Origine, évolution et exhumation des leucogranites peralumineux de la chaîne hercynienne armoricaine : implication sur la métallogénie de l'uranium

Christophe Ballouard

ANNÉE 2016

THÈSE / UNIVERSITÉ DE RENNES 1
sous le sceau de l'Université Bretagne Loire

pour le grade de

DOCTEUR DE L'UNIVERSITÉ DE RENNES 1

Mention : Sciences de la Terre

Ecole doctorale Sciences de la Matière

présentée par

Christophe Ballouard

Préparée à l'unité de recherche Géosciences Rennes
OSUR (Observatoire des sciences de l'Univers) – UMR 6118
UFR Sciences et Propriétés de la Matière

Origine, évolution et exhumation des leucogranites peralumineux de la chaîne hercynienne armoricaine : implication sur la métallogénie de l'uranium

Thèse soutenue à Rennes
le 2 décembre 2016

devant le jury composé de :

Laurence Robb
Professeur, University of Oxford / *rapporteur*

Jean-Louis Paquette
Directeur de recherche, Université Blaise Pascal – Clermont-Ferrand II / *rapporteur*

Robin Shail
Senior lecturer, University of Exeter / *examinateur*

Antonin Richard
Maître de Conférences, Université de Lorraine/ *examinateur*

Denis Gapais
Directeur de recherche, Université de Rennes 1 / *examinateur*

Marc Poujol
Maître de Conférences, Université de Rennes 1 / *directeur de thèse*

Marc Jolivet
Directeur de recherche, Université de Rennes 1 / *co-directeur de thèse*

Remerciements

Mes remerciements vont tout d'abord à mes deux encadrants Marc et Marc ainsi qu'à Philippe. Marc P. je te remercie de m'avoir fait confiance depuis mon master 1 en m'envoyant faire ce fantastique stage dans les contrés éloignées de l'Abitibi. Ensuite, tu m'as initié (avec Philippe) à l'étude des granites bretons, la géochronologie et la métallogénie de l'uranium en me proposant ce stage de master 2 sur le granite de Guérande. Cela m'a beaucoup plu, la preuve en est que j'ai remballé pour 3 ans supplémentaires ! Durant ces années, j'ai beaucoup aimé travailler avec toi. Tu m'as toujours soutenu et tu m'as laissé la liberté de penser et d'action dont j'avais besoin pour m'épanouir dans ce domaine qu'est la recherche. J'ai aussi beaucoup apprécié les « repas » aux tournebrides ! Merci Marc J. de m'avoir initié à l'art des traces de fission. Tu vois malgré toutes les lames de standards Durango que j'ai cassé et que tu as du réparé au vernis j'ai fini par l'avoir mon Zeta ! J'ai aussi beaucoup aimé travailler avec toi. Philippe, tu as été mon co-encadrant de master 2 et tu es l'encadrant officieux de cette thèse. Tu m'as toujours encouragé (en particulier sur mon travail du « dimanche »), et j'ai beaucoup apprécié les discussions scientifiques (et autres !) qu'on a eu ensemble. Un très grand merci à tous les trois !

Je remercie tous les membres de mon jury pour avoir accepté d'évaluer cette thèse ainsi que pour les discussions scientifiques qui ont suivi ma soutenance. Un grand merci à mes deux rapporteurs qui ont relu le manuscrit en détail. Laurence, j'ai bien rajouté un petit paragraphe sur le Nb/Ta dans le résumé, mais désolé je suis limité à une page ! Jean-Louis, vous verrez que j'ai bien remis les ellipses à 2σ dans mes diagrammes concordia ! Robin et Antonin, j'espère que vous avez apprécié la sortie à Piriac sur Mer ! Moi, j'ai eu du mal à me lever… Merci président Gapais pour les discussions sur la tectonique hercynienne !

Merci à toutes les personnes avec qui j'ai travaillé et discuté « sciences » durant cette thèse. Merci Julien pour ton enthousiasme dans l'étude des gisements d'uranium bretons et pour m'avoir accueilli à Nancy ! Jean-Louis, merci de m'avoir accompagné sur le chemin du fractionnement du Nb-Ta ! Merci beaucoup aux deux Michels pour vos conseils et le prêt d'échantillons ! Yannick, merci pour tes encouragements et les discussions qu'on a eu ensemble ! Armin, merci pour l'accueil à Frankfurt et l'initiation à l'Hf ! Torsten, merci, j'ai beaucoup apprécié les analyses en isotopes de l'oxygène avec toi à Lausanne ! Romain, merci pour tes encouragements et tes conseils, promis maintenant j'arrête de t'envoyer mes posters ! Etienne, merci pour l'initiation à la sonde ionique ! Marie-Pierre, merci, heureusement que tu étais là pour l'échantillonnage à Crozon ! Pipo, merci pour les discussions qu'on a eu ensemble ! David, un grand merci pour ta bonne humeur et les analyses en Sr et Nd ! Dominique, je ne sais pas comment j'aurai fini mon Powerpoint sans tes paquets de chips ! Merci à Yann et Xavier pour le broyage d'échantillons et la réalisation de lames minces sans quoi cette thèse n'aurait jamais pu aboutir. Marie-Anne, merci pour ton aide dans toutes les tâches administratives ! Merci à Jessica à l'Ifremer et tout le personnel du CMEBA à Rennes et du SCMEM à Nancy pour l'aide durant les analyses au MEB et à la microsonde électronique. Merci à Cédric D. pour tous les coups de main à Nancy. Merci à Areva pour

le prêt d'échantillons. Enfin, je tiens à remercier l'ensemble du personnel de Géosciences Rennes pour ces 4 années inoubliables !

Bien évidemment je tiens à remercier ma famille qui m'a toujours soutenu même à l'époque où j'essayais (en vain) de déterrer des fossiles de dinosaures dans le remblai derrière la maison de Saint-Lô. Papa, Maman vous avez toujours été là pour moi, MERCI. Sophie, t'es une sœur fantastique et toi aussi tu as toujours été là. Merci aux petits dragons (Juliette et Alexis) et à Rico ! Felix, tu fais aussi partie de ma famille et toi et tes parents je vous remercie. Merci à mes papis, mes mamies, Christine, Marie-Paule et Jacques, tous mes tontons, tatas et cousins – cousines.

Bien sûr un énorme merci à tous les copains de Rennes et d'ailleurs !!! Tout d'abord, merci à mes deux fantastiques colocataires du bureau 115/1 : Benoît, il faut qu'on se l'avoue une bonne fois pour toute : on a partagé une chambre d'ado pendant deux ans pas un bureau ! Gemmouuu !!! on s'est bien marré pendant toutes ces années et je n'aurai pas pu espérer une meilleure colocataire pour cette fin de thèse ! Thomas que dire…. Et bien pour résumé : sodium, russe blanc, Hellfest, bière, fléchettes, bière, 206, guitares, hamburgers au micro-onde, Gojira, kinder delices, O'Connels ! Bob, je ne peux plus aller dans le Finistère ou regarder un navet au cinéma sans penser à toi ! Antoni, on se refait un karaoké sur Bohemian Rhapsody au Yumi bar quand tu veux ! Cholenn, je suis sûr que tu lis ces remerciements juste pour ça : merci d'avoir corrigé mon résumé !! Marylou, on se revoit à Johannesburg ! Merci à JP, Caro, Matthieu (alias Barthi), Guillaume, Justine, Antoine (alias La Deul), Marie, Youssef, Benjamin, Paul, Dani, Roman, Camille, Sylvia, Loïc, Massi, Charlotte, Marion, Inoussa, Maxime, Frank, Antoine, Tristan, Olivier, Louise, Charline, Regis, Vicky, Luc… les potes de Nancy : Matthieu (Baloo), Kévin, Cédric, Florence, Matthieu (Harlaux), François, Glin… bref tous les doctorants et autres étudiants « géologues » que j'ai côtoyé durant ces années !! Merci à tous les copains « non géologues »: Virginie, Morgane, Johan, Beber, Antoine, Vince, … (Désolé je n'ai pas mis tout le monde !) Merci aussi à Mario et Matthieu, les deux amis d'enfance de la cité de l'automne !

Résumé

Les granites peralumineux sont les acteurs principaux de la différentiation de la croûte continentale et représentent un enjeu sociétal important car ils sont associés à de nombreux gisements métallifères. Dans la chaîne hercynienne européenne, la majorité des gisements hydrothermaux d'uranium (filons ou épisyenites) sont associés à des leucogranites peralumineux d'âge tardi-carbonifère. Ainsi dans le Massif armoricain, 20000 t d'uranium (U) (~20% de la production française), ont été extraites des gisements associés aux leucogranites de Mortagne, Pontivy et Guérande. L'objectif de ce travail est de mieux comprendre le cycle de l'U dans la chaîne hercynienne armoricaine depuis la source des leucogranites, leur évolution et leur mise en place dans la croûte supérieure jusqu'à leur lessivage par des fluides, la formation des gisements puis leur exhumation en sub-surface. Dans ce but, des données pétro-géochimiques, géochronologiques et thermochronologiques ont été obtenues sur les leucogranites de Guérande, Pontivy et leurs gisements d'U associés.

Les leucogranites de Guérande et de Pontivy se sont mis en place, respectivement, à ca. 310 Ma dans une zone de déformation extensive dans le domaine interne de la chaîne et ca. 315 Ma dans le domaine externe le long du cisaillement sud armoricain, une faille décrochante d'échelle lithosphérique. Les deux leucogranites sont issus d'un faible taux de fusion partielle de métasédiments détritiques et d'orthogneiss peralumineux, la fusion de ces derniers ayant vraisemblablement joué un rôle majeur dans la richesse en U des leucogranites. La fusion de la croûte continentale dans la zone interne de la chaîne a été induite par l'extension tardi-orogénique alors que la fusion de la croûte mais aussi du manteau dans la zone externe était probablement contrôlée par une déformation décrochante diffuse. La cristallisation d'oxydes d'uranium magmatiques dans les facies les plus évolués des leucogranites a été vraisemblablement rendue possible grâce à l'action combinée de la cristallisation fractionnée et d'une activité magmatique-hydrothermale diffuse. De ca. 300 Ma à 270 Ma, une activité tectonique fragile le long du CSA et des détachements a permis l'infiltration de fluides météoriques oxydants en profondeur induisant la mise en solution des oxydes d'uranium des leucogranites. Ensuite, les fluides ont précipité leur U dans des failles ou des fentes de tension à proximité du contact avec des lithologies sédimentaires avec un caractère réducteur variable. Les leucogranites étaient toujours en profondeur à des températures supérieures à 120°C au moment de la formation des gisements et leur exhumation en sub-surface n'est pas enregistrée avant le Trias ou le Jurassique. Ce modèle métallogénique n'est probablement pas exclusif au Massif armoricain car la période de formation des gisements d'U dans la région entre 300 et 270 Ma est la même que dans l'ensemble de la chaîne hercynienne européenne.

A une échelle plus globale, le fractionnement d'éléments géochimiques « jumeaux » comme le niobium (Nb) et le tantale (Ta) dans les leucogranites peralumineux est principalement lié à l'action combinée de la cristallisation fractionnée et d'une altération magmatique-hydrothermale. La valeur Nb/Ta ~ 5 apparait comme un bon outil d'exploration pour différencier les granites spatialement associés à des gisements de métaux comme l'étain, le tungstène, l'uranium ou les métaux rares.

Abstract

Peraluminous leucogranites are the principal actors for the differentiation of the continental crust and play an important economic role because they are commonly associated with significant metalliferous deposits. Most hydrothermal uranium (U) deposits (vein or episyenite types) from the European Hercynian belt are spatially associated with Carboniferous peraluminous leucogranites and in the French Armorican Massif (western part of the European Hercynian belt) 20000 t of U (~20 % of the French production) were extracted from the deposits associated with the Mortagne, Pontivy and Guérande leucogranites. The objective of this work is to improve our knowledge about the U cycle in the Armorican Hercynian Belt from the leucogranites sources, their evolution and emplacement in the upper crust to U leaching, deposit formation and leucogranites exhumation at the subsurface level. For that purpose, petro-geochemical, geochronological and thermochronological data were obtained on the Guérande and Pontivy leucogranites as well as their spatially associated U deposits.

The Guérande leucogranite was emplaced ca. 310 Ma ago in an extensional deformation zone in the internal domain of the belt whereas the Pontivy leucogranite was emplaced ca. 315 Ma ago in the external domain along the South Armorican Shear Zone (SASZ), a lithospheric scale wrench fault. Both leucogranites were formed by a low degree of partial melting of detrital metasediments and peraluminous orthogneisses; the fusion of the latter probably played a major role in the generation of U rich leucogranites. Partial melting of the crust in the internal zone of the belt was triggered by late orogenic extension whereas partial melting of the crust but also the mantle in the external zone was likely controlled by pervasive wrenching. The crystallization of magmatic uranium oxides in the most evolved leucogranitic facies was induced by fractional crystallization and probably enhanced by magmatic-hydrothermal processes. From ca. 300 to 270 Ma, a fragile tectonic activity along detachments and the SASZ, allowed for the infiltration at depth of meteoric oxidizing fluids, able to dissolve magmatic uranium oxides in the leucogranites. These fluids have then precipitated their U in faults or tension gashes close to the contact with sediments having a variable reducing character. The leucogranites were at depth above 120°c during the formation of U deposits and the exhumation of these intrusions did not occur before the Trias or the Jurassic. The proposed metallogenic model is likely not exclusive to the Armorican Massif as the timing of U deposits formation in the region from ca. 300 to 270 Ma is similar to the main U mineralizing event in the whole European Hercynian belt.

On a larger scale, the fractionation of “twin” elements such as niobium (Nb) and tantalum (Ta) in peraluminous leucogranites is mostly the result of both fractional crystallization and magmatic-hydrothermal alteration. From an exploration point of view, the value Nb/Ta ~5 appears to be a good geochemical indicator to differentiate barren peraluminous granites from granites spatially associated with tin, tungsten, uranium or rare metal deposits.

Table des matières

Introduction générale

Les magmas granitiques sont les acteurs principaux de la différentiation et de la formation de la croûte continentale et les granitoïdes représentent plus de 50% de sa composition (e.g. Hans Wedepohl, 1995). A partir de la fin de l'Archéen, la nature des roches granitiques a évolué en passant globalement de compositions de tonalites-trondhjémites-granodiorites (TTG) à celles de granodiorites et granites, en réponse au refroidissement progressif de la Terre (e.g. Taylor and McLennan, 1985; Martin, 1994). La diversité des roches granitiques sur Terre reflète la variabilité de leur source, de leurs processus d'évolution et de leur environnement géodynamique de mise en place. Les granitoïdes peralacalins se forment généralement par fusion du manteau en contexte de rifting continental, les granitoïdes paralumineux proviennent principalement de la fusion partielle de la croûte continentale en contexte de collision et les roches granitiques métalumineuses calco-alcalines ont pour, une grande partie, une origine hybride et sont caractéristiques des environnements de subduction (e.g. Barbarin, 1999). Les roches granitiques présentent un fort enjeu sociétal car elles sont associées à de nombreux gisements de métaux dont la nature varie en même temps que la source, l'évolution, le niveau structural et le contexte tectonique de mise en place des magmas. Les granites hyperalcalins et leurs pegmatites sont communément associés à des gisements de métaux rares comme le niobium (Nb), le tantale (Ta), les terres rares (ETR), le zirconium (Zr), l'uranium (U) et le thorium (Th) (e.g. Jébrak and Marcoux, 2008). Les gisements porphyriques à cuivre (Cu) et molybdène (Mo) et les gisements épithermaux à or (Au), argent (Ag) et Cu sont typiques des environnements géodynamiques de subduction où se mettent en place des granitoïdes calco-alcalins (e.g. Robb, 2005). Enfin, les granitoïdes peralumineux sont communément associés à des gisements d'étain (Sn), tungstène (W) et d'U, voir même de métaux rares comme le lithium (Li), césium (Cs) et tantale (Ta) pour leurs termes les plus évolués (e.g. Robb, 2005). Tous ces gisements sont rarement purement magmatiques et ils mettent aussi en jeu des processus hydrothermaux.

Les gisements d'U ont des origines extrêmement variées et peuvent se former à toutes les étapes du cycle géologique depuis des conditions métamorphiques, plutoniques et volcaniques jusqu'à des environnements de surfaces, sédimentaires ou diagénétiques (Cuney, 2009) (Fig. 1). Les ressources mondiales (raisonnablement assurées + déduites) en U sont estimées à 5.9 millions de tonnes en 2014 (world nuclear association : www.world-nuclear.org) et 2 à 5% de cette U (entre 130000 et 300000 t) est présent dans des gisements associés à des granites selon la base de données UDEPO (www.infcis.iaea.org). Une grande partie de ces gisements sont des minéralisations hydrothermales filoniennes ou d'imprégnation (type épisyenite) qui sont, comme dans le cas de la chaine hercynienne européenne, spatialement associées à des leucogranites peralumineux à deux micas (e.g. Cuney et al., 1990). Le modèle de genèse le plus admis pour la genèse de ces gisements est que l'uranium provient du lessivage des oxydes d'uranium des leucogranites environnent par des fluides hydrothermaux oxydants dérivés de la surface (e.g. Friedrich et al., 1987 ; Cuney et Kyser, 2008 ; Cuney, 2014). Néanmoins, il existe peu d'études récentes sur les leucogranites uranifères de la chaîne hercynienne

européenne et leurs gisements associés (e.g. André et al., 1999 ; Cathelineau, 1981, 1982 ; Dubessy et al., 1987 ; Friedrich et al., 1987 ; Cathelineau et al., 1990 ; Cuney et al., 1990 ; Dill, 1983 ; Hofmann and Eikenberg, 1991 ; Peiffert et al., 1994, 1996 ; Pérez del Villar and Moro, 1991 ; Scaillet et al., 1996 ; Tartèse et al., 2013 ; Turpin et al., 1990a, 1990b ; Velichkin et al., 2011 ; Vigneresse et al., 1989). Ainsi, les processus qui contrôlent la fertilité des leucogranites mais aussi le timing et les conditions du lessivage de l'U, son transport par les fluides et sa précipitation dans les pièges restent mal compris.

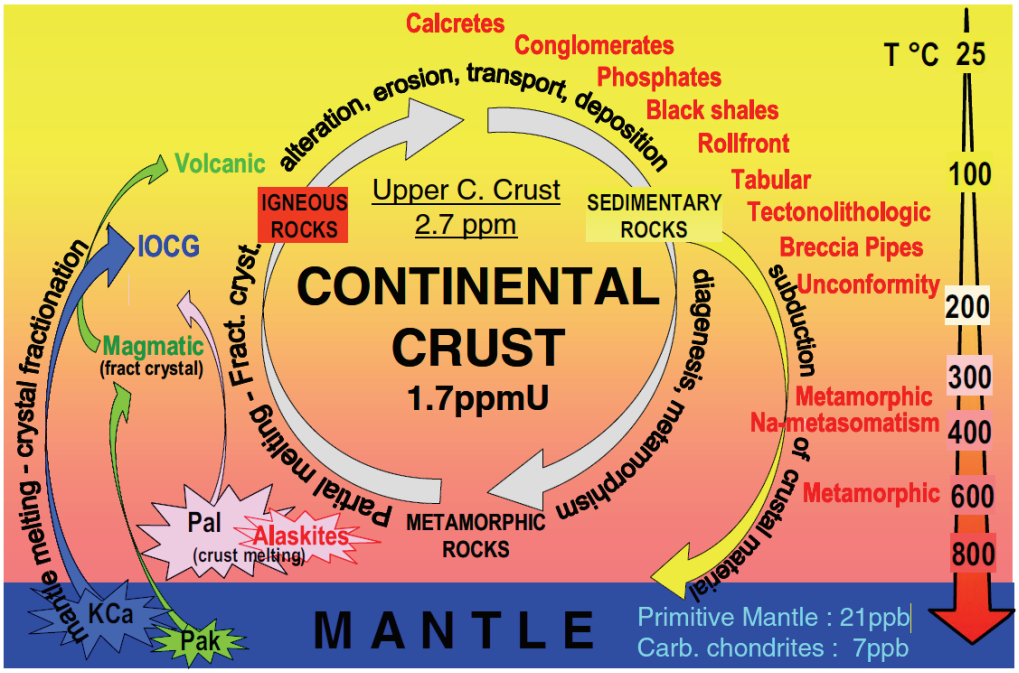

Figure 1 : position des gisements d'uranium par rapport aux principaux processus de fractionnement du cycle géologique. Les principaux types de magmas riches en U sont indiqués. Pak : peralcalin, KCa calc-alcalin potassique, Pal : peralumineux. D'après Cuney (2009).

Dans le Massif armoricain, situé à l'ouest de la chaîne hercynienne européenne, environ 20000 t d'U (~20 % de la production historique française) ont été extraites des gisements hydrothermaux associés aux leucogranites peralumineux tardi-carbonifères de Mortagne, Pontivy et Guérande. Le leucogranite voisin de Questembert n'est pas directement associé à des minéralisations mais l'étude de Tartèse et al. (2013) a montré que ce granite a libéré plus d'une centaine de millier de tonnes d'U lors d'une phase d'altération hydrothermale en profondeur. A ce jour, et cela malgré une compréhension limitée de la métallogénie de l'U au sein de la chaîne hercynienne, il n'existe pas d'études modernes sur les granites minéralisés de la chaîne hercynienne armoricaine. L'objectif de cette thèse est de mieux comprendre et de contraindre dans le temps le cycle de l'uranium dans la région, depuis la source des leucogranites, leur évolution et leur mise en place dans la croûte supérieure jusqu'à leur lessivage par des fluides, la formation des gisements et leur exhumation. Pour cela, nous nous sommes focalisés sur les leucogranites fertiles de Guérande et de Pontivy. En effet, ces deux leucogranites mis en place, respectivement, en contexte tectonique d'extension crustale et décrochant sont associés à un style de

minéralisation uranifère différent (majoritairement périgranitique dans le district de Guérande et intragranitique dans le district de Pontivy) et peuvent être considérés comme représentatifs de la région.

Le manuscrit s'organise en cinq parties qui mêlent des articles scientifiques, publiés ou en préparation, en anglais avec des chapitres ou des développements en français. Les articles scientifiques sont précédés d'un bref résumé en français.

La **Partie I** s'articule sur le thème du magmatisme peralumineux, des gisements uranifères et du Massif armoricain. Elle a pour objectif de présenter des généralités sur les granites peralumineux et leurs associations métallifères et sur les processus qui contrôlent la fertilité d'une roche ignée pour former des gisements d'uranium hydrothermaux. Un aperçu de l'évolution du Massif armoricain au cours de l'orogenèse hercynienne est aussi retranscrit et a pour but d'illustrer le cadre général de mise en place des granites peralumineux et des gisements d'uranium.

La **Partie II** est axée sur la transition magmatique-hydrothermale dans les granites peralumineux et les travaux qui y sont présentés, ayant fait l'objet d'une publication dans le journal Geology, se basent sur une compilation d'analyses géochimiques roches totales issues de la littérature. Cette étude vise à comprendre les fractionnements élémentaires qui se produisent au cours de la transition magmatique-hydrothermale en se basant plus particulièrement sur l'évolution du Nb et du Ta, deux éléments « jumeaux » dont le comportement dans les magmas et les fluides hydrothermaux fait débat depuis le début des années 90. Les résultats de ce travail suggèrent que la diminution du rapport Nb/Ta dans les granites peralumineux est la conséquence de la cristallisation fractionnée et d'une altération sub-solidus. De plus, la valeur Nb/Ta ~5 est proposée comme outil d'exploration pour discriminer les granites stériles des granites associés à des gisements d'Sn, W, U et métaux rares. Cette publication, qui a fait l'objet d'un commentaire par Stepanov et al. (2016 ; fourni en annexe), est suivie d'une réponse elle aussi publiée dans Geology. Enfin, cette partie se termine avec une discussion complémentaire sur les évidences minéralogiques de fractionnements hydrothermales en Nb-Ta ainsi que sur les implications par rapport à la pétrogenèse des CPG (granite peralumineux à cordiérite) et des MPG (leucogranite peralumineux à muscovite) (Barbarin, 1996, 1999) et sur le comportement de l'U à la transition magmatique-hydrothermale.

La **Partie III** porte sur le magmatisme tardi-carbonifère de la chaîne hercynienne armoricaine et sur les relations géodynamiques. Les travaux présentés se basent sur l'étude pétro-géochimique et géochronologique du leucogranite de Guérande et du complexe magmatique de Pontivy-Rostrenen, deux intrusions caractéristiques de la région, que ce soit du point de vue du contexte structurale de mise en place ou de la nature des roches ignées qui les constituent. Nos interprétations sont principalement basées sur des observations et des mesures de terrain combinées à de la pétrographie, des analyses en éléments majeurs et traces sur roches totales, des analyses en éléments majeurs sur minéraux, des analyses en isotopes radiogéniques sur roches totales (Nd et Sr) et zircon (Hf) ainsi que sur de la

géochronologie U-Pb sur zircon et monazite. Les études des deux massifs visent à comprendre l'origine et l'évolution des magmas qui ont formé ces intrusions et contraindre l'évolution spatiale et temporelle du magmatisme dans la région. En plus de poser un cadre général pour travailler sur les processus minéralisateurs en U dans le Massif armoricain (Partie IV), ces travaux apportent des informations clés sur la géodynamique hercynienne et sur les modalités du recyclage et de la formation de la croûte continentale dans les orogènes de collision. Les travaux sur l'histoire magmatique, hydrothermale et tectonique du leucogranite de Guérande ont fait l'objet d'une publication dans la revue Lithos et l'étude sur le complexe de Pontivy-Rostrenen est rédigée sous la forme d'un article soumis à Gondwana Research. Une sous-partie complémentaire est consacrée à la datation U-Pb sur zircon du granite à cordiérite de Huelgoat.

La **partie IV** est consacrée à la compréhension du cycle de l'U dans le Massif armoricain depuis la source des leucogranites minéralisés en U jusqu'à leur lessivage par des fluides et la formation des gisements. Il est divisé en deux chapitres. Le ***Chapitre 1*** est consacré à la métallogénie de l'uranium dans les districts de Guérande et de Pontivy-Rostrenen. L'étude des leucogranites et de leurs gisements associés est basée sur plusieurs méthodes comme la géochimie en éléments majeurs et traces sur roches totales et minéraux, l'isotopie de l'oxygène, la datation U-Pb de l'apatite des granitoïdes et des oxydes d'uranium issus des gisements, les analyses d'inclusions fluides, la themochronologie par traces de fission sur apatite et la radiométrie spectrale aéroportée ou in situ. L'accès aux mines d'U est impossible depuis leur fermeture au début des années 90 mais nous avons eu la chance d'avoir accès à des échantillons historiques d'oxydes d'uranium, d'episyenites et de peignes de quartz issus des collections privées du CREGU à Nancy (centre de recherche sur la géologie de l'uranium) et d'AREVA à Bessines. Les travaux sur le leucogranite de Guérande et ses gisements associés ont fait l'objet d'une publication dans le journal Ore Geology Reviews alors que pour le district de Pontivy-Rostrenen, les travaux réalisés sont présentés sous la forme d'un article en préparation pour la revue Mineralium Deposita. Le ***chapitre 2*** porte sur la caractérisation de la ou les source(s) des leucogranites uranifères du Massif armoricain. Cette étude se base sur la comparaison de la signature isotopique (U-Pb et Hf) des cristaux de zircon hérités des leucogranites fertiles avec celle des grains de zircon détritiques ou néoformés issus des sources potentielles métasédimentaires et métaignées de la région. Les interprétations sont appuyées par des données sur roches totales en isotopes radiogéniques (Sr et Nd) et en éléments traces sur les leucogranites fertiles et leurs sources potentielles.

La **partie V** porte sur une discussion préliminaire des résultats des analyses en traces de fission sur apatite obtenus durant cette thèse sur les granites tardi-carbonifères du Massif armoricain et leur implication sur l'évolution post hercynienne de la région.

Partie I : granites peralumineux, uranium et Massif armoricain

Chapitre 1 : Le magmatisme peralumineux et ses spécificités métallogéniques

Les magmas à l'origine des roches plutoniques et volcaniques sont l'expression de la fusion du manteau et de la croûte terrestre. Ils sont donc les acteurs principaux de la formation et du recyclage de la croûte continentale sur laquelle nous vivons. De même, les roches magmatiques sont la source directe ou indirecte de nombreux métaux et représentent un fort enjeux sociétal. Dans ce chapitre, nous allons définir les caractéristiques pétrographiques et pétrologiques des roches magmatiques qui font l'objet de cette thèse : les granitoïdes peralumineux. Puis nous discuterons de leur genèse, de leur évolution et des processus magmatique-hydrothermaux qui vont mener à la formation de gisements métallifères.

1.1. Définition et caractéristiques générales

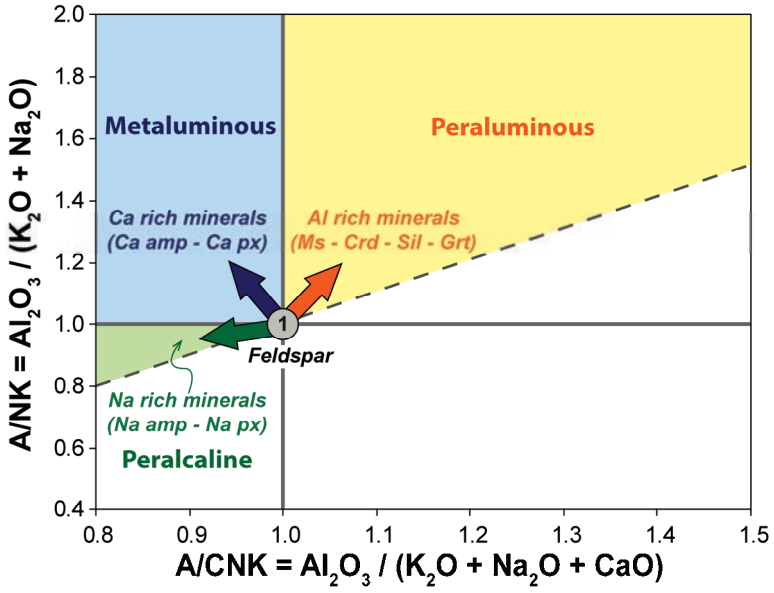

Figure I.1 : Diagramme de Shand (1943). Ms : muscovite ; Crd : cordiérite ; Grt : grenat ; Ca amp : amphibole calcique ; Ca px : clinopyroxène ; Na amp : amphibole sodique ; Na px : pyroxène sodique. Les rapports sont calculés en proportions molaires.

Les roches volcaniques ou granitoïdes peralumineux sont des roches magmatiques issues principalement de la fusion de la croûte continentale et participent donc au recyclage de celle-ci. Ces roches se caractérisent géochimiquement par un excès d'aluminium (Al) par rapport aux calcium (Ca) et aux alcalins [sodium (Na) et potassium (K)] et donc possèdent un rapport A/CNK > 1 [Al_2O_3 / (CaO + Na_2O + K_2O) : proportion molaire] (Fig. I.1). Cette peraluminosité se traduit minéralogiquement par la présence de minéraux riches en aluminium comme la muscovite ou la cordiérite car tout l'Al présent dans le magma ne peut pas être incorporé dans les feldspaths. Au contraire, les magmas métalumineux et peralcalins sont sous saturés en Al et se caractérisent, respectivement, par un excès de Ca et de Na. Les roches peralcalines qui sont principalement d'origine mantelliques vont donc présenter des minéraux secondaires particuliers riches en Na comme l'Aegyrine. Quant aux magmas métalumineux qui ont une origine hybride, ils vont contenir des minéraux secondaires riches en Ca comme l'amphibole

calcique et le clinopyroxène. Communément, les magmas peralumineux sont considérés comme réduits ce qui se traduit par la cristallisation d'ilménite et l'absence de magnétite alors que les magmas métalumineux et surtout alcalins sont considérés comme oxydants ce qui se traduit par la cristallisation de magnétite.

Bien qu'il existe plusieurs classifications des granitoïdes peralumineux, Barbarin (1999) en définie deux grands types avec les granites peralumineux à muscovite (MPG) et les granitoïdes peralumineux à cordiérite (CPG) (Table I.1). Les magmas métalumineux peuvent devenir légèrement peralumineux via des processus de différentiations ou d'assimilation mais ces cas restent relativement minoritaires et ne seront pas discutés ici. La muscovite peut être un minéral accessoire dans de nombreux granitoïdes mais n'est abondante que dans les MPG. Ces leucogranites à muscovite (± biotite) vont communément contenir de la tourmaline et du grenat mais les enclaves de xénolithes ou restites et de roches mafiques sont rares. La cordiérite, fréquemment associée à la sillimanite (± andalousite), au grenat et à de rare grains de muscovite primaire, caractérise les CPG. Ces roches de composition granitique à granodioritique sont souvent associées à des intrusions d'origine mantellique et contiennent communément des enclaves de xénolithes ou restites et de roches microgrenues mafiques. Les CDG incluent les granites de type S (sédimentaires) définies par Chappell et White (1974, 1992) dans le Lachlan Fold Belt (Australie). Les équivalents volcaniques des CPG et surtout des MPG sont rares. Nous discuterons plus loin pourquoi.

	Bt	**Ms**	**Crd**	**Sil-And**	**Amp**	**Px**	**Ap**	**Zrn**
MPG	x	xxx	o	o	o	o	xxx	x
CPG	xxx	x	xx	x	o	o	xxx	xx
	Mnz	**Grt**	**Turm**	**Aln**	**Ttn**	**Ilm**	**Mnt**	**Pl - An%**
MPG	x	xx	xxx	o	o	x	o	0 - 20
CPG	x	x	xx	o	o	x	o	15 - 40
	Petrographic type			**A/CNK**	**I_{sr}**	**εNd(t)**	**$\delta^{18}O$ (‰)**	**$\delta^{34}S$ (‰)**
MPG	Leucogranites - (granites)			>1	> 0.705	< 0	+ 10 to + 14	- 12 to + 2
CPG	(Leucogranites) - granites - granodiorites - Qtz diorites							
	Enclaves						**Associated mafic rocks**	
	Restite or xenoliths	*Felsic M.E.*	*Mafic M.E.*					
MPG	x	x	o				o	
CPG	xxx	o-x	x				x	

Table I.1 : Caractéristique pétrographiques et géochimiques générales des granites peralumineux à muscovite (MPG) et des granites peralumineux à cordiérites (CPG) selon Barbarin (1999). o = absent ; x = rare ; xx = commun ; xxx = abondant. Abréviation minéralogiques selon Kretz (1983). I_{Sr} représente le rapport ^{87}Sr / ^{86}Sr initial. M.E. : Enclaves microgrenues

1.2. Origines

Les CPG et les MPG sont communément interprétés comme résultant de la fusion partielle de métasédiments alumineux (pélites et graywackes principalement) mais ils peuvent aussi provenir de la fusion d'orthogneiss (e.g. Turpin et al., 1990). La fusion partielle de la croûte est mis en évidence par

les migmatites et l'extraction des magmas peralumineux depuis les zones partiellement fondues est probablement dépendante du régime de déformation (e.g. Sawyer, 1998; Brown, 2001; Vanderhaeghe, 2009).

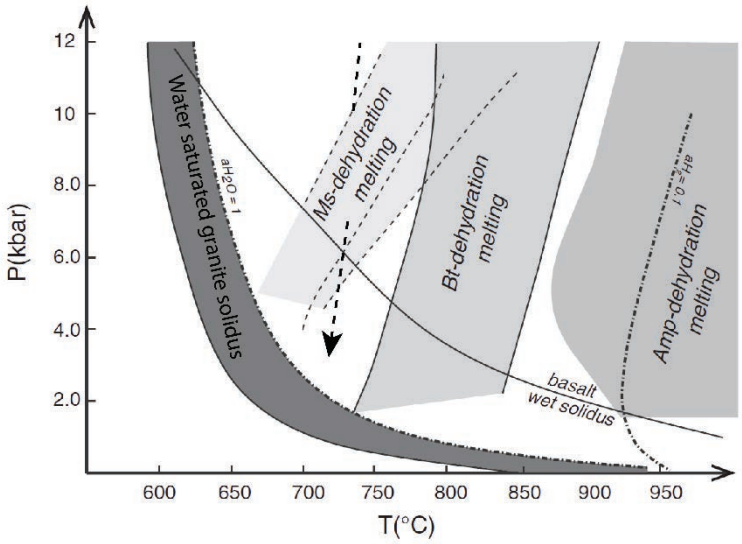

Figure I.2 : Diagramme de phase simplifié des principales réactions de fusion partielles d'après Weinberg and Hasalová (2015) et références y contenues. La flèche en tirés noirs représente un exemple de décompression adiabatique en contexte d'extension tardi-orogénique.

Les conditions de formations des magmas peralumineux dépendent de la nature de leur source et des conditions de fusion partielles (pression, température et activité en eau). L'eau a un rôle essentiel dans la fusion et on identifie deux types principaux de réaction de fusion qui sont les réactions hydratées et anhydres (Fig. I.2). Dans le cas de la fusion hydratée s.s., l'eau est en excès dans le métasédiment et un liquide silicaté saturé en eau va être formé lors de la réaction de fusion. La fusion hydratée peut se produire à des températures relativement faibles d'environ 650 °C (pour une activité en eau $aH_2O = 1$) mais cela implique un apport continue de fluides aqueux. La fusion anhydre implique, quant à elle, la déstabilisation des micas blancs ou de la biotite. Ces réactions se produisent à plus haute température et près de 60 % de la roche d'origine peut fondre lors la déstabilisation de la biotite à partir de 750 °C (Vielzeuf et Montel, 1994). La déstabilisation des phases hydratées lors des réactions de fusion incongruentes (anhydres ou hydratées) va s'accompagner de la formation de minéraux péritectiques comme la sillimanite lors de la déshydratation de la muscovite ou le grenat et l'orthopyroxène lors de la déshydratation de la biotite (e.g. Vielzeuf et Montel, 1994 ; Weinberg et Hasalová, 2015). Certains auteurs défendent que la majorité des granites se forment par des réactions de fusion anhydres (Clemens et Watkins, 2001; Clemens et Stevens, 2015, Patiño-Douce, 1999). Ainsi, les granites type S, comparables aux CPG, se formeraient majoritairement par des taux de fusion partielle élevés (~ 50 %) via la réaction de déshydratation de la biotite (Vielzeuf et Holloway, 1988; Vielzeuf et Montel, 1994 ; Clemens et Watkins, 2001; Clemens et Stevens, 2015). En parallèle, Patiño-Douce et Harris (1998) et Patiño-Douce (1999) suggèrent que les MPG sont, pour la plus part, issues de la déshydratation de sédiments riches en muscovite avec probablement des faibles taux de fusions partielles (< 30 %). Néanmoins, il est aussi évident que l'eau, en excès ou non, va pouvoir jouer un rôle dans les processus de fusion crustale et cela plus particulièrement dans les zones de déformation qui vont pouvoir localiser

les circulations de fluides (Le Fort et al., 1987; Johnson et al., 2001; Sawyer, 2010; Weinberg and Hasalová, 2015a, 2015b).

Les CPG et les MPG sont typiques des zones de collision continentales. Néanmoins, les MPG sont généralement associés à des grandes zones de cisaillements alors que les CPG sont plus dispersés, contiennent fréquemment des enclaves mafiques et sont souvent associées à des roches mantelliques (Table 1). Cela mène Barbarin (1996, 1999) a proposé que les CPG, se forment via une fusion crustale anhydre induite par le sous plaquage de magmas mantéliques alors que pour les MPG, la fusion serait favorisée par des circulations de fluides le long de zones de cisaillement d'échelle crustale. En effet, La richesse en muscovite des leucogranites témoignent de leur plus forte teneur en eaux (~7 – 8%) comparée aux CPG (< 4 %) (Barbarin, 1996 et références y contenues). Parallèlement, Patiño-Douce (1999) suggère que la décompression adiabatique en contexte d'extension tardi-orogénique va favorisée la fusion par déshydratation de la muscovite par rapport à la fusion par déstabilisation de la biotite et ainsi faciliter la formation de MPG (Fig. I.2). La forte teneur en eaux des MPG comparée aux CPG ainsi que leur plus faible température de fusion favorise l'intersection de leur solidus avant qu'ils atteignent la surface. Cela explique la rareté des roches volcaniques équivalentes aux MPG.

1.3. Processus d'évolution

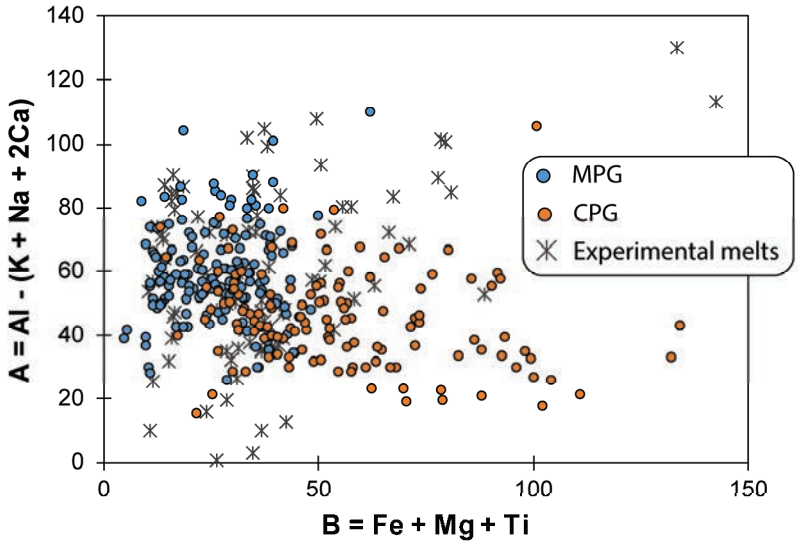

Figure I.3 : Diagramme A-B (d'après Debon et Le Fort, 1988) qui compare la composition de CPG et de MPG de la chaîne hercynienne d'Europe de l'ouest avec celle des liquides produits lors de la fusion expérimentale de sédiments (Patiño-Douce et Harris, 1998; Patiño-Douce et Johnston, 1991; Montel et Vielzeuf, 1997; Spicer et al., 2004; Vielzeuf et Holloway, 1988). La composition des CPG est issue de cette étude, Bea et al. (1994), Bechennec (2006, 2009), Euzen (1993), Ramirez et Grundvig (2000), Solgadi et al. (2007) et Tartèse et Boulvais (2010). La composition des CPG est issue de Cotten (1975), Georget (1986), Euzen (1993), Fernández-Suárez et al. (2011) , Rolin (2006), Solgadi (2007), Tabaud et al. (2015). Les paramètres A et B qui représentent, respectivement, la peralumonosité et la proportion de biotite des échantillons sont exprimés en proportion molaire multiplié par mille (millication).

De nombreuses études expérimentales ont permis de caractériser la chimie en éléments majeurs des liquides silicatés produit lors de la fusion partielle de sédiments (e.g. Patiño-Douce et Harris, 1998; Patiño-Douce et Johnston, 1991; Montel et Vielzeuf, 1997; Spicer et al., 2004; Vielzeuf et Holloway,

1988) et les liquides produits ont quasiment toujours une composition leucogranitique (Fig. I.3). Cela suggère que les MPG représentent majoritairement des purs jus anatectiques. Au contraire, beaucoup de CPG ont un degré de maficité (Paramètre B sur la Fig. I.3) qui diffère des liquides produits lors de la fusion expérimentale de sédiments ce qui implique l'interventions d'autre processus chimiques.

Les variations géochimiques en éléments majeurs et traces observer dans les granitoïdes peralumineux peuvent refléter différents processus comme (1) le mélange avec des magmas mafiques d'origine mantélique (e.g. Castro et al., 1999; Patiño-Douce, 1999), (2) l'assimilation d'encaissant (e.g. DÍaz-Alvarado et al., 2011), (3) l'entrainement de restites (Chappell et al., 1987) ou (4) de minéraux péritectiques (Stevens et al., 2007; Villaros et al., 2009) depuis la source et (5) la cristallisation fractionnée (e.g. Morfin et al., 2014; Tartèse et Boulvais, 2010). Le processus de cristallisation fractionnée, qui va impliquer la séparation préférentielle de minéraux ferro-magnésien du liquide initial, va induire une diminution du degré de maficité et ne peut donc pas expliquer les variations géochimiques observées au sein des CPG (Fig. I.3). Ensuite, bien que les quatre premiers processus cités ci-dessus sont théoriquement susceptibles d'expliquer l'évolution des CPG, certains sont susceptibles de se produire plus facilement dans la nature. Tout d'abord, les CPG contiennent souvent des enclaves mafiques et ils sont souvent associés à des roches d'origine mantelliques sur le terrain. Néanmoins, le mélange en proportion significative de magmas avec des températures et des viscosités différentes sont difficiles et implique une quantité importante de roches mafiques probablement supérieure aux roches felsiques (e.g. Laumonier et al., 2014, 2015). De plus, les évidences minéralogiques d'hybridation importante comme des feldspath rapakivi (e.g. Baxter et Feely, 2002) manquent généralement dans les CPG. De même, l'assimilation de roches encaissantes consomme beaucoup d'énergie et va rapidement induire la cristallisation du magma empêchant ainsi son mouvement (Glazner, 2007). Ainsi, l'assimilation va être limitée aux parties les plus marginales des intrusions. Ensuite, le modèle d'entrainement de restite implique que les CPG représentent un mélange entre un liquide silicaté et des roches non fondues entrainées depuis la source. Néanmoins, la plus part des granitoïdes manquent d'évidences minéralogiques et texturales de la présence de restite en proportion significative (Clemens and Stevens, 2012). Enfin, plusieurs études ont montré que l'entrainement de minéraux péritéctiques, comme le grenat ou l'orthopyroxène, depuis la source était un processus majeurs dans l'évolution des CPG (e.g. Clemens et Stevens, 2012; Stevens et al., 2007; Villaros et al., 2009). Les minéraux péritectiques ne sont pas censés être identifiables dans les roches granitiques car leur faible taille va les amener à se rééquilibrer facilement avec le magma pour former des minéraux comme la biotite ou la cordiérite.

Le fait que l'entrainement de minéraux péritectiques depuis la source est un processus majeur dans l'évolution des CPG mais pas des MPG est probablement le résultat des conditions de genèse spécifiques des deux types de granitoïdes. En effet, le fort taux de fusion partielle dont sont issues les CPG ainsi que leur plus forte viscosité, due à leur faible teneur en eau, doit faciliter l'entrainement de

phases péritectiques. En revanche, les MPG se forment via un taux de fusion plus faible et leur plus forte teneur en eau diminue leur viscosité. Ces deux facteurs vont limiter l'entrainement de cristaux péritectiques depuis la source mais, comme nous le discuterons dans la partie suivante, probablement faciliter le processus de cristallisation fractionnée qui est surement le processus majeur d'évolution des MPG.

1.4. Spécificités métallogéniques des granites peralumineux

Il existe un lien entre la nature des granitoïdes et leurs associations métalliques. Ainsi, Chappell et White (1974) met en évidence dans le Lachlan Fold Belt en Australie que de façon générale les minéralisations en Cuivre (Cu) – Molybdène (Mo) – Or (Au) sont associées aux granitoïdes de type I (ignées), plutôt métalumineux et oxydés. Au contraire, les minéralisations en étain (Sn) – tungstène (W) sont associées aux granitoïdes de type S (sédimentaires), généralement peralumineux et réduits.

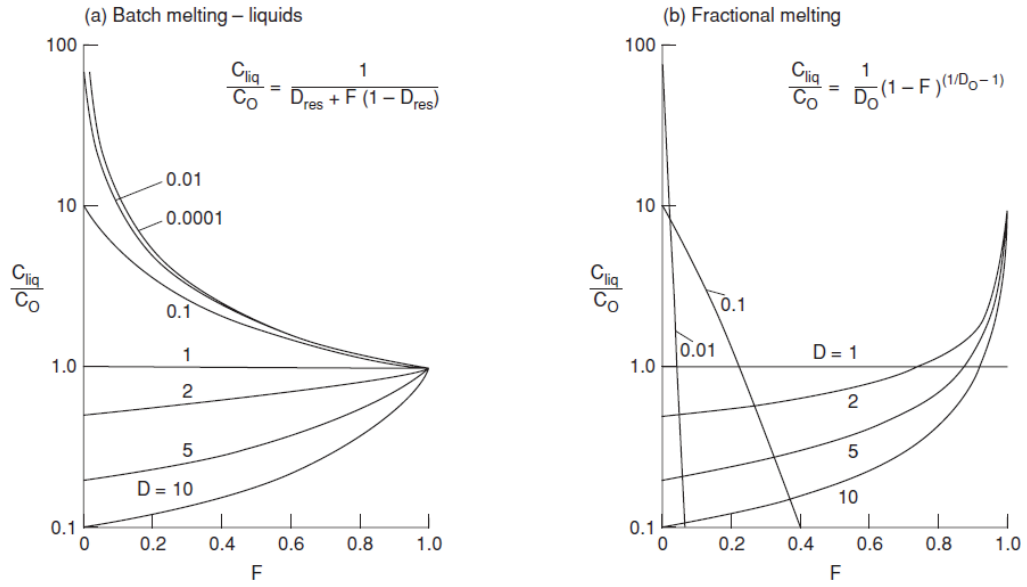

Figure I.4 : Distribution des éléments traces dans les processus de fusion partielle à l'équilibre (a) et en déséquilibre (b). L'enrichissement ou l'appauvrissement d'un élément trace dans le liquide par rapport à sa source (C_{liq}/C_0) sont calculés en fonction du degré de fusion partielle (F) et de son coefficient de partage (D). D'après Robb (2005) et Rollinson (1993).

Deux processus magmatiques majeurs qui vont contrôler les enrichissements en métaux dans les magmas peralumineux sont la fusion partielle et la cristallisation fractionnée. Ainsi, l'Sn et le W, qui ont un comportement incompatible (D << 1), vont fortement s'enrichir dans le liquide par rapport à leur source lors de la fusion partielle et l'enrichissement va être d'autant plus fort (jusqu'à deux ordres de grandeur) que le taux de fusion partiel (F) est faible (Fig. I.4). Ainsi, la teneur initiale en Sn et W de la source va être primordiale pour former des granites associés à des gisements. C'est la notion de province métallogénique (e.g. Romer et Kroner, 2014). De même, les éléments incompatibles comme l'Sn et le W vont s'enrichir au cours de la cristallisation fractionnée mais cela va nécessiter des taux de fractionnement très importants (1-F > 0.8) pour induire un enrichissement de plus d'un ordre de grandeur

par rapport au liquide initial (Fig. I.5). Ainsi, les MPG qui se forment à des taux de fusion partielle relativement faibles (< 30 %) et dont la richesse en eau diminue la viscosité et facilite le processus de cristallisation fractionnée sont nettement plus susceptibles d'être riches en éléments incompatibles comparé aux CPG. Les gisements de métaux comme l'Sn et le W sont donc à prospecter en priorité à proximité des MPG.

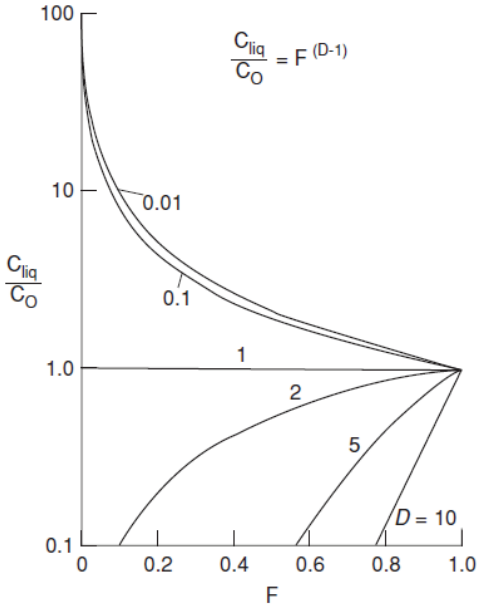

Figure I.5 : Distribution des éléments traces dans les processus de cristallisation fractionnée. L'enrichissement ou l'appauvrissement d'un élément trace dans le liquide résiduel par rapport au liquide initial (C_{liq}/C_0) sont calculés en fonction du taux de cristallisation fractionnée (1-F) et de son coefficient de partage entre le liquide résiduelle et l'assemblage minéralogique fractionné (D). D'après Robb (2005) et Rollinson (1993).

La teneur en eau des magmas et les fractionnements élémentaires entre fluides (H_2O, CO_2, …) et magmas vont jouer aussi un rôle essentiel dans la distribution des métaux dans et autour des intrusions granitiques. Tout d'abord, comme nous en avons parlé précédemment la température et la teneur en eau initiale des magmas vont contrôler leur profondeur de mise en place. Ainsi, les magmas « froids » issus de la déshydratation de la muscovite (~7 – 8 % d'eau) type MPG vont cristalliser à une profondeur plus élevée que les magmas « chauds » issus de la déshydratation de la biotite ou de l'amphibole (~ 3-4 % d'eau) (Fig. I.6a). Il existe deux phases majeurs appelées « première » et « seconde » ébullition au cours desquels les magmas granitiques peuvent exsolver de l'eau. La « première » ébullition est liée à la remontée du magma vers la surface car la solubilité de l'eau dans les liquides silicatés est corrélée à la pression. La « seconde » a lieu lors de la cristallisation du magma car toute l'eau présente dans le liquide silicaté ne peut pas être incorporée dans les phases hydratées comme la biotite ou la muscovite.

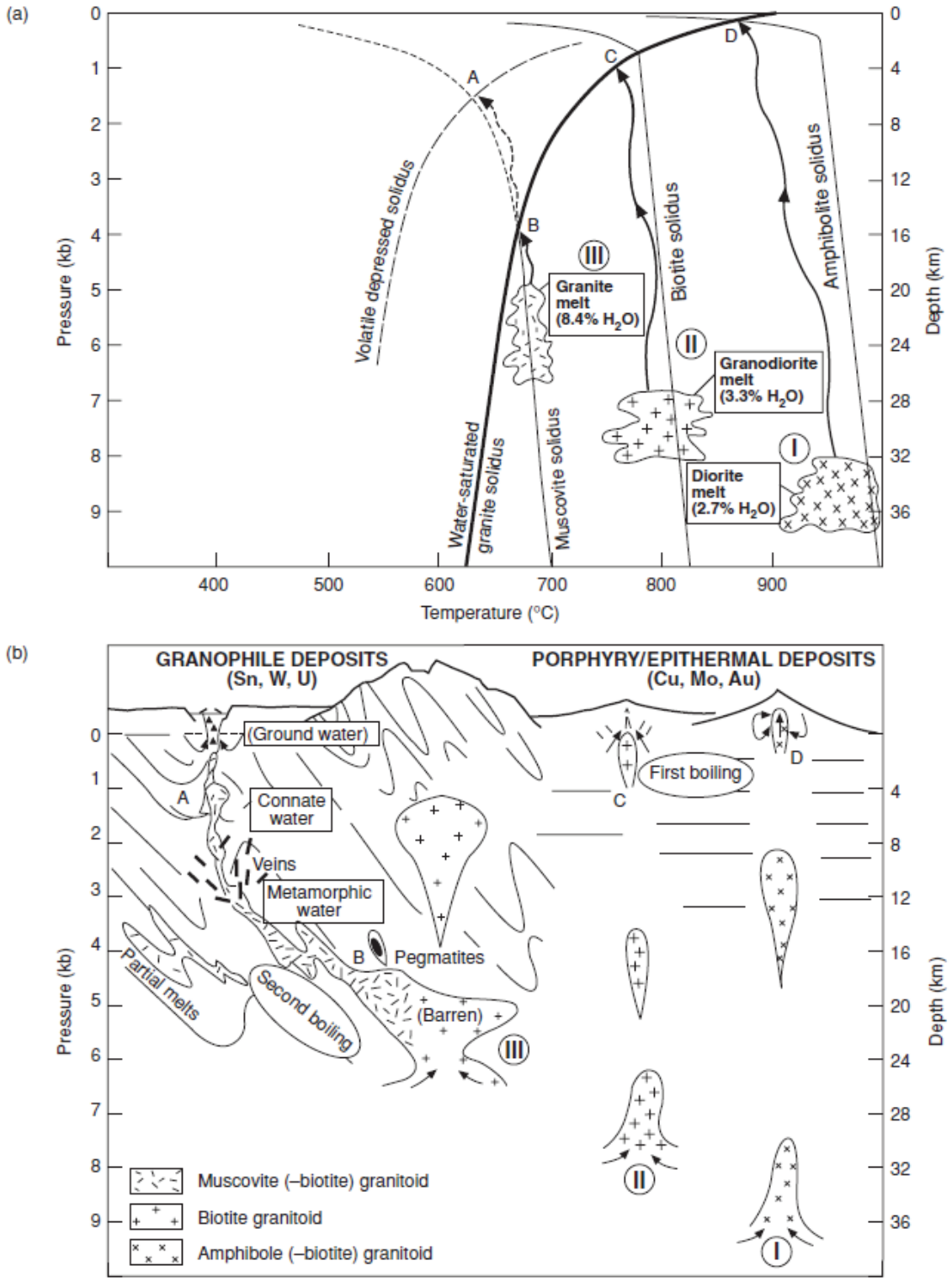

Figure I.6 : Modèle montrant la relation entre profondeur de mise en place des granites et leur caractère métallogénique d'après Strong (1988) et Robb (2005). (a) Diagramme pression-température (P-T) montrant les conditions approximatives de fusion partielle par déshydratation de l'amphibole (I), de la biotite (II) et de la muscovite (III). Le diagramme indique aussi à quelle condition P-T le magma produit va intercepter son solidus en cas de décompression adiabatique. (b) Schéma illustrant les modalités d'emplacement et le caractère métallogénique des granitoïdes formées dans les conditions P-T, repérées par les points A, B, C et D.

Ainsi, pour les granitoïdes initialement pauvres en eau et issus de la déshydratation de l'amphibole (plutôt métalumineux), la première ébullition d'une phase vapeur peut arriver dans les niveaux superficiels de la croûte induisant fracturation hydraulique, bréchification et circulations hydrothermales diffuses. Ce scénario courant en contexte de subduction est favorable à la formation de gîtes magmatique-hydrothermaux type porphyres ou épithermaux minéralisés en Cu-Mo-Au (Fig I.6b).

Les MPG, quant à eux, vont théoriquement commencer à cristalliser proche de leur zone de genèse dans la croûte inférieure à moyenne (Fig. I.6). A cette profondeur ces granites à deux micas sont généralement stériles mais ils peuvent se différencier par cristallisation fractionnée au cours de leur remontée vers la surface (e.g. Tartèse et Boulvais, 2010 ; Yamato et al., 2015). De cette façon, les liquides résiduels vont s'enrichir en eau et en éléments volatiles comme le bore (B), le fluor (F), le phosphore (P) et le lithium (Li). Cela va induire la diminution de la viscosité du magma et de la température du solidus saturé en eau (e.g. London, 1987) et faciliter leur ascension dans la croûte supérieure (Fig. I.6). Les fluides libérés lors de la remontée (« première » ébullition) et la cristallisation (« seconde » ébullition) de ces magmas vont induire des circulations magmatique-hydrothermales qui peuvent promouvoir la mise en place de pegmatites potentiellement minéralisés en lithium (Li), césium (Cs), tantale (Nb) (type LCT, Černý, 1991) (Fig. I.6b). Au niveau de la zone apicale des intrusions, ces circulations de fluides orthomagmatiques, enrichies en éléments incompatibles, vont être plus diffuses et peuvent induire des mobilités élémentaires importantes qui peuvent se traduire par la formation de roches métasomatiques comme les greisens communément minéralisées en Sn et W (e.g. Schwartz et Surjono, 1990) (Fig. I.6b). La greisenisation, communément précédée d'un metasomatisme sodique (albitite), est liée à la circulation de fluides acides (enrichies en ion H^+) qui vont induire la destruction de la biotite et des feldspaths du granite original pour former un assemblage quartz + mica blanc (muscovite, phengite, lepidolite, ...) (e.g. Pirajno, 2013).

Les pegmatites LCT (Černý, 1991) et les granites à métaux rares (Linnen et Cuney, 2005) sont communément interprétés comme les produits de la différenciation extrême des MPG et représentent un enjeu économique important. Néanmoins, comme plusieurs champs de pegmatites LCT n'ont pas de liens génétiques ou spatiaux directs avec des intrusions granitiques un modèle alternatif d'anatexie crustale direct peut, dans certains cas, être proposé (e.g. Kontak et al., 2005; Dill et al., 2012; Deveaud et al., 2013; 2015). Les travaux expérimentaux de Jahns et Burnham (1969) suggèrent que les pegmatites se forment en présence d'une phase fluide exsudée immiscible. Ainsi, les pegmatites se formeraient en milieu biphasé et le point de saturation en eau du magma marquerait la transition entre granites et pegmatites. Néanmoins, des études plus récentes (e.g. London, 1990, 2005; London et Morgan, 2012) ont suggéré que les pegmatites pouvaient se former à partir d'un magma granitique sous saturée en eau dans des conditions métastables de surfusion (undercooling). Dans ce scénario, la chute rapide de la température du liquide silicaté en dessous de son solidus va induire une cristallisation hors équilibre du magma des bordures vers le cœur du filon. Cela va aussi entrainer la formation d'une couche de liquide

enrichie en éléments fluants (B, P, Li, F, H_2O) à la frontière du front de cristallisation. Ce mécanisme va permettre de reproduire la majorité des caractéristiques texturales des pegmatites comme la grande taille des minéraux, leur zonation symétrique et les textures graphites. Pourtant des études récentes n'excluent pas le rôle important de l'eau dans la formation des pegmatites et certains auteurs (Thomas et al., 2012; Thomas et Davidson, 2012) suggèrent que le processus de surfusion n'est pas nécessairement dominant dans la formation de ces roches. En effet, les études sur les inclusions de liquides silicatés (« melt inclusions ») menées par ces auteurs montrent que les phénomènes d'immiscibilité entre différents liquides silicatés et phases fluides doivent être prépondérants lors de la genèse des pegmatites. Ainsi, il n'existe pas encore de consensus sur le modèle de formation de ces roches mais il semble que l'enrichissement en H_2O, dont la teneur peut dépasser les 50% dans les inclusions de « melt », et la présence d'autres éléments fluants (Li, B, F, CO_2, …) soient des paramètres clés pour leur genèse et leur enrichissement en métaux.

Outre le Sn, l'W et les métaux rares, les MPG sont fréquemment associés à des gisements d'uranium hydrothermaux (Fig. I.6b). C'est ce que nous allons discuter dans le prochain chapitre.

Chapitre 2 : Gisements d'uranium et granites

L'uranium (U) est un des matériaux énergétiques les plus importants de la planète. Ainsi, l'énergie nucléaire représente 10.8 % de la production mondiale d'électricité en 2014 (IAEA : international atomic energy agency - www.iaea.org) et 76.3 % de la production française en 2015 (RTE : réseau de l'intelligence électrique - www.rte-france.com/). Il existe une grande variété de gisements d'uranium sur terre et dans de nombreux cas l'uranium provient du lessivage des roches magmatiques environnantes par des fluides hydrothermaux ou de surface (Cuney, 2009). Dans la chaîne hercynienne européenne dont le Massif armoricain, la majorité des gisements d'uranium sont associés à des granites peralumineux d'âge Carbonifère. Ici, nous allons discuter des paramètres qui contrôle la fertilité d'une roche ignée pour former des gisements d'uranium hydrothermaux. Ce chapitre est en grande part basé sur les travaux de M. Cuney et co-auteurs et les lecteurs intéressés sont invités à se référer à Cuney et Kyser (2008) et Cuney (2014) pour plus de détails.

L'uranium est un élément lithophile et sa forte charge et son rayon ionique élevé lui confèrent généralement un caractère incompatible lors des processus de fusion partielle et de cristallisation fractionnée (Goldschmidt, 1937). Ainsi, l'uranium est enrichi dans la croûte continentale supérieur ([U] = 2.7 ppm ; Rudnick et Gao, 2005) par rapport au manteau primitif ([U] = 0.0203 ppm ; Hofmann, 1988) et à la croûte continentale globale ([U] = 1.3 ppm ; Rudnick et Gao, 2005). Pourtant, les gisements d'uranium issus essentiellement de processus magmatiques sont rares et le gisement le plus important se situe à Rössing en Namibie. Là-bas, des filons de leucogranites minéralisés en uraninite (UO_2), localement appelés alaskites, se sont mis en place proche de leur source dans des roches métamorphiques de haut grade partiellement migmatisées. Ces filons à texture pegmatitique sont pour la plus part

légèrement peralumineux et leur forte teneur en U (300 ppm en moyenne) est probablement liée à un faible taux de fusion partielle d'un protholithe métasédimentaire ou métaigné préenrichi en U (Nex et al., 2001; Robb, 2005; Cuney et Kyser, 2008; Cuney, 2014).

La fertilité d'une roche ignée pour faire des gisements d'uranium hydrothermaux n'est pas seulement dépendante de son degré d'enrichissement. En effet, cette fertilité est aussi dépendante de la nature du site dans lequel l'uranium est localisé et de la capacité de ce site à être lessivé par des fluides.

Dans les magmas peralcalins, la température élevée et l'excès d'alcalins par rapport à l'aluminium ((Na + K) / Al > 1 ; Fig. I.1) favorise la dépolymérisation du liquide silicaté et la forte solubilité des HFSE (High Field Strength Elements) comme l'U, le Th, le Nb (niobium), le Ta (tantale), le Zr (zirconium), l'Hf (hafnium) et les ETR (terres rares) (Montel, 1993; Peiffert et al., 1996, 1994; Linnen et Keppler, 1997, 2002). Ainsi, U, Th et autres HFSE vont tous s'enrichir de la même façon au cours de la cristallisation fractionnée et le rapport Th/U va rester constant proche de la valeur moyenne de la croute continentale supérieure (Fig. I.7). Cela va induire la cristallisation de phases minérales complexes porteuses de HFSE, comme par exemple le pyrochlore $[(Ca,U,REE)(Nb,Ta,Ti)_2O_6(O,OH,F)]$, avec l'U comme élément mineur dans leur structure. Dans ces minéraux, l'U n'est pas facilement lessivable par les fluides donc malgré des taux d'enrichissements parfois extrêmes, de l'ordre d'une centaine ou du millier de ppm, les roches plutoniques peralcalines ne représentent généralement pas de source significatives d'uranium. Elles peuvent toutefois devenir des sources importantes d'uranium si les phases porteuses silicatées deviennent métamictes. De même, les roches volcaniques peraclalines évoluées sont d'excellentes sources d'uranium car une majorité de l'U peut être incorporé dans du verre qui est facilement lessivable en présence de fluides.

En ce qui concerne les roches peralumineuses, les granitoïdes à cordiérites (CPG) ne représentent pas des sources favorables d'uranium. En effet, le fort taux de fusion partielle via lequel ils se forment et les processus d'entrainement peritectiques ou d'assimilation ne vont pas permettre un fort enrichissement en uranium du magma (cf. Chap. 1). Au contraire les leucogranites à muscovite (MPG) peuvent représenter d'excellentes sources d'uranium sous réserve de certaines conditions :

(1) Le protholithe soumis à la fusion partielle doit être suffisamment riche en uranium pour qu'une proportion importante de l'U soit présent en dehors des phases accessoires peu solubles dans les magmas peralumineux comme le zircon (Watson et Harrison, 1983) et la monazite (Montel, 1993).
(2) Le degré de fusion partielle doit rester faible pour induire un fort enrichissement en éléments incompatibles comme l'U dans le magma (Fig. I.4).
(3) Le magma doit se différencier suffisamment pour atteindre la saturation en uraninite magmatique. En effet, dans les magmas peralumineux de faibles températures, qui sont fortement polymérisés, la monazite et le zircon sont peu solubles et ils vont fractionner du

liquide silicaté au cours de la différentiation (Watson et Harrison, 1983; Montel, 1993). Ainsi, le magma va s'appauvrir en Th, ETR et Zr au cours de la cristallisation fractionnée mais il va s'enrichir en U car seulement une faible proportion de l'U va être incorporée dans ces minéraux accessoires. Ce processus va induire la diminution du rapport Th/U jusqu'à des valeurs < 1 permettant ainsi la cristallisation de l'uraninite. Les teneurs en U de l'ordre de 10 à 30 ppm mesurés dans les MPG associés à des gisements (e.g. Friedrich et al., 1987) sont cohérentes avec les études expérimentales sur la solubilité de l'uraninite dans les magmas peralumineux (Peiffert et al., 1994, 1996).

Les équivalents volcaniques des MPG sont rares dans la nature (cf. Chap. 1). Néanmoins, une occurrence de roche volcanique peralumineuses à deux micas riche en U existe à Macusani au Péru. Ces tufs pyroclastiques peuvent atteindre des teneurs en U d'une vingtaine de ppm similaires aux MPG (Pichavant et al., 1988a., 1988b) et la dévitrification de leur verre par des fluides oxydants peut libérer une quantité significative d'U.

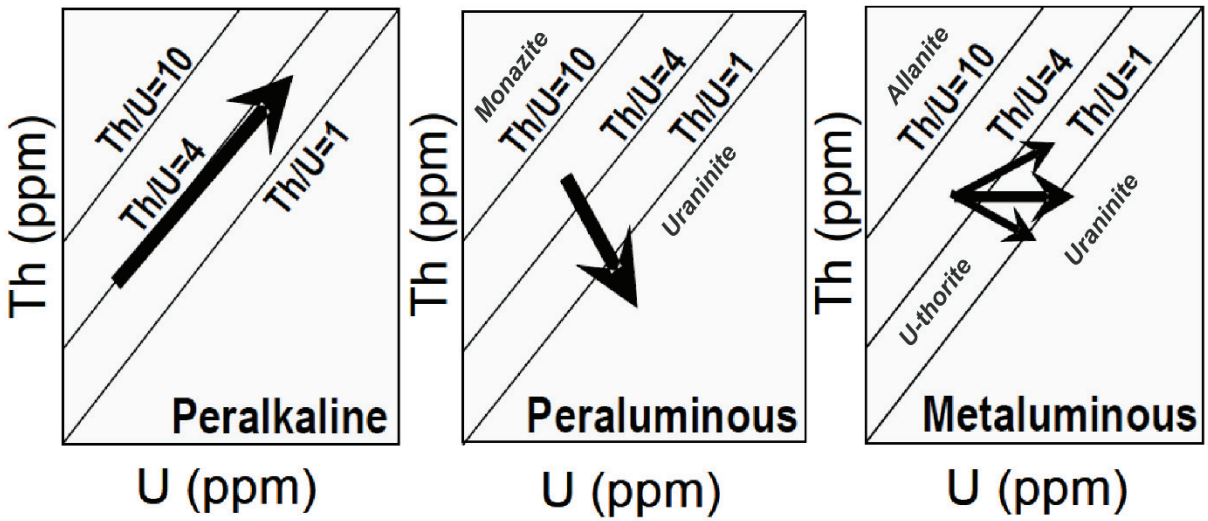

Figure I.7 : Evolution générale de la teneur en U, Th et du rapport Th/U dans les magmas peralcalins, peralumineux et métalumineux au cours de la cristallisation fractionnée. Dans les granites métalumineux, le Th et l'U peuvent se comporter différemment selon la température et le degré de peraluminosité du magma. Les principaux minéraux porteurs d'U ont été identifiés en fonction du rapport Th/U. D'après Cuney et Kyser (2008) et Cuney (2014).

Les liquides silicatés dont sont issus les séries métalumineuses évoluées vont présenter une température élevée à modérée et vont se caractériser par un degré de polymérisation variable qui sera intermédiaire entre les liquides peralcalins et fortement peralumineux. Ainsi, la solubilité des ETR et du Th dans ces liquides va être variable et leur teneur peut rester constante, augmenter ou diminuer au cours de la cristallisation fractionnée. L'U augmentant lors de la différenciation, il va en résulter une évolution incertaine du rapport Th/U (Fig. I.7). Les rapports Th/U autour de 4 vont faciliter la cristallisation de l'uranothorite [(Th,U)SiO_4] qui est une phase minérale où l'U sera difficilement mobilisable par les fluides mis à part si celle-ci devient métamicte. De même, les rapports ETR/Th et Nb/Th élevés, vont induire, respectivement, l'incorporation d'une majeure partie de l'U dans des phases réfractaires comme

l'allanite [$(Ce,Ca,Y,La)_2(Al,Fe^{3+})_3(SiO_4)_3(OH)$] et les oxydes de Nb. Enfin, si le liquide diminue de température et devient légèrement peralumineux (baisse de l'activité en calcium), la monazite peut devenir stable et fractionner du magma. Cela va induire une diminution du rapport Th/U et peut potentiellement permettre la cristallisation d'uraninite magmatique. La présence d'uraninite dans ces séries granitiques reste néanmoins exceptionnelle et ces roches ne représentent généralement pas des sources d'U idéals pour les gisements mis à part si les minéraux porteurs deviennent métamictes. Au contraire, les roches volcaniques métalumineuses évoluées peuvent être des sources favorables si l'U est porté par du verre.

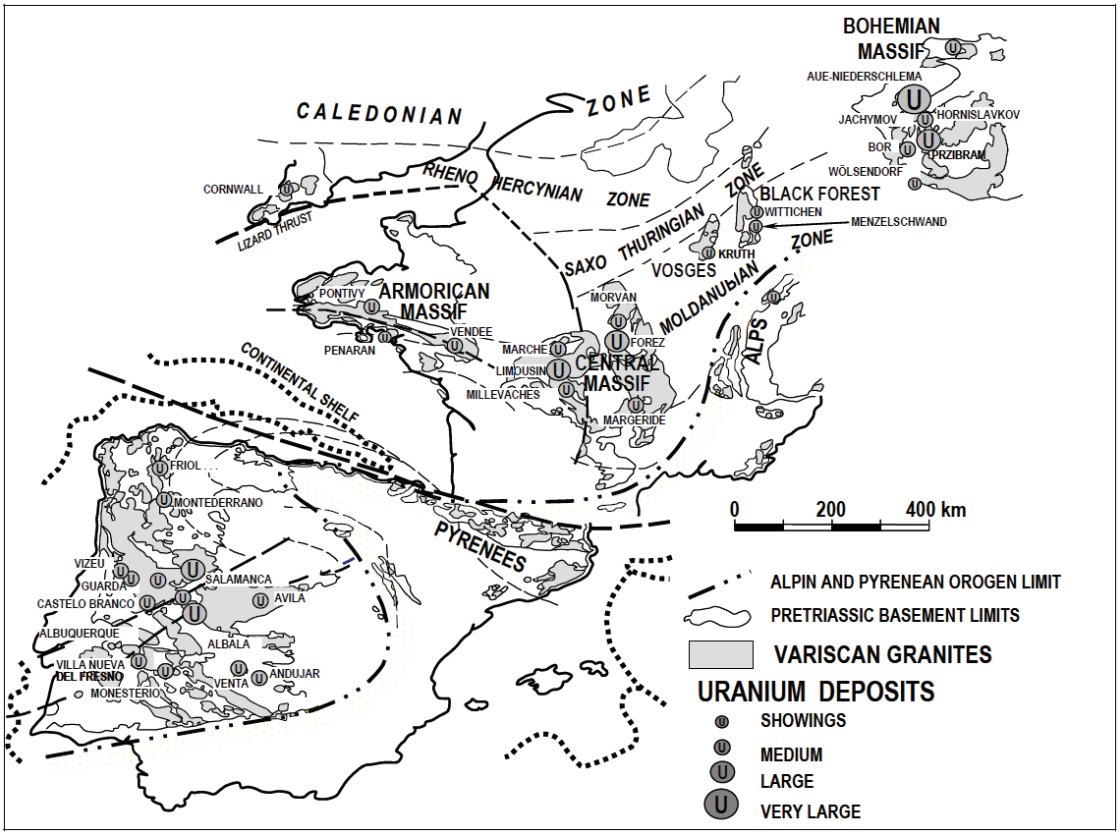

Figure I.8 : Distribution des granites varisques et des gisements d'uranium hydrothermaux dans la chaîne hercynienne ouest européenne avant l'ouverture du Golfe de Gascogne. D'après Cuney et Kyser (2008).

Ainsi les leucogranites peralumineux (MPG) représentent une des sources les plus favorables pour former des gisements d'uranium hydrothermaux et cette association est particulièrement évidente dans la chaîne hercynienne ouest européenne qui s'étend du Massif de Bohème à la péninsule ibérique (Fig. I.8). Dans le Massif central (France), les minéralisations en uraninite, intra à périgranitiques, sont filoniennes ou disséminées dans des granites déquartzifiés (épisyénites) et l'âge des gisements (~290 – 260 Ma) postdatent la mise en place des leucogranites (~335 – 305 Ma) d'au moins 20 Ma (Cathelineau et al., 1990). Dans le complexe leucogranitique de Saint-Sylvestre (Limousin), la localisation des gisements est contrôlée par des structures magmatiques tardi-carbonifères qui ont été réactivées en fragile au Permien et ont canalisé les circulations de fluides hydrothermaux (Cuney et al., 1990). L'étude

en isotope stable réalisée par Turpin et al. (1990) sur des épisyénites du complexe de Saint-Sylvestre suggère l'intervention de deux fluides dans la genèse des minéralisations : un fluide aqueux oxydant d'origine météorique capable de lessiver l'U de l'uraninite des leucogranites environnants et un fluide réducteur d'origine présumée sédimentaire. Les études d'inclusions fluides réalisées sur les gisements indiquent des fluides minéralisateurs peu salés avec des températures généralement faibles entre 150 et 250 °C qui sont en accord avec la contribution de fluides météoriques (Cathelineau et al., 1990). Le rôle des fluides météoriques est crucial dans la genèse de ces minéralisations car leur forte fugacité en oxygène va leur permettre de transporter l'uranium en quantité importante (Dubessy et al., 1987).

Cette association entre leucogranites peralumineux à muscovite et gisements d'uranium hydrothermaux est aussi présente dans le Massif armoricain (Fig. I.8.) dont le contexte géologique est traité dans le chapitre suivant.

Chapitre 3 : La chaîne hercynienne armoricaine

Le Massif armoricain est une des expressions de l'orogenèse hercynienne en Europe de l'ouest. A la fin du Carbonifère, ce domaine est soumis à un magmatisme important et hétérogène qui nous donne l'opportunité de mieux comprendre les conditions de recyclage et de formation de la croûte continentale au cours d'un orogène de collision. Enfin, le Massif armoricain dispose d'un passé minier significatif et de nombreuses ressources comme, par exemple, l'or (Au), l'antimoine (Sb), le fer (Fe), le plomb (Pb), l'étain (Sn) et l'uranium (U) (Chauris, 1977). L'U représente une ressource majeure de la région et environ 20 % de la production historique française (~20000 t) a été extraite des gisements associés aux leucogranites peralumineux carbonifères du Massif armoricain (IRSN, 2004). Ce chapitre a pour but de retranscrire de façon générale l'évolution de ce massif à la fin du Paléozoïque et d'illustrer le cadre de mise en place des granites peralumineux et des gisements d'uranium.

3.1. Evolution tectono-magmatique de la chaîne hercynienne armoricaine

La chaîne hercynienne (ou varique) européenne résulte de la collision des super continents Laurussia (= Laurentia + Baltica) et Gondwana au cours du Paléozoïque. Cette collision entraine aussi la subduction de plusieurs océans et la rencontre de blocs continentaux de tailles plus modestes comme Avalonia et Armorica (Fig. I.9) (Ballèvre et al., 2009, 2013).

Figure I.9 : Carte illustrant la position du Massif armoricain dans la chaîne hercynienne ouest européenne avant l'ouverture du Golfe de Gascogne. Les couleurs indiquent les corrélations possibles entre les différents domaines continentaux de la chaîne. D'après Ballèvre et al. (2009).

Le Massif armoricain est divisé en trois domaines principaux par le cisaillement nord armoricain (CNA) et le cisaillement sud armoricain (CSA) : deux failles décrochantes dextres d'échelle crustale à lithosphérique (Fig. I.10) (Gumiaux et al., 2004a, 2004b). Le domaine nord armoricain est composé principalement de socle protérozoïque déformé au cours de l'orogenèse cadomienne (620 – 530 Ma) et il appartient à la croûte supérieure au cours du Paléozoïque (Brun et al., 2001). Le domaine centre armoricain est composé de sédiments protérozoïques (Briovérien) à carbonifères généralement faiblement déformés en conditions schiste vert durant l'orogenèse varisque mais la déformation augmente du nord vers le sud et de l'est vers l'ouest (e.g. Hanmer et al., 1982). Les décrochements dextres le long du CSA et du CNA sont accommodés par une déformation distribuée de l'ensemble du domaine centre armoricain et cela se traduit par une foliation verticale portant une linéation sub-

horizontale (Jégouzo, 1980; Gumiaux et al., 2004a). Le domaine sud armoricain et le Léon appartiennent aux zones internes de la chaîne hercynienne et se caractérisent par la présence de roches de haut grade métamorphique et une forte déformation (e.g. Gapais et al., 2015).

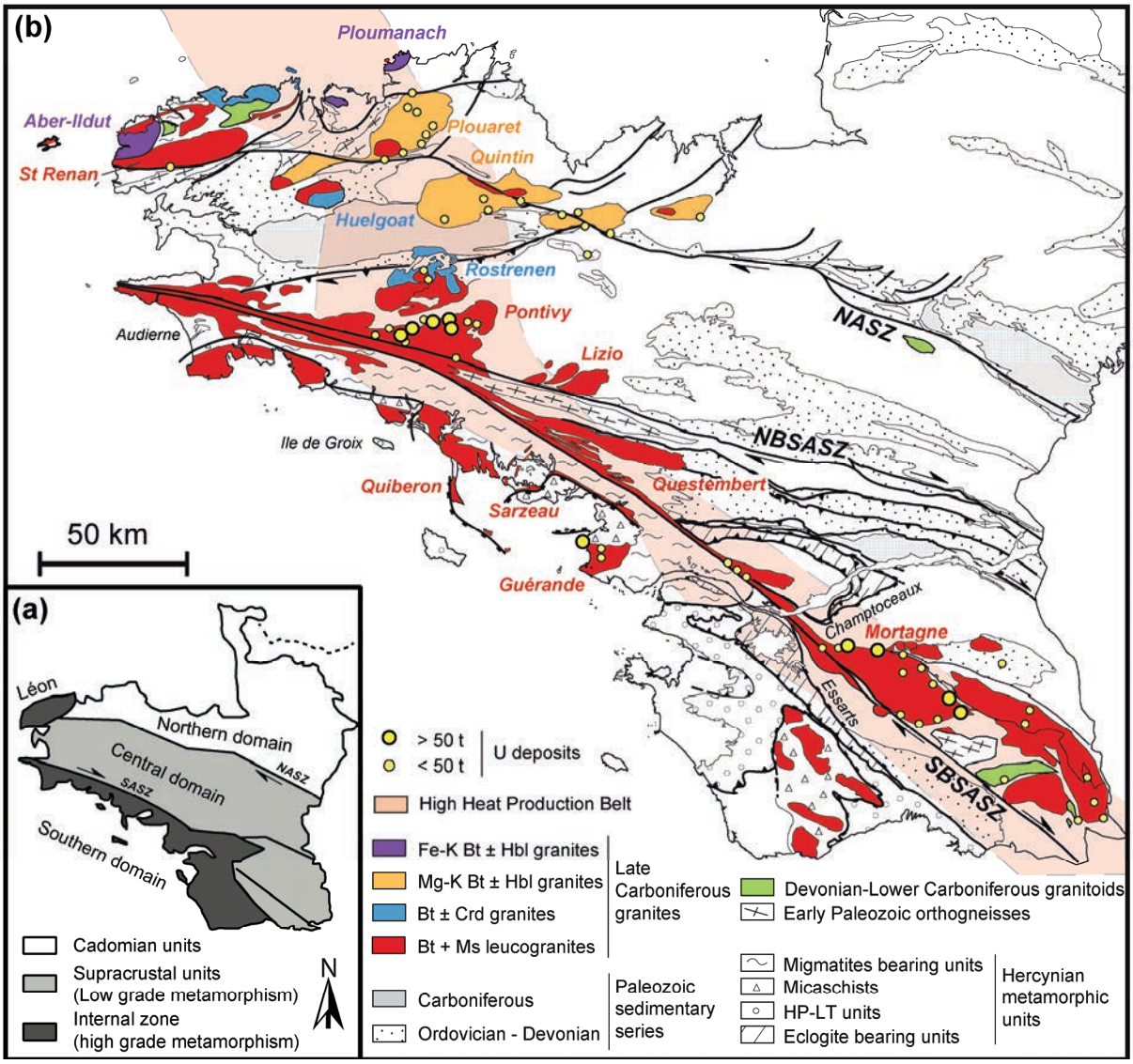

Figure I.10 : (a) Domaines structuraux principaux du Massif armoricain. (b) Carte géologique générale du Massif armoricain [modifiée d'après Chantraine et al. (2003) et Gapais et al. (2015)] montrant les différents types de granites carbonifères d'après Capdevila (2010) et localisant les gîtes d'uranium. NASZ: cisaillement nord armoricain; NBSASZ: branche nord du cisaillement sud armoricain. SBSASZ: branche sud du cisaillement sud armoricain. Fe-K granites: granites ferro-potassiques. Mg-K granites: granites magneso-potassiques. Calk-alk granites: granites calco-alcalins. La high heat production belt de Vigneresse et al. (1989) est indiquée. Abréviation minéralogique d'après Kretz (1983).

On distingue trois groupes principaux d'unités tectono-métamorphiques dans le domaine sud-armoricain avec du haut vers le bas (Fig. I.10) :

- des unités supérieures associées à un métamorphisme de haute pression-basse température (HP-BT) qui comprennent en haut de la pile des schistes bleus comme à l'île de Groix et à la base la formation des porphyroïdes de Vendée composée principalement de

métavolcanites ordoviciennes (Ballèvre et al., 2012) et de schiste noirs. Les schistes bleus et les porphyroïdes ont été soumis, respectivement, à des conditions de pression-température maximum de 1.4-1.8 Gpa, 500-550 °C (Bosse et al., 2002) et 0.8 Gpa, 350-400 °C (Le Hébel et al., 2002). La subduction et l'exhumation de ces unités a lieu entre 370 et 350 Ma (Le Hébel, 2002; Bosse et al., 2005).

- des unités intermédiaires composées principalement de micaschistes affectées par un métamorphisme barrovien du facies schiste vert à amphibolite (Bossiere, 1988; Triboulet et Audren, 1988).
- des unités inférieures constitués de migmatites, de gneiss et de granitoïdes qui ont atteint des conditions pression-température maximum de 0.8 Gpa et 700-750 °C (Jones et Brown, 1990).

Une ou plusieurs zones de sutures océaniques sont reconnues dans le domaine sud armoricain (Fig. I.9) du fait de la présence de complexes ophiolitiques (Audierne et Champtoceaux ; Fig. I.10) (Ballèvre et al, 2009 ; 2013). De même, l'identification d'unités de HP-BT (schistes bleus et porphyroïdes de Vendée) et d'éclogites (Audierne, Cellier et Essarts ; Fig. I.10) impliquent l'existence d'au moins une zone de subduction (Fig. I.11). Le métamorphisme de haute pression vers 360 Ma est synchrone de la fusion du manteau sous le domaine centre et nord armoricain se traduisant par la mise en place de nombreux dykes de dolérites (Pochon et al., 2016). La présence d'un vestige de lithosphère océanique à pendage vers le NE sous le domaine centre armoricain est mis en évidence par la tomographie du manteau (Gumiaux et al., 2004b). Ces auteurs suggèrent que ce panneau plongeant ait été déchiré à la limite lithosphère-asthénosphère (~130 km) lors de la déformation diffuse en décrochement du domaine centre armoricain. A Champtoceaux, l'empilement de nappes induit un métamorphisme inverse qui fait suite à l'éclogitisation entre 370 et 360 Ma (Ballèvre at al., 2013 et références y contenues) (Fig. I.11). Ces nappes sont ensuite plissées aux alentours de 335 Ma (Gumiaux et al., 2004a).

Entre 315 et 300 Ma (Tartèse et al., 2012), le CSA joue le rôle de zone de transfert entre le domaine centre armoricain, une zone non épaissie en décrochement, et le domaine sud armoricain, une zone épaissie en extension (e.g. Gapais et al., 1993, 2015). A cette période, l'amincissement crustal au sud du CSA induit l'exhumation de dômes migmatitiques bordés de leucogranites peralumineux comme Quiberon, Sarzau et Guérande qui viennent se mettre en place à la limite fragile-ductile sous les unités de HP-BT (e.g. Gapais et al., 1993, 2015; Turrillot et al., 2009) (Fig. I.12).

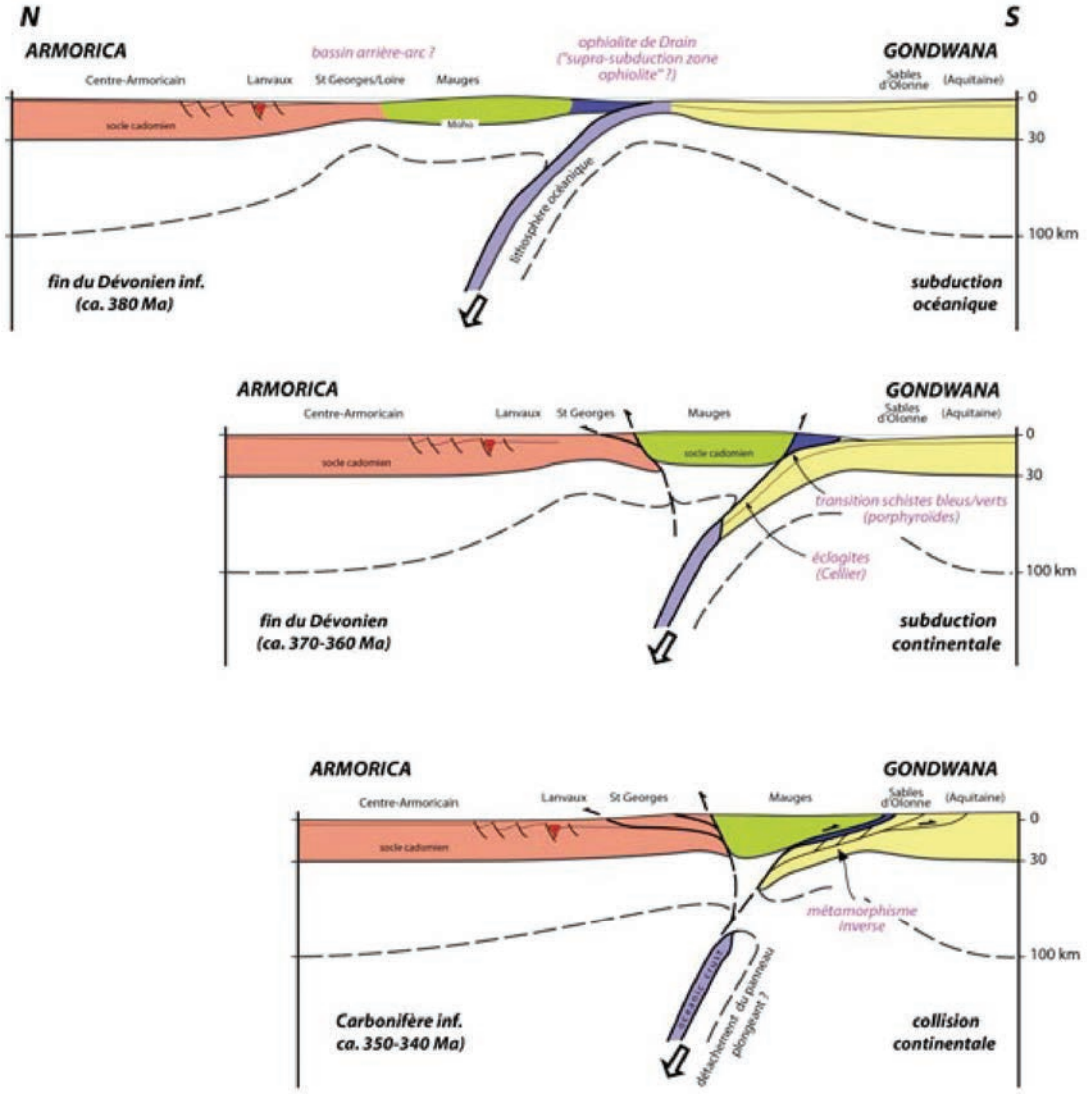

Figure I.11 : Schéma évolutif de la partie sud du Massif armoricain de la fin du Dévonien au Carbonifère Inférieur. D'après Ballèvre et al. (2013).

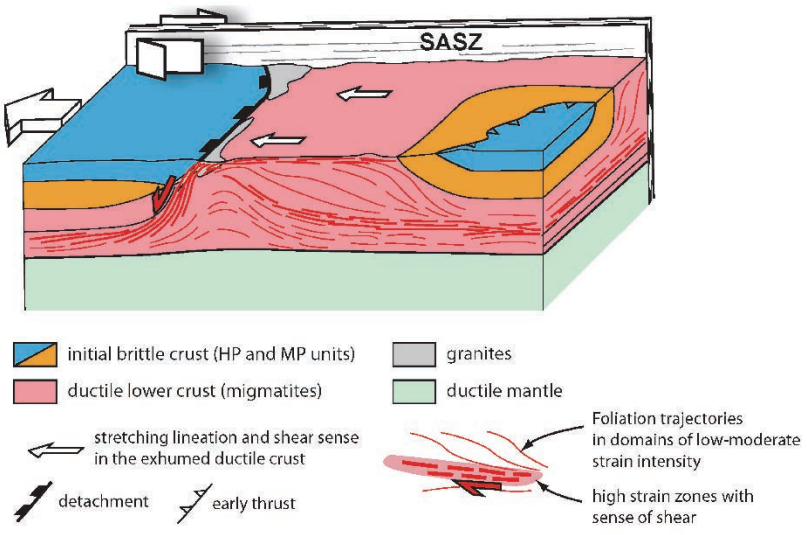

Figure I.12 : Schéma représentant la relation entre la formation de « core complex » dans la zone sud armoricaine et le décrochement le long du cisaillement sud armoricain (SASZ) à la fin du Carbonifère (~310 – 300 Ma). La relation avec les unités de HP qui forment la croûte supérieure à cette période est aussi illustrée. D'après Gapais et al. (2015).

A la fin du Carbonifère, le Massif armoricain est donc soumis à un magmatisme important qui résulte en la mise en place depuis, globalement, le sud vers le nord de quatre grandes suites granitiques (Capdevila, 2010) (Fig. I.10) :

- une suite magnéso – potassique peralumineuse composée de leucogranites à muscovite - biotite (type MPG d'après Barbarin, 1999). La plus part de ces intrusions se sont mis en place le long de zones de déformation extensives dans la zone sud armoricaine comme les leucogranites de Quiberon, Sarzeau et Guérande (e.g. Gapais et al., 1993, 2015; Turrillot et al., 2009) ou le long du CSA comme les leucogranites de Pontivy, Lizio et Questembert (Berthé et al., 1979). Ces leucogranites présentent généralement des structures C/S caractéristiques d'un refroidissement syntectonique (Gapais, 1989). Parmi eux, les leucogranites de Lizio et Questembert ont été datés en U-Pb sur zircon à, respectivement, 316.4 ± 5.6 Ma (Tartèse et al., 2011a) et 316.1 ± 2.9 Ma (Tartèse et al., 2011b). En parallèle, le long du CNA, l'intrusion de Saint-Renan a été datée par la méthode U-Pb sur zircon à 316.0 ± 2.0 Ma (Le Gall et al., 2014). Des intrusions leucogranitiques de tailles plus modestes sont communément associés aux granites des autres suites.
- une suite magneso-potassique peralumineuse composée de granites ou monzogranites à biotite – cordiérite (type CPG selon Barbarin, 1999). A Rostrenen, le monzogranite est associé à des petites intrusions de quartz-monzodiorite d'origine mantellique (Euzen, 1993). Le granite de Huelgoat est daté en Rb-Sr via la méthode isochrone sur roches totales à 336 ± 13 Ma (Peucat et al., 1979).
- une suite magneso-potassique métalumineuse composée de monzogranites à biotite – hornblende et associées avec des roches mafiques à intermédiaires. Ces intrusions se sont mis en place le long de CNA et les granites de Quintin et de Plouaret ont été datés, respectivement, en Rb-Sr via la méthode isochrone sur roches totales à 291 ± 9 Ma et 329 ± 5 Ma (Peucat et al., 1984).
- une suite ferro-potassique métalumineuse constituée principalement part des monzogranites ou des syénites à biotite-hornblende accompagnés d'intrusions mafiques à intermédiaires d'origine mantellique (série des granites rouges). Dans cette suite, le monzogranite de l'Alber-Ildut est daté en U-Pb sur zircon à 303.8 ± 0.9 Ma (Caroff et al., 2015) alors que pour l'intrusion de Ploumanac'h, l'unité la plus ancienne et la plus jeune sont datés par U-Pb sur zircon, respectivement, à 308.8 ± 2.5 et 301.3 ± 1.7 Ma (Dubois, 2014).

Au permien, les évidences de magmatisme dans le Massif armoricain sont rares ou inexistantes. Pourtant, cette période se caractérise par un plutonisme important, tout d'abord outre-manche, avec la mise en place du batholithe de Cornwall de ~295 à 275 Ma (Chen et al., 1993) mais aussi dans la péninsule ibérique avec la mise en place des granitoïdes post-orogéniques de ~310 à 285 Ma (Fernández-Suárez et al., 2000; Gutiérrez-Alonso et al., 2011). De même, les bassins sédimentaires permiens sont

peu représentés dans le Massif armoricain et le rare exemple est localisé à l'extrémité NE près de Carentan. Là-bas, la sédimentation détritique terrigène se traduit par le dépôt de grès et d'argiles rouges (Ballèvre et al., 2013). Ce bassin est interprété comme l'extrémité méridionale de bassins plus importants, maintenant localisés sous la mer de la Manche, et alimentés par les produits d'érosion de la chaîne hercynienne armoricaine et de la partie sud-ouest de l'Angleterre. En effet, à cette période le domaine de la Manche est soumis à un rifting important qui se traduit par une forte sédimentation détritique terrigène pouvant atteindre jusqu'à 9 km d'épaisseur (Ballèvre et al., 2013).

3.2. L'uranium dans le Massif armoricain

La grande majorité des gisements d'uranium du Massif armoricain sont associés aux leucogranites peralumineux d'âge tardi-carbonifère de Guérande, Pontivy et Mortagne (Cathelineau et al., 1990; Cuney et al., 1990) (Fig. I-10). Les autres occurrences sont mineures et n'ont pas fait l'objet d'exploitation importante (IRSN, 2004). Les minéralisations d'uraninite, intra à perigranitiques, peuvent être filoniennes comme celles associées au granite de Guérande (Cathelineau, 1981) ou disséminées dans des granites épisyenitisés comme, localement, à Pontivy (Marcoux, 1982 ; Alabosi, 1984). Les datations U-Pb réalisées à la sonde ionique sur les uraninites des gisements associés au leucogranite de Mortagne ont permis d'estimer l'âge de mise en place des minéralisations entre ca. 290 et 260 Ma (Cathelineau et al., 1990). Ces âges permiens sont comparables à ceux obtenus dans le Massif central (Cathelineau et al., 1990).

Le granite de Questembert (Fig. I.10) n'est pas directement associé à des gisements uranifères mais l'étude pétro-géochimique et géochronologique de Tartèse et al. (2013) (Fig. I.13) suggère qu'une centaine de millier de tonnes d'U ont été libérées de ce leucogranite lors d'une phase d'altération hydrothermale en profondeur avec des fluides dérivés de la surface. Dans le leucogranite de Questembert, les teneurs anormalement faibles en U des échantillons les plus évolués (i.e. les plus riches en SiO_2) sont associées à un déséquilibre isotopique en oxygène entre le quartz et le feldspath (Fig. I.13). Ce déséquilibre isotopique est interprété comme le reflet d'une altération hydrothermale sub-solidus avec des fluides à bas $\delta^{18}O$, d'origine probablement météorique, et l'infiltration en profondeur de ces fluides aurait été facilitée par les structures C/S qui affectent l'ensemble de l'intrusion. Cette épisode d'altération hydrothermale avec des fluides oxydants a pu induire le lessivage de l'U de l'uraninite présente originellement dans les échantillons les plus évolués. Les âges ^{40}Ar-^{39}Ar sur muscovite obtenus sur le leucogranite suggèrent que ce lessivage a eu lieu durant une période de 15 Ma à partir de sa mise en place (i.e. de 315 à 300 Ma) (Tartèse et al., 2013). Néanmoins, la muscovite des échantillons lessivés ne présente pas de déséquilibre isotopique en oxygène avec le quartz donc ces âges peuvent être le reflet d'une activité magmatique-hydrothermale plus précoce et le lessivage en U a pu avoir lieu plus tardivement. Tartèse et al. (2013) ont suggéré que l'U libéré par ces fluides météoriques a été dispersé dans les bassins permiens sus-jacent maintenant érodés.

Jolivet et al. (1989) et Vigneresse et al. (1989) ont défini, à partir d'une étude sur les flux de chaleur et la production de chaleur des formations géologique du Massif armoricain, la « high heat production and flow belt » (HHPFB), une ceinture NO-SE d'une cinquantaine de kilomètre de large qui intègre la majorité des occurrences uranifères de la région (Fig. I.10). Cette zone, qui recoupe la plupart des structures géologiques de la chaîne, se caractérise par un flux de chaleur anormalement élevé et les granites qu'elle englobe ont une production de chaleur par deux fois supérieure aux autres formations environnantes. Les auteurs ont suggéré que cette ceinture soit le reflet d'une croute supérieure à moyenne pré-enrichie en éléments radioactifs dont la fusion partielle aurait permis la mise en place de leucogranites fertiles. La HHPFB se poursuit jusqu'au NO du Massif central et en Cornwall de l'autre côté de la Manche.

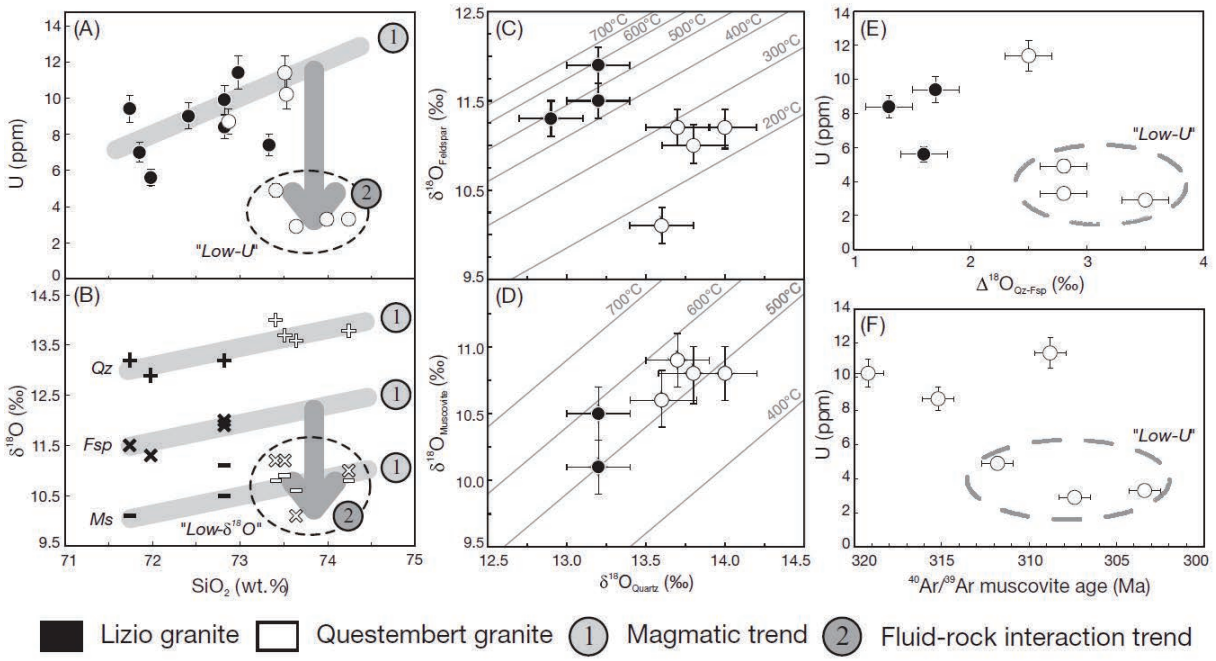

Figure I.13 : Sélection de données géochimiques (Tartèse et Boulvais, 2010) et géochronologiques (Tartèse et al., 2011b) pour les leucogranites de Lizio et Questembert. D'après Tartèse et al. (2013). (A) Teneur roche totale en U des échantillons en fonction leur teneur en SiO_2. (B) Valeur du $\delta^{18}O$ du quartz (Qz), du feldspath (Fsp) et de la muscovite (Ms) des échantillons en fonction de leur teneur roche totale en SiO_2. (C) $\delta^{18}O$ du Fsp en fonction du $\delta^{18}O$ du Qz. (D) $\delta^{18}O$ de la Ms en fonction du $\delta^{18}O$ du Qz. Dans ces deux diagrammes, les températures d'équilibre isotopique sont calculées à partir des coefficients de fractionnement de (Zheng, 1993a, 1993b). (E) Teneur roche totale en U des échantillons en fonction du $\Delta^{18}O_{Qtz\text{-}Fsp}$. (F) Teneur roche totale en U des échantillons en fonction de leur date Ar-Ar sur muscovite.

Partie II : La transition magmatique-hydrothermale dans les systèmes peralumineux

Préambule

Comme nous l'avons discuté dans le chapitre I, les magmas peralumineux peuvent contenir une contenir une quantité importante d'eau qui va généralement varier entre 3-4 % pour les CPG (granites peralumineux à cordiérite) et 7-8 % pour les MPG (leucogranites peralumineux à muscovite). La majeure partie de cette eau, qui ne va pas pouvoir être incorporée dans les phases hydratées comme les micas, va s'exsolver au cours de la remonté du magma vers la surface (« première ébullition ») et au moment de sa cristallisation (« seconde ébullition »). Par définition, la transition magmatique-hydrothermale sépare un système dominé par des interactions magma-cristaux d'un système dominé par des interactions magmas-cristaux-phases fluides (Fig. I.1). Cette étape critique dans l'évolution des granites peralumineux présente un fort enjeu économique car elle va se traduire par des mobilités élémentaires importantes pouvant conduire à la formation de gisements métallières. Les granites ayant subi une altération magmatique-hydrothermale importante n'en garde pas nécessairement une trace macroscopique significative mais la géochimie élémentaire peut aider à distinguer les granites « sains » des granites « altérés ».

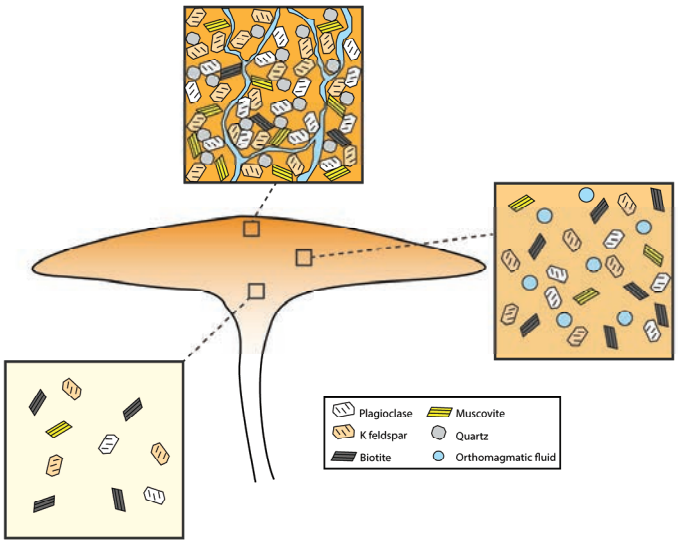

Figure II.1. : Schéma de laccolite illustrant le concept de transition magmatique-hydrothermale. Les interactions entre fluides, magmas et cristaux augmentent en ce dirigeant de la racine vers la zone apicale de l'intrusion.

Les travaux présentés dans cette Partie se basent sur une compilation d'analyses géochimiques roches totales, issues de la littérature, réalisées sur plus de 400 échantillons de granites peralumineux. Cette étude vise à documenter les fractionnements élémentaires qui se produisent au cours de la transition magmatique-hydrothermale en se basant plus particulièrement sur le niobium (Nb) et le tantale (Ta), deux éléments lithophiles jumeaux dont le comportement dans les fluides et les magmas est soumis à débat depuis le début des années 90. Cette étude a fait l'objet d'une publication dans le journal Geology ainsi que d'une réponse à un commentaire écrit par Stepanov et al. (2016). Le commentaire en question est fourni en annexe du manuscrit.

Résumé de l'article #1 : le fractionnement du Nb-Ta dans les granites peralumineux : un marqueur de la transition magmatique-hydrothermale

Au cours des derniers stades de leur évolution, les magmas peralumineux exsolvent une quantité importante de fluides qui peuvent modifier la composition chimique des échantillons de granites. Le rapport Nb/Ta est censé décroitre au cours de la différentiation des magmas granitiques mais le comportement de ces deux éléments lors de la transition magmatique-hydrothermale reste mal compris. En se basant sur une compilation de données géochimiques roches totales disponibles dans la littérature, nous démontrons que la cristallisation fractionnée seule n'est pas suffisante pour expliquer la distribution du Nb et du Ta dans la plupart des granites peralumineux. Néanmoins, nous observons que la majorité des granites qui présentent des évidences d'interactions avec des fluides a un rapport Nb/Ta inférieur à 5. Nous proposons que la décroissance du rapport Nb/Ta dans les magmas les plus évolués est la conséquence de la cristallisation fractionnée et d'une altération hydrothermale sub-solidus. Nous proposons la valeur Nb/Ta~5 comme un marqueur de la transition magmatique-hydrothermale dans les granites peralumineux. En parallèle, la valeur Nb/Ta~5 apparait utile pour discriminer les granites stériles des granites minéralisés en métaux.

Nb-Ta fractionation in peraluminous granites: A marker of the magmatic-hydrothermal transition

Christophe Ballouard[1], Marc Poujol[1], Philippe Boulvais[1], Yannick Branquet[1,2], Romain Tartèse[3,4], and Jean-Louis Vigneresse[5]
[1]Géosciences Rennes, UMR CNRS 6118, OSUR, Université Rennes 1, 35042 Rennes Cedex, France
[2]Institut des Sciences de la Terre d'Orléans (ISTO), UMR 6113 CNRS, Université d'Orléans, BRGM, Campus Géosciences, 1A rue de Férollerie, F-45071 Orléans Cedex 2, France
[3]Institut de Minéralogie, de Physique des Matériaux et de Cosmochimie, Muséum National d'Histoire Naturelle, Sorbonne Universités, CNRS, UPMC, IRD, 75005 Paris, France
[4]Department of Physical Sciences, The Open University, Walton Hall, Milton Keynes MK7 6AA, UK
[5]Université de Lorraine, UMR 7539 GéoRessources, BP 23, F-54501 Vandoeuvre Cedex, France

ABSTRACT

In their late stages of evolution, peraluminous granitic melts exsolve large amounts of fluids which can modify the chemical composition of granitic whole-rock samples. The niobium/tantalum (Nb/Ta) ratio is expected to decrease during the magmatic differentiation of granitic melts, but the behavior of both elements at the magmatic-hydrothermal transition remains unclear. Using a compilation of whole-rock geochemical data available in the literature, we demonstrate that fractional crystallization alone is not sufficient to explain the distribution of Nb-Ta in most peraluminous granites. However, we notice that most of the granitic samples displaying evidence of interactions with fluids have Nb/Ta < 5. We propose that the decrease of the Nb/Ta ratio in evolved melts is the consequence of both fractional crystallization and sub-solidus hydrothermal alteration. We suggest that the Nb/Ta value of ~5 fingerprints the magmatic-hydrothermal transition in peraluminous granites. Furthermore, a Nb/Ta ratio of ~5 appears to be a good marker to discriminate mineralized from barren peraluminous granites.

INTRODUCTION

In granitic systems, the magmatic-hydrothermal transition separates a purely magmatic system dominated by a crystal-melt interaction from a system dominated by a crystal–melt–magmatic fluid phase interaction (Halter and Webster, 2004). Hydrothermal activity in peraluminous granites can be either localized, as evidenced by pegmatites and/or quartz veins, or pervasive, leading to significant element mobility and, in the most extreme cases, to the formation of greisens (Pirajno, 2013). These alteration events occur during the sub-solidus stage of granitic magma emplacement and may lead to the deposition of economically significant mineralization such as tin (Sn) or tungsten (W).

Niobium (Nb) and tantalum (Ta) are lithophile elements considered to be "geochemical twins" because they have the same charge and a similar ionic radius. As a result they have similar geochemical properties and should not be fractionated during most geological processes (Goldschmidt, 1937). However, Nb/Ta ratios are variable in several types of igneous rocks, more particularly in granites (<2–25; Green, 1995). Some authors have demonstrated that the Nb/Ta ratios decrease in granites during fractional crystallization (Raimbault et al., 1995; Linnen and Keppler, 1997; Stepanov et al., 2014). Other studies have suggested that Nb and Ta could be fractionated in evolved peraluminous granites during the interaction with late magmatic fluids (Dostal and Chatterjee, 2000; Tartèse and Boulvais, 2010; Ballouard et al., 2015; Dostal et al., 2015).

In order to decipher the specific role of magmatic and hydrothermal processes in the evolution of Nb/Ta ratios, we compiled the whole-rock geochemical data available in the literature for peraluminous granites having various mineralogy and geochemical properties and emplaced in various tectonic contexts at different times.

PRESENT KNOWLEDGE

Magmatic Behavior of Nb-Ta

In highly evolved granites and pegmatites, columbite [$(Fe,Mn)Nb_2O_6$] and tantalite [$(Fe,Mn)Ta_2O_6$] are the main mineral phases hosting Nb and Ta. Experimental studies have shown that the solubility of these two minerals in granitic melts increases with temperature but decreases with increasing the aluminum saturation index (ASI), a parameter related to the degree of polymerization of the melt (e.g., Linnen and Keppler, 1997).

Partial melting can produce granitic peraluminous melts with Nb/Ta ratios higher or lower than that of their source, depending on the temperature (Stepanov et al., 2014). Melts formed during high-temperature anatexis tend to have high Nb/Ta ratios, as a result of the complete consumption of biotite and the high abundance of titanium (Ti)-bearing oxides in the residue, which preferentially incorporate Ta over Nb (Stepanov et al., 2014). Conversely, low-temperature partial melting generates melts with low Nb/Ta ratios because residual biotite preferentially incorporates Nb over Ta (Stepanov et al., 2014). Because biotite and Ti-bearing minerals can also be involved during the differentiation of granitic melts, fractional crystallization also changes the Nb/Ta ratios: Nb/Ta increases during high-temperature fractional crystallization of Ti-rich melts due to the preferential saturation of Ti-oxide minerals over biotite, whereas Nb/Ta ratios decrease during low-temperature differentiation of granitic melts due to the fractionation of biotite and/or muscovite (Stepanov et al., 2014). In the most evolved peraluminous melts, the lower solubility of manganocolumbite ($MnNb_2O_6$) compared with manganotantalite ($MnTa_2O_6$) also enhances the decrease of the Nb/Ta ratio in the melt (Linnen and Keppler, 1997). In lithium-fluorine (Li-F) granites, melt inclusions indicate a separation of an immiscible F-rich hydrosaline melt that can induce a decrease of the Nb and Ta contents in the residual melt (Badanina et al., 2010).

Nb-Ta Behavior in Hydrothermal Systems

Nb and Ta are generally poorly soluble in aqueous solutions, Ta being even less soluble than Nb (Zaraisky et al., 2010). Experiments with aqueous F-rich fluids and aluminosilicate melt indicate that Nb and Ta preferentially partition into the melt (Chevychelov et al., 2005). However, the solubility and hydrothermal transfer of Ta and Nb are greatly enhanced in F-rich solutions under reducing conditions (Zaraisky et al., 2010). These experimental results are consistent with the fact that several F-rich cupolas of greisenized peraluminous granites are significantly enriched in both Nb and Ta (e.g., Zaraisky et al., 2009).

VARIATIONS OF WHOLE-ROCK Nb/Ta RATIOS IN PERALUMINOUS GRANITES

We compiled data for peraluminous granites [i.e., with an $Al_2O_3/(CaO + Na_2O + K_2O)$ ratio (A/CNK) >1; excluding aplites and pegmatites], as well as for some greisens, of different ages (Archean to Mesozoic) that were emplaced in various geodynamical contexts (see Table DR1 in the GSA Data Repository[1]).

[1]GSA Data Repository item 2016069, synthesis of peraluminous granites reported in this study, is available online at www.geosociety.org/pubs/ft2016.htm, or on request from editing@geosociety.org or Documents Secretary, GSA, P.O. Box 9140, Boulder, CO 80301, USA.

Nb-Ta Fractionation During Magmatic Processes

As shown in Figure 1, the Nb/Ta ratios in the compiled data are highly variable, between ~15 and ~0.1, and the lowest values are shown by whole rocks displaying the highest Nb and Ta contents. Mica fractionation in granitic melt induces a decrease of the Nb/Ta ratios (Stepanov et al., 2014). Figure 1 also shows our model of the evolution of a melt with initial Ta and Nb contents of 1.5 ppm and 12 ppm (Nb/Ta = 8), respectively. This melt undergoes extraction of a cumulate made of 80 wt% (quartz + feldspar) + 10 wt% muscovite + 10 wt% biotite, using the Rayleigh distillation law and the silicate-melt partition coefficients compiled by Stepanov et al. (2014). The modeling qualitatively reproduces the behaviors of Nb and Ta, but it requires an unrealistic amount of mineral fractionation (>90 wt%) to reach low Nb/Ta ratios of ~2 and Nb and Ta contents of ~20 and 10 ppm, respectively (Fig. 1). The addition of 0.5 wt% Fe-Ti oxide (e.g., ilmenite or rutile) in the cumulate, in which Ta and Nb are highly compatible (Stepanov et al., 2014), makes things even worse. Indeed, the fractionation of this cumulate causes a decrease of the Nb content (Fig. 1A), resulting in a trend opposite to the trend displayed by the peraluminous granites.

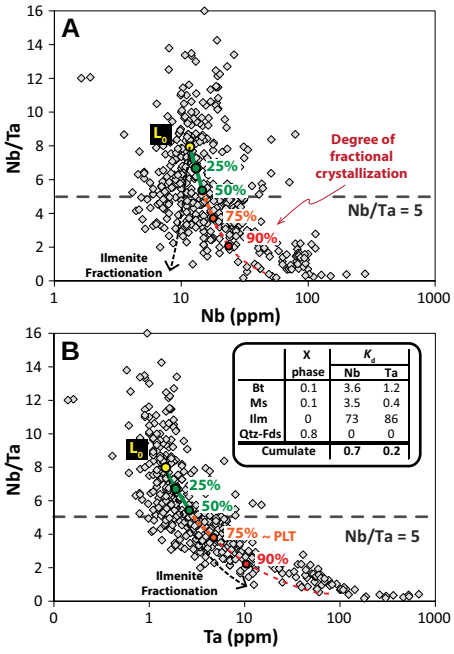

Figure 1. Nb/Ta versus Nb (A) and Ta (B) abundances for peraluminous granites. Colored curves represent model of evolution of Nb and Ta in liquid L_0 (Nb = 12 ppm, Ta = 1.5 ppm, Nb/Ta = 8) during fractionation of assemblage made of 10 wt% biotite + 10 wt% muscovite + 80 wt% (quartz + feldspar). Numbers above curves indicate amount of fractional crystallization. Black dashed line represents same model during fractionation of assemblage composed of 10 wt% biotite + 10 wt% muscovite + 0.5 wt% ilmenite + 79.5 wt% (quartz + feldspar). Bulk partition coefficient (K_d) values used and presented in inset are from Stepanov et al. (2014, and references therein). X phase—proportion of a mineral phase in the cumulate; PLT—particle locking threshold (Vigneresse et al., 1996); Bt—biotite; Ms—muscovite; Ilm—ilmenite; Qtz—quartz; Fds—feldspar.

Crystal-melt fractionation is likely to occur during the crystallization of granitic melts in magmatic bodies (Dufek and Bachmann, 2010) and during magma ascent in dikes (Tartèse and Boulvais, 2010; Yamato et al., 2015). However, numerical modeling shows that the efficiency of crystal-melt segregation in dikes is restricted to cases where crystals represent a low percentage of the total magma volume (<45%; Yamato et al., 2015). Indeed, 70%–75% crystallization marks the particle locking threshold (PLT in Fig. 1B; Vigneresse et al., 1996) where the interstitial residual melt cannot escape from the crystal framework without deformation. The extraction of low-fraction residual melts (with an amount of fractional crystallization >75%) is thus restricted to areas affected by strong shear stress such as magmatic shear zones (Vigneresse et al., 1996) and dike walls, which represent a small percentage of the granites compiled in this study (Fig. 1). The model presented here thus suggests that fractional crystallization alone is not sufficient to explain the behaviors of Nb and Ta in most peraluminous granitic rocks.

Nb-Ta Fractionation during Magmatic-Hydrothermal Processes

Mineralogical Markers

Secondary muscovitization and greisenization occur under sub-solidus conditions during the interaction between crystallized granites and acidic late magmatic fluids (Pirajno, 2013). Figure 2 shows that the Nb/Ta ratios of whole-rock granites and greisens are anti-correlated with the average $MgO/(Na_2O + TiO_2)$ ratios of the muscovite they host (a chemical marker for secondary muscovitization; Miller et al., 1981). This observed anti-correlation suggests that the fluids involved in the secondary muscovitization processes could also be responsible for the decrease of the Nb/Ta whole-rock values. Whole-rock hydrothermal enrichment of Ta during secondary muscovitization is, for example, observed in ongonites (topaz-bearing microleucogranites), and this process is associated with the crystallization of late Ta-rich overgrowth on Nb-Ta oxides (Dostal et al., 2015).

Geochemical Markers

The whole-rock Nb/Ta ratios of peraluminous granites are anti-correlated with their Sn contents, Sn being an element highly mobilized at the magmatic-hydrothermal transition (Fig. 3A): high Sn contents (30–10,000 ppm) are only encountered in granitic samples (or

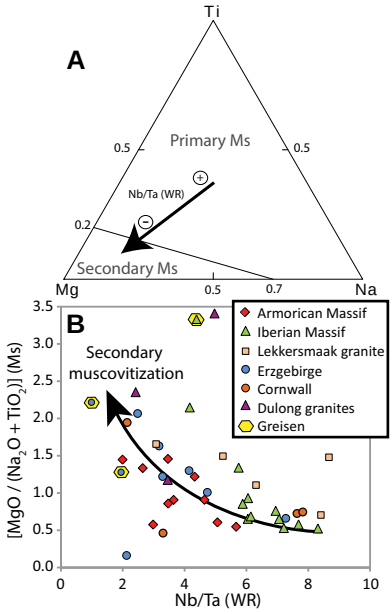

Figure 2. A: Mg-Na-Ti ternary classification diagram of muscovite (Ms) (Miller et al., 1981). B: Diagram reporting evolution of Nb/Ta ratios for whole-rock (WR) samples from different peraluminous granites against average value of $MgO/(Na_2O + TiO_2)$ ratios of their diochtaedral micas.

greisens) with low Nb/Ta (<5). These samples also display high contents of Cs (35–1000 ppm), F (>0.4%–4%), Li (250–2000 ppm), W (10–1000 ppm) and Rb (>500 ppm). Because such incompatible elements have a strong affinity for magmatic fluids, their enrichment is commonly used as a marker of a magmatic-hydrothermal alteration in highly evolved crustal granites. In Figure 3A, the Sn content of granites increases from ~10 to ~1000 ppm. During fractional crystallization, an increase by two orders of magnitude of highly incompatible elements, with a bulk partition coefficient K_d between the mineral phases and the melt close to 0, requires a degree of fractionation of up to 99 wt%. This unrealistic degree of fractionation suggests that hydrothermal processes are also involved. Such enrichments in highly incompatible elements, attributed to interaction with magmatic fluids, have been noticed in the Erzgebirge (Germany and the Czech Republic; Förster et al., 1999), in the South Mountain batholith (Nova Scotia, Canada) (e.g., Dostal and Chatterjee, 2000), and in the Armorican Massif (France; Tartèse and Boulvais, 2010; Ballouard et al., 2015).

Also, the Nb/Ta ratios correlate with the K/Rb ratios (Fig. 3B). Most granites with low Nb/Ta display K/Rb values <150, characteristic of pegmatite-hydrothermal evolution (Shaw, 1968). This tendency is observed in the South Mountain batholith, where it was interpreted as evidence for a magmatic-hydrothermal alteration (Dostal and Chatterjee, 2000).

Finally, the whole-rock Nb/Ta ratios can be compared with the degree of the tetrad effect,

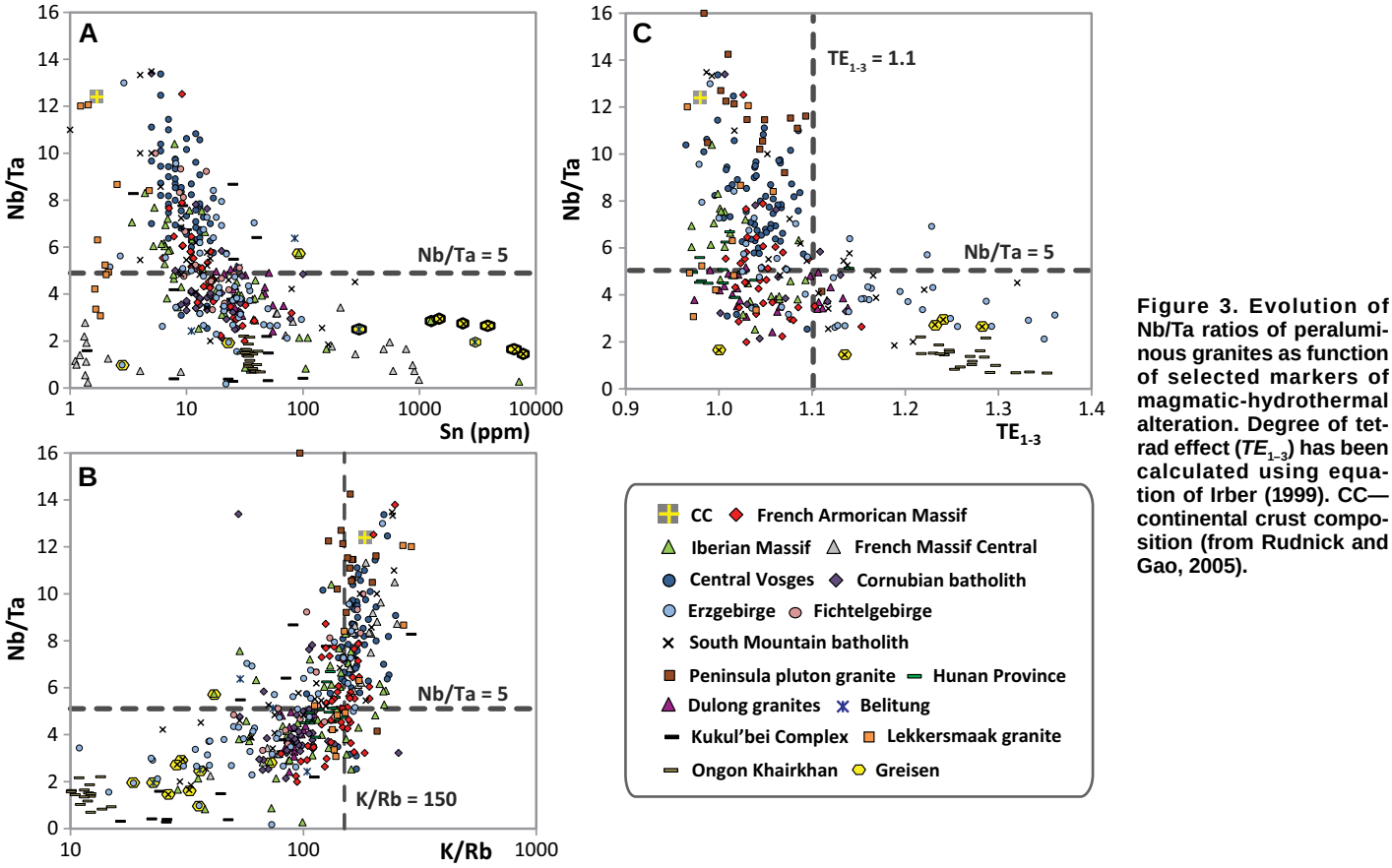

Figure 3. Evolution of Nb/Ta ratios of peraluminous granites as function of selected markers of magmatic-hydrothermal alteration. Degree of tetrad effect (TE_{1-3}) has been calculated using equation of Irber (1999). CC—continental crust composition (from Rudnick and Gao, 2005).

which corresponds to the intra-REE (rare earth element) fractionation observed in the REE patterns of highly fractionated magmatic rocks and hydrothermal precipitates (e.g., Irber, 1999). Although Duc-Tin and Keppler (2015) have recently suggested that the tetrad effect could result from monazite and xenotime fractionation, most authors have argued that such REE patterns actually reflect a selective complexation of REE during the interaction of granitic melts with F-rich and Cl-rich aqueous fluids (e.g., Bau, 1996; Irber, 1999; Monecke et al., 2007). Irber (1999) quantified the degree of tetrad effect (TE_{1-3}) by determining the deviation of the first and third tetrad of granite REE patterns from a hypothetical tetrad effect–free REE pattern. The large majority of the samples with a significant tetrad effect ($TE_{1-3} > 1.1$) are also characterized by low Nb/Ta ratios (<~5) (Fig. 3C).

Metallogenic Markers

The Nb/Ta ratio is commonly compared to the zirconium/hafnium (Zr/Hf) ratio, as the latter has been proposed as a marker of either magmatic-hydrothermal interactions (Bau, 1996) or fractional crystallization (Linnen and Keppler, 2002; Claiborne et al., 2006). The Zr/Hf ratio is a geochemical indicator of the fertility of granitic rocks, as a Zr/Hf ratio <~25 (corresponding to the lower limit of the charge and radius control [CHARAC] range; Bau, 1996) is expected in granites where Sn, W, Mo, Be, and Ta mineralization is described (Zaraisky et al., 2009). In a Nb/Ta versus Zr/Hf diagram (Fig. 4), most barren granites plot in the field defined by 26 < Zr/Hf < 46 (CHARAC range of Bau, 1996) and 5 < Nb/Ta < 16, whereas peraluminous granites associated with Sn, W, and/or U deposits have comparable Zr/Hf ratios between 18 and 46 and Nb/Ta ratios <5. Rare-metals granites are characterized by even lower Zr/Hf ratios (<18) with Nb/Ta ratios that are still <5.

From the diagrams presented in Figures 2, 3, and 4, we highlight significant mineralogical (secondary muscovitization), geochemical (Sn contents, K/Rb ratio, tetrad effect), and metallogenic (Sn-W-U and rare-metal mineralization) evidence that magmatic-hydrothermal processes account for the decrease of the Nb/Ta ratio in peraluminous granites. In reduced F-rich aqueous solutions, the solubility and hydrothermal transfer of Nb and Ta are greatly enhanced by up to three orders of magnitude with some fractionation of Nb over Ta, Ta being less soluble (Zaraisky et al., 2010). Therefore, the sub-solidus alteration of peraluminous granites leads to deposition of a mineral assemblage with Ta > Nb. Consequently, we suggest here that the decrease of the Nb/Ta ratios to values <~5 in peraluminous granites reflects the concomitant effect of fractional crystallization and sub-solidus hydrothermal alteration, likely by F-rich acidic reduced fluids of magmatic origin.

Nb/Ta ~5: A Critical Ratio for Granite Petrogenesis and Mineral Exploration Strategies

Peraluminous granites that show significant evidence of interaction with fluids (i.e., Sn and Cs contents >30 ppm and >35 ppm,

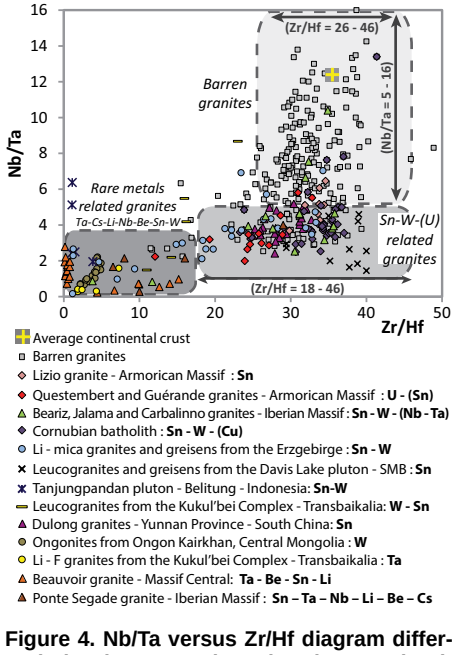

Figure 4. Nb/Ta versus Zr/Hf diagram differentiating barren and ore-bearing peraluminous granites.

respectively, K/Rb values <150, and/or TE_{1-3} > 1.1) systematically display Nb/Ta ratios <5. In such cases, we suggest that Nb/Ta of ~5 represents a threshold between a purely magmatic system (Nb/Ta > 5) and a magmatic-hydrothermal one (Nb/Ta < 5).

Finally, the use of an approximate cut-off value of 5 for the Nb/Ta ratio as a marker of the magmatic-hydrothermal transition in peraluminous granites bears some implications for exploration strategies as it can also help to define the economic potential of these granites. Figure 4 demonstrates that a Nb/Ta ratio of 5 can be used as a geochemical indicator to differentiate barren granites from granites that are spatially related to Sn-W(-U) or rare-metals mineralization. Because whole-rock trace element analyses (including Nb and Ta) are routinely performed in most laboratories around the world, the simple calculation of whole-rock Nb/Ta ratios can therefore help exploration geologists define potential targets for Sn-W(-U) and rare-metal deposits.

CONCLUSION

The mineralogical and geochemical evidence of a fluid interaction recorded in granitic whole-rock samples indicates that the value Nb/Ta of ~5 is a good marker of the magmatic-hydrothermal transition in peraluminous granites. The decrease of the Nb/Ta ratio in peraluminous granites is associated with an increase of the degree of secondary muscovitization and with geochemical and metallogenic evidence of hydrothermal interactions, suggesting that a subsolidus alteration is involved in the fractionation of Nb-Ta. To further constrain the mechanisms involved in the fractionation of the Nb/Ta ratios in peraluminous granites at the magmatic-hydrothermal transition, mineral-scale analyses would now be required. From an exploration point of view, and based on the large compilation of data presented in this study, the Nb/Ta ratio appears to be a good geochemical indicator to differentiate barren from ore-bearing peraluminous granites.

ACKNOWLEDGMENTS

Nelson Eby and two anonymous reviewers helped to improve the present version of the manuscript. We thank B. Murphy for editorial handling.

REFERENCES CITED

Badanina, E.V., Syritso, L.F., Volkova, E.V., Thomas, R., and Trumbull, R.B., 2010, Composition of Li-F granite melt and its evolution during the formation of the ore-bearing Orlovka massif in Eastern Transbaikalia: Petrology, v. 18, p. 131–157, doi:10.1134/S0869591110020037.

Ballouard, C., Boulvais, P., Poujol, M., Gapais, D., Yamato, P., Tartèse, R., and Cuney, M., 2015, Tectonic record, magmatic history and hydrothermal alteration in the Hercynian Guérande leucogranite, Armorican Massif, France: Lithos, v. 220–223, p. 1–22, doi:10.1016/j.lithos.2015.01.027.

Bau, M., 1996, Controls on the fractionation of isovalent trace elements in magmatic and aqueous systems: Evidence from Y/Ho, Zr/Hf, and lanthanide tetrad effect: Contributions to Mineralogy and Petrology, v. 123, p. 323–333, doi:10.1007/s004100050159.

Chevychelov, V.Y., Zaraisky, G.P., Borisovskii, S.E., and Borkov, D.A., 2005, Effect of melt composition and temperature on the partitioning of Ta, Nb, Mn, and F between granitic (alkaline) melt and fluorine-bearing aqueous fluid: Fractionation of Ta and Nb and conditions of ore formation in rare-metal granites [translated from Petrologiya, v. 13, no. 4, p. 339–357]: Petrology, v. 13, p. 305–321.

Claiborne, L.L., Miller, C.F., Walker, B.A., Wooden, J.L., Mazdab, F.K., and Bea, F., 2006, Tracking magmatic processes through Zr/Hf ratios in rocks and Hf and Ti zoning in zircons: An example from the Spirit Mountain batholith, Nevada: Mineralogical Magazine, v. 70, p. 517–543, doi:10.1180/0026461067050348.

Dostal, J., and Chatterjee, A.K., 2000, Contrasting behaviour of Nb/Ta and Zr/Hf ratios in a peraluminous granitic pluton (Nova Scotia, Canada): Chemical Geology, v. 163, p. 207–218, doi:10.1016/S0009-2541(99)00113-8.

Dostal, J., Kontak, D.J., Gerel, O., Shellnutt, J.G., and Fayek, M., 2015, Cretaceous ongonites (topaz-bearing albite-rich microleucogranites) from Ongon Khairkhan, Central Mongolia: Products of extreme magmatic fractionation and pervasive metasomatic fluid:rock interaction: Lithos, v. 236–237, p. 173–189, doi:10.1016/j.lithos.2015.08.003.

Duc-Tin, Q., and Keppler, H., 2015, Monazite and xenotime solubility in granitic melts and the origin of the lanthanide tetrad effect: Contributions to Mineralogy and Petrology, v. 169, 8, doi:10.1007/s00410-014-1100-9.

Dufek, J., and Bachmann, O., 2010, Quantum magmatism: Magmatic compositional gaps generated by melt-crystal dynamics: Geology, v. 38, p. 687–690, doi:10.1130/G30831.1.

Förster, H.-J., Tischendorf, G., Trumbull, R.B., and Gottesmann, B., 1999, Late-collisional granites in the Variscan Erzgebirge, Germany: Journal of Petrology, v. 40, p. 1613–1645, doi:10.1093/petroj/40.11.1613.

Goldschmidt, V.M., 1937, The principles of distribution of chemical elements in minerals and rocks: The seventh Hugo Müller Lecture delivered before the Chemical Society on March 17th, 1937: Journal of the Chemical Society, v. 1937, p. 655–673, doi:10.1039/JR9370000655.

Green, T.H., 1995, Significance of Nb/Ta as an indicator of geochemical processes in the crust-mantle system: Chemical Geology, v. 120, p. 347–359, doi:10.1016/0009-2541(94)00145-X.

Halter, W.E., and Webster, J.D., 2004, The magmatic to hydrothermal transition and its bearing on ore-forming systems: Chemical Geology, v. 210, p. 1–6, doi:10.1016/j.chemgeo.2004.06.001.

Irber, W., 1999, The lanthanide tetrad effect and its correlation with K/Rb, Eu/Eu*, Sr/Eu, Y/Ho, and Zr/Hf of evolving peraluminous granite suites: Geochimica et Cosmochimica Acta, v. 63, p. 489–508, doi:10.1016/S0016-7037(99)00027-7.

Linnen, R.L., and Keppler, H., 1997, Columbite solubility in granitic melts: Consequences for the enrichment and fractionation of Nb and Ta in the Earth's crust: Contributions to Mineralogy and Petrology, v. 128, p. 213–227, doi:10.1007/s004100050304.

Linnen, R.L., and Keppler, H., 2002, Melt composition control of Zr/Hf fractionation in magmatic processes: Geochimica et Cosmochimica Acta, v. 66, p. 3293–3301, doi:10.1016/S0016-7037(02)00924-9.

Miller, C.F., Stoddard, E.F., Bradfish, L.J., and Dollase, W.A., 1981, Composition of plutonic muscovite: Genetic implications: Canadian Mineralogist, v. 19, p. 25–34.

Monecke, T., Dulski, P., and Kempe, U., 2007, Origin of convex tetrads in rare earth element patterns of hydrothermally altered siliceous igneous rocks from the Zinnwald Sn–W deposit, Germany: Geochimica et Cosmochimica Acta, v. 71, p. 335–353, doi:10.1016/j.gca.2006.09.010.

Pirajno, F., 2013, Effects of metasomatism on mineral systems and their host rocks: Alkali metasomatism, skarns, greisens, tourmalinites, rodingites, black-wall alteration and listevenites, *in* Harlov, D.E., and Austrheim, H., eds, Metasomatism and the Chemical Transformation of Rock: Lecture Notes in Earth System Sciences: Berlin, Springer Berlin Heidelberg, p. 203–252.

Raimbault, L., Cuney, M., Azencott, C., Duthou, J.-L., and Joron, J.L., 1995, Geochemical evidence for a multistage magmatic genesis of Ta-Sn-Li mineralization in the granite at Beauvoir, French Massif Central: Economic Geology and the Bulletin of the Society of Economic Geologists, v. 90, p. 548–576, doi:10.2113/gsecongeo.90.3.548.

Rudnick, R., and Gao, S., 2005, Composition of the continental crust, *in* Holland, H.D., and Turekian, K.K., eds., Treatise on Geochemistry: Amsterdam, Elsevier, v. 3, p. 1–64.

Shaw, D., 1968, A review of K-Rb fractionation trends by covariance analysis: Geochimica et Cosmochimica Acta, v. 32, p. 573–601, doi:10.1016/0016-7037(68)90050-1.

Stepanov, A., Mavrogenes, J.A., Meffre, S., and Davidson, P., 2014, The key role of mica during igneous concentration of tantalum: Contributions to Mineralogy and Petrology, v. 167, p. 1009–1016, doi:10.1007/s00410-014-1009-3.

Tartèse, R., and Boulvais, P., 2010, Differentiation of peraluminous leucogranites "en route" to the surface: Lithos, v. 114, p. 353–368, doi:10.1016/j.lithos.2009.09.011.

Vigneresse, J.L., Barbey, P., and Cuney, M., 1996, Rheological transitions during partial melting and crystallization with application to felsic magma segregation and transfer: Journal of Petrology, v. 37, p. 1579–1600, doi:10.1093/petrology/37.6.1579.

Yamato, P., Duretz, T., May, D.A., and Tartèse, R., 2015, Quantifying magma segregation in dykes: Tectonophysics, v. 660, p. 132–147, doi:10.1016/j.tecto.2015.08.030.

Zaraisky, G.P., Aksyuk, A.M., Devyatova, V.N., Udoratina, O.V., and Chevychelov, V.Y., 2009, The Zr/Hf ratio as a fractionation indicator of rare-metal granites: Petrology, v. 17, p. 25–45, doi:10.1134/S0869591109010020.

Zaraisky, G.P., Korzhinskaya, V., and Kotova, N., 2010, Experimental studies of Ta_2O_5 and columbite–tantalite solubility in fluoride solutions from 300 to 550°C and 50 to 100 MPa: Mineralogy and Petrology, v. 99, p. 287–300, doi:10.1007/s00710-010-0112-z.

Manuscript received 29 October 2015
Revised manuscript received 26 January 2016
Manuscript accepted 27 January 2016

Printed in USA

Forum Reply

doi:10.1130/ G38169Y.1

Nb-Ta fractionation in peraluminous granites: A marker of the magmatic-hydrothermal transition

Christophe Ballouard[1], Yannick Branquet[1,2], Romain Tartèse[3], Marc Poujol[1], Philippe Boulvais[1], and Jean-Louis Vigneresse[4]

[1]Géosciences Rennes, UMR CNRS 6118, OSUR, Université Rennes 1, 35042 Rennes Cedex, France
[2]Institut des Sciences de la Terre d'Orléans (ISTO), UMR 6113 CNRS, Université d'Orléans, BRGM, Campus Géosciences, F-45071 Orléans Cedex 2, France
[3]Institut de Minéralogie, de Physique des Matériaux et de Cosmochimie, Muséum National d'Histoire Naturelle, Sorbonne Universités, CNRS, UPMC, IRD, 75005 Paris, France
[4]Université de Lorraine, UMR 7539 GéoRessources, BP 23, F-54501 Vandoeuvre Cedex, France

We thank A. Stepanov and co-authors (Stepanov et al., 2016) for giving us the opportunity to clarify some important points made in our original manuscript (Ballouard et al., 2016) and to discuss the issues raised in their Comment. In Ballouard et al. (2016), we propose that the decrease of the Nb/Ta ratios to <~5 in peraluminous granites "is the consequence of both fractional crystallization and sub-solidus hydrothermal alteration," an interpretation challenged by Stepanov et al. (2016) who argue that low Nb/Ta ratios in peraluminous granites are better explained by magmatic fractionation and that the role of magmatic-hydrothermal processes is not significant.

In their Comment, Stepanov et al. (2016) repeatedly mention "post-magmatic" alteration, implying that the fluid-rock interaction processes we propose as responsible for the decrease in the Nb/Ta ratios occurred when the bulk of the peraluminous magmas were fully crystallized. This is not the case, and we clearly define in the first sentence of our introduction ("the magmatic-hydrothermal transition separates a purely magmatic system dominated by a crystal-melt interaction from a system dominated by a crystal–melt–magmatic fluid phase interaction") that we consider sub-solidus alteration with primary magmatic fluids/brines exsolved from crystallizing melts. Also, Stepanov et al. (2016) frequently refer to mineralized pegmatites in their Comment, which are complex objects involving, for example, undercooling processes. As stated in Ballouard et al. (2016), we took care not to include pegmatite/aplite in our database and only focused on pervasive hydrothermal activity in peraluminous granites.

Stepanov et al. (2014) demonstrated, on the basis of fractional crystallization modeling, that the fractionation of biotite and muscovite will induce a decrease of the Nb/Ta ratios in granitic melts. In Ballouard et al. (2016), we did not overlook the important role of mica fractionation in the decrease of the Nb/Ta ratios, but we show that fractional crystallization alone is not sufficient to explain the behavior of Nb-Ta in most peraluminous granites. In their Comment, Stepanov et al. (2016) argue that low Nb/Ta granites contain insufficient ilmenite to counteract the decrease in Nb/Ta due to the fractionation of micas. This is likely true. However, the authors missed the major point of our argument. The results of our modeling suggest that, even during magmatic fractionation of an ilmenite-free cumulate composed of quartz, feldspar, biotite and muscovite (micas accounting for 20% of the cumulate), unrealistic amounts of fractional crystallization (>90 wt%) are needed to significantly decrease the Nb/Ta ratio from ~8 to 2. As detailed by Ballouard et al. (2016), such amounts of fractionation cannot be reached in most of the granites compiled in our study. Moreover, we would like to underline again that small magmatic bodies like pegmatite or aplite, which can reach an extreme rate of fractional crystallization, were not included in our compilation.

Stepanov et al. (2016) also point out that low abundances of "immobile elements," such as Ti, Zr, and rare earth elements (REEs), in low-Nb/Ta granites likely resulted from fractional crystallization process. We agree with this point but we would like to specify once again that in our paper we suggested that the decrease of Nb/Ta in peraluminous granites is the consequence of both fractional crystallization and sub-solidus hydrothermal alteration.

Stepanov et al. (2016) argue that fluid-rock interactions decrease Sn concentrations in granites and that a high Sn enrichment cannot be used as a marker of magmatic-hydrothermal alteration. The simple fact that greisens (i.e., granites resulting from extreme sub-solidus hydrothermal alteration) are highly enriched in Sn (up to 1 wt% Sn; see Ballouard et al., 2016, our figure 3A) refutes this assumption.

Mineralogical evidence for Ta hydrothermal enrichment exists in ongonites, but also in several rare metal granites of Southern China where hydrothermal overgrowths of tantalite are commonly observed on magmatic columbite (e.g., Zhu et al., 2015; Xie et al., 2016). For example, Zhu et al. (2015, their figure 4a) show columbo-tantalite crystals (CGM) with a CGM-I core with a columbite composition surrounded by a CGM-II rim with a tantalite composition (including some CGM-II veinlets within the CGM-I). Few experimental studies exist on Nb and Ta solubility in aqueous solution, but Ta seems to be less soluble than Nb (e.g., Zaraisky et al., 2010). Therefore, we suggest that during magmatic-hydrothermal alteration, Ta will preferentially form overgrowths around Nb-Ta–bearing minerals, whereas Nb will be carried away by fluids, resulting in a decrease of the whole-rock Nb/Ta ratios.

At the magmatic-hydrothermal transition, granitic melts exsolve large amounts of fluids with variable compositions, ranging from aqueous to hydrosaline, having a variable capacity to transport economic lithophile elements such as Nb and Ta. Many unknowns remain regarding the behavior of Nb and Ta in such systems, warranting further experimental work on this topic. However, we maintain that it is hard to account for a decrease of the Nb/Ta ratios < ~5 in peraluminous granites by magmatic fractionation alone, and that it is likely the consequence of both fractional crystallization and magmatic-hydrothermal alteration processes.

REFERENCES CITED

Ballouard, C., Poujol, M., Boulvais, P., Branquet, Y., Tartèse, R., and Vigneresse, J.-L., 2016, Nb-Ta fractionation in peraluminous granites: A marker of the magmatic-hydrothermal transition: Geology, v. 44, p. 231–234, doi:10.1130/G37475.1.

Stepanov, A., Mavrogenes, J.A., Meffre, S., and Davidson, P., 2014, The key role of mica during igneous concentration of tantalum: Contributions to Mineralogy and Petrology, v. 167, p. 1–8, doi:10.1007/s00410-014-1009-3.

Stepanov, A., Meffre, S., Mavrogenes, J.A., and Steadman, J., 2016, Nb-Ta fractionation in peraluminous granites: A marker of the magmatic-hydrothermal transition: Comment: Geology v. 44, doi:10.1130/G38086C.1.

Xie, L., Wang, R.-C., Che, X.-D., Huang, F.-F., Erdmann, S., Zhang, W.-L., 2016, Tracking magmatic and hydrothermal Nb–Ta–W–Sn fractionation using mineral textures and composition: A case study from the late Cretaceous Jiepailing ore district in the Nanling Range in South China: Ore Geology Reviews, v. 78, p. 300–321, doi:10.1016/j.oregeorev.2016.04.003.

Zaraisky, G.P., Korzhinskaya, V., and Kotova, N., 2010, Experimental studies of Ta_2O_5 and columbite–tantalite solubility in fluoride solutions from 300 to 550°C and 50 to 100 MPa: Mineralogy and Petrology, v. 99, p. 287–300, doi:10.1007 /s00710 -010-0112-z.

Zhu, Z.-Y., Wang, R.-C., Che, X.-D., Zhu, J.-C., Wei, X.-L., Huang, X.E., 2015, Magmatic–hydrothermal rare-element mineralization in the Songshugang granite (northeastern Jiangxi, China): Insights from an electron-microprobe study of Nb–Ta–Zr minerals: Ore Geology Reviews, v. 65, p. 749–760, doi:10.1016/j.oregeorev.2014.07.02.

Discussion complémentaire

1. Evidences texturales de fractionnement hydrothermal du Nb-Ta

Dans la réponse au commentaire de Stepanov et al. (2016), nous mettons l'accent sur l'existence d'évidences texturales d'enrichissement hydrothermal en Ta dans plusieurs granites à métaux rares de Chine du Sud. Sur les images en électrons rétrodiffusés de la Figure II.2, les oxydes de Nb-Ta issues de ces granites spécialisés sont caractérisés par des cœurs magmatique avec une composition de colombite (zones gris-sombres ; CGM-I) et des zonations irrégulières avec une composition de tantalite (zones gris-claires ; CGM-II). Sur la Figure II.2a, le cœur riche en Nb d'un de ces oxydes (CGM I) est recoupé par une veinule avec une composition de tantalite (flèche blanche sur la figure) alors que dans la Figure II.b, la seconde génération d'oxyde enrichie en Ta (CGM II) semble brèchifier un zircon (Zrn) et une première génération d'oxyde CGM I. De tels textures sont les témoins indéniables d'un enrichissement hydrothermal en Ta dans les derniers stades d'évolution de ces granites à métaux rares.

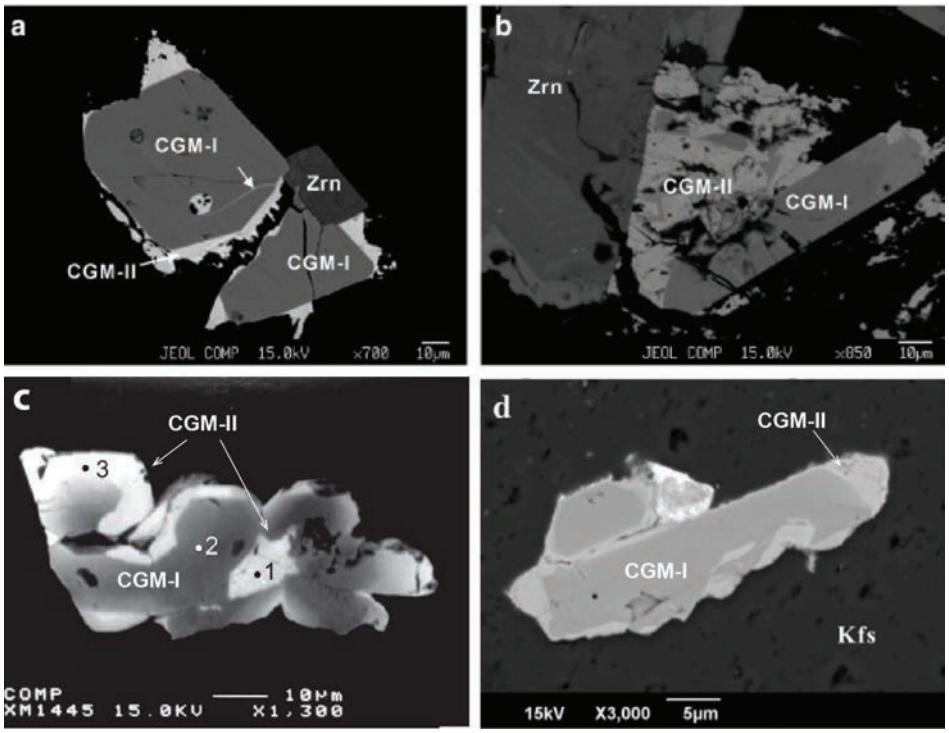

Figure II.2. : Sélections d' images en électrons rétrodiffusés de cristaux de colombo-tantalite (CGM) dans les granite à métaux rares de Songshugang (a-b: Zhu et al., 2015), Yichun (c: Huang et al., 2002) et Jiepailing (Xie et al., 2016) en Chine du Sud. Zrn : zircon ; Kfs : feldspath potassique.

2. Implication sur la pétrogenèse des CPG et des MPG

Dans le chapitre I, il est mis en évidence les différences importantes qui existent du point de vue petrogénétique entre les granites peralumineux à deux micas (MPG) et les granites peralumineux à cordiérite (CPG). Ce contraste est bien marqué dans le diagramme Nb/Ta versus Zr/Hf (Fig. II.3) où les CPG se caractérisent généralement par des valeurs de Nb/Ta > 5 et des rapports Zr/Hf entre 26 et 40,

caractéristiques des granites stériles, alors que les MPG montrent une gamme de variation beaucoup plus importante des deux rapports, située entre ~10 et 0.1 pour le Nb/Ta et ~40 et 0.1 pour le Zr/Hf, s'étendant du champ des granites stériles aux champs des granites minéralisés. Cette différence peut, tout d'abord, s'expliquer par la température, le taux de fusion partielle et les réactions de fusion dont sont issus ces deux grands types de granites peralumineux. Les CPG se forment à des températures généralement > 750°C qui vont induire la déstabilisation de la biotite et un taux de fusion partielle de l'ordre de 50 % (e.g. Clemens et Watkins, 2001). Dans ces conditions, l'abondance d'oxyde de Fe-Ti, où le Ta est plus compatible que le Nb, au résidu induit la genèse d'un magma silicaté avec un rapport Nb/Ta élevé (Stepanov et al., 2014). Au contraire, les réactions de fusion hydratées ou anhydres par déstabilisation de la muscovite dont sont issus les MPG (Barbarin, 1996; Patinño-Douce, 1999) vont laisser la biotite, où le Nb est plus compatible que le Ta, au résidu favorisant la formation d'un liquide avec un rapport Nb/Ta relativement faible. Ensuite, la richesse en eau des MPG comparée aux CPG va leur conférer une viscosité plus faible qui va favoriser le processus de cristallisation fractionnée des phases micacés, plus abondantes en parallèle dans les MPG, et des zircons induisant, respectivement, une décroissance du rapport Nb/Ta (Stepanov et al., 2014) et Zr/Hf (e.g. Claiborne et al., 2006). Pour finir, la richesse en eau des MPG va évidemment favoriser les processus magmatique-hydrothermaux qui induisent une décroissance des rapports Zr/Hf (Bau, 1996) et Nb/Ta.

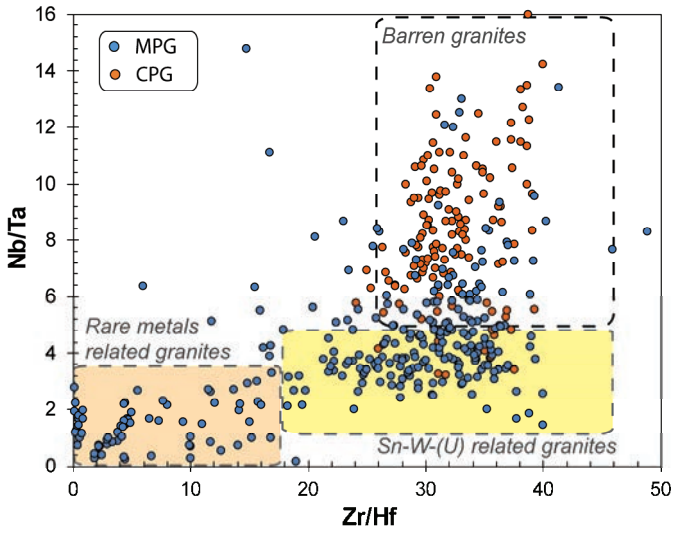

Figure II.3 : Diagramme reportant la composition roche totale en Nb/Ta et Zr/Hf des CPG et des MPG

3. Implication sur le comportement de l'U

Dans la Figure II.4, la composition en Nb/Ta des échantillons de roches totales des granites peralumineux est reportée en fonction de leur teneur en U et du rapport Th/U. Il n'existe pas de corrélation entre l'U et le rapport Nb/Ta mais on remarque tout de même une augmentation de la dispersion des points pour les faibles rapports Nb/Ta et la majorité des granites avec des teneurs en U > 10 ppm et < 3 ppm présente des rapports Nb/Ta < ~5. Ensuite, une corrélation grossière apparait entre

le rapport Nb/Ta et le rapport Th/U. Ce diagramme illustre bien la différence de comportement qui existe entre l'U et les autres éléments incompatibles avec une forte affinité pour les fluides magmatiques comme l'Sn, le W ou le Cs (cf. article #1). Une façon d'interpréter ce comportement particulier est que l'U s'enrichie en même temps que les autres éléments incompatibles pendant la cristallisation fractionnée et les processus magmatiques-hydrothermaux (e.g. Friedrich et al., 1987). Au contraire, le Th est extrait du magma durant la cristallisation fractionnée de la monazite entrainant ainsi la diminution du rapport Th/U et expliquant cette corrélation grossière observée entre les rapports Nb/Ta et Th/U. L'enrichissement en U et la diminution du rapport Th/U du liquide silicaté au cours de la différentiation a vraisemblablement permis la cristallisation d'oxydes d'uranium dans les échantillons les plus évolués (e.g. Friedrich et al., 1987 ; Cuney, 2014). Néanmoins, les oxydes d'uranium sont très instables en condition de surface et dans les fluides hydrothermaux post-magmatiques à caractère oxydant (Dubessy et al., 1987). Ainsi la forte dispersion des teneurs en U pour les faibles rapports Nb/Ta (< ~5) est probablement la conséquence d'une combinaison complexe entre enrichissement magmatique et/ou magmatique-hydrothermal permettant la cristallisation d'oxydes d'uranium suivit d'une déstabilisation de ces oxydes lors de circulations de fluides post magmatiques et/ou de l'altération de surface. Ainsi les gisements d'U sont généralement associés à des leucogranites peralumineux (MPG) avec des rapports Nb/Ta < ~5 car ce sont les plus à même à avoir pu cristalliser des oxydes d'uranium facilement lessivables par les fluides hydrothermaux (Fig. II.3). Ces processus impliqués dans la genèse de minéralisations uranifères seront discutés en détails dans la partie IV de ce manuscrit.

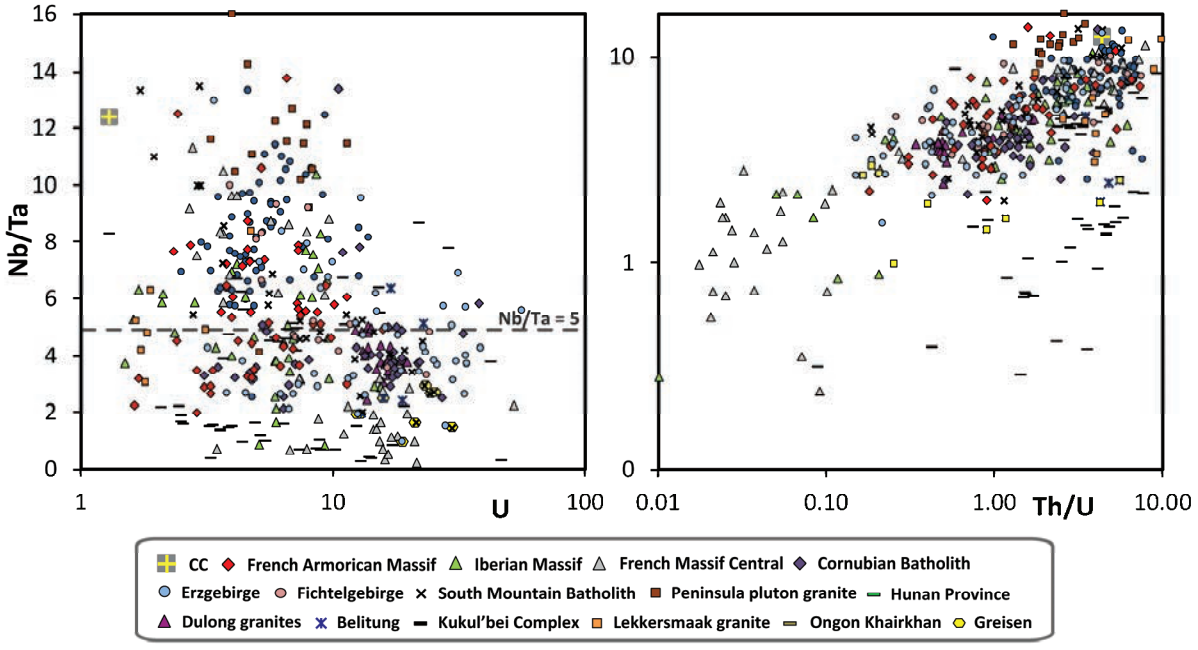

Figure II.4 : Diagrammes Nb/Ta versus U et Nb/Ta versus Th/U pour les granites peralumineux.

Location	Igneous province	Granite	Age	Related deposit		Reference
Western Europe	French Armorican Massif	Lizio	ca. 316 Ma	Sn		Tartèse and Boulvais, 2010
		Questembert	ca. 316 Ma	(U)	U leached during hydrothermal alteration	Tartèse and Boulvais, 2010; Tartèse et al., 2013
		Guérande	ca. 310 Ma	U - Sn	Apical zone facies	Ballouard et al., 2015
		Huelgat	Late Carboniferous	-		Georget, 1986
		Brignogan	Late Carboniferous	-		Georget, 1986
	Iberian massif	Ponte Segade	Late Carboniferous	Sn - Ta - Nb -Li -Be -Cs		Canosa et al., 2012
		Jalama	Late Carboniferous	Sn-W-(Nb-Ta)		Ramírez and Grundvig, 2000
		Beariz (Avion)	Late Carboniferous	-		Gloaguen, 2006
		Beariz	Late Carboniferous	Sn -W		Gloaguen, 2006
		Boboraz	Late Carboniferous	-		Gloaguen, 2006
		Carballino	Late Carboniferous	Sn-W-(Nb-Ta)		Gloaguen, 2006
		Irixo	Late Carboniferous	-		Gloaguen, 2006
		Pedrobernardo	c.a. 300 Ma	-		Bea et al., 1994
		S. Mamede de Ribatua	Hercynian	Sn-W		Nieva, 2002
		Panasqueira	Hercynian	Sn-W		Nieva, 2002
	French Massif Central	Colette	ca. 310 Ma	-		Raimbault et al., 1995
		Beauvoir	ca. 310 Ma	Ta - Be -Sn - Li		Raimbault et al., 1995
		Guéret	ca. 350 Ma	-		Rolin et al., 2006
	Cornubian Batholith	-	295-275 Ma	Sn - W – (Cu)		Chappell and Hine, 2006; Müller et al., 2006
	Erzgebirge	-	Late Carboniferous - Early Permian	Sn - U -W	Li - mica granites and greisens	Förster et al., 1999; Breiter, 2012; Štemprok et al., 2005
	Fichtelgebirge	-	Late Carboniferous - Early Permian	?		Hecht et al., 1997
	Central Vosges	-	329 - 322 Ma	-		Tabaud et al., 2015
Nova Scotia - Canada	South Mountain Batholith	-	Late Devonian	-		MacDonald et al., 1992
		Davis Lake	Late Devonian	Sn	Topaz muscovite leucogranites and greisens	Dostal and Chatterjee, 1995
South Africa	Kaapvaal Craton	Lekkersmaak granite suite	ca. 2800 Ma	-		Jaguin, 2012
	Cape Granite Suite	Peninsula pluton	556-534 Ma	-		Farina et al., 2012
South China	Hunan Province	Indosinian granites	210 – 243 Ma	?		Wang et al., 2007
	Yunnan Province	Dulong granites	ca. 90 Ma	Sn		Xu et al., 2015
Indonesia	Belitung	Tanjungpandan pluton	ca. 215 Ma	Sn - W		Schwartz and Surjono, 1990
Eastern Transbaikalia	-	Kukul'bei complex	ca. 140 Ma	W – Sn Ta	Muscovite leucogranites (phase 2) Albite-amazonite Li-F granites (phase 3)	Zaraisky et al., 2009
Central Mongolia	-	Ongon Khairkhan	Ca. 120 Ma	W	Ongonites (topaz bearing albite-rich microleucogranites	Dostal et al., 2015

Table DR1: Synthesis of the peraluminous granites reported in this study with their location, their age, their associated metal deposits when available and the corresponding reference

Partie III : Le magmatisme tardi-carbonifère du Massif armoricain et ses implications sur la géodynamique hercynienne

Préambule

De ca. 320 à 300 Ma, le Massif armoricain est soumis à un magmatisme intense qui se traduit par la mise en place de nombreux granitoïdes de compositions hétérogènes. Au sud du cisaillement sud armoricain (CSA), des magmas exclusivement crustaux formés de leucogranites peralumineux (MPG) se sont mis en place le long de zones de déformation extensive alors qu'au nord du CSA des granitoïdes de compositions peralumineuses (MPG - CPG) à métalumineuses, dont l'ascension dans la croûte supérieure a été favorisée par une tectonique décrochante, sont les témoins d'une fusion crustale et mantellique.

Les travaux présentés dans cette partie se basent sur l'étude pétro-géochimique et géochronologique du leucogranite de Guérande et du complexe magmatique de Pontivy-Rostrenen, deux intrusions tardi-carbonifères caractéristiques, respectivement, des domaines sud et centre armoricain. Cette étude vise à mieux comprendre l'évolution spatiale du magmatisme de la région et à intégrer cela à la géodynamique hercynienne. En parallèle, ce travail permet de poser un cadre métallogenique qui permettra dans la partie suivante de discuter des processus minéralisateurs en uranium qui ont pris cours dans la région. A une échelle plus globale, ces travaux participent à la compréhension des processus magmatiques et magmatique-hydrothermaux qui entrent jeu lors de la genèse des roches granitiques et permettent d'apporter des informations sur les processus de recyclage et de formation de la croute continentale dans les orogènes de collision. L'article #2 sur le leucogranite de Guérande a fait l'objet d'une publication dans la revue Lithos alors que l'article #3 sur l'intrusion composite de Pontivy-Rostrenen est soumis à Gondwana Research.

Résumé de l'article #2 : Enregistrement tectonique, histoire magmatique et altération hydrothermale dans le leucogranite hercynien de Guérande, Massif armoricain, France.

Le leucogranite de Guérande s'est mis en place à la fin du Carbonifère dans la partie sud du Massif armoricain. A l'échelle de l'intrusion, ce granite montre des hétérogénéités structurales avec une faible déformation dans la partie sud-ouest alors que la partie nord-ouest est marquée par la présence de structures extensives C/S et mylonitiques. L'orientation des veines de quartz et des filons de pegmatite ainsi que les directions de la linéation d'étirement dans le granite et son encaissant démontrent une extension E-O et N-S contemporaines. Ainsi, pendant son emplacement en régime extensif, le leucogranite de Guérande a probablement subi un partitionnement de la déformation. La partie sud-ouest de l'intrusion est caractérisée par un assemblage à muscovite-biotite, la présence de restites et d'enclaves de migmatites et une faible abondance de veines de quartz comparée aux filons de pegmatites. Au contraire, la partie nord-ouest est caractérisée par un assemblage à muscovite-tourmaline, des évidences d'albitisation, de greisenisation et une dominance de veines de quartz par rapport aux pegmatites. Ainsi, la partie sud-ouest de l'intrusion est interprétée comme sa zone d'alimentation alors que la partie nord-ouest est interprétée comme sa zone apicale. Les rapports initiaux $^{87}Sr/^{86}Sr$ élevés et les valeurs négatives

en εNd(T) des échantillons suggèrent que le leucogranite peralumineux de Guérande (A/CNK > 1.1) s'est formé via la fusion partielle de métasédiments. Dans les diagrammes d'Harker, les échantillons de leucogranite présentent des tendances évolutives continues pour des teneurs en SiO_2 qui varient entre 69.8 et 75.3 %.pds. L'évolution magmatique du leucogranite de Guérande est contrôlée par la cristallisation fractionnée du feldspath potassique, du plagioclase et de la biotite. Les échantillons de la zone apicale présentent des évidences de muscovitisation secondaire et sont caractérisés par un fort enrichissement en éléments incompatibles comme l'Sn et le Cs ainsi que des faibles valeurs en K/Rb (< 150) et en Nb/Ta (< 5). L'apex du granite a été soumis à une altération magmatique-hydrothermale diffuse. Les datations U-Th-Pb sur zircon et monazite révèlent que le leucogranite de Guérande s'est mis en place à 309.7 ± 1.3 Ma et qu'à ca. 300 Ma la mise en place de dykes leucogranitiques était synchrone de circulations hydrothermales. Cette nouvelle étude structurale, pétrologique et géochronologique permet de documenter l'évolution magmatique et hydrothermale d'une intrusion leucogranitique lors de sa mise en place en contexte d'extension crustale. De même, ce travail fournit un cadre général pour mieux comprendre les conditions de formation de certains gisements de métaux comme l'étain et l'uranium dans la chaîne hercynienne ouest européenne.

Lithos 220–223 (2015) 1–22

Contents lists available at ScienceDirect

Lithos

journal homepage: www.elsevier.com/locate/lithos

Tectonic record, magmatic history and hydrothermal alteration in the Hercynian Guérande leucogranite, Armorican Massif, France

C. Ballouard [a,*], P. Boulvais [a], M. Poujol [a], D. Gapais [a], P. Yamato [a], R. Tartèse [b], M. Cuney [c]

[a] UMR CNRS 6118, Géosciences Rennes, OSUR, Université, Rennes 1, 35042 Rennes Cedex, France
[b] Planetary and Space Sciences, The Open University, Walton Hall, Milton Keynes MK7 6AA, UK
[c] GeoRessources UMR 7359, CREGU, Campus Sciences-Aiguillettes, BP 70239, 54506 Vandoeuvre-lès-Nancy, France

ARTICLE INFO

Article history:
Received 11 July 2014
Accepted 19 January 2015
Available online 14 February 2015

Keywords:
Leucogranite petrogenesis
Geochemistry
U–Th–Pb LA-ICP-MS geochronology
Structure
Hercynian
Armorican Massif

ABSTRACT

The Guérande peraluminous leucogranite was emplaced at the end of the Carboniferous in the southern part of the Armorican Massif. At the scale of the intrusion, this granite displays structural heterogeneities with a weak deformation in the southwestern part, whereas the northwestern part is marked by the occurrence of S/C and mylonitic extensional fabrics. Quartz veins and pegmatite dykes orientations as well as lineations directions in the granite and its country rocks demonstrate both E–W and N–S stretching. Therefore, during its emplacement in an extensional tectonic regime, the syntectonic Guérande granite has probably experienced some partitioning of the deformation. The southwestern part is characterized by a muscovite–biotite assemblage, the presence of restites and migmatitic enclaves, and a low abundance of quartz veins compared to pegmatite dykes. In contrast, the northwestern part is characterized by a muscovite–tourmaline assemblage, evidence of albitization and gresenization and a larger amount of quartz veins. The southwestern part is thus interpreted as the feeding zone of the intrusion whereas the northwestern part corresponds to its apical zone. The granite samples display continuous compositional evolutions in the range of 69.8–75.3 wt.% SiO_2. High initial $^{87}Sr/^{86}Sr$ ratios and low $\varepsilon_{Nd}(T)$ values suggest that the peraluminous Guérande granite (A/CNK > 1.1) was formed by partial melting of metasedimentary formations. Magmatic evolution was controlled primarily by fractional crystallization of K-feldspar, biotite and plagioclase (An20). The samples from the apical zone show evidence of secondary muscovitization. They are also characterized by a high content in incompatible elements such as Cs and Sn, as well as low Nb/Ta and K/Rb ratios. The apical zone of the Guérande granite underwent a pervasive hydrothermal alteration during or soon after its emplacement. U–Th–Pb dating on zircon and monazite revealed that the Guérande granite was emplaced 309.7 ± 1.3 Ma ago and that a late magmatic activity synchronous with hydrothermal circulation occurred at ca. 303 Ma. These new structural, petrological and geochronological data presented for the Guérande leucogranite highlight the interplay between the emplacement in an extensional tectonic regime, magmatic differentiation and hydrothermal alteration, and provide a general background for the understanding of the processes controlling some mineralization in the western European Hercynian belt.

1. Introduction

Peraluminous leucogranites are widespread throughout orogenic belts especially those associated with continental collision (Barbarin, 1999). They formed mostly by partial melting of metasedimentary rocks buried at low crustal depths (Le Fort et al., 1987; Puziewicz and Johannes, 1988; Patiño Douce and Johnston, 1991; Patiño Douce, 1999), while their exhumation within the crust is generally favored by crustal-scale faults or shear zones (Hutton, 1988; D'lemos et al., 1992; Collins and Sawyer, 1996; Searle, 1999). Peraluminous leucogranite can display geochemical heterogeneities from the sample scale to that of the magmatic chamber. These variations can reflect several processes such as progressive partial melting, partial melting of heterogeneous metasedimentary sources (Deniel et al., 1987; Brown and Pressley, 1999), variable degree of entrainment of peritectic assemblages (Stevens et al., 2007; Clemens and Stevens, 2012), entrainment of unmelted restite (Chappell et al., 1987), magma mixing (Słaby and Martin, 2008), wall rock assimilation (Ugidos and Recio, 1993) and fractional crystallization (e.g. Tartèse and Boulvais, 2010).

During the magma ascent and its final crystallization at the emplacement site, magmatic fluids may exsolve from the melt and give rise to numerous pegmatite and quartz veins. Alteration induced by the pervasive circulation of fluids in the late stage of the leucogranites evolution can induce consequent element mobility (Dostal and Chatterjee, 1995; Förster et al., 1999; Tartèse and Boulvais, 2010).

In the Hercynian belt, peraluminous leucogranites are mostly Carboniferous in age (Bernard-Griffiths et al., 1985; Lagarde et al., 1992).

* Corresponding author. Tel.: +33 223 23 30 81.
E-mail address: christophe.ballouard@univ-rennes1.fr (C. Ballouard).

http://dx.doi.org/10.1016/j.lithos.2015.01.027
0024-4937/

They are present throughout the belt in the Bohemian Massif (Förster et al., 1999), in Cornwall (Willis-Richards and Jackson, 1989; Chen et al., 1993), in the Iberian Massif (Capdevila et al., 1973) as well as in the French Armorican and Central Massifs (La Roche et al., 1980; Lameyre, 1980; Bernard-Griffiths et al., 1985; Tartèse et al., 2011a, 2011b).

In the Armorican Massif, the peraluminous leucogranites are syntectonic (Cogné, 1966; Jégouzo, 1980) and mostly located in its southern part. They are closely associated with either strike-slip lithospheric shear zones, the so-called "South Armorican Shear Zone" (Berthé et al., 1979; Strong and Hanmer, 1981; Tartèse and Boulvais, 2010), or with extensional shear zones (Gapais et al., 1993; Turrillot et al., 2009).

The Guérande granite is one of the leucogranites emplaced in an extensional deformation zone during the Carboniferous synconvergence extension of the internal zone of the Hercynian belt (Gapais et al., 1993). The Guérande granite offers a unique opportunity to characterize the internal differentiation of a granitic pluton, and to study the relationships between crustal magmatism and (i) regional tectonics and (ii) fluid driven alteration, in the heart of the Hercynian belt. The purpose of this paper is therefore to address these different issues, based on new field descriptions and new petrological, geochemical and geochronological data. These data are the first obtained for this strategic intrusion over the last thirty years (Bouchez et al., 1981; Ouddou, 1984).

2. Geological setting

2.1. The South Armorican Massif

The southern part of the Armorican Massif (Fig. 1) belongs to the internal zone of the Hercynian orogenic belt of Western Europe. It is bounded to the north by the South Armorican Shear Zone (SASZ), a lithospheric dextral strike-slip shear zone divided into two branches (Gumiaux et al., 2004). From top to bottom, three main tectono-metamorphic units can be structurally distinguished in the South Armorican domain (Fig. 1):

- High pressure–low temperature units, represented at the top of the pile by the blueschist klippes of the Groix island and the Bois-de-Cené (1.4–1.8 GPa, 500–550 °C, Bosse et al., 2002) and at the bottom by the Vendée Porphyroid Nappe made of metamorphosed metavolcanics and black shales (0.8 GPa, 350–400 °C; Le Hébel et al., 2002). Ductile deformations, metamorphism and exhumation of these units relate to early tectonic events, around 360 Ma (Bosse et al., 2005)
- Intermediate units mostly made of micaschists affected by a Barrovian metamorphism from greenschist to amphibolite facies conditions (Bossière, 1988; Triboulet and Audren, 1988; Goujou, 1992)
- Lower units constituted by high grade metamorphic rocks comprising gneiss, granitoids and abundant migmatites related to metamorphism with PT condition of 0.8 GPa, 700–750 °C (Jones and Brown, 1990).

The Barrovian metamorphism developed during crustal thickening and was followed by a major extensional shearing event that occurred during Upper Carboniferous, around 310 Ma (Gapais et al., 1993; Burg et al., 1994; Cagnard et al., 2004; Gapais et al., 2015). Crustal extension was accompanied by the exhumation and the rapid cooling of migmatites (about 40 °C per Ma; Jones and Brown, 1990; Gapais et al., 1993). At a regional scale, the structural patterns can be described as lower crustal, migmatite-bearing, extensional domes, covered by micaschist units and overlying HP-LT units that belonged to the upper brittle crust during the Upper Carboniferous extension.

Several leucogranites (Quiberon, Sarzeau, Guérande) are intrusive within the micaschists, above migmatite bearing units and below the contact with the porphyroids (Figs. 1 and 2). On the basis of structural features and geochronological works, it has been argued that these granites were emplaced during the Upper Carboniferous extension (Gapais et al., 1993, in press; Le Hébel, 2002; Turrillot et al., 2009).

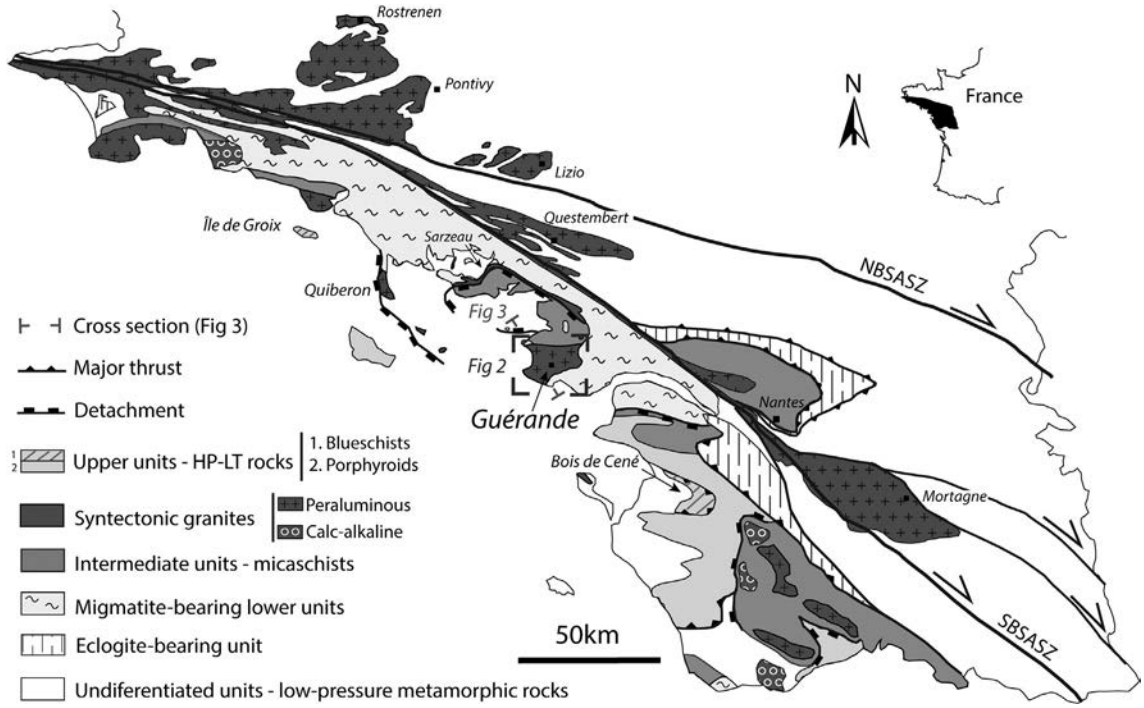

Fig. 1. Structural map of the southern part of the Armorican Massif showing the localization of the Guérande granite. Modified from Gapais et al. (1993), Gumiaux (2003), the 1/1,000,000 geological map of France (Chantraine et al., 2003) and the 1/250,000 geological map of Lorient (Proust et al., 2009). NBSASZ: Northern Branch of the South Armorican Shear Zone; SBSASZ: Southern Branch of the South Armorican Shear Zone.

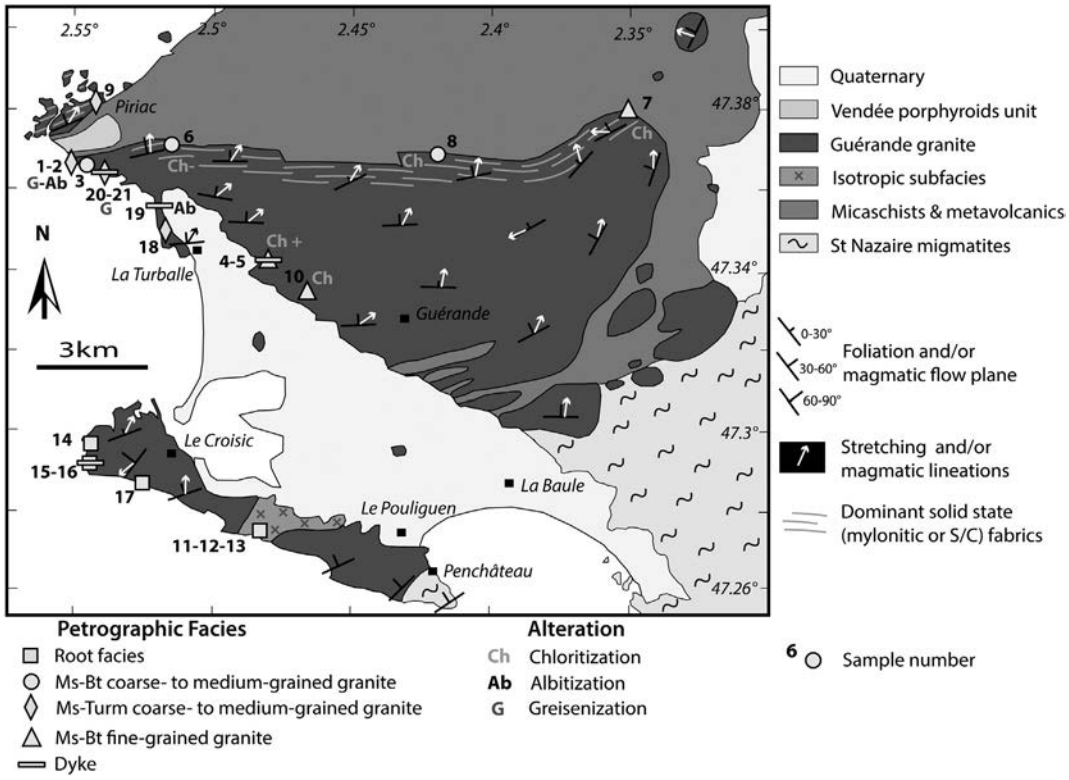

Fig. 2. Geological map of the Guérande granite modified after the 1/50,000 geological maps of La Roche Bernard (Audren et al., 1975) and St-Nazaire (Hassenforder et al., 1973). The different petrographic facies and the alteration types are reported. Sampling sites with sample numbers are also indicated. Structural data (foliation planes orientations and strikes of lineation) are from Bouchez et al. (1981) and our own observations. Mineral abbreviations are from Kretz (1983).

Several leucogranite intrusions occur also along the SASZ (Berthé et al., 1979) and present S/C structures which indicate syn-cooling shearing (Gapais, 1989). Among them, the Questembert and Lizio granites (Fig. 1), that have been dated at 316 ± 3 Ma (Tartèse et al., 2011b) and 316 ± 6 Ma (Tartèse et al., 2011a) respectively, were formed by the partial melting of Upper Proterozoic metasediments, and shared a similar magmatic history, marked by the fractionation of feldspar and biotite together with the zircon and monazite grains included in biotite (Tartèse and Boulvais, 2010).

Some giant quartz veins are also located along the SASZ, in a network of regionally distributed vertical fractures oriented N160°. Isotopic and fluid inclusion studies suggest that the fluids involved originated both from the exhuming lower crust and downward meteoric circulation (Lemarchand et al., 2012). These authors interpreted these veins as giant tension gashes and proposed that these veins attest for crustal-scale fluid circulation during the exhumation of the lower crust and the concomitant regional strike-slip deformation.

2.2. Previous studies on the Guérande granite

The Guérande leucogranite (Figs. 2 and 3), a ca. 1 km thick 3-D blade shaped structure dipping slightly northward (Bouchez et al., 1981; Vigneresse, 1983), was emplaced along an extensional deformation zone (Gapais et al., 1993). To the north, the granite presents an abrupt contact with micaschists and metavolcanics that recorded a contact metamorphism as demonstrated by the presence of staurolite and garnet (Valois, 1975). To the southwest, the contact is different and presents a progressive evolution with the Saint-Nazaire migmatites, which may represent the source of the Guérande granite (Bouchez et al., 1981). Several enclaves of micaschists occur within the granite and a "kilometer-size" body of isotropic subfacies crosscuts its southwestern edge (Figs. 2 and 3). Within the granite, the foliations are generally weakly expressed and basically of magmatic type. They dip generally 20–30° northward and bear weak dip-slip mineral lineations (Fig. 2). The southwestern part of the intrusion is also characterized by magmatic- or migmatitic-like foliations and mineral lineations. In contrast, S/C fabrics affect its northern edge (Bouchez et al., 1981). The occurrences of migmatites to the south, below the intrusion, and of micaschists to the north above it, underline that the southwestern part corresponds to the base of the granite and the northwestern part to its roof (Bouchez et al., 1981). By shearing, the top-to-the-north extensional deformation zone (Figs. 2 and 3) likely induced translation of the upper part of the granitic body. As a consequence, both the root zone in the southwestern part and the apical zone in the northwestern part are exposed to the surface today. The general shape of the intrusion as it appears today (thin laccolith intrusion with a large horizontal extension) likely relates to this peculiar tectonic context at the time of emplacement.

A fluid-inclusions study performed on quartz veins occurring near the roof of the Guérande granite reveals that it was probably emplaced at shallow depth (around 3 km; Le Hébel et al., 2007). An extensional graben (the so-called "Piriac synform"; Valois, 1975), where rocks from the HP-LT upper unit (Vendée porphyroid unit) crop out (Fig. 3), affects the northwestern part of the granite. Valois (1975) and Cathelineau (1981) interpreted this structure as the result of roof collapse of the intrusion.

Although its age is not well constrained yet, the Guérande granite was emplaced during the Upper Carboniferous: muscovite $^{40}Ar/^{39}Ar$ data yielded dates of 307 ± 0.3 Ma for an undeformed sample that could be interpreted as a cooling age and 304 ± 0.6 Ma for a mylonitized sample which could represent the age of the deformation (Le Hébel, 2002). Le Hébel (2002) also reported $^{40}Ar/^{39}Ar$ dates of 303.3 ± 0.5 Ma obtained on muscovite grains from a quartz vein intrusive within the Guérande granite and 303.6 ± 0.5 Ma for a sheared granite sample.

3. Field description and sampling

Since the Guérande granite is largely covered by salt marsh (Fig. 2), it crops out only in a few inland quarries and along the coastline. Overall,

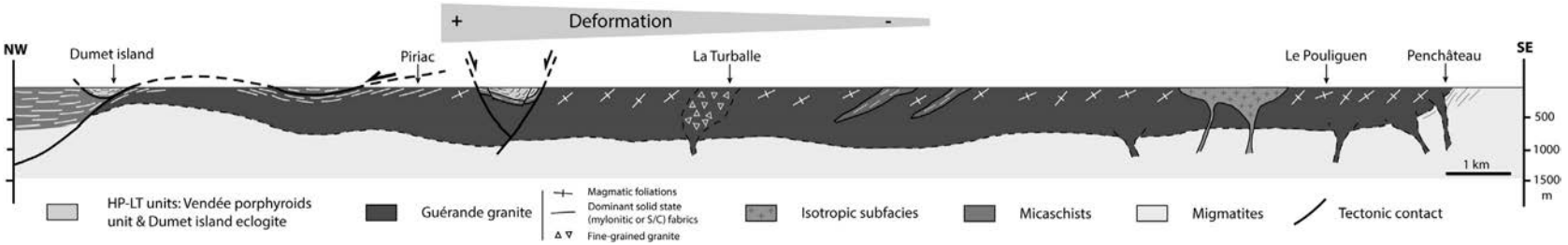

Fig. 3. Simplified cross section of the Guérande granite. The localization of the cross section is in Fig. 1. Modified after Bouchez et al. (1981).

these coastal outcrops are of good quality and are therefore suitable for establishing cross sections from the southwestern to the northwestern parts of the intrusion.

3.1. Petrographic zonation within the Guérande granite

At the scale of the intrusion, the Guérande granite displays petrographic heterogeneities with variable proportions of muscovite, biotite and tourmaline (Fig. 2). The southwestern part of the pluton is characterized by a muscovite–biotite assemblage (Fig. 4a) whereas the northwestern part is characterized by a muscovite–tourmaline assemblage (Fig. 4b). Moreover, numerous meter-size zones of isotropic granite (I granite in Fig. 4c), as well as enclaves of restites and migmatites are present in the southwestern part of the granite, whereas greisens and albitized rocks occur in the northwestern part (Fig. 2). These observations, together with the fact that the foliation dips northward, are consistent with the zonation of the pluton, the southwestern part corresponding to the feeding zone of the granite whereas the northwestern part corresponds to the apical zone which typically concentrates the hydrothermal activity.

3.2. Structures and dykes

The central and southwestern parts of the intrusion display magmatic and roughly defined foliations (Fig. 4a and d) whereas S/C structures and mylonites (Fig. 4e) occur along the northern edge. This strain localization, responsible for the development of solid state fabrics, occurred to the north, at the roof of the pluton, in association with the extensional deformation zone which caps the Guérande granite (Figs. 2 and 3).

In the granite, the lineation dips generally northward but a significant scattering exists (Fig. 2). To the northwest, at the roof of the granite, dip-slip type lineations (Fig. 5a) associated with top to the north S/C fabrics occur. However, the adjacent country-rocks show evidence of E–W stretching, with outcrop-scale tilted blocks and rocks affected by a contact metamorphism bearing E–W elongated patches of retrogressed cordierite (Fig. 5b).

Many pegmatitic dykes (Fig. 4c) together with a few aplitic dykes and quartz veins (Fig. 4f) crosscut the Guérande granite. To the northwest, pegmatites are biotite-free and contain muscovite ± tourmaline whereas, to the south-west, the pegmatites are biotite-bearing. These differences in the pegmatite compositions mimic the petrographic heterogeneities previously described for the pluton (i.e., biotite is absent to the north-west and present to the south-west while tourmaline appears only in the northwestern part of the intrusion). Fig. 5 shows the strike directions for 180 of these dykes and veins in three different locations. In the northernmost area (Piriac) located close to the roof of the intrusion and associated, in part, with the mylonitized granite (Fig. 4e), the pegmatites contain a Qtz–Fsp–Ms assemblage. Quartz veins are less present than pegmatites (Fig. 5c). The strike of the dykes and veins in this zone is mostly oriented N110°—N140° and is nearly perpendicular to the strike of the lineation recorded in the granite. Further to the south, close to La Turballe, pegmatitic dykes contain a Qtz–Fsp–Ms ± Turm assemblage. The proportion of pegmatite dykes over quartz veins (Fig. 5d) is comparable to that in Piriac. In this area, dykes are mainly oriented N160°—N170° and are slightly oblique to the strike of the lineation in the granite. In the southernmost area (Le Croisic), pegmatite dykes contain a Qtz–Fsp–Ms ± Bt assemblage and appear in a greater proportion than quartz veins (Fig. 5e). Dykes in this zone strike dominantly N000°–N020°, i.e. roughly parallel to the strike of the lineation in the granite. In most parts of the intrusion, the dykes and veins record an E–W stretching, which is different from that recorded by the granite itself, although a significant scattering of the lineations is observed (Fig. 2).

3.3. Sampling and samples

A sampling strategy was developed in order to take into account the petrographic variability observed in the field at the scale of the intrusion. For this purpose, we targeted all the inland ancient quarries in

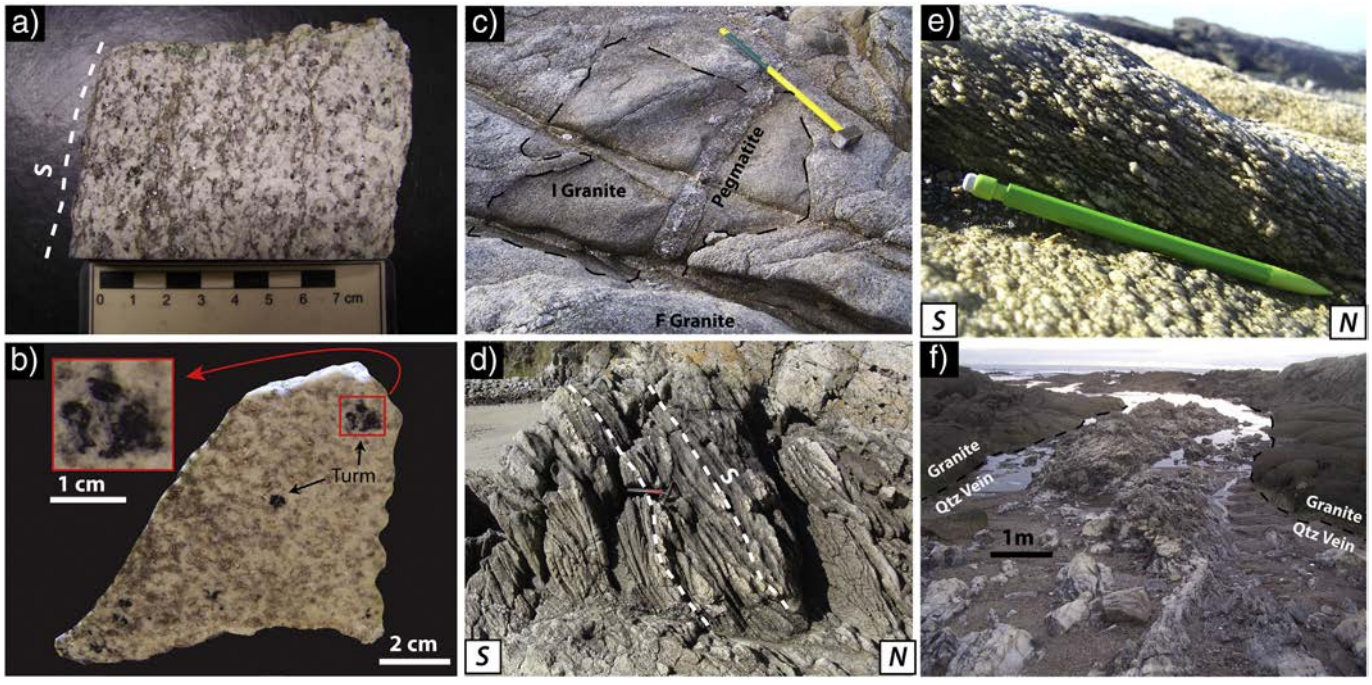

Fig. 4. Representative pictures from the southwestern part (a, c, d) and the northwestern part (b, e, f) of the Guérande granite. a) Ms–Bt bearing root facies (sample GUE-13). The roughly defined foliation (S) is marked by muscovite and biotite stretching. b) Ms–Turm coarse- to medium-grained granite (sample GUE-18). c) Typical outcrop of the root facies with granite marked by a roughly defined foliation (F Granite) and a zone of isotropic granite (I Granite). Both facies are crosscut by a pegmatite dyke. d) Root facies with a roughly defined foliation (S). e) Mylonitic S/C granite (sample GUE-9). f) Large quartz vein cross cutting Ms–Turm coarse- to medium-grained granite near the contact with the micaschists and metavolcanics.

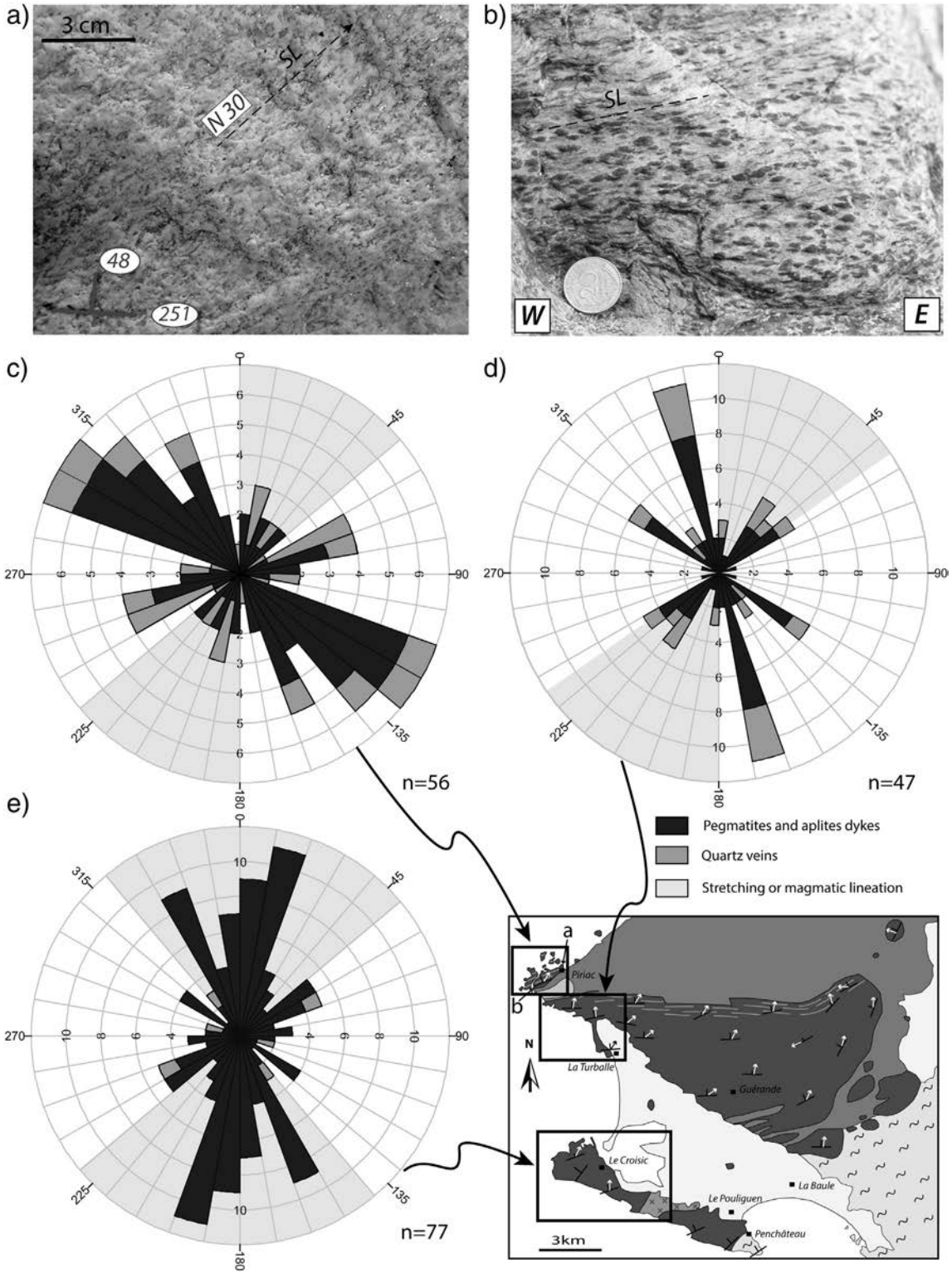

Fig. 5. a–b) Pictures of stretching lineation (SL) in the Guérande massif: d) N030° stretching lineation in the mylonitic S/C sample GUE-9, e) E–W stretching lineation marked by contact metamorphism minerals in the micaschists localized at the contact with the Guérande granite. Both pictures are localized on the map. (c–d–e) Rose diagram displaying the strikes of pegmatites, aplite dykes and quartz veins of three strategic areas from the south-west to the north-west of the Guérande granite. The numbers inside the diagrams (horizontal and vertical axes) represent the amount of measured dykes displaying a range of strike. The light gray areas represent the main strike of lineation (most of the lineation data are from Bouchez et al., 1981). n: number of measured dykes.

addition to the outcrops available along the coast. A total of 21 samples were collected.

All the samples contain a Qtz–Kfs–Pl–Ms assemblage (Fig. 6a) with a variable amount of Bt and Turm. Quartz is normally anhedral, commonly forms polycrystalline cluster (Fig. 6b) and some grains show undulose extinction characteristic of intracrystalline deformation. The alkali feldspar is generally anhedral and some grains display Carlsbad twining and rare string-shaped sodic perthitic exsolutions.

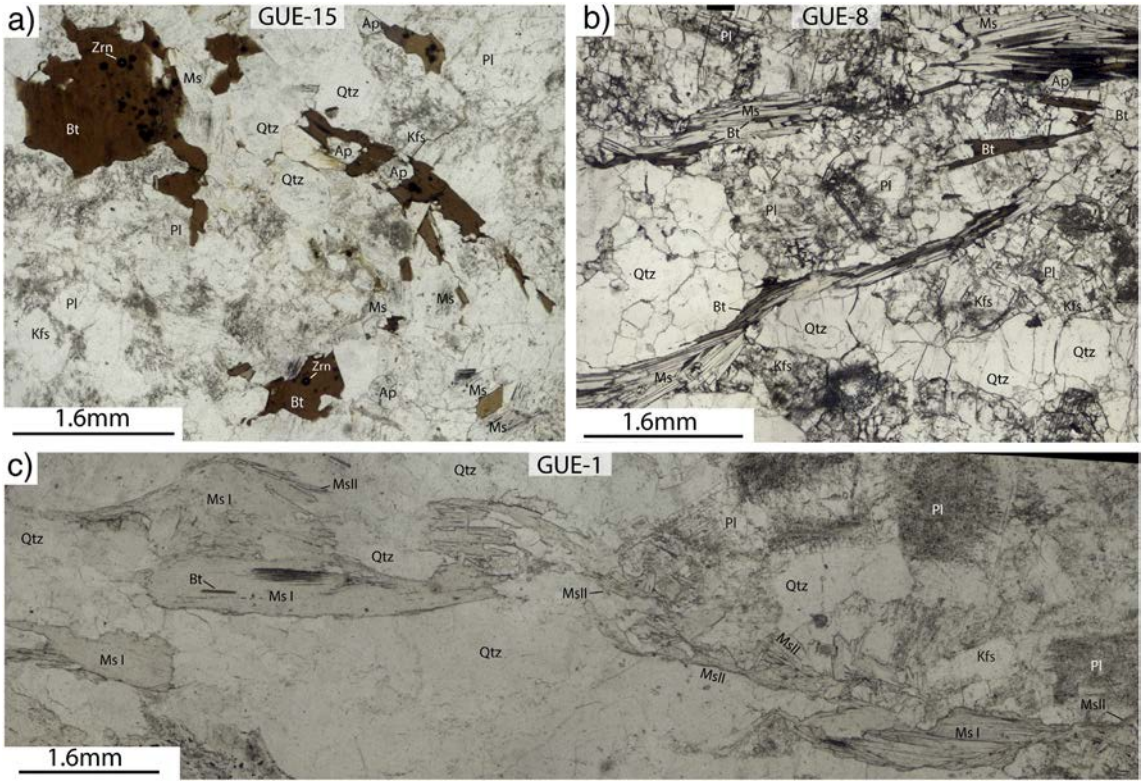

Fig. 6. Thin section photomicrographs showing the different petrographic facies of the Guérande granite. a) Root facies (Bt > Ms), b) Ms–Bt coarse- to medium grained granite (Ms > Bt) and c) Ms–Turm coarse- to medium-grained with two generation of Ms (MsI: primary muscovite; MsII: secondary muscovite). Mineral abbreviation from Kretz (1983).

The plagioclase is anhedral to sub-euhedral, shows polysynthetic twinning and can be associated with myrmekites. Muscovite is generally euhedral, flake shaped and occur also with a fish-like habit (Ms I in Fig. 6c). Fine-grained secondary muscovite can be abundant in some facies. It developed as sericite inclusion in feldspar, as small grains around coarse primary muscovite or within foliation planes (Ms II in Fig. 6c). Biotite is brown, sub-euhedral to euhedral and commonly appears as intergrowth within muscovite flakes (Fig. 6b). Biotite hosts most of the accessory minerals such as apatite, Fe–Ti oxide, zircon and monazite (Fig. 6a).

The 21 samples have been divided into five different groups, based on their respective petrographic characteristics (see Table 1, and sample location on Fig. 2):

(1) The *root facies* (southern part of the intrusion) is heterogeneous and includes facies marked by a roughly defined foliation (Fig. 4a and d) and zones of fine- to medium-grained isotropic granites (0.5–3 mm; Fig. 4c). In the root facies, muscovite is normally more abundant than biotite and this facies contains numerous accessory minerals (Fe–Ti oxide, apatite, zircon and

Table 1
GPS coordinates and simplified petrographic description of the Guérande granite samples. Ms–Bt: Ms–Bt coarse- to medium-grained granite; Ms–Turm: Ms–Turm coarse- to medium-grained granite; Fine: Ms–Bt fine-grained granite; Root: root facies; Ch: chloritization; Ab: albitization; G: greisenization.

Sample	Longitude (°)	Latitude (°)	Facies	Texture	Strain	Mineralogy	Alteration
GUE-11	−2.484200	47.274183	Root	Medium-grained (2 mm), roughly defined foliation	+	Ms > > Bt	
GUE-12	−2.484200	47.274183	Root	Fine- to medium-grained (1–3 mm), isotropic		Ms > Bt	
GUE-13	−2.484533	47.274367	Root	Medium-grained (2–3 mm), roughly defined foliation	+	Ms > > Bt	
GUE-14	−2.546383	47.296217	Root	Fine-grained (1 mm), isotropic		Ms > Bt	
GUE-15	−2.546417	47.291733	Root	Medium-grained (2–3 mm), roughly defined foliation		Bt > Ms	
GUE-17	−2.526550	47.286967	Root	Fine-grained (1–2 mm), solid state fabric	+	Ms > > Bt > Grt	
GUE-3	−2.547297	47.368122	Ms–Bt	Medium-to coarse grained (2–4 mm), magmatic foliation	+	Ms > Bt	
GUE-6	−2.515918	47.370945	Ms–Bt	Medium- to fine-grained (1–3 mm), S/C fabric	++	Ms > Bt	
GUE-8	−2.417652	47.368925	Ms–Bt	Coarse-grained (3–5 mm), isotropic		Ms > Bt	Ch −
GUE-1	−2.552081	47.369195	Ms–Turm	Coarse-grained (3–5 mm), magmatic foliation	+	Ms > > Turm > Bt	
GUE-2	−2.552081	47.369195	Ms–Turm	Coarse-grained (3–4 mm), shear zone	++	Ms > > Turm	Ab −
GUE-9	−2.548596	47.381192	Ms–Turm	Fine- to medium-grained (<0.5–2 mm), S/C mylonite	+++	Ms > > Turm	
GUE-18	−2.517417	47.350167	Ms–Turm	Medium- to coarse-grained (2–3 mm), isotropic		Ms > > Bt > Turm	
GUE-21	−2.541317	47.365750	Ms–Turm	Coarse-grained (3–5 mm), magmatic foliation	+	Ms > > Turm	G?
GUE-4	−2.481191	47.342346	Fine	Fine-grained (0.5–2 mm), isotropic		Ms > Bt	
GUE-7	−2.346883	47.380000	Fine	Fine-grained (0.5–2 mm), solid state fabric	+	Ms > Bt	Ch
GUE-10	−2.466283	47.334767	Fine	Fine-grained (1–2 mm), isotropic		Ms > Bt	Ch
GUE-5	−2.481191	47.342346	Dyke	Medium-grained (2 mm), isotropic		Ms > > Bt	Ch +
GUE-16	−2.546417	47.291733	Dyke	Fine-grained (1–2 mm), isotropic		Ms = Bt	
GUE-19a	−2.520933	47.356367	Dyke	Aplitic texture (0.5–1 mm), shear zone	++	Ms > Turm > Grt	Ab +
GUE-19b	−2.520933	47.356367	Dyke	Aplitic texture (0.5–1 mm), shear zone	++	Ms > Bt > Turm	Ab
GUE-20	−2.544000	47.366067	Dyke	Aplitic texture (0.5–1 mm), isotropic		Ms	Ab − ?

monazite) (Fig. 6a). Small garnet grains occur in sample GUE-17 (Table 1).

(2) The *Ms–Bt coarse- to medium-grained granite* (3–5 mm) represents the most common facies in the intrusion. The muscovite is commonly coarse (>1 mm) and is more abundant than biotite (<1 mm, Fig. 6b). Fine secondary muscovite (<1 mm) is rarely observed inside the foliation.

(3) The *Ms–Turm coarse- to medium-grained granite* (3–5 mm) occurs only in the northwestern part of the intrusion (apex, Fig. 2). Tourmaline (<5%) is normally several millimeters long, green brown in color, presents coarse cracks and hosts inclusions of quartz and feldspar. Fine secondary muscovite (<1 mm) is abundant in this facies (Fig. 6c) where it occurs inside foliation planes or around coarse primary muscovite flakes (>1 mm). Biotite is rare and generally appears as inclusions inside primary muscovite crystals (Fig. 6c).

(4) The *Ms–Bt fine-grained granite* (0.5–2 mm) occurs mainly near La Turballe and in the northeastern extremity of the intrusion. Ouddou (1984) has reported some occurrences of this facies in the eastern and the southwestern parts. Bouchez et al. (1981) interpreted this facies as kilometer thick dykes (Fig. 3), but the existence of mingling features at the contact between this fine-grained facies and the coarse- to medium-grained granites suggests that they are contemporaneous (Ouddou, 1984). In this granite, perthitic orthoclase is common and muscovite is more abundant than biotite. This facies contains numerous monazite grains.

(5) *Granitic meter-thick dykes* have been sampled in different locations within the intrusion. They normally show similar mineralogical and textural features, and commonly display an aplitic texture (Table 1).

Chloritization, albitization and greisenization occur at different locations in the Guérande intrusion (Table 1 and Fig. 2). Chloritization of biotite is visible at the microscopic scale and is localized to the northern central part of the granite (Fig. 2). The chlorite commonly hosts small (<50 μm) highly pleochroic anhedral grains, likely anatase. Albitization is linked to shear zones and results in a greater proportion of albite relative to quartz and micas; it may be discrete (sample GUE 2) or more intense (sample GUE 19a). Garnet is present in the albitized sample GUE-19a (Table 1). Meter-scale greisenization occurs and both albitization and greisenization are restricted to the northwestern part of the Guérande granite (Fig. 2).

4. Analytical techniques

4.1. Mineral compositions

Mineral compositions were measured using a Cameca SX-100 electron microprobe at IFREMER, Plouzané, France. Operating conditions were a 15 kV acceleration voltage, a beam current of 20 nA and a beam diameter of 5 μm. Counting times were approximately 13–14 s. For a complete description of the analytical procedure and the list of the standards used, see Pitra et al. (2008).

4.2. Major and trace-elements analyses

Large samples (5 to 10 kg) were crushed following a standard protocol to obtain adequate powder fractions using agate mortars. Chemical analyses were performed by the Service d'Analyse des Roches et des Minéraux (SARM; CRPG-CNRS, Nancy, France) using a ICP-AES for major-elements and a ICP-MS for trace-elements following the techniques described in Carignan et al. (2001).

4.3. Isotopic analyses

Sm–Nd and Sr isotopic values were determined on whole-rock samples. All the analyses were carried out at the Géosciences Rennes Laboratory using a 7 collectors Finnigan MAT-262 mass spectrometer. Samples were spiked with a ^{149}Sm-^{150}Nd and ^{84}Sr mixed solution and dissolved in a HF-HNO_3 mixture. They were then dried and taken up with concentrated HCl. In each analytical session, the unknowns were analyzed together with the Ames Nd-1 Nd or the NBS-987 Sr standards, which during the course of this study yielded an average of 0.511956 (±5) and 0.710275 (±10) respectively. All the analyses of the unknowns have been adjusted to the long-term value of $^{143}Nd/^{144}Nd$ value of 0.511963 for Ames Nd-1 and reported $^{87}Sr/^{86}Sr$ values were normalized to the reference value of 0.710250 for NBS-987. Mass fractionation was monitored and corrected using the value $^{146}Nd/^{144}Nd = 0.7219$ and $^{88}Sr/^{86}Sr = 8.3752$. Procedural blanks analyses yielded values of 400 pg for Sr and 50 pg for Nd and are therefore considered to be negligible.

4.4. U–Th–Pb analyses

A classic mineral separation procedure has been applied to concentrate minerals suitable for U–Th–Pb dating using the facilities available at Géosciences Rennes. Rocks were crushed and only the powder fraction with a diameter of <250 μm has been kept. Heavy minerals were successively concentrated by Wilfley table and heavy liquids. Magnetic minerals were then removed with an isodynamic Frantz separator. Zircon and monazite grains were carefully handpicked under a binocular microscope and embedded in epoxy mounts. The grains were then hand-grounded and polished on a lap wheel with a 6 μm and 1 μm diamond suspension successively. Zircon grains were imaged by cathodoluminescence (CL) using a Reliotron CL system equipped with a digital color camera available in Géosciences Rennes, whereas monazite grains were imaged using the electron microprobe facility in IFREMER, Brest.

U–Th–Pb geochronology of zircon and monazite was conducted by in-situ laser ablation inductively coupled plasma mass spectrometry (LA-ICPMS) at Géosciences Rennes using a ESI NWR193UC excimer laser coupled to a quadripole Agilent 7700x ICP-MS equipped with a dual pumping system to enhance sensitivity. The instrumental conditions are reported in Table 2.

Table 2
Operating conditions for the LA-ICP-MS equipment.

Laser-ablation system ESI NWR193UC	
Laser type/wavelength	Excimer 193 nm
Pulse duration	<5 ns
Energy density on target	~7 J/cm^2
ThO^+/Th^+	<0.5%
He gas flow	~800 ml/min
N_2 gas flow	4 ml/min
Laser repetition rate	3–5 Hz (zircon);1–2 Hz (monazite)
Laser spot size	26–44 μm (zircon); 20 μm (monazite)
ICP-MS Agilent 7700x	
RF power	1350 W
Sampling depth	5.0–5.5 mm (optimized daily)
Carrier gas flow (Ar)	~0.85 l/min (optimized daily)
Coolant gas flow	16 l/min
Data acquisition protocol	Time-resolved analysis
Scanning mode	Peak hopping, one point per peak
Detector mode	Pulse counting, dead time correction applied, and analog mode when signal intensity >~10^6 cps
Isotopes determined	^{204}(Hg + Pb), ^{206}Pb, ^{207}Pb, ^{208}Pb, ^{232}Th, ^{238}U
Dwell time per isotope	10 ms (30 ms for ^{207}Pb)
Sampler, skimmer cones	Ni
Extraction lenses	X type

The ablated material was carried into helium, and then mixed with nitrogen and argon, before injection into the plasma source. The alignment of the instrument and mass calibration was performed before each analytical session using the NIST SRM 612 reference glass, by inspecting the ^{238}U signal and by minimizing the ThO^+/Th^+ ratio (<0.5%). During the course of an analysis, the signals of $^{204}(Pb + Hg)$, ^{206}Pb, ^{207}Pb, ^{208}Pb and ^{238}U masses were acquired. The occurrence of common Pb in the sample can be monitored by the evolution of the $^{204}(Pb + Hg)$ signal intensity, but no common Pb correction was applied owing to the large isobaric interference with Hg. The ^{235}U signal is calculated from ^{238}U on the basis of the ratio $^{238}U/^{235}U = 137.88$. Single analyses consisted of 20 s of background integration, followed by a 60 s integration with the laser firing and then a 10 s delay to wash out the previous sample. Ablation spot diameters of 26–44 μm and 20 μm with repetition rates of 3–5 Hz and 1–2 Hz were used for zircon and monazite, respectively. Data were corrected for U–Pb and Th–Pb fractionation and for the mass bias by standard bracketing with repeated measurements of the GJ-1 zircon (Jackson et al., 2004) or the Moacir monazite standards (Gasquet et al., 2010). Repeated analyses of 91500 zircon (1061 ± 3 Ma (n = 20)); (Wiedenbeck et al., 1995) or Manangoutry monazite (554 ± 3 Ma (n = 20); Paquette and Tiepolo, 2007) standards treated as unknowns were used to control the reproducibility and accuracy of the corrections. Data reduction was carried out with the GLITTER® software package developed by the Macquarie Research Ltd. (Jackson et al., 2004). Concordia ages and diagrams were generated using Isoplot/Ex (Ludwig, 2001). All errors given in Supplementary Tables 1 and 2 are listed at one sigma, but where data are combined for regression analysis or to calculate weighted means, the final results are provided with 95% confidence limits.

5. Mineralogical composition

Five samples from the Guérande granite representative of the different petrographic varieties have been selected for chemical analyses on feldspar, biotite and muscovite. These are two Ms–Bt coarse- to medium-grained granite (GUE-3 and GUE-8), one Ms–Turm coarse- to medium-grained granite (GUE-1), one Ms–Bt fine-grained granite (GUE-4) and one granitic dyke (GUE-5).

5.1. Feldspar and biotite (Supplementary Table 3)

Plagioclase chemical compositions display a well-defined trend in the Ab–An–Or ternary diagram (Fig. 7a). The plagioclase calcium contents decrease from the Ms–Bt fine-grained granite (GUE-4; An = 0.09) to the Ms–Turm coarse- to medium-grained granite (GUE-1; An = 0.02), whereas the Ms–Bt coarse- to medium-grained granites and the dyke display intermediate contents (An = 0.07–0.05). In alkali feldspar, the potassium content is merely constant (Or = 0.90–0.93) irrespective of the petrographic facies.

Biotite displays typical chemical composition for peraluminous granites with an elevated content in Al (Al_{TOT} > 3.5 pfu; Nachit et al., 1985) and X_{Mg} = 0.27–0.28. GUE-3 displays a lower Mg content (X_{Mg} = 0.22).

5.2. Muscovite (Supplementary Table 4)

Muscovite grains in the Ms–Bt fine-grained granite (GUE-4) and the granitic dyke (GUE-5) fall in the primary muscovite field defined by Miller et al. (1981) and display homogenous Mg content (Fig. 7b). The Mg content of the muscovite grains increases in the other samples and

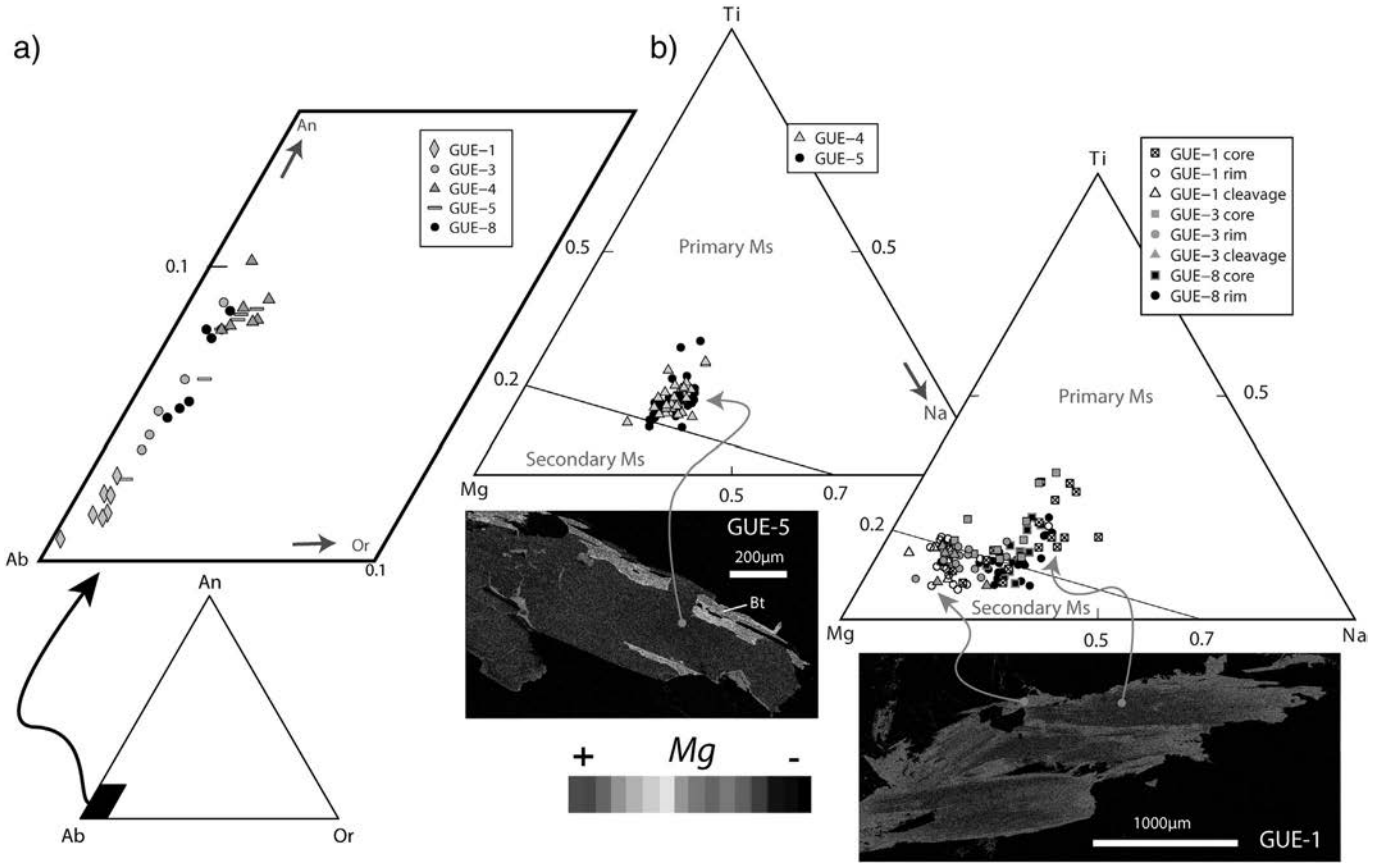

Fig. 7. Chemical compositions of plagioclase and muscovite from the Guérande granite. a) Triangular classification of plagioclase. b) Ternary Ti–Na–Mg diagram for muscovite and chemical map of Mg distribution in muscovite for the Ms–Turm granite sample GUE-1 and the Ms-Bt granite dyke GUE-5. The primary and secondary fields of muscovite are from Miller et al. (1981). In figure the inset "cleavage" refers to small muscovite grains located within foliation planes.

Table 3
Whole-rock chemical compositions of the Guérande granite samples. Root: root facies; Ms–Bt: Ms–Bt coarse- to medium-grained granite; Ms–Turm: Ms–Turm coarse- to medium-grained granite; Fine: Ms–Bt fine-grained granite; LOI: Loss on ignition; A/NK: molar $Al_2O_3/(Na_2O + K_2O)$; A/CNK: molar $Al_2O_3/(CaO + Na_2O + K_2O)$; bdl: below detection limit.

Sample		GUE-11	GUE-12	GUE-13	GUE-14	GUE-15	GUE-17	GUE-3	GUE-6	GUE-8	GUE-1	GUE-2	GUE-9	GUE-18	GUE-21	GUE-4	GUE-7	GUE-10	GUE-5	GUE-16	GUE-20	GUE-19a	GUE-19b
Facies		Root	Root	Root	Root	Root	Root	Ms–Bt	Ms–Bt	Ms–Bt	Ms–Turm	Ms–Turm	Ms–Turm	Ms–Turm	Ms–Turm	Fine	Fine	Fine	Dyke	Dyke	Dyke	Dyke	Dyke
SiO_2	wt.%	72.9	74.2	72.8	72.3	71.6	73.6	72.5	72.5	73.3	73.2	73.5	72.9	73.7	69.8	72.1	72.3	71.8	73.4	72.9	75.3	74.4	74.1
Al_2O_3	wt.%	14.76	14.50	15.27	15.34	15.04	15.01	14.95	15.43	14.97	14.66	15.01	15.27	14.81	16.11	15.04	14.92	15.18	14.28	14.79	14.01	15.20	15.14
Fe_2O_3	Wt.%	0.45	0.73	0.59	0.87	1.16	0.22	0.68	0.38	0.78	0.52	0.67	0.45	0.71	0.81	0.96	0.92	0.99	0.53	0.51	0.26	bdl	0.36
MnO	Wt.%	0.01	0.02	0.01	0.01	0.01	0.01	0.01	0.01	0.01	0.01	0.02	0.01	0.02	0.01	0.01	0.01	0.01	0.01	0.01	0.01	0.01	0.03
MgO	Wt.%	0.14	0.16	0.16	0.24	0.32	0.07	0.20	0.15	0.24	0.16	0.15	0.16	0.21	0.22	0.24	0.26	0.30	0.12	0.14	0.06	bdl	0.05
CaO	Wt.%	0.71	0.48	0.59	0.83	0.82	0.62	0.57	0.46	0.75	0.43	0.40	0.62	0.59	0.83	0.78	0.80	0.73	0.55	0.71	0.21	0.37	0.27
Na_2O	Wt.%	4.40	4.00	4.05	3.54	3.85	3.83	3.79	3.73	4.01	4.18	4.51	4.07	3.66	3.28	3.78	3.61	3.26	3.77	3.93	4.68	8.71	7.10
K_2O	Wt.%	4.01	4.08	4.65	4.70	4.59	5.03	4.61	4.57	4.44	4.03	3.51	4.26	4.51	6.64	4.61	4.93	4.94	5.11	5.14	3.63	0.42	1.29
TiO_2	Wt.%	0.07	0.09	0.09	0.15	0.18	0.06	0.12	0.12	0.10	0.08	0.06	0.11	0.10	0.11	0.12	0.15	0.16	0.06	0.08	0.02	bdl	bdl
P_2O_5	Wt.%	0.16	0.25	0.14	0.25	0.23	0.22	0.23	0.23	0.23	0.24	0.29	0.21	0.35	0.59	0.25	0.22	0.23	0.18	0.25	0.14	0.23	0.19
LOI	Wt.%	0.94	0.95	0.79	1.00	0.89	0.05	1.14	1.54	0.98	1.10	1.09	1.19	1.25	1.09	1.04	0.74	1.34	0.63	0.67	0.84	0.39	0.80
Total	Wt.%	98.51	99.47	99.11	99.27	98.69	98.75	98.83	99.15	99.79	98.57	99.19	99.23	99.86	99.49	98.95	98.83	98.93	98.63	99.16	99.18	99.72	99.27
Cs	ppm	8	18	10	6	14	5	35	16	31	77	95	26	50	88	24	25	16	17	11	28	11	36
Rb	ppm	202	271	223	195	230	218	353	239	251	357	365	244	384	459	245	293	252	266	222	325	14	150
Sr	ppm	139	76	106	161	212	125	121	145	147	75	46	163	113	187	134	114	119	129	183	17	15	16
Ba	ppm	243	153	191	296	411	241	215	284	288	133	57	269	185	362	293	294	339	279	346	13	4	8
Be	ppm	5.7	11.0	7.0	3.9	9.2	9.2	18.4	11.3	13.7	18.7	12.9	15.0	34.5	6.0	15.4	9.8	9.2	24.0	12.6	131.3	129.3	158.5
Y	ppm	6.7	4.5	5.5	7.6	7.7	9.7	5.9	7.2	6.6	5.1	3.8	6.3	7.7	9.1	7.6	5.1	6.0	4.1	5.9	2.2	2.4	1.8
Zr	ppm	33	32	22	58	81	37	45	46	46	30	19	41	38	50	49	61	67	20	48	13	20	23
Hf	ppm	1.19	1.10	0.77	1.77	2.46	1.37	1.54	1.54	1.53	1.26	0.96	1.44	1.41	1.78	1.65	2.00	2.03	0.73	1.70	1.10	1.30	1.46
Nb	ppm	4.68	7.75	6.34	7.96	8.61	10.64	6.39	6.70	5.70	6.81	10.57	6.51	11.39	11.09	8.03	5.67	6.66	4.95	7.02	8.63	1.59	11.14
Ta	ppm	0.61	1.45	0.80	0.64	1.55	1.76	1.85	1.48	1.32	3.41	3.31	1.44	3.97	5.19	1.73	0.97	1.03	1.36	1.27	3.85	1.59	4.23
Th	ppm	2.64	3.72	1.97	5.24	9.15	2.20	3.46	3.52	3.14	2.59	1.44	3.04	2.94	3.59	3.89	5.63	6.36	1.49	5.49	0.29	0.59	0.61
U	ppm	2.35	3.99	2.74	2.44	4.75	4.02	3.35	4.24	6.42	2.90	1.71	2.41	3.09	4.05	5.98	7.24	3.78	6.21	3.64	1.63	1.96	1.87
Pb	ppm	73	41	74	68	77	83	54	68	65	61	41	73	66	92	55	44	52	76	85	42	15	15
V	ppm	1.9	1.7	2.8	4.2	8.2	1.0	3.9	4.3	3.5	2.2	1.4	3.8	4.5	3.7	4.0	3.5	5.0	1.1	2.2	bdl	bdl	bdl
Ni	ppm	bdl	bdl	bdl	bdl	bdl	bdl	bdl	bdl	bdl	bdl	bdl	10.0	bdl	bdl	bdl	bdl	bdl	bdl	bdl	bdl	bdl	bdl
Cr	ppm	4.6	12.2	9.0	6.3	17.2	bdl	9.9	11.0	15.9	10.3	5.7	25.7	10.7	13.9	14.9	16.7	5.5	36.3	5.3	5.1	4.1	bdl
Co	ppm	0.5	0.4	0.6	0.6	1.4	bdl	0.8	1.3	0.8	bdl	bdl	0.5	0.8	0.9	0.8	0.8	1.1	0.4	bdl	bdl	bdl	bdl
Cu	ppm	bdl	bdl	bdl	bdl	bdl	bdl	bdl	bdl	bdl	bdl	bdl	bdl	bdl	bdl	bdl	bdl	bdl	bdl	bdl	bdl	bdl	bdl
Zn	ppm	24	45	33	35	52	14	48	27	48	31	57	25	44	52	54	69	56	30	23	23	bdl	32
Ga	ppm	22.4	22.4	24.9	23.4	26.9	21.8	26.2	25.9	24.0	25.1	30.8	25.8	25.8	31.7	26.6	29.1	25.7	21.5	20.0	23.7	18.8	25.4
Sn	ppm	7.1	15.2	9.2	9.2	11.1	9.2	20.8	15.5	14.1	31.6	79.9	16.7	38.3	102.3	16.8	16.1	11.0	12.4	6.3	19.7	2.9	32.6
W	ppm	0.85	2.10	0.98	3.17	2.47	1.65	1.12	1.18	1.09	1.69	1.92	1.00	1.57	2.87	1.77	0.86	1.82	1.03	1.96	0.51	bdl	0.44
Bi	ppm	1.7	0.7	1.9	0.1	0.6	2.7	1.7	1.6	1.6	2.3	1.7	1.7	1.8	0.5	1.9	0.9	1.2	3.5	1.0	0.4	0.6	0.7
Cd	ppm	0.1	bdl	bdl	0.7	0.1	0.4	bdl	bdl	0.1	bdl	0.2	bdl	0.3	0.2	0.1	bdl	0.1	0.4	0.3	0.2	0.3	0.2
Ge	ppm	1.2	1.6	1.2	1.2	1.4	1.5	1.6	1.3	1.4	1.8	2.2	1.4	1.9	2.0	1.3	1.2	1.2	1.5	1.5	2.4	2.7	2.6
La	ppm	8.04	9.26	5.73	13.71	19.08	6.06	9.50	10.10	9.00	8.00	4.43	9.04	8.48	9.10	10.54	13.88	14.91	3.94	10.39	1.28	1.65	1.08
Ce	ppm	15.55	17.96	11.33	26.65	36.36	11.52	18.84	19.86	17.42	15.58	8.74	17.51	16.61	18.23	20.55	27.54	28.75	7.82	19.49	2.34	2.86	1.95
Pr	ppm	1.69	1.98	1.26	2.90	3.93	1.23	2.09	2.19	1.95	1.71	0.94	1.92	1.83	2.08	2.27	3.06	3.18	0.88	2.06	0.25	0.28	0.20
Nd	ppm	6.85	7.77	5.08	11.58	15.65	4.93	8.50	8.85	7.92	6.89	3.66	7.75	7.65	8.81	9.15	12.42	12.80	3.60	8.19	0.89	0.95	0.76
Sm	ppm	1.73	1.68	1.34	2.42	3.31	1.35	2.19	2.23	1.97	1.55	0.92	1.97	1.99	2.46	2.30	3.01	2.88	0.99	1.90	0.24	0.27	0.24
Eu	ppm	0.60	0.38	0.44	0.55	0.85	0.53	0.63	0.74	0.68	0.37	0.20	0.75	0.54	0.86	0.67	0.68	0.61	0.58	0.65	0.08	0.09	0.09
Gd	ppm	1.65	1.27	1.30	1.82	2.46	1.38	1.80	2.12	1.81	1.32	0.81	1.80	1.89	2.46	2.08	2.47	2.32	0.95	1.62	0.29	0.27	0.23
Tb	ppm	0.26	0.18	0.21	0.28	0.34	0.27	0.26	0.31	0.27	0.20	0.13	0.27	0.29	0.37	0.32	0.31	0.32	0.15	0.24	0.06	0.05	0.05
Dy	ppm	1.35	0.88	1.09	1.43	1.59	1.64	1.19	1.54	1.31	0.99	0.68	1.34	1.51	1.87	1.59	1.26	1.41	0.81	1.21	0.33	0.34	0.26
Ho	ppm	0.21	0.13	0.16	0.22	0.23	0.28	0.18	0.23	0.20	0.15	0.11	0.20	0.23	0.27	0.23	0.16	0.18	0.12	0.17	0.06	0.06	0.05
Er	ppm	0.50	0.35	0.40	0.58	0.58	0.74	0.43	0.53	0.48	0.38	0.28	0.47	0.56	0.65	0.53	0.35	0.41	0.30	0.45	0.15	0.16	0.13
Tm	ppm	0.07	0.05	0.05	0.08	0.08	0.11	0.06	0.07	0.07	0.05	0.04	0.07	0.08	0.09	0.07	0.04	0.06	0.04	0.06	0.03	0.03	0.03
Yb	ppm	0.42	0.38	0.34	0.53	0.51	0.71	0.39	0.44	0.41	0.35	0.30	0.41	0.48	0.52	0.44	0.26	0.38	0.28	0.41	0.18	0.22	0.20
Lu	ppm	0.05	0.05	0.05	0.07	0.07	0.10	0.05	0.06	0.06	0.05	0.04	0.05	0.07	0.08	0.06	0.04	0.06	0.04	0.06	0.02	0.03	0.03
A/NK		1.28	1.32	1.31	1.41	1.33	1.28	1.33	1.39	1.31	1.30	1.34	1.35	1.36	1.28	1.34	1.32	1.42	1.22	1.23	1.20	1.03	1.16
A/CNK		1.15	1.22	1.2	1.24	1.18	1.17	1.22	1.29	1.17	1.22	1.26	1.23	1.24	1.14	1.19	1.17	1.26	1.12	1.11	1.17	0.98	1.12

the secondary affinity of muscovite tends to increase from the Ms–Bt coarse- to medium-grained granites (GUE-3 and 8) to the Ms–Turm coarse- to medium-grained granite (GUE-1, Fig. 7b). In these samples, several grains of coarse muscovite display heterogeneous Mg contents: the cores are poorer in Mg and belong to the primary muscovite field whereas their rims are richer in Mg and fall in the secondary muscovite field (Fig. 7b). Regarding the small muscovite grains present in the foliation (labeled MsII in Fig. 6c), they all plot in the secondary field.

6. Whole-rock geochemistry

6.1. Major elements (Table 3)

The chemical diagram of Hughes (1973) is useful to identify magmatic rocks that have undergone metasomatism, which may be responsible for the loss of their initial igneous composition. In this diagram (Fig. 8a), three samples fall outside or at the limit of the field for igneous rocks. These are the two samples from the aplite dyke GUE-19a and GUE-19b and a Ms–Turm coarse- to medium-grained granite (sample GUE-21). The chemical mineralogical Q-P diagram (Debon and Le Fort, 1988) is suitable to evidence the mineralogical changes linked to chemical composition modification in igneous rocks because it is sensitive to the proportion of quartz (Q parameter) and to the proportion of alkali feldspar relative to plagioclase (P parameter). In this diagram (Fig. 8b), samples GUE-19a and GUE-19b display a trend characteristic of an albitic alteration where albitization and dequartzification are associated with the neoformation of albite. Samples GUE-2 and 20 display weak albitization. Sample GUE-21 displays dequartzification associated with the neoformation of alkali feldspar. These results are consistent with field and petrographic descriptions, which indicate that albitization affected samples GUE-19 and GUE-2 whereas greisens occur in the vicinity of sample GUE-21 (Fig. 2 and Table 1). According to the Hughes and Q-P diagrams (Fig. 8a and b), the Guérande granite samples can be divided into two groups: the unaltered samples, which display igneous compositions and the altered samples GUE-19 and GUE-21 that show evidence of hydrothermal alteration.

Similarly to some neighboring granites such as the Questembert and Lizio leucogranites (Tartèse and Boulvais, 2010), all the unaltered samples from the Guérande granite display a peraluminous affinity in the A/NK vs A/CNK diagram(A/CNK values ranging from 1.11 to 1.29; Fig. 8c and Table 3). However, the altered sample GUE-19a shows A/CNK and A/NK values close to 1, which is typical for an albitized granite (Boulvais et al., 2007) and reflects the disappearance of muscovite during albitization.

As shown in Fig. 9a, unaltered samples display high SiO_2 contents ranging from 71.6 wt.% (GUE-15) to 75.3 wt.% (GUE-20). The altered sample GUE-21 yields a low SiO_2 content of 69.8 wt.% whereas albitized samples show high SiO_2 contents of 74.1 to 74.4 wt.%. Most of the major elements for the unaltered samples display well defined evolution trends with increasing SiO_2, i.e., decreasing K_2O, CaO and $Fe_2O_3 + MgO + TiO_2$ contents whereas Na_2O content increases. Conversely, the altered samples rarely follow these trends (Fig. 9a).

6.2. Trace-elements (Table 3)

Whereas some incompatible trace-elements such as Rb, Cs, W, U or Sn are not correlated with SiO_2, several other trace-elements from the unaltered samples display well-defined evolution trends and show large variations against SiO_2. Sr and Ba mimic the trends defined by K_2O, CaO and $Fe_2O_3 + MgO + TiO_2$ (Fig. 9a). Zr, Th and La are also inversely correlated with SiO_2 and they decrease respectively from 81 to 13 ppm, 9.2 to 0.3 ppm and 19.1 to 1.3 ppm (Fig. 9a). Zr correlates well with $Fe_2O_3 + TiO_2 + MgO$ while a very good correlation exists between Zr, Th and La (Fig. 9b). Among altered samples, GUE-21 does not follow the general trend provided by the unaltered samples in the Harker diagrams reported in function of SiO_2 (Fig. 9a). Nevertheless, sample GUE-21 is indistinguishable from unaltered samples in the diagrams involving Zr, La and Th (Fig. 9b). Samples GUE-19a and GUE-19b plot at the lower extremity of these trends (Fig. 9b). GUE-19a, 19b and 20 are highly enriched in Be when compared to the other samples (Be > 120 ppm).

The REE patterns obtained on the unaltered samples are somewhat variable (Fig. 10), show high fractionation ($(La/Lu)_N = 10.8–28$) and display either positive or negative Eu anomalies ($Eu/Eu^* = 0.7–1.2$), the largest positive anomaly being recorded in the dyke sample GUE-5. These patterns are similar to those obtained for the other Armorican Massif leucogranites (Bernard-Griffiths et al., 1985; Tartèse and Boulvais, 2010). The aplite dyke GUE-20 is remarkable because of its large depletion in REE. Concerning the altered samples, GUE-19a and GUE-19b show REE patterns similar to the ones from the aplite dyke GUE-20. Sample GUE-21 displays a REE spectrum comparable with the other unaltered samples suggesting that the REE distribution in this sample was not affected during fluid-rock interaction.

The evolution of some of the geochemical tracers sensitive to the interaction with fluids is reported in Fig. 11a with respect to the distance to the northwestern edge of the Guérande granite, identified as the apical zone of the intrusion. In the apical zone, the Cs and Sn contents increase by about one order of magnitude, from around 10 ppm to 100 ppm for both elements. This behavior is similar for Rb, which increases from 200 to 450 ppm. Also, samples from the Guérande granite display fractionation of the Nb/Ta ratios from about 6–8 down to about 2–4 in the apical zone, similarly to the hydrothermal alteration trends identified in the nearby Questembert granite (Tartèse and Boulvais, 2010). Taking the Cs content as a qualitative tracer for an increasing fluid-rock alteration (e.g. Förster et al., 1999; Fig. 11b), the Sn contents show a very well correlated evolution, whereas the Nb/Ta ratios are rather anti-correlated with the Cs contents. Both trends are defined by the unaltered and altered samples.

7. Radiogenic isotopes: Rb–Sr and Sm–Nd

Sr and Sm–Nd isotope analyses for some of the samples from the Guérande granite are reported in Table 4 and Fig. 12. Initial $^{87}Sr/^{86}Sr$ (I_{Sr}) and εNd(T) values have been recalculated for an age of 310 Ma (see part 8). I_{Sr} values are high and vary from 0.7148 to 0.7197 while εNd(T) varies from −7.8 to −9.0. T_{DM} values are old and vary from 1642 to 1736 Ma. In the εNd(T) vs I_{Sr} diagram (Fig. 12), a regional trend is defined by the Rostrenen, Pontivy, Lizio, Questembert and Guérande peraluminous granites: εNd(T) values decrease while I_{Sr} increases. This evolution may indicate an increase of crustal recycling going southward in the southern part of the Armorican Massif as already noticed by Bernard-Griffiths et al. (1985).

8. Geochronology

Sample GUE-3, a Ms–Bt coarse- to medium-grained granite collected in the northwestern part of the intrusion (Fig. 2), provided both zircon and monazite grains. Thirty-six analyses were carried out on nineteen zircon grains (Supplementary Table 1). The zircon population is characterized by translucent colorless euhedral to sub-euhedral grains. Cathodoluminescence imaging reveals the presence of inherited cores surrounded by zoned rims for most of the grains (Fig. 13a). They plot in a concordant to discordant position (Fig. 14a) and yield $^{207}Pb/^{206}Pb$ dates ranging from 2604 ± 18 Ma down to 307 ± 27 Ma. A group of nine concordant to sub-concordant analyses allow to calculate a mean $^{206}Pb/^{238}U$ date of 309 ± 2.6 Ma (MSWD = 1.0). The remaining 5 data (dashed line on Fig. 14a) plot in a sub-concordant to discordant

position and can be best explained by the presence of initial common Pb together with a complex Pb loss.

In addition, sixteen monazite grains have also been analyzed (Supplementary Table 2). In a $^{206}Pb/^{238}U$ vs $^{208}Pb/^{232}Th$ concordia diagram, they plot in a concordant to sub-concordant position. All sixteen analyses yield a mean $^{206}Pb/^{238}U$ date of 311.3 ± 2.2 Ma (MSWD = 0.5) and the fifteen most concordant analyses allow to calculate an equivalent (within error) concordia date of 309.4 ± 1.9 Ma (MSWD = 1.08).

Within the same facies (ie. Ms–Bt coarse- to medium-grained granite), a large zircon grain from sample GUE-8 was analyzed. It displays a well-defined magmatic zoning without any evidence of inherited core (Fig. 13b). Eight analyses were performed and allow to calculate a poorly constrained concordia date of 309.3 ± 6.1 Ma (MSWD = 2.4) for the 6 most concordant points (not shown in this paper).

Zircon and monazite grains were also extracted from a third sample, GUE-4, a Ms–Bt fine grain granite collected within the La Turballe quarry (Fig. 2). All the zircon grains were characterized by the presence of cores and rims. Unfortunately, all the analyses performed on the zircon rims were perturbated by a large amount of common Pb together with variable degrees of Pb loss. Furthermore these zircon grains yielded uranium contents up to 20,000 ppm. Therefore, no ages could be calculated from these zircon grains.

Forty-one analyses were carried out on twelve monazite grains. The monazite grains are rather large (up to 300 μm), euhedral, and characterized by a Th distribution from heterogeneous (patchy) to zoned (Fig. 13c) with a systematic Th enrichment around the edges of the grains. Independently from where the spot analyses were located, all the acquired data are consistent and plot in a concordant to sub-concordant position in a $^{206}Pb/^{238}U$ vs $^{208}Pb/^{232}Th$ concordia diagram (Fig. 14c). Thirty-two concordant analyses allow to calculate a concordia date of 309.7 ± 1.3 Ma (MSWD = 0.81) which is equivalent within error with a mean $^{206}Pb/^{238}U$ date of 310.9 ± 1.6 Ma (n = 41; MSWD = 1.3).

Finally, sample GUE-5 corresponds to a dyke intrusive into GUE-4. It provided abundant zircon and monazite grains. Here again, all the zircon grains display cores and rims and all of them but one were common-Pb rich and affected by variable degree of Pb loss. The only

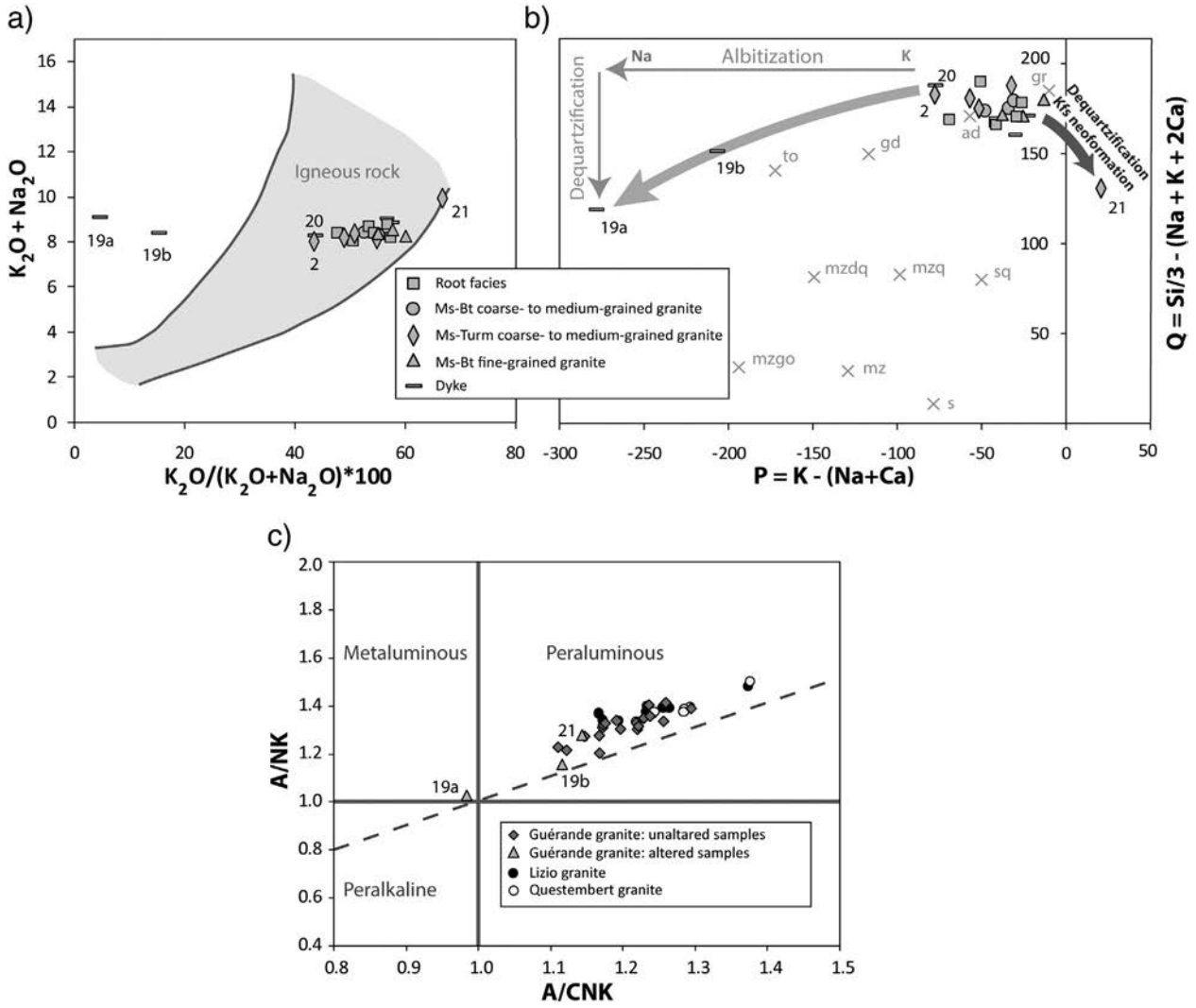

Fig. 8. a) Chemical (after Hughes, 1973) and b) chemical–mineralogical (after Debon and Le Fort, 1988) diagrams for the Guérande granite samples. Samples GUE-19a, 19b and 21 show evidences of alteration. In diagram b), the crosses indicate the location of common igneous rock: gr = granite, ad = adamellite, gd = granodiorite, to = tonalite, sq = quartz syenite, mzq = quartz monzonite, mzdq = quartz monzodiorite, s = syenite, mz = monzonite, and mzgo = monzogabbro. Q and P parameters are expressed in molar proportion multiplied by 1000. c) Shand (1943) diagram (A/CNK = $Al_2O_3/(CaO + Na_2O + K_2O)$; A/NK = $(Al_2O_3/Na_2O + K_2O)$; molar proportions) where unaltered and altered samples are distinguished on the basis of figures a) and b). Lizio and Questembert granite samples are shown for comparison (Tartèse and Boulvais, 2010).

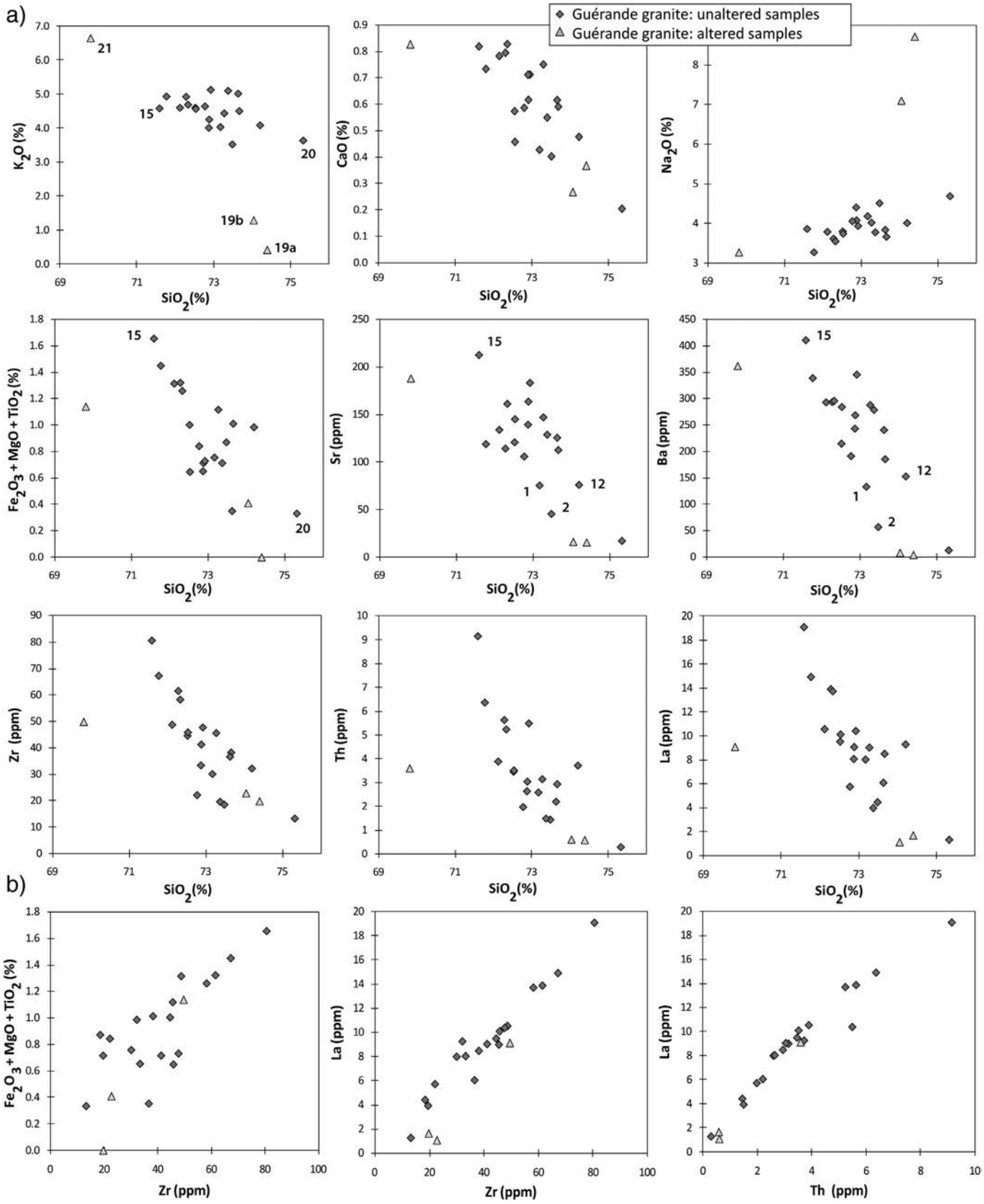

Fig. 9. Harker (a) and bivariate diagrams (b) of selected major- and trace-elements for the Guérande granite.

zircon that was not common-Pb rich (Fig. 13d) yields a concordia date of 299.6 ± 5.4 Ma (MSWD = 0.49) for the two analyses performed in the rim.

Twenty-three analyses out of sixteen monazite grains were realized. They all plot in a concordant to sub-concordant position in a $^{206}Pb/^{238}U$ vs $^{208}Pb/^{232}Th$ concordia diagram (Fig. 14d). The eighteen most

concordant points yield a concordia date of 302.5 ± 1.6 Ma (MSWD = 0.86), equivalent within error with a mean $^{206}Pb/^{238}U$ date of 303.7 ± 1.7 Ma (MSWD = 0.9) computed for all the analyses. These dates of 302.5 ± 1.6 Ma and 303.7 ± 1.7 Ma are equivalent within error with the Concordia date of 299.6 ± 5.4 Ma obtained on the rim of the zircon grain.

9. Discussion

9.1. Tectonic evolution

The Guérande granite and its country rock record puzzling kinematic patterns which suggest a particular deformation regime at the time of the granite emplacement.

First, to the northwest, S/C granites bear dip-slip type N–S lineation whereas in the country rock, elongated patch of contact metamorphism minerals indicate an E–W stretching direction (Fig. 5). Second, the main emplacement directions of the pegmatite dykes and quartz veins intrusive into the Guérande granite indicate either NE–SW or E–W stretching direction depending on the area (Fig. 5). To the northwest extremity, veins strike mostly NW–SE and their emplacement is compatible with the main strike of the lineation recorded in the granite (i.e. N–S to NE–SW). In contrast, to the southwest, veins strike mostly N–S and record an E–W stretching direction incompatible with the strike of the lineation in the granite (i.e. N–S).

From the local occurrence of S/C fabrics and contact metamorphism indicators attesting for potentially coeval N–S and E–W motions, we must consider the possibility that extension in the area resulted in subhorizontal flattening strains, with local partitioning of dominant extension directions. At a more regional scale, Gapais et al. (1993) showed that the extension direction was variable to the north of the Guérande area, from E–W to N–S, according to the local orientation of the foliation, the stretching lineations associated with the extension tending to show dominant dip-slip attitudes. Field evidences do not support successive deformation events for these variable local kinematics. As a consequence, the emplacement of pegmatite dykes and quartz veins, either from the southwest area which recorded E–W stretching or from the northwest area which in contrast recorded NE–SW stretching, could be synchronous and linked to the same deformation event.

It has been previously argued that extension in south Brittany was coeval with the dextral wrenching along the South Armorican Shear Zone (Gumiaux et al., 2004). A combination of regional EW extension and WNW–SSE strike-slip shearing might have contributed to the observed local scattering of extension directions (Gapais et al., 2015). Another additional working hypothesis could be a tendency of the brittle upper crust to record chocolate-tablet type strains (Ramsay and Huber, 1983) induced by a regional vertical shortening, which could constrain the partitioning of the kinematics in the underlying ductile middle crust (Gapais et al., 2015). Further arguments would require a detailed analysis of the brittle strain patterns within the upper HP-LT units.

9.2. Magmatism

9.2.1. Source

As expected from the CL imaging (Fig. 13a), zircon grains from the sample GUE-3 yield a large range of $^{207}Pb/^{206}Pb$ dates (Fig. 14a) suggesting the presence of heterogeneous inherited material. Because most of the data are not concordant, it is impossible to discuss individual group of ages but basically two main periods of inheritance can be seen with a few Late Archean–Proterozoic and numerous Paleozoic cores (oldest and youngest $^{207}Pb/^{206}Pb$ dates of 2604 ± 18 Ma and 341 ± 27 Ma respectively). This spread of ages is well known in the leucogranites from the Armorican Massif (see for example Tartèse et al., 2011a).

The high peraluminous index (Fig. 8c and Table 3), the high I_{Sr} ratios and the low εNd(T) values (Fig. 12) of the samples, together with the presence of inherited cores, with variable apparent ages, within the dated zircon grains (Figs. 13 and 14a), and the old T_{DM} (Table 4), suggest a metasedimentary source for the Guérande granite. The value of I_{Sr} and εNd(T) plot at the transition between the fields defined for the Brioverian and the Paleozoic sediments (Michard et al., 1985; Dabard et al., 1996; Fig. 12). This observation as well as the presence of inherited cores within the zircon grains with apparent ages ranging from the Archean–Proterozoic to the Paleozoic suggest that both the Brioverian and the Paleozoic sedimentary formations may have been involved in the partial melting event that produced the Guérande granite.

Along a transect roughly perpendicular to the South Armorican Shear Zone, the Guérande granite together with the others, mostly contemporaneous, syntectonic granites yield a peculiar evolution in the I_{Sr} vs εNd(T) diagram (Figs. 1 and 12). Indeed, from roughly north to south, the I_{Sr} values increase while the εNd(T) decrease from the Rostrenen (316 ± 3 Ma, U–Pb zircon; Euzen, 1993), Pontivy (344 ± 8 Ma, Rb–Sr whole-rock isochron; Bernard-Griffiths et al., 1985; 311 ± 2 Ma, $^{40}Ar/^{39}Ar$ muscovite; Cosca et al., 2011), Lizio (316 ± 6 Ma, U–Pb zircon; Tartèse et al., 2011a), Questembert (316 ± 3 Ma,

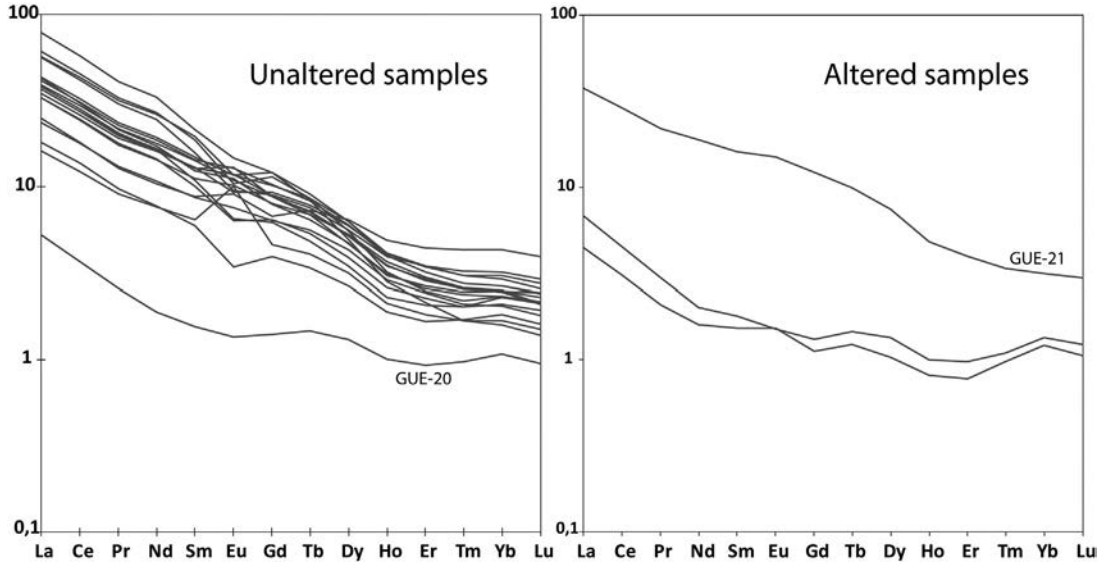

Fig. 10. Chondrite normalized REE patterns of the Guérande granite samples. Normalization values from Evensen et al. (1978).

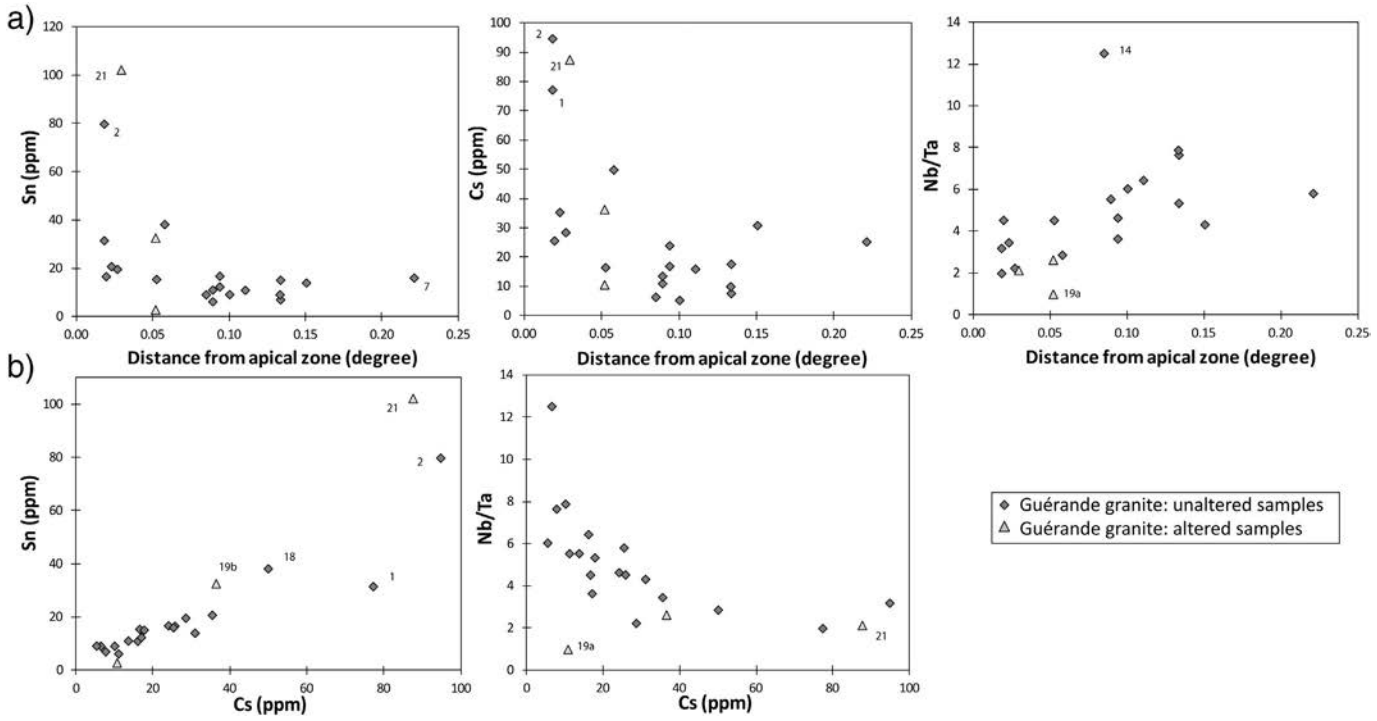

Fig. 11. a) Evolution of some geochemical tracers sensible to the interaction with fluids as a function of the distance to the NW edge of the Guérande granite. b) Evolution of chosen tracers as a function of the concentration of Cs.

U–Pb zircon; Tartèse et al., 2011b) to the Guérande granite (309.7 ± 1.3 Ma, U–Pb zircon and monazite; this study, see part 9.4). We can propose three hypotheses at two different spatial scales to account for this trend:

(1) The Lizio, Questembert and Guérande granites have a pure metasedimentary source (Fig. 12). Consequently, the N–S trend displayed by these three granites in Fig. 12 could be explained by a mixing between two metasedimentary end-members. To the north, the source of the peraluminous granites is almost exclusively constituted by the Brioverian sediments whereas, going south, the proportion of Paleozoic sediments, characterized by older model ages, increases. This would be consistent with the fact that, the further south the granites are located, the further away they are from the Cadomian domain, i.e. from the source for the Brioverian sediments (Dabard et al., 1996), that are well expressed in the northern part of the Armorican Massif.

(2) Comparing the Rostrenen–Pontivy granites to the Lizio–Questembert–Guérande granites in Fig. 12, the εNd(T) and I_{Sr} values for some of the samples from the Rostrenen and Pontivy granites suggest a mantle contribution (two points with positive εNd(T) values). This hypothesis is supported by the fact that granitoids with a mantle affinity have been described in the Rostrenen massif (Plélauff monzodiorite; Euzen, 1993). We could tentatively link the mantle contribution in the Rostrenen and Pontivy granites to the thickness of the continental crust, which decreased from south to north at the end of the Carboniferous in Southern Brittany: the crust was very thick below the Guérande and the Questembert massifs because these granites were emplaced close to the core of the Hercynian belt whereas the crust was thinner below the Lizio–Pontivy granites and almost not thickened at all below the Rostrenen massif (Ballèvre et al., 2009). To the south of the South Armorican Shear Zone, the important thickness of the crust could have prevented a mantle-derived underplated magma to reach the upper crustal level, whereas such a process might have been possible to the north.

(3) Another hypothesis to explain the low I_{Sr} and the high εNd(T) measured for the northernmost granites (Peucat et al., 1988) could be the contribution of juvenile components from the St-Georges-sur-Loire synclinorium, located a few tens of kilometers to the east of the Questembert region, and interpreted by some authors as the trace of an early Devonian back-arc basin (Ballèvre et al., 2009 and references therein).

These three hypotheses are not individually exclusive and could have all contributed to the southward evolution of the granitic sources during the Carboniferous evolution of the Hercynian belt in the region.

Table 4
Rb–Sr and Sm–Nd whole-rock data for the Guérande granite. Rb concentrations have been obtained by ICP-MS, other concentrations by isotopic dilution.

Sample	Rb (ppm)	Sr (ppm)	$^{87}Rb/^{86}Sr$	$^{87}Sr/^{86}Sr$	±	$(^{87}Sr/^{86}Sr)$ 310 Ma	Sm (ppm)	Nd (ppm)	$^{147}Sm/^{144}Nd$	$^{143}Nd/^{144}Nd$	±	εNd (310 Ma)	T_{DM}[a]
GUE-3	353	101	10.2	0.759868	11	0.7149	2.0	8.1	0.149821	0.512081	5	−9.0	1736
GUE-4	245	131	5.4	0.741854	11	0.7179	2.3	9.3	0.147638	0.512088	6	−8.8	1718
GUE-5	266	121	6.4	0.744704	12	0.7165	0.9	3.5	0.163489	0.512128	6	−8.6	1707
GUE-8	251	147	5.0	0.741599	11	0.7197	2.1	8.5	0.149165	0.512099	5	−8.6	1707
GUE-15	230	197	3.4	0.729724	10	0.7148	3.1	15.3	0.123199	0.512089	5	−7.8	1642

[a] Two stages T_{DM} calculated using the equation of Liew and Hofmann (1988) for an age of 310 Ma.

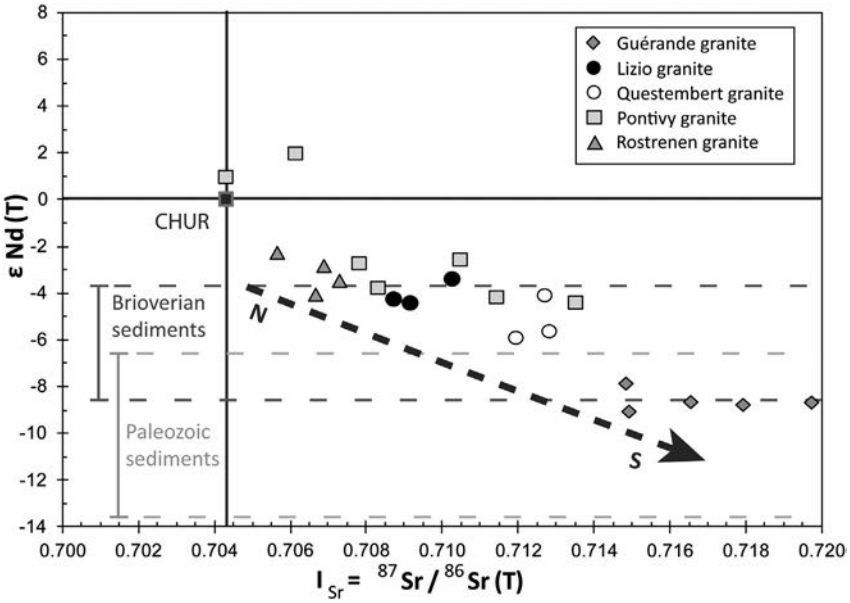

Fig. 12. Sr and Nd isotopic compositions of the Guérande granite compared with the Lizio, Questembert (Tartèse and Boulvais, 2010), Pontivy and Rostrenen granite (Peucat et al., 1979; Euzen, 1993). εNd and I_{Sr} are calculated for an age of 310 Ma. The vertical bars representing εNd(T) composition of the Brioverian and Paleozoic sediments from Central Brittany are calculated from Michard et al. (1985) and Dabard et al. (1996). The exceptionally high εNd(T) value of 0.5 measured in the Paleozoic sediments (Michard et al., 1985) is not reported in the figure. The arrow in the figure represents north–south evolution of the isotopic compositions of the Carboniferous peraluminous granites of the Armorican Massif.

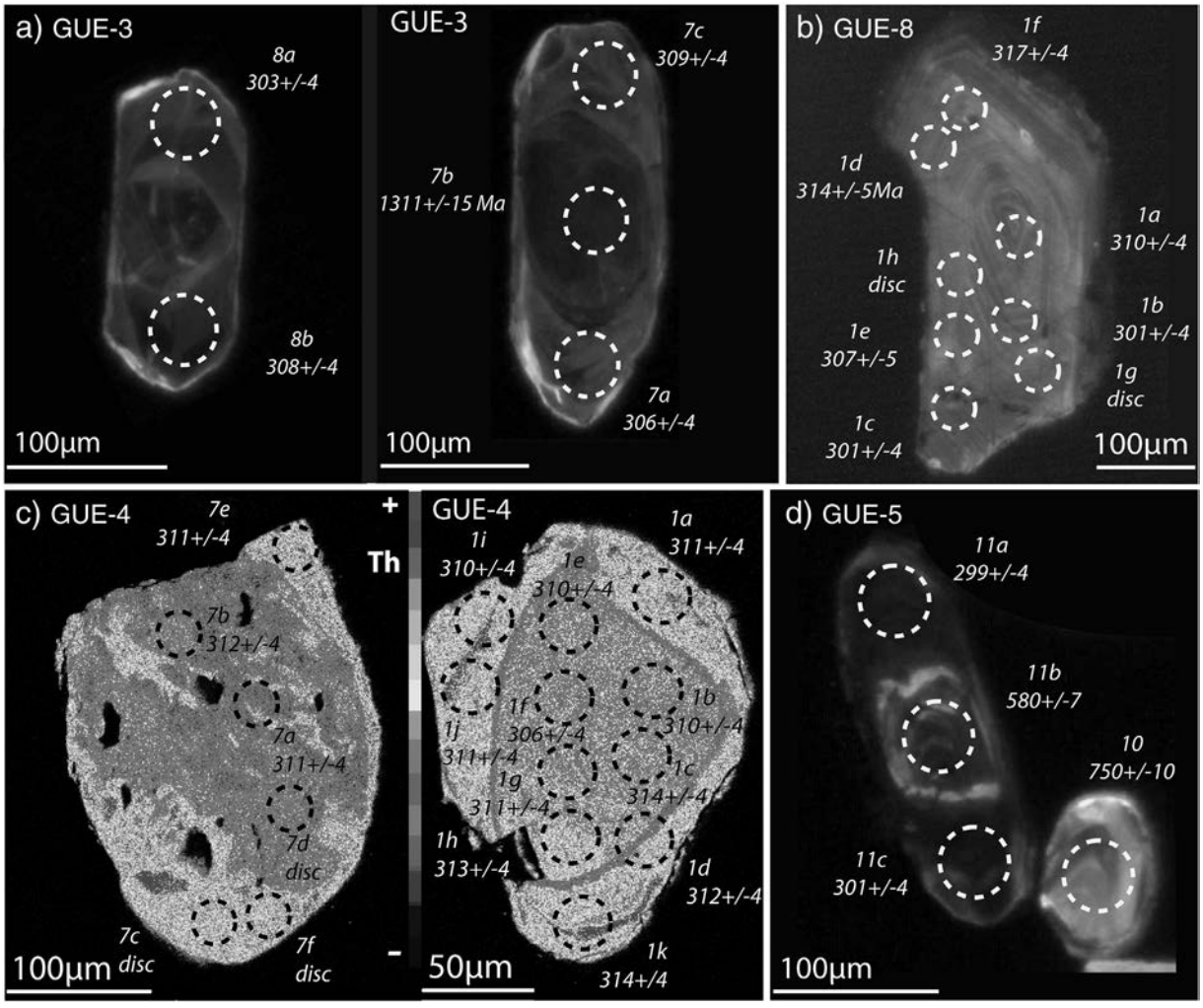

Fig. 13. Selected images of zircon and monazite grains. a–b-d) Cathodoluminescence images of zircons from the sample GUE-3, GUE-8 and GUE-5. c) Th chemical map of monazite from the sample GUE-4. Dashed circles represent the location of LA-ICP-MS analyses with the corresponding $^{206}Pb/^{238}U$ ages in Ma.

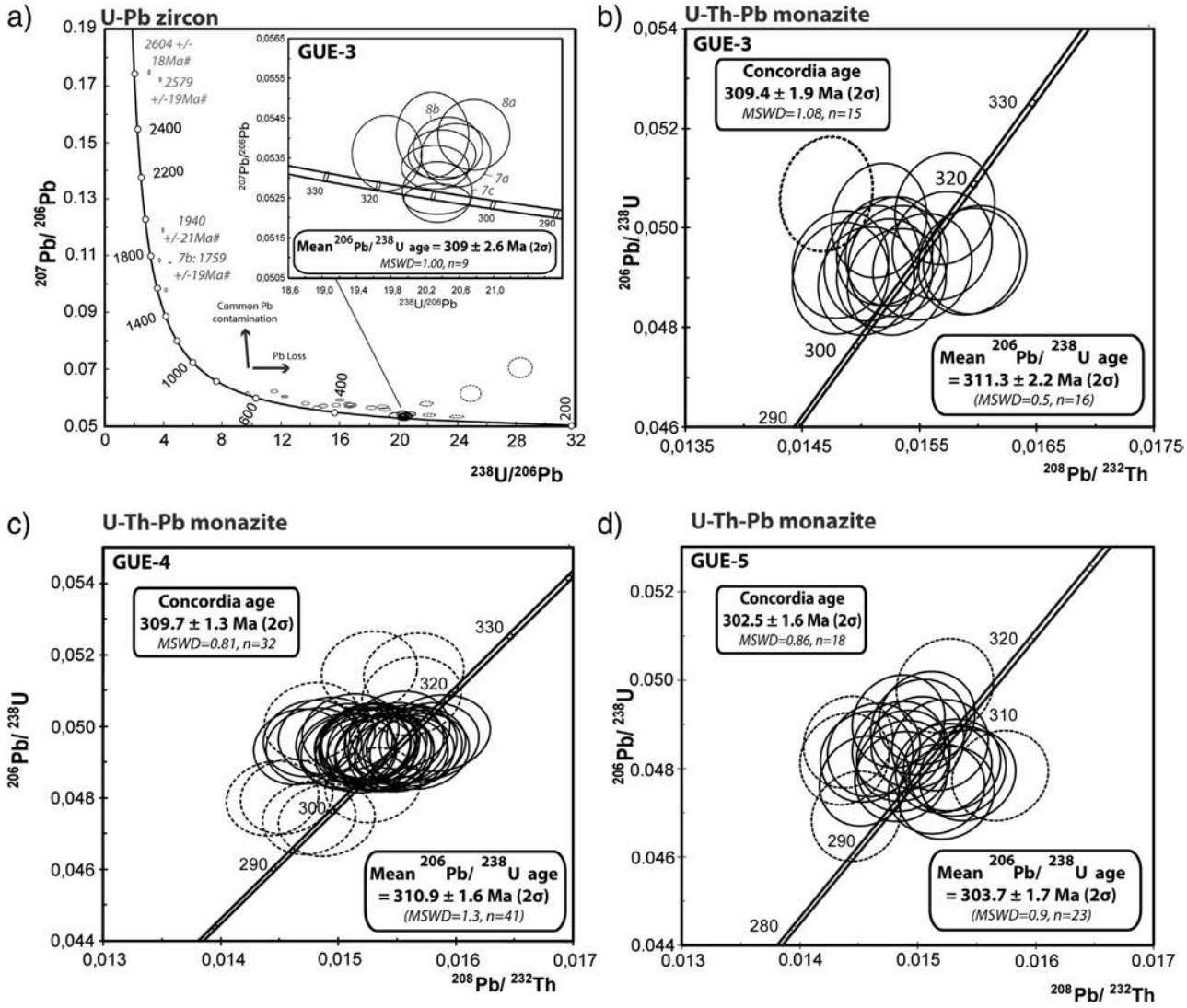

Fig. 14. a) Tera–Wasserburg diagram displaying the analyses made on zircon of the sample GUE-3. The gray ellipses represent the inherited zircons and the dashed ellipses represent zircon submitted to a lost or a gain in common lead. #: $^{207}Pb/^{206}Pb$ ages at 1 σ. b–c–d) $^{206}Pb/^{238}U$ vs $^{208}Pb/^{232}Th$ concordia diagram for monazite of the sample GUE-3, GUE-4 and GUE-5. The dashed ellipses represent the analyses not used for the calculation of Concordia ages. In the diagrams error ellipses are plotted at 1σ.

9.2.2. Differentiation process

In the Harker diagrams (Fig. 9), several major- and trace-elements display well defined correlations with SiO_2. These chemical variations could reflect a number of processes such as the melting of heterogeneous sources combined with variable entrainment of peritectic assemblages and accessory minerals in the melt (Stevens et al., 2007; Clemens and Stevens, 2012), a variable degree of partial melting, wall-rock assimilation, a variation in the amount of mineral-melt segregation during differentiation (Tartèse and Boulvais, 2010; Yamato et al., 2012) or a coalescence of several magma batches issued from different sources followed by differentiation of these melts (Deniel et al., 1987; Le Fort et al., 1987). For the Guérande granite, we believe that a process of fractional crystallization implying the segregation of feldspar and biotite, hosting most accessory minerals, is the main process behind the observed chemical variations. First, despite the fact that we cannot exclude source heterogeneities, the similar εNd and the limited variation of I_{Sr} for the analyzed samples (Fig. 12) suggest a derivation from a relatively homogeneous melt. Second, the low SiO_2 samples from the Guérande granite display geochemical characteristics comparable to that of the liquids produced during experimental melting of metasediments (Vielzeuf and Holloway, 1988; Patiño Douce and Johnston, 1991; Montel and Vielzeuf, 1997), with low content of ferromagnesian and CaO ($Fe_2O_3 + MgO + TiO_2 < 2\%$; $CaO < 1\%$), suggesting that they are close to anatectic melts (Patiño Douce, 1999) and that the amount of peritectic or restitic minerals entrained from the source is negligible. Moreover, the K_2O content of the Guérande samples is correlated with the sum $Fe_2O_3 + MgO + TiO_2$, as both parameters decrease with SiO_2 (Fig. 9), which is the opposite behavior expected for a process of entrainment of peritectic garnets (Stevens et al., 2007; Clemens and Stevens, 2012). Third, two main observations based on trace-elements behavior are in favor of a fractional crystallization process:

(1) The Ba and Sr contents, two elements compatible in biotite and feldspar, decrease largely with increasing SiO_2 (Fig. 9a). Such variations in compatible elements (212 to 75 ppm for Sr and 411 to 133 ppm for Ba from GUE-15 to GUE-1) are very difficult to explain with a simple partial melting process. In fact, by modeling the process of "partial or batch melting" (details in Janoušek et al., 1997) using $D(Sr)^{res/liq} = 4.4$ for a pure plagioclase and $D(Ba)^{res/liq} = 6.36$ for a pure biotite, the measured contents in Ba and Sr could be matched by a variation of the degree of partial melting from about 0 to 80%, which is an unrealistic large range. On the other hand, such important variations in compatible elements can be easily explained by a fractional crystallization

process involving a few tenths of a percent of mineral fractionation (Hanson, 1978; see part 9.2.3.2. for quantitative details).

(2) In Fig. 9b, the excellent correlation between Zr and La reveals a common process between zircon (which hosts Zr) and monazite (which hosts La), while the good correlation between Zr and Fe_2O_3 + Mgo + TiO_2, which both display the same overall range of variation (factor of 4 between 80 and 20 ppm for Zr and factor 4 between 1.6 and 0.4 wt.% for Fe_2O_3 + Mgo + TiO_2), indicates that zircon and biotite shared a common magmatic history. In thin sections, zircon and monazite occur mostly as inclusions within biotite, which suggests that the common magmatic process which controls the distribution of Zr and La is the fractional crystallization of zircon- and monazite-bearing biotite.

9.2.3. Fractional crystallization modeling

The inverse correlation between Fe_2O_3 + MgO + TiO_2 and SiO_2 is consistent with the fractionation of biotite and the depletions in CaO and K_2O for the SiO_2-rich samples are consistent with the fractionation of plagioclase (CaO), potassic feldspar and biotite (K_2O) (Fig. 9). Here, we propose a quantification of the amount of minerals that was segregated from the melt during the process of fractional crystallization, first by using major elements and then by using trace-elements hosted by the main rock forming minerals. The aplitic sample GUE-20 has been removed from these calculations because it displays a much more evolved composition than the other samples, which is difficult to model solely by fractional crystallization processes. Some of the characteristics of this sample may indeed be attributed to the interaction with a fluid phase (discrete albitization as seen in the Q-P diagram (Fig. 8b) and enrichment in Be (Table 3)).

9.2.3.1. Major elements. In Fig. 15a and b, the whole-rock compositions of the unaltered samples from the Guérande granite are plotted in Harker diagrams together with the theoretical composition of an An20 plagioclase and the average composition of biotite and potassic feldspar from the most primitive sample (GUE-4) out of all the samples where chemical analyses of minerals have been carried out. In these diagrams, the prolongation of the trends displayed by the granite samples allows to calculate the mineralogical composition of the segregate assemblage (see Tartèse and Boulvais, 2010 for details about the calculation), which yields an assemblage composed by 40–55 wt.% Kfs + 20–40 wt.% Bt + 5–40 wt.% An20.

Independently, we used the "inverse major" plugin included in the GCD Kit software (Janoušek et al., 2006) to calculate the amount and the mineralogical composition of the segregated cumulate required to produce the chemical composition of the more evolved sample GUE-12 from the composition of the less evolved sample GUE-15. The results obtained with this modeling (Table 5) are consistent with those obtained with the first method and the differences between the calculated and the actual compositions are small as indicated by a ΣR^2 (sum of the squared residuals) of 0.16. This modeling also implies that apatite had a non-negligible contribution to the fractionating assemblage, as shown by the modal composition of the calculated segregate assemblage that contains 45 wt.% Kfs + 21 wt.% Bt + 31 wt.% An20 + 4 wt.% Ap. Such amount of apatite is rather high but it allows for a good reproduction of the CaO behavior. The P_2O_5 behavior is not well reproduced, as already noticed by Tartèse and Boulvais (2010), and could perhaps be attributed to the mobility of P_2O_5 in deuteric systems (Kontak et al., 1996). The calculated amount of fractional crystallization in this model is 13 wt.%. These results are similar to those obtained for the Lizio and Questembert granites by Tartèse and Boulvais (2010), who estimated that the high SiO_2 samples from the Questembert granite could have derived from magmas similar to the low SiO_2 samples of the Lizio granite if a fractionation of 16 wt.% of an assemblage composed of 51 wt.% Kfs + 22 wt.% Bt + 27 wt.% Pl occurred.

9.2.3.2. Trace-elements. Ba is a compatible element in biotite and potassic feldspar whereas Sr is compatible in plagioclase and apatite. In Fig. 15c, the whole-rock compositions of the unaltered Guérande granite samples are plotted in a Ba versus Sr diagram, with two theoretical models of evolution for the Ba and Sr contents for a variable amount of fractional crystallization of the assemblage 0.45 Kfs + 0.21 Bt + 0.31 Pl + 0.04 Ap. The two models have been calculated using the Rayleigh distillation-type fractional crystallization for two different ranges of Kd displayed in the table in Fig. 15c. The two calculated trends reproduce the trend defined by the Guérande granite samples and the calculated amount of crystallization between 10 and 30% is consistent with the previous amount of fractionate (13 wt.%) calculated using the major elements. Sample GUE-2 displays higher degrees of mineral-melt segregation, but as noticed previously, this sample underwent a weak albitization (Table 1). Therefore, its Sr and Ba contents could have been modified during this hydrothermal process. Regarding other trace-elements whose behavior are controlled by accessory minerals (Th, Zr, REE), an example of modeling developed by Tartèse and Boulvais (2010) showed that even a minute fraction of mineral fractionation can account for the content variations actually measured in the rocks. Such a modeling is not reproduced here and the interested readers are invited to refer to these authors.

9.2.4. Mechanism of differentiation

The physical mechanism by which minerals segregated from the melt is still unclear. In fact, the process of fractional crystallization is considered to be difficult to initiate in granitic magmas because of the high viscosity of the melt and the low density contrast between crystals and melt (Yamato et al., 2012). Tartèse and Boulvais (2010) proposed, on the basis of a petro-geochemical study of the Lizio and Questembert granites (Fig. 1), that mineral-melt segregation could have occurred during magma ascent in dykes and that, the largest amount of vertical motion the magma underwent, the most evolved the magma becomes via differentiation. This hypothesis was tested by Yamato et al. (2012) using numerical modeling, which showed that crystal segregation of rigid crystals from an ascending magma is physically possible in a granitic melt, with typical density of 2400 $kg.m^{-3}$ and viscosity of 10^4 Pa.s, as soon as (i) crystals involved are denser than the melt and (ii) the magma migration velocity, or pressure gradient, within the dyke is low (see Fig. 9 in Yamato et al., 2012).

In the Guérande granite, the most differentiated facies are overall located at the apical zone of the intrusion (i.e. Ms–Turm coarse- to medium-grained granite, Fig. 2) suggesting that they originated from a magma that traveled more distance than the magma involved in the root zone (i.e. Root facies: Ms–Bt bearing, Fig. 2). As a consequence, the differentiation from the less to the more evolved samples of the granite could have occurred when the magma was migrating toward the apical zone.

9.3. Hydrothermal history

Evidence for fluid-rock interaction in the Guérande granite includes:

(1) Numerous pegmatitic dykes and quartz veins crosscut the granite and recorded localized magmato-hydrothermal activity.

(2) Greisens and albitized rocks have been described in the northwestern part of this intrusion (Figs. 2 and 8b). Greisenization generally occurs during the interaction with hot magmatic fluids (400–600 °C; Jébrak and Marcoux, 2008) whereas albitization can be related to the interaction with fluids of variable origins, either magmatic (Lee and Parsons, 1997) or post-magmatic (Boulvais et al., 2007). Here, the facts that these albitized rocks are concentrated near the apical zone of the intrusion and are spatially associated with greisenization, (i.e., a magmato-hydrothermal process where albitization is complementary; Schwartz and Surjono, 1990), suggest that both alterations

resulted from the interaction with high temperature fluids at the apex of the Guérande granitic body. Fig. 8a allows to discriminate samples which have lost their igneous compositions during such a hydrothermal alteration. Among them, the albitized dyke samples GUE-19a and GUE-19b (Fig. 8b) display textural similarities with the aplitic dyke GUE-20 (Table 1) suggesting that they share the same origin. This hypothesis is supported by the fact that samples GUE-20, GUE-19a and 19b display similar REE patterns (Fig. 10). Also, these three samples are enriched in Be, an independent feature related to the interaction with a fluid phase.

(3) In Fig. 11a, some samples (mostly the Ms–Turm bearing ones) display a strong increase in their Cs and Sn contents, up to one order of magnitude, towards the apical zone of the granite where cassiterite (SnO_2) occurs in quartz veins (Audren et al., 1975). In Fig. 11b, Cs and Sn are very well correlated; this trend could be interpreted as reflecting the magmatic behavior of Sn and Cs, two highly incompatible elements, during fractional crystallization. Nevertheless, the increase in the Cs content from 5 (GUE-17) to 77 ppm (GUE-1), for example, would imply an unrealistic amount of fractional crystallization (more than 90%) even if we consider that Cs displays a purely incompatible behavior. The high Cs and Sn contents rather reflect an enrichment in samples that interacted with fluids where Sn and Cs were strongly concentrated (e.g., Förster et al., 1999).

(4) K/Rb values for the Guérande granite samples range from 243 down to 71, with values for the Ms–Turm bearing samples always below 150. Such values below 150 are characteristic of the pegmatite-hydrothermal evolution of Shaw (1968).

(5) The ratios between twin elements, such as Nb/Ta, may be fractionated during magmato-hydrothermal processes either by muscovite and biotite fractionation (Stepanov et al., 2014) or by fluid-rock interaction (Dostal and Chatterjee, 2000). Here, the Nb/Ta ratios decrease below a value of 5 toward the apical zone (Fig. 11a) and is anti-correlated with Cs (Fig. 11b), likely indicating that the decrease of the Nb/Ta ratios is the witness of the interaction with fluids, as already noticed by Tartèse and Boulvais (2010) for the most evolved samples from the Questembert granite.

(6) Chemical analyses of the muscovite grains (Fig. 7b) reveal that a secondary muscovitization process occurred in the Guérande granite. This phenomenon increases from the Ms–Bt to the Ms–Turm bearing samples and seems to be correlated with the decrease of the Nb/Ta ratios and the increase of the Cs and Sn contents. These observations suggest that secondary muscovitization could also be related to an interaction with fluids.

To sum up, the Guérande granite experienced both localized and pervasive magmato-hydrothermal activity. Localized fluid circulation is recorded at the scale of the intrusion by the presence of numerous quartz and pegmatitic veins whereas the pervasive hydrothermal interaction was prevalent at the apical zone of the pluton.

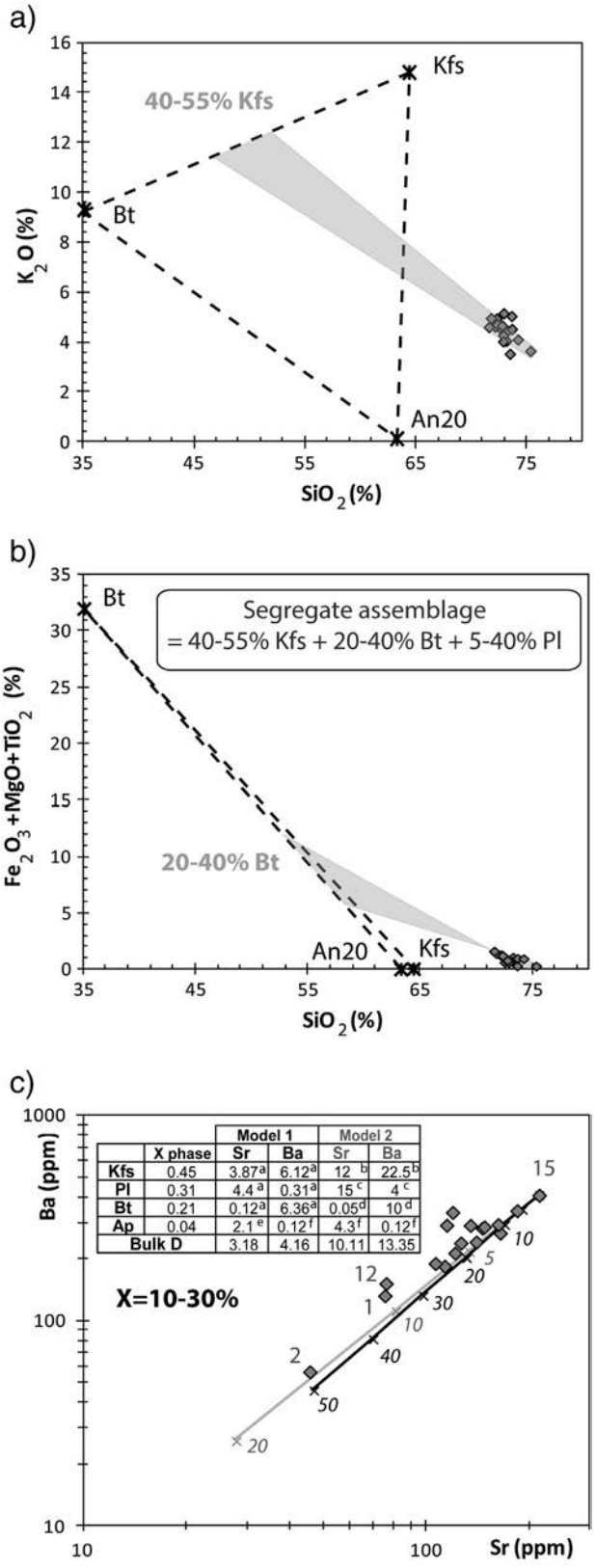

Fig. 15. a–b) Harker diagrams displaying the whole-rock compositions of the unaltered samples from the Guérande granite. The black stars represent the average compositions of potassic feldspar and biotite from the sample GUE-4 and the composition of a theoretical plagioclase (An20). The gray areas represent the magmatic trends defined by the whole-rock data including the errors. The intersection of this trend with the assemblage Bt + An20 + Kfs encompasses the mineralogical composition of the segregate. c) Ba vs Sr diagram displaying the whole-rock compositions of the unaltered samples from the Guérande granite. The two lines represent two different models of evolution of Ba and Sr compositions in a liquid during the fractional crystallization of an assemblage made of 0.45Kfs + 0.31Pl + 0.21Bt + 0.04Ap. The numbers under the line indicate the amount of the assemblage fractionated from the melt in wt.%. The primitive composition of the liquid used to model fractional crystallization is the composition of sample GUE-15. Kd used and presented in the table in inset in the diagram are from a. Hanson (1978); b. Icenhower and London (1996); c. Ren et al. (2003); d. Icenhower and London (1995); e. Watson and Green (1981); and f. Prowatke and Klemme (2006).

9.4. Timing of events

U–Th–Pb dating of zircon and monazite from two samples from the Ms–Bt coarse- to medium-grained granite (Fig. 14a and b) yielded dates equivalent within error (309 ± 2.6 Ma: Zrn GUE-3; 309.3 ± 6.1 Ma: Zrn

Table 5
Result of fractional crystallization modeling between the less differentiated sample GUE-15 and more differentiated sample GUE-12.

	Less differentiated GUE-15 sample	More differentiated GUE-12 sample			Segregate composition
		Measured	Computed	Difference	
SiO_2	71.60	74.21	74.07	0.140	55.52
Al_2O_3	15.04	14.50	14.35	0.151	19.54
Fe_2O_3	1.16	0.73	0.53	0.195	5.23
MgO	0.32	0.16	0.21	−0.054	1.01
CaO	0.82	0.48	0.42	0.058	3.41
Na_2O	3.85	4.00	3.92	0.080	3.40
K_2O	4.59	4.08	3.98	0.097	8.54
TiO_2	0.18	0.09	0.13	−0.040	0.51
P_2O_5	0.23	0.25	0.02	0.232	1.61
Segregating minerals, wt.%					
Kfs					44.5
Bt					21.1
An20					30.7
Ap					3.7
Amount of solid segregate removed, wt.%					13.3
Sum residuals squared ΣR^2					0.16

GUE-8; 309.4 ± 1.9 Ma: Mnz GUE-3) and the analyses of the monazite grains from a sample from the Ms–Bt fine-grained facies (GUE-4) yielded a Th–Pb date of 309.7 ± 1.3 Ma (Fig. 14c). Both zircon and monazite ages are identical within error and are consistent with the field observation of Ouddou (1984) that revealed mingling features at the contact between these two facies attesting for their synchronous emplacement. We therefore conclude that the Guérande granite was emplaced ca. 310 Ma ago. The muscovite Ar–Ar age of 307 ± 0.3 Ma, obtained by Le Hébel, 2002 for the undeformed granite, could therefore be interpreted as a cooling age.

U–Th–Pb analysis of monazite and zircon grains from the dyke sample GUE-5 (Fig. 14d) yielded dates equivalent within error (Zrn: 299.6 ± 5.4 Ma; Mnz: 302.5 ± 1.6 Ma), so this dyke was emplaced ca. 303 Ma ago, which is indicative of a second magmatic event in the vicinity. This age is directly comparable to the muscovite Ar–Ar ages of 303.3 ± 0.5 Ma obtained for a quartz vein and of 303.6 ± 0.5 Ma and 304 ± 0.5 Ma obtained on a sheared granite and on a mylonitic granite, respectively (Le Hébel, 2002).

To summarize, considering that the Guérande granite displays S/C and mylonitic structures, it is likely that the main phase of granite emplacement occurred syntectonically at ca. 310 Ma. Late magmatic activity at ca. 303 Ma was still coeval with deformation. The circulation of fluids responsible for the quartz veins emplacement and possibly for the secondary muscovitization process that pervasively affected the apical zone of the Guérande granite (Fig. 7) likely occurred during both stages. If large amounts of exsolved fluids are expected during the main emplacement stage of the Guérande granite at ca. 310 Ma, the Ar–Ar age on muscovite grains from a quartz vein shows that hydrothermal circulation was still active at ca. 303 Ma.

10. Conclusion

This study provides new constraints on the tectonic and magmatic history of the Guérande peraluminous leucogranite and allows to shed some light on the mobility of elements during hydrothermal activity. These new structural and petro-geochemical data lead to the following conclusions:

(1) Structural and petrographic observations throughout the intrusion indicate that the southwestern part of the Guérande granite represents the feeding zone whereas its northwestern part corresponds to the apical zone.
(2) The Guérande granite was emplaced in an extensional tectonic regime and probably underwent a partitioning of the deformation during its cooling. Indeed, the strike of quartz veins and pegmatitic dykes and the lineations directions measured within the massif suggest that both N–S and E–W stretching occurred synchronously in this area.
(3) Sr and Nd isotope data suggest that the Guérande granite formed by partial melting of metasedimentary formations. When compared to others syntectonic peraluminous granites from both the central and southern part of the Armorican Massif, from north to south, the increase of I_{Sr} and the decrease of εNd could be explained by sedimentary sources becoming gradually dominated by Paleozoic sediments relative to Brioverian sediments, combined with a mantle contribution limited to the central part of the Armorican Massif.
(4) The magmatic history of the Guérande granite is controlled by fractional crystallization where an amount of ~15% of fractionation of an assemblage composed of Kfs + Pl + Bt (± Ap ± Zrn ± Mnz ± Fe–Ti oxide) can explain the chemical variations observed between the samples.
(5) The apex of the Guérande leucogranite experienced pervasive hydrothermal alteration which induced an enrichment in incompatible elements such as Sn and Cs, secondary muscovitization and the decrease of geochemical ratio such as K/Rb and Nb/Ta in the samples.
(6) U–Th–Pb dating on zircon and monazite reveal that the Guérande granite was emplaced 309.7 ± 1.3 Ma ago and that a late magmatic activity synchronous with a hydrothermal circulation occurred ca. 303 Ma ago. The magmatic and fluid–rock interaction events documented here likely provides some key information for the U and Sn mineralization geometrically associated with the Guérande intrusion.

Supplementary data to this article can be found online at http://dx.doi.org/10.1016/j.lithos.2015.01.027.

Acknowledgments

This study is based on the work carried out by C. Ballouard for his Master's degree and was supported by the 2012 and 2013 NEEDS-CNRS (AREVA–CEA) grants to M. Poujol. Rémi Sarrazin helped during field work. The authors want to thank D. Vilbert (Géosciences Rennes) and J. Langlade (IFREMER, Brest) for their contributions during the radiogenic isotopes and the electron microprobe analyses respectively. This paper benefited from comments from P. Barbey and an anonymous reviewer on an earlier version of the manuscript and from D.B. Clarke and A. Patiño Douce on the present version.

References

Audren, C., Jegouzo, P., Barbaroux, L., Bouysse, P., 1975. La Roche-Bernard, 449. Bureau de Recherches Géologiques et Minières.
Ballèvre, M., Bosse, V., Ducassou, C., Pitra, P., 2009. Palaeozoic history of the Armorican Massif: models for the tectonic evolution of the suture zones. Comptes Rendus Geosciences 341, 174–201.
Barbarin, B., 1999. A review of the relationships between granitoid types, their origins and their geodynamic environments. Lithos 46, 605–626.
Bernard-Griffiths, J., Peucat, J.J., Sheppard, S., Vidal, P., 1985. Petrogenesis of Hercynian leucogranites from the southern Armorican Massif: contribution of REE and isotopic (Sr, Nd, Pb and O) geochemical data to the study of source rock characteristics and ages. Earth and Planetary Science Letters 74, 235–250.
Berthé, D., Choukroune, P., Jegouzo, P., 1979. Orthogneiss, mylonite and non coaxial deformation of granites: the example of the South Armorican Shear Zone. Journal of Structural Geology 1, 31–42.
Bosse, V., Ballevre, M., Vidal, O., 2002. Ductile thrusting recorded by the garnet isograd from blueschist-facies Metapelites of the Ile de Groix, Armorican Massif, France. Journal of Petrology 43, 485–510.
Bosse, V., Féraud, G., Ballèvre, M., Peucat, J.-J., Corsini, M., 2005. Rb–Sr and $^{40}Ar/^{39}Ar$ ages in blueschists from the Ile de Groix (Armorican Massif, France): implications for closure mechanisms in isotopic systems. Chemical Geology 220, 21–45.
Bossière, G., 1988. Evolutions chimico-minéralogiques du grenat et de la muscovite au voisinage de l'isograde biotite-staurotide dans un métamorphisme prograde de type barrovien: un exemple en Vendée littorale (Massif Armoricain). Comptes Rendus de l'Académie des Sciences, Paris, série II 306, 135–140.

Bouchez, J., Guillet, P., Chevalier, F., 1981. Structures d'écoulement liées à la mise en place du granite de Guérande (Loire-Atlantique, France). Bulletin de la Societe Geologique de France XXIII-4, 387–399.
Boulvais, P., Ruffet, G., Cornichet, J., Mermet, M., 2007. Cretaceous albitization and dequartzification of Hercynian peraluminous granite in the Salvezines Massif (French Pyrénées). Lithos 93, 89–106.
Brown, M., Pressley, R.A., 1999. Crustal melting in nature: prosecuting source processes. Physics and Chemistry of the Earth Part A: Solid Earth and Geodesy 24, 305–316.
Burg, J.P., Van Den Driessche, J., Brun, J.P., 1994. Syn- to post thickening extension in the Variscan Belt of Western Europe: modes and structural consequences. Géologie de la France 3, 33–51.
Cagnard, F., Gapais, D., Brun, J.P., Gumiaux, C., Van den Driessche, J., 2004. Late pervasive crustal-scale extension in the south Armorican Hercynian belt (Vendée, France). Journal of Structural Geology 26, 435–449.
Capdevila, R., Corretgé, G., Floor, P., 1973. Les granitoides Varisques de la Meseta Ibérique. Bulletin de la Societe Geologique de France XV-3–4, 209–228.
Carignan, J., Hild, P., Mevelle, G., Morel, J., Yeghicheyan, D., 2001. Routine analyses of trace elements in geological samples using flow injection and low pressure on-line liquid chromatography coupled to ICP-MS: a study of geochemical reference materials BR, DR–N, UB–N, AN–G and GH. Geostandards Newsletter 25, 187–198.
Cathelineau, M., 1981. Les Gisements Uraniferes de la Presqu'ile Guerandaise (Sud Bretagne); Approche Structurale et Metallogenique. Mineralium Deposita 16, 227–240.
Chantraine, J., Autran, A., Cavelier, C., 2003. Carte géologique de la france à l'échelle du millionième, 6ème édition. Bureau de Recherches Géologiques et Minières.
Chappell, B.W., White, A.J.R., Wyborn, D., 1987. The importance of residual source material (Restite) in granite petrogenesis. Journal of Petrology 28, 1111–1138.
Chen, Y., Clark, A.H., Farrar, E., Wasteneys, H.A.H.P., Hodgson, M.J., Bromley, A.V., 1993. Diachronous and independent histories of plutonism and mineralization in the Cornubian Batholith, southwest England. Journal of the Geological Society 150, 1183–1191.
Clemens, J.D., Stevens, G., 2012. What controls chemical variation in granitic magmas? Lithos 134–135, 317–329.
Cogné, J., 1966. Les grands cisaillement hercyniens dans le Massif Armoricain et les phénomènes de granitisation. Etages tectoniques. Edition de la Braconièrepp. 179–192.
Collins, W.J., Sawyer, E.W., 1996. Pervasive granitoid magma transfer through the lower–middle crust during non-coaxial compressional deformation. Journal of Metamorphic Geology 14, 565–579.
Cosca, M., Stunitz, H., Bourgeix, A.L., Lee, J.P., 2011. 40Ar* loss in experimentally deformed muscovite and biotite with implications for $^{40}Ar/^{39}Ar$ geochronology of naturally deformed rocks. Geochimica et Cosmochimica Acta 75, 7759–7778.
D'lemos, R.S., Brown, M., Strachan, R.A., 1992. Granite magma generation, ascent and emplacement within a transpressional orogen. Journal of the Geological Society 149, 487–490.
Dabard, M.P., Loi, A., Peucat, J.J., 1996. Zircon typology combined with Sm–Nd whole-rock isotope analysis to study Brioverian sediments from the Armorican Massif. Sedimentary Geology 101, 243–260.
Debon, F., Le Fort, P., 1988. A cationic classification of common plutonic rocks and their magmatic associations: principles, method, applications. Bulletin de Mineralogie 111 (5), 493–510.
Deniel, C., Vidal, P., Fernandez, A., Fort, P.L., Peucat, J.J., 1987. Isotopic study of the Manaslu granite (Himalaya, Nepal): inferences on the age and source of Himalayan leucogranites. Contributions to Mineralogy and Petrology 96, 78–92.
Dostal, J., Chatterjee, A.K., 1995. Origin of topaz-bearing and related peraluminous granites of the Late Devonian Davis Lake pluton, Nova Scotia, Canada: crystal versus fluid fractionation. Chemical Geology 123, 67–88.
Dostal, J., Chatterjee, A.K., 2000. Contrasting behaviour of Nb/Ta and Zr/Hf ratios in a peraluminous granitic pluton (Nova Scotia, Canada). Chemical Geology 163, 207–218.
Euzen, T., 1993. Pétrogenèse des granites de collision post-épaississement. Le cas des granites crustaux et mantelliques du complexe de Pontivy-Rostrenen (Massif Armoricain, France). Memoires Géosciences Rennes 51 (360 pp.).
Evensen, N.M., Hamilton, P.J., O'Nions, R.K., 1978. Rare-earth abundances in chondritic meteorites. Geochimica et Cosmochimica Acta 42, 1199–1212.
Förster, H.-J., Tischendorf, G., Trumbull, R.B., Gottesmann, B., 1999. Late-Collisional Granites in the Variscan. Erzgebirge, Germany. Journal of Petrology 40, 1613–1645.
Gapais, D., 1989. Shear structures within deformed granites: mechanical and thermal indicators. Geology 17, 1144–1147.
Gapais, D., Lagarde, J.L., Le Corre, C., Audren, C., Jegouzo, P., Casas Sainz, A., Van Den Driessche, J., 1993. La zone de cisaillement de Quiberon: témoin d'extension de la chaine varisque en Bretagne méridionale au Carbonifère. Comptes Rendus de l'Académie des Sciences, Paris, série II 316, 1123–1129.
Gapais, D., Brun, J.P., Gumiaux, C., Cagnard, F., Ruffet, G., Le Carlier de Veslud, C., 2015. Extensional tectonics in the Hercynian Armorican belt (France). An overview. Bulletin de la Société Géologique de France 186, 117–129.
Gasquet, D., Bertrand, J.-M., Paquette, J.-L., Lehmann, J., Ratzov, G., Guedes, R.D.A., Tiepolo, M., Boullier, A.-M., Scaillet, S., Nomade, S., 2010. Miocene to Messinian deformation and hydrothermal activity in a pre-Alpine basement massif of the French western Alps: new U–Th–Pb and argon ages from the Lauzière massif. Bulletin de la Societe Geologique de France 181, 227–241.
Goujou, J.C., 1992. Analyse pétro-structurale dans un avant-pays métamorphique: influence du plutonisme tardi-orogénique varisque sur l'encaissant épi à mésozonal de Vendée. Document du Bureau de Recherches Géologique et Minière 216.
Gumiaux, C., 2003. Modelisation du cisaillement hercynien de Bretagne Centrale: deformation crustale et implications litosphériques. Thèse, Université de Rennes 1 (266 pp.).
Gumiaux, C., Gapais, D., Brun, J.P., Chantraine, J., Ruffet, G., 2004. Tectonic history of the Hercynian Armorican Shear belt (Brittany, France). Geodinamica Acta 17, 289–307.
Hanson, G.N., 1978. The application of trace elements to the petrogenesis of igneous rocks of granitic composition. Earth and Planetary Science Letters 38, 26–43.
Hassenforder, B., Cogné, J., Barbaroux, L., Ottman, F., Berthois, L., 1973. Saint-Nazaire, 479. Bureau de Recherches Géologiques et Minières.
Hughes, C.J., 1973. Spilites, keratophyres, and the igneous spectrum. Geological Magazine 109, 513–527.
Hutton, D.H.W., 1988. Granite emplacement mechanisms and tectonic controls: inferences from deformation studies. Earth and Environmental Science Transactions of the Royal Society of Edinburgh 79, 245–255.
Icenhower, J., London, D., 1995. An experimental study of element partitioning among biotite, muscovite, and coexisting peraluminous silicic melt at 200 MPa (H_2O). American Mineralogist 80, 1229–1251.
Icenhower, J., London, D., 1996. Experimental partitioning of Rb, Cs, Sr, and Ba between alkali feldspar and peraluminous melt. American Mineralogist 81, 719–734.
Jackson, S.E., Pearson, N.J., Griffin, W.L., Belousova, E.A., 2004. The application of laser ablation-inductively coupled plasma-mass spectrometry to in situ U–Pb zircon geochronology. Chemical Geology 211, 47–69.
Janoušek, V., Rogers, G., Bowes, D.R., Vaòková, V., 1997. Cryptic trace-element variation as an indicator of reverse zoning in a granitic pluton: the Ricany granite, Czech Republic. Journal of the Geological Society 154, 807–815.
Janoušek, V., Farrow, C.M., Erban, V., 2006. Interpretation of whole-rock geochemical data in igneous geochemistry: introducing geochemical data toolkit (GCDkit). Journal of Petrology 47, 1255–1259.
Jébrak, M., Marcoux, É., 2008. Géologie des Ressources Minérales. Ministère des ressources naturelles et de la faune.
Jégouzo, P., 1980. The South Armorican Shear Zone. Journal of Structural Geology 2, 39–47.
Jones, K.A., Brown, M., 1990. High-temperature "clockwise" P–T paths and melting in the development of regional migmatites: an example from southern Brittany, France. Journal of Metamorphic Geology 8, 551–578.
Kontak, D.J., Martin, R.F., Richard, L., 1996. Patterns of phosphorus enrichment in alkali feldspar, South Mountain Batholith, Nova Scotia, Canada. European Journal of Mineralogy 8, 805–824.
Kretz, R., 1983. Symbols for rock-forming minerals. American Mineralogist 68, 277–279.
La Roche, H., Sussi, J., Chauris, L., 1980. Les granites à deux micas hercyniens français. Sciences de la Terre 24, 5–121.
Lagarde, J.L., Capdevila, R., Fourcade, S., 1992. Granites et collision continentale; l'exemple des granitoides carboniferes dans la chaine hercynienne ouest-europeenne. Bulletin de la Societe Geologique de France 163, 597–610.
Lameyre, J., 1980. Les magmas granitiques: leurs comportements, leurs associations et leurs sources. Mémoire hors-série de la Société Géologique de France 10, 51–62.
Le Fort, P., Cuney, M., Deniel, C., France-Lanord, C., Shepard, S.M.F., Upreti, B.N., Vidal, P., 1987. Crustal generation of the Himalayan leucogranites. Tectonophysics 134, 39–57.
Le Hébel, F., 2002. Déformation continentale et histoire des fluides au cours d'un cycle subduction, exhumation, extension. Thèse, Exemple des porphyroïdes Sud-Armoricains. Université de Rennes 1 (218 pp.).
Le Hébel, F., Vidal, O., Kienast, J.-R., Gapais, D., 2002. Les Porphyroides de Bretagne méridionale: une unité de HP–BT dans la chaîne hercynienne. Comptes Rendus Geoscience 334, 205–211.
Le Hébel, F., Fourcade, S., Boiron, M.-C., Cathelineau, M., Capdevila, R., Gapais, D., 2007. Fluid history during deep burial and exhumation of oil-bearing volcanics, Hercynian Belt of southern Brittany, France. American Journal of Science 307, 1096–1125.
Lee, M.R., Parsons, I., 1997. Dislocation formation and albitization in alkali feldspars from the Shap Granite. American Mineralogist 82, 557–570.
Lemarchand, J., Boulvais, P., Gaboriau, M., Boiron, M.-C., Tartèse, R., Cokkinos, M., Bonnet, S., Jégouzo, P., 2012. Giant quartz vein formation and high-elevation meteoric fluid infiltration into the South Armorican Shear Zone: geological, fluid inclusion and stable isotope evidence. Journal of the Geological Society 169, 17–27.
Liew, T.C., Hofmann, A.W., 1988. Precambrian crustal components, plutonic associations, plate environment of the Hercynian Fold Belt of central Europe: indications from a Nd and Sr isotopic study. Contributions to Mineralogy and Petrology 98, 129–138.
Ludwig, K.R., 2001. Isoplot/Ex Version 2.49. A Geochronological Toolkit for Microsoft Excel. Berkeley Geochronology Center, Special, Publication 1app. 1–55.
Michard, A., Gurriet, P., Soudant, M., Albarede, F., 1985. Nd isotopes in French Phanerozoic shales: external vs. internal aspects of crustal evolution. Geochimica et Cosmochimica Acta 49, 601–610.
Miller, C.F., Stoddard, E.F., Bradfish, L.J., Dollase, W.A., 1981. Composition of plutonic muscovite; genetic implications. The Canadian Mineralogist 19, 25–34.
Montel, J.-M., Vielzeuf, D., 1997. Partial melting of metagreywackes, Part II. Compositions of minerals and melts. Contributions to Mineralogy Petrology 128, 176–196.
Nachit, H., Razafimahefa, N.J.M.S., Carron, J., 1985. Composition chimique des biotites et typologie magmatique des granitoïdes. Comptes Rendus de l'Académie des Sciences, Paris, série II 301, 813–818.
Ouddou, D., 1984. Le Massif de Guérande-Le Croisic (Loire-Atlantique): Caractérisation géochimique et minéralogique de l'évolution magmatique. Comportement de l'uranium (Thèse, INPL-CREGU Nancy, 309 pp.).
Paquette, J.L., Tiepolo, M., 2007. High resolution (5 μm) U–Th–Pb isotope dating of monazite with excimer laser ablation (ELA)-ICPMS. Chemical Geology 240, 222–237.
Patiño Douce, A.E., 1999. What do experiments tell us about the relative contributions of crust and mantle to the origin of granitic magmas? Geological Society of London, Special Publication 168, 55–75.

Patiño Douce, A.E., Johnston, A.D., 1991. Phase equilibria and melt productivity in the pelitic system: implications for the origin of peraluminous granitoids and aluminous granulites. Contributions to Mineralogy and Petrology 107, 202–218.
Peucat, J., Charlot, R., Mifdal, A.J.C., Autran, A., 1979. Définition géochronologique de la phase bretonne en Bretagne centrale, étude Rb–Sr de granites en domaine Centre-Armoricain. Bulletin du Bureau de Recherches Geologiques et Minieres, BRGM 2 (I4), 349–356.
Peucat, J.J., Jegouzo, P., Vidal, P., Bernard-Griffiths, J., 1988. Continental crust formation seen through the Sr and Nd isotope systematics of S-type granites in the Hercynian belt of western France. Earth and Planetary Science Letters 88, 60–68.
Pitra, P., Boulvais, P., Antonoff, V., Diot, H., 2008. Wagnerite in a cordierite–gedrite gneiss: witness of long-term fluid-rock interaction in the continental crust (Ile d'Yeu, Armorican Massif, France). American Mineralogist 93, 315–326.
Proust, J., Guennoc, P., Thinon, I., Menier, D., 2009. Carte géologique de la France à 1/250 000 de la marge continentale: Lorient, Bretagne Sud. Bureau de Recherches Géologiques et Minières; Centre National de La Recherche Scientifique.
Prowatke, S., Klemme, S., 2006. Trace element partitioning between apatite and silicate melts. Geochimica et Cosmochimica Acta 70, 4513–4527.
Puziewicz, J., Johannes, W., 1988. Phase equilibria and compositions of Fe–Mg–Al minerals and melts in water-saturated peraluminous granitic systems. Contributions to Mineralogy and Petrology 100, 156–168.
Ramsay, J.G., Huber, M.I., 1983. Strain Analysis, The Techniques of Modern Structural Geology, Vol. 1. Strain Analysis. Academic Press, London.
Ren, M., Parker, D.F., White, J.C., 2003. Partitioning of Sr, Ba, Rb, Y, and LREE between plagioclase and peraluminous silicic magma. American Mineralogist 88, 1091–1103.
Schwartz, M.O., Surjono, 1990. Greisenization and albitization at the Tikus tin–tungsten deposit, Belitung, Indonesia. Economic Geology 85, 691–713.
Searle, M.P., 1999. Emplacement of Himalayan leucogranites by magma injection along giant sill complexes: examples from the Cho Oyu, Gyachung Kang and Everest leucogranites (Nepal Himalaya). Journal of Asian Earth Sciences 17, 773–783.
Shand, S., 1943. Eruptive Rocks. Their genesis, composition, classification, and their relations to ore-deposits 2. Wiley, New York, p. 444.
Shaw, D., 1968. A review of K–Rb fractionation trends by covariance analysis. Geochimica et Cosmochimica Acta 32, 573–601.
Słaby, E., Martin, H., 2008. Mafic and felsic magma interaction in granites: the Hercynian karkonosze pluton (Sudetes, Bohemian Massif). Journal of Petrology 49, 353–391.
Stepanov, A., Mavrogenes, J.A., Meffre, S., Davidson, P., 2014. The key role of mica during igneous concentration of tantalum. Contributions to Mineralogy and Petrology 167, 1–8.
Stevens, G., Villaros, A., Moyen, J.-F., 2007. Selective peritectic garnet entrainment as the origin of geochemical diversity in S-type granites. Geology 35, 9–12.
Strong, D.F., Hanmer, S.K., 1981. The leucogranites of southern Brittany; origin by faulting, frictional heating, fluid flux and fractional melting. The Canadian Mineralogist 19, 163–176.
Tartèse, R., Boulvais, P., 2010. Differentiation of peraluminous leucogranites "en route" to the surface. Lithos 114, 353–368.
Tartèse, R., Poujol, M., Ruffet, G., Boulvais, P., Yamato, P., Košler, J., 2011a. New U–Pb zircon and 40Ar/39Ar muscovite age constraints on the emplacement of the Lizio syntectonic granite (Armorican Massif, France). Comptes Rendus Geoscience 343, 443–453.
Tartèse, R., Ruffet, G., Poujol, M., Boulvais, P., Ireland, T.R., 2011b. Simultaneous resetting of the muscovite K–Ar and monazite U–Pb geochronometers: a story of fluids. Terra Nova 23, 390–398.
Triboulet, C., Audren, C., 1988. Controls on P–T–t deformation path from amphibole zonation during progressive metamorphism of basic rocks (estuary of the River Vilaine, South Brittany, France). Journal of Metamorphic Geology 6, 117–133.
Turrillot, P., Augier, R., Faure, M., 2009. The top-to-the-southeast Sarzeau shear zone and its place in the late-orogenic extensional tectonics of southern Armorica. Bulletin de la Societe Geologique de France 180, 247–261.
Ugidos, J.M., Recio, C., 1993. Origin of cordierite-bearing granites by assimilation in the Central Iberian Massif (CIM), Spain. Chemical Geology 103, 27–43.
Valois, J., 1975. Les formations métamorphiques de Pénaran (presqu'île de Guérande, Loire Atlantique) et leur minéralisation uranifère (Thèse 3e cycle, Nancy, 136 pp.).
Vielzeuf, D., Holloway, J.R., 1988. Experimental determination of the fluid-absent melting relations in the pelitic system. Contributions to Mineralogy and Petrology 98, 257–276.
Vigneresse, J., 1983. Enracinement des granites armoricains estimé d'après la gravimétrie. Bulletin de la societé Géologique et minéralogique de Bretagne C (15 (1)), 1–15.
Watson, E.B., Green, T.H., 1981. Apatite/liquid partition coefficients for the rare earth elements and strontium. Earth and Planetary Science Letters 56, 405–421.
Wiedenbeck, M., Allé, P., Corfu, F., Griffin, W.I., Meier, M., Oberli, F., Quadt, A.V., Roddick, J.C., Spiegel, W., 1995. Three natural zircon standards for U–Th–Pb, Lu–Hf, trace element and REE analyses. Geostandards Newsletter 19, 1–23.
Willis-Richards, J., Jackson, N.J., 1989. Evolution of the Cornubian ore field, Southwest England; Part I, Batholith modeling and ore distribution. Economic Geology 84, 1078–1100.
Yamato, P., Tartèse, R., Duretz, T., May, D.A., 2012. Numerical modelling of magma transport in dykes. Tectonophysics 526–529, 97–109.

Données en isotopes radiogéniques complémentaires sur le leucogranite de Guérande

Lors de la publication de l'article #2, nous ne disposions pas d'analyses en isotopes radiogéniques sur les facies à muscovite-tourmaline de la zone apicale du leucogranite de Guérande. Il était donc légitime de se demander si la richesse en éléments incompatibles de ces échantillons n'était pas en partie liée à une différence de source. Des analyses sur roches totales complémentaires en isotopes du Sr et Nd ont donc été réalisées sur deux échantillons (GUE-1 et GUE-9) de leucogranite à Ms-Turm (Table III.1). Le protocole d'analyse est le même que celui décrit dans l'article #3. Les rapports $^{87}Sr/^{86}Sr$ initiaux [I_{Sr}(310 Ma)] des deux échantillons varient entre 0.7158 et 0.7196 et sont comparables à ceux obtenus précédemment sur les autres facies de l'intrusion (Fig. III.1). Il en va de même pour les valeurs en εNd(310 Ma) qui varient entre -9.61 et -7.96 pour des âges modèle Nd (T_{DM}) entre 1.65 et 1.78 Ga (Fig. III.1). Ainsi, il n'existe pas de différences majeures entre la source des facies à muscovite-tourmaline et des facies à muscovite-biotite. On peut donc en conclure, que le fort enrichissement en éléments incompatibles de ces échantillons, y compris les rapports Nb/Ta < 5, relate bien de processus secondaires comme la cristallisation fractionnée et l'activité magmatique-hydrothermale.

Table III.1 : Composition isotopique roche totale en Rb-Sr et Sm-Nd de deux échantillons à muscovite-tourmaline du leucogranite de Guérande. Les concentrations en Rb ont été obtenues par ICP-MS et les autres par dilution isotopique.

Sample	Rb (ppm)	Sr (ppm)	$^{87}Rb/^{86}Sr$	$^{87}Sr/^{86}Sr$	±	$^{87}Sr/^{86}Sr$ (310 Ma)	Sm (ppm)	Nd (ppm)	$^{147}Sm/^{144}Nd$	$^{143}Nd/^{144}Nd$	±	εNd (310 Ma)	T_{DM}*
GUE-1	356.9	70.7	14.7	0.780550	9	0.715679	1.6	6.0	0.144798	0.512125	4	-7.96	1.65
GUE-9	243.6	163.3	4.5	0.739690	10	0.719621	2.0	8.0	0.147867	0.512047	5	-9.61	1.78

** Two stages T_{DM} calculated using the equation of Liew and Hofmann (1988) for an age of 315 Ma.*

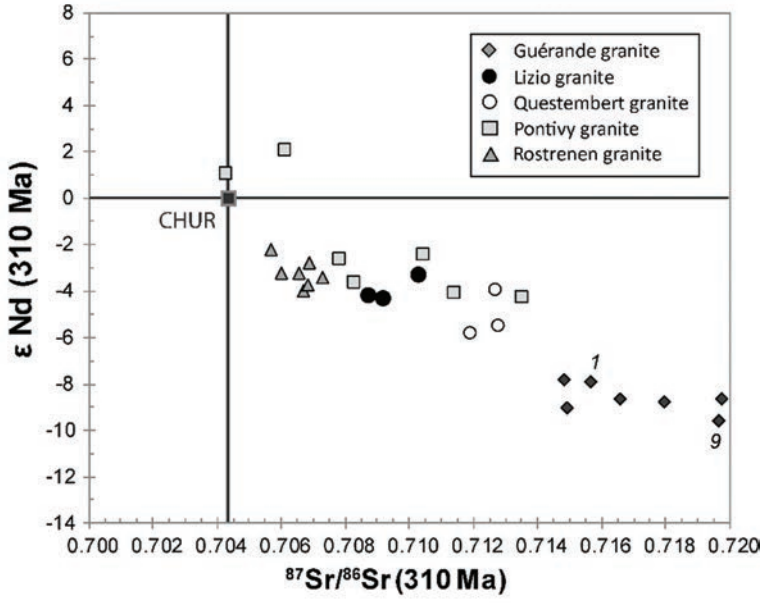

Fig. III.1 : Composition isotopique en Sr et Nd, calculés à 310 Ma, des échantillons du leucogranite de Guérande comparée aux autres granites peralumineux de la région. Les références dont sont issus les données sont les même que dans l'article #2.

Supplementary Table 3 : Feldspar and biotite average chemical compositions from selected Guérande granite samples.

		Plagioclase						K feldspar						Biotite			
		GUE-1	**GUE-3**	**GUE-4**	**GUE-5**	**GUE-8**		**GUE-1**	**GUE-3**	**GUE-4**	**GUE-5**	**GUE-8**		**GUE-3**	**GUE-4**	**GUE-5**	**GUE-8**
		n=7	n=6	n=7	n=6	n=7		n=4	n=6	n=4	n=6	n=6		n=6	n=7	n=2	n=8
Na_2O	%	10.8	10.3	10.0	10.2	10.4		0.8	0.8	1.1	0.9	1.0		0.0	0.1	0.1	0.1
MgO	%	0.0	0.0	0.0	0.0	0.0		0.0	0.0	0.0	0.0	0.0		3.5	4.8	4.7	4.6
Al_2O_3	%	19.9	20.5	20.9	20.7	20.8		18.3	18.4	18.6	18.5	18.5		20.4	20.0	20.2	20.3
SiO_2	%	68.0	66.8	66.5	66.5	67.0		64.3	64.2	64.5	64.7	64.8		35.8	35.1	35.3	35.3
P_2O_5	%	0.2	0.1	0.1	0.0	0.1		0.0	0.1	0.0	0.0	0.1		0.0	0.0	0.0	0.0
K_2O	%	0.2	0.2	0.3	0.3	0.3		15.3	15.1	14.8	14.7	14.6		9.2	9.3	9.4	8.9
CaO	%	0.4	1.1	1.7	1.4	1.4		0.0	0.0	0.0	0.0	0.0		0.0	0.0	0.0	0.1
MnO	%	0.0	0.0	0.0	0.0	0.0		0.0	0.0	0.0	0.0	0.0		0.4	0.3	0.4	0.4
FeO	%	0.0	0.0	0.0	0.0	0.0		0.0	0.0	0.0	0.1	0.0		21.8	22.3	22.7	21.7
TiO_2	%	0.0	0.0	0.0	0.0	0.0		0.0	0.0	0.0	0.0	0.0		2.4	2.4	2.2	2.1
Total	%	99.3	99.0	99.5	99.2	99.9		98.7	98.6	98.9	99.0	99.0		93.5	94.3	95.0	93.3
		Structural formula based on 8 oxygen atoms												Structural formula based on 22 oxygen atoms			
Na		0.91	0.88	0.85	0.87	0.89		0.07	0.07	0.10	0.08	0.09		0.01	0.02	0.02	0.02
Mg		0.00	0.00	0.00	0.00	0.00		0.00	0.00	0.00	0.00	0.00		0.81	1.12	1.10	1.08
Al		1.02	1.06	1.08	1.07	1.07		1.00	1.01	1.01	1.01	1.01		3.75	3.67	3.68	3.74
Si		2.98	2.95	2.92	2.94	2.94		3.00	3.00	2.99	3.00	3.00		5.60	5.47	5.48	5.52
P		0.01	0.00	0.00	0.00	0.00		0.00	0.00	0.00	0.00	0.00		0.00	0.00	0.00	0.00
K		0.01	0.01	0.02	0.02	0.01		0.91	0.90	0.88	0.87	0.86		1.83	1.84	1.85	1.78
Ca		0.02	0.05	0.08	0.07	0.07		0.00	0.00	0.00	0.00	0.00		0.00	0.00	0.00	0.01
Mn		0.00	0.00	0.00	0.00	0.00		0.00	0.00	0.00	0.00	0.00		0.06	0.04	0.05	0.05
Fe		0.00	0.00	0.00	0.00	0.00		0.00	0.00	0.00	0.01	0.00		2.83	2.90	2.94	2.83
Ti		0.00	0.00	0.00	0.00	0.00		0.00	0.00	0.00	0.00	0.00		0.28	0.28	0.25	0.24
Total		4.95	4.96	4.96	4.97	4.98		4.99	4.98	4.98	4.97	4.97		15.16	15.35	15.36	15.27
%An		1.79	5.42	8.58	7.00	6.77	**%Or**	92.90	92.61	90.12	91.12	90.56	**X_{Mg}**	0.22	0.28	0.27	0.28

Supplementary Table 4 : Muscovite average chemical composition from selected Guérande granite samples.

		GUE-1			GUE-3			GUE-8		GUE-4	GUE-5
		core	**rim**	**cleavage**	**core**	**rim**	**cleavage**	**core**	**rim**		
		n=18	n=18	n=8	n=10	n=16	n=5	n=14	n=20	n=26	n=29
Na_2O	%	0.34	0.2	0.2	0.29	0.24	0.22	0.4	0.4	0.4	0.4
MgO	%	0.96	1.23	1.33	1.01	1.26	1.29	1.1	1.13	0.89	0.88
Al_2O_3	%	32.62	30.87	30.31	32.96	31.92	32	33.5	33.34	33.73	33.72
SiO_2	%	45.94	45.97	46.2	46.27	46.35	47	47.31	47.21	46.74	46.77
P_2O_5	%	0.02	0.02	0.02	0.01	0.01	0	0.01	0.00	0.01	0.01
K_2O	%	8.89	8.58	8.76	9.05	8.99	7.95	8.11	8.02	8.61	8.36
CaO	%	0.02	0.01	0.00	0.00	0.01	0.01	0.01	0.01	0.02	0.02
MnO	%	0.06	0.12	0.13	0.04	0.06	0.05	0.03	0.03	0.03	0.04
FeO	%	2.86	4.33	4.62	2.66	3.3	3.31	2.45	2.46	2.14	2.04
TiO_2	%	0.62	0.45	0.5	0.71	0.5	0.45	0.57	0.48	0.58	0.57
Total	%	92.33	91.8	92.07	93.01	92.64	92.28	93.51	93.08	93.15	92.81
		Structural formula based on 22 oxygen atoms									
Na		0.09	0.05	0.05	0.08	0.06	0.06	0.1	0.1	0.1	0.1
Mg		0.2	0.26	0.28	0.21	0.26	0.26	0.22	0.23	0.18	0.18
Al		5.26	5.04	4.95	5.28	5.15	5.14	5.29	5.29	5.36	5.36
Si		6.3	6.39	6.42	6.3	6.35	6.42	6.35	6.36	6.31	6.32
P		0.00	0.00	0.00	0.00	0.00	0.00	0.00	0.00	0.00	0.00
K		1.56	1.52	1.55	1.57	1.57	1.38	1.39	1.38	1.48	1.44
Ca		0.00	0.00	0.00	0.00	0.00	0.00	0.00	0.00	0.00	0.00
Mn		0.01	0.01	0.01	0.01	0.01	0.01	0.00	0.00	0.00	0.00
Fe		0.33	0.5	0.53	0.30	0.38	0.38	0.27	0.28	0.24	0.23
Ti		0.06	0.05	0.05	0.07	0.05	0.05	0.06	0.05	0.06	0.06
Total		13.82	13.83	13.86	13.81	13.84	13.69	13.69	13.69	13.74	13.71

« core » and « rim » refer to analyses of cores and rims of plurimillimetric muscovite. “cleavage” refers to inframillimetric muscovite localized within the foliation planes.

Résumé de l'article #3 : Recyclage crustale et addition juvénile pendant un décrochement d'échelle lithosphérique : le complexe magmatique de Pontivy-Rostrenen, Massif Armoricain (France), chaîne hercynienne.

Le cisaillement sud armoricain (CSA), chaîne hercynienne armoricaine, est une faille décrochante d'échelle lithosphérique qui, au cours du Carbonifère supérieur, joue le rôle de zone de transfère entre un domaine en extension au sud, dominé par un magmatisme crustal, et un domaine en décrochement au nord qui est soumis à un magmatisme crustal et mantellique. Le complexe de Pontivy-Rostrenen est une intrusion composite qui s'est mis en place le long du CSA. Au sud, le complexe est formé de leucogranites peralumineux alors que des monzogranites affleurent dans la partie nord avec des intrusions de monzodiorites quartziques. Les datations U-Pb sur zircon révèlent que les trois facies magmatiques se sont mis en place de façon synchrone à ca. 315 Ma alors qu'une intrusion leucogranitique tardive (Langonnet) s'est mise en place à 304.7 ± 2.7 Ma. Les échantillons de leucogranites (A/CNK > 1.1) représentent des liquides silicatés purement crustaux formés à partir de la fusion partielle d'une source métasédimentaire avec une contribution probable d'orthogneiss peralumineux. Les monzogranites (1 < A/CNK < 1.3) sont issus de la fusion partielle d'un orthogneiss probablement métalumineux alors que les monzodiorites quartziques de composition métalumineuse (0.7 < A/CNK < 1.1) proviennent de la fusion d'un manteau lithosphérique métasomatisé. L'évolution des magmas était contrôlée par des processus de cristallisation fractionnée, d'hybridation et d'entrainement de minéraux péritectiques. A l'époque, la fusion partielle de la croûte et les processus d'hybridation sont promus par le sous plaquage de magmas d'origine mantellique. La déformation le long du CSA a probablement facilité l'ascension des magmas dans la croûte supérieure. A l'échelle de la chaine, la fusion partielle de la croûte au sud du CSA était contrôlée par un amincissement lithosphérique qui a eu lieu en réponse de l'extension tardi-orogénique de la zone interne. Au contraire, au nord du CSA, la remonté de l'asthénosphère pendant le décrochement en transtension de l'ensemble du domaine centre-armoricain a induit la fusion de la croûte et du manteau fertilisé pendant les épisodes de subduction antérieurs. De même, la remontée asthénosphérique a été potentiellement promue par le démembrement d'une relique de panneau océanique a la transition lithosphère – asthénosphère.

Crustal recycling and juvenile addition during lithospheric wrenching: The Pontivy-Rostrenen magmatic complex, Armorican Massif (France), Hercynian Belt.

Submitted to Gondwana Research

Ballouard C.[a], Poujol M.[a], Boulvais P.[a], Zeh A.[b, c]

[a]UMR CNRS 6118, Géosciences Rennes, OSUR, Université Rennes 1, 35042 Rennes cedex, France;
*correspondance: christopheballouard@hotmail.fr

[b]Institute for Geosciences, Goethe University Frankfurt, Section Mineralogy, Petrology and Geochemistry, Altenhöferallee 1, D-60438 Frankfurt, Germany

[c]Institute for Applied Geosciences – Karlsruhe Institute of Technology (KIT), Campus South, Mineralogy and Petrology, Adenauerring 20b, 50.4, D-76131 Karlsruhe, Germany

Keywords: Peraluminous and metaluminous magmatism; Strike-slip fault; mantle fertilization; Variscan belt; South Armorican Shear Zone.

Abstract

The South Armorican Shear Zone (SASZ), French Armorican Hercynian Belt, is a lithospheric wrench fault which acted during the Late Carboniferous as a transition zone between a domain in extension to the south dominated by crustal magmatism and a domain submitted to dextral wrenching to the north where both crustal and mantle magmatism occurred. The Pontivy-Rostrenen complex is a composite intrusion which was emplaced along the SASZ. To the south, the complex is formed of peraluminous leucogranites whereas monzogranites outcrops in the north with small stocks of quartz monzodiorites. U-Pb dating of magmatic zircon reveals that the three magmatic facies were emplaced synchronously at ca. 315 Ma whereas a late leucogranitic intrusion was emplaced at 304.7 ± 2.7 Ma. The leucogranite samples (A/CNK > 1.1) represent pure crustal melts formed by partial melting of metasedimentary rocks with a probable contribution from peraluminous orthogneisses. The monzogranites (1 < A/CNK < 1.3) formed by partial melting of an orthogneiss with a probable metaluminous composition whereas the metaluminous quartz monzodiorites (0.7 < A/CNK < 1.1) formed by partial melting of a metasomatized lithospheric mantle. Magmas evolution was triggered by fractional crystallization, magma mixing and/or peritectic mineral entrainment. Partial melting of the crust and magma hybridation were likely promoted by underplating of mantle-derived magmas. Shearing along the SASZ facilitated the ascent of the melts in the upper crust. At the scale of the belt, partial melting of the crust to the south of the SASZ was triggered by lithospheric thinning during crustal

extension. In contrast, to the north, asthenosphere upwelling during strike-slip deformation (transtension) promoted the melting of both the crust and the mantle fertilized during previous subduction events. Asthenosphere upwelling was also potentially promoted by the dismembering of a slab remnant at the lithosphere-asthenosphere transition during pervasive wrenching.

1. Introduction

Continental scale strike-slip faults represent major features in orogenic belts as they are able to crosscut the whole lithosphere and to accommodate horizontal displacement for several hundreds of kilometers (Sylvester, 1988; Storti et al., 2003; Vauchez and Tommasi, 2003). These structures commonly mark the boundaries between distinct continental domains, each bearing its own deformation, metamorphic and geomorphologic history. For example, in East Asia, the Tun-Lu fault delimitates ultra-high pressure rocks bearing metamorphic units from low grade sediments (e.g. Gilder et al., 1999). In New Zealand, high grade metamorphic rocks exhumed from a depth of ~20 km depth outcrop at high altitude in the hanging wall of the Alpine Fault (e.g. Norris and Cooper, 2000). Lithospheric wrench faults also represent major conduits for hydrothermal fluids as well as magmas with crustal and/or mantle origins (e.g. Pirajno, 2010). Partial melting of the crust and the mantle in strike-slip deformation belts can be triggered by hydrous fluxing (e.g. Hutton and Reavy, 1992), shear heating (Leloup et al., 1999) and asthenospheric upwelling during transtensional regime (Rocchi et al., 2003; Barak and Klemperer, 2016; Yang et al., 2016). Shearing and pressure gradient along wrench faults also promote the ascent of magmas to the upper crust (e.g. D'lemos et al., 1992; De Saint Blanquat et al., 1998) and deformation driven filter pressing enhance their differentiation (e.g. Bea et al., 2005).

In the French Armorican Massif, western European Hercynian Belt, the South Armorican Shear Zone (SASZ) is a major crustal to lithospheric scale strike slip fault which, during the Late Carboniferous, delimitated a crustal domain in extension thickened during the Hercynian orogeny to the south and a non-thickened domain submitted to pervasive dextral wrenching and belonging to the external zone of the belt to the north (Berthé et al., 1979; Gapais and Le Corre, 1980; Jégouzo, 1980; Gapais et al., 1993, 2015; Gumiaux et al., 2004a, 2004b). During this period, the Armorican Massif experienced an intense post-collisional magmatism resulting in the emplacement of numerous granitoidic intrusions of various types (Carron et al., 1994; Capdevila, 2010) (Fig. 1). In the internal part of the belt, along or to the south of the SASZ, these intrusions are almost exclusively peraluminous leucogranites which represent pure crustal melts (Bernard-Griffiths et al., 1985; Patiño-Douce, 1999; Tartèse and Boulvais, 2010; Ballouard et al, 2015a). In contrast, to the north of the SASZ, in the external domains, the composition of the granitic intrusions is more variable (ranging from metaluminous to peraluminous) and the granites display variable degree of interaction with juvenile mantle-derived magmas (Carron et al., 1994; Capdevila, 2010).

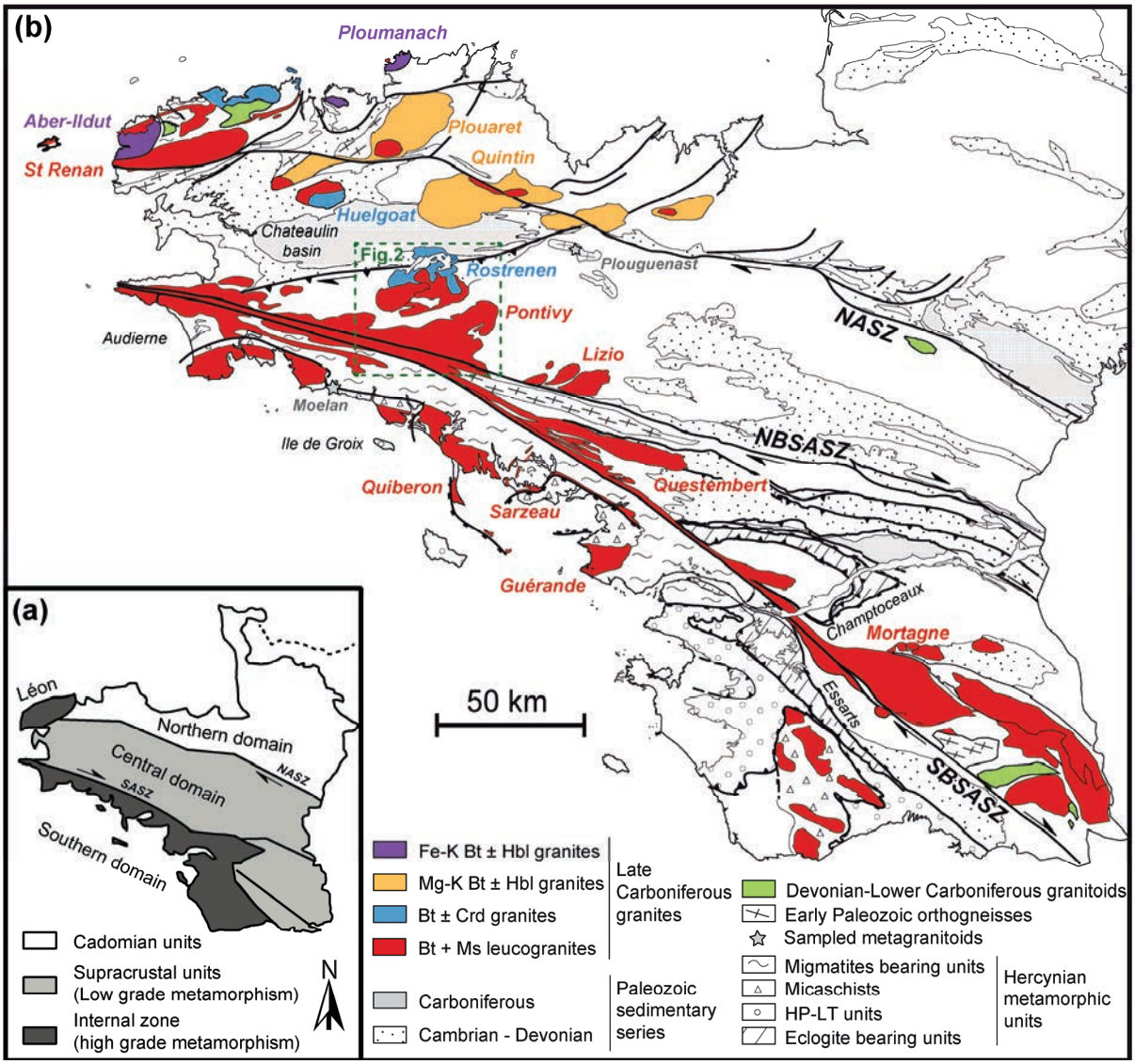

Figure 1: (a) main structural domains of the Armorican Massif. (b) General geological map of the Armorican Massif showing the four types of late Carboniferous granites according to Ca 0pdevila (2010). The map is modified from Chantraine et al. (2003) and Gapais et al. (2015). NASZ: North Armorican Shear Zone; NBSASZ: Northern Branch of the South Armorican Shear Zone. SBSASZ: Southern Branch of the South Armorican Shear Zone. Fe-K granites: ferro-potassic granites. Mg-K granites: magnesio-potassic granites. Calk-alk granites: calco – alkaline granites. Mineral abbreviation according to Kretz (1983).

The Pontivy-Rostrenen magmatic complex, which is the object of this study, is a composite intrusion localized in the central part of the Armorican Massif. The granitoids forming the complex were emplaced along or to the north of the SASZ at the transition between the internal and the external zones of the belt. The spatial evolution of the magmatism in the complex mimics that of the whole Armorican Massif as the contribution of mantle-derived magmas appears to increase from south to north. Thus, this composite intrusion represents a unique opportunity to document crustal recycling and juvenile addition in a key zone of the Hercynian belt localized at the transition between a domain in post-thickening extension and a non-thickened domain dominated by wrenching.

To understand the spatial evolution of magmatism in the Pontivy-Rostrenen complex as well as in the Armorican Massif, the characterization of both primary and secondary magmatic processes at the origin of the different facies forming this composite intrusion is necessary and has to be combined with geochronological data. Consequently, in this study, we used zircon U-Pb and Hf analyses together with whole rock major, trace elements and radiogenic isotope data to (i) specify the different sources involved in the generation of the magmas, (ii) estimate their timing and duration of emplacement and (iii) identify the secondary magmatic processes controlling their evolution. These new constraints are integrated within the tectono-magmatic evolution of the Armorican Hercynian belt and bring information about the magmatic evolution of belts affected by strike slip deformation in general.

2. Geological Context

2.1. The Armorican Massif

The French Armorican Massif belongs to the West-European Hercynian belt which resulted from the convergence of the Laurussia and Gondwana continents at the end of the Paleozoic (e.g. Ballèvre et al., 2009). The Armorican Massif is divided into three main domains by the South Armorican Shear Zone (SASZ) and the North Armorican Shear Zone (NASZ), two dextral crustal to lithospheric scale strike-slip faults (Fig. 1). The northern domain is mostly made of Proterozoic basement that belonged to the upper-crust during Hercynian orogeny (Brun et al., 2001 and references therein). The central domain is composed of Proterozoic (Brioverian) to Carboniferous sediments generally moderately deformed under greenschist facies conditions. Deformation and metamorphism increase from north to south and from east to west (e.g. Hanmer et al., 1982; Gumiaux et al., 2004). The deformation is commonly marked by a vertical foliation which bear a lineation either sub-horizontal or dipping 5-10° eastward (Jégouzo, 1980). The southern domain, which belongs to the internal zone of the belt, is characterized by a higher degree of deformation and by the presence of high grade metamorphic rocks represented from top to bottom by high pressure-low temperature rocks (HP-LT), micaschists and migmatites bearing units (Gapais et al., 2015 and references therein; Fig. 1). HP-LT rocks are mostly composed of blueschists (e.g. Ile de Groix on Fig. 1b) and metavolcanics which reach peak P-T condition of 1.4 – 1.8 Ga, 500-550°C (Bosse et al., 2002) and 0.8 GPa, 350-400°C (Le Hébel et al., 2002), respectively. Subduction and exhumation of these units relate to early tectonic events, around 360 Ma (Bosse et al., 2005). Lower units are composed of gneisses, granitoides and migmatites with peak PT condition of 0.8 GPa, 700-750°C (Jones and Brown, 1990). At the end of the Carboniferous, between ~315 to 300 Ma (Tartèse et al., 2012), the SASZ acted as a transfer zone between the southern domain which experienced crustal extension, leading to the formation of core complex cored by migmatites and syncinematic leucogranites, while the central domain was affected by dextral wrenching (Gapais et al., 2015). During this period, the Armorican Massif experienced an important magmatism which resulted in the emplacement, from overall south to north, of four main granitoidic suites (Capdevilla, 2010; Fig. 1):

- A magneso-potassic peraluminous suite composed of Ms – Bt leucogranites. Most of these leucogranites were emplaced either along extensional deformation zones in the southern domain, such as the Quiberon (Gapais et al., 1993, 2015), Sarzeau (Turrillot et al., 2009) and Guérande (Ballouard et al., 2015a) leucogranites, or along the SASZ such as the Pontivy, Lizio and Questembert leucogranites (Berthé et al., 1979). Among them, the Lizio, Questembert and Guérande leucogranites were dated at 316.4 ± 5.6 Ma (Zrn U-Pb ; Tartèse et al., 2011a), 316.1 ± 2.9 Ma (Zrn U-Pb ; Tartèse et al., 2011b) and 309.7 ± 1.3 Ma (Zrn and Mnz U-Th-Pb; Ballouard et al., 2015a), respectively. In parallel, the intrusion of Saint Renan emplaced along the NASZ was dated at 316.0 ± 2.0 Ma (Zrn U-Pb; Le Gall et al., 2014). Moderate size intrusions of two micas peraluminous leucogranites are commonly found associated with the granitic intrusions from other suites (Fig. 1).
- A magneso-potassic peraluminous suite composed of Bt ± Crd monzogranites and granites associated with small stocks of quartz monzodiorites. Among these intrusions, the Huelgoat granite was emplaced at 314.8 ± 2.0 Ma (U-Pb Zrn; Ballouard, unpublished data).
- A magneso-potassic metaluminous suite composed of Bt ± Hbl (hornblende) monzogranites associated with mafic to intermediate rocks (Mg-K Bt ± Hbl granites in Fig.1). Among these granites which were emplaced along the NASZ, the Quintin and Plouaret granites were dated at 291 ± 9 Ma and 329 ± 5 Ma, respectively using the whole-rock Rb-Sr isochron method (Peucat et al., 1984).
- A ferro-potasic metaluminous suite mostly constituted by Bt ± Hbl monzogranites and syenites associated with mafic to intermediate rocks with a mantle origin (Fe-K Bt ± Hbl granites in Fig.1). In this suite, the Aber-Ildut monzogranite was emplaced at 303.8 ± 0.9 Ma (U-Pb Zrn; Caroff et al., 2015) whereas for the Ploumanach composite intrusion, the oldest unit was emplaced at 308.8 ± 2.5 Ma and the youngest at 301.3 ± 1.7 Ma (Ballouard et al., 2015b).

2.2. The Pontivy-Rostrenen magmatic complex

The Pontivy–Rostrenen magmatic complex (Figs. 1 and 2) is composed, to the south, of peraluminous leucogranites whereas, to the north, it is made of peraluminous leucogranites, peraluminous monzogranites and metaluminous quartz monzodiorites (Euzen, 1993; Fig. 2a). The Langonnet intrusion is composed exclusively of peraluminous leucogranites and crosscut the other facies (Fig. 2a).

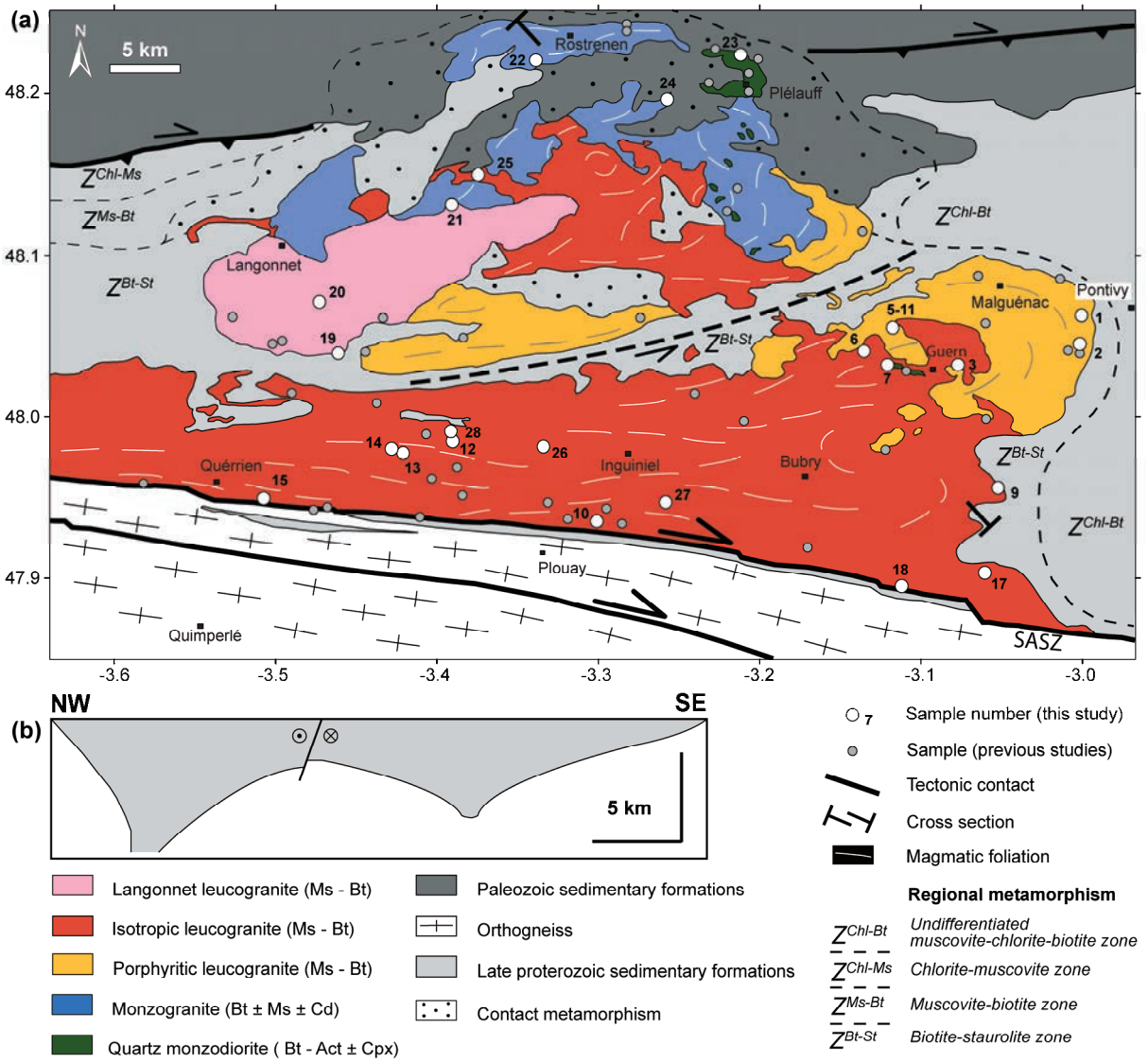

Figure 2: (a) Geological map of the Pontivy-Rostrenen granitic complex showing the different magmatic units, the magmatic foliation and the country rock metamorphism. Samples from this study and from previous studies are localized on the map. The map is redrawn from Euzen (1993) and from the 1/50000 BRGM geological maps of Pontivy (Dadet et al., 1988), Rostrenen (Bos et al., 1997), Plouay (Bechennec et al., 2006) and Bubry (Bechennec and Thiéblemont, 2009). (b) Cross section of the Pontivy-Rostrenen granitic complex redrawn from Vigneresse (1999). Mineral abbreviation from Kretz (1983).

The Pontivy-Rostrenen intrusions are syntectonic and the shape of the Pontivy leucogranite, to the south, marks the dextral shearing of the SASZ (Fig. 1 and 2). The main part of the magmatic rocks forming the complex presents magmatic foliations which commonly follow the edges of the intrusions (Fig. 2). In the southern edge of the Pontivy leucogranite, syn-cooling shearing is revealed by the development of C/S structures (Gapais, 1989) and mylonites visible in 100 m wide N100-110 oriented dextral shear zones (Jégouzo, 1980; Tartèse et al, 2012). Leucogranites intrudes Late-Proterozoic (Brioverian) sediments, to the south, whereas leucogranites, monzogranites and quartz monzodiorites were emplaced into both Late-Proterozoic and Paleozoic (Ordovician to Lower-Carboniferous) sediments, to the north. The regional metamorphism in the Late-Proterozoic sediments increases from

north to south and from east to west: the north-eastern area is characterized by a chlorite-biotite assemblage whereas the south-western zone is characterized by a biotite-staurolite assemblage (e.g. Bos et al., 1997) (Fig. 2a). A contact metamorphism also affected the sediments to the north of the complex (e.g. Bos et al., 1997) and attests for a higher emplacement temperature for the Rostrenen monzogranite than for the Pontivy leucogranite. This metamorphism is characterized by a prograde evolution andalusite + (± cordierite), biotite +, garnet +, muscovite -, sillimanite +. The gravimetric data obtained by Vigneresse and Brun (1983; Fig. 2b) reveal that the Pontivy-Rostrenen magmatic complex represents a continuous intrusion with the main root localized to the north. The depth of the root is around 6 km but the intrusion is relatively flat as 80 % of its volume present a thickness between 0 and 3 km (Vigneresse, 1999). Based on an estimation of the depth of the brittle-ductile transition using the shape of several intrusions in the Hercynian belt, including the Pontivy-Rostrenen complex, Vigneresse (1999) suggested that these intrusions were emplaced at a depth around 6 – 8 km.

The previous petro-geochemical and isotopic studies of Bernard-Griffiths et al. (1985) and Euzen (1993) on the Pontivy-Rostrenen magmatic complex suggested that the leucogranites formed by the partial melting of a metasedimentary source. Euzen (1993) also proposed that the partial melting of a metasomatized mantle was involved in the formation of the quartz monzodiorites, whereas the monzogranites would represent a hybrid magma resulting from the mixing between a leucogranitic melt and a mantellic magma. A previous dating on the Pontivy leucogranite using the whole-rock Rb-Sr isochron method (Peucat et al., 1979) yielded a date of 344 ± 8 Ma but more recently a date of 311 ± 2 Ma was obtained by Cosca et al. (2011) using the muscovite ^{40}Ar-^{39}Ar method.

3. Field and samples description

Due to the poor outcropping conditions in the area, the sampling was mostly limited to quarries. A total of 25 samples representative of the petrographic heterogeneities have been collected in the Pontivy-Rostrenen magmatic complex (Fig. 2). Our samples have been divided into different facies according to petro-textural and cartographic criteria as leucogranites (Fig. 3a-b), monzogranites (Fig. 3c-d) and quartz monzodiorites (Fig.3d) (Table 1).

Table 1: GPS coordinates and simplified petrographic description of the Pontivy-Rostrenen granitoid samples. The description and the coordinates of Early Paleozoic metagranitoids samples used for supplementary Sm-Nd analyses are also reported.

Longitude (°)	Lattitude (°)	Sample	Facies	Mineralogy	Texture	Strain	Chloritization
-3.000557	48.062879	PONT-1	Porphyritic leucogranite	Bt > Ms	Porphyritic (1-2 cm), coarse grained (2-5 mm), magmatic foliation		Chl+
-3.001773	48.045242	PONT-2	Porphyritic leucogranite	Ms > Bt	Porphyritic (1-2 cm), coarse grained (3-5 mm)		Chl
-3.117447	48.055276	PONT-5	Porphyritic leucogranite	Bt > Ms	Moderatley porphyritic (0.5-2 cm), medium to coarse grained (1-4 mm), magmatic foliation	+	Chl
-3.117447	48.055276	PONT-11	Porphyritic leucogranite	Bt > Ms	Porphyritic (1-2 cm), medium to coarse grained (2-4 mm)	+	Chl-
-3.461017	48.039550	PONT-19	Porphyritic leucogranite	Bt > Ms	Porphyritic (1-2 cm), coarse grained (3-5 mm)		Chl +++
-3.077133	48.032150	PONT-3	Isotropic leucogranite	Bt > Ms	Medium to fine grained (0.5-2 mm), slightly porphyritic (1-2 cm), magmatic foliation	+	Chl-
-3.135274	48.040860	PONT-6	Isotropic leucogranite	Bt > Ms	Fine to medium grained, magmatic foliation	+	Chl ++
-3.052191	47.955898	PONT-9	Isotropic leucogranite	Ms > Bt	Medium grained (1-3 mm), solid state deformation	++	Chl
-3.300926	47.935201	PON-10	Isotropic leucogranite	Ms > Bt	Coarse grained (2-5 mm), slightly porphyritic, magmatic foliation	++	Chl
-3.390235	47.984733	PONT-12	Isotropic leucogranite	Ms > Bt	Coarse grained (2-7 mm), slightly porphyritic (1 cm)		Chl
-3.420917	47.976350	PONT-13	Isotropic leucogranite	Ms > Bt	Medium to coarse grained (1-7 mm), slightly porphyritic (1 cm)		Chl+
-3.428067	47.980217	PONT-14	Isotropic leucogranite	Ms	Medium to coarse grained (2-6 mm)		
-3.507400	47.949383	PONT-15	Isotropic leucogranite	Ms > Bt	Fine grained (0.5-3 mm), magmatic foliation	+	Chl-
-3.060517	47.903217	PONT-17	Isotropic leucogranite	Bt = Ms	Coarse grained (2-8 mm), slightly porphyritic (2 cm), magmatic foliation	++	
-3.112083	47.895200	PONT-18	Isotropic leucogranite	Bt > Ms	Fined grained (≤ 2 mm), ligtly porphyritic, solid state deformation	+++	Chl+++
-3.374485	48.149737	PONT-25	Isotropic leucogranite	Ms >> Bt	Medium to fine grained (2-3 mm), slightly porphyritic (1-2cm)		Chl-
-3.333955	47.981447	PONT-26	Isotropic leucogranite	Ms = Bt	Medium grained (1-5 mm), slightly porphyritic (1 cm), magmatic foliation	+	Chl+
-3.258245	47.947043	PONT-27	Isotropic leucogranite	Ms > Bt	Medium to coarse grained (1-3 mm), magmatic foliation	+	Chl-
-3.391240	47.990710	PONT-28	Isotropic leucogranite	Bt =Ms	Coarse grained (0.5-1cm), slightly porphyritic (1-2 cm), magmatic foliation	+	Chl-
-3.472679	48.071121	PONT-20	Langonnet leucogranite	Bt > Ms	Fine grained (1-4 mm), ligtly porphyritic (1-2 cm)		Chl - -
-3.390833	48.131267	PONT-21	Langonnet leucogranite	Fs - Ms	Medium to coarse grained (2-4 mm)		
-3.338700	48.220583	PONT-22	Monzogranite	Bt - (Ms)	Highly porphyritic (1-4 cm), medium grained (2-4 mm)		Chl - -
-3.257395	48.196251	PONT-24	Monzogranite	Bt - (Ms - Cd?)	Porphyritic(1-2 cm), medium to fine grained (1-3 mm)		Chl-
-3.116167	48.031867	PONT-7	Quartz monzodiorite	Bt > Act	Fine grained (0.5-1 mm)		Chl-
-3.211867	48.224141	PONT-23	Quartz monzodiorite	Bt > Act > CPx	Medium grained (2-4 mm)		
-3.740952	47.811525	QIMP-1	Moelan Metagranitoid (tonalite)	Ms > Bt	Fine grained (≤ 1 mm), mylonitic	++++	Chl-
-2.63975	48.274317	PLG-1	Plouguenast Metagranitoid (granite)	Bt > Ms	Medium Grained (2-5 mm), ductile deformation	+++	
-2.545533	48.270633	PLG-2	Plouguenast Metagranitoid (tonalite)	Bt > Ms	Fine grained (≤ 1 mm), slightly porphyritic (2 - 5 mm), ductile deformation	++++	
-2.55685	48.255217	PLG-3	Plouguenast Metagranitoid (granite)	Ms > Bt	Medium grained (1 -4 mm), semi-brittle deformation	++	
-2.615186	48.19458	PLG-4	Plouguenast Metagranitoid (tonalite)	Ms >> Chl (Bt)	Fine grained (≤ 1 mm), semi-brittle deformation	++	Chl++

The deformation in the leucogranites increases when getting closer to the South Armorican Shear Zone with an evolution from slightly marked magmatic foliations in the north to solid state deformation in the south (Table 1). The leucogranite samples contain a Qtz-Kfs-Pl-Ms (mineral

abbreviation according to Kretz, 1983) assemblage with a variable amount of biotite (Fig. 4a-b). Quartz is mostly anhedral and can display undulose extinction or forms polycrystalline clusters due to intracrystalline deformation. K-feldspar is more or less porphyritic depending on the sub-facies and is euhedral to sub-euhedral. Plagioclase is generally sub-euhedral, shows polysynthetic twining and commonly displays myrmekites. Micas are commonly oriented in the foliation (Fig. 4a). Muscovite is generally euhedral and flake-shaped (Fig. 4a-b) but locally displays fish-like habit due to deformation. Secondary muscovite commonly occurs as small inclusions in feldspar (sericite) or as small grains either in the foliation or around primary micas. Biotite is brown, euhedral to sub-euhedral and is commonly found in intergrowth with primary muscovite. The accessory minerals, commonly hosted by biotite, are apatite, zircon, Fe-Ti oxide, monazite and rare sulfides. Needles of sillimanite are occasionally found as inclusions in quartz or muscovite. The leucogranites can be divided in three different sub-facies:

(1) The porphyritic leucogranite facies outcrops in the northeastern part of the Pontivy intrusion and in the southern part of the Rostrenen intrusion (Fig. 2). This facies is marked by the abundance of porphyritic K-feldspar crystals (1 - 2 cm) which commonly mark the magmatic foliation (Fig. 3a). The matrix is coarse grained (0.2 – 0.5 cm) and the biotite is generally more abundant than muscovite. In this facies, the K-feldspar commonly displays Carlsbad twining and perthitic exsolutions. Plagioclase is locally zoned. Schlierens and acid microgranular enclaves are commonly observed in this facies. The latter are interpreted to form by the breaking up of microgranitic dykes also described in this facies (Euzen and Capdevila, 1991).
(2) The isotropic leucogranite facies represents the most common type of leucogranites which outcrop in the Pontivy-Rostrenen complex (Fig. 2). This facies display a variable grain size from fine grained (0.05 – 0.3 cm) to coarse grained (0.5 – 1 cm) and is characterized by the absence or by a low abundance of porphyritic K-feldspar (1-2cm). The proportion of muscovite and biotite is variable (Fig. 4a-b) and biotite can be totally absent. In this facies, K-feldspar generally displays tartan twinning characteristic of microcline and perthitic exsolutions. The poor outcropping conditions did not allow to observe the relationship between this facies and the porphyritic leucogranitic facies.
(3) The Langonnet leucogranite forms an elliptic stock which crosscuts cartographically the others magmatic facies of the Pontivy-Rostrenen complex (Fig. 2). No contact has been observed on the field. This intrusion is mostly composed of medium to coarse grained (0.2 – 0.4 cm) isotropic leucogranites characterized by a small proportion of biotite. Yet, a fine grained (0.1 – 0.4 cm) weakly porphyritic (1 – 2 cm) leucogranite with a higher proportion of biotite than muscovite was also observed. In this facies, K-feldspar commonly displays Carlsbad twinning. Secondary muscovitization is generally weak in the samples.

Several veins of quartz, pegmatite and aplite crosscut these leucogranites. Pegmatites commonly host Qtz-Fsp-Ms-(Bt-Turm). Pegmatite stocksheiders were also described along the western edge of the

Langonnet leucogranite, whereas greisenization locally affects the more evolved term of the isotropic leucogranite facies as well as the Langonnet leucogranite (Euzen, 1993; Bos et al., 1997). Chloritization also commonly affects the biotite of the leucogranite samples (Table 1). Chlorite is visible at a microscopic scale and commonly host Fe-Ti oxides.

Figure 3: Representative pictures of the Pontivy (a-b) and the Rostrenen (c-d) granitoids. (a) Porphyritic leucogranite (PONT-1). (b) Isotropic leucogranite. (c) Porphyritic monzogranite with a mafic enclave (ME). (d) Mingling features at the contact between a porphyritic monzogranite (Mgr) and a quartz monzodiorite (Mdr). The scale bar represents 5 cm.

The monzogranites (i.e. the Rostrenen granite s.s.) outcrop in the northern part of the Rostrenen intrusion (Fig. 2; Fig. 3c). This facies is generally highly porphyritic and K-feldspar phenocrysts can reach 15 cm in length. The matrix (0.1 – 0.4 cm) contains a Qtz-Pl-Bt assemblage with a small amount of muscovite (Fig. 4c) and punctual apparition of cordierite. Quartz is generally anhedral. K-feldspar is generally perthitic, euhedral and commonly contains perthitic exsolution. Plagioclase is also generally euhedral and is commonly zoned. Biotite is brown and generally sub-euhedral. Muscovite is rare and generally occurs as inclusions in either biotite or K-feldspar (Fig. 4c). Cordierite was not observed in our samples but was described by Euzen (1993) as euhedral pinitized crystals almost completely replaced by an association of green biotite + muscovite. Apatite, zircon and Fe-Ti oxide are the most common accessory minerals and generally occur as inclusions in biotite. This facies commonly contains mafic enclaves similar in composition to the ones found in the quartz monzodiorite facies (Euzen, 1993;

Fig. 3c). Biotite can be slightly chloritized. The relationship between the leucogranites and the monzogranite cannot be observed in the field.

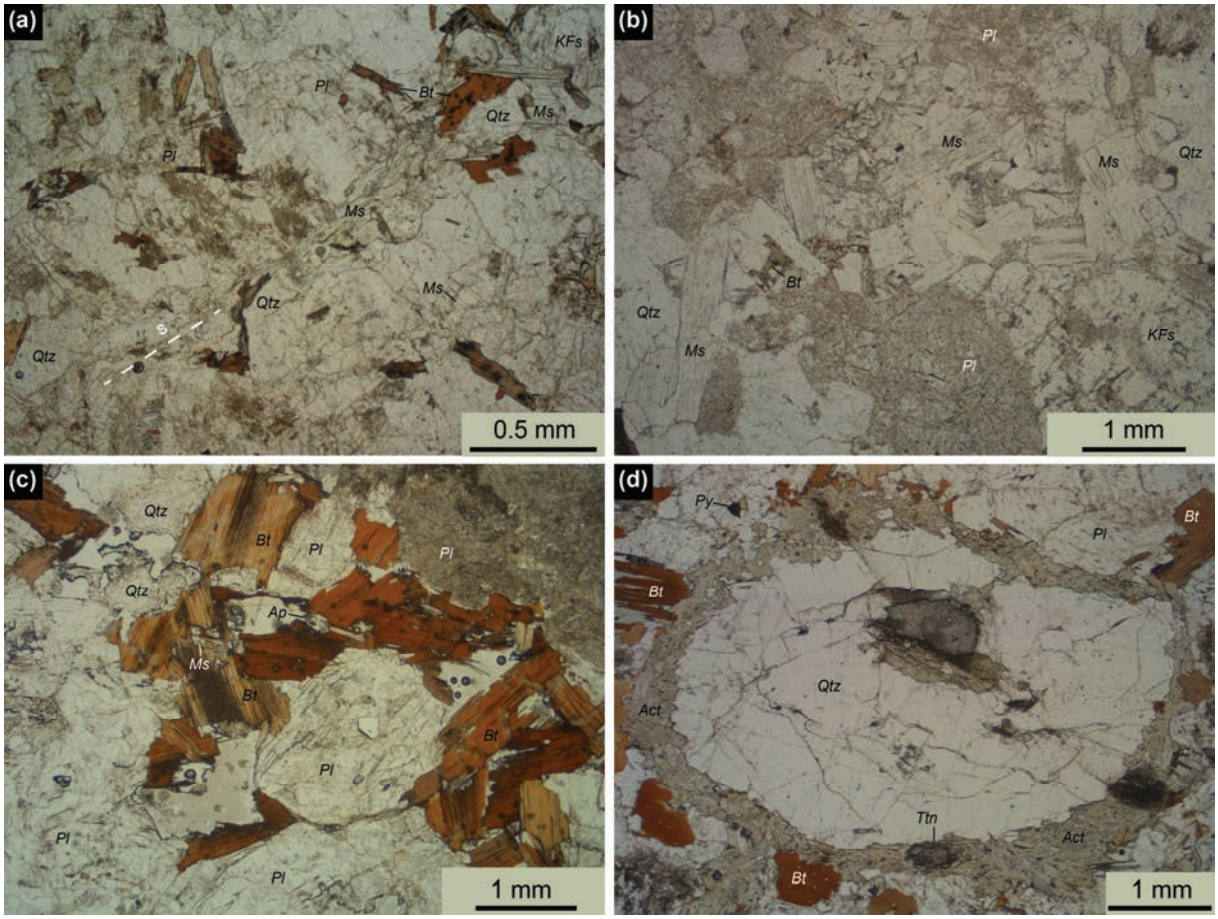

Figure 4: Thin section photomicrographs of some representative samples of the Pontivy (a-b) and Rostrenen granitoids (c-d). (a): PONT-3: Bt > Ms leucogranite. The magmatic foliation (S) is marked by micas. (b) PONT-12: Ms > Bt leucogranite. (c) PONT-22: Bt monzogranite. (d) PONT-23: Bt > Act quartz monzodiorite with an ocelli quartz (Qtz) surrounded by amphibole (Act). Mineral abbreviation according to Kretz (1983).

The quartz monzodiorite facies appears as small stocks (few square kilometers on the map) mostly in the eastern part of the monzogranitic intrusion. The most important intrusion occurs near Plélauff and a stock also occurs in the isotropic leucogranite (Fig. 2). This facies is fine to medium grained (0.05 – 0.4 cm) and generally contains Qtz-Pl-Kfs-Bt-Act (± Cpx). Quartz is anhedral and locally forms ocellar textures with amphiboles (Fig. 4d) or Cpx. Plagioclase is euhedral to sub-euhedral, can display mirmekites and light sericitisation. K-feldspar is not abundant (< 10 %) and commonly displays tartan twining characteristic of microcline. Biotite is brown to green and euhedral to sub euhedral. Amphibole is pale green, generally anhedral and commonly forms cluster of crystals together with biotite. Clinopyroxene is rare and was observed as sub-euhedral, partly resorbed, crystals. The most common accessory minerals are apatite, titanite, zircon, Fe-Ti oxide and sulfide. A weak chloritization of biotite is occasionally observed (Table 1). Mingling features are visible at the contact between the monzogranite and the quartz-monzodiorite (Fig. 3d).

4. Analytical techniques

4.1. Mineral chemistry

Mineral compositions were measured using a Cameca SX-100 electron microprobe at IFREMER, Plouzané, France. Operating conditions were a 15 kV acceleration voltage, a beam current of 20 nA and a beam diameter of 5 μm. Counting times were approximately 13–14 s. For a complete description of the analytical procedure and the list of the standards used, see Pitra et al. (2008).

4.2. Major and trace whole rock element analyses

Large samples (5 to 10 kg) were crushed in Geosciences Rennes following a standard protocol to obtain adequate powder fractions using agate mortars. Chemical analyses were performed by the Service d'Analyse des Roches et des Minéraux (SARM; CRPG-CNRS, Nancy, France) using a ICP-AES for major-elements and a ICP-MS for trace-elements following the techniques described in Carignan et al. (2001).

4.3. Whole rock Isotopic analyses

Sm–Nd and Sr isotope analyses values were carried out on whole-rock samples at the Geosciences Rennes Laboratory using a 7 collectors Finnigan MAT-262 mass spectrometer. Samples were spiked with a ^{149}Sm-^{150}Nd and ^{84}Sr mixed solution and dissolved in a HF-HNO_3 mixture. They were then dried and taken up with concentrated HCl. In each analytical session, the unknowns were analyzed together with the Ames Nd-1 Nd or the NBS-987 Sr standards, which during the course of this study yielded an average of 0.511969 (±5) and 0.710263 (±10) respectively. All the analyses of the unknowns have been adjusted to the long-term value of $^{143}Nd/^{144}Nd$ value of 0.511963 for Ames Nd-1 and reported $^{87}Sr/^{86}Sr$ values were normalized to the reference value of 0.710250 for NBS-987. Mass fractionation was monitored and corrected using the value $^{146}Nd/^{144}Nd = 0.7219$ and $^{88}Sr/^{86}Sr = 8.3752$. Procedural blanks analyses yielded values of 400 pg for Sr and 50 pg for Nd and were therefore considered as negligible.

4.4. Zircon U-Pb and Hf analyses

A classic mineral separation procedure has been applied to concentrate zircon grains suitable for U–Pb dating using the facilities available at Géosciences Rennes (Ballouard et al., 2015). Zircon grains were imaged either by cathodoluminescence (CL) using a Reliotron CL system equipped with a digital color camera available in Geosciences Rennes or by back-scattered electron imaging using a JEOL JSM 7100 F scanning electron microscope available in the Centre de Microscopie Electronique à Balayage et MicroAnalyse (CMEBA; University of Rennes 1).

U–Th–Pb geochronology of zircon was conducted by in-situ laser ablation inductively coupled plasma mass spectrometry (LA-ICPMS) at Geosciences Rennes using a ESI NWR193UC excimer laser

coupled to a quadripole Agilent 7700x ICP-MS equipped with a dual pumping system to enhance sensitivity. The methodology used to perform the analyses can be found in Ballouard et al. (2015) and in Supplementary file 1. All errors given in Supplementary file 2 are listed at one sigma, but where data are combined to calculate concordia dates, the final results are provided with 2σ confidence limits. Only the analyses with a degree of concordance between 90 and 110 % have been reported in supplementary file 2.

Hafnium (Hf) isotope analyses were performed at Goethe-University Frankfurt with a Thermo-Finnigan NEPTUNE multi collector ICP-MS coupled to a Resolution M-50 (Resonetics) 193 nm ArF excimer laser (ComPexPro 102F, Coherent), using the procedure as outlined in detail in Gerdes and Zeh (2006, 2009) and summarized in Supplementary file 1. The epsilon Hf values [εHf(t)] were calculated using the chondritic uniform reservoir (CHUR) as recommended by Bouvier et al. (2008; $^{176}Lu/^{177}Hf$ = 0.0336 and $^{176}Hf/^{177}Hf$ = 0.282785) and a decay constant of $1.867.10^{-11}$ yr^{-1} (Scherer et al., 2001; Söderlund et al., 2004). Initial $^{176}Hf/^{177}Hf_t$ and εHf(t) were calculated using intrusion ages for magmatic rims or grains whereas for inherited zircon, with a degree of concordance between 90 and 110% ,$^{206}Pb/^{238}U$ date were used for zircon with a $^{206}Pb/^{207}Pb$ date < 1.0 Ga and $^{206}Pb/^{207}Pb$ date were used for zircon with a $^{206}Pb/^{207}Pb$ date > 1.0 Ga.

5. Mineral composition

Seven samples, including one porphyritic leucogranite (PONT-1), four isotropic leucogranites (PONT-10-14-15-26), one Langonnet leucogranite (PONT-21), one monzogranite (PONT-22) and one quartz monzodiorite (PONT-7) have been selected for chemical analyses of feldspar, amphibole, biotite and muscovite. Average minerals chemical composition are provided in Supplementary file 4.

5.1. Feldspar

The chemical composition of plagioclase displays a well-defined trend in the Ab-An-Or ternary diagram (Fig. 5a) and the average anorthite content of the plagioclase decreases from the quartz monzodiorite (% An = 42.2; mostly andesine), the monzogranite (% An = 27.5; oligoclase), the porphyritic leucogranite (% An = 9.3; albite-oligoclase), the isotropic leucogranites (% An = 2.8; albite) to the Langonnet leucogranite (% An = 0.3; albite). In contrast, the average orthoclase content of K-feldspar is nearly constant and vary from % Or = 91.1 in the monzogranite to % Or = 92.6 in the leucogranites.

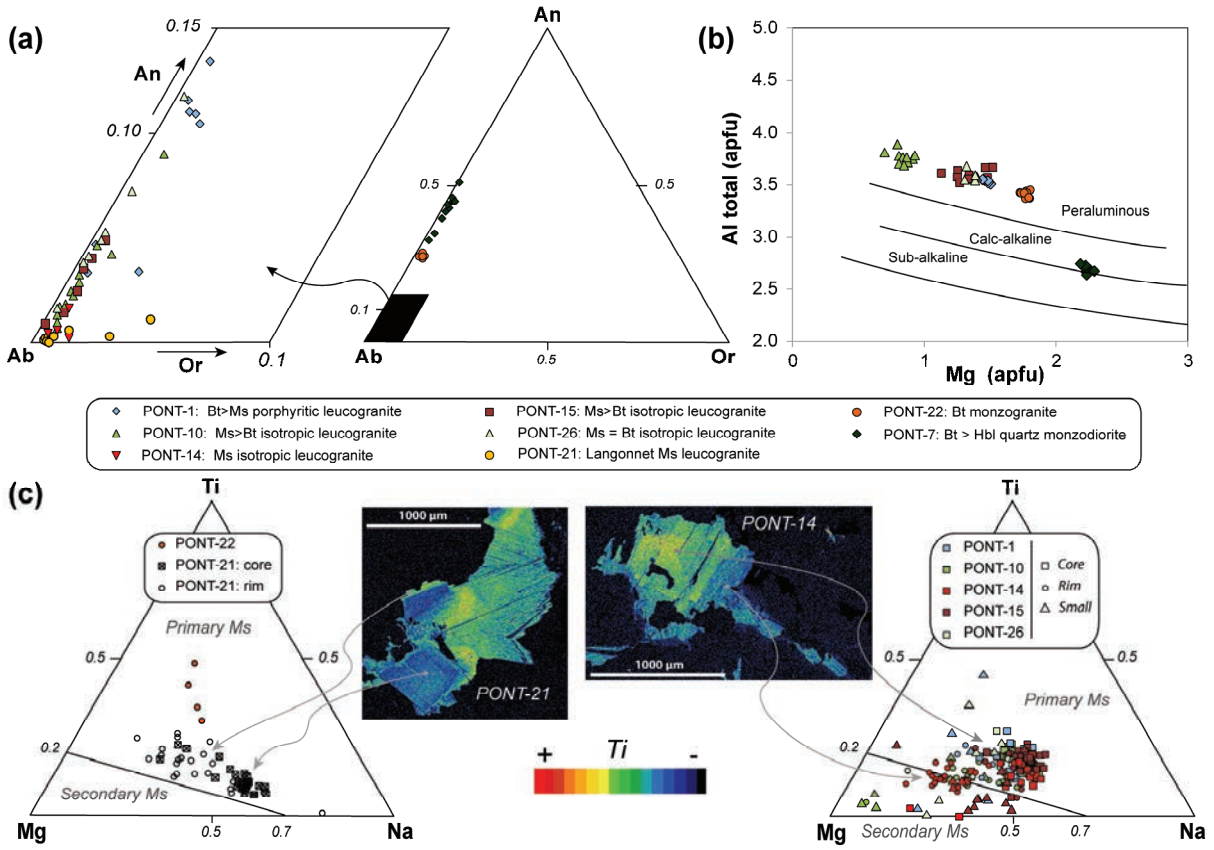

Figure 5: Chemical composition of plagioclase, biotite and muscovite of the Pontivy and Rostrenen granitoids. (a) Triangular classification of the plagioclase. (b) Altot vs. Mg plot for biotite. The fields are from Nachit et al., 1985. (c) Ternary Ti-Na-Mg diagram for muscovite and chemical maps of Ti distribution in muscovite for a Ms Langonnet leucogranite (PONT-21) and a Ms isotropic leucogranite (PONT-14). The primary and secondary fields of muscovite are from Miller et al. (1981). In figure legend, "small" refers to small muscovite inside the foliation planes.

5.2. Amphibole and biotite

The amphibole from the quartz monzodiorite is a calcic amphibole [(Ca + Na) > 1.34] with a relatively elevated content in magnesium [Mg / (Mg + Fe^{2+}) > 0.5] and its composition vary mostly from actinolite-hornblende to actinolite (Leake, 1978).

In the Al_{tot} versus Mg diagram (Nachit et al., 1985) (Fig. 5b), the compositions of the biotite found in the leucogranites and the monzogranite (Al_{tot} > 3.38) plot in the field of the peraluminous granites whereas the biotite compositions from the quartz monzodiorite (average Al_{tot} = 2.69) mostly falls in the cal-alkaline field. The average X_{Mg} ranges from 0.35 to 0.33 in the leucogranites whereas average X_{Mg} = 0.41 in the monzogranite and X_{Mg} = 0.46 in the quartz monzodiorite.

5.3. Muscovite

For the monzogranite (PONT-22), the compositions of the rare and small muscovite crystals systematically plot in the primary field defined by Miller et al. (1981) (Fig. 5c). For the Langonnet leucogranite sample (PONT-21), the muscovite flakes display concentric zonation on the Ti distribution

maps but all the analyses fall also in the primary muscovite field (Fig. 5c). Regarding the others leucogranites samples, most of the analyses performed on the muscovite grains from the porphyritic leucogranite (PONT-1; Bt > Ms) fall in the primary muscovite field whereas for the isotropic leucogranites, the affinity for secondary compositions tends to increase from PONT-26 (Ms = Bt), PONT-15 (Ms > Bt), PONT-10 (Ms > Bt) to PONT-14 (Ms) sample (Fig. 5c). In the PONT-10 and PONT-14 samples, the muscovite flakes commonly display cores and rims with distinct compositions on the Ti distribution chemical map (Fig. 5c). Cores generally display high Ti contents and plot in the primary field whereas the rims are depleted in Ti, enriched in Mg-Fe and plot in the secondary field. In the leucogranites, small muscovite grains which developed in the foliation planes generally plot in the secondary muscovite field and are characterized by elevated Mg contents.

6. Whole rock composition

The chemical composition of the 25 whole rock granitic samples from the Pontivy-Rostrenen complex collected during this study are reported in Table 2.

6.1. Major elements

In the A/NK versus A/CNK diagram (Shand, 1943) (Fig. 6a), both the monzogranites and the leucogranites plot in the peraluminous field characteristic of crustal granites. The leucogranites are highly peraluminous (A/CNK in the range 1.18 – 1.47) whereas the monzogranites are moderately peraluminous (A/CNK in the range 1.03 – 1.30). The quartz monzodiorite samples fall in the metaluminous field, except for 2 peraluminous samples, and have A/CNK values in the range 0.69 – 1.10. In the Q-P diagram (Debon et Le Fort, 1988) (Fig. 6b), the leucogranites mostly fall in the field of granites, the monzogranites fall in the field of adamellites (monzogranites) and the quartz monzodiorite samples plot in the field characteristic of quartz monzodiorites and quartz monzonites. In the Q-P (Fig. 6b) and A-B (Fig. 6c) diagrams, the leucogranites have a similar composition than the melts produced during the partial melting experiments of both sedimentary and peraluminous igneous rocks. Numerous monzogranite samples display a composition similar to the melts produced during the experimental partial melting of metaluminous igneous rocks in the A-B diagram (Fig. 6c). Finally, all the quartz monzodiorite samples plot out of the field of experimental melts (Fig. 6b and c). In the diagrams of Figure 6a, 6b and 6c, the monzogranites plot in an intermediate position between leucogranites and quartz monzodiorites. In the AFM diagram (Fig. 6d), the quartz monzodiorite samples fall in the calc-alkaline field consistently with their biotite compositions (Fig. 5b).

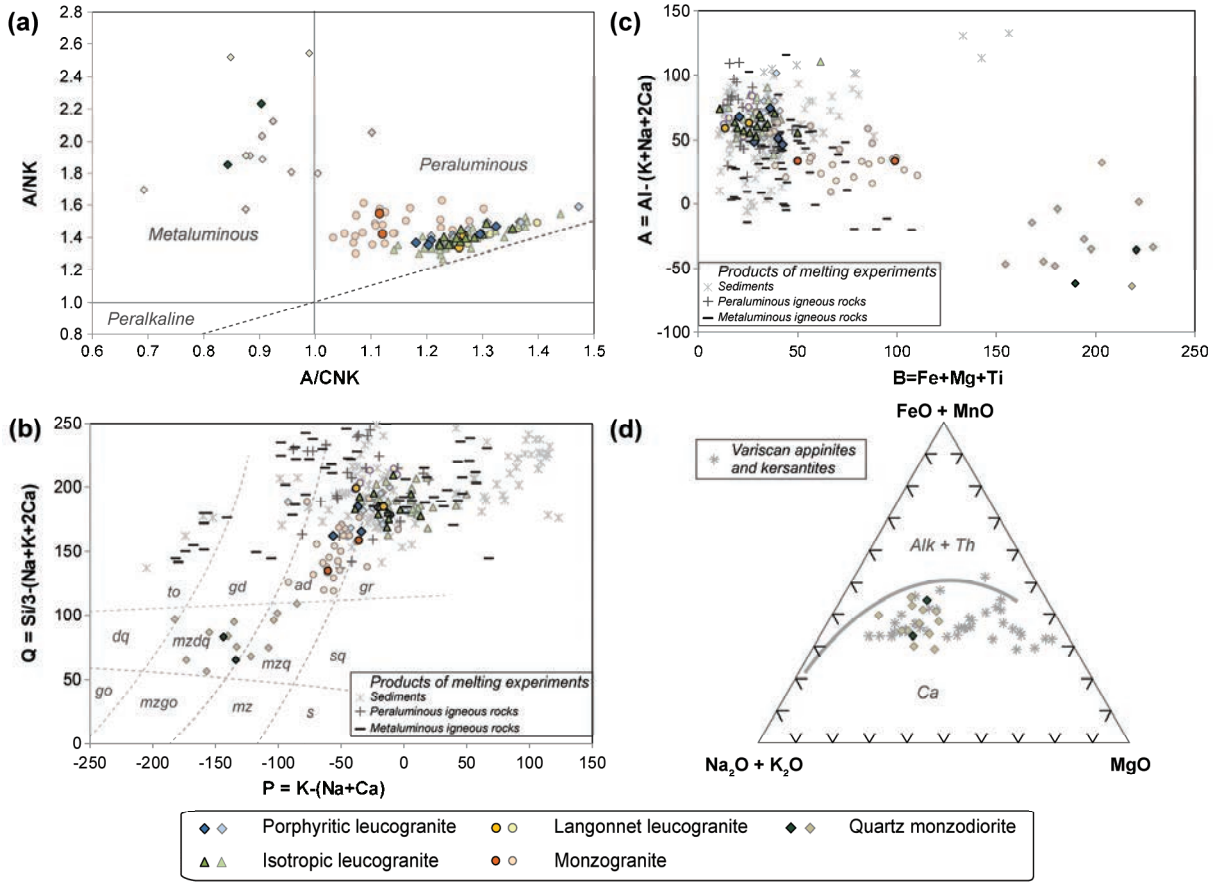

Figure 6: In all the diagrams, symbols in light colors represent Pontivy-Rostrenen granitoid samples from the literature (Cotten, 1975; Euzen, 1993; Bechennec et al., 2006, 2009; Tartèse et al., 2012) whereas the symbols in darker colors represent the samples from this study. (a) Shand (1943) diagram [A/CNK = Al_2O_3 / (CaO + Na_2O + K_2O); A/NK = Al_2O_3 / (Na_2O + K_2O); molar proportions] for the Pontivy-Rostrenen granitoid samples. (b-c) Q-P and A-B diagrams (after Debon and Le Fort, 1988) showing the mineral-chemical composition of the Pontivy-Rostrenen granitoid samples. The composition of melts produced by experimental partial melting are from Vielzeuf and Holloway (1988), Patiño-Douce and Johnston (1991), Patiño-Douce and Harris (1998), Montel and Vielzeuf (1997) and Spicer et al. (2004) for sediments, Castro et al. (1999) for peraluminous igneous rocks and Conrad et al. (1988), Patiño-Douce and Beard (1995) and Patiño-Douce (1997) for metaluminous igneous rocks. The fields in dashed (a) delimitate the location of common igneous rock: gr = granite, ad = adamellite (monzogranite), gd = granodiorite, to = tonalite, sq = quartz syenite, mzq = quartz monzonite, mzdq = quartz monzodiorite, s = syenite, mz = monzonite, and mzgo= monzogabbro. Q and P parameters are expressed in molar proportion multiplied by 1000. (d) AFM (Na_2O + K_2O–FeO + MnO-MgO; wt.%) diagram for the quartz monzodiorites from the Pontivy-Rostrenen complex. The composition of Variscan appinites and kersantites (Turpin et al., 1988; Scarrow et al., 2009; Molina et al., 2012) are reported for comparison. Ca: calco-alkaline; Alk: alkaline; Th: tholeiitic.

In the Harker diagrams (Fig. 7a), the monzogranites (SiO_2 = 55.0 – 60.1 wt.%) and the quartz monzodiorites (SiO_2 = 64.7 – 71.5 wt.%) samples generally define continuous evolution trends but with more scattering for the quartz monzodiorite samples. CaO, Al_2O_3 and the sum Fe_2O_3 + MgO + TiO_2 correlate negatively with SiO_2 whereas K_2O and Na_2O are nearly constant or correlate positively with SiO_2. Regarding the leucogranite samples (SiO_2 = 69.5 – 74.9 wt.%; Fig. 7b), CaO, K_2O, the sum Fe_2O_3 + MgO + TiO_2 and Al_2O_3 anticorrelates with SiO_2 whereas Na_2O displays a positive correlation with

SiO_2, despite a significant scattering. Among the leucogranites, the isotropic leucogranites display the larger compositional range (SiO_2 = 70.0 – 74.6 wt.%) whereas the porphyritic leucogranites display the most primitive compositions (SiO_2 = 69.5 – 73.1 wt.%) and the Langonnet leucogranites samples (SiO_2 = 72.3 – 74.9 wt.%) mostly plot at the end of the evolution trends.

6.2. Trace elements

In Figure 7c, the Rb contents of leucogranites poorly correlate with SiO_2 and vary from ~100 to 600 ppm whereas Sr (~10 - 250 ppm), Ba (~20 - 500 ppm), Zr (~30 – 150 ppm) and La (~5 – 35 ppm) anticorrelate with SiO_2. Among the leucogranites, the Langonnet leucogranite samples display the lowest contents in Ba, Sr, Zr, La and the highest contents in Rb. Regarding the monzogranites, Sr (~150 - 450 ppm), Ba (~300 – 1300 ppm), Zr (~150 - 300 ppm) and La (~45 - 75 ppm) contents are anticorrelated with SiO_2 and the samples display continuous evolution with the leucogranites. In contrast the Rb contents (~150 - 200 ppm) are low and nearly constant. The quartz monzodiorite samples display variable content in Sr (~300 - 650 ppm), Ba (~250 - 1600 ppm) and La (~20 - 70 ppm) without correlation with SiO_2. The Zr contents increase with SiO_2 from ~175 to 250 ppm. The Rb contents are comparable to those of monzogranites and vary slightly between ~100 to 200 ppm. No well-defined correlation can be observed in the different granitic samples between SiO_2 and incompatible elements such as U, Cs, Li, Ta, W or Sn.

The REE patterns of the different leucogranites are comparable (Fig. 8). They show generally high fractionation (La_N/Lu_N = 5.8 - 49.2) and are marked by a negative Eu anomaly (Eu/Eu* = 0.08 – 0.90), the largest negative anomaly being displayed by a Langonnet leucogranite sample (PONT-21). In the monzogranite (Fig. 8), the REE patterns also show high fractionation (La_N/Lu_N = 25.4 – 47.1) and can display a light negative Eu anomaly (Eu/Eu* = 0.61 – 0.88). The REE patterns of the quartz monzodiorite (Fig. 8) display less fractionation (La_N/Lu_N = 9.1 – 18.7) without significant Eu anomaly (Eu/Eu* = 0.87 – 0.89).

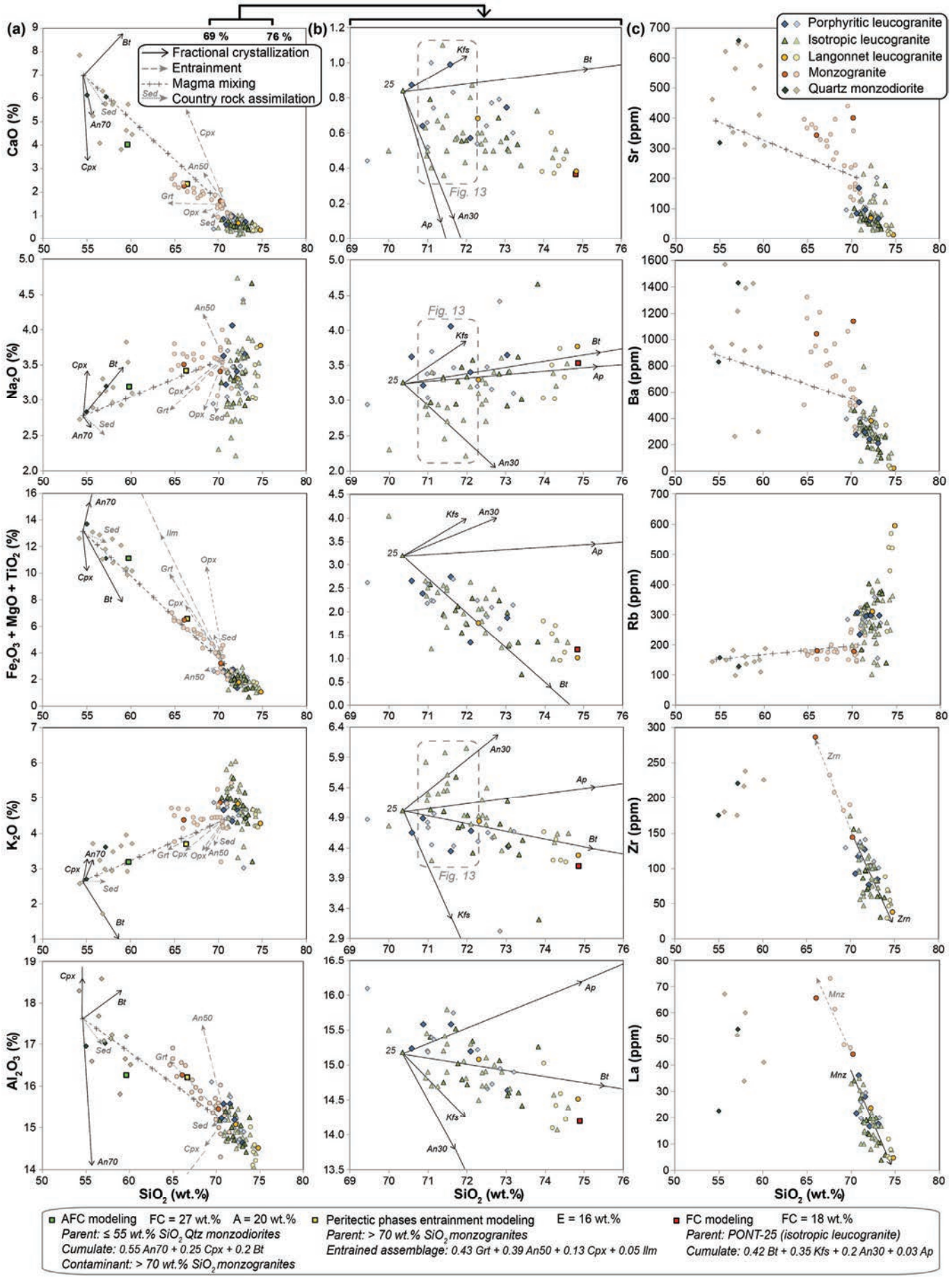
(a)
(b)
(c)
69 %
76 %
Fractional crystallization
Entrainment
Magma mixing
Country rock assimilation
Porphyritic leucogranite
Isotropic leucogranite
Langonnet leucogranite
Monzogranite
Quartz monzodiorite
CaO (%)
Na2O (%)
Fe2O3 + MgO + TiO2 (%)
K2O (%)
Al2O3 (%)
Sr (ppm)
Ba (ppm)
Rb (ppm)
Zr (ppm)
La (ppm)
SiO2 (wt.%)
Fig. 13
Bt
Cpx
An70
An50
An30
Grt
Opx
Sed
Kfs
Ap
Ilm
Zrn
Mnz
AFC modeling FC = 27 wt.% A = 20 wt.%
Parent: ≤ 55 wt.% SiO2 Qtz monzodiorites
Cumulate: 0.55 An70 + 0.25 Cpx + 0.2 Bt
Contaminant: > 70 wt.% SiO2 monzogranites
Peritectic phases entrainment modeling E = 16 wt.%
Parent: > 70 wt.% SiO2 monzogranites
Entrained assemblage: 0.43 Grt + 0.39 An50 + 0.13 Cpx + 0.05 Ilm
FC modeling FC = 18 wt.%
Parent: PONT-25 (isotropic leucogranite)
Cumulate: 0.42 Bt + 0.35 Kfs + 0.2 An30 + 0.03 Ap

Figure 7: (a) Harker diagrams for Pontivy-Rostrenen granitoid samples. (b) Harker diagram for the leucogranitic samples. The dashed boxes delimit the samples in the range 70.8 – 72.3 wt.% SiO_2 which are reported in the Figure 13. (c) Selected trace elements versus SiO_2 diagrams for Pontivy-Rostrenen granitoid samples. In (a) and (c), the dashed grey line with crosses illustrates the mixing model between the composition of the average high SiO_2 (> 70 wt.%) monzogranites samples and the average composition of low SiO_2 (≤ 55 wt.%) quartz monzodiorite samples. The crosses represent increments of 10 wt.%. In (a) and (b) the black and grey arrows represent 20 wt.% of fractional crystallization or entrainment of different minerals. Parent compositions used in modeling are the average of high SiO_2 (> 70 wt.%) monzogranites samples, low SiO_2 (≤ 55 wt.%) quartz monzodiorite samples and the low SiO_2 PONT-25 isotropic leucogranite sample. In Zr vs. SiO_2 and La vs. SiO_2 diagrams the arrows representing the fractional crystallization or the entrainment of zircon (Zrn) and monazite (Mnz) are theoretical. Sed represents the assimilation of 20 wt.% of the mean composition of Brioverian to Paleozoic sediments from central Brittany (Georget, 1986). The details of AFC modeling (assimilation – fractional crystallization) for quartz monzodiorites as well as peritectic minerals entrainment or magma mixing modeling for the monzogranites and fractional crystallization modeling (FC) for the leucogranites are provided in Supplementary file 5.

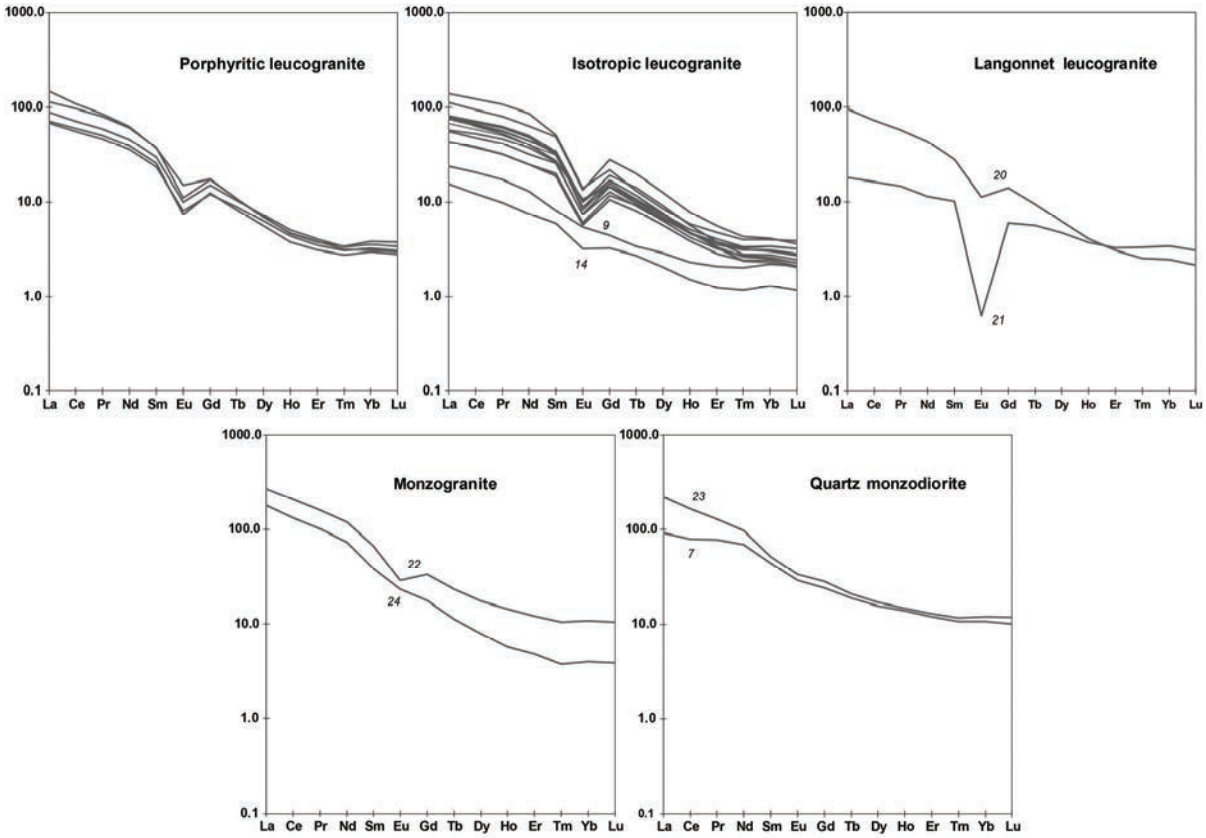

Figure 8: Chondrite normalized REE patterns of the Pontivy-Rostrenen granitoid samples. Normalization values from Evensen et al. (1978).

Table 2: Whole rock chemical composition of the Pontivy-Rostrenen granitoid samples. Langonnet lg: Langonnet leucogranite; LOI: loss on ignition; bdl: below detection limit.

Sample		PONT-1	PONT-2	PONT-5	PONT-11	PONT-19	PONT-3	PONT-6	PONT-9	PONT-10	PONT-12	PONT-13	PONT-14	PONT-15
Facies		**Porphiritic leucogranite**					**Isotropic leucogranite**							
SiO_2	**Wt.%**	70.59	72.10	73.05	71.59	70.88	72.15	71.77	73.83	73.33	73.07	71.88	73.42	72.01
Al_2O_3	**Wt.%**	15.23	15.19	14.64	15.58	15.58	15.34	15.02	15.26	14.61	14.60	14.79	14.42	14.72
Fe_2O_3	**Wt.%**	1.82	0.86	1.28	1.80	1.58	1.53	1.46	0.94	0.98	0.90	1.10	0.38	1.23
MnO	**Wt.%**	0.03	0.01	0.03	0.03	0.02	0.02	0.02	0.04	0.02	0.01	0.02	0.01	0.01
MgO	**Wt.%**	0.57	0.29	0.39	0.64	0.51	0.50	0.42	0.32	0.22	0.22	0.28	0.19	0.33
CaO	**Wt.%**	0.87	0.57	0.74	0.99	0.64	0.87	0.58	0.73	0.53	0.51	0.56	0.42	0.56
Na_2O	**Wt.%**	3.63	3.41	3.65	4.06	3.22	3.57	3.28	4.66	3.62	3.40	3.48	3.02	3.34
K_2O	**Wt.%**	4.66	4.69	4.43	4.35	4.89	4.33	4.74	3.22	4.29	4.45	4.77	4.53	4.95
TiO_2	**Wt.%**	0.28	0.21	0.21	0.31	0.31	0.26	0.24	0.11	0.15	0.15	0.18	0.09	0.19
P_2O_5	**Wt.%**	0.37	0.36	0.38	0.42	0.30	0.35	0.34	0.26	0.45	0.44	0.47	0.41	0.42
LOI	**Wt.%**	1.16	1.54	0.73	1.01	1.89	1.77	1.42	1.13	1.33	1.29	1.34	1.82	1.34
Total	**Wt.%**	99.20	99.21	99.52	100.77	99.80	100.69	99.29	100.49	99.54	99.05	98.85	98.71	99.09
Li	**ppm**	257	202	205	224	66	174	188	225	310	272	251	135	184
Cs	**ppm**	29.5	16.9	19.6	16.6	4.6	22.8	15.3	19.9	34.0	33.2	31.4	30.3	19.1
Rb	**ppm**	309	300	300	298	236	261	301	141	380	376	403	372	305
Sn	**ppm**	14.1	11.1	10.9	10.1	5.8	12.2	12.6	11.6	24.1	26.8	24.1	22.0	15.3
W	**ppm**	1.30	1.53	1.39	1.39	1.18	0.49	1.76	0.33	3.56	3.58	2.75	2.86	1.58
Ba	**ppm**	277	239	210	293	518	327	283	260	146	167	184	101	229
Sr	**ppm**	83.9	62.3	67.7	96.4	167.6	78.8	63.4	176.7	41.5	46.1	55.4	32.9	49.4
Be	**ppm**	12.1	5.8	7.1	7.3	5.2	7.5	6.4	18.2	6.1	7.5	14.6	19.3	7.3
U	**ppm**	7.76	4.30	9.75	8.15	5.89	5.22	6.75	3.04	5.60	8.88	7.36	4.02	5.08
Th	**ppm**	12.08	9.29	10.87	17.79	15.07	9.59	17.34	1.34	6.57	6.26	13.48	2.63	8.37
Nb	**ppm**	6.74	6.39	5.72	8.41	5.54	5.50	5.69	4.88	9.27	9.21	7.52	6.34	6.54
Ta	**ppm**	1.27	1.41	1.02	1.47	0.78	1.19	1.05	1.80	2.35	2.38	2.44	2.17	1.41
Zr	**ppm**	92.6	76.5	84.3	127.3	117.2	101.5	96.8	58.2	60.6	59.7	69.9	30.7	72.2
Hf	**ppm**	2.96	2.48	2.67	3.92	3.51	3.17	2.99	2.00	2.07	2.04	2.21	1.21	2.37
Bi	**ppm**	1.05	0.36	1.63	1.01	1.02	0.73	0.85	1.45	1.45	1.53	1.68	1.36	0.83
Cd	**ppm**	0.13	bld	0.15	0.21	0.15	bld	0.12	bld	0.14	bld	0.13	bld	0.14
Co	**ppm**	3.85	1.16	1.56	1.93	3.88	1.80	1.68	1.05	0.57	0.67	0.55	0.73	0.88
Cr	**ppm**	27.95	11.62	20.04	18.76	10.53	15.29	14.54	9.273	10.15	11.16	10.7	8.07	14.57
Cu	**ppm**	bld	bld	bld	bld	bld	bld	bld	bld	bld	bld	bld	bld	bld
Ga	**ppm**	24.4	24.0	24.4	26.1	25.3	23.9	23.4	20.0	24.0	25.0	24.8	23.5	22.7
Ge	**ppm**	1.76	1.86	1.70	1.64	1.35	1.64	1.71	1.81	1.97	1.95	1.98	2.01	1.71
In	**ppm**	bld	bld	bld	bld	bld	bld	bld	bld	0.128	0.138	0.097	0.108	0.082
Mo	**ppm**	bld	bld	bld	bld	bld	bld	bld	bld	bld	bld	bld	bld	bld
Ni	**ppm**	bld	bld	bld	bld	bld	bld	bld	bld	bld	bld	bld	bld	bld
Pb	**ppm**	27.5	25.7	23.5	25.4	34.2	26.3	26.7	19.8	21.6	24.8	23.3	19.8	28.1
Sc	**ppm**	3.76	2.93	2.93	3.84	3.44	3.34	3.33	2.03	3.15	3.74	2.4	1.8	2.2
Sb	**ppm**	bld	0.37	bld	bld	bld	bld	bld	bld	bld	bld	bld	bld	bld
V	**ppm**	14.4	9.5	8.9	18.4	16.4	15.8	13.8	7.3	5.9	5.7	6.0	1.7	6.6
Y	**ppm**	7.86	6.78	6.03	7.25	7.14	7.26	7.20	3.76	6.28	7.84	7.10	2.53	7.69
Zn	**ppm**	86.94	39.97	83.15	100.6	62.86	71.51	78.21	43.32	75.61	64.34	58.67	36.8	83
As	**ppm**	bld	1.591	2.22	bld	1.823	bld	bld	1.689	2.583	8.871	4.251	bld	3.969
La	**ppm**	21.62	16.72	17.52	27.94	36.00	19.81	18.84	5.79	10.47	10.49	14.12	3.77	13.68
Ce	**ppm**	45.39	35.38	38.43	61.99	69.47	40.70	43.96	12.97	23.84	23.69	33.65	7.80	30.46
Pr	**ppm**	5.68	4.48	4.88	7.73	8.21	5.04	5.84	1.64	3.02	3.04	4.47	0.95	3.95
Nd	**ppm**	21.42	16.92	18.42	28.92	29.92	18.97	22.91	6.14	11.63	11.64	17.55	3.54	15.05
Sm	**ppm**	4.52	3.61	3.91	5.74	5.64	4.17	4.76	1.26	2.87	3.07	4.02	0.91	3.93
Eu	**ppm**	0.58	0.47	0.43	0.64	0.87	0.63	0.52	0.31	0.33	0.35	0.43	0.19	0.43
Gd	**ppm**	3.06	2.48	2.54	3.49	3.56	2.96	2.94	0.90	2.15	2.38	2.61	0.66	2.98
Tb	**ppm**	0.39	0.33	0.31	0.41	0.41	0.38	0.37	0.13	0.30	0.35	0.34	0.10	0.40
Dy	**ppm**	1.84	1.60	1.41	1.76	1.74	1.75	1.67	0.74	1.43	1.71	1.59	0.53	1.85
Ho	**ppm**	0.29	0.25	0.21	0.26	0.27	0.26	0.27	0.13	0.22	0.27	0.24	0.09	0.27
Er	**ppm**	0.68	0.58	0.52	0.63	0.64	0.59	0.63	0.35	0.48	0.59	0.54	0.21	0.56
Tm	**ppm**	0.09	0.08	0.07	0.09	0.08	0.08	0.08	0.05	0.06	0.08	0.07	0.03	0.07
Yb	**ppm**	0.59	0.54	0.50	0.63	0.51	0.51	0.57	0.37	0.40	0.50	0.43	0.22	0.42
Lu	**ppm**	0.09	0.08	0.07	0.10	0.08	0.07	0.08	0.05	0.05	0.07	0.06	0.03	0.06
A/NK		1.38	1.42	1.35	1.37	1.47	1.45	1.43	1.37	1.38	1.40	1.36	1.46	1.36
A/CNK		1.21	1.30	1.20	1.18	1.32	1.26	1.30	1.22	1.26	1.29	1.24	1.35	1.24

Sample		PONT-17	PONT-18	PONT-25	PONT-26	PONT-27	PONT-28	PONT-20	PONT-21	PONT-22	PONT-24	PONT-7	PONT-23
Facies		Isotropic leucogranite						Langonnet lg		Monzogranite		Quartz monzodiorite	
SiO_2	**Wt.%**	72.84	71.07	70.36	71.40	71.72	73.04	72.32	74.86	66.12	70.29	55.00	57.18
Al_2O_3	**Wt.%**	15.06	15.40	15.18	14.75	15.52	14.56	15.07	14.51	16.26	15.44	16.97	17.03
Fe_2O_3	**Wt.%**	1.57	1.75	2.04	1.35	1.38	1.37	1.21	0.81	4.24	1.98	8.31	5.93
MnO	**Wt.%**	0.02	0.01	0.02	0.02	0.01	0.01	0.02	0.02	0.04	0.02	0.12	0.09
MgO	**Wt.%**	0.45	0.51	0.79	0.39	0.43	0.40	0.34	0.12	1.52	0.85	3.98	4.08
CaO	**Wt.%**	0.69	0.79	0.84	0.63	0.57	0.57	0.68	0.38	2.24	1.61	6.14	6.05
Na_2O	**Wt.%**	3.38	2.97	3.26	3.33	2.95	2.92	3.29	3.77	3.50	3.40	2.83	3.19
K_2O	**Wt.%**	4.80	5.03	5.02	5.01	5.58	5.18	4.83	4.28	4.37	4.86	2.70	3.62
TiO_2	**Wt.%**	0.24	0.32	0.38	0.21	0.24	0.21	0.22	0.08	0.69	0.36	1.39	1.11
P_2O_5	**Wt.%**	0.39	0.45	0.30	0.41	0.49	0.37	0.24	0.39	0.27	0.20	0.40	0.45
LOI	**Wt.%**	1.05	1.50	1.35	1.15	1.55	1.31	1.67	1.19	1.09	1.06	1.24	1.20
Total	**Wt.%**	100.5	99.80	99.53	98.64	100.4	99.95	99.87	100.4	100.3	100.1	99.07	99.94
Li	**ppm**	208	100	110	176	145	120	119	168	56	57	72	43
Cs	**ppm**	25.8	5.3	10.9	15.0	15.0	13.7	21.1	22.9	5.3	3.9	5.5	4.8
Rb	**ppm**	350	185	306	328	335	266	310	593	178	178	157	129
Sn	**ppm**	14.4	6.8	5.7	12.4	13.5	8.8	9.7	22.5	2.4	2.2	2.9	2.7
W	**ppm**	2.43	0.57	1.16	1.32	1.86	0.83	1.19	4.38	0.39	0.31	0.55	0.69
Ba	**ppm**	252	373	461	310	327	245	377	21	1038	1132	830	1429
Sr	**ppm**	59.3	85.5	101.3	64.7	64.9	55.1	67.2	11.4	341.7	399.1	319.3	657.5
Be	**ppm**	6.3	6.3	6.2	6.1	6.5	7.9	5.3	2.0	3.1	1.4	5.6	3.4
U	**ppm**	13.28	7.58	6.41	6.04	8.40	6.54	5.83	27.28	4.23	3.53	2.88	4.27
Th	**ppm**	18.48	15.65	31.75	12.91	11.99	11.51	13.15	3.71	26.58	19.22	9.30	17.30
Nb	**ppm**	6.89	6.20	3.96	6.30	7.56	5.54	6.23	9.35	9.76	4.75	10.02	14.46
Ta	**ppm**	1.33	0.68	0.45	1.26	1.51	0.95	1.08	2.10	0.66	0.41	0.62	1.03
Zr	**ppm**	101.0	137.6	155.1	86.0	97.2	82.3	103.3	36.7	285.5	143.6	174.7	220.5
Hf	**ppm**	3.14	4.14	4.46	2.73	3.03	2.56	3.29	1.66	7.20	4.14	4.41	5.31
Bi	**ppm**	0.89	0.32	0.25	0.66	0.77	0.47	0.60	1.28	bld	bld	bld	0.13
Cd	**ppm**	0.19	0.20	0.19	0.14	0.14	0.17	bld	0.19	0.31	0.13	0.24	0.24
Co	**ppm**	1.48	1.45	3.09	1.30	1.12	1.14	1.46	0.43	7.539	3.268	18.92	16.72
Cr	**ppm**	19.18	21.46	28.97	16.98	11.25	7.89	9.505	7.339	38.66	16.38	156.6	110.8
Cu	**ppm**	bld	bld	6.12	bld	6.39	bld	bld	bld	12.77	bld	6.49	12.39
Ga	**ppm**	24.8	23.3	25.9	24.0	23.3	21.7	26.5	31.8	25.6	22.5	22.8	21.6
Ge	**ppm**	1.65	1.35	1.33	1.51	1.59	1.34	1.48	2.13	1.35	1.15	1.61	1.53
In	**ppm**	0.097	bld	0.072	0.1	0.113	0.087	bld	0.178	bld	bld	0.098	0.08
Mo	**ppm**	bld	bld	bld	bld	bld	bld	bld	bld	bld	bld	bld	0.779
Ni	**ppm**	bld	bld	7.174	bld	bld	bld	bld	bld	13.87	6.076	5.926	20.78
Pb	**ppm**	24.8	35.2	27.9	28.1	32.8	29.4	25.9	8.2	36.3	40.8	13.9	25.4
Sc	**ppm**	3.68	3.16	3.91	2.22	2.4	2	2.58	3.95	9.87	4.32	22.79	19.4
Sb	**ppm**	bld	bld	bld	bld	bld	bld	bld	bld	bld	bld	bld	0.35
V	**ppm**	12.8	12.5	27.1	8.2	9.4	7.4	10.7	1.9	50.0	27.7	132.1	121.7
Y	**ppm**	8.20	12.69	8.95	7.48	9.04	7.79	6.37	6.39	20.85	8.47	20.03	21.64
Zn	**ppm**	91.08	41.72	97.25	87.6	72.71	83.44	94.1	86.51	98.36	60.17	102	78.58
As	**ppm**	bld	bld	10.21	1.528	2.292	3.15	2.292	10.71	bld	bld	bld	4.085
La	**ppm**	19.88	27.43	34.10	18.47	19.08	16.63	23.44	4.39	65.52	43.98	22.54	53.80
Ce	**ppm**	45.63	59.93	77.97	41.16	42.10	37.50	46.61	10.35	131.8	84.05	50.60	104.70
Pr	**ppm**	6.05	7.74	10.39	5.36	5.45	4.88	5.56	1.41	15.34	9.79	7.56	12.34
Nd	**ppm**	23.97	30.26	40.82	20.86	20.91	18.85	20.32	5.39	56.70	34.99	33.32	46.18
Sm	**ppm**	5.15	7.57	7.88	5.03	5.25	4.76	4.31	1.57	10.44	5.95	6.85	8.10
Eu	**ppm**	0.48	0.77	0.81	0.58	0.59	0.51	0.65	0.04	1.68	1.35	1.70	1.96
Gd	**ppm**	3.20	5.64	4.42	3.45	3.87	3.36	2.86	1.21	6.89	3.64	4.96	5.81
Tb	**ppm**	0.41	0.75	0.49	0.44	0.53	0.44	0.36	0.21	0.88	0.42	0.71	0.78
Dy	**ppm**	1.88	3.22	2.15	1.89	2.34	1.94	1.59	1.20	4.42	1.99	3.98	4.34
Ho	**ppm**	0.29	0.44	0.33	0.27	0.32	0.27	0.23	0.21	0.82	0.32	0.79	0.84
Er	**ppm**	0.67	0.92	0.79	0.55	0.63	0.55	0.51	0.54	2.03	0.79	1.99	2.16
Tm	**ppm**	0.09	0.11	0.10	0.06	0.07	0.06	0.07	0.09	0.27	0.10	0.27	0.30
Yb	**ppm**	0.56	0.67	0.66	0.40	0.46	0.38	0.41	0.56	1.78	0.65	1.77	1.98
Lu	**ppm**	0.08	0.09	0.10	0.05	0.06	0.05	0.06	0.08	0.27	0.10	0.26	0.30
A/NK		1.40	1.49	1.40	1.35	1.42	1.40	1.41	1.34	1.55	1.42	2.23	1.85
A/CNK		1.25	1.31	1.23	1.22	1.30	1.27	1.27	1.26	1.12	1.12	0.90	0.84

7. Geochronology

Five samples representative of the different magmatic facies were chosen for zircon U-Pb LA-ICP-MS analyses. In the leucogranites, the zircon population is characterized by generally euhedral translucent grains which can be colorless, grayish or creamy. Cathodoluminescence (CL) imaging reveals numerous zoned grains which commonly display inherited cores (Fig. 9a, b, c). For the porphyritic leucogranite (PONT-1), 53 analyses were performed on 45 zircon grains and 27 analyses have a degree of concordance between 90 and 110 % (Fig. 10a). $^{207}Pb/^{206}Pb$ dates range from 1750.6 ± 19.3 Ma down to 304.1 ± 27.8 Ma and 8 concordant to sub-concordant analyses allow to calculate a concordia date of 316.7 ± 2.5 Ma (MSWD = 1.2) that is interpreted as the crystallization age for this sample. 4 analyses display younger apparent $^{206}Pb/^{238}U$ and $^{207}Pb/^{235}U$ dates (dashed ellipses in Fig. 10a). They plot in concordant to discordant position and likely reflect slight Pb loss combined with initial common Pb contamination.

74 analyses on 45 zircon grains were carried out for the isotropic leucogranite sample (PONT-26) and 48 analyses have a degree of concordance between 90 and 110 % (Fig. 10b). $^{207}Pb/^{206}Pb$ dates range from 1982.5 ± 21.6 Ma down to 289.2 ± 26.0 Ma. One group of 6 analyses allows to calculate a poorly constrained concordia date of 310.3 ± 4.7 Ma (MSWD = 2.5) which is in the same range than for the porphyritic sample. In Figure 10b, dashed ellipses can be best explained by the presence of inherited common Pb and complex Pb loss. 59 analyses out of 42 grains were performed on zircon grains from a Langonnet leucogranite sample (PONT-20). 43 analyses have a degree of concordance between 90 and 110 % and among those, the $^{207}Pb/^{206}Pb$ dates range from 2637.9 ± 17.6 Ma to 287.2 ± 31.9 Ma (Fig. 10c). Six analyses in concordant position allow the calculation of a concordia date of 304.7 ± 2.7 Ma (MSWD = 0.57) that we interpret as the crystallization age for this sample. Three analyses, represented by dashed ellipses in Figure 10c, plot in discordant position and likely reflect complex Pb loss and initial common Pb contamination.

The monzogranite sample (PONT-22) provided an important number of generally euhedral translucent zircon grains characterized by an euhedral shape with a colorless, milky, grayish or yellowish color. On the CL images, most zircon grains display growing zonation (Fig. 9d). 29 analyses were performed on 22 zircon grains and 26 analyses have a degree of concordance between 90 and 110 % (Fig. 10d). $^{207}Pb/^{206}Pb$ dates range from 487.5 ± 30.4 Ma to 299.1 ± 30.5 Ma and a group of 18 concordant to sub-concordant analyses allow to calculate a concordia date of 315.5 ± 2.0 Ma (MSWD = 1.5) which is the same rage than the porphyritic and isotropic leucogranite. As a consequence, we suggest that this sample crystallized 315.5 ± 2.0 Ma ago. The analyses represented by dashed ellipses in Figure 10d can be explained by complex Pb loss and common Pb contamination.

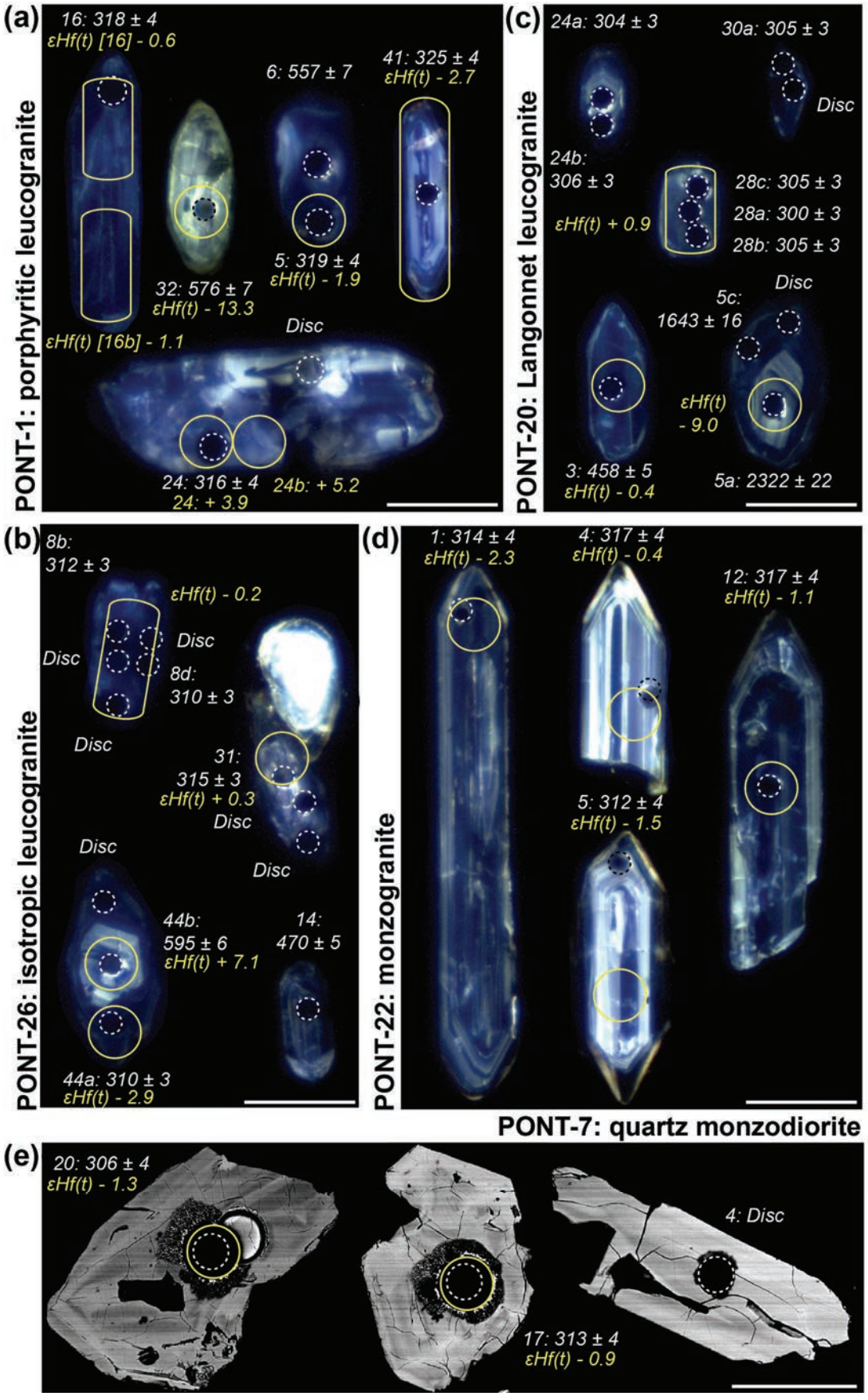

Figure 9: Selected (a-d) cathodoluminescence and (e) BSE image of zircon grains. Dashed white circles represent the location of U-Pb LA-ICP-MS analyses with the corresponding $^{206}Pb/^{238}U$ age in Ma and yellow zones represent the location of Hf isotopic LA-MC-ICP-MS analysis with the corresponding εHf(t) values. The white bar represents 100 µm.

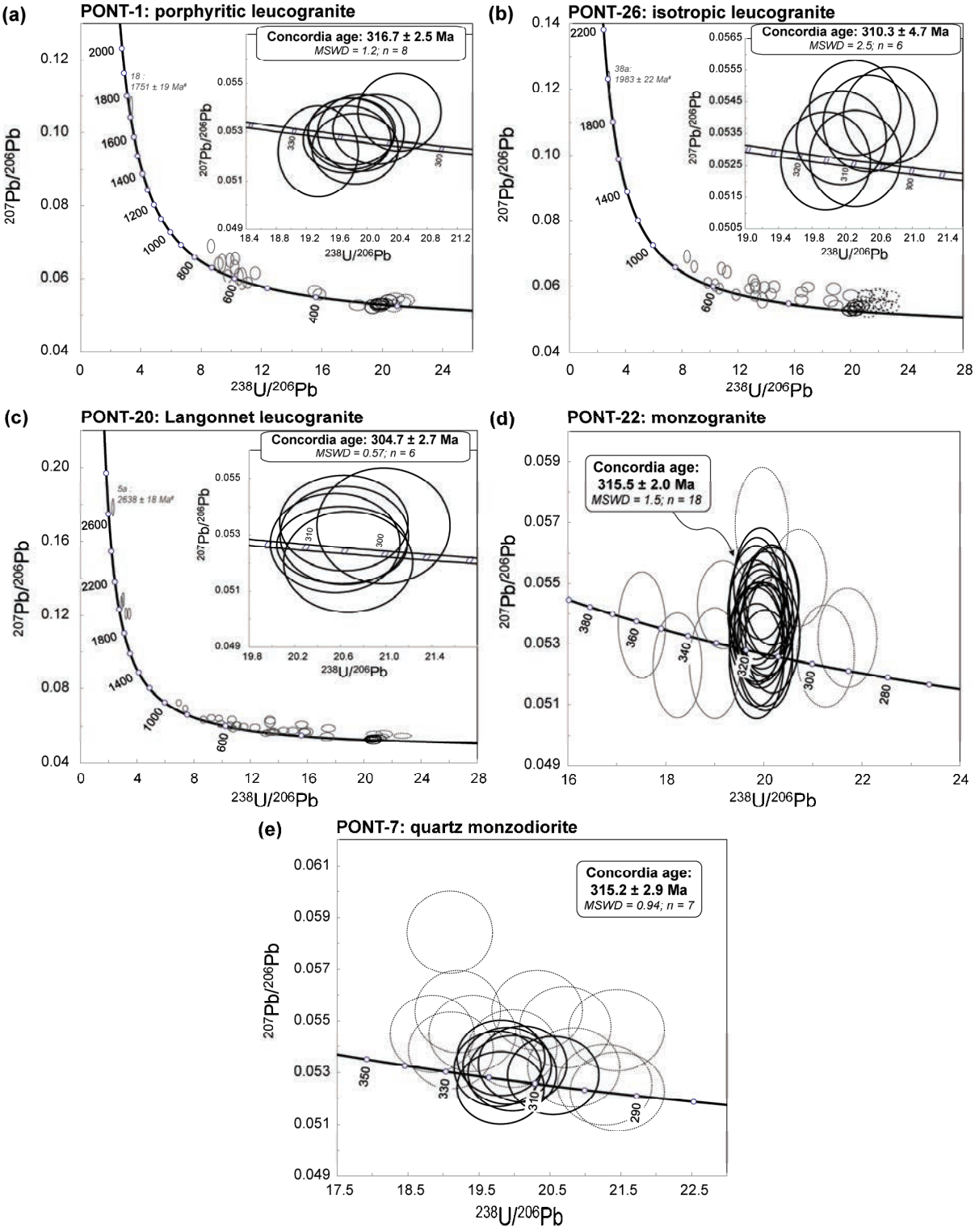

Figure 10: Terra-Wasserburg diagram displaying the analyses (degree of concordance between 90 and 110%) made on zircon of granitoid samples from the Pontivy-Rostrenen complex. The gray ellipses represent inherited zircon and the dashed ellipses represent zircon submitted to a loss or a gain in common lead. Black ellipses represent the analyses used for the calculation of concordia ages. #: $^{207}Pb/^{206}Pb$ ages at 1σ. In the diagrams error ellipses are plotted at 2σ.

In the quartz monzodiorite sample (PONT-7), zircon grains are abundant, generally sub-euhedral and characterized by a brownish-honey color. The grains are not luminescent on the CL images but they reveal discreet zonings on the BSE images (Fig. 9e). 24 analyses were carried out on 24 grains and 19 analyses have a degree of concordance between 90 and 110 % (Fig. 10e). Among them, a group of 7 analyses plot in concordant positions and allow the calculation of a concordia date of 315.2 ± 2.9 Ma (MSWD = 0.94) which is comparable with the dates obtained on the porphyritic and isotropic leucogranite as well as the monzogranite. We suggest that this sample crystallized 315.2 ± 2.9 Ma ago. Dashed ellipses in Figure 10e are interpreted to result from complex Pb loss and common Pb contamination.

8. Radiogenic isotopes

Whole rock Sr and Sm-Nd analyses from the Pontivy-Rostrenen magmatic complex are reported in Figures 11a-b and Table 3. The initial Nd isotope compositions [εNd(315)] are comparable between the different facies and mostly range from - 4.79 to -2.46 with Nd Model ages ($T_{DM.Nd}$) ranging between 1.49 Ga and 1.23 Ga. Two isotropic leucogranites (data from Euzen, 1993) have positive εNd(315) values of 1.08 and 2.08 ($T_{DM.Nd}$ = 0. 846 and 0.9 Ga) which suggest juvenile contributions. Initial Sr isotopic [ISr(315)] values range from 0.7056 to 0.7068 in the quartz monzodiorites and from 0.7064 to 0.7071 in the monzogranites. These two facies describe a well-defined evolution trend in the I_{Sr}(315) vs. SiO_2 diagram (Fig. 11b). For the isotropic and porphyritic leucogranites most I_{Sr}(315) values range from 0.7041 to 0.7122. For the Langonnet leucogranite and one isotropic leucogranite (PONT-14), the I_{Sr}(315) values are anomalously low and range from 0.6114 to 0.7012. No correlation exists between I_{Sr}(315) values of the leucogranites and their SiO_2 content (Fig. 12b).

In Table 3, we provide five Sm-Nd whole-rock sample analyses on Early Paleozoic peraluminous metagranitoids from the Central Armorican domain (Plouguenast) and the South Armorican Domain (Moelan) (Fig. 1, Table 1). The εNd(T) values of these samples, recalculated at 315 Ma, range from -2.83 to 0.54 with $T_{DM.Nd}$ values between 0.99 and 1.25 Ga.

Table 3: Rb-Sr and Sm-Nd whole rock data for the Pontivy-Rostrenen granitoids. Additional Sm-Nd analyses on Early Paleozoic metagranitoids are also reported. Rb concentrations have been obtained by ICP-MS whereas other concentrations have been obtained by isotopic dilution.

Sample	Intrusion	Facies	Rb (ppm)	Sr (ppm)	$^{87}Rb/^{86}Sr$	$^{87}Sr/^{86}Sr$	±	$^{87}Sr/^{86}Sr$ (315 Ma)	S m (ppm)	Nd (ppm)	$^{147}Sm/^{144}Nd$	$^{143}Nd/^{144}Nd$	±	εNd (315 Ma)	T_{DM}*
PONT-3	Pontivy	Isotropic lg	260.6	78.8	9.61	0.750650	10	0.707547	3.8	18.4	0.125637	0.512322	5	-3.30	1.29
PONT-6	Pontivy	Isotropic lg	301.1	63.4	13.83	0.771012	11	0.709021	4.6	22.8	0.121104	0.512256	5	-4.42	1.38
PONT-10	Pontivy	Isotropic lg	379.6	41.5	26.76	0.825829	10	0.705845	2.8	11.8	0.143538	0.512337	4	-3.73	1.33
PONT-14	Pontivy	Isotropic lg	372.1	32.9	33.20	0.850024	12	0.701194	0.8	3.5	0.145109	0.512286	6	-4.79	1.41
PONT-15	Pontivy	Isotropic lg	304.7	49.4	18.00	0.790331	10	0.709617	3.7	14.7	0.151254	0.512310	5	-4.58	1.39
PONT-26	Pontivy	Isotropic lg	327.7	64.7	14.74	0.774110	10	0.708009	4.7	20.5	0.140117	0.512334	5	-3.65	1.32
PONT-20	Langonnet	Langonnet lg	310.3	63.6	14.18	0.763911	10	0.700323	4.2	20.9	0.120593	0.512355	5	-2.46	1.23
PONT-21	Langonnet	Langonnet lg	593.2	11.7	155.38	1.308011	13	0.611438	1.5	5.6	0.162937	0.512363	5	-4.00	1.35
PONT-22	Rosrenen	Monzogranite	178.4	320.2	1.61	0.713663	11	0.706431	9.8	56.0	0.117271	0.512311	5	-3.19	1.28
PONT-24	Rosrenen	Monzogranite	177.6	374.7	1.37	0.712872	11	0.706722	5.6	34.7	0.108900	0.512346	4	-2.17	1.20
PONT-7	Pontivy	Qtz monzodiorite	157.3	303.6	1.50	0.712591	10	0.705868	6.6	33.9	0.117600	0.512335	2	-2.73	1.25
QIMP-1	Moelan	Metagranitoid							3.9	16.5	0.143344	0.512548	4	0.39	1.00
PLG-1	Plouguenast	Metagranitoid							3.8	17.0	0.134942	0.512498	4	-0.25	1.05
PLG-2	Plouguenast	Metagranitoid							5.4	28.5	0.113956	0.512323	5	-2.81	1.25
PLG-3	Plouguenast	Metagranitoid							2.5	9.9	0.154841	0.512407	5	-2.83	1.26
PLG-4	Plouguenast	Metagranitoid							1.6	6.9	0.141894	0.512553	5	0.54	0.99

** Two stages T_{DM} calculated using the equation of Liew and Hofmann (1988) for an age of 315 Ma*

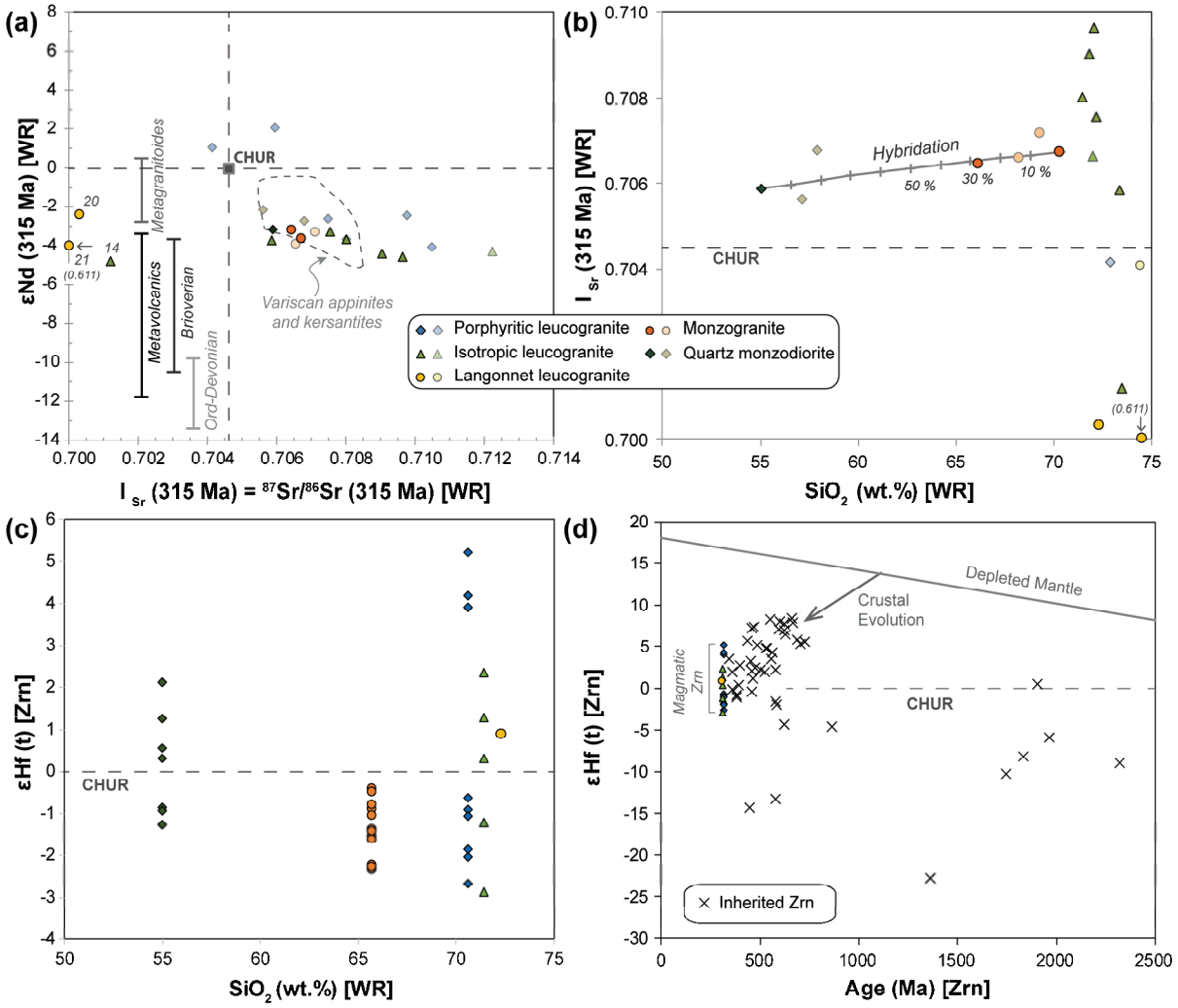

Figure 11: (a) Initial Sr and Nd isotopic composition of the Pontivy-Rostrenen granitoid samples. I_{Sr} and εNd values have been calculated for an age of 315 Ma. Analyses in light color are from Euzen (1993) and Peucat et al. (1979). The vertical bars represent the εNd composition of Ordovician acid metavolcanics (Vendée Porphyroids, Ballèvre et al., 2012), Ordovician metagranitoids (this study), Brioverian sediments (Dabard et al., 1996; Dabard, 1997) and Ordovician to Devonian sediments (Michard et al., 1985) from the Armorican Massif. The isotopic composition of Variscan appinites and kersantites (Turpin et al., 1988; Molina et al., 2012) has also been reported for comparison. (b) I_{Sr} (315 Ma) versus SiO_2 diagram for the Pontivy-Rostrenen granitoid samples. The dashed line with gray crosses represents the mixing model between the monzogranite sample PONT-24 and the quartz monzodiorite sample PONT-7. Crosses represent increment of 10 %. (c) diagram reporting the εHf(t) composition of magmatic zircon in function of the SiO2 whole rock content of granitic samples of the Pontivy-Rostrenen complex. (d) εHf(t) versus U-Pb ages for magmatic and inherited zircon from the leucogranites samples of the Pontivy-Rostrenen complex. The crustal evolution trend is calculated using a $^{176}Lu/^{177}Hf$ ratio of 0.0113 (Taylor and McLennan, 1985; Wedepohl, 1995).

The Hf isotope compositions of zircon are reported in Figures 11c-d and in the supplementary file 3. For the leucogranite samples (PONT-1, 20 and 26), both magmatic (15 analysis) and inherited (46 analysis) zircon grains/domains (Fig. 9a, b and c) were analyzed whereas for the monzogranite (sample PONT-22) and quartz-monzogranite (sample PONT-7) only the magmatic grains were analyzed. For the Langonnet leucogranite (PONT-20), only one analysis of magmatic zircon was performed due to the small size of the grains in this sample. For all the samples, the magmatic zircon

grains/domains reveal mostly subchondritic to chondritic εHf(t) values ranging from -2.9 to +2.4, and corresponding to two stage hafnium model ages ($T_{DM2.Hf}$) between 1.40 and 1.11 Ga, respectively (Leucogranites: PONT-1 = -0.6 to -2.7, n = 6; PONT-20 = +0.9, n=1; PONT-26 = -2.9 to +2.4, n = 5; Monzogranite: PONT-22 = –2.3 to –0.4, n=14; Quartz monzodiorite: PONT-7 = -1.3 to +2.1, n=7). Only three grains/domains in sample PONT-1 show significantly higher εHf(t) values of +3.9 to +5.2 (corresponding to lower $T_{DM2.Hf}$ =1.03 - 0.96), pointing to a bimodal Hf isotope distribution. The inherited zircon grains/domains show a much wider scatter in εHf(t) than the magmatic grains, ranging from -22.8 to +8.4 (Fig. 11b). However, most of the inherited grains (~75%) have similar overlapping initial $^{176}Hf/^{177}Hf$ than the magmatic grains, and consequently they are aligned on the same crustal evolutionary trend than the magmatic grains, and show comparable $T_{DM2.Hf}$ between 0.95 and 1.4 Ga (see trend in Figure 11d). The other 25% reveal much older hafnium model ages ranging between ca. 2.0 and 3.0 Ga.

9. Discussion

9.1. Petrogenesis

9.1.1. Source characterization

CL imaging (Fig. 9a, b, c) and U-Pb analyses (Fig. 10a, b, c) on zircon provide direct evidence for the presence of inherited material in the leucogranites from the Pontivy-Rostrenen magmatic complex. Inherited $^{207}Pb/^{206}Pb$ dates range from Late Archean (2637.9 ± 17.6 Ma; PONT-1) to Paleozoic (376.9 ± 25.7 Ma; PONT-26). This spread of ages is well known in other rocks from the Armorican Massif, e.g. from the Guérande, Lizio and Questembert leucogranites (Ballouard et al., 2015a, Tartèse et al., 2011a and b) (Fig.1). All these leucogranites are interpreted to be mostly formed by the partial melting of a metasedimentary source, because of (i) their highly peraluminous characters (A/CNK > 1.1; Fig. 6a; Fig. 5b), (ii) their compositions similar to melts produced experimentally by partial melting of sedimentary rocks (Fig. 6b and c), (iii) their crustal Nd and Sr isotopic signatures (Fig. 11a), and (iv) the presence of inherited zircon grains. This interpretation is also in agreement with the elevated $\delta^{18}O$ whole rock values of 12.5 and 12.8 ‰ obtained on a porphyritic and isotropic leucogranite, respectively, by Bernard-Griffiths et al. (1985). In Figure 11a, the εNd(315) signatures of most of the leucogranites overlap with those of Brioverian (Neoproterozoic) sediments from the Armorican Massif (Dabard et al., 1996; Dabard, 1997). However, the presence of two porphyritic leucogranite samples with positive εNd(315) can potentially reflect the contribution of Early Paleozoic peraluminous metagranitoids in their source (Fig. 11a), in agreement with the ages and Hf isotope signatures of the Paleozoic inherited zircon grains (Fig. 11d). Moreover, the Ordovician peraluminous metavolcanics (~470 - 500 Ma) from the South Armorican Massif also display an εNd(315) signature (Ballèvre et al., 2012) mostly comparable with those of the leucogranites. As a consequence, we suggest that the leucogranites from the Pontivy-Rostrenen complex formed by the partial melting of a metasedimentary source Neoprotorozoic in age with the probable contribution of Early Paleozoic peraluminous orthogneisses.

This suggestion is consistent with the hypothesis of Tartèse and Boulvais (2010) and Ballouard et al. (2015a) who suggested that the Lizio - Questembert leucogranites and the Guérande leucogranite formed by the partial melting of Neoproterozoic and Neo-Proteorozoic to Paleozoic metasediments, respectively.

The proposed sources are furthermore in good agreement with the fact that ca. 75 % of the inherited Neoproterozoic-Paleozoic zircon grains (700-480 Ma) in the leucogranite samples are aligned on the same crustal evolutionary trend (having all similar model ages) than the ca. 315 Ma old magmatic grains, and that the inherited and magmatic grains show a similar spread in εHf(t) (ca.7 epsilon units) (Fig. 11d). This feature is similar to that of the S-type Cape granite suite of South Africa, where the εHf(t) variability in the magmatic zircon matches well with that of the inherited zircon population, suggesting that the heterogeneity is directly inherited from the source (Villaros et al., 2012; Farina et al., 2014). Thus, it seems possible to state that the observed Hf-isotope heterogeneity of the magmatic zircon grains in our samples (comprising the bimodality in sample PONT-1) is a result of an incomplete homogenization of the (inherited) Hf isotope system (on a sample scale) during the formation of the leucogranites. Modeling of zircon dissolution by Farina et al. (2014), suggests that sub-mm domains with variable Hf isotope compositions can indeed be created in a granitic melt, whereby the composition of such domains is controlled by the size and the isotopic signature of the nearest dissolving zircon crystal as well as the cooling rate of the magma. Nevertheless, there are also many other examples, showing that nearly perfect Hf-isotope homogenization (on sample scale) can be achieved during new zircon (over)growth in the presence of partial melts at >750°C (e.g., Gerdes & Zeh, 2009, Zeh et al., 2007, 2010).

The whole rock I_{Sr}(315) values for the leucogranites are highly variable. The I_{Sr}(315) mostly range from ~ 0.7040 to 0.7125 and three samples display abnormally low I_{Sr}(315) values below 0.7015 (Fig. 11a). This spread of I_{Sr} values could reflect heterogeneities in the source of the leucogranites or can be the result of mineral-scale isotopic disequilibrium during partial melting reactions (Farina and Stevens, 2011). Moreover, this variability of the I_{Sr} values could reflect hydrothermal alteration processes as Rb has a strong affinity for orthomagmatic fluids (e.g. Shaw, 1968). Two of the samples with abnormally low I_{Sr}(315) values below 0.7015 are highly evolved Ms leucogranites (PONT-14 and 21) which likely experienced significant hydrothermal interaction suggesting that magmatic-hydrothermal alteration processes are involved in the decrease of the I_{Sr} values.

The monzogranites display high I_{Sr}(315) and negative εNd(315) values as well as subchondritic zircon εHf(t) values (Fig. 11a). These results combined with the moderately peraluminous signature of the samples (~ 1 < A/CNK< 1.3; Fig. 6a; Fig. 5b), the whole rock composition of several samples close to the experimental melts produced by partial melting of metaluminous igneous rocks (Fig. 6c) and the absence or the scarcity of inherited zircon grains (Fig. 9d and 10d) suggest that the monzogranites were mostly formed by the partial melting of a metaluminous metaigneous source.

The quartz monzodiorite samples display also high I_{Sr}(315) as well as subchondritic εNd(315) and chondritic zircon εHf(t) values (Fig. 11a, 11c), that would normally be characteristic of a crustal source. However, their metaluminous signature (Fig. 6a) and their major elements composition, including their maficity (Fe + Mg + Ti > 150 millications in Fig. 6c), largely differ from the products of partial melting experiment of igneous and sedimentary rocks (Fig. 6b and c) and suggest a mantle-derived origin. In fact, the quartz monzodiorite samples display whole rock major elements (Fig. 6d) and radiogenic isotopic compositions (Fig. 11a) similar to others magneso-potassic (Mg-K) calc-alkaline igneous mafic rocks from the west European Hercynian belt locally called appinites in Iberia (e.g. Scarrow et al., 2009; Molina at al., 2012) and kersantites or vaugnerites in the French Hercynian belt (e.g. Turpin et al., 1988; Couzinié et al., 2014, Moyen et al., in press). Mg-K mafic magmatic rocks are commonly found associated with post collisional granites and are interpreted as being formed by the partial melting of a metasomatized lithospheric mantle (Turpin et al., 1988; Bonin, 2004; Scarrow et al., 2009; Zhong et al., 2016; Moyen et al., in press). The metasomatization of the subcontinental lithospheric mantle during Variscan subduction events by fluid and/or melt interactions could explain the apparent crustal Sr, Nd and Hf isotopic signatures of theses rocks (e.g. Yoshikawa et al., 2010; Gordon Medaris Jr. et al., 2015; Laurent and Zeh, 2015). The origin of the quartz monzodiorites predominately from an enriched mantle source is also in agreement with the absence of inherited zircon grains.

9.1.2. Timing and duration of emplacement

The zircon U-Pb concordia ages (Fig. 10) obtained on porphyritic (316.7 ± 2.5 Ma) and isotropic leucogranite (310.3 ± 4.7 Ma) as well as monzogranite (315.5 ± 2.0 Ma) and quartz monzodiorite (315.2 ± 2.9 Ma) samples are comparable within error and suggest that the majority of the Pontivy-Rostrenen magmatic complex was emplaced ca. 315 Ma ago. The synchronous emplacement age of the different magmatic units forming the complex is consistent with field observations which revealed mingling features at the contact between the monzogranite and the quartz monzodiorite (Fig. 3d). The slightly younger and poorly constrained concordia date of 310.3 ± 4.7 Ma (MSWD =2.5) obtained on the isotropic leucogranite sample is likely due to a complex combination of Pb loss and common Pb contamination (Fig. 10b). The zircon U-Pb age of ca. 315 Ma obtained on our samples is younger than the Rb-Sr isochron date of 344 ± 8 Ma previously obtained by Peucat et al. (1979) for the Pontivy leucogranite samples but is in agreement with the muscovite ^{40}Ar-^{39}Ar date obtained by Cosca et al. (2011) which can now be interpreted as a cooling age. The fact that the Rb-Sr isochron method yielded an older date is surprising but not exclusive to the Pontivy leucogranite as it was already the case for the neighboring Lizio (Tartèse et al., 2011a) and Questembert (Tartèse et al., 2011b) leucogranites (Fig. 1). In any case, these differences seem to demonstrate that the Rb-Sr isotopic system is not suitable to date the emplacement and/or to trace the sources of peraluminous leucogranite intrusions. In agreement with cartographic criteria (Fig. 2), zircon U-Pb dating of a Langonnet leucogranite sample yields a concordia age of 304.7 ± 2.7 Ma (Fig. 10c) which demonstrates that this intrusion was emplaced late when

compared to the bulk part of the complex. At a regional scale, the crystallization age of ca. 315 Ma obtained on the Pontivy-Rostrenen granitoids is consistent with the ages found for other syntectonic granites emplaced along the SASZ such as the Lizio (316.4 ± 5.6 Ma; U-Pb Zrn; Tartèse et al., 2011a) and Questembert (316.1 ± 2.9 Ma; U-Pb Zrn; Tartèse et al., 2011b) leucogranites. The emplacement of the Langonnet leucogranite at 304.7 ± 2.7 Ma is synchronous with the late magmatic pulse recorded in the Guérande leucogranite ca. 303 Ma ago (Ballouard et al., 2015a) and with hydrothermal circulations in the Questembert leucogranite (Tartèse et al., 2011b).

9.1.3. Magmatic history

Peraluminous granites mostly form by the partial melting of the crust and the diversity of their mineralogical assemblages and chemical compositions can reflect different petrogenetic processes such as (i) fractional crystallization (e.g. Tartèse and Boulvais, 2010; Morfin et al., 2014; Ballouard et al., 2015a), (ii) mixing with mantellic magmas (e.g. Castro et al., 1999; Patiño-Douce, 1999; Healy et al., 2004), (iii) country rock assimilation (e.g. DÍaz-Alvarado et al., 2011), (iv) restite unmixing (Chappell et al., 1987) and (v) peritectic phases entrainment (e.g. Stevens et al., 2007; Villaros et al., 2009a, 2009b; Clemens and Stevens, 2012). Metaluminous granitic rocks associated with peraluminous granites in post-orogenic context are commonly interpreted as the result of a mixing between crustal and mantellic melts (e.g. Barbarin, 1999; Patiño-Douce, 1999).

The peraluminous leucogranites from the Pontivy-Rostrenen complex display major elements compositions similar to the products of partial melting experiments of sedimentary and igneous rocks (Fig. 6b and c) suggesting that they are pure crustal melts (Patiño-Douce, 1999) and that the degree of mixing with mantle-derived magmas, assimilation of country rocks or entrainment of peritetic and restite minerals from the source are negligible. In bivariate diagrams (Fig. 7b and c), the leucogranite samples display trends of evolution which likely reflect the fractional crystallization of biotite, K-feldspar and plagioclase (± apatite). Modeling using major elements (Fig. 7b) suggests that the evolution from low to high SiO_2 leucogranite samples can be best explained by the segregation of ~ 20 wt.% of a cumulate composed of these minerals (details on the modeling are provided in Fig. 7 and Supplementary file 5). The scattering of the analyses could be the result of source heterogeneities. Indeed, in Figure 12, the compositions in K_2O, CaO and Na_2O of the more primitive leucogranite samples, with low SiO_2 contents between 70.8 and 72.3 wt.% (Fig. 7b), are reported cartographically. On this map of the southern part of the complex, we can observe a zonation of the K_2O and CaO-Na_2O contents independently of the petrographic facies: the southwestern part of the massif is mostly characterized by high K_2O content above 5.0 wt.% and low CaO content below 0.7 wt.% whereas the eastern and northern parts are mostly characterized by low K_2O content below 5.0 wt.% and high CaO and Na_2O contents above 0.7 and 3.0 wt.% respectively. This zonation suggests a partial melting of a K rich source to the SW whereas a Ca-Na rich source was involved to the N and to the E. This spatial variation of the source correlates with the evolution of the regional metamorphism which increases from NE to SW (Fig. 1b) and suggests a

difference for the depth of the metasedimentary source involved during partial melting. In Figure 7c, Ba and Sr are both anticorrelated with SiO_2 for the leucogranites (Fig. 7c). These trends are also consistent with the fractional crystallization of feldspar and biotite (± apatite) as Sr is a compatible element in plagioclase, K-feldspar and apatite and Ba a compatible element in plagioclase, K-feldspar and biotite. The roughly defined correlation between Rb and SiO_2 for leucogranite samples reflects its incompatible behavior in peraluminous melts and the potential interaction with orthomagmatic fluids (e.g. Shaw, 1968). In Figure 7c, Zr and La anticorrelate with SiO_2 for the leucogranites. This trend is consistent with the fractionation of zircon and monazite commonly hosted in biotite. Among the leucogranites, the SiO_2 rich Langonnet leucogranite samples fall at the extremity of the evolution trends and experienced the higher degree of differentiation (Fig. 7).

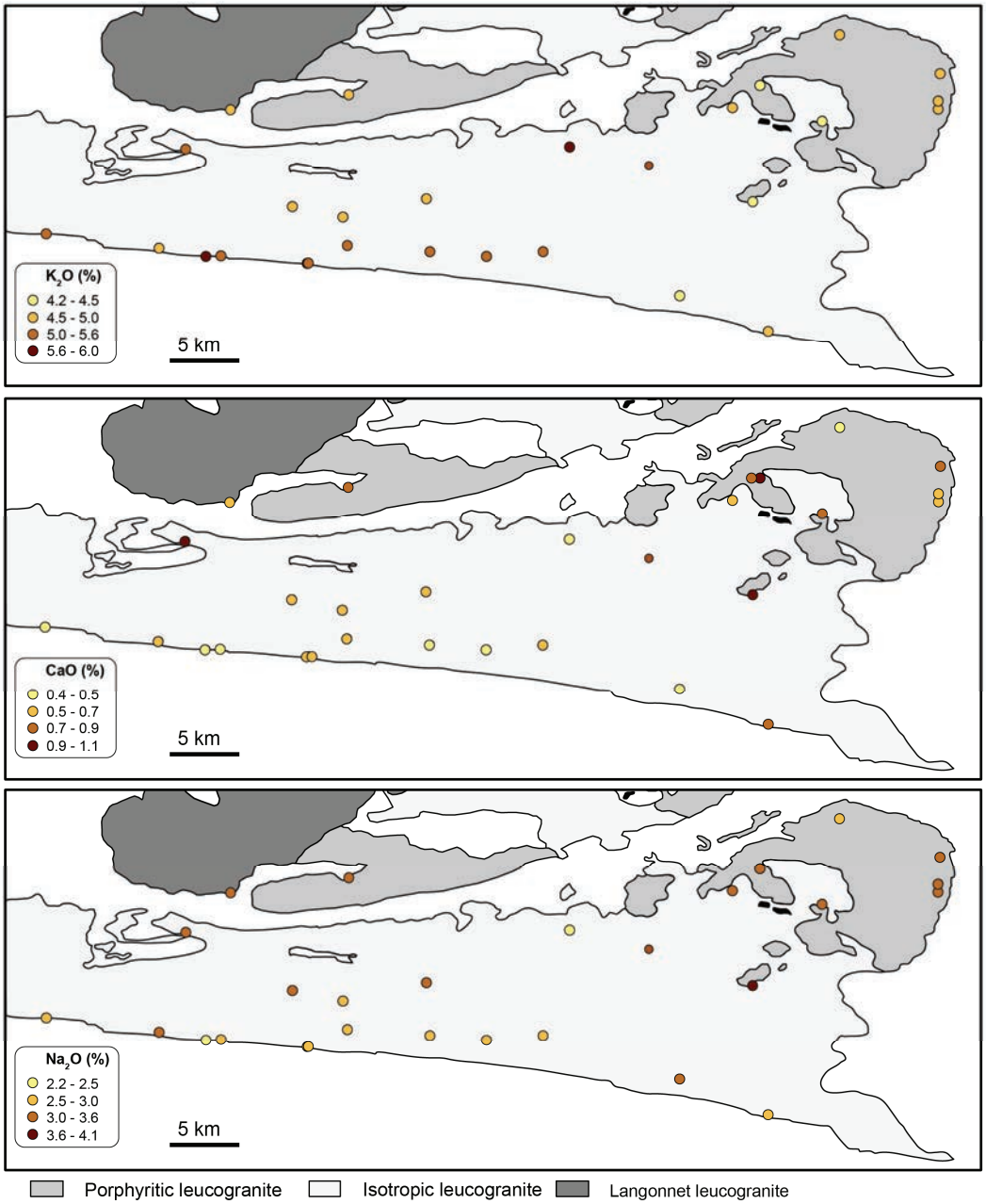

Figure 12: Maps displaying the K_2O, the CaO and the Na_2O contents of low SiO_2 (70.8 – 72.3 wt.%) leucogranite samples.

Then, the compositions and the isotopic signatures of the quartz monzodiorite samples suggest that they mostly formed by partial melting of a metasomatized mantle source (see section 9.1.1) but some evidences suggest that these rocks also experienced variable degree of interaction with crustal derived melts. Indeed, ocelli quartz grains which correspond to corroded quartz crystals surrounded by mafic minerals such as clinopyroxene or amphibole are commonly observed in the quartz monzodiorite samples (Fig. 4d). Such textures are commonly used as a marker of magma mixing and generally interpreted as reflecting the introduction of quartz crystals from a felsic magma into a more mafic hybrid magma which leads to localized under cooling and crystallization of fine grained mafic minerals around the quartz xenocrysts (e.g. Baxter and Feely, 2002 and reference therein). Then, mingling features, commonly observed at the contact between monzogranites and quartz monzodiorites (Fig. 3d), as well as U-Pb geochronology, attest for the synchronous emplacement of crustal and mantle-derived melts and suggest an interaction between these two. The Hf isotopic signatures of zircon grains from the quartz monzodiorite, ranging from subchondritic to slightly superchondritic (Fig. 11c), and the mixing model with a monzogranitic magma based on SiO_2 contents and I_{Sr} compositions (Fig. 11b), also point to a hybrid origin. However, magma hybridation modeling based on major element compositions necessitates an amount of mixing of ~ 40 wt.% between low SiO_2 ($\leq$ 55 wt.%) quartz monzodiorite and high SiO_2 (> 70 wt.%) monzogranite samples to explain the compositional variation observed in Harker diagrams (Fig. 7a). Such amount of mixing is likely unrealistic due to the expected differences in viscosity between the two magmas and requires an enormous amount of mafic melts (e.g. Laumonier et al., 2015 and reference therein). Moreover, the scattering of the analyses in bivariate diagrams (Fig. 7a and c) suggest that high SiO_2 samples also experienced fractional crystallization of biotite, plagioclase and clinopyroxene. The AFC (assimilation-fractional crystallization) modeling is consistent with this hypothesis and reveals that the chemical variation of the samples can be explained by ~25 wt.% segregation of a cumulate composed of An70 + Cpx + Bt and 20 wt.% assimilation of an acid magma with the average composition of high SiO_2 (> 70wt.%) monzogranite samples (details of the modeling are provided in Fig. 7 and Supplementary file 5). The large variability of the Ba, Sr and La contents for the quartz monzodiorite samples is likely due to the combination of both processes whereas Zr behaves as an incompatible element and increases during differentiation (Fig. 7c). In contrast to magma mixing and fractional crystallization, sedimentary country rock assimilation cannot explain the chemical variations displayed by the samples (Fig. 7a).

In contrast with the leucogranites, several monzogranite samples display whole rock chemical compositions that differ from the composition of a melt produced during the experimental partial melting of natural rocks. As a consequence, several samples do not represent pure crustal melts and the well-defined evolution trends displayed by the monzogranites in the bivariate diagrams (Fig. 7a and 7c) can result from different processes such as country rocks assimilation, entrainment of restite and peritectic minerals from the source as well as mixing with mantle-derived magmas. In the Harker diagrams (Fig. 7a), the assimilation of country rocks cannot reproduce the different trends displayed by the

monzogranites and the samples lack the mineralogical and textural evidence characteristic of the presence of significant restitic materials (i.e. unmolten source rocks). Therefore, neither of these two processes can be accounted for the evolution of the monzogranites. In contrast, the model of mixing between high SiO_2 monzogranite and quartz monzodiorite samples matches generally well with the trends displayed by the monzogranite samples (Fig. 7a and c) as well as in the diagrams reporting the I_{Sr} composition as a function of SiO_2 (Fig. 11b). However, the hybridation modeling, based on major elements (Fig. 7a) and Sr isotopic compositions (Fig. 11b), involve an amount of mixing of about 30 wt.% between the two end members. As discussed above for the quartz monzodiorites, such an amount of mixing is likely unrealistic and even if field observations (Fig. 3c and d) demonstrate that both monzogranite and quartz monzodiorite magmas interacted and were emplaced together, the monzogranite samples do not present the mineralogical textures attributable to a significant amount of magma mixing such as rapakivi feldspar (e.g. Baxter and Feely, 2002). On the other hand, we have shown previously that the quartz monzodiorites already represent hybrid magmas which were formed by a mixing between crustal and mantle-derived melts. As a consequence, we do not have access to the initial mantle melt composition and the amount of mixing between the crustal and the mantle end members can be much lower than 30 wt.%. This hypothesis could account for the elevated Ba content of the monzogranites which cannot be explained solely by a mixing with the quartz monzodiorites. Alternatively, entrainment of peritectic minerals can induce significant change in the composition of granitic magmas and metaluminous igneous rocks will typically melt via the reaction: Bt + Hbl + Qtz + Pl^1 = melt + Pl^2 + Cpx + Opx + Ilm ± Grt (Clemens et al., 2011). The entrainment of a mixture of the peritectic minerals formed during this partial melting reaction could potentially account for the trend displayed by the monzogranites (Fig. 7a). Peritectic minerals entrainment modeling shows that the evolution from a high SiO_2 (> 70 wt.%) to the low SiO_2 sample PONT-22 can be explained by the addition of ~15 wt.% of an assemblage composed of Grt + Cpx + Pl ± Ilm (details on the modeling are provided in Fig. 7 and Supplementary file 5). Peritectic minerals are not expected to be identified in granitic rocks as the small grain size of these crystals will facilitate a reequilibration with the magma during ascent and emplacement. Ferromagnesian minerals such as clinopyroxene can react with a melt to form biotite, and garnet can break down into cordierite or biotite at low pressure (Stevens et al., 2007; Clemens and Stevens, 2012). The anticorrelation between SiO_2 and trace elements such as Zr and La should reflect variable degrees of entrainment of zircon and monazite from the source, respectively (Villaros et al., 2009) (Fig. 7c). However, these accessory minerals likely reequilibrated with the melt as evidenced by the scarcity of inherited zircon grains in the monzogranite. In contrast to the less viscous H_2O rich leucogranites which experienced significant fractional crystallization, we suggest that monzogranites were more affected by a peritectic and accessory phase entrainment due to their higher viscosity and because they likely result from a higher degree of partial melting. Finally, we propose that the monzogranites could have evolved via the combination of peritectic phase entrainment and hybridation with a mantle-derived melt.

9.2. Magma generation model and implication for the tectono-magmatic evolution of the Hercynian Armorican belt

In the previous section, we propose that the leucogranites from the Pontivy-Rostrenen complex represent pure crustal melts which formed by the partial melting of metasediments and peraluminous orthogneisses. The partial melting zone from which the leucogranite melts escaped could be the equivalent of the migmatites from South Brittany (Marchildon and Brown, 2003) which reached peak P-T condition of 0.8 Gpa (~30 km) and 800-850°C (Jones and Brown, 1990). If we consider a thermal gradient of 40°C/km, partial melting could have occurred at a depth of 20 km as previously estimated by Strong and Hanmer (1981). In contrast, the quartz monzodiorite likely formed by the partial melting of a metasomatized lithospheric mantle and experienced variable degree of mixing with crustal derived melts with a possible monzogranitic composition. Metasomatization of the sub-continental lithospheric mantle could have occurred during oceanic then continental subduction below the Armorican microplate until 350 - 370 Ma (Bosse et al., 2005; Ballèvre et al., 2013, 2014) which was synchronous with the emplacement of dolerite dikes in the Central and Northern Domain (Pochon et al., in press). This hypothesis is in agreement with the tomographic images of the mantle which show the presence of a remnant of an oceanic lithosphere steeply dipping to the NE below the Armorican Massif (Gumiaux et al., 2004b). The fact that this slab remained below the Armorican Massif since the Carboniferous suggest that it is still connected laterally to the South Armorican continental crust. Concerning the monzogranites, they are likely derived from the melting of a metaluminous metaigneous source. The initial melts likely sampled variable amount of peritectic minerals from the source and/or were subjected to different degrees of mixing with mantle-derived melts. Partial melting of igneous rocks can result from underplating of mafic magma and hybridation could have occurred during crustal melting and ascent of the two melts (e.g. Huppert and Sparks, 1988; Petford and Gallagher, 2001 and Annen and Sparks, 2002). Rising of the different magmas in the upper crust levels to a depth of ~6 – 8 km (Vigneresse, 1999) was likely promoted by the shearing along the SASZ and second order strike slip faults (Hutton, 1988; D'lemos et al., 1992) (Fig. 1b and 13).

At the scale of the Pontivy-Rostrenen complex and the Armorican Massif, the influence of mantle-derived melts increases from south to north (Capdevila, 2010) (Fig. 1b). A first hypothesis is that mantle melting occurred independently of the latitude below the Armorican Massif but that the thickness of the crust to the south of the SASZ prevented the ascent of mantle-derived magma in the upper crustal levels. However, it would have been unlikely that none mantle-derived magmas reached the upper crust considering their low viscosity when compared to crustal melts. Thus we suggest that mantle melting was mostly restricted to the north of the SASZ. The main geodynamic processes allowing concomitant crustal and mantle melting in late orogenic context are the delamination of a lithospheric mantle root (e.g. Houseman et al., 1981; Molnar and Houseman, 2004), crustal extension or collapse

(e.g. Gapais et al., 1993, 2015; Gardien et al., 1997; Vanderhaeghe and Teyssier, 2001), orocline-driven lithospheric thinning (Gutiérrez-Alonso et al., 2011) and slab breakoff (Davies and von Blanckenburg, 1995; van de Zedde and Wortel, 2001; Janoušek and Holub, 2007). The first process cannot be expected to the north of the SASZ, as it necessitates a thickened continental crust. Also, no significant evidence for an extension exists in the Northern and Central Domain posterior to the doleritic swarn emplacement near 360Ma (Pochon et al., in press), so a process of crustal thinning, occurring for example during a slab retreat (e.g. Vanderhaeghe and Duchêne, 2010; Moyen et al, in press), is precluded. Gutiérrez-Alonso et al. (2011) also proposed that the formation of the Iberian-Armorican Arc around 310-300 Ma (Weil et al., 2010) induced the thinning of the sub-continental lithospheric mantle below the outer arc which resulted in asthenosphere upwelling and lithospheric mantle partial melting. However, this model, which involves the bending of a highly thickened lithosphere in the inner part of the belt, is not in agreement with the evidence of crustal extension in the South Armorican Domain around 310-300 Ma and the absence of a major extension in the Central and Northern Domains (e.g. Gapais et al., 2015). Concerning slab breakoff, this process would have been expected to happen during the early carboniferous time following the end of subduction events at the end of Devonian around 360 Ma ago (Bosse et al., 2005) and hardly explains the main granitic magmatism event recorded in the Armorican Massif from 315 to 300 Ma. On the other hand, Gumiaux et al. (2004a) showed that a pervasive strike slip deformation affected the whole Central Domain during Carboniferous. Gumiaux et al. (2004b) proposed that this lithospheric scale wrenching induce a cutting of the oceanic slab remnant localized below this area by a horizontal shear zone at a depth of around 130 km close to the lithosphere-asthenosphere boundary. This event, by creating an asthenospheric window, potentially induced the upwelling of the asthenospheric mantle below the Central and Northern Armorican Domains resulting in the partial melting of the mantle and the crust (Fig. 13). In parallel, the end of sedimentation in the Chateaulun transpressive basin (Fig. 1) in Lower Namurian time, ca. 320 Ma ago, likely marks the end of transpression regime in the western part of the Central Armorican Domain (Gumiaux et al., 2004a and reference therein) and can indicate a transition toward a transtension regime. Transtension in the western part of the Central Armorican Domain potentially enhanced asthenospheric upwelling as proposed in the Ross Sea region (Antartica; Rocchi et al., 2003) or in the SE Tibetan plateau (Yang et al., 2016) and evidenced by geophysics below the Salton Through in the San Andreas fault zone (Barak et al., 2015; Barak and Klemperer, 2016).

The fact that mantle melting mostly occurred to the north of the SASZ may result from a specific composition of the corresponding sub-continental lithospheric mantle. Overall, the SASZ represents the suture zone between Gondwana and Armorica in this part of the Armorican Massif (Ballèvre et al., 2009, 2013, 2014) indicating that subduction only fertilized the mantle localized below the Central and Northern Domains. Refertilization of the sub-continental lithospheric mantle during oceanic subduction by melt or fluid interactions is commonly evidenced by the study of mantles xenoliths and ophiolites (e.g. Chin et al., 2014; Dokuz et al., 2015; Gordon Medaris Jr. et al., 2015; Uysal et al., 2015). Moreover,

the subduction of crustal materials to the north of the SASZ, could explain why the mantle below the Central and Northern Domains was more favorable to be affected by partial melting than the one below the Southern Domain. To sum up, in the internal part of the belt to the south of the SASZ, crustal magmatism was likely triggered by lithosphere thinning during extensional tectonics whereas to the north of the SASZ in the external parts, thinning of the sub-continental lithospheric mantle during wrenching (transtension) and slab dismembering induced an upwelling of the asthenosphere and the concomitant melting of the crust and a mantle fertilized during earlier subductions events. South-north zonation in the Pontivy-Rostrenen magmatic complex, localized at the transition between these two zones, highlight the role of the SASZ in delimiting lithospheric domains with distinct magmatic systems.

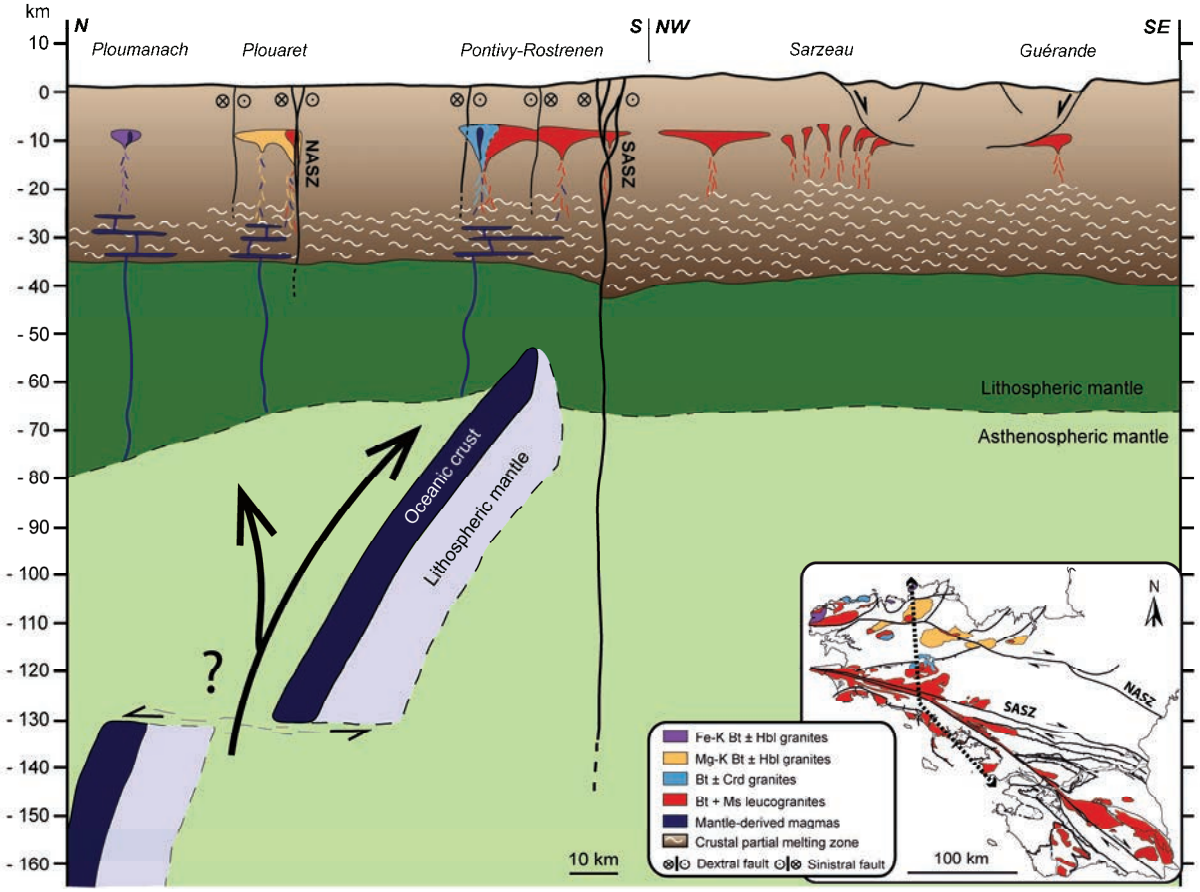

Figure 13: Schematic cross section of the Armorican Massif ca. 315 – 310 Ma ago. The colored tails below the intrusion represent feeding dikes. In the Southern Armorican Domain, lithospheric thinning is triggered by crustal extension whereas to the south of the South Armorican Shear Zone (SASZ), asthenospheric upwelling (black arrows) is promoted by lithospheric wrenching (transtension) and potentially slab dismembering at the lithosphere-asthenosphere boundary. See the text for details.

10. Conclusion

The Pontivy-Rostrenen magmatic complex was emplaced along the SASZ at the transition between a domain in extension to the south and a non-thickened domain submitted to dextral wrenching to the north. The southern part of the intrusion is almost exclusively composed by peraluminous leucogranites whereas moderately peraluminous monzogranites and metaluminous quartz

monzodiorites outcrop in the northern part. This magmatic complex displays compositional spatial evolution which mimics that of Late Carboniferous magmatism in the whole Armorican Massif and suggests the increase of the contribution of mantle-derived melts going northward. The petro-geochemical and geochronological study of the Pontivy-Rostrenen complex leads to the following conclusions:

(1) The major elements and Sr-Nd isotope compositions of bulk rocks, combined with zircon U-Pb ages and Hf isotope data suggest that the leucogranites predominately formed by the partial melting of Neoproterozoic sediments with contribution of Early Paleozoic orthogneisses. In contrast, monzogranites result from partial melting of metaluminous igneous rocks in the lower crust, and the quartz monzodiorites by the partial melting of a metasomatized lithospheric mantle source.

(2) The magmatic evolution of the leucogranites is controlled by fractional crystallization whereas the compositional trend of the monzogranites can be explained either by mixing between a crust and mantle-derived magmas and/or the selective entrainment of peritectic minerals into the crustal melt. In general, monzogranite are more subjected to peritectic mineral entrainment because they are more viscous and likely formed by a higher degree of partial melting than the H_2O rich leucogranites. The magmatic history of the quartz monzodiorite samples is mainly controlled by fractional crystallization as well as hybridation with a crustal derived magma of potential monzogranitic composition.

(3) U-Pb dating of magmatic zircon grains is in agreement with field observations and demonstrate that leucogranites, monzogranites and quartz monzodiorites were synchronously emplaced at ca. 315 Ma. A late leucogranite intrusions (i.e. the Langonnet leucogranite) was emplaced at ca. 305 Ma.

Underplating of metasomatized mantle-derived melts beneath the Pontivy-Rostrenen complex triggered crustal partial melting and hybridation processes between crustal and mantle-derived melts. Shearing along the SASZ additionally promoted magmas ascent in the upper crust. At the scale of the Armorican Massif, crustal melting to the South of the SASZ is triggered by crustal extension whereas the partial melting of the mantle and the crust to the north of the SASZ from ~315 to 300 Ma is potentially due to an asthenosphere upwelling during transtension of the western part of the Central Armorican Domain and dismembering of an oceanic slab remnant. Due to the injection of crustal materials during earlier subduction events until ca. 360 Ma, the mantle below the Central and northern domains was more prone to partial melting than the mantle to the south of the suture zone (i.e. the SASZ in the western part of the Armorican Massif). At a larger scale, this study highlights the role of lithospheric wrenching to trigger crustal and mantle magmatism in an unthickened continental domain. Moreover, earlier subduction of continental material seems to have a primary control on the capacity of melting of the sub-continental lithospheric mantle in a post-collisional context.

Acknowledgment

This study was supported by 2012-2013 NEEDS-CNRS and 2015-CESSUR-INSU (CNRS) research grants attributed to Marc Poujol. Many thanks to Y. Lepagnot, X. Le Coz and D. Vilbert (Geosciences Rennes) for crushing the samples, realizing the thin sections and performing radiogenic isotope analyses (Sm-Nd and Sr), respectively. We are grateful to F. Gouttefangeas (CMEBA – Université de Rennes 1) and J. Langlade (IFREMER, Brest) for technical supports during SEM and EPMA analyses, respectively. This paper benefited from fruitful discussion with A. Villaros and J.P. Brun.

Discussion complémentaire

Dans l'article #3, nous n'avons pas discuté des processus magmatique-hydrothermaux qui ont possiblement prit part à l'évolution des roches magmatiques présentes au sein du complexe de Pontivy-Rostrenen. Tout d'abord, l'abondance des filons de pegmatite et d'aplite au sein des leucogranites est la trace d'une activité magmatique-hydrothermale localisée qui a affecté ces derniers après ou au cours de leur mise en place. Au contraire, cette activité magmatique-hydrothermale était peu marquée pour les monzodiorites quartziques et les monzogranites. En parallèle, les leucogranites ont été soumis à une altération magmatique-hydrothermale diffuse qui se traduit par :

- La formation de greisens dans les facies les plus évolués des leucogranites isotropes et de Langonnet (Euzen, 1993; Bos et al., 1997).
- Le développement de muscovite secondaire dans les facies les plus évolués des leucogranites isotropes (Ms > Bt), soit sous la forme de petits grains néoformés dans la formation ou au dépend de cristaux de muscovite primaire (article #3 : Fig. 5c).
- La chloritisation fréquente de la biotite.
- La décroissance des rapports K/Rb à des valeurs inférieures à 150 caractéristiques de l'évolution pegmatitique-hydrothermale de Shaw (1968) et des valeurs de Nb/Ta < 5 (Fig. III.2a) qui marquent la transition magmatique-hydrothermale (cf. article #1).
- Un fort enrichissement en éléments incompatibles avec une forte affinité pour les fluides orthomagmatiques comme le Cs (~5 à 35 ppm), l'Sn (~5 à 25 ppm) et le W (~1 à 6 ppm) cohérent avec l'association entre le leucogranite de Langonnet et des indices à Sn-W (Marcoux, 1982).
- L'hétérogénéité de la signature isotopique en Sr des leucogranites qui résulte vraisemblablement de la forte mobilité du Rb dans les fluides hydrothermaux.

Au contraire, les échantillons de monzogranite et monzodiorite quartzique se caractérisent par des faibles teneurs en Cs (< 10 ppm), Sn (< 10 ppm) et W (< 1 ppm) ainsi que des rapports K/Rb (> 200) et Nb/Ta (> 10) élevés (Fig. III.2) qui ne suggèrent pas une interaction significative avec des fluides

hydrothermaux. Pour conclure, de nombreux indices font valoir le caractère riche en fluides des leucogranites comparé aux monzogranites et monzodiorites quartziques

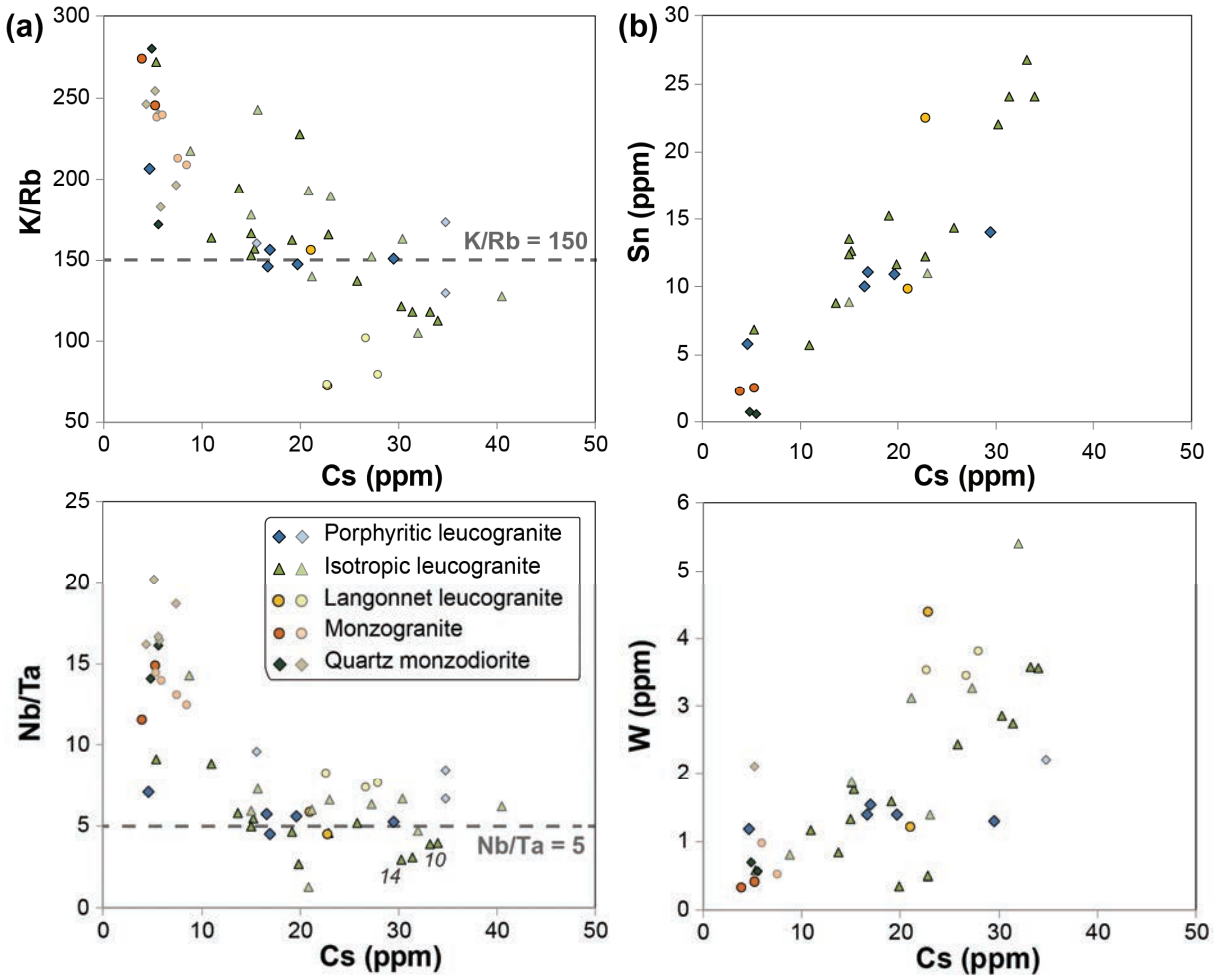

Figure III.2: évolution de (a) rapports géochimiques et de (b) teneurs en éléments incompatibles sensibles à l'intéraction avec des fluides en fonction de la teneur en Cs des échantillons de roches totales du complexe de Pontivy-Rostrenen.

Supplementary Table 1 :

(a) Operating conditions for the LA-ICP-MS equipment

Laboratory & Sample Preparation	
Laboratory name	Géosciences Rennes, UMR CNRS 6118, Rennes, France
Sample type/mineral	Magmatic zircons
Sample preparation	Conventional mineral separation, 1 inch resin mount, 1µm polish to finish
Imaging	CL: RELION CL instrument, Olympus Microscope BX51WI, Leica Color Camera DFC 420C. BSE: JEOL JSM 7100 F (CMEBA, University of Rennes 1)
Laser ablation system	
Make, Model & type	ESI NWR193UC, Excimer
Ablation cell	ESI NWR TwoVol2
Laser wavelength	193 nm
Pulse width	< 5 ns
Fluence	6 – 8.8 J/cm-2
Repetition rate	4 - 5 Hz
Spot size	20 – 30 µm
Sampling mode / pattern	Single spot
Carrier gas	100% He, Ar make-up gas and N_2 (3 ml/mn) combined using in-house smoothing device
Background collection	20 seconds
Ablation duration	60 seconds
Wash-out delay	15 seconds
Cell carrier gas flow (He)	0.75 l/min
ICP-MS Instrument	
Make, Model & type	Agilent 7700x, Q-ICP-MS
Sample introduction	Via conventional tubing
RF power	1350W
Sampler, skimmer cones	Ni
Extraction lenses	X type
Make-up gas flow (Ar)	0.85 l/min
Detection system	Single collector secondary electron multiplier
Data acquisition protocol	Time-resolved analysis
Scanning mode	Peak hopping, one point per peak
Detector mode	Pulse counting, dead time correction applied, and analog mode when signal intensity > ~ 10^6 cps
Masses measured	^{204}(Hg + Pb), ^{206}Pb, ^{207}Pb, ^{208}Pb, ^{232}Th, ^{238}U
Integration time per peak	10-30 ms
Sensitivity / Efficiency	28000 cps/ppm Pb (50µm, 10Hz)
Data Processing	
Gas blank	20 seconds on-peak
Calibration strategy	GJ1 zircon standard used as primary reference material, Plešovice used as secondary reference material (quality control)
Reference Material info	GJ1 (Jackson et al., 2004) Plešovice (Slama et al., 2008: 337.13 ± 0.37 Ma)
Data processing package used	GLITTER ® (van Achterbergh et al., 2001)
Quality control / Validation	Plešovice: concordia age = 336.4 ± 1.2 Ma (N=42; MSWD=0.52; probability=0.3)

(b) Operating conditions for the LA-MC-ICP-MS equipment

Laboratory	
Laboratory name	Institute for Geosciences, Goethe University Frankfurt, Germany
Laser ablation system	
Make, Model & type	ComPexPro 102F, Coherent (Excimer)
Ablation cell	Two-volume ablation cell (Laurin Technic, Australia)
Laser wavelength	193 nm
Pulse width	
Fluence	6 J/cm-2
Repetition rate	5.5 Hz
Spot size	40-50 µm
Sampling mode / pattern	Single spot or line
Carrier gas	0.89 l min^{-1} Ar + "squid" smoothing device directly after ablation cell
Background collection	30 seconds
Ablation duration	40 seconds
Wash-out delay	ca. 30 seconds
Cell carrier gas flow	(0.63 l/min He + 0.006 l/min N_2 sample gas)
ICP-MS Instrument	
Make, Model & type	Thermo-Finnigan NEPTUNE MC ICP-MS
Sample introduction	Via conventional tubing
RF power	1310 W
Sampler, skimmer cones	Ni
Extraction lenses	X-cone
Make-up gas flow (Ar)	0.89 l/min
Detection system	Multi collector, 9 faraday detectors and amplifiers (10^{11} Ω resistors)
Data acquisition protocol	
Scanning mode	
Detector mode	
Masses measured	^{172}Yb, ^{173}Yb, ^{175}Lu, ^{176}Hf-Yb-Lu, ^{177}Hf, ^{178}Hf, ^{179}Hf, ^{180}Hf,^{181}Hf-Ta
Integration time per peak	0.48 sec.
Sensitivity / Efficiency	120 mV/pg Hf
Data Processing	
Gas blank	
Calibration strategy	GJ1 zircon standard used as primary reference material. 91500, Plešovice, Temora 2 used as secondary reference material (quality control)
Reference Material info	Woodhead and Hergt, 2005; Gerdes and Zeh, 2006
Data processing package used	Excel spreadsheet (Gerdes & Zeh, 2006, 2009)
Quality control / Validation	Plešovice: $^{176}Lu/^{177}Hf = 0.00017 \pm 0.00012$, $^{176}Hf/^{177}Hf = 0.282474 \pm 0.000022$ (N=11); 91500: $^{176}Lu/^{177}Hf = 0.00032 \pm 0.00005$, $^{176}Hf/^{177}Hf = 0.282293 \pm 0.000031$ (N=9); Temora 2: $^{176}Lu/^{177}Hf = 0.00126 \pm 0.00035$, $^{176}Hf/^{177}Hf = 0.282674 \pm 0.000041$ (N=7)

Supplementary Table 4a : Average chemical composition of feldspar from the Pontivy-Rostrenen granitoids

		Por. leuc.	*Isotropic leucogranite*				*Lgt leuc.*	*Mzgt*	*Qtz-mzdt*	*Por. leuc.*	*Isotropic leucogranite*				*Mzgt*
		PONT-1	PONT-10	PONT-14	PONT-15	PONT-26	PONT-21	PONT-22	PONT-7	PONT-1	PONT-10	PONT-14	PONT-15	PONT-26	PONT-22
		Plagioclase								K feldspar					
		n=7	n=11	n=5	n=5	n=7	n=11	n=6	n=10	n=3	n=5	n=4	n=6	n=4	n=3
Na_2O	%	10.47	11.36	11.51	10.82	10.78	11.47	8.25	6.50	0.81	0.60	0.82	0.85	0.91	1.02
MgO	%	0.01	0.01	0.00	0.01	0.01	0.01	0.00	0.01	0.01	0.01	0.00	0.00	0.01	0.01
SiO_2	%	66.06	68.02	68.64	67.11	66.73	68.51	61.17	57.50	64.02	63.78	63.54	63.91	63.88	63.96
Al_2O_3	%	21.40	20.22	20.03	20.78	20.56	19.67	24.26	26.80	18.81	18.83	18.96	18.93	18.88	18.71
CaO	%	1.96	0.48	0.12	1.44	1.15	0.05	5.79	8.77	0.01	0.01	0.00	0.02	0.04	0.04
TiO_2	%	0.01	0.02	0.02	0.02	0.01	0.01	0.03	0.02	0.01	0.03	0.03	0.02	0.01	0.05
FeO	%	0.01	0.01	0.02	0.03	0.02	0.01	0.02	0.09	0.01	0.03	0.05	0.02	0.02	0.03
MnO	%	0.01	0.01	0.01	0.00	0.00	0.01	0.00	0.01	0.00	0.00	0.00	0.00	0.00	0.00
P_2O_5	%	0.15	0.10	0.05	0.02	0.02	0.01	0.05	0.01	0.38	0.34	0.58	0.42	0.24	0.06
K_2O	%	0.18	0.11	0.15	0.14	0.08	0.23	0.32	0.22	15.56	15.65	15.02	15.40	15.08	15.28
Total	%	100.26	100.35	100.55	100.36	99.36	99.99	99.90	99.93	99.63	99.27	99.01	99.59	99.08	99.15
Na	Structural formula based on 8oxygen atoms	0.89	0.96	0.97	0.96	0.92	0.97	0.71	0.56	0.07	0.05	0.07	0.07	0.08	0.09
Mg		0.00	0.00	0.00	0.00	0.00	0.00	0.00	0.00	0.00	0.00	0.00	0.00	0.00	0.00
Si		2.89	2.96	2.98	2.97	2.94	2.99	2.72	2.58	2.96	2.96	2.95	2.96	2.97	2.97
Al		1.10	1.04	1.03	1.03	1.07	1.01	1.27	1.42	1.03	1.03	1.04	1.03	1.03	1.03
Ca		0.09	0.02	0.01	0.03	0.05	0.00	0.28	0.42	0.00	0.00	0.00	0.00	0.00	0.00
Ti		0.00	0.00	0.00	0.00	0.00	0.00	0.00	0.00	0.00	0.00	0.00	0.00	0.00	0.00
Fe		0.00	0.00	0.00	0.00	0.00	0.00	0.00	0.00	0.00	0.00	0.00	0.00	0.00	0.00
Mn		0.00	0.00	0.00	0.00	0.00	0.00	0.00	0.00	0.00	0.00	0.00	0.00	0.00	0.00
P		0.01	0.00	0.00	0.00	0.00	0.00	0.00	0.00	0.01	0.01	0.02	0.02	0.01	0.01
K		0.01	0.01	0.01	0.01	0.00	0.01	0.02	0.01	0.92	0.93	0.89	0.91	0.89	0.90
Total		5.00	4.99	4.99	4.99	4.99	4.99	5.00	5.00	5.00	4.99	4.98	5.00	4.99	5.00
% Ab		89.68	97.09	98.58	96.75	94.04	98.42	70.76	56.53	7.34	5.53	7.70	7.44	8.38	8.74
%An		9.29	2.28	0.58	2.68	5.48	0.26	27.46	42.19	0.06	0.04	0.00	0.07	0.22	0.13
%Or		1.03	0.64	0.84	0.56	0.48	1.32	1.78	1.27	92.60	94.44	92.30	92.48	91.40	91.13

Por. leuc.: porphyritic leucogranite; Lgt leuc.: Langonnet leucogranite; Qtz-mzdt: quartz monzodiorite; Mzgt: monzogranite

Supplementary Table 4b : Average chemical composition of biotite from leucogranite and monzogranite samples as well as biotite and amphibole from a monzodiorite quartzique sample.

		Por. leuc.	***Isotropic leucogranite***			***Mzgt***	***Qtz-mzdt***		***Qtz-mzdt***
		PONT-1	**PONT-10**	**PONT-15**	**PONT-26**	**PONT-22**	**PONT-7**		**PONT-7**
		Biotite							**Amphibole**
		n=6	**n= 11**	**n=11**	**n=5**	**n=9**	**n=8**		n=11
Na_2O	**%**	0.11	0.04	0.03	0.09	0.13	0.08		0.52
MgO	**%**	6.36	3.58	5.78	5.87	7.80	9.75		12.16
SiO_2	**%**	34.83	34.74	34.94	34.85	35.14	36.19		50.11
Al_2O_3	**%**	19.35	20.45	19.58	19.59	19.01	14.87		4.81
CaO	**%**	0.01	0.01	0.02	0.04	0.01	0.02		12.28
TiO_2	**%**	3.20	2.47	2.42	2.73	3.79	4.11		0.60
FeO	**%**	20.63	23.31	21.91	21.33	19.74	20.72		16.24
MnO	**%**	0.23	0.28	0.24	0.21	0.18	0.22		0.39
P_2O_5	**%**	0.01	0.05	0.01	0.03	0.02	0.01		0.01
K_2O	**%**	9.68	9.30	9.41	9.63	9.98	9.74		0.43
Total	**%**	94.42	94.23	94.35	94.38	95.80	95.71		97.56
Na	**Structural formula based on 22 oxygen atoms**	0.03	0.01	0.01	0.03	0.04	0.02	**Structural formula based on 23 oxygen atoms**	0.15
Mg		1.47	0.83	1.34	1.36	1.77	2.23		2.68
Si		5.40	5.44	5.44	5.42	5.35	5.56		7.41
Al		3.54	3.78	3.59	3.59	3.41	2.69		0.84
Ca		0.00	0.00	0.00	0.01	0.00	0.00		1.94
Ti		0.37	0.29	0.28	0.32	0.43	0.47		0.07
Fe		2.67	3.05	2.85	2.77	2.51	2.66		2.01
Mn		0.03	0.04	0.03	0.03	0.02	0.03		0.05
P		0.00	0.01	0.00	0.00	0.00	0.00		0.00
K		1.92	1.86	1.87	1.91	1.94	1.91		0.08
Total		15.43	15.31	15.42	15.43	15.49	15.59		15.22
X Mg		0.35	0.21	0.32	0.33	0.41	0.46		

Por. leuc.: porphyritic leucogranite; Qtz-mzdt: quartz monzodiorite; Mzgt: monzogranite

Supplementary Table 4c : Average chemical composition of muscovite from the Pontivy-Rostrenen granites. "small" refers to muscovite inside foliation planes

		Porphyritic leucogranite			***Isotropic leucogranite***												***Langonnet leucogranite***			***Mzgt***
		PONT-1			**PONT-10**			**PONT-14**			**PONT-15**			**PONT-26**			**PONT-21**			**PONT-22**
		core n=12	rim n=8	small n=7	core n=21	rim n=15	small n=8	core n=20	rim n=19	small n=4	core n=19	rim n=12	small n=12	core n=13	rim n=7	small n=9	core n=26	rim n=21	small n=2	n=4
Na_2O	**%**	0.64	0.55	0.56	0.68	0.47	0.33	0.65	0.36	0.38	0.71	0.56	0.49	0.65	0.58	0.46	0.70	0.39	0.75	0.48
MgO	**%**	0.80	0.95	0.88	0.83	0.97	1.27	0.84	1.04	0.98	0.77	0.79	0.99	0.78	0.93	0.87	0.65	0.65	0.40	0.84
SiO_2	**%**	45.72	45.82	45.22	45.87	45.92	45.44	45.79	45.80	45.52	45.87	45.85	45.93	45.54	45.78	48.43	45.65	45.24	45.92	45.77
Al_2O_3	**%**	35.21	34.82	34.42	35.13	34.31	32.48	34.92	33.77	34.11	35.58	35.54	34.89	34.99	34.64	32.73	33.72	31.22	34.75	34.36
CaO	**%**	0.01	0.02	0.02	0.01	0.01	0.62	0.02	0.02	0.01	0.01	0.01	0.02	0.02	0.03	0.04	0.01	0.02	0.01	0.03
TiO_2	**%**	0.76	0.70	0.75	0.70	0.46	0.38	0.48	0.43	0.34	0.71	0.50	0.43	0.72	0.65	0.66	0.39	0.45	0.14	1.88
FeO	**%**	1.06	1.24	1.15	1.40	1.96	2.75	1.63	2.36	2.33	1.19	1.28	1.58	1.23	1.40	1.41	3.03	5.06	2.30	1.05
MnO	**%**	0.00	0.01	0.01	0.01	0.01	0.02	0.01	0.02	0.03	0.00	0.01	0.00	0.01	0.01	0.00	0.02	0.05	0.03	0.01
P_2O_5	**%**	0.05	0.03	0.03	0.05	0.04	0.51	0.04	0.01	0.04	0.05	0.03	0.01	0.03	0.02	0.02	0.04	0.04	0.03	0.00
K_2O	**%**	10.32	10.30	10.16	9.89	10.31	10.20	10.05	10.32	10.47	10.05	10.15	10.19	9.93	9.85	9.64	10.19	10.16	9.97	10.18
Total	**%**	94.57	94.44	93.20	94.58	94.48	94.00	94.44	94.13	94.21	94.93	94.70	94.53	93.89	93.90	94.28	94.42	93.29	94.31	94.60
Na	**Structural data based on 22 oxygen units**	0.17	0.14	0.15	0.18	0.12	0.09	0.17	0.09	0.10	0.18	0.15	0.13	0.17	0.15	0.12	0.18	0.11	0.20	0.12
Mg		0.16	0.19	0.18	0.17	0.20	0.26	0.17	0.21	0.20	0.15	0.16	0.20	0.16	0.19	0.18	0.13	0.13	0.08	0.17
Si		6.12	6.15	6.15	6.14	6.18	6.18	6.15	6.20	6.16	6.11	6.13	6.16	6.14	6.17	6.43	6.19	6.28	6.19	6.13
Al		5.56	5.51	5.51	5.54	5.44	5.21	5.53	5.39	5.45	5.59	5.60	5.52	5.56	5.50	5.19	5.39	5.10	5.52	5.43
Ca		0.00	0.00	0.00	0.00	0.00	0.09	0.00	0.00	0.00	0.00	0.00	0.00	0.00	0.00	0.01	0.00	0.00	0.00	0.00
Ti		0.08	0.07	0.08	0.07	0.05	0.04	0.05	0.04	0.03	0.07	0.05	0.04	0.07	0.07	0.07	0.04	0.05	0.01	0.19
Fe		0.12	0.14	0.13	0.16	0.22	0.31	0.18	0.27	0.26	0.13	0.14	0.18	0.14	0.16	0.16	0.35	0.59	0.26	0.12
Mn		0.00	0.00	0.00	0.00	0.00	0.00	0.00	0.00	0.00	0.00	0.00	0.00	0.00	0.00	0.00	0.00	0.01	0.00	0.00
P		0.01	0.00	0.00	0.01	0.00	0.06	0.00	0.00	0.00	0.01	0.00	0.00	0.00	0.00	0.00	0.00	0.00	0.00	0.00
K		1.76	1.76	1.76	1.69	1.77	1.77	1.72	1.78	1.81	1.71	1.73	1.74	1.71	1.69	1.65	1.76	1.80	1.71	1.74
Total		13.98	13.97	13.97	13.95	13.99	14.01	13.98	14.00	14.03	13.96	13.96	13.97	13.95	13.93	13.79	14.05	14.07	13.99	13.90

Mzgt: monzogranite

Supplementary Table 5 : results of magmatic processes modeling

Peritectic minerals entrainment modeling (monzogranites)

	Parent	**Contaminated sample**			**Entrained peritectic assemblage**				
	Average of high SiO_2 (> 70 wt.%) monzogranite samples	monzogranite sample PONT-22	Computed	Difference	Average	Grt[a]	Cpx[b]	An50	Ilm
SiO_2	70.6	66.1	66.4	-0.3	44.2	38.4	46.3	55.6	0.0
Al_2O_3	15.2	16.3	16.2	0.0	21.5	21.7	8.3	28.3	0.0
Fe_2O_{3t}	2.1	4.2	4.4	-0.2	16.5	31.2	5.8	0.0	47.4
MgO	0.8	1.5	1.4	0.1	4.6	6.5	14.7	0.0	0.0
CaO	1.4	2.2	2.4	-0.2	7.6	2.1	20.5	10.4	0.0
Na_2O	3.6	3.5	3.4	0.1	2.4	0.0	1.3	5.7	0.0
K_2O	4.4	4.4	3.7	0.7	0.0	0.0	0.0	0.0	0.0
TiO_2	0.3	0.7	0.8	-0.1	3.1	0.0	3.2	0.0	52.7

Entrained minerals, wt.%	Grt	43
	Cpx	13
	An50	39
	Ilm	0.05
Amount of entrainment, wt.%	wt.%	16
Sum residual squared, ΣR^2	0.64	

a: peritectic garnet composition from Stevens et al. (2007); b: augite theroretical composition

Magma mixing modeling (monzogranites)

	Parent	**Contaminated sample**			**Contaminant**
	Average of high SiO_2 (> 70 wt.%) monzogranite samples	monzogranite sample PONT-22	Computed	Difference	Average of low SiO_2 (≤ 55 wt.%) quartz monzodiorite samples
SiO_2	70.6	66.1	66.2	-0.1	54.6
Al_2O_3	15.2	16.3	15.9	0.4	17.6
Fe_2O_3	2.1	4.2	3.6	0.7	7.5
MgO	0.8	1.5	1.8	-0.2	4.4
CaO	1.4	2.2	2.9	-0.7	7.0
Na_2O	3.6	3.5	3.4	0.1	2.8
K_2O	4.4	4.4	3.9	0.5	2.6
TiO_2	0.3	0.7	0.6	0.1	1.2

Amount of mixing, wt.%	wt.%	27
Sum residual squared	ΣR^2	1.39

Assimilation - fractional crystallization (AFC) modeling (quartz monzodiorites)

	Parent	**Residual hybrid melt**			**Cumulate**				**Contaminant**
	Average of low SiO_2 (≤ 55 wt.%) quartz monzodiorite samples	Average of high SiO_2 (> 59 wt.%) quartz monzodiorite samples	Computed	Difference	Average	Cpx [a]	An70	Bt [b]	Average of high SiO_2 (> 70 wt.%) monzogranite samples
SiO_2	54.6	59.8	57.0	0.1	48.1	52.5	50.5	36.2	70.6
Al_2O_3	17.6	16.8	16.5	0.5	20.5	0.5	31.7	14.9	15.2
Fe_2O_{3t}	7.5	6.0	7.6	-0.5	7.4	12.9	0.0	20.7	2.1
MgO	4.4	3.1	4.2	-0.4	5.0	12.0	0.0	9.8	0.8
CaO	7.0	5.0	4.6	0.9	13.3	21.8	14.3	0.0	1.4
Na_2O	2.8	3.5	3.1	0.3	1.9	0.2	3.4	0.1	3.6
K_2O	2.6	3.5	2.9	0.3	2.0	0.0	0.0	9.7	4.4
TiO_2	1.2	1.0	1.4	-0.1	0.8	0.1	0.0	4.1	0.3

Segragating minerals, wt.%	Bt	20
	An70	55
	Cpx	25
Amount of mixing/assimilation (A), wt.%	20	
Amount of solid segregate removed, wt.%	27	
Sum residual squared, ΣR^2	1.81	

a : average Cpx composition from quartz monzodiorite samples (Euzen, 1993); b: average Bt composition from PONT-7 quartz-monzodiorite sample

Fractional crystallization modeling (leucogranites)

	Parent	**Residual melt**			**Cumulate**				
	Low SiO_2 PONT-25 isotropic leucogranite sample	High SiO_2 PONT-21 langonnet leucogranite sample	Computed	Difference	Average	An30	Bt[a]	Kfs[a]	Ap
SiO_2	70.4	74.9	74.9	0.0	49.2	60.7	34.9	63.9	0.0
Al_2O_3	15.2	14.5	14.2	0.3	19.8	24.9	19.6	18.9	0.0
Fe_2O_3	2.0	0.8	0.5	0.3	9.1	0.0	21.6	0.0	0.0
MgO	0.8	0.1	0.4	-0.3	2.5	0.0	5.8	0.0	0.0
CaO	0.8	0.4	0.4	0.0	3.0	6.3	0.0	0.0	56.8
Na_2O	3.3	3.8	3.5	0.2	2.0	8.1	0.1	0.9	0.0
K_2O	5.0	4.3	4.1	0.2	9.3	0.0	9.5	15.2	0.0
TiO_2	0.4	0.1	0.2	-0.1	1.1	0.0	2.6	0.0	0.0
P_2O_5	0.3	0.4	0.1	0.3	1.4	0.0	0.0	0.3	43.2

Segregating minerals, wt.%	Kfs	35
	Bt	42
	An30	20
	Ap	3
Amount of solid segregate removed, wt.%	18	
Sum residuals squared ΣR^2	0.49	

a : average Bt and Kfs composition from PONT-15 and PONT-26 isotropic leucogranite samples

Datation U-Pb sur zircon du granite de Huelgoat

Le granite de Huelgoat appartient, comme le granite de Rostrenen, à la suite magnéso-potassique peralumineuse définie par Capdevila (2010) (article #3 : Fig. 1). C'est une intrusion composite formée de 4 faciès principaux (Georget, 1986 ; Castaing, 1988) (Fig. III.3) :

- Le faciès La Feuillée est un granite à gros grain dont la composition varie de celle d'un monzogranite à Bt > Ms à un leucogranite à Ms > Bt.
- Le faciès Le Cloitre est un monzogranite à grains fins à Bt-Ms ± Cd
- Le faciès Huelgoat s.s. est un monzogranite porphyrique à Bt-Cd. Il contient localement des enclaves du facies Le Cloitre.
- Les microdiorites quartziques qui recoupent sous forme de filons d'orientation N130° les facies Le cloitre et Huelgoat s.s. et qu'on retrouve aussi en enclaves dans les 3 facies définies précédemment.

Ces intrusions ont des contacts francs et Georget (1986) a définit la chronologie de mise en place suivante : (1) intrusion de La Feuillée puis (2) intrusion de Huelgoat s.s. et Le Cloitre. Néanmoins, le facies Le Cloitre étant interprété comme une enclave dans le facies Huelgoat s.s., il est considéré comme plus vieux que le facies Huelgoat s.s. et il possiblement antérieur au faciès la Feuillée. Les microdiorites quartziques semblent contemporaines de la mise en place des deux ensembles. La méthode isochrone Rb-Sr sur roches totales réalisée en regroupant les 3 faciès de granites a fourni deux dates comparables de 336 ± 13 (Peucat et al., 1979) et 340 ± 9 Ma (Georget, 1986).

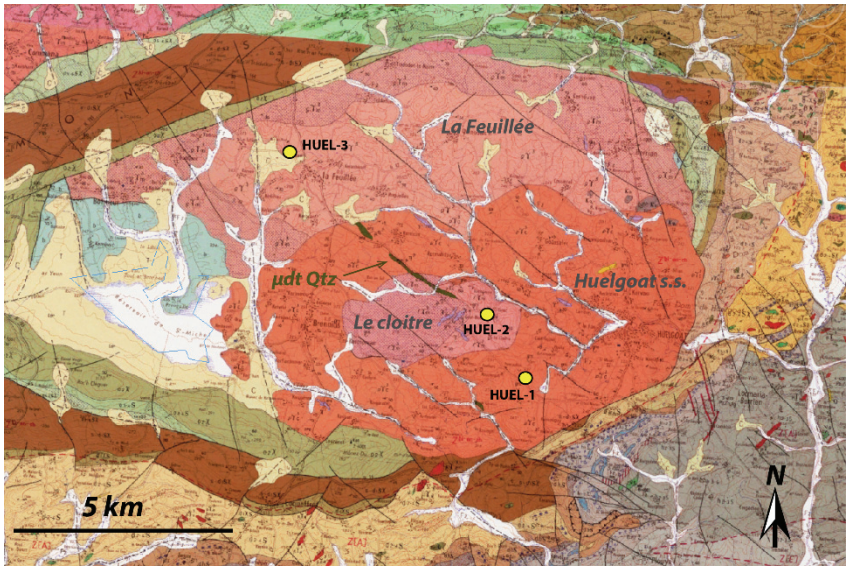

Fig. III.3 : carte géologique du granite de Huelgoat identifiant les 4 facies magmatiques principaux et localisant les échantillons prélevés. D'après la carte 1/50000 BRGM n° 276 de Huelgoat (Castaing, 1988). µdt Qtz = microdiorite quartzique.

HUEL-1 : x = -3.778958 ; y = 48.351317. HUEL-2 : x = -3.793344 ; y = 48.363371. HUEL-3 : - 3.860646 ; y = 48.394754

Dans le cadre de ces travaux de thèse, nous avons réalisé des datations U-Pb sur zircon par LA-ICP-MS d'un échantillon du facies de La Feuillée (HUEL-3) et du Cloitre (HUEL-2). La méthode utilisée est la même que celle décrite dans l'article #3. Un âge concordia de 337.6 ± 2.6 Ma (MSWD = 0.99 ; n = 8) obtenu sur le zircon Plešovice (Slama et al., 2008 ; 337.13 ± 0.37 Ma) utilisé comme

standard externe au cours de la session analytique permet de valider la justesse des résultats. Les résultats finaux des analyses avec un degré de concordance entre 90 et 110 % sont fournis en annexe de ce manuscrit avec une incertitude de 1σ mais les âges sont calculés avec une incertitude de 2σ.

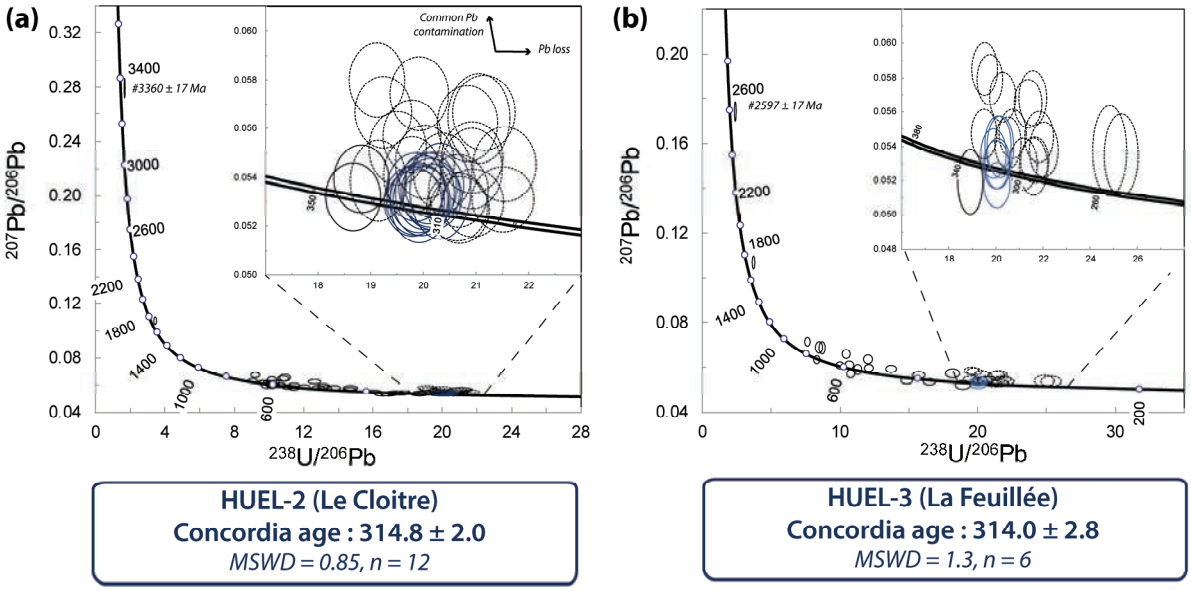

Fig. III.4 : Diagrammes Terra-Wasserburg reportant les analyses U-Pb réalisées sur les grains de zircon des échantillons HUEL-2 (Le Cloitre) et HUEL-3 (La Feuillée). Les ellipses en bleues sont utilisées pour le calcul des âges concordia alors que les ellipses en pointillés sont interprétées comme le reflet de pertes en Pb, d'une contamination en Pb commun ou d'un mélange complexe entre les deux. Les ellipses en traits pleins noirs sont interprétées comme liées à de l'héritage. # : date $^{207}Pb/^{206}Pb$ à 1 σ. Les ellipses sont reportées à 2σ.

Les deux échantillons ont fourni un nombre important de grains de zircon qui se caractérisent généralement par la présence d'un cœur et de bordures zonées en cathodoluminescence. Pour l'échantillon HUEL-2, un total de 90 analyses sur 70 grains ont été réalisées et 70 de ces analyses ont un degré de concordance entre 90 et 110 % (Fig. III.4a). Les dates $^{207}Pb/^{206}Pb$ varient entre 3360 ± 17 et 315 ± 24 Ma et un groupe de 12 analyses (ellipses bleues) en positions concordantes à sub-concordantes permet de calculer une date concordia de 314.8 ± 2.0 Ma (MSWD = 0.85) qui est interprétée comme l'âge de cristallisation de cette échantillon. Les analyses en pointillés sur le diagramme Terra-Wasserburg sont vraisemblablement le reflet de pertes en Pb et/ou d'une contamination en Pb commun. Les ellipses en traits pleins noirs sont interprétées comme liées à de l'héritage. Pour l'échantillon HUEL-3 (La Feuillée), 71 analyses ont été réalisées à partir de 48 grains et 41 de ces analyses ont un degré de concordance entre 90 et 110 %. Les dates $^{207}Pb/^{206}Pb$ varient entre 2597 ± 17 et 322 ± 29 Ma et un groupe de 6 analyses en positions concordantes à sub-concordantes (ellipses bleues) permet de calculer une date concordia de 314.0 ± 2.8 Ma (MSWD = 1.3) identique dans l'erreur à celle obtenue sur l'échantillon HUEL-2 et interprétée comme l'âge de cristallisation de cette échantillon. Comme précédemment, les ellipses en pointillés sont interprétées comme le reflet de perte en Pb et/ou d'une contamination en Pb commun alors que les ellipses en traits pleins noirs sont liées à de l'héritage.

Les âges hérités archéens à paléozoïques obtenus sur les deux échantillons sont en accord avec leur nature peralumineuse et la source métasédimentaire proposée par Georget (1986) pour l'intrusion granitique de Huelgoat. Comme observé pour les leucogranites Carbonifères du Massif Armoricain (e.g. Tartèse et al., 2011a, 2011b, cf. article #3), les âges de mise en place obtenus par U-Pb sur zircon sur l'intrusion de Huelgoat à ca. 315 Ma sont plus jeunes que ceux obtenus précédemment par la méthode isochrone Rb-Sr sur roches totales à 336 ± 13 (Peucat et al., 1979) et 340 ± 9 Ma (Georget, 1986). Le fait d'avoir des dates isochrones Rb-Sr plus vieilles que les dates U-Pb sur zircon est surprenant mais cela confirme l'utilité de redater ces intrusions avec une méthode de géochronologie moderne.

A l'échelle de l'intrusion, ces deux âges de mise en place à ca. 315 Ma donnent l'âge maximum du magmatisme dans la région de Huelgoat. Néanmoins, les microdiorites quartziques étant en enclave dans les 3 facies granitiques et recoupant aussi sous forme de filons le facies granitique le plus jeune (Huelgoat s.s.), il est fort probable que les 4 facies qui forment l'intrusion se soient tous mis en place à ca. 315 Ma. Il pourrait être toutefois utile de dater aussi le facies Huelgoat s.s. et le facies microdioritique par U-Pb sur zircon pour vérifier cette hypothèse. A l'échelle régionale, cette âge de mise en place à ca. 315 Ma est comparable à ceux obtenus sur les leucogranites mis en place le long du CSA comme Questembert (tartèse et al., 2011b), Lizio (Tartèse et al., 2011a) et Pontivy (cf. aticle #3) ainsi que le monzogranite de Rostrenen (cf. article #3). Comme pour le complexe de Pontivy-Rostrenen, l'association spatiale et temporelle entre monzogranites à cordiérite et facies mafiques est compatible avec un modèle de fusion crustale par sous plaquage de magmas mantelliques durant une remonté asthénosphérique induite par la déformation en décrochement du domaine centre armoricain.

Partie IV : Le cycle de l’uranium dans le Massif armoricain - de la source des leucogranites aux gisements

Préambule

Dans la chaîne hercynienne européenne la majorité des gisements d'uranium (U) est spatialement associée à des leucogranites peralumineux d'âge tardi-carbonifère. Le modèle le plus admis concernant la genèse de ces minéralisations et que l'U est issu du lessivage par des fluides météoriques des oxydes d'uranium présents dans les leucogranites environnants. Il existe néanmoins peu d'étude récentes sur ces gisements. Ainsi, les processus qui contrôlent la richesse en U de ces intrusions, le transport de l'U par les fluides hydrothermaux et sa précipitation dans des pièges restent mal compris.

Avec environ 20000 t d'U extraits (~20% de la production historique française), le Massif armoricain représente une des province minière majeure de la chaîne hercynienne européenne pour l'uranium et la majorité des gisements est spatialement associée aux leucogranites de Mortagne, Pontivy et Guérande. Dans la partie III, il a été discuté du contexte géodynamique de mise en place ainsi que de l'histoire magmatique et magmatique-hydrothermale du leucogranite de Guérande et du complexe de Pontivy-Rostrenen. Ce chapitre a permis de poser les bases pour pouvoir comprendre le paysage métallogénique dans lequel s'est formée la minéralisation uranifère associée aux leucogranites du Massif armoricain.

La partie IV a pour but de comprendre et de contraindre dans le temps le cycle de l'uranium à l'échelle du Massif armoricain depuis la source des leucogranites minéralisés jusqu'à leur lessivage par des fluides et la précipitation de l'uranium dans les gisements. Le chapitre 1 est consacré à l'étude de la métallogénie de l'uranium dans les districts de Guérande et de Pontivy-Rostrenen. L'étude du leucogranite de Guérande et de ses gisements d'uranium associés a fait l'objet d'une publication (Article #4) dans le journal Ore Geology Reviews et les travaux sur le complexe de Pontivy sont présentés sous la forme d'un article (#5) en préparation pour la revue Mineralium Deposita. Ces travaux ont fait appel à plusieurs méthodes comme la datation U-Pb de l'apatite et des oxydes d'uranium, les traces de fissions sur apatite, l'isotopie de l'oxygène, les analyses d'inclusions fluides, la géochimie en éléments majeurs et traces de minéraux et de roches totales ainsi que l'utilisation de données de radiométrie spectrale aéroportée. Le chapitre 2 a pour but de préciser la ou les source(s) des leucogranites fertiles en uranium du Massif armoricain. Ce chapitre se base sur la comparaison des données isotopiques en U-Pb et Hf obtenues sur les cœurs hérités de zircon des leucogranites avec celles obtenues sur des grains magmatiques d'orthogneisses paléozoïques et des grains détritiques des formations sédimentaires protérozoïques à paléozoïques du Massif armoricain.

Chapitre 1 : Modèle de genèse des gisements d'uranium hydrothermaux associés aux leucogranites peralumineux du Massif armoricain

Résumé de l'article #4 : Comportement magmatique et hydrothermal de l'uranium dans les leucogranites syntectoniques : la minéralisation en uranium associée au granite hercynien de Guérande (Massif armoricain, France)

La majorité des gisements d'uranium (U) de la chaîne hercynienne européenne est spatialement associée à des leucogranites peralumineux carbonifères. Dans la partie sud du Massif armoricain (partie française de la chaîne hercynienne européenne), le leucogranite peralumineux de Guérande, qui s'est mis en place dans une zone de déformation extensive à ca. 310 Ma, est spatialement associé à plusieurs gisements et indices d'U. La zone apicale de l'intrusion est située structuralement en dessous du gisement d'U de Pen Ar Ran, un gisement filonien périgranitique où la minéralisation est localisée au contact entre des schistes noirs et des métavolcanites ordoviciennes. Dans le gisement intragranitique de la Métairie-Neuve, les minéralisations filoniennes sont sécantes au leucogranite à une enclave métasédimentaire.

Les données radiométriques aéroportées et les analyses en éléments traces sur roches totales publiées sur le leucogranite de Guérande suggèrent un lessivage de l'U à l'apex de l'intrusion. L'enrichissement primaire en U au niveau de la zone apicale du leucogranite est vraisemblablement lié à la cristallisation fractionnée et à l'interaction avec des fluides orthomagmatiques. Les faibles rapports Th/U (< 2) mesurés sur le leucogranite de Guérande ont probablement favorisé la cristallisation d'oxydes d'uranium magmatiques. La composition isotopique en oxygène du leucogranite de Guérande ($\delta^{18}O_{\text{roche totale}}$ = 9.7-11.6‰ pour les échantillons déformés et $\delta^{18}O_{\text{roche totale}}$ = 12.2-13.6‰ pour les autres échantillons) indique que les échantillons déformés de la zone apicale ont été soumis à une altération hydrothermale sub-solidus en profondeur avec des fluides oxydants d'origine météorique. Les analyses des inclusions fluides d'un peigne de quartz issu d'une veine à quartz-oxydes d'uranium du gisement de Pen Ar Ran indiquent la contribution d'un fluide peu salé (1-6 wt.% NaCl eq.) en accord avec la contribution d'un fluide météorique. La température de piégeage des fluides dans la gamme 250-350°C suggère un gradient géothermique élevé, probablement lié à l'extension régionale et à un magmatisme tardif dans l'environnement du gisement au moment de sa formation. La datation U-Pb des oxydes d'uranium du gisement de Pen Ar Ran et de la Métairie-Neuve révèle trois événement minéralisateurs. Le premier événement à 296.6 ± 2.6 Ma (Pen Ar Ran) est sub-synchrone de circulations hydrothermales et de la mise en place de filons leucogranitiques dans le massif de Guérande. Les deux derniers événements minéralisateurs se sont produits, respectivement, à 286 ± 1.0 Ma (Métairie-Neuve) et 274.6 ± 0.9 Ma (Pen Ar Ran). L'imagerie en électrons rétrodiffusés combinée à la chimie des éléments majeurs

et des éléments de terres rares des oxydes d'uranium indiquent des conditions minéralisatrices similaires lors des deux événements à Pen Ar Ran à ca. 300 et 275 Ma. Les analyses traces de fission sur apatites révèlent que le leucogranite de Guérande était en profondeur et à une température au-dessus de 120°C quand ces évènements minéralisateurs se sont produits.

En nous basant sur ces nouvelles données, nous proposons que le leucogranite de Guérande est la source principale pour l'U des gisements de Pen Ar Ran et de la Métairie-Neuve. L'altération sub-solidus avec des fluides oxydants peu salés dérivés de la surface a induit le lessivage des oxydes d'uranium de la zone apicale du leucogranite. L'uranium lessivé a ensuite précipité dans l'environnement réducteur représenté par des schistes noirs et des quartzites graphiteux. De tels événements minéralisateurs impliquant l'infiltration en profondeur de fluides dérivés de la surface se sont répétés vraisemblablement plusieurs fois dans la région jusqu'à 275 Ma. Les âges des minéralisations (300 – 275 Ma) dans le district de Guérande sont similaires à ceux obtenus sur la majorité des gisements d'U de la chaîne hercynienne européenne. Cela suggère des conditions minéralisatrices similaires dans l'ensemble de la chaîne avec des circulations de fluides météoriques d'échelle crustale à long termes capables de lessivés l'U des leucogranites peralumineux fertiles au moment de l'extension tardi-carbonifère à permienne.

Ore Geology Reviews 80 (2017) 309–331

Contents lists available at ScienceDirect

Ore Geology Reviews

journal homepage: www.elsevier.com/locate/oregeorev

Magmatic and hydrothermal behavior of uranium in syntectonic leucogranites: The uranium mineralization associated with the Hercynian Guérande granite (Armorican Massif, France)

C. Ballouard [a,*], M. Poujol [a], P. Boulvais [a], J. Mercadier [b], R. Tartèse [c,d], T. Venneman [e], E. Deloule [f], M. Jolivet [a], I. Kéré [a], M. Cathelineau [b], M. Cuney [b]

[a] UMR CNRS 6118, Géosciences Rennes, OSUR, Université Rennes 1, 35042 Rennes Cedex, France
[b] Université de Lorraine, CNRS, CREGU, GeoRessources, Boulevard des Aiguillettes, BP 70239, 54506 Vandoeuvre-lès-Nancy, France
[c] Institut de Minéralogie, de Physique des Matériaux et de Cosmochimie, Muséum National d'Histoire Naturelle, Sorbonne Universités, CNRS, UPMC & IRD, 75005 Paris, France
[d] Department of Physical Sciences, The Open University, Walton Hall, Milton Keynes MK7 6AA, United Kingdom
[e] Institute of Earth Surface Dynamics, Géopolis, University of Lausanne, CH-1015 Lausanne, Switzerland
[f] CRPG, UMR 7358 CNRS-Université de Lorraine, BP20, 54501 Vandœuvre Cedex, France

ARTICLE INFO

Available online 03 July 2016

Keywords:
Hercynian
Peraluminous leucogranites
Sub-solidus alteration
Uranium deposit

ABSTRACT

Most of the hydrothermal uranium (U) deposits from the European Hercynian belt (EHB) are spatially associated with Carboniferous peraluminous leucogranites. In the southern part of the Armorican Massif (French part of the EHB), the Guérande peraluminous leucogranite was emplaced in an extensional deformation zone at ca. 310 Ma and is spatially associated with several U deposits and occurrences. The apical zone of the intrusion is structurally located below the Pen Ar Ran U deposit, a perigranitic vein-type deposit where mineralization occurs at the contact between black shales and Ordovician acid metavolcanics. In the Métairie-Neuve intragranitic deposit, uranium oxide-quartz veins crosscut the granite and a metasedimentary enclave.

Airborne radiometric data and published trace element analyses on the Guérande leucogranite suggest significant uranium leaching at the apical zone of the intrusion. The primary U enrichment in the apical zone of the granite likely occurred during both fractional crystallization and the interaction with magmatic fluids. The low Th/U values (<2) measured on the Guérande leucogranite likely favored the crystallization of magmatic uranium oxides. The oxygen isotope compositions of the Guérande leucogranite ($\delta^{18}O_{whole\ rock}$ = 9.7–11.6‰ for deformed samples and $\delta^{18}O_{whole\ rock}$ = 12.2–13.6‰ for other samples) indicate that the deformed facies of the apical zone underwent sub-solidus alteration at depth with oxidizing meteoric fluids. Fluid inclusion analyses on a quartz comb from a uranium oxide-quartz vein of the Pen Ar Ran deposit show evidence of low-salinity fluids (1–6 wt.% NaCl eq.), in good agreement with the contribution of meteoric fluids. Fluid trapping temperatures in the range of 250–350 °C suggest an elevated geothermal gradient, probably related to regional extension and the occurrence of magmatic activity in the environment close to the deposit at the time of its formation. U-Pb dating on uranium oxides from the Pen Ar Ran and Métairie-Neuve deposits reveals three different mineralizing events. The first event at 296.6 ± 2.6 Ma (Pen Ar Ran) is sub-synchronous with hydrothermal circulations and the emplacement of late leucogranitic dykes in the Guérande leucogranite. The two last mineralizing events occur at 286.6 ± 1.0 Ma (Métairie-Neuve) and 274.6 ± 0.9 Ma (Pen Ar Ran), respectively. Backscattered uranium oxide imaging combined with major elements and REE geochemistry suggest similar conditions of mineralization during the two Pen Ar Ran mineralizing events at ca. 300 Ma and ca. 275 Ma, arguing for different hydrothermal circulation phases in the granite and deposits. Apatite fission track dating reveals that the Guérande granite was still at depth and above 120 °C when these mineralizing events occurred, in agreement with the results obtained on fluid inclusions at Pen Ar Ran.

Based on this comprehensive data set, we propose that the Guérande leucogranite is the main source for uranium in the Pen Ar Ran and Métairie-Neuve deposits. Sub-solidus alteration via surface-derived low-salinity oxidizing fluids likely promoted uranium leaching from magmatic uranium oxides within the leucogranite. The leached out uranium may then have been precipitated in the reducing environment represented by the surrounding black shales or graphitic quartzites. As similar mineralizing events occurred subsequently until ca. 275 Ma, meteoric oxidizing fluids likely percolated during the time when the Guérande leucogranite was still at depth. The age of the U mineralizing events in the Guérande region (300–275 Ma) is consistent with that obtained on other U deposits in the EHB and could suggest a similar mineralization condition, with long-term upper to middle crustal infiltration of meteoric fluids likely to have mobilized U from fertile peraluminous leucogranites during the Late Carboniferous to Permian crustal extension events.

* Corresponding author.
E-mail address: christophe.ballouard@univ-rennes1.fr (C. Ballouard).

http://dx.doi.org/10.1016/j.oregeorev.2016.06.034
0169-1368/

1. Introduction

Uranium (U) deposits resulting solely from magmatic processes such as partial melting or fractional crystallization are rare (IAEA, 2012). In most cases, U is initially mobilized from igneous rocks by hydrothermal and/or surficial fluids (e.g., Cuney, 2014). However, the U fertility of igneous rocks not only depends on their total U content but also on the capacity of the igneous U-bearing phases they host to be dissolved by the fluids. In peralkaline or high K calc-alkaline granites, most of the uranium is hosted in refractory minerals such as zircon, monazite and/or uranothorite, and, therefore, not easily leachable by fluids. In contrast, in peraluminous leucogranites, uranium is mainly hosted as uranium oxides and, as such, represent an ideal source for the formation of U deposits (e.g., Cuney, 2014) as uranium oxide is an extremely unstable mineral and consequently easily leachable during oxidizing fluid circulations.

In the European Hercynian belt (EHB), a large proportion of the uraniferous deposits is spatially associated with Late-Carboniferous peraluminous leucogranites or, less frequently, monzogranites. The vein-type, episyenite-type, breccia-hosted or shear zone-hosted U deposits related to these granites can be either intra- or perigranitic. This spatial relationship can be observed in the Iberian Massif (e.g. Pérez del Villar and Moro, 1991), in the French part of the EHB (Armorican Massif and Massif Central; Cathelineau et al., 1990; Cuney et al., 1990), in the Black Forest (e.g. Hofmann and Eikenberg, 1991) and in the Bohemian Massif (e.g. Dill, 1983; Barsukov et al., 2006; Velichkin and Vlasov, 2011; Dolníček et al., 2013). In the Bohemian Massif, Black Forest, Massif Central and Armorican Massif, most of the U mineralization was emplaced between 300 and 260 Ma (e.g. Wendt et al., 1979; Carl et al., 1983; Eikenberg, 1988; Cathelineau et al., 1990; Hofmann and Eikenberg, 1991; Kříbek et al., 2009; Velichkin and Vlasov, 2011 and references therein). Regarding the genesis of these deposits, Turpin et al. (1990) proposed that in the Massif Central, the U deposition resulted from the mixing of two types of fluids: an oxidizing surface-derived aqueous fluid able to leach U from uranium oxides in the leucogranites and a reduced fluid with an inferred sedimentary origin. Similarly, meteoric and basin derived fluids were involved during the genesis of the shear zone-hosted U mineralization of Okrouhlá Radouň and Rožná in the Bohemian Massif (Kříbek et al., 2009; Dolníček et al., 2013) and their mixing likely promoted the precipitation of the U leached out from the basement. For the Schlema and Schneebergs vein-type deposits (Bohemian Massif), Barsukov et al. (2006) showed that the U ore originated from the leaching of the cupola of the Aue syeno-monzo-granite during the interaction with oxidizing hydrothermal fluids and that the reducing nature of the metasedimentary host rocks promoted the precipitation of U. In the western edge of the Bohemian Massif, the age of vein type deposits at ca. 295 Ma (Carl et al., 1983; Dill, 2015 and reference therein) is synchronous with the emplacement of intragranitic uranium oxides bearing pegmatites in the Hagendorf-Pleystein province from 302.8 ± 1.9 Ma to 299 0.6 ± 1.9 Ma (Dill, 2015). On the other hand, for the U vein-type deposits spatially associated with the Falkenberg monzogranite, Dill (1983) suggested that monzogranite was the major heat source for the U deposition but that the U mostly originated from the proterozoic black shales and phosphorites hosting the mineralization. For the Krunkelbach intragranitic uranium deposit in the Black Forest, the vein type mineralization mainly formed at 297 ± 7 Ma (Hofmann and Eikenberg, 1991). However, this deposit displays a complex history as a first uranium mineralizing event is dated at 310 ± 3 Ma (Wendt et al., 1979) and fluid circulations episodes likely occurred in the deposit during the Mesozoic and Paleogene times (Hofmann and Eikenberg, 1991). These authors suggest that uranium probably derived from the leaching of magmatic uranium oxides present in the host leucogranite by near surface oxidizing ground waters. The uranium was then precipitated either because of mixing with hot reducing fluids of sedimentary or metamorphic origin or because of a reaction with a previously deposited reduced ore assemblage. In the Iberian Massif, a Permian age has been proposed for the Saguazal breccia-hosted intragranitic U deposit (Pérez del Villar and Moro, 1991), and these authors suggested that the U was leached out from the host leucogranite. In contrast, for the Fé breccia-hosted deposit, it has been argued that U was mobilized from the Upper-Proterozoic host metasediments in response to hydrothermal circulations involving meteoric fluids during the Eocene due to Alpine tectonics (Both et al., 1994). Therefore, in the EHB alone, numerous metallogenic models have been proposed for the genesis of U mineralization. For some deposits however, several questions remain unanswered regarding the source(s) of the U but also the timing of the mineralization, the nature of the fluid(s) involved and the conditions for the U precipitation.

This is the case in the French Armorican Massif (western part of the EHB), where most of the uranium deposits are associated with the peraluminous leucogranites from Mortagne, Pontivy and Guérande (Fig. 1). The Guérande leucogranite was emplaced in an extensional deformation zone at ca. 310 Ma (Gapais et al., 1993, 2015; Ballouard et al., 2015). This leucogranite is associated with several U deposits and occurrences, the most important one being the Pen Ar Ran deposit (Figs. 2 and 3), a perigranitic vein-type deposit structurally located above the apical zone of the Guérande intrusion (Ballouard et al., 2015). In the Pen Ar Ran deposit, the U mineralization is found at the contact between Ordovician felsic metavolcanics and black shales (Cathelineau, 1981). Other U occurrences and deposits are known in the area, in particular in Métairie-Neuve, where uranium oxide-bearing quartz veins crosscut both the Guérande leucogranite and the metasedimentary rocks. One of the questions still debated is the origin of the U found in the Pen Ar Ran deposit and other minor occurrences. Bonhoure et al. (2007) proposed that the metavolcanic country rocks were the source for the U, based on the peculiar REE concentrations measured in the UO_2 oxides. However, another possibility is that at least some of the U was leached out from the Guérande leucogranite itself, which potentially represents a major source of available uranium because of the known existence of magmatic uranium oxides (Ouddou, 1984).

This contribution follows the study of Ballouard et al. (2015) in which the tectonic, magmatic and hydrothermal framework for the Guérande leucogranite was presented. Here we provide a comprehensive set of radiometric data, oxygen isotope and fluid inclusion analyses, together with apatite fission track thermochronology, mineralogical, geochemical and geochronological data in an attempt to answer the following questions:

(1) What was the main source of U (i.e. the metamorphic country rocks or the Guérande leucogranite) for the Pen Ar Ran and associated uranium deposits?
(2) What were the processes (magmatic or hydrothermal) responsible for the U pre-enrichment of this source?
(3) What was the nature of the fluid(s) involved in the uranium mobilization, the geological conditions that prevailed during this mobilization (i.e. thermal and tectonic) and the uranium precipitation condition (i.e. lithological or fluid-controlled)?
(4) What was the precise timing for these events and how do they fit with the geodynamical framework of this part of the EHB?

2. Geological framework

The aim of this section is to present the state-of-the-art geology of the South Armorican Massif in general, and the Guérande leucogranite vicinity in particular, which is relevant for the

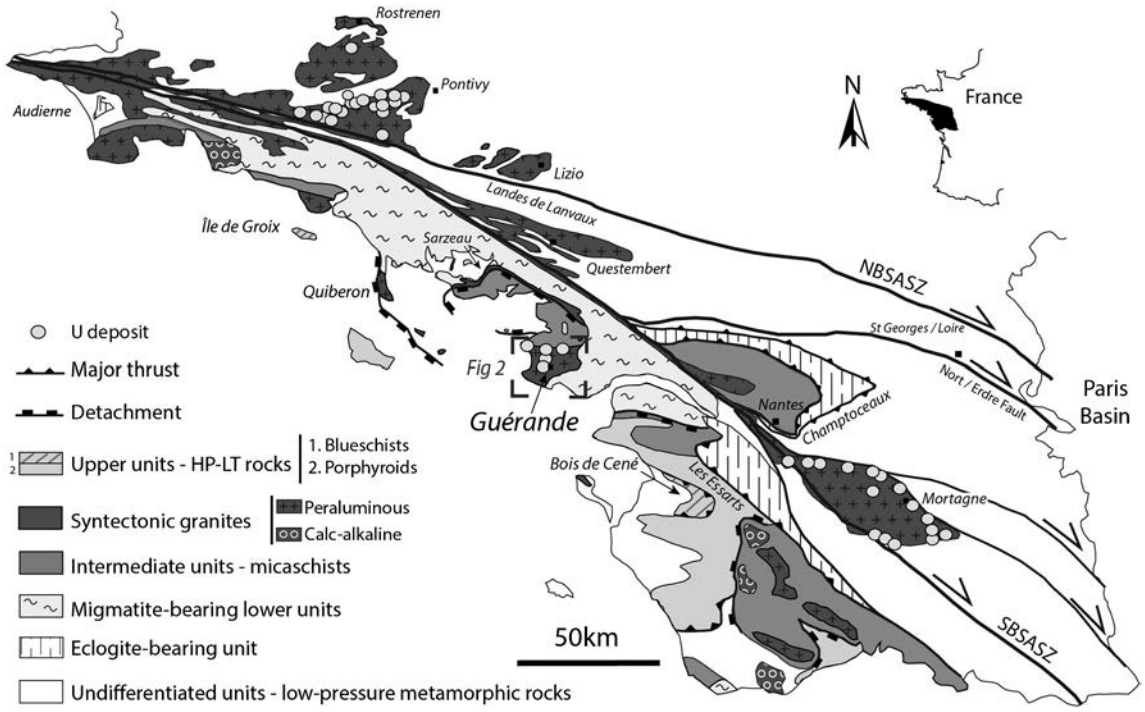

Fig. 1. Structural map of the southern part of the Armorican Massif showing the localization of the uranium deposits and carboniferous peraluminous granites. Modified from Ballouard et al. (2015). SBSASZ: southern branch of the South Armorican Shear Zone. NBSASZ: northern branch of the South Armorican Shear Zone.

understanding and study of the Pen Ar Ran and associated uranium deposits.

2.1. The South Armorican Massif

The southern part of the Armorican Massif belongs to the internal zone of the Hercynian belt in Western Europe and results from the collision of the Gondwana supercontinent with the Armorica microplate (Ballèvre et al., 2009). The South Armorican Massif is bounded to the north by the South Armorican Shear Zone (SASZ) (Fig. 1), a lithospheric-scale dextral strike-slip fault zone (Gumiaux et al., 2004) divided into two branches. North of the SASZ, the terranes belong to the Armorica microplate whereas two major suture zones have been identified in the South Armorican Domain. The first one, marked by

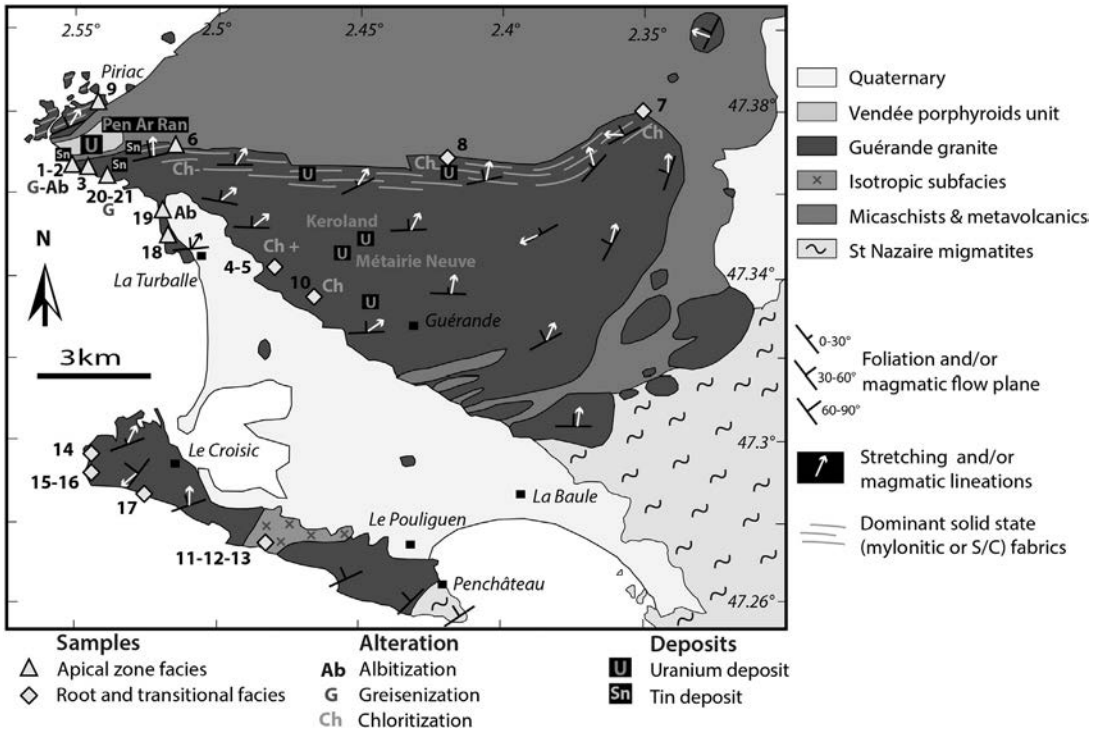

Fig. 2. Geological and structural map of the Guérande granite modified after Ballouard et al. (2015). The localization of the studied samples and U deposits and Sn showings, together with the alteration types, are also reported.

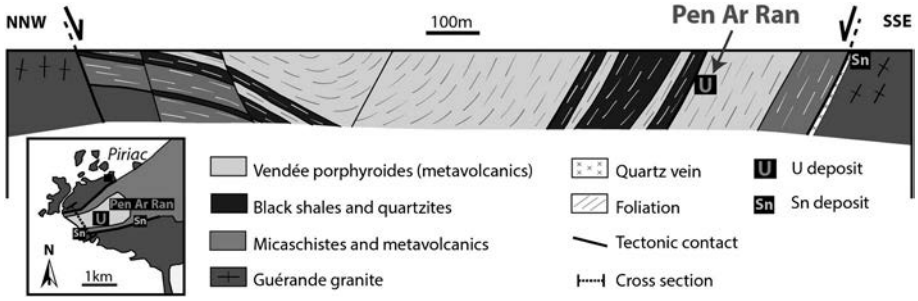

Fig. 3. Simplified cross-section of the extensional graben ("Piriac graben") affecting the apical zone of the Guérande granite, with a projection of the Pen Ar Ran U deposit and Sn showing. The cross-section is localized on the map.

the eclogites of Les Essarts and Audierne, separates terranes with a Gondwanian affinity to the south (lower allochton and parautochton) from the terranes belonging to the Moldanubian zone to the north (upper allochton). The second suture zone, materialized by the Nort-sur-Erdre fault, the Champtoceaux eclogites and the southern branch of the SASZ, separates the upper allochton terranes from the Lanvaux-Saint Georges sur Loire unit, which is interpreted as a Devonian back arc basin (Ballèvre et al., 2009) (Fig. 1). From the bottom to the top, three main groups of tectono-metamorphic units can be distinguished in the South Armorican Domain (e.g. Gapais et al., 1993, 2015) (Fig. 1):

(1) Lower units constituted of migmatites, gneisses and granitoids related to high grade metamorphism reaching P-T conditions of 0.8 GPa and 700–750 °C (Jones and Brown, 1990)
(2) Intermediate units mostly composed of micaschists affected by a Barrovian metamorphism from greenschist to amphibolite facies conditions (Bossière, 1988; Triboulet and Audren, 1988)
(3) Upper units related to the HP-LT metamorphism represented at the base of the pile by the Vendée porphyroid Formation, made of Ordovician felsic metavolcanics (Ballèvre et al., 2012) and black shales, and, at the top of the pile, by the blueschist klippes of Groix Island and Bois-de-Cené. The porphyroid and blueschist formations reached peak P-T conditions of 0.8 GPa, 350–400 °C (Le Hébel et al., 2002) and 1.4–1.8 GPa, 500–550 °C (Bosse et al., 2002), respectively. The subduction and exhumation of these units are related to early tectonic events that occurred between 370 and 350 Ma (Le Hébel, 2002; Bosse et al., 2005).

The Barrovian metamorphism affecting the lower and intermediate units occurred during the continental collision and was followed by a major episode of extension which induced the exhumation of migmatite domes between 310 and 300 Ma (Gapais et al., 1993, 2015; Burg et al., 1994; Brown and Dallmeyer, 1996; Cagnard et al., 2004). During this episode of crustal thinning, several sheets of syntectonic leucogranites such as Quiberon, Sarzeau and Guérande (Fig. 1) were emplaced in the micaschists and below the porphyroid unit, which represented the upper brittle crust during the Upper Carboniferous (Gapais et al., 1993, 2015; Turrillot et al., 2009; Ballouard et al., 2015).

Numerous syntectonic leucogranites were also emplaced along the SASZ (Berthé et al., 1979) (Fig. 1). Among them, the Lizio and Questembert granites, which were dated at 316 ± 6 Ma (Tartèse et al., 2011a) and 316 ± 3 Ma (Tartèse et al., 2011b), respectively, formed through the partial melting of metasediments (Tartèse and Boulvais, 2010). Some giant quartz veins are also associated with the SASZ. Isotopic and fluid inclusion studies revealed that the quartz originated from both meteoric and lower crustal fluid circulations (Lemarchand et al., 2012). These veins are evidence of a crustal-scale fluid circulation that occurred between ~315 and 300 Ma during a strike slip deformation along the SASZ (Tartèse et al., 2012).

Within this part of the Armorican Massif, several metal deposits, mainly Sn and U mineralization (Chauris, 1977), are spatially associated with the peraluminous leucogranites. Uranium represents the most important resource in the region and has been mined within the three uraniferous districts of Pontivy, Mortagne and Guérande up until the end of the 90s (Cathelineau et al., 1990; Cuney et al., 1990) (Fig. 1). These three districts provided around 20% of the uranium extracted in France (IRSN, 2004).

2.2. The Guérande leucogranite

2.2.1. General framework

The Guérande leucogranite (Fig. 2) is an ~1 km thick blade-shaped structure dipping slightly northward (Bouchez et al., 1981; Vigneresse, 1983, 1995). The granite was emplaced ca. 310 Ma ago (U-Pb on zircon and monazite, Ballouard et al., 2015) in an extensional deformation zone (Gapais et al., 1993, 2015; Ballouard et al., 2015). To the north, the granite intrudes micaschists that were affected by contact metamorphism as indicated by the occurrence of staurolite and garnet (Valois, 1975). In contrast, to the south, the Guérande leucogranite presents a progressive contact with migmatites. Several micaschist bodies, hectometers to kilometers in size, are found within the leucogranite. The southwestern edge of the intrusion is crosscut by a kilometer-size isotropic leucogranitic intrusion which does not present any evidence of deformation (leucogranite isotropic sub-facies intrusion; Fig. 2).

In the Guérande leucogranite, the foliation dips generally 20–30° to the north with a dip-slip type lineation. A zone of intense strain is localized in the northern zone of the granite and is characterized by S/C and mylonitic fabrics. The northwestern part of the intrusion is also affected by an extensional graben, the so-called "Piriac graben" where metavolcanics and black shales from the Vendée porphyroid formation crop out (Fig. 3). Some authors interpreted this structure as the result of the collapse of the roof of the intrusion (Valois, 1975; Cathelineau, 1981; Cottaz et al., 1989). The Ordovician metavolcanics of the Piriac graben were affected by the emplacement of the Guérande leucogranite as demonstrated by muscovite $^{40}Ar/^{39}Ar$ dates at 311.8 ± 0.5 Ma and 313.4 ± 0.4 Ma (Le Hébel, 2002).

2.2.2. Tectonic evolution and magmatic-hydrothermal history of the Guérande leucogranite

The aim of this section is to summarize the recent structural, petro-geochemical and geochronological study performed on the Guérande leucogranite by Ballouard et al. (2015). The Guérande leucogranite displays structural heterogeneities at the scale of the intrusion with a weak deformation in the southwestern part, whereas the northern part is marked by the occurrence of S/C and mylonitic extensional fabrics. Quartz veins and pegmatite dykes orientations, as well as stretching lineation directions in the granite and its country rocks, both show E-W and N-S stretching directions. Therefore, during its emplacement in an

extensional regime, the leucogranite experienced some partitioning of the deformation and the main top to the north stretching direction recorded in the area is locally accommodated by E-W motions.

The southwestern part of the intrusion is characterized by a muscovite-biotite assemblage, the presence of restite and migmatite enclaves and a low abundance of quartz veins compared to pegmatitic dykes. In contrast, the northwestern part is characterized by a muscovite-tourmaline assemblage, evidence for both albitization and greisenization (Fig. 2) and a higher number of quartz veins. These observations, together with the northward dipping foliation, are consistent with the fact that the southwestern part corresponds to the feeding zone of the intrusion while the northwestern part corresponds to its apical zone.

The samples studied by Ballouard et al. (2015) have variable grain-size, from aplitic (0.5–1 mm, in dykes) to coarse-grained (3–5 mm). All the samples contain a quartz-feldspar-muscovite assemblage with variable amounts of biotite and tourmaline. Biotite hosts most of the accessory minerals such as apatite, Fe-Ti oxide, zircon and monazite. No magmatic uranium oxide was observed during this study. However, such oxides have been reported by Ouddou (1984) and Friedrich et al. (1987) in a drilled core of a highly evolved coarse-grained facies from this leucogranite. This sample, which has a U content of 20 ppm, was recovered at a depth of 160 m in the northwestern part of the leucogranite at the contact with the micaschists.

In terms of alteration, indices of chloritization are localized in the northern central part of the intrusion whereas muscovitization, greisenization and albitization are restricted to the apical zone to the northwest (Fig. 2). In this area, albitization, associated with dequartzification, largely affected the chemical composition of some of the samples.

High initial $^{87}Sr/^{86}Sr$ ratios (0.7149 to 0.7197) and low εNd(T) (−9.0 to −7.8) values suggest that the Guérande leucogranite (A/CNK > 1.1) was formed by partial melting of Upper-Proterozoic to Paleozoic metasediments. Fractional crystallization affected the granitic melts, reaching 15–30% fractionation of K-feldspar, plagioclase, biotite and accessory minerals (apatite, zircon and monazite) in the most evolved samples. The apical zone is characterized by high contents of highly incompatible elements, such as Sn or Cs, which cannot be solely explained by a fractional crystallization process. Rather these distributions are consistent with a pervasive hydrothermal alteration that took place during (or soon after) crystallization of the magma. Zircon and monazite U-Th-Pb dating indicate that the Guérande leucogranite was emplaced ca. 310 Ma ago and that a second magmatic event, represented by the emplacement of leucogranite dykes, occurred at ca. 303 Ma. This age of ca. 303 Ma is directly comparable with the muscovite $^{40}Ar/^{39}Ar$ dates of 303.3 ± 0.5 Ma obtained for a quartz vein and of 303.6 ± 0.5 Ma and 304 ± 0.5 Ma obtained for a sheared granite and on a mylonitic S/C granite sampled in the apical zone of the intrusion, respectively (Le Hébel, 2002). This information suggests that deformation and hydrothermal circulations were both active at ca. 303 Ma and were contemporaneous with a late magmatic event.

2.2.3. The U mineralization

The Guérande leucogranite and its surrounding host rocks are spatially associated with Sn and U mineralization (Fig. 2). The Sn mineralization, represented by cassiterite-bearing quartz veins, is located in the northwestern part of the leucogranite (Audren et al., 1975) (Figs. 2 and 3), whereas U deposits are found exclusively in the central and northern parts of the intrusion. They are either perigranitic, hosted in the metamorphic country rocks (Pen Ar Ran), or intragranitic, hosted within the leucogranite itself or within pluridecametric metamorphic enclaves (Keroland, Métairie-Neuve; Cathelineau, 1981) (Fig. 2).

The most important deposit is the Pen Ar Ran deposit where around 600 tons of uranium have been extracted (IRSN report, 2004). In this deposit, uranium oxide veins crosscut the metavolcanics (Fig. 4a) and are localized at the contact with black shales in a sub-vertical sinistral N 110° shear zone within the "Piriac graben" (Cathelineau, 1981) (Fig. 3). The mineralization fills brittle structures oriented N 90° and N 70° that crosscut the foliation of the metavolcanics but are blocked at the contact with reducing black shales (Fig. 4b). These mineralized fractures correspond to Riedel or to tension gashes associated with sinistral N 110° faults (Cathelineau, 1981) (Fig. 4c). Cathelineau (1981) described a quartz-pitchblende mineralization event which represents >90% of the vein infilling. This event began with the development of a millimeter-size quartz comb where spherulitic pitchblende crystallized first, followed by prismatic pitchblende. The axial zone of the veins is locally filled with sulfides (mostly pyrite, marcasite, and chalcopyrite) commonly fracturing the previous pitchblende filling. Finally, a late reworking of the uranium oxides induced the precipitation of secondary hexavalent U-bearing minerals such as phosphates, oxides or vanadates (Fig. 4b and c).

In the Métairie-Neuve deposit (Fig. 2) (production of around 10 tons of UO_2), the uranium mineralization was formed in a hectometer-size enclave made up of micaschists and graphitic quartzites. The mineralization is expressed as centimeter-thick quartz-uranium veins, similar to the Pen Ar Ran deposit, but with a smaller size and volume. The uranium oxide veins crosscut both the metasediments and leucogranite (Cathelineau, 1981).

A pioneer fluid inclusion study (Cathelineau, 1982) on a quartz comb associated with an uranium oxide vein from the Pen Ar Ran deposit has shown that a low salinity (3–5 wt.% NaCl eq.) mineralizing fluid was trapped at a temperature between 340 and 380 °C and a low pressure; this temperature is anomalously high when compared to other U deposits in the EHB (150–250 °C, Cathelineau et al., 1990).

The REE concentrations measured in the uranium oxides from the Pen Ar Ran deposit are typically low but the patterns show a significant fractionation from LREE to HREE with an enrichment in Sm, Eu and Gd (Bonhoure et al., 2007). Based on the comparison with some clearly volcanic-related U deposits, these spectra have been interpreted as an indicator that the probable U source for the Pen Ar Ran deposit was the enclosing metavolcanic rocks (Bonhoure et al., 2007).

3. Analytical techniques

3.1. Oxygen isotope analyses

Oxygen isotope analyses were performed in the stable isotope laboratory at the University of Lausanne, Switzerland. The oxygen isotope composition of whole-rock samples and minerals (quartz and feldspar) from the Guérande granite, reported in the standard $\delta^{18}O$ notation, were measured using a CO_2-laser fluorination line coupled to a Finnigan MAT 253 mass spectrometer. The detailed methodology is provided as Supplementary material. For each run, the results, reported in per mill (‰) relative to VSMOW (Vienna Standard Mean Ocean Water), were normalized using the analyses carried out on the quartz standard LS1 (reference value: $\delta^{18}O = 18.1‰$ vs. VSMOW). The precision, based on replicate analyses of the standard run together with the samples, was generally better than 0.2‰.

3.2. Radiometric data

A detailed airbone radiometric survey was performed over the Armorican Massif by the BRGM (Bureau de Recherche Géologique et Minière). The detailed acquisition and treatment methods applied to the airborne radiometric data are provided in Bonijoly et al. (1999). To get complementary radiometric data at a smaller scale, qualitative measurement of the U, Th and K contents were carried out on selected outcrops using a portable spectral gamma ray (RS-230 BGO Super-Spec – Radiation Solution, this study). The duration of analysis was 3 min and the results reported in Table 1 correspond to the average of three analyses performed on an outcrop surface of about 4 m^2. No analytical biases were noticed whether the measurements were done perpendicularly or parallel to the foliation planes.

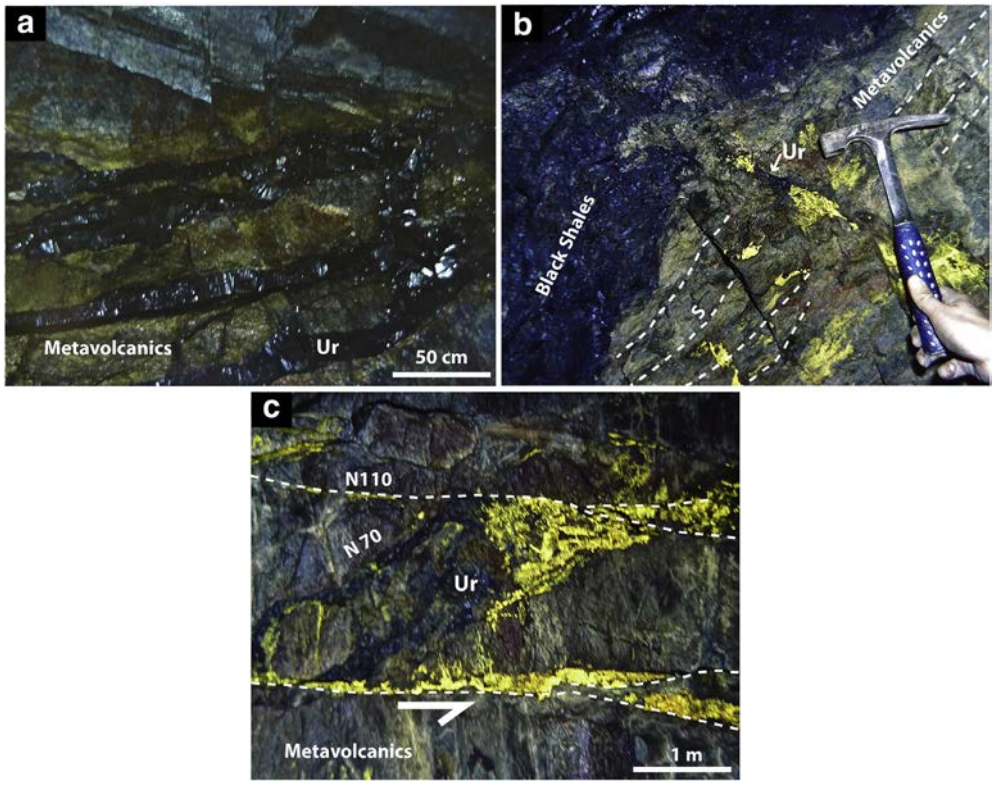

Fig. 4. U mineralization of the Pen Ar Ran deposit. (a) U oxide–quartz bearing veins (Ur) intruding the metavolcanics. (b) The uranium oxide–quartz bearing veins (Ur) are blocked at the contact between the reducing black shales and crosscut the foliation (S) of the metavolcanics. (c) The mineralization filled N 70° tension gashes associated with the development of a N 110° sub-vertical sinistral fault inside the metavolcanics. Yellow minerals (b–c) correspond to hexavalent U minerals formed quickly after the mine gallery opening, and revealing the distribution of the U ores. (For interpretation of the references to color in this figure legend, the reader is referred to the web version of this article.)

3.3. Apatite fission tracks analysis

Apatite fission track (AFT) analysis was performed on three samples from the Guérande leucogranite using the external detector method (see Supplementary material for details on the method). The AFT measurements were made in Géosciences Rennes using a Zeiss Axioplan 2 microscope with a 1250× magnification under dry lenses. For each sample, a total of 20 inclusion-free apatite grains oriented parallel to the c-axis were measured using the TrackWorks software (on manual mode) developed by the Autoscan company (Australia). Age calculations were done using the TrackKey software (Dunkl, 2002). A weighted mean zeta value of 335.9 ± 6.8 yr cm^2 (CB) obtained on both the Durango (McDowell et al., 2005) and Mount Dromedary (Green, 1985; Tagami, 1987) apatite standards was used. All ages reported in this study are central ages (Galbraith and Laslett, 1993) reported at ±2σ. Measurements of the horizontal track lengths and their respective angle with c axis, as well as the mean D_{par} value (e.g. Jolivet et al., 2010; Sobel and Seward, 2010) were obtained for each sample. The D_{par} value corresponds to the etched trace of the intersection of a fission track with the surface of the analyzed apatite (parallel to the c axis). The mean D_{par} value used for each sample was obtained by measuring >300 D_{par}. Inverse time-temperature history modeling was performed using the QTQt software (Gallagher et al., 2009; Gallagher, 2012) with the annealing model of Ketcham et al. (2007) that takes into account the D_{par} parameter to constrain the annealing kinetic of fission tracks. The time-temperature history modeling is only well constrained in the temperature interval 60–120 °C which corresponds to the partial annealing zone (PAZ) of apatite fission tracks.

Table 1
Average spectral gamma ray radiometric data.

		K (%)		U (ppm)		Th (ppm)		Th/U	
	n	Mean	σ	Mean	σ	Mean	σ	Mean	σ
Granite	102	4.3	0.6	3.3	1.1	4.6	5.0	1.3	0.6
Metavolcanics	22	6.0	2.0	5.5	1.5	18.6	1.5	3.5	0.8
Black shales	12	2.5	0.8	5.4	1.8	8.1	2.3	1.6	0.6

3.4. Fluid inclusion analyses

The petrography, microthermometry and Raman analyses of the fluid inclusions were carried out at the GeoRessources laboratory (Nancy, France) on a thick section of a quartz comb associated with a uranium oxide vein from the Pen Ar Ran deposit. Microthermometric measurements were performed on a Linkam THMS600 heating–cooling stage connected to an Olympus BX51 microscope. The fluid inclusions used for the calibration were a CO_2 standard fluid inclusion (triple point at −56.9 °C) and two H_2O standard fluid inclusions with an ice melting and a homogenization temperature of 0.0 °C and 165 °C, respectively. Raman microspectrometry analyses were performed on both the vapor and liquid phases of the fluid inclusions using a LabRAM HR Raman spectrometer (Horiba Jobin Yvon) equipped with a 1800 gr.mm^{-1} grating and an Edge filter. The confocal hole aperture was 500 μm and the slit aperture 100 μm. The excitation beam was provided by a Stabilite 2017 Ar^+ laser (Spectra Physics, Newport Corporation) at 514 nm and a power of 200 mW, focused on the sample using a 100× optical zoom lens (Olympus). The acquisition time and the number of accumulations were chosen in order to optimize the signal-to-noise ratio (S/N). Salinity is expressed as weight equivalent percent NaCl (wt.% NaCl eq.) and has been calculated using the measured ice melting temperature (Tm Ice) with the equation of Bodnar (1993) and Raman analyses (Caumon et al., 2013, 2015).

3.5. U oxide analyses and dating

Petrography, imaging, as well as major and trace element analyses of selected polished thin sections and mounts of uranium oxide samples from the Pen Ar Ran and Métairie-Neuve deposits were carried out at the GeoRessources laboratory (Nancy, France). U-Pb dating was carried out at the Centre de Recherches Pétrographiques et Géochimiques (CRPG, Nancy, France) by secondary ion mass spectrometry (SIMS). The U oxide samples were first examined using reflected light microscopy. We then selected appropriate areas suitable for laser ablation-inductively coupled plasma mass spectrometry (LA-ICP-MS) and SIMS analyses (areas without evidence of post-crystallization alterations and having high radiogenic lead contents) based on back-scattered electron (BSE) images obtained using both a JEOL J7600F and a HITACHI S-4800 scanning electron microscopes and major element analyses obtained using a CAMECA SX100 electron microprobe (EPMA). The rare earth element (La, Ce, Pr, Nd, Sm, Eu, Gd, Tb, Dy, Ho, Er, Tm, Yb, Lu) concentrations in the uranium oxides were quantified using a LA-ICP-MS system composed of a GeoLas excimer laser (ArF, 193 nm, Microlas) coupled to an Agilent 7500c quadrupole ICP-MS. The detailed methodology is provided as Supplementary material and followed the one proposed by Lach et al. (2013). U-Pb isotope analyses were performed using a CAMECA IMS 1270 ion microprobe. The complete methodology is described in Mercadier et al. (2010). Ages, calculated using the ISOPLOT software (Ludwig, 2012), are provided with their 2σ uncertainties. All the isotopic ratios are provided in Supplementary Table 1.

4. Results

In this section we successively present the petrographic and geochemical characteristics of the deposits (uranium oxides and fluid inclusion analyses) and the country rocks (Guérande leucogranite, black shales and metavolcanics).

4.1. Uranium deposits

4.1.1. Uranium oxide petrography

Three uranium oxide samples from the Pen Ar Ran deposit and two from the Métairie-Neuve deposit were analyzed in detail. The selection of these samples, representative of the different types and habitus of the uranium oxides and host rocks described for the two deposits, was based on the initial work on the deposits carried out by Cathelineau (1981, 1982).

The three uranium oxide samples from the Pen Ar Ran deposit have specific morphologies: (1) a spherulitic facies ("PAR-spherulitic"; Fig. 5a), (2) a pseudo-spherulitic facies ("PAR-pseudo-spherulitic"; Fig. 5b and c) and (3) a prismatic facies ("PAR-prismatic"; Fig. 5d). In the spherulitic facies, the spherules, which have grown on a millimeter-size quartz comb, have a diameter of 500 μm to 2 mm and display micrometer-size concentric zoning, likely reflecting overgrowth of uraninite zones around a more homogeneous uraninite core (Fig. 5a). On the BSE images, the rims of the spherules commonly display a dark-grey color (lowest mean atomic mass Z) whereas the cores display a light-grey color (higher Z; Fig. 5a). The spherules (Ur1) are locally brecciated by sulfides (mostly pyrite, chalcopyrite, marcasite). Some micrometric fractures crosscut the spherules and induced the alteration of the first generation of uranium oxides (alt Ur1). The pseudo-spherulitic facies is characterized by millimeter- to centimeter-size partially developed spherules which have grown on ~500 μm thick quartz comb (Qtz, Fig. 5b). Sulfide minerals fill the central parts of the vein and locally crosscut Ur1 as micrometer-size veinlets (Py and CPy, Fig. 5b) that are related to the alteration of Ur1 (Alt Ur1). Ur1 is also characterized by chemically homogenous areas within the uranium oxide which were chosen for U-Pb dating (Fig. 5c; see the geochronological section below). In the prismatic facies, the BSE imaging also revealed large-scale homogenous areas within the uranium oxide (Fig. 5d).

For the Métairie-Neuve deposit, one sample comes from a vein crosscutting the Guérande leucogranite ("MN-granitic C.R."; Fig. 5e) and the second sample from a vein crosscutting metasedimentary rock enclaves in the leucogranite ("MN-metased. C.R."; Fig. 5f). Both uranium oxides display a prismatic morphology. In the "MN-granitic C.R." sample, the uranium oxide (Ur1) is crosscut by micro-fractures associated with the alteration of Ur1 (Alt Ur1) and the crystallization of micrometer-size crystals of galena (Gn, Fig. 5e). Some fractures can be filled with a late fibrous uranium phosphate mineral (U-Ca-K-PO_4; Fig. 5e). In the "MN-metased. C.R." sample, the uranium oxide displays a homogenous composition on the BSE image (Fig. 5f).

The precise and small-scale observations of the different uranium oxides Ur1 from the Pen Ar Ran and Métairie-Neuve deposits clearly indicate that they present limited alteration patterns, and that consequently the measured isotopic ratios and trace element contents in these minerals can be considered as reflecting the crystallization processes rather than later alteration events.

4.1.2. Uranium oxide geochemistry

The average major and REE element compositions of the uranium oxides analyzed in this study are reported in Table 2. For the "PAR-spherulitic" sample, the analyses performed on the core of the spherules were distinguished from the analyses made on the rim. We also separated the analyses carried out on the altered uranium oxides (Alt Ur1).

For the Pen Ar Ran deposit, the average UO_2 contents of the uranium oxides Ur1 range from 80.2 to 82.8 wt.% (Table 2) whereas the Th content is below the detection limit (<0.1 wt.%). These uranium oxides are characterized by an elevated but variable content in PbO which ranges from 3 wt.% to 9 wt.%, the maximum PbO content being recorded in the core of the spherules of the "PAR-spherulitic" sample (Fig. 6a). The CaO content is also highly variable, ranging from 4 wt.%, in the core of the spherules of the "PAR-spherulitic" sample, to >10 wt.% in the "PAR-pseudo-spherulitic" sample; the other uranium oxides present intermediate contents (Fig. 6a). The PbO content in the "PAR-spherulitic" sample is *anti*-correlated with the CaO contents (Fig. 6a). In the uranium oxides Ur1, the average content in SiO_2 ranges from 1.0 to 1.4 wt.% while FeO is generally below the detection limit. The analyses performed on the altered uranium oxides (Alt Ur1) from the "PAR-spherulitic" sample revealed lower UO_2, CaO and PbO contents and an increase in the P_2O_5 and FeO contents (Table 2). In the Métairie-Neuve deposit, both uranium oxides display overall similar major element compositions (average UO_2 content of 84.4 and 84.9 wt.% in the "MN-granitic C.R." and "MN-metased. C.R." samples, respectively), comparable with the composition of the uranium oxides Ur1 from the Pen Ar Ran deposit (Table 2). However, the PbO content is less variable in the "MN-granitic C.R." sample (3.5–3.8 wt.%) than in the "MN-metased. C.R." sample (2.7–8.6 wt.%).

The REE spectra of the uranium oxides from the Pen Ar Ran and Métairie-Neuve deposits display variable patterns, but are all characterized by relatively low REE contents (Fig. 6b-c-d). In the spherulitic facies from Pen Ar Ran (Fig. 6b), the REE spectra display a progressive evolution from the core to the rim of the spherules with a decrease in the total REE content (mean Σ REE from 145 to 24 ppm; Table 2) mainly based on a decrease in the MREE and HREE contents, introducing an increase in the fractionation of LREE (mean La_N/Sm_N from 33 to 782). Some of the spectra (e.g. 5a, 5b, 6a; Fig. 6b) display a saddle-shape from La to Gd whereas some patterns from the cores (1a, 1b, 3a, 3b and 6b) are marked by a negative Eu anomaly (average $Eu/Eu^* = 0.4$). The pseudo-spherulitic and prismatic facies of Pen Ar Ran display homogenous REE spectra (Fig. 6c) characterized by a fractionation from La to Sm (mean La_N/Sm_N of 4.5 for the "PAR-pseudo-spherulitic" sample and 3.9 for the "PAR-prismatic" sample) and a negative Eu anomaly (average $Eu/Eu^* = 0.7$). The prismatic facies displays a higher total REE content than the pseudo-spherulitic facies (mean Σ REE of 120 and 34 ppm, respectively).

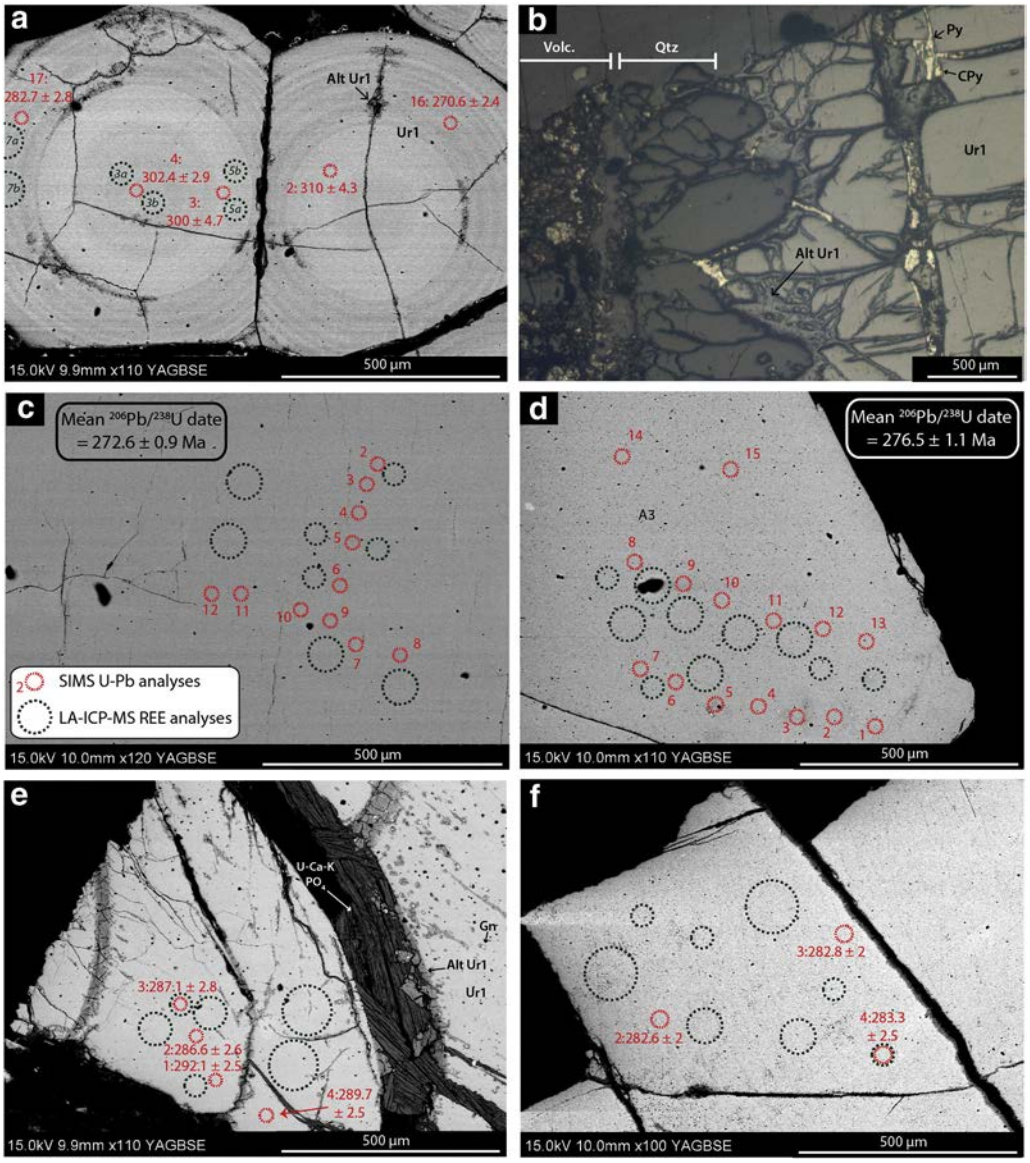

Fig. 5. Back-scattered electron (BSE; a–c–d–e–f) and reflected light (b) images of the uranium oxide samples analyzed in this study. The dates associated with SIMS analyses correspond to the common Pb-corrected punctual $^{206}Pb/^{238}U$ ages (Ma). The numbers associated with LA-ICP-MS analyses (a) refer to the REE patterns presented in Fig. 6b. (a) Spherulitic uranium oxide from the Pen Ar Ran deposit (PAR-spherulitic). The spherulites (Ur1) are characterized by concentric zonation and the borders display a darker color than the cores. Alteration products of Ur1 (Alt Ur1) occur along micro-fractures (b–c) Pseudo-spherulitic uranium oxide from the Pen Ar Ran deposit (PAR-pseudo-spherulitic). In (b), the filling of the vein sample intruding the metavolcanics (Volc.) begins with a 500 µm thick quartz comb (Qtz) on which uranium oxides (Ur1) have grown. The central part of the vein and fractures are commonly filled with sulfide such as pyrite (Py), chalcopyrite (CPy) and are associated with a product of alteration of Ur1 (Alt Ur1). (d) Prismatic uranium oxide from the Pen Ar Ran deposit (PAR-prismatic). (e–f) Uranium oxide from the Métairie-Neuve deposit. In (e), the uranium oxides occur within a granitic country rock (MN-granitic C.R.) and the first generation of uranium oxide (Ur1) is crosscut by fractures associated with the alteration of Ur1 (Alt Ur1), and the crystallization of galena and U-Ca-K phosphate (U-Ca-K-PO_4). In (f), Uranium oxides occur within the metasedimentary country rock in enclaves in the Guérande granite (MN-metased. C.R.).

The REE patterns of the two uranium oxide samples from the Métairie-Neuve deposits are similar (Fig. 6d) but differ from the majority of the spectra from the Pen Ar Ran deposit (Fig. 6b). Their REE content is very low with a mean Σ REE of 18.3 and 3.7 ppm for the "MN-granitic C.R." and "MN-metased. C.R." samples, respectively (Table 2). Two different LREE patterns are displayed, either a linear negative slope or a saddle shape from La to Sm (mean La_N/Sm_N of 3.5 for the "MN-granitic C.R." sample and 5.3 for the "MN-metased. C.R." sample). All the patterns are marked by a positive Eu anomaly (average Eu/Eu* of 1.6 for "MN-granitic C.R." and 2.0 for "MN-metased. C.R.") and a fractionation from Gd to Lu.

4.1.3. Fluid inclusions in quartz

The fluid inclusion study was performed on a quartz comb from a uranium oxide vein from Pen Ar Ran such as shown in Fig.5b. Most of the fluid inclusions are generally found in clusters or along quartz growth zones and have been identified as primary in origin. Secondary fluid inclusions are small and rare, and have not been studied. The primary fluid inclusions (Fig. 7) have a moderate size (10–30 µm), and can be elongated in the direction of the growth of their host quartz crystal (Fig. 7a). Several inclusions of muscovite occur in the quartz and can be locally observed inside or at the border of the fluid inclusions (Fig. 7d). The inclusions are all biphasic at room temperature with a highly variable degree of gas filling (Fig. 7) from 10 to 90%. The result of the microthermometric and Raman analyses of the representative fluid inclusions are reported in Table 3. All the fluid inclusions are aqueous and the volatile phase contains a variable amount of O_2-H_2-N_2. The salinity of the liquid phase varies significantly from 0.9 to 6.4 wt.% NaCl eq. (Fig. 8a). The homogenization temperatures (T_h) range from 287 to 461 °C (Fig. 8b). Lowest T_h (<360 °C) are characteristic of inclusions

Table 2
Chemical composition of the studied uranium oxides, measured by EPMA and LA-ICP-MS. bdl = below detection limit, Alt Ur1 = product of alteration of Ur1. PAR = Pen Ar Ran. MN-granitic C.R. = Métairie-Neuve granitic country rock. MN-metased. C.R. = Métairie-Neuve metasedimentary country rock.

	PAR-spherulitic: Ur1 (rim)		PAR-spherulitic: Ur1 (core)		PAR-spherulitic: Alt Ur1		PAR-pseudo-spherulitic		PAR-prismatic		MN-granitic C.R.		MN-metased. C.R.	
Analyses	15	σ	26	σ	2	σ	48	σ	70	σ	15	σ	65	σ
UO_2 (wt.%)	82.83	1.60	82.13	1.39	71.77	17.56	82.70	0.79	80.17	1.90	84.38	0.83	84.86	0.99
PbO	4.49	1.98	6.73	1.28	1.24	0.45	3.59	0.42	5.60	0.23	3.65	0.10	3.57	1.02
CaO	6.58	0.73	5.57	0.71	1.67	0.40	9.55	0.46	9.17	1.18	6.88	0.39	7.77	0.22
SiO_2	1.35	0.37	1.31	0.39	0.33	0.00	0.98	0.07	1.19	0.08	1.43	0.22	0.54	0.06
FeO	0.16	0.10	bdl		0.70	0.16	bdl		bdl		bdl		bdl	
P_2O_5	0.14	0.09	0.13	0.03	3.06	0.21	0.23	0.17	0.21	0.15	0.13	0.15	0.17	0.01
Total	95.55	1.53	95.87	0.66	78.76	18.46	97.06	0.57	96.34	1.00	96.47	0.51	96.90	0.69
Analyses	4	σ	10	σ			4	σ	10	σ	12	σ	8	σ
Σ REE	24.35	9.62	145.39	118.99			33.89	1.77	119.82	8.65	18.26	18.66	3.66	2.56
Eu/Eu*	0.4	0.4	0.5	0.2			0.7	0.1	0.7	0.0	1.6	0.3	2.0	0.5
LaN/SmN	782.0	1456.6	33.3	43.6			4.5	0.7	3.9	0.3	3.5	2.1	5.3	4.4
La	15.13	2.21	41.23	22.70			7.69	0.49	27.66	2.60	5.65	6.45	0.83	0.71
Ce	5.67	3.85	39.60	43.87			11.55	1.31	38.03	3.75	6.72	7.95	1.12	1.05
Pr	0.40	0.38	3.67	4.42			1.06	0.06	4.12	0.39	0.60	0.65	0.11	0.08
Nd	1.79	2.00	16.80	18.56			5.14	0.36	18.85	0.78	2.32	2.31	0.56	0.35
Sm	0.26	0.35	4.08	4.26			1.09	0.12	4.47	0.19	0.52	0.32	0.24	0.09
Eu	0.13	0.11	1.31	1.10			0.29	0.04	1.18	0.04	0.40	0.18	0.14	0.04
Gd	0.38	0.42	9.71	8.06			1.70	0.09	6.46	0.32	0.89	0.48	0.32	0.14
Tb	0.06	0.04	1.36	1.20			0.31	0.02	1.05	0.12	0.10	0.05	0.04	0.02
Dy	0.30	0.30	10.60	9.83			2.11	0.03	8.10	0.29	0.51	0.24	0.27	0.05
Ho	0.06	0.06	2.29	1.98			0.49	0.02	1.54	0.17	0.08	0.05	0.04	0.02
Er	0.27	0.16	7.28	6.52			1.29	0.03	4.44	0.17	0.23	0.13	0.12	0.04
Tm	0.02	0.02	0.85	0.74			0.18	0.01	0.50	0.07	0.03	0.02	0.02	0.00
Yb	0.10	0.12	5.96	5.44			0.90	0.07	3.11	0.10	0.20	0.13	0.09	0.05
Lu	0.02	0.01	0.80	0.64			0.11	0.02	0.31	0.04	0.03	0.02	0.02	0.01

homogenizing in the liquid phase whereas the highest T_h were obtained for fluid inclusions which homogenize in the vapor phase (Fig. 8b). Overall, the ranges of T_h and liquid phase salinities measured in this study are larger than those obtained by Cathelineau (1982). There is no evident correlation between T_h and liquid salinity (Fig. 8c), although the highest salinities are mostly found within the inclusions presenting the highest T_h and homogenizing in the vapor phase. Finally, the T_h are correlated with the gas bubble size (Fig. 8d).

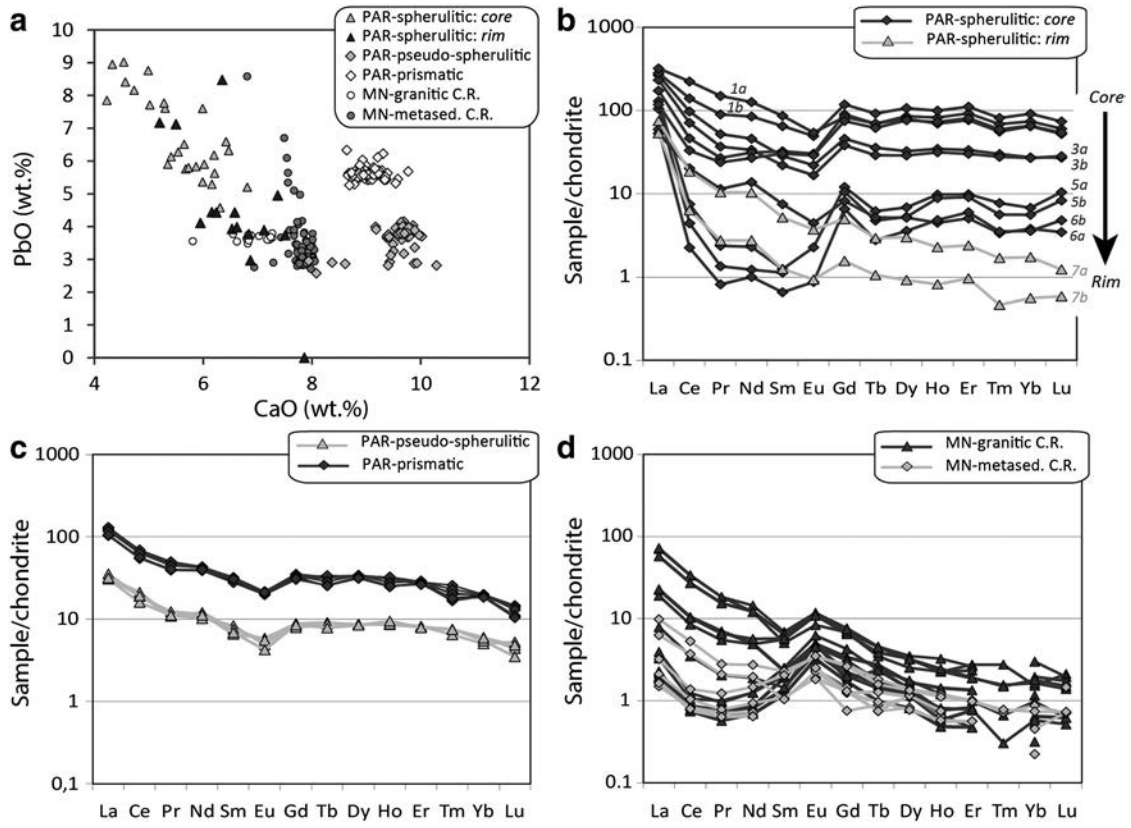

Fig. 6. (a) PbO vs. CaO diagram displaying the chemical composition of the uranium oxide samples analyzed in this study. (b–c–d) Chondrite-normalized REE patterns for uranium oxides from the Pen Ar Ran (PAR) and Métairie-Neuve (MN) deposits. The chondrite REE abundances used for normalization are from McDonough and Sun (1995).

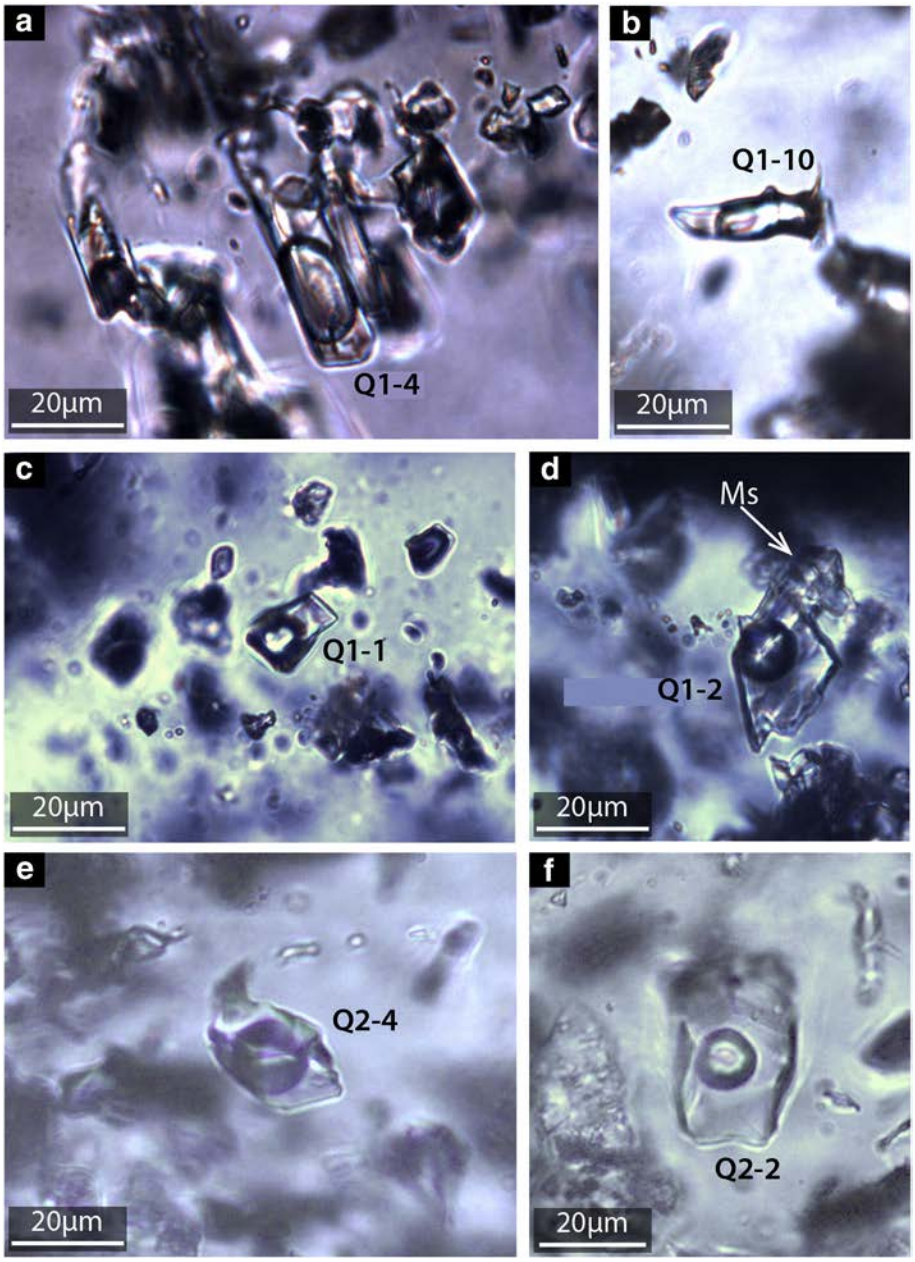

Fig. 7. Photomicrographs of some fluid inclusions observed in the quartz comb associated to a uranium oxide vein from the Pen Ar Ran deposit showing a variable degree of volatile filling. Notably, some fluid inclusions are oriented in the direction of growth of the host quartz crystal (a), and some are associated with mineral inclusions such as muscovite (d). The reference numbers of the fluid inclusions are the same as in Table 3.

Table 3
Microthermometric data and chemical composition of some representative fluid inclusions from a quartz comb associated with a uranium oxide vein of the Pen Ar Ran deposit.

Inclusion	Homogenization Type	Degree of volatile filling (%)	Microthermometry (°C)		Salinity (wt.% NaCl eq.)		Volatile phase (mol.%)		
			Tm Ice	Th	Microthermometry	Raman	O_2	N_2	H_2
Q1–1	Vapor	60	−2.4	420	4.0	3.8	74.9	3.0	22.1
Q1–6	Liquid	20	−3.5	285	5.6	6.3	78.3	2.0	19.7
Q1–9	Liquid	60	−1.4	390	2.4	3.0	39.0	14.0	47.0
Q1–13	Vapor	60	−3.7	461	5.9	5.2	79.8	1.1	19.1
Q1–16	Vapor	70		407		3.4	71.7	2.6	25.7
Q2–2	Liquid	20	−1.2	353	2.0	2.0	60.8	6.2	33.0
Q2–3	Vapor	80		406		3.4	67.0	9.0	24.0
Q2–4	Liquid	50	−1.7	360	2.9	3.1	65.5	3.3	31.2
Q2–5	Liquid	60		350		4.1	45.0	9.0	46.0

4.1.4. U-Pb geochronology

The results of the SIMS U-Pb isotope analyses on the uranium oxides from the Pen Ar Ran and Métairie-Neuve deposits are reported in Supplementary Table 1. All the analyses, performed on homogenous and fresh uranium oxide areas, display highly elevated common Pb contents with $^{204}Pb/^{206}Pb$ values ranging from 0.0010 ("MN-metased. C.R." sample) to 0.020 ("PAR-spherulitic" sample). For this reason, a common Pb correction was applied, based on the measured ^{204}Pb content and using Stacey and Kramers (1975) common Pb isotopic composition calculated for the estimated age of the uranium oxide crystallization.

4.1.4.1. Pen Ar Ran: spherulitic facies. Among the 18 analyses performed on the "PAR-spherulitic" sample, 16 were performed in the cores of the spherules and two in the rims (Fig. 5a). For the cores, the 16 common Pb-corrected analyses plot in a concordant to sub-concordant position in a Wetherill concordia diagram and allow to calculate a concordia date of 296.6 ± 2.6 Ma (MSWD = 1.2; Fig. 9a). In a Tera-Wasserburg diagram (Fig. 9b), these 16 analyses, uncorrected for common Pb, plot in a discordant position. A regression line anchored to the composition of common Pb at 300 Ma, following Stacey and Kramers (1975) model for Pb evolution, yields a lower intercept date of 294.4 ± 3.4 Ma (MSWD = 11.7). This less well-constrained date is comparable within error with the concordia date calculated above so we conclude that the cores of the spherules from this uranium oxide sample crystallized at 296.6 ± 2.6 Ma. The two common Pb-corrected analyses for the rim of the spherules (Fig. 5a) plot in apparent sub-concordant positions in the Wetherill concordia diagram (Fig. 9a) and yielded apparent $^{206}Pb/^{238}U$ dates of 270.6 ± 2.4 and 282.7 ± 2.8 Ma and $^{207}Pb/^{235}U$ dates of 278.1 ± 4.7 and 285.2 ± 5.1 Ma, respectively.

4.1.4.2. Pen Ar Ran: pseudo-spherulitic and prismatic facies. A total of 23 and 29 analyses were carried-out on the "PAR-pseudo-spherulitic" and "PAR-prismatic" samples, respectively (Figs. 5c and d). For the "PAR-pseudo-spherulitic" sample, all the common Pb corrected analyses plot in a concordant position in the Wetherill concordia diagram (Fig. 9c). For the "PAR-prismatic" sample, 28 analyses out of 29 are concordant (Fig. 9c). Together, 51 analyses from the two samples allow us to calculate a well-defined concordia date of 274.6 ± 0.9 Ma (MSWD = 1.4). The only discordant analysis (not shown here) obtained on the prismatic facies yields apparent $^{206}Pb/^{238}U$ and $^{207}Pb/^{235}U$ dates of 152 ± 2 and 159 ± 5 Ma, respectively, and likely underwent Pb loss. In a Tera Wasserburg diagram, the 51 analyses, uncorrected for common Pb and used for the calculation of the concordia date, plot in a discordant position (Fig. 9d). A regression line, anchored to the common Pb composition at 275 Ma (Stacey and Kramers, 1975), yields a lower intercept date of 274.9 ± 1.1 Ma (MSWD = 5.7) that is identical within error to the concordia date of 274.6 ± 0.9 Ma. Consequently, we argue that these two uranium oxide types crystallized 274.6 ± 0.9 Ma ago.

4.1.4.3. Métairie-Neuve. A total of 12 analyses were performed on each sample from the Métairie-Neuve deposit ("MN-granitic C.R." and "MN-metased. C.R."; Fig. 5e and f). All together, these 24 analyses, corrected for common Pb, plot in a concordant to sub-concordant position in the Wetherill concordia diagram and allow us to calculate a concordia date of 286.6 ± 1.0 Ma (MSWD = 1.4; Fig. 9e). These 24 analyses, uncorrected for common Pb, plot in a discordant position in the Tera Wasserburg diagram (Fig. 9f). A regression line anchored to the composition of common Pb at 285 Ma (Stacey and Kramers, 1975) allows us to calculate a lower intercept date of 286.5 ± 1.2 Ma (MSWD = 3.3). These two dates are identical within error. As a consequence, we infer that these uranium oxides crystallized at 286.6 ± 1.0 Ma.

4.2. The Guérande leucogranite and surrounding country rocks

4.2.1. U and Th distribution

The U airborne radiometric map of the Guérande leucogranite and its country rocks is displayed in Fig. 10a. The variations of U contents allow to differentiate two main domains within the intrusion. The southern and the northeastern part of the leucogranite are

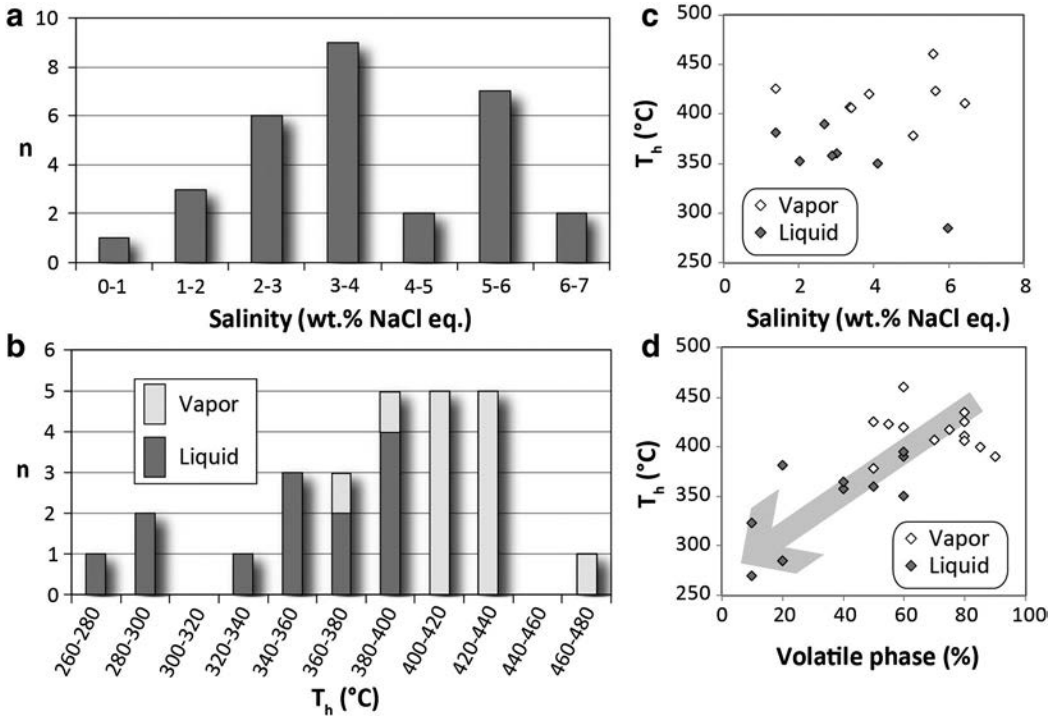

Fig. 8. (a–b) Histograms reporting the (a) salinity and (b) homogenization temperature (T_h) of the fluid inclusions of the quartz comb associated with a uranium oxide vein from the Pen Ar Ran deposit. (c–d) Diagram reporting the homogenization temperature (T_h) of fluid inclusions as a function of the (c) salinity and (d) degree of volatile filling. (b–c–d) Fluid inclusions homogenizing in the liquid phase (liquid) are differentiated from those homogenizing in the vapor phase (Vapor).

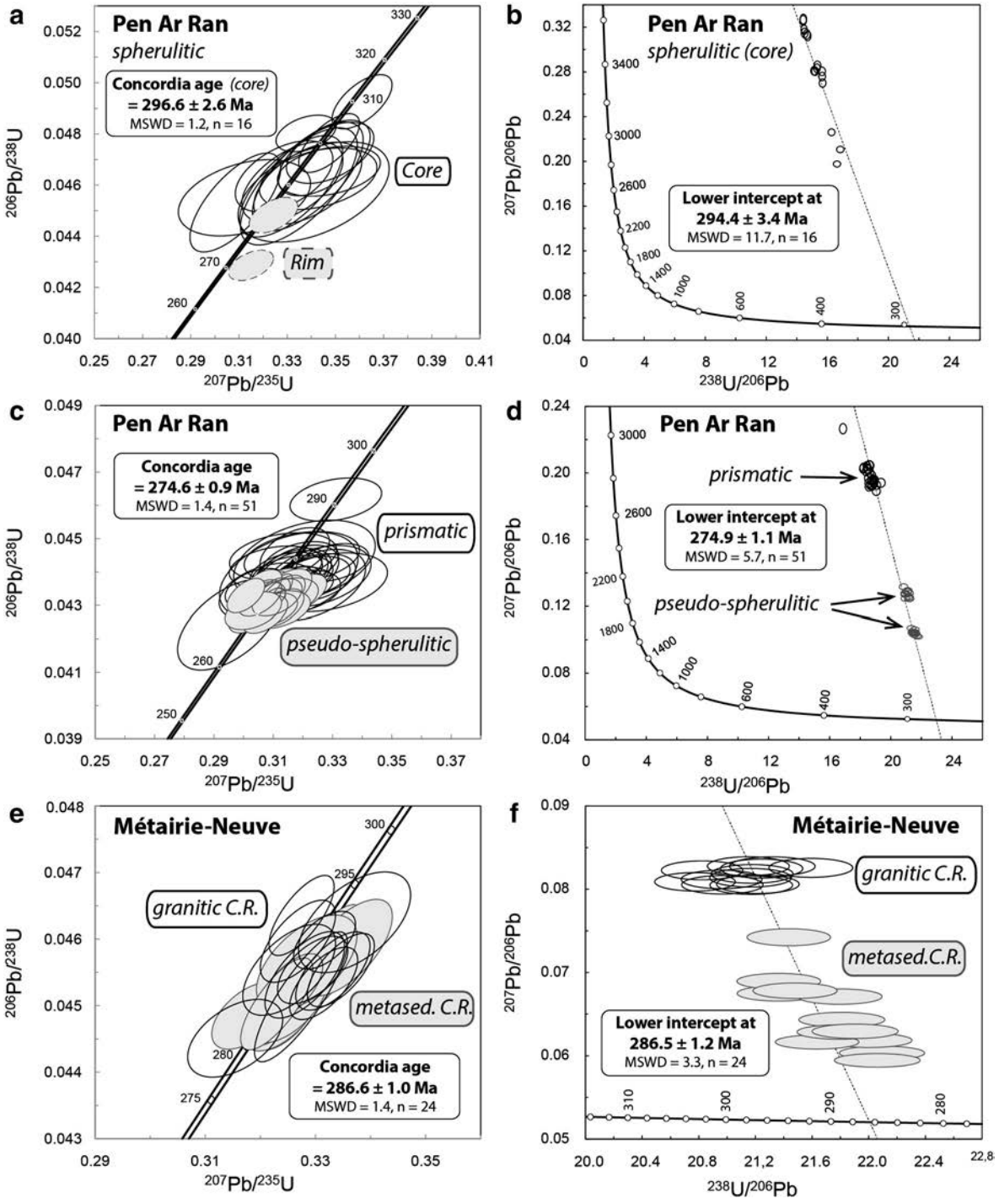

Fig. 9. (a–c–e) Wetherill concordia diagrams and (b–d–f) Tera Wasserburg diagrams displaying the analyses performed on the uranium oxides from the Pen Ar Ran and Métairie-Neuve deposits. The analyses reported in the Wetherill concordia diagrams are corrected from common Pb whereas the analyses reported on the Tera Wasserburg diagrams are not. Dashed ellipses correspond to analyses not used for date calculations. In all the diagrams, error ellipses are plotted at 1σ.

characterized by high U contents (brown color) whereas the northwestern part, interpreted as the apical zone of the intrusion by Ballouard et al. (2015), is characterized by low U contents (yellow to white colors). U deposits are systematically located inside or at the border of the "high U content" zones. For the country rock, the U contents are variable but the metavolcanics (Vendée porphyroid unit) and migmatites (south-east) are characterized by a high U content (brown color).

We also performed U, Th and K gamma-ray analyses on the Guérande leucogranite and its metamorphic country rocks (metavolcanics and black shales of the Piriac graben, Fig. 3) using a portable gamma-ray spectrometer. The measurements were mostly taken along the coastline from La Turballe to Piriac (Fig. 2) as there are only a few outcrops inland. The results of the analyses are reported in Table 1 and in a U vs. Th diagram (Fig. 10b) together with the ICP-MS data from the leucogranite (Ballouard et al., 2015) and metavolcanics (Le Hébel, 2002). In this diagram, the analyses performed on the Guérande leucogranite using the gamma-ray spectrometer are in a good agreement with the ICP-MS analyses made on whole-rock samples (Ballouard et al., 2015) and mostly have Th/U values below 2. For the metavolcanics (of the Vendée porphyroid unit), the Th/U values are between 2 and 5. These values

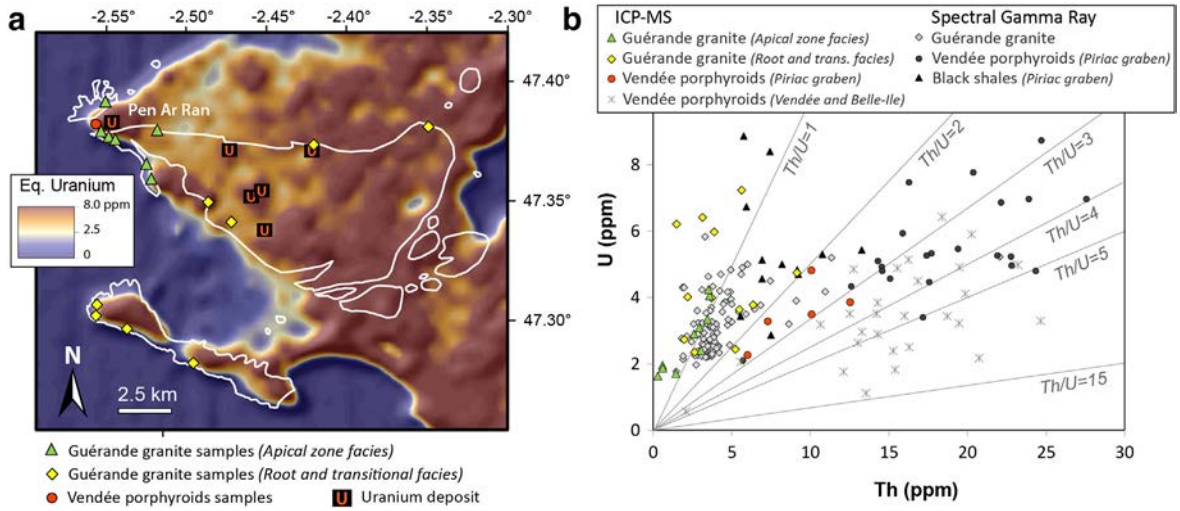

Fig. 10. (a) Airborne radiometric map of U in the Guérande granite area. The contour of the granite is shown in white. Radiometric data were obtained during an airborne survey of the Armorican Massif (Bonijoly et al., 1999). (b) U vs. Th diagram displaying the ICP-MS analyses of the Guérande granite (Ballouard et al., 2015) and of the metavolcanics of the Vendée porphyroid formation (Piriac graben and other areas of the South Armorican Massif: Belle-Ile en Mer and Vendée; Le Hébel, 2002) and spectral gamma ray radiometric data obtained on the Guérande granite and the metamorphic formations of the Piriac graben (metavolcanics and black shales of the Vendée porphyroid formation).

are comparable with the values obtained by the ICP-MS method on whole-rock porphyroid samples from the Piriac graben ($2 < Th/U < 4$; Le Hébel, 2002) and on other Ordovician metavolcanic samples from the South Armorican Massif ($2 < Th/U < 15$: porphyroids from Vendée and Belle-Ile) (Le Hébel, 2002). Finally, the black shales have intermediate Th/U values between 0.5 and 3.

4.2.2. Oxygen isotope compositions

The oxygen isotope compositions measured on whole-rock and mineral separates (quartz and feldspar) from the Guérande leucogranite samples are reported in Table 4 and summarized in Fig. 11. The whole-rock $\delta^{18}O$ values have a range from 12.2 to 12.9‰ in the root and transitional facies and a range from 9.7 to 13.6‰ in the apical zone facies. The high $\delta^{18}O$ values are comparable with the values obtained on other Carboniferous leucogranites from the Armorican Massif (Bernard-Griffiths et al., 1985; Tartèse and Boulvais, 2010) and are consistent with the metasedimentary source proposed for the Guérande leucogranite by Ballouard et al. (2015).

In Fig. 11a, the $\delta^{18}O$ values of the minerals (quartz and feldspar) are reported as a function of the $\delta^{18}O$ values of the whole-rock samples. Four samples (GUE-6, 7, 9 and 21) have feldspar and/or whole-rock $\delta^{18}O$ values below the values of the other samples ($\delta^{18}O_{WR} < 12$ and $\delta^{18}O_{Fds} < 10$). These low $\delta^{18}O$ samples have $\Delta^{18}O_{(Qz\text{-}Fds)}$ between 4.4 and 4.9, which would correspond to meaningless low temperatures of equilibration between 7060 and 90 °C, whereas the other samples have high equilibration temperatures between 460 and 610 °C (s4).

In Fig. 11b, most of the $\delta^{18}O$ values of the whole-rock and minerals correlate with the geographic latitude of the samples and the highest $\delta^{18}O$ values have been measured for rocks in the apical zone facies. Whole-rock, quartz and feldspar $\delta^{18}O$ values increase by about 1‰ from south to north of the intrusion. The four samples with the low $\delta^{18}O$ values of the feldspar and/or the whole-rock (GUE-6, 7, 9 and 21) are localized to the north of the intrusion and plot below the trend defined by the other samples whereas the quartz displays a continuous trend. These low $\delta^{18}O$ samples which belong either to the apical zone facies or to the root and transitional facies, are a mylonitic S/C granite (GUE-9), a S/C granite (GUE-6), a fine grained granite affected by solid state deformation (GUE-7) and an altered granite (GUE-21) collected near a greisen affected by dequartzification and potassic feldspar neoformation (Ballouard et al., 2015). These observations suggest a relationship between solid-state deformation and the isotopic disequilibrium between quartz and feldspar recorded by these samples.

4.2.3. Apatite fission track (AFT) thermochronology

The results of the AFT analysis performed on three samples from the Guérande leucogranite are reported in Table 5 and Fig. 12. The GUE-5 granite is a dyke intrusive into the GUE-4 granite whereas the GUE-3 granite sample was collected in the northwestern edge of the intrusion (Fig. 2). No tectonic discontinuity has been identified between the two sampling areas. The crystallization ages of GUE-3, GUE-4 and GUE-5 leucogranite have previously been obtained on zircon and monazite by LA-ICPMS U-Th-Pb dating at 309 ± 1.9 Ma, 309.7 ± 1.3 Ma and 302.5 ± 1.6 Ma, respectively (Ballouard et al., 2015).

The three granite samples GUE-3, GUE-4 and GUE-5 yield slightly different central AFT dates of 168 ± 7 Ma, 177 ± 8 Ma and 156 ± 6 Ma, respectively (Fig. 12). The mean track lengths of the samples are similar, ranging from 13.1 to 13.3 μm. Yet, the GUE-5 sample displays a mean D_{par} value of 1.2 μm, slightly lower than the values obtained for the

Table 4
Oxygen isotope data.

Sample	Location	$\delta^{18}O$ WR	$\delta^{18}O$ Qtz	$\delta^{18}O$ Fds	$\Delta_{(Qtz\text{-}Fds)}$	$T_{(Qtz\text{-}Fds)}$[a]
GUE-1	Apex	13.3	14.5	12.9	1.6	461
GUE-2	Apex	12.8	14.4			
GUE-3	Apex	12.9	13.8			
GUE-4	Root	12.4	13.8	12.3	1.5	492
GUE-5	Root	12.2	13.4			
GUE-6	Apex	9.7	13.9	9.2	4.7	72
GUE-7	Root	11.6	13.5			
GUE-8	Root	12.8	13.9			
GUE-9	Apex	10.8	13.2	8.3	4.9	62
GUE-10	Root	12.9	13.7			
GUE-11	Root	12.8	13.4	11.9	1.6	461
GUE-12	Root	12.3	13.2			
GUE-13	Root	12.9	13.3			
GUE-14	Root	12.4	13.4			
GUE-15	Root	12.6	13.6	12.4	1.2	608
GUE-16	Root	12.6	13.4			
GUE-17	Root	12.3	12.6			
GUE-18	Apex	13.6	14.3			
GUE-19.A	Apex	13.4	13.6			
GUE-19.B	Apex	13.3	13.9			
GUE-20	Apex	13.1	14.3			
GUE-21	Apex	11.1	13.8	9.3	4.4	89

[a] Temperature calculation (°C) following the calibration of Zheng (1993).

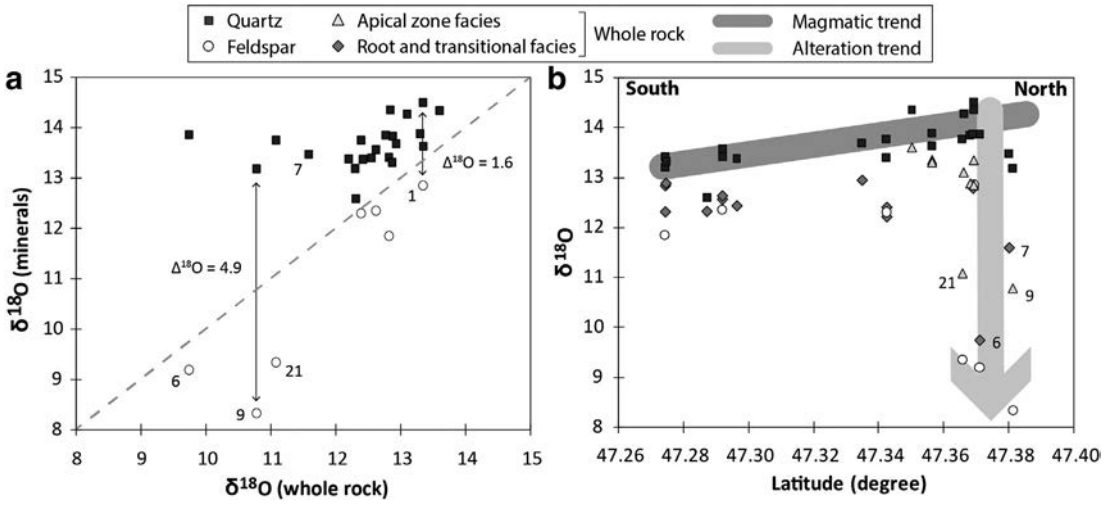

Fig. 11. (a) Minerals (quartz and feldspar) vs. whole-rock $\delta^{18}O$ values for the Guérande granite samples. $\Delta^{18}O_{(Qtz\text{-}Fds)}$ of two representative samples is indicated. (b) Evolution of the $\delta^{18}O$ values of whole-rock, quartz and feldspar of the samples as a function of the latitude.

GUE-3 and GUE-4 samples (D_{par} = 1.5 μm). The lower D_{par} value of the GUE-5 granite, which reflects a relatively faster rate of fission track annealing, could account for its younger apparent age. Data from the three leucogranite samples were used together to model the low-temperature thermal history of the Guérande leucogranite using the QTQt software (Fig. 12a) (Gallagher, 2012). The muscovite $^{40}Ar/^{39}Ar$ dates available on the Guérande leucogranite range from ca. 307 to ca. 303 Ma (Le Hébel, 2002). Consequently, based on the closure temperature for the muscovite $^{40}Ar/^{39}Ar$ geochronometer (Harrison et al., 2009), we assumed that the Guérande intrusion reached a temperature of 450 ± 100 °C at 300 ± 10 Ma and used these data as a constraint in the QTQt model. As suggested by the unimodal distribution of the fission track lengths (Fig. 12b, c, d), the Guérande leucogranite shows a monotonous cooling through the partial annealing zone (PAZ: 60–120 °C) at a rate of about 3 °C per Ma from ca. 195 to 175 Ma. Following this initial exhumation phase, the samples remained below 60 °C at or near the surface.

5. Discussion

5.1. Fluid-rock interaction in the Guérande leucogranite

In Fig. 11, the $\delta^{18}O$ values of all the quartz and most of the whole-rock and feldspar samples from the Guérande leucogranite samples display a correlation with the latitude. This evolution can in part be explained by the fractional crystallization process proposed by Ballouard et al. (2015). Indeed, the most differentiated samples (apical zone facies) are located in the northwestern part of the intrusion and the segregation of low-$\delta^{18}O$ biotite may increase the $\delta^{18}O$ of the evolving melt. Yet, Ballouard et al. (2015) showed that the chemical variation between the samples with the lowest and highest SiO_2 contents from the Guérande leucogranite can be explained by a fractionation of 15–30 wt.% of a cumulate composed of 0.44 Kfs (potassic feldspar), 0.31 Pl (plagioclase-An20), 0.21 Bt (biotite) and 0.04 Ap (apatite). Consequently, if the initial magma had a $\delta^{18}O$ value of 12.3‰ (e.g. sample GUE-17), the assemblage 0.75 Fs (Feldspar) + 0.21 Bt + 0.04 Ap would have had a $\delta^{18}O$ value of 11.4‰, taking a feldspar value of 12‰ (0.3‰ lower than the whole-rock) and considering equilibrium isotopic fractionation factors between the granitic melt, feldspar, biotite and apatite at 600 °C (Zheng, 1993; Valley, 2003). This indicates that in order to increase the $\delta^{18}O$ of the melt from 12.3 to 13.5‰, such as observed in the whole-rock values from our samples (Fig. 11), 55 wt.% of the cumulate would have to be separated from the granitic melt, a value that is too high when compared to our prediction. Alternatively, Ballouard et al. (2015) demonstrated that the apical zone of the Guérande leucogranite experienced a pervasive magmatic-hydrothermal alteration. Given that the Sr and Nd isotopic compositions of the Guérande leucogranite do not favor source heterogeneities or country rock assimilation (Ballouard et al., 2015), the high $\delta^{18}O$ values of the samples may relate to this hydrothermal event. This process was already proposed by Dubinina et al. (2010) to explain the high $\delta^{18}O$ values recorded in the apical zone samples from the Miocene leucogranites from the Caucasian mineral water region (Russia). The results of the geochemical modeling performed by these authors indicated that a change of up to 1‰ in the O isotope composition of a cooling granitic rock can occur, as a result of the interaction with exsolved magmatic fluids in isotopic equilibrium with the granitic melt, if this rock was localized in the zones that crystallized at an early stage (i.e. the outer zone of the intrusion).

Whereas the quartz retained its magmatic oxygen isotope composition ($\delta^{18}O_{Qtz}$ = 12.6–14.5‰), the whole-rock and feldspars of four samples from the north of the Guérande leucogranite (Fig. 11) have low $\delta^{18}O$ values ($\delta^{18}O_{WR}$ = 9.7–11.6‰; $\delta^{18}O_{Fs}$ = 8.3–9.3‰). The isotopic disequilibrium between quartz and feldspar recorded in these low $\delta^{18}O$ samples argue for an open system alteration (Gregory and Criss, 1986) with a sub-solidus interaction between the feldspar and a low $\delta^{18}O$ fluid. Indeed, close to the granite solidus temperature (about 600 °C), an exsolved magmatic fluid in equilibrium with a quartz with an $\delta^{18}O$ of 14‰ (Fig. 11) would have an $\delta^{18}O$ of around 12‰ (Zheng, 1993), and the feldspar is always enriched in ^{18}O with regard to H_2O

Table 5
Apatite fission track data. Pd is the density of the induced fission tracks (per cm^2) that would be obtained in each sample if its U concentration was equal to the concentration of the CN5 glass dosimeter. Ps and Pi are the spontaneous and induced track densities per cm^2 measured in the samples, respectively. The numbers in parentheses are the total number of tracks counted. U is the calculated average U concentration of apatite for each sample. P (χ^2) is the probability in % of χ^2 for ν degrees of freedom (where ν = number of crystals). The age is the central age. Dpar is the measured mean diameter (in μm) of the etched trace of the intersection of a fission track with the surface of the analyzed apatite crystal, measured parallel to the c axis.

Sample	Number of grains	ρd × 10^5 (cm^2)	ρs × 10^5 (cm^2)	ρi × 10^5 (cm^2)	U (ppm)	P (χ^2)	Age (Ma)	±2σ	MTL	SD	D_{par}
GUE-3	20	3.409 (6127)	35.998 (4579)	12.17 (1548)	44	33.4	168	7	13.39	0.96	1.5
GUE-4	20	3.457 (4485)	56.923 (3404)	18.411 (1081)	61	97.4	177	8	13.16	1.11	1.46
GUE-5	20	3.361 (5510)	55.589 (4058)	19.89 (1452)	69	35.2	156	6	13.22	0.99	1.19

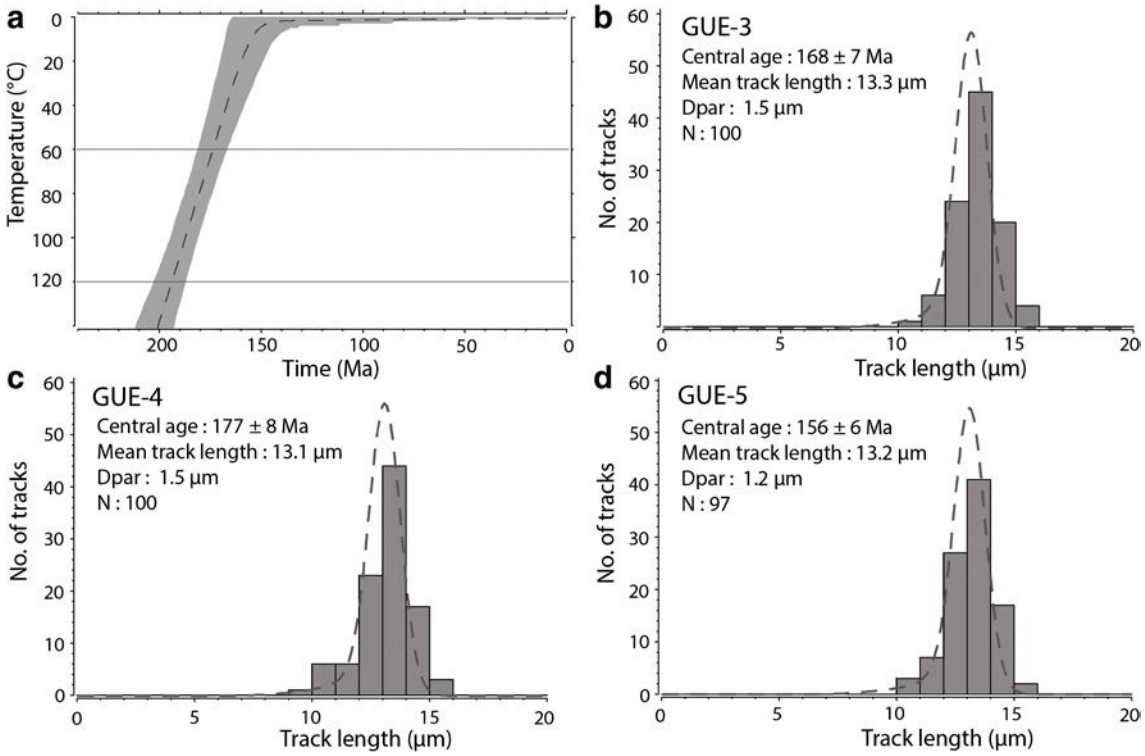

Fig. 12. Apatite fission track (AFT) thermal modeling of the Guérande granite samples using the QTQt software (Gallagher et al., 2009). (a) Time-temperature history of the Guérande granite using fission track data of the GUE-3, GUE-4 and GUE-5 samples. The horizontal lines represent the apatite partial annealing zone. The model is well constrained only in this temperature interval. The grey area represents the 95% credible interval for the thermal history. The dashed line represents the expected weighted mean thermal history. (b–c–d) Apatite fission track lengths histogram of the Guérande granite samples. The histograms represent the measured data while the dashed lines represent the calculated data. N: number of track lengths measured.

(by about 0.6 to 8‰ for temperature from 600 to 200 °C, respectively; Zheng, 1993). Thus, the only possibility to lower the $\delta^{18}O$ of feldspar (from ~12 to 9‰ in our samples, Fig. 11) during hydrothermal alteration is to involve a low $\delta^{18}O$ fluid. A temperature of alteration cannot be estimated using a feldspar-H_2O equilibrium, as the isotopic composition of the water and the fluid/rock ratio remains unknown. However, it is obvious that this fluid alteration event occurred when the granite was still at depth as the degree of fractionation of O isotope is anti-correlated with temperature. In fact, at a low temperature of 50 °C, the O isotope fractionation value between feldspar and water ($\Delta^{18}O_{feldspar-H_2O}$) is high and around 25‰ (Zheng, 1993). This fact precludes a decrease in the feldspar $\delta^{18}O$ values (i.e. from 12‰ to 9‰) during the fluid-feldspar interaction, as observed in the altered granite samples, even if we consider a fluid with an $\delta^{18}O$ value down to −10‰. The different behavior between quartz and feldspar is consistent with the fact that quartz is believed to be more resistant to an oxygen isotope exchange with fluids than feldspar (e.g. Gregory and Criss, 1986).

The most probable source for an input of low-$\delta^{18}O$ fluid is oxidizing meteoric waters. Indeed, this part of the Hercynian belt was likely above sea level at ca. 300 Ma (Lemarchand et al., 2012), and meteoric water infiltration at depth is well documented in the South Armorican Massif during the regional deformation from ca. 315 to 300 Ma (Tartèse and Boulvais, 2010; Tartèse et al., 2012, 2013; Lemarchand et al., 2012). Furthermore, as evidenced by Gapais et al. (1993) and Ballouard et al. (2015), the Guérande granite was emplaced syntectonically along an extensional deformation zone and is characterized by the presence of S/C and mylonitic extensional fabrics at the apex. All these features represent permeable planar discontinuities that can facilitate downward fluid infiltration.

To summarize, the Guérande leucogranite recorded two different events of fluid-rock interactions. The first at high temperature, already described by Ballouard et al. (2015), is recorded at the apical zone of the intrusion by an increase in incompatible elements such as Cs and Sn, secondary muscovitization and possibly an increase in the quartz and feldspar $\delta^{18}O$ values. This magmatic-hydrothermal event likely occurred during the emplacement of the Guérande leucogranite at ca. 310 Ma. The second fluid-rock interaction event, which took place at a lower temperature and in relation with a probable meteoric-derived fluid, mostly affected the deformed part of the northern side of the leucogranite and is evidenced by low-$\delta^{18}O$ feldspar and whole-rock values. As proposed by Tartèse and Boulvais (2010) for the neighboring Questembert leucogranite (Fig. 1), the pervasive S/C structures that affected the roof of the Guérande leucogranite likely facilitated the infiltration of oxidizing meteoric fluids at depth. The implication of these two hydrothermal events on the uranium mobility in the Guérande leucogranite and the formation of U mineralization will be discussed in the following section.

5.2. U leaching in the Guérande leucogranite

The U distribution in the Guérande leucogranite samples does not correlate with hydrothermally-immobile markers of fractional crystallization such as SiO_2, La or Th (Fig. 10b). Therefore, it is unlikely that the U distribution was solely controlled by magmatic processes. In the U vs. Cs (Fig. 13a), U vs. Sn (Fig. 13b) and U vs. K/Rb (Fig. 13c) diagrams, U shows a complex behavior with two different trends. The first trend mostly concerns the samples from the root and transitional facies whereas the second trend exclusively concerns the samples from the apical zone (Fig. 2).

In the trend for the root and transitional facies (Fig. 13), U is correlated with both Cs and Sn: U content increases from 2 to 7 ppm whereas Cs and Sn contents increase from 5 to 30 ppm and 3 to 20 ppm, respectively. In contrast, the K/Rb ratio is anti-correlated with U and decreases from 200 to 150. The positive correlation between U and Cs (Fig. 13a) or U and Sn (Fig. 13b) could be explained by a common magmatic evolution as U, Cs and Sn all behave as incompatible elements in a

peraluminous melt. However, the increase in the Cs content from 5 to 30 ppm can hardly be explained solely by fractional crystallization as it would require about 85% of mineral fractionation, an amount far higher than the 15–30% mineral fractionation estimated from geochemical modeling (Ballouard et al., 2015), and therefore likely implies some interaction with orthomagmatic fluids. Such correlations between U and incompatible elements such as Cs, Sn or Rb have already been observed in the St-Sylvestre peraluminous granite by Friedrich et al. (1987) and were attributed to the behavior of U during magmatic-hydrothermal processes. It is known that the simultaneous transport of U and elements such as Sn in the same fluid is not common because they generally display an opposite behavior, notably because their affinity toward the fluid depends on different oxygen fugacities. In fact, in a hydrothermal fluid, a low oxygen fugacity (fO_2 below the Ni-NiO buffer; i.e. a magmatic fluid exsolved from a peraluminous magma) favors the transport of Sn whereas a high oxygen fugacity (fO_2 above the hematite-magnetite buffer; i.e. a surface-derived hydrothermal fluid) favors the transport of U (Dubessy et al., 1987). However, the solubility of U in reducing magmatic fluid exsolved from a peraluminous melt increases greatly if these fluids are enriched in chlorine (Peiffert et al., 1996). Therefore, we suggest that the first evolution trend (Fig. 13) represents a concomitant enrichment in U, Sn, Cs and a decrease in the K/Rb ratio through combined fractional crystallization and an interaction with late-magmatic fluids.

In the apical zone facies trend (Fig. 13), the U contents remain rather low, below 4 ppm, whereas the Cs and Sn contents increase from 20 to 100 ppm and the K/Rb values decrease from 150 to 75. The difference in U contents between the apical zone in the northwestern part and the root in the southwestern part can also be observed on the airborne radiometric map (Fig. 10a). The hypothesis which can be proposed to explain the low U contents of the apical zone is that this area has been depleted by the dissolution of magmatic uranium oxides from evolved samples during a late fluid circulation event, at depth or during surface weathering. Indeed, the samples from both the root and transitional facies and the apical zone facies share the same magmatic history controlled by fractional crystallization (Ballouard et al., 2015), so the highest uranium content was expected in the highly evolved samples from the apical zone. Uraninite, which is one of the most easily leachable U-bearing mineral (e.g. Cuney, 2014), has not been directly observed in our samples but its presence has been reported by Ouddou (1984) in the northwestern part of the intrusion. In peraluminous magmas, uraninite typically crystallizes when bulk U contents reach around 10 ppm (Peiffert et al., 1996). Therefore, the maximum U content of 8 ppm observed in the studied Guérande samples does not seem to be representative of the initial value. Indeed, it is likely that values higher than 10 ppm have been reached by the most evolved samples during the magmatic-hydrothermal evolution of the intrusion, following the trend defined by the root and transitional facies in the U vs. Cs diagrams for example (Fig. 13a), and that later uraninite alteration at depth or during surface weathering lowered the U contents of the apical zone facies. Furthermore, most of the samples localized near the apical zone present Th/U ratios below or equal to 1 (Th/U = 0.3–1.3; Fig. 10b). Taking into account the possibility that some uranium has been leached out from these rocks, this implies that the initial (pre-leaching) ratios were even lower than that. Such low Th/U values suggest that most of the uranium was incorporated into uranium oxides (up to 80% for Th/U = 1) at the expense of refractory U-bearing minerals such as monazite or zircon (Friedrich et al., 1987).

As the solubility of uraninite in fluids is highly dependent on the oxygen fugacity (Dubessy et al., 1987), it is unlikely that the leaching of uranium oxide at the apical zone of the intrusion occurred during the interaction with reducing high temperature Cs- and Sn-rich fluids. This leaching of U could have occurred either during surface weathering or at depth during a hydrothermal alteration event with oxidizing surface-derived fluids, similar to what has been documented in the neighboring Questembert granite (Tartèse et al., 2013). A sub-solidus interaction with oxidizing fluids of meteoric origin is recorded via oxygen isotope analyses in samples from the northern edge of the Guérande leucogranite and three of these samples belong to the apical zone facies. This result suggests that even if surface weathering likely contributes to some U leaching at the apex of the granite, the sub-solidus alteration event at depth with surface-derived fluids recorded in the deformed facies likely liberated substantial amounts of uranium. Finally, the uranium behavior in the late magmatic/hydrothermal processes observed in the Guérande leucogranite, such as chloritization or albitization (Fig. 2), is unclear and no loss or gain of U has been noticed.

5.3. Metallogenesis

5.3.1. Mineralizing fluids

In the Pen Ar Ran deposit, the study of the primary fluid inclusions from a quartz comb associated with a uranium oxide-bearing vein provides precious information about the chemical and physical properties of the uranium mineralizing fluid.

Raman and microthermometric analyses indicate low salinity fluids with a NaCl eq. content between 1 and 6 wt.% in the liquid (Fig. 8a). The fluid inclusions contain H_2O-NaCl-O_2-H_2-(N_2) (Table 3) and display variable homogenization temperatures (T_h), ranging from 250 to 450 °C (Fig. 8b). In Fig. 8c, the inclusions homogenizing in the vapor phase (T_h ~ 400–450 °C) generally display a higher salinity (3–6 wt.% NaCl eq.) than those homogenizing in the liquid phase (Th ~ 350–400; salinity ~1–4 wt.% NaCl eq.) and this observation could suggest a mixing between a low temperature-low salinity fluid and a high temperature-moderate salinity fluid. A mixing process between meteoric-derived and basinal fluids has been invoked for the genesis of numerous uranium deposits of the EHB such as in the French Massif Central (Turpin et al., 1990) or Bohemian Massif (Kříbek et al., 2009; Dolníček et al., 2013). For the Pen Ar Ran deposit, the low salinity of the fluid inclusions

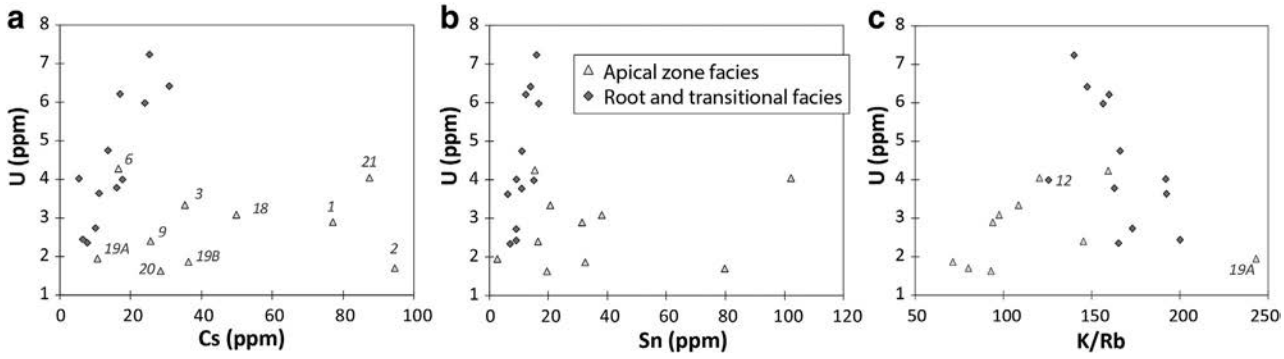

Fig. 13. Evolution of the U whole-rock content of the Guérande granite samples as a function of geochemical tracers sensitive to magmatic differentiation and interaction with orthomagmatic fluids.
Data from Ballouard et al. (2015).

(1–6 wt.% eq. NaCl) suggests that a fluid with a meteoric origin was involved in the genesis of the mineralization, but does not imply the involvement of basinal brines. In contrast, the elevated T_h measured on the inclusions suggest a contribution of deep fluids with probably metamorphic origins. On the other hand, O_2 and H_2 gases are both characteristic of the radiolysis of water that has been in contact with uranium minerals (Dubessy et al., 1988). Their presence in fluid inclusions can likely result from the heterogeneous entrapment of radiolytic O_2 and H_2 and this process could account for the variability in the measured T_h (Derome et al., 2005). In Fig. 8d, T_h correlate with the degree of volatile filling in the inclusion suggesting that the highest T_h are mostly disturbed by radiolytic gases and that the lowest T_h (250–350 °C) should be taken as the best estimate for the trapping temperature. As a consequence, the fluid inclusion data alone does not allow us to unambiguously interpret the highest T_h measured in the fluid inclusions as indicating a mixing of fluids with various origins or the entrapment of radiolytic H_2 and O_2. In any case, both hypothesis are in agreement with the contribution of low salinity meteoric fluids with temperatures in the range of 250–350 °C. These temperatures are relatively high when compared to other vein type deposits from the French Hercynian belt, which are generally in the range of 150–250 °C (Cathelineau et al., 1990), and therefore, reflect specific conditions for the Pen Ar Ran mineralization.

Around 300 Ma ago (first mineralizing event in the Pen Ar Ran deposit, see Section 5.3.2 for details), the metavolcanics that host the Pen Ar Ran uranium mineralization were part of the brittle upper crust and were already below 450 °C, based on the muscovite ^{40}Ar-^{39}Ar dates of 311.8 ± 0.5 Ma and 313.4 ± 0.4 Ma obtained on the porphyroids from the Piriac graben (Le Hébel, 2002) and the closure temperature of the muscovite ^{40}Ar-^{39}Ar geochronometer (Harrison et al., 2009). However, this period around 300 Ma ago marks the end of the extension regime in the South Armorican Massif (e.g. Gapais et al., 2015), and notably the end of the ductile deformation in the Guérande leucogranite, as attested by muscovite ^{40}Ar-^{39}Ar dates of 304 ± 0.6 Ma and 303.6 ± 0.5 Ma on a S/C granite and on a sheared granite from the northwestern part of the intrusion, respectively (Le Hébel, 2002). The exhumation of the lower crust in the South Armorican Massif during extension likely induced an increase in the geothermal gradient at a regional scale. Moreover, this period was accompanied by a late magmatic event at depth in the Guérande region as demonstrated by the emplacement of leucogranitic dykes at 302.5 ± 2.0 Ma (Ballouard et al., 2015), which also likely contributed to this abnormal heat flow in the environment of the deposit. Finally, according to the apatite fission track thermal modeling, the Guérande leucogranite was still at a temperature above 120 °C, so at a depth greater than about 4 km (for a geothermal gradient of 30 °C/km), 200 Ma ago (Fig. 12).

5.3.2. Timing of the uranium mineralization

The U-Pb analyses performed on the uranium oxide samples from the Pen Ar Ran and Métairie-Neuve deposits revealed three different events (Fig. 9) dated at 296.6 ± 2.6 Ma (PAR-spherulitic: core), 286.6 ± 1.0 Ma (Métairie-Neuve) and 274.6 ± 0.9 Ma (PAR-pseudo-spherulitic and PAR-prismatic), respectively. The low content in FeO and SiO_2 of the uranium oxides Ur1 (Table 2) and the concordance of most of the U-Pb analyses (Fig. 9) suggest that these uranium oxides did not undergo a significant post-crystallization alteration and that the concordia dates obtained in this study reflect the crystallization age of the uranium-oxides.

In the uranium oxide "PAR-spherulitic" sample, the CaO content increases from the core to the rim of the spherules and is inversely correlated with the PbO content (Fig. 6a). This inverse correlation is likely primary, reflecting the concentric zoning displayed by the spherules in the BSE images and could account for the lower mean atomic mass (darker color) of the rims compared to the cores of the spherules (Fig. 5a). The REE contents of the spherules (Σ REE) also decrease from the core to the rim (Table 2 and Fig. 6b) and likely reflect the composition of the mineralizing fluid. The saddle shape displayed by some REE patterns (Fig. 6b) is however not specific of the location of the analyses. U-Pb analyses performed on the cores of the spherules allow us to calculate their crystallization at 296.6 ± 2.6 Ma (Fig. 9a). The two sub-concordant analyses performed on the rim of the spherules yield apparent $^{206}Pb/^{238}U$ dates of 270.6 ± 2.4 Ma and 282.7 ± 2.8 Ma (Figs. 5a and 9a) that may reflect slight Pb loss.

The two other samples from the Pen Ar Ran deposit ("PAR-pseudo-spherulitic" and "PAR-prismatic") display major element compositions (CaO and PbO contents; Fig. 6a) and REE patterns (Fig. 6c) mostly comparable with those from the "PAR-spherulitic" sample. In particular, the REE patterns and REE concentrations obtained on the rim of the spherules of the "PAR-spherulitic" sample are almost identical to those obtained on the "PAR-pseudo-spherulitic" sample, likely reflecting a similar mineralization condition. U-Pb analyses on the "PAR-pseudo-spherulitic" and "PAR-prismatic" samples allow us to define their crystallization age at 274.6 ± 0.9 Ma.

As a consequence, we suggest that at least two U mineralizing events occurred at Pen Ar Ran: a first one at 296.6 ± 2.6 Ma and a second one at 274.6 ± 0.9 Ma. These two different events, separated by ca. 20 Ma, are surprising but in fact consistent with the description of Cathelineau (1981) who described that the prismatic facies postdated the spherulitic facies in the Pen Ar Ran deposit. The Pb loss recorded by the rims on some of the spherules from the "PAR-spherulitic" sample, which yield apparent $^{206}Pb/^{238}U$ dates of 270.6 ± 2.4 Ma and 282.7 ± 2.8 Ma, possibly occurred during the second mineralizing event.

The concordia age of 286.6 ± 1.0 Ma obtained on the uranium oxides from the Métairie-Neuve deposit probably dates another mineralizing event. The REE patterns of the samples suggest different conditions for the mineralization than in the Pen Ar Ran deposit. For example, the positive Eu anomaly could reflect more oxidizing conditions at the moment of uranium precipitation. Indeed, the much larger ionic radius of Eu^{2+}, compared to Eu^{3+}, limits the substitution of Eu^{2+} for U^{4+} in the uranium oxide structure. Therefore, the Eu anomaly in uranium oxide could be a good proxy for oxygen fugacity in the U precipitation environment as it reflects the oxidation state of Eu (Fryer and Taylor, 1987; Eglinger et al., 2013).

On a larger scale, the dates of ca. 285 Ma and ca. 275 Ma obtained for the uranium mineralizing events in the Guérande district (Métairie-Neuve and Pen Ar Ran deposits) are comparable with those obtained by Cathelineau et al. (1990) in other vein type deposits from the Mortagne district in the South Armorican Massif (Fig. 1) and French Massif Central with a major stage of U mineralization between 290 and 260 Ma. In the Bohemian massif and Black Forest, most vein-type uranium deposits are also Permian in age (e.g. Carl et al., 1983; Hofmann and Eikenberg, 1991; Velichkin and Vlasov, 2011 and reference therein).

5.4. Is the Guérande leucogranite the source for the uranium of the Pen Ar Ran deposit?

Based on the REE patterns of uranium oxides from the Pen Ar Ran mineralization, Bonhoure et al. (2007) proposed that the metavolcanics of the Piriac graben (Vendée porphyroids; Fig. 3) were the likely source for the uranium concentrated in this deposit. Our study does not favor this hypothesis as we did not obtain the same REE patterns as these authors (i.e. no positive anomaly in Sm, Eu and Gd in our REE patterns; Fig. 6). Because of this difference, we tested our LA-ICP-MS analytical protocol using an UO_2 reference material (Mistamisk, Lach et al., 2013), and did not notice any significant difference between the measured REE contents and the reference ones. Consequently, we believe that our data are accurate.

Moreover, the Th/U ratios obtained on the Vendée porphyroids using radiometric data and ICP-MS analyses are rather high, between 2 and 5 (Fig. 10b). These Th/U ratios favor the crystallization of refractory U-bearing minerals at the expense of uranium oxides from which U is

more easily leachable in the presence of hydrothermal fluids (Friedrich et al., 1987; Cuney, 2014). Also, the Th/U ratios of the porphyroids from the Piriac graben (Th/U between 2 and 5) are comparable with those obtained for the same Ordovician metavolcanics elsewhere in the South Armorican Massif (Th/U between 2 and 15; Fig. 10b), which does not favor U leaching from the Guérande district metavolcanics. The HP-LT metamorphism, which affected the Vendée porphyroid formation around 360 Ma (Bosse et al., 2005; Le Hébel, 2002), also preclude the presence of easy leachable volcanic glass with free U in the metavolcanics at ca. 300 Ma. It should be noted that the presence of uraninite was never described for these porphyroids. Finally, the fluid inclusion analyses and stable isotope characterization of the Vendée porphyroid formation at a regional scale, including the Piriac locality (Le Hébel et al., 2007), indicate that this unit was deformed within a system closed to fluids at the time of the HP-LT metamorphism and during the Guérande leucogranite emplacement, precluding significant chemical alteration of these porphyroids.

In the black shales, the Th/U ratios between 0.5 and 2 (Fig. 10b) point to the presence of free U but the highly reducing character of these lithologies, combined with the effect of the HP-LT metamorphism, preclude a high U mobility.

In the Guérande leucogranite, the low Th concentrations reflect the magmatic fractionation of monazite and zircon (see for example the good correlation of Th with La, Zr and SiO_2 documented by Ballouard et al., 2015, their Fig. 9). This magmatic evolution likely induced the increase in the U content in the differentiated melts and led to uraninite saturation as only a limited amount of uranium is incorporated in monazite and other accessory minerals such as zircon or apatite (Cuney, 2014; Friedrich et al., 1987). However, the actual U content of the Guérande leucogranite is lower than what is expected for uraninite saturation. One way to understand this apparent paradox is to consider that uraninite actually crystallized in the differentiated melts when the uranium content reached around 10 ppm or more (some uraninite grains have been actually observed in a drill core, see above), but uraninite was then dissolved, likely by infiltrating fluids, and a significant fraction of the bulk uranium leached out from the granite. In this scenario (magmatic evolution overprinted by hydrothermal alteration and surface weathering), the Th/U ratios may have widely varied, resulting in the measured low and erratic values ($0.2 < Th/U < 2.1$; ICP-MS data from Ballouard et al., 2015; Fig. 10b).

Several lines of evidence favor the Guérande leucogranite as the main source for the uranium of the Pen Ar Ran deposit:

(1) The U airborne radiometric map (Fig. 10a) and trace element geochemistry (Fig. 13) suggest that some U has been leached out from the highly differentiated facies from the apical zone of the intrusion.
(2) Oxygen isotope analyses show that a sub-solidus alteration event with surface-derived fluids affected the deformed facies from the roof of the intrusion when this granite was still at depth (Fig. 11). These oxidizing fluids were likely able to dissolve the magmatic uranium oxides and to liberate U (Dubessy et al., 1987).
(3) The REE patterns obtained on the uranium oxides from the Pen Ar Ran deposit (Fig. 6b and c) are overall comparable with the patterns of the uranium oxides from other vein-type deposits from the French Hercynian belt where uranium is expected to originate from the leaching of the surrounding leucogranites (Mercadier et al., 2011). The saddle shape displayed by LREE on some spectra obtained on the "PAR-spherulitic" sample (Fig. 6b) and two samples from Métairie-Neuve (Fig. 6d) point to peculiar REE fractionation processes likely resulting from a variation of the physical-chemical conditions in the mineralizing fluids or in the U precipitation environment. The parameters controlling the solubility of REE in aqueous fluids are various (temperature, oxygen fugacity, presence of ligands…) and it is difficult to precisely determine which one is responsible for this peculiar LREE behavior. Moreover, the interaction of the mineralizing fluid with various lithologies such as leucogranites, micaschists, metavolcanics and black shales, in which REE can be host in different mineral phases, could induce specific fractionation between REE.
(4) The U-Pb dating on uranium oxides from the Pen Ar Ran deposit revealed that a first mineralizing event occurred at 296.6 ± 2.6 Ma. This event was sub-synchronous with an early hydrothermal circulation event (constrained by muscovite ^{40}Ar-^{39}Ar dates obtained on deformed granite samples and on a quartz vein from the apex; Le Hébel, 2002) and with the emplacement of late leucogranitic dykes in the Guérande leucogranite at ca. 303 Ma (Ballouard et al., 2015; Fig. 14).
(5) Fluid inclusions analyses on a quartz comb associated with a uranium oxide-bearing vein from the Pen Ar Ran deposit argue for low-salinity mineralizing fluid, consistent with the involvement of meteoric fluids (Fig. 8a). The elevated estimated fluid trapping temperatures (250–350 °C) reflect an abnormal heat flux in the near environment of the deposit, possibly reflecting lower crust exhumation during regional extension and magmatic activity at depth, as reflected by the emplacement of the leucogranitic dykes at ca. 303 Ma.

5.5. Mass balance calculation

The oxygen isotope, radiometric data and trace element analyses in the Guérande leucogranite combined with the geochemical and geochronological characterization of the uranium mineralization, lead us to the hypothesis that the highly evolved deformed facies from the apical zone of the intrusion represents a likely source for the U found in the surrounding deposits. In the apical zone of the intrusion, pervasive solid-state deformation is mostly observed to the north of the graben in the harbor of Piriac-sur-Mer (sample GUE-9, Fig. 2). In this area, we can consider, based on cartographic criteria, that the extensional deformation zone, with an approximate thickness of 100 m and a minimum extension of 2×10^6 m^2, has a minimum volume of 2×10^8 m^3. If we consider that this volume had an initial uranium content of 20 ppm (as attested by the drill core sample of Ouddou, 1984), and that 50% of this uranium was hosted by uranium oxides, this volume represents an initial available mass of U of about 5400 t. Around 600 t of U have been extracted from the Pen Ar Ran deposit which is located structurally above the apical zone of the intrusion (Figs. 2 and 3). Therefore, this mass balance estimate suggests that most, if not all, of the U extracted from the Pen Ar Ran deposit could have originated from the leaching of the highly evolved deformed facies of the apical zone of the Guérande leucogranite.

5.6. Uranium mineralizing process

In Fig. 14, we have reported the major events that occurred in the Guérande district from 310 to 270 Ma. These events and their implications for the uranium metallogenesis are also represented as a drawing in Fig. 15.

At ca. 310 Ma, the Guérande leucogranite was emplaced in a mainly top to the north extensional deformation zone (Fig. 2). This tectonic-magmatic event was contemporaneous with the beginning of a synconvergence crustal thinning in the southern part of the Armorican Massif and with dextral wrenching along the South Armorican Shear Zone (Gumiaux et al., 2004; Gapais et al., 2015) (Fig. 1). The main N-S stretching direction in the Guérande area is different from the overall W-E stretching direction recorded in the South Armorican domain and could be the consequence of a regional sub-horizontal flattening regime (Ballouard et al., 2015; Gapais et al., 2015). This crustal extension event, which led to the development of core complex cored by migmatites and

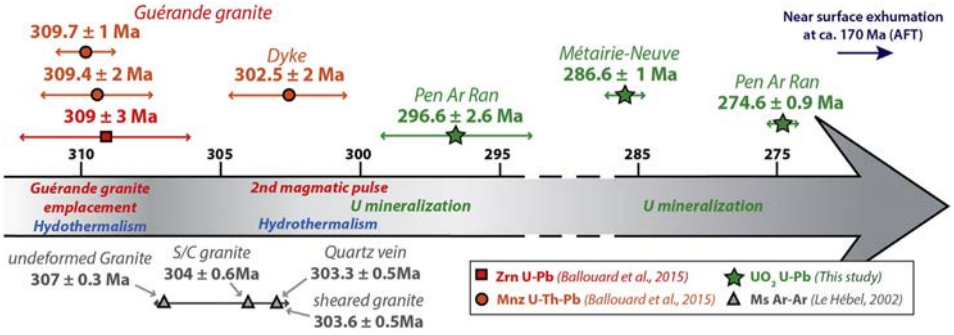

Fig. 14. Chronological sequence of the different events that occurred in the Guérande district between 310 and 270 Ma.

syntectonic leucogranites, such as the Saint-Nazaire migmatites and the Guérande leucogranite (Fig. 2), was likely accommodated by brittle extensional tectonics in the upper crust as tentatively illustrated in Fig. 15. During the emplacement of the Guérande leucogranite, fractional crystallization and interaction with late magmatic fluids allowed for the crystallization of magmatic uranium oxides at the apical zone of the intrusion.

At ca. 300 Ma, the deformation was still active in the Guérande region, as evidenced by the muscovite ^{40}Ar-^{39}Ar dates of 304 ± 0.6 Ma and 303.6 ± 0.5 Ma obtained on a S/C granite and a sheared granite, respectively (Le Hébel, 2002), but with probably a transition from a ductile to a brittle regime. At a regional scale, this date also marks the end of the ductile deformation along the South Armorican Shear Zone and the Quiberon detachment (Gapais et al., 2015) (Fig. 1). In the Guérande region, meteoric fluids could have percolated into the fault zones and in the deformed facies of the leucogranite as the S/C structures likely facilitate the infiltration of surface derived waters at depth (e.g. Tartèse and Boulvais, 2010). Moreover, the isotopic study of Lemarchand et al. (2012) on syntectonic quartz veins along the South Armorican Shear Zone suggests that meteoric fluids were involved in their formation, and that a significant relief in this part of the Armorican Massif at this period likely facilitated meteoric fluid circulations at depth. In Fig. 15, these oxidizing surface derived fluids became enriched in U by leaching the magmatic uranium oxides from the evolved facies of the apical zone of the Guérande leucogranite. When these fluids percolated in the structures at the contact between the metavolcanics and reducing black shales, uranium was precipitated. In the Pen Ar ran deposit, the U mineralization filled brittle structures which correspond to the riedel or tension gashes of the N 110° strike-slip faults (Cathelineau, 1981) (Fig. 4), showing that the mineralizing processes were deeply linked with the tectonic activity. The heat flux that allows for the convection of these fluids was probably provided by late magmatism, as evidenced by the intrusion of leucogranitic dykes at about 300 Ma, and at a larger scale, by the exhumation of a hot lower crust during the late-orogenic extension of this part of the Hercynian Belt (e.g. Gapais et al., 2015).

The recognition that U mineralizing events occurred until ca. 275 Ma in the Guérande district suggests that oxidizing surface-derived fluids have continued to percolate, probably by pulse, in the Guérande leucogranite during a long time period of ca. 25 Ma and that a discreet extensional tectonic activity was present until the middle Permian. Tectonic and hydrothermal events have not yet been documented in

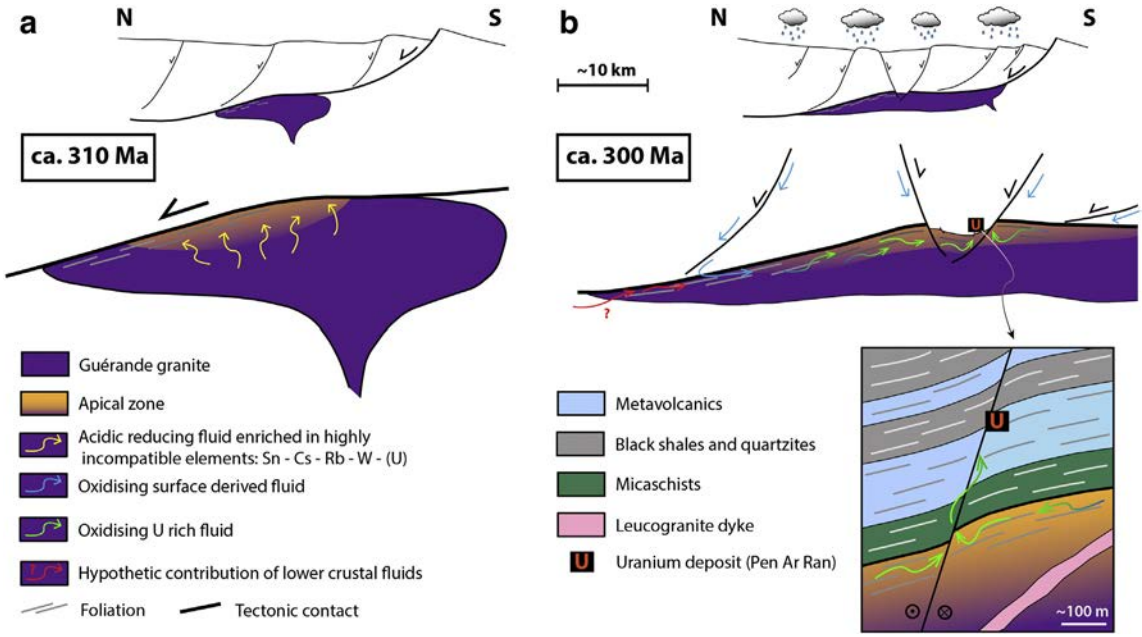

Fig. 15. Drawing representing the uranium behavior evolution in the Guérande granite from ca. 310 to ca. 300 Ma. (a) At ca. 310 Ma, the Guérande leucogranite emplaces and differentiates in an extensional deformation zone. The most evolved U-rich magmas migrate toward the apical zone of the intrusion. U enrichment at the apical zone is enhanced by the interaction with orthomagmatic fluids that trigger the crystallization of "magmatic" uranium oxides. (b) At ca. 300 Ma, the regional deformation is still active. Oxidizing fluids derived from the surface circulate in the deformed facies of the apical zone of the Guérande leucogranite and become enriched in U due to leaching of magmatic uranium oxides. The heat provided by a late magmatic event, as expressed by the emplacement of late leucogranite dykes, likely contributes to maintain the convective fluid circulations. U-rich fluids migrate toward the faults and precipitate U at the contact with reducing environments, such as the black shales. Such a hydrothermal system was likely active until ca. 275 Ma.

this part of the Armorican Massif during the Lower Permian but apatite fission track analysis reveals that the Guérande leucogranite was still at depth at that time (Fig. 12). Moreover, lithospheric extensional events are well described during this period, for example in the French Massif Central, and induced the coeval exhumation of metamorphic domes and the formation of Late Carboniferous to Permian continental sedimentary basins with a dominant half-graben structural style (e.g. Van Den Driessche and Brun, 1989, 1992; Faure, 1995).

On a continental scale, the Permian period hosts the main U mineralizing events for the EHB (Fig. 16) and most U ore deposits in the Moldanubian zone or terranes with Gondwanian affinities are sub-synchronous or postdate, up to 35 Ma, the end of peraluminous leucogranitic magmatism. One hypothesis is that Carboniferous peraluminous leucogranites, which are characterized by high heat production due to their high content in radioactive elements (Vigneresse et al., 1989; Jolivet et al., 1989), can maintain the convection of surface derived hydrothermal fluids at depth several million years after their emplacement as long as these intrusions remain buried at depth. Moreover, the Permian period in Europe is characterized by an abnormal heat flux in the mantle, evidenced, for example, by the emplacement of the Cornubian Batholith in southwest England from ~295 Ma to 275 Ma (Chen et al., 1993) and the emplacement of post-orogenic granitoids in Iberia from 310 to 285 Ma (Fernández-Suárez et al., 2000; Gutiérrez-Alonso et al., 2011) (Fig. 16). This abnormal mantellic heat flux may have helped maintain an elevated geothermal gradient.

5.7. Implication for the Mesozoic evolution of the Armorican Massif

The apatite fission track analysis shows that the Guérande leucogranite experienced a slow cooling from 120 to 60 °C (PAZ) from 210 to 175 Ma and that this intrusion remained below 60 °C after 175 Ma (Fig. 12). The exhumation of the Guérande leucogranite between the Upper Triassic and lower Jurassic could be related to the extensional crustal deformation events that have been well recorded in the sediments of the Paris Basin (e.g. Guillocheau et al., 2000). Based on a detailed mapping of planation surfaces in the Armorican Massif, Bessin et al. (2015) showed that at least two major burring and denudation phases occurred in the Armorican Massif during the Mesozoic-Cenozoic: the burial during the Middle to Upper Jurassic time was followed by a denudation episode during the early Cretaceous then a burial during late Cretaceous was followed by a denudation event from the latest Cretaceous to Eocene times. These authors also suggest that the burial depths of the sediments during the Middle to Upper Jurassic and Late Cretaceous times were shallow due to the lack of a significant volume of Early Cretaceous and Cenozoic siliciclastic sediments in the basins surrounding the Armorican Massif. Our data

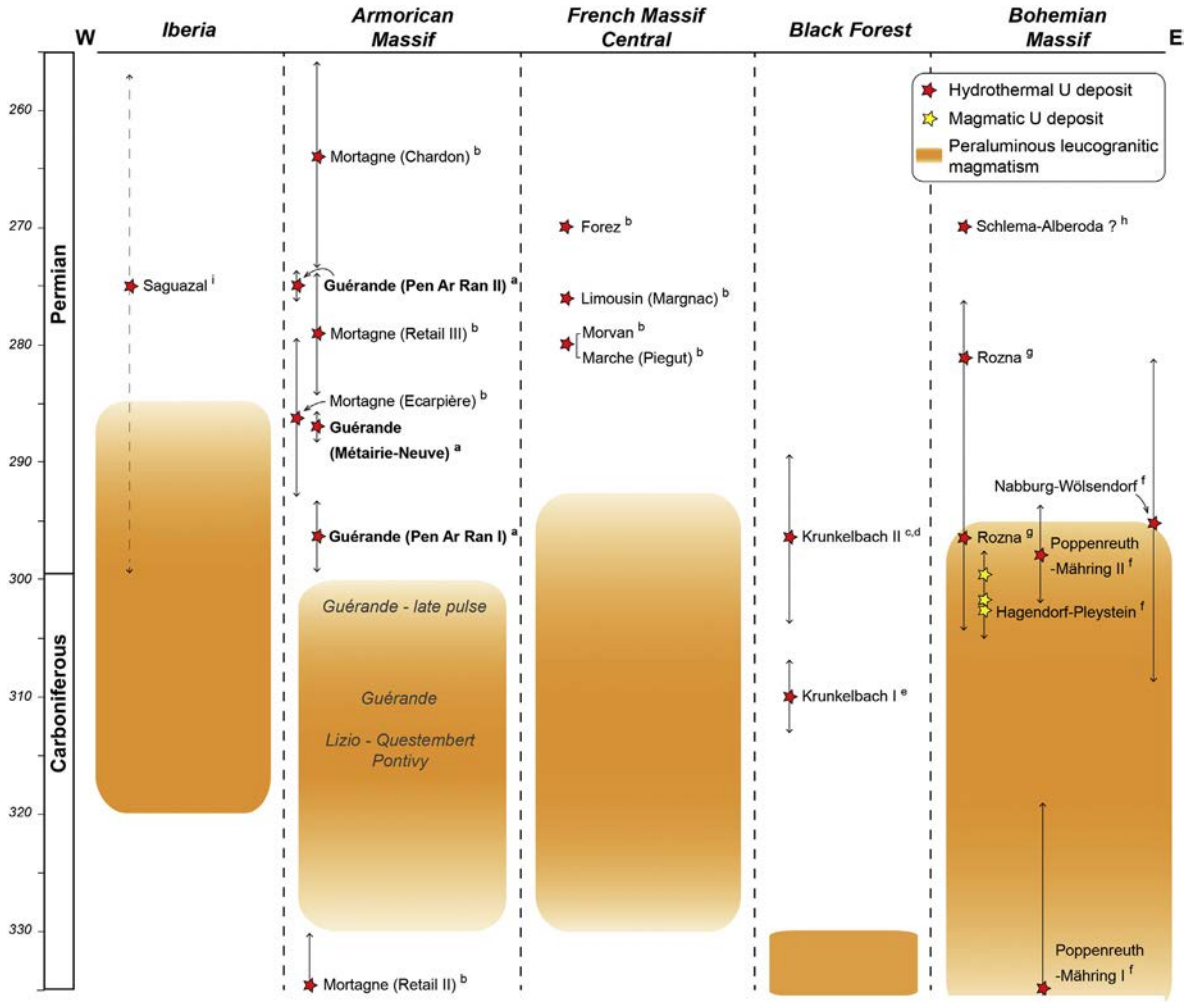

Fig. 16. Chronological sequence comparing the ages of U mineralization with the period of peraluminous leucogranitic magmatism in the west European Hercynian belt. The period of leucogranites emplacement is from Fernández-Suárez et al. (2000); Gutiérrez-Alonso et al. (2011) for the Iberian Peninsula, Ballouard et al. (2015) and reference therein for the Armorican Massif, Couzinié et al. (2014); Laurent et al. (2015) and Teyssier et al. (2015) for the French Massif Central, Schaltegger (2000) for the Black Forest, Finger et al. (1997) and Breiter (2012) for the Bohemian Massif. The ages of U mineralization are from (a) this study, (b) Cathelineau et al. (1990), (c) Hofmann and Eikenberg (1991), (d) Eikenberg (1988) (e) Wendt et al. (1979), (f) Dill (2015) and reference therein (g), Kříbek et al. (2009), (h) Velichkin and Vlasov (2011) and reference therein, (i) Pérez Del Villar and Moro (1991).

confirm this hypothesis as no thermal event above 60 °C is recorded by the samples after 175 Ma, suggesting that the burial depth of the sediments was lower than 2–3 km if we consider a geothermal gradient of 20 °C/km in the sediment cover. The Lower-Mesozoic exhumation event recorded by apatite fission tracks analyses on the Guérande granite samples does not seem responsible for a uranium remobilization in the area.

6. Conclusion

The multi-approach study on the leucogranite and uranium deposits from the Guérande district led us to the following conclusions:

(1) The trace element geochemistry and airborne radiometric data on the Guérande leucogranite show anomalously low uranium content in the highly evolved facies from the apical zone. These low U contents are likely a consequence of uranium leaching at the apex of the intrusion during hydrothermal alteration at depth, although we cannot exclude that some of the uranium was leached out during sub-surface weathering. Previous uranium enrichment at the apical zone was due to a fractional crystallization process and an interaction with late magmatic fluids.
(2) The ICP-MS and radiometric analyses carried out on the Guérande leucogranite show low Th/U values (<2) which are in favor of the crystallization of magmatic uranium oxide.
(3) The oxygen isotope study performed on the Guérande leucogranite shows an isotopic disequilibrium between feldspar and quartz in the deformed samples from the roof of the intrusion. The low $\delta^{18}O$ of the feldspar reflects a sub-solidus hydrothermal alteration by meteoric fluids whereas the quartz retained its magmatic signature. Solid-state extensional deformation likely facilitated the infiltration of surface-derived fluids at depth. These oxidizing fluids were able to leach uranium from the deformed facies sufficiently evolved to contain crystallized magmatic uranium oxides.
(4) The mass balance calculation suggests that the deformed facies from the apical zone could have liberated a sufficient amount of uranium to form the Pen Ar Ran deposit (i.e. 600 t UO_2 mined).
(5) The fluid inclusion analyses on a quartz comb from a uranium oxide-bearing vein of the Pen Ar Ran deposit revealed a low salinity mineralizing fluid consistent with the contribution of meteoric waters. The elevated estimated fluid trapping temperatures (250 to 350 °C) reflect an abnormal heat flux, likely related to the regional extensional regime that prevailed at the time of their circulation and possibly to magmatic activity at depth, in the near environment of the deposit.
(6) The REE patterns obtained on the uranium oxides from the Pen Ar Ran deposit are mostly comparable with the patterns of other vein-type deposits from the French Hercynian belt and are not consistent with the metavolcanic source previously proposed for the uranium of the deposit.
(7) The geochemistry and U-Pb dating on the uranium oxides from the Pen Ar Ran and Métairie-Neuve deposits revealed three mineralizing events. The first event, dated at 296.6 ± 2.6 Ma, is sub-contemporaneous with hydrothermal circulations and a late magmatic event in the Guérande leucogranite at ca. 303 Ma. The two following mineralizing events occurred at ca. 285 and 275 Ma. The apatite fission track analysis indicates that the Guérande leucogranite was still at depth, above 120 °C, when these two mineralizing events occurred.

All these new data allow us to propose the Guérande leucogranite as the main source for the uranium of the Pen Ar Ran and Métairie-Neuve deposits. We suggest that the uranium was leached out from the deformed facies of the apical zone by oxidizing meteoric fluids at depth. The U leached by these fluids could have then precipitated in the reducing environment constituted by the surrounding black shales (Pen Ar Ran) or graphitic quartzite (Métairie-Neuve) to form the uranium deposits. As the different mineralizing events can be separated by ca. 25 Ma, percolation of oxidizing surface-derived fluids could have occurred, probably by pulses, during a long period of time when the Guérande leucogranite was still at depth. The model proposed in this study to constrain the U mineralizing process in deposits spatially associated with the Guérande leucogranite could possibly be applied to other U deposits related to peraluminous granites in the Hercynian Belt. Indeed, the ages of the U mineralizing events in the Guérande region (300–275 Ma) are in the same range as most U deposits in the European Hercynian Belt (e.g. French Massif Central and Erzgebirge). In Europe, this period could be characterized by regional scale infiltration of oxidizing meteoric fluids down to upper-middle crustal levels that were then able to mobilize uranium from the peraluminous granites. To verify this hypothesis, the present study must be applied to other U fertile intrusions, such as the Pontivy granite in the case of the Armorican Massif for example.

Supplementary data to this article can be found online at http://dx.doi.org/10.1016/j.oregeorev.2016.06.034.

Acknowledgments

This work was supported by the 2012-2013 NEED-CNRS (AREVA-CEA) and 2014-CESSUR-INSU (CNRS) grants attributed to Marc Poujol. We are grateful to AREVA (in particular to D. Virlogeux and J-M. Vergeau) for providing uranium oxide samples and for fruitful discussions. Many thanks to S. Matthieu, L. Salsi, O. Rouer from the SCMEM (GeoRessources – Nancy), M.C. Caumon (GeoRessources - Nancy) and B. Putlitz (UNIL - Lausanne) for technical support during the SEM, EPMA, Raman and oxygen isotope analyses. We thank G. Martelet (BRGM) for providing the airborne radiometric data. The manuscript benefited from the comments of two anonymous reviewers and the associated editor H.G. Dill. S. Mullin, a professional translator, proof-read the manuscript.

References

Audren, C., Jegouzo, P., Barbaroux, L., Bouysse, P., 1975. La Roche-Bernard, 449. Bureau de Recherches Géologiques et Minières.
Ballèvre, M., Bosse, V., Ducassou, C., Pitra, P., 2009. Palaeozoic history of the Armorican Massif: models for the tectonic evolution of the suture zones. Compt. Rendus Geosci. 341, 174–201. http://dx.doi.org/10.1016/j.crte.2008.11.009.
Ballèvre, M., Fourcade, S., Capdevila, R., Peucat, J.-J., Cocherie, A., Fanning, C.M., 2012. Geochronology and geochemistry of Ordovician felsic volcanism in the Southern Armorican Massif (Variscan belt, France): implications for the breakup of Gondwana. Gondwana Res. 21, 1019–1036. http://dx.doi.org/10.1016/j.gr.2011.07.030.
Ballouard, C., Boulvais, P., Poujol, M., Gapais, D., Yamato, P., Tartèse, R., Cuney, M., 2015. Tectonic record, magmatic history and hydrothermal alteration in the Hercynian Guérande leucogranite, Armorican Massif, France. Lithos 220–223, 1–22. http://dx.doi.org/10.1016/j.lithos.2015.01.027.
Barsukov, V.L., Sokolova, N.T., Ivanitskii, O.M., 2006. Metals, arsenic, and sulfur in the Aue and Eibenstock granites, Erzgebirge. Geochem. Int. 44, 896–911. http://dx.doi.org/10.1134/S0016702906090059.
Bernard-Griffiths, J., Peucat, J.J., Sheppard, S., Vidal, P., 1985. Petrogenesis of Hercynian leucogranites from the southern Armorican Massif: contribution of REE and isotopic (Sr, Nd, Pb and O) geochemical data to the study of source rock characteristics and ages. Earth Planet. Sci. Lett. 74, 235–250. http://dx.doi.org/10.1016/0012-821X(85)90024-X.
Berthé, D., Choukroune, P., Jegouzo, P., 1979. Orthogneiss, mylonite and non coaxial deformation of granites: the example of the South Armorican Shear Zone. J. Struct. Geol. 1, 31–42. http://dx.doi.org/10.1016/0191-8141(79)90019-1.
Bessin, P., Guillocheau, F., Robin, C., Schroëtter, J.-M., Bauer, H., 2015. Planation surfaces of the Armorican Massif (western France):Denudation chronology of a Mesozoic land surface twice exhumed in response to relative crustal movements between Iberia and Eurasia. Geomorphology 233, 75–91. http://dx.doi.org/10.1016/j.geomorph.2014.09.026.
Bodnar, R.J., 1993. Revised equation and table for determining the freezing point depression of H_2O-Nacl solutions. Geochim. Cosmochim. Acta 57, 683–684. http://dx.doi.org/10.1016/0016-7037(93)90378-A.
Bonhoure, J., Kister, P., Cuney, M., Deloule, E., 2007. Methodology for rare earth element determinations of uranium oxides by ion microprobe. Geostand. Geoanal. Res. 31, 209–225. http://dx.doi.org/10.1111/j.1751-908X.2007.00865.x.

Bonijoly, D., Perrin, J., Truffert, C., Asfirane, F., 1999. Couverture géophysique aéroportée du Massif armoricain, magnétisme et radiométrie spectrale. Rapport B.R.G.M. R40471 (75 pp.).

Bosse, V., Ballevre, M., Vidal, O., 2002. Ductile thrusting recorded by the garnet isograd from blueschist-facies metapelites of the Ile de Groix, Armorican Massif, France. J. Petrol. 43, 485–510. http://dx.doi.org/10.1093/petrology/43.3.485.

Bosse, V., Féraud, G., Ballèvre, M., Peucat, J.-J., Corsini, M., 2005. Rb–Sr and $^{40}Ar/^{39}Ar$ ages in blueschists from the Ile de Groix (Armorican Massif, France): implications for closure mechanisms in isotopic systems. Chem. Geol. 220, 21–45. http://dx.doi.org/10.1016/j.chemgeo.2005.02.019.

Bossière, G., 1988. Evolutions chimico-minéralogiques du grenat et de la muscovite au voisinage de l'isograde biotite-staurotide dans un métamorphisme prograde de type barrovien: un exemple en Vendée littorale (Massif Armoricain). C. R. Acad. Sci. Paris II 306, 135–140.

Both, R.A., Arribas, A., De Saint-Andre, B., 1994. The origin of breccia-hosted uranium deposits in carbonaceous metasediments of the Iberian Peninsula; U-Pb geochronology and stable isotope studies of the Fe Deposit, Salamanca Province. Spain. Econ. Geol. 89, 584–601. http://dx.doi.org/10.2113/gsecongeo.89.3.584.

Bouchez, J.L., Guillet, P., Chevalier, F., 1981. Structures d'ecoulement liées à la mise en place du granite de Guérande (Loire-Atlantique, France). Bull. Soc. Geol. Fr. S7-XXIII, 387–399. http://dx.doi.org/10.2113/gssgfbull.S7-XXIII.4.387.

Breiter, K., 2012. Nearly contemporaneous evolution of the A- and S-type fractionated granites in the Krušné hory/Erzgebirge Mts., Central Europe. Lithos 151, 105–121. http://dx.doi.org/10.1016/j.lithos.2011.09.022.

Brown, M., Dallmeyer, R.D., 1996. Rapid Variscan exhumation and the role of magma in core complex formation: southern Brittany metamorphic belt, France. J. Metamorph. Geol. 14, 361–379. http://dx.doi.org/10.1111/j.1525-1314.1996.00361.x.

Burg, J.P., Van Den Driessche, J., Brun, J.P., 1994. Syn- to post thickening extension in the Variscan Belt of Western Europe: modes and structural consequences. Géol. Fr. 3, 33–51.

Cagnard, F., Gapais, D., Brun, J.P., Gumiaux, C., Van den Driessche, J., 2004. Late pervasive crustal-scale extension in the south Armorican Hercynian belt (Vendée, France). J. Struct. Geol. 26, 435–449. http://dx.doi.org/10.1016/j.jsg.2003.08.006.

Carl, C., Dill, H.G., Kreuzer, H., Wendt, I., 1983. U-Pb dating of ores in NE Bavaria. Terra Cognita 3, 195–196.

Cathelineau, M., 1981. Les Gisements Uraniferes de la Presqu'ile Guerandaise (Sud Bretagne); Approche Structurale et Metallogenique. Miner. Deposita 16, 227–240. http://dx.doi.org/10.1007/BF00202737.

Cathelineau, M., 1982. Les gisements d'uranium liés spatialement aux leucogranites sud-armoricains et à leur encaissant métamorphique: relations et interactions entre les minéralisations et divers contextes géologiques et structuraux. Sciences de la Terre, Mémoires 42. Université de Nancy (375 pp.).

Cathelineau, M., Boiron, M.C., Holliger, P., Poty, B., 1990. Metallogenesis of the French part of the Variscan orogen. Part II: time-space relationships between U, Au and Sn-W ore deposition and geodynamic events — mineralogical and U-Pb data. Tectonophysics 177, 59–79. http://dx.doi.org/10.1016/0040-1951(90)90274-C.

Caumon, M.-C., Dubessy, J., Robert, P., Tarantola, A., 2013. Fused-silica capillary capsules (FSCCs) as reference synthetic aqueous fluid inclusions to determine chlorinity by Raman spectroscopy. Eur. J. Mineral. 25, 755–763. http://dx.doi.org/10.1127/0935-1221/2013/0025-2280.

Caumon, M.-C., Tarantola, A., Mosser-Ruck, R., 2015. Raman spectra of water in fluid inclusions: I. Effect of host mineral birefringence on salinity measurement. J. Raman Spectrosc. http://dx.doi.org/10.1002/jrs.4708.

Chauris, L., 1977. Les associations parageneticques dans la metallogenie varisque du massif armoricain. Mineral. Deposita 12, 353–371. http://dx.doi.org/10.1007/BF00206172.

Chen, Y., Clark, A.H., Farrar, E., Wasteneys, H.A.H.P., Hodgson, M.J., Bromley, A.V., 1993. Diachronous and independent histories of plutonism and mineralization in the Cornubian Batholith, southwest England. J. Geol. Soc. 150, 1183–1191. http://dx.doi.org/10.1144/gsjgs.150.6.1183.

Cottaz, Y., Barthes, V., Berne, S., Crochon, P., Lericolais, G., Robach, F., 1989. Acoustic, magnetic and seismic investigation of the sea floor off the uraniferous district of Piriac, France. Mar. Geol. 86, 201–220. http://dx.doi.org/10.1016/0025-3227(89)90049-2.

Couzinié, S., Moyen, J.-F., Villaros, A., Paquette, J.-L., Scarrow, J.H., Marignac, C., 2014. Temporal relationships between Mg-K mafic magmatism and catastrophic melting of the Variscan crust in the southern part of Velay Complex (Massif Central, France). J. Geosci. 69–86. http://dx.doi.org/10.3190/jgeosci.155.

Cuney, M., 2014. Felsic magmatism and uranium deposits. Bull. Soc. Geol. Fr. 185, 75–92. http://dx.doi.org/10.2113/gssgfbull.185.2.75.

Cuney, M., Friedrich, M., Blumenfeld, P., Bourguignon, A., Boiron, M.C., Vigneresse, J.L., Poty, B., 1990. Metallogenesis in the French part of the Variscan orogen. Part I: U preconcentrations in pre-Variscan and Variscan formations — a comparison with Sn, W and Au. Tectonophysics 177, 39–57. http://dx.doi.org/10.1016/0040-1951(90)90273-B.

Derome, D., Cathelineau, M., Cuney, M., Fabre, C., Lhomme, T., Banks, D.A., 2005. Mixing of Sodic and calcic brines and uranium deposition at McArthur River, Saskatchewan, Canada: a Raman and laser-induced breakdown spectroscopic study of fluid inclusions. Econ. Geol. 100, 1529–1545. http://dx.doi.org/10.2113/gsecongeo.100.8.1529.

Dill, H.G., 1983. Vein-and metasedimentary-hosted carbonaceous matter and phosphorus from NE Bavaria (FR Germany) and their implication on syngenetic and epigenetic uranium concentration. Neues Jb. Mineral. Abh. 148, 1–21.

Dill, H.G., 2015. The Hagendorf-Pleystein Province: the center of pegmatites in an ensialic orogen. Modern Approaches in Solid Earth Sciences. Springer, Dortrecht, Heidelberg, London, New York (475 pp.).

Dolníček, Z., René, M., Hermannová, S., Prochaska, W., 2013. Origin of the Okrouhlá Radouň episyenite-hosted uranium deposit, Bohemian Massif, Czech Republic: fluid inclusion and stable isotope constraints. Miner. Deposita 49, 409–425. http://dx.doi.org/10.1007/s00126-013-0500-5.

Dubessy, J., Ramboz, C., Nguyen Trung, C., Cathelineau, M., Charoy, B., Cuney, M., Leroy, J., Poty, B., Weisbrod, A., 1987. Physical and chemical control (pO_2, T, pH) of the opposite behaviour of U and Sn-W as exemplified by hydrothermal deposits in France and Great Britain, and solubility data. Bull. Minér. 262–281.

Dubessy, J., Pagel, M., Beny, J.-M., Christensen, H., Hickel, B., Kosztolanyi, C., Poty, B., 1988. Radiolysis evidenced by H_2-O_2 and H_2-bearing fluid inclusions in three uranium deposits. Geochim. Cosmochim. Acta 52, 1155–1167. http://dx.doi.org/10.1016/0016-7037(88)90269-4.

Dubinina, E.O., Nosova, A.A., Avdeenko, A.S., Aranovich, L.Y., 2010. Isotopic (Sr, Nd, O) systematics of the high Sr-Ba Late Miocene granitoid intrusions from the Caucasian Mineral Waters region. Petrology 18, 211–238. http://dx.doi.org/10.1134/S086959111003001X.

Dunkl, I., 2002. Trackkey: a Windows program for calculation and graphical presentation of fission track data. Comput. Geosci. 28, 3–12.

Eglinger, A., André-Mayer, A.-S., Vanderhaeghe, O., Mercadier, J., Cuney, M., Decrée, S., Feybesse, J.-L., Milesi, J.-P., 2013. Geochemical signatures of uranium oxides in the Lufilian belt: from unconformity-related to syn-metamorphic uranium deposits during the Pan-African orogenic cycle. Ore Geol. Rev. 54, 197–213. http://dx.doi.org/10.1016/j.oregeorev.2013.04.003.

Eikenberg, J., 1988. Vergleichende Datierungen von Uranmineralen mit den U-Xe, U-Kr und U-Pb-Systemen sowie Untersuchungen der Produktion von Ne und Ar durch Kemprozesse (Ph.D. Thesis) Comparative Dating of U Minerals Using the U-Xe, U-Kr and U-Pb Systems and Supplementary Investigations Concerning the Production of Ne and Ar by Nuclear Processes. ETH Zürich.

Faure, M., 1995. Late orogenic carboniferous extensions in the Variscan French Massif Central. Tectonics 14, 132–153. http://dx.doi.org/10.1029/94TC02021.

Fernández-Suárez, J., Dunning, G.R., Jenner, G.A., Gutiérrez-Alonso, G., 2000. Variscan collisional magmatism and deformation in NW Iberia: constraints from U–Pb geochronology of granitoids. J. Geol. Soc. 157, 565–576. http://dx.doi.org/10.1144/jgs.157.3.565.

Finger, F., Roberts, M.P., Haunschmid, B., Schermaier, A., Steyrer, H.P., 1997. Variscan granitoids of central Europe: their typology, potential sources and tectonothermal relations. Mineral. Petrol. 61, 67–96. http://dx.doi.org/10.1007/BF01172478.

Friedrich, M., Cuney, M., Poty, B., 1987. Uranium geochemistry in peraluminous leucogranites. Uranium 3, 353–385.

Fryer, B.J., Taylor, R.P., 1987. Rare-earth element distributions in uraninites: implications for ore genesis. Chem. Geol. 63, 101–108. http://dx.doi.org/10.1016/0009-2541(87)90077-5.

Galbraith, R.F., Laslett, G.M., 1993. Statistical models for mixed fission track ages. Nucl. Tracks Radiat. Meas. 21, 459–470. http://dx.doi.org/10.1016/1359-0189(93)90185-C.

Gallagher, K., 2012. Transdimensional inverse thermal history modeling for quantitative thermochronology. J. Geophys. Res. Solid Earth 117, B02408. http://dx.doi.org/10.1029/2011JB008825.

Gallagher, K., Charvin, K., Nielsen, S., Sambridge, M., Stephenson, J., 2009. Markov Chain Monte Carlo (MCMC) Sampling Methods to Determine Optimal Models, Model Resolution and Model Choice for Earth Science Problems. Mar. Petrol. Geol. Thematic Set on Basin Modeling Perspectives 26, pp. 525–535. http://dx.doi.org/10.1016/j.marpetgeo.2009.01.003.

Gapais, D., Lagarde, J.L., Le Corre, C., Audren, C., Jegouzo, P., Casas Sainz, A., Van Den Driessche, J., 1993. La zonede cisaillement de Quiberon: témoin d'extension de la chaine varisque en Bretagne méridionale auCarbonifère. C. R. Acad. Sci. Paris II 316, 1123–1129.

Gapais, D., Brun, J.-P., Gumiaux, C., Cagnard, F., Ruffet, G., Le Carlier de Veslud, C., 2015. Extensional tectonics in the Hercynian Armorican belt (France). An overview. Bull. Soc. Geol. Fr. 186, 117–129. http://dx.doi.org/10.2113/gssgfbull.186.2-3.117.

Green, P.F., 1985. Comparison of zeta calibration baselines for fission-track dating of apatite, zircon and sphene. Chem. Geol. Isot. Geosci. Sect. 58, 1–22. http://dx.doi.org/10.1016/0168-9622(85)90023-5.

Gregory, R.T., Criss, R.E., 1986. Isotopic exchange in open and closed systems. Rev. Mineral. Geochem. 16, 91–127.

Guillocheau, F., Robin, C., Allemand, P., Bourquin, S., Brault, N., Dromart, G., Friedenberg, R., Garcia, J.-P., Gaulier, J.-M., Gaumet, F., Grosdoy, B., Hanot, F., Strat, P.L., Mettraux, M., Nalpas, T., Prijac, C., Rigoltet, C., Serrano, O., Grandjean, G., 2000. Meso-Cenozoic geodynamic evolution of the Paris Basin: 3D stratigraphic constraints. Geodin. Acta 13, 189–245. http://dx.doi.org/10.1080/09853111.2000.11105372.

Gumiaux, C., Gapais, D., Brun, J.P., Chantraine, J., Ruffet, G., 2004. Tectonic history of the Hercynian Armorican Shear belt (Brittany, France). Geodin. Acta 17, 289–307. http://dx.doi.org/10.3166/ga.17.289-307.

Gutiérrez-Alonso, G., Fernández-Suárez, J., Jeffries, T.E., Johnston, S.T., Pastor-Galán, D., Murphy, J.B., Franco, M.P., Gonzalo, J.C., 2011. Diachronous post-orogenic magmatism within a developing orocline in Iberia, European Variscides. Tectonics 30, TC5008. http://dx.doi.org/10.1029/2010TC002845.

Harrison, T.M., Célérier, J., Aikman, A.B., Hermann, J., Heizler, M.T., 2009. Diffusion of ^{40}Ar in muscovite. Geochim. Cosmochim. Acta 73, 1039–1051. http://dx.doi.org/10.1016/j.gca.2008.09.038.

Hofmann, B., Eikenberg, J., 1991. The Krunkelbach uranium deposit, Schwarzwald, Germany; correlation of radiometric ages (U-Pb, U-Xe-Kr, K-Ar, ^{230}Th-^{234}U). Econ. Geol. 86, 1031–1049. http://dx.doi.org/10.2113/gsecongeo.86.5.1031.

International Atomic Energy Agency (IAEA), 2012. UDEPO – World Distribution of Uranium Deposits.

IRSN, 2004. Inventaire national des sites miniers d'uranium. Institut de Radioprotection et de Sureté Nucléaire.

Jolivet, J., Bienfait, G., Vigneresse, J.L., Cuney, M., 1989. Heat flow and heat production in Brittany (Western France). Tectonophysics 159, 61–72. http://dx.doi.org/10.1016/0040-1951(89)90170-4.

Jolivet, M., Dominguez, S., Charreau, J., Chen, Y., Li, Y., Wang, Q., 2010. Mesozoic and Cenozoic tectonic history of the Central Chinese Tian Shan: reactivated tectonic structures and active deformation. Tectonics 29, 6. http://dx.doi.org/10.1029/2010TC002712.

Jones, K.A., Brown, M., 1990. High-temperature "clockwise"P-T paths and melting in the development of regional migmatites: an example from southern Brittany, France. J. Metamorph. Geol. 8, 551–578. http://dx.doi.org/10.1111/j.1525-1314.1990.tb00486.x.

Ketcham, R.A., Carter, A., Donelick, R.A., Barbarand, J., Hurford, A.J., 2007. Improved modeling of fission-track annealing in apatite. Am. Mineral. 92, 799–810. http://dx.doi.org/10.2138/am.2007.2281.

Kříbek, B., Žák, K., Dobeš, P., Leichmann, J., Pudilová, M., René, M., Scharm, B., Scharmová, M., Hájek, A., Holeczy, D., Hein, U.F., Lehmann, B., 2009. The Rožná uranium deposit (Bohemian Massif, Czech Republic): shear zone-hosted, late Variscan and post-Variscan hydrothermal mineralization. Mineral. Deposita 44, 99–128. http://dx.doi.org/10.1007/s00126-008-0188-0.

Lach, P., Mercadier, J., Dubessy, J., Boiron, M.-C., Cuney, M., 2013. In situ quantitative measurement of rare earth elements in uranium oxides by laser ablation-inductively coupled plasma-mass spectrometry. Geostand. Geoanal. Res. 37, 277–296. http://dx.doi.org/10.1111/j.1751-908X.2012.00161.x.

Laurent, O., Couzinié, S., Vanderhaeghe, O., Zeh, A., Moyen, J.F., Villaros, A., Gardien, V., 2015. U-Pb dating of Variscan igneous rocks from the eastern French Massif Central: southward migration of coeval crust- and mantle-melting witnesses late-orogenic slab retreat. Variscan Conference, Rennes.

Le Hébel, F., 2002. Déformation continentale et histoire des fluides au cours d'un cycle subduction, exhumation, extension. Exemple des porphyroïdes Sud-Armoricains 1 (Thèse Université de Rennes). (218 pp.).

Le Hébel, F., Vidal, O., Kienast, J.-R., Gapais, D., 2002. Les Porphyroïdes de Bretagne méridionale: une unité de HP–BT dans la chaîne hercynienne. Compt. Rendus Geosci. 334, 205–211.

Le Hébel, F., Fourcade, S., Boiron, M.-C., Cathelineau, M., Capdevila, R., Gapais, D., 2007. Fluid history during deep burial and exhumation of oil-bearing volcanics, Hercynian Belt of southern Brittany, France. Am. J. Sci. 307, 1096–1125. http://dx.doi.org/10.2475/09.2007.03.

Lemarchand, J., Boulvais, P., Gaboriau, M., Boiron, M.-C., Tartèse, R., Cokkinos, M., Bonnet, S., Jégouzo, P., 2012. Giant quartz vein formation and high-elevation meteoric fluid infiltration into the South Armorican Shear Zone: geological, fluid inclusion and stable isotope evidence. J. Geol. Soc. 169, 17–27. http://dx.doi.org/10.1144/0016-76492010-186.

Ludwig, K.R., 2012. Isoplot, a geochronological toolkit for Microsoft Excel. Berkeley Geochronology Center, Special Publication No. 5, p. 75.

McDonough, W.F., Sun, S.S., 1995. The composition of the earth. Chem. Geol., Chemical Evolution of the Mantle 120, pp. 223–253. http://dx.doi.org/10.1016/0009-2541(94)00140-4.

McDowell, F.W., McIntosh, W.C., Farley, K.A., 2005. A precise ^{40}Ar–^{39}Ar reference age for the Durango apatite (U–Th)/He and fission-track dating standard. Chem. Geol. 214, 249–263. http://dx.doi.org/10.1016/j.chemgeo.2004.10.002.

Mercadier, J., Cuney, M., Cathelineau, M., Lacorde, M., 2010. U redox fronts and kaolinisation in basement-hosted unconformity-related U ores of the Athabasca Basin (Canada): late U remobilisation by meteoric fluids. Mineral. Deposita 46, 105–135. http://dx.doi.org/10.1007/s00126-010-0314-7.

Mercadier, J., Cuney, M., Lach, P., Boiron, M.-C., Bonhoure, J., Richard, A., Leisen, M., Kister, P., 2011. Origin of uranium deposits revealed by their rare earth element signature. Terra Nova 23, 264–269. http://dx.doi.org/10.1111/j.1365-3121.2011.01008.x.

Ouddou, D., 1984. Le Massif de Guérande-Le Croisic (Loire-Atlantique): Caractérisation géochimique et minéralogique de l'évolution magmatique. Comportement de l'uranium. INPL-CREGU Nancy (Thèse). (309pp.).

Peiffert, C., Nguyen-Trung, C., Cuney, M., 1996. Uranium in granitic magmas: part 2. Experimental determination of uranium solubility and fluid-melt partition coefficients in the uranium oxide-haplogranite-H_2O-NaX (X = Cl, F) system at 770 °C, 2 kbar. Geochim. Cosmochim. Acta 60, 1515–1529. http://dx.doi.org/10.1016/0016-7037(96)00039-7.

Pérez Del Villar, L., Moro, C., 1991. Las mineralizaciones intragraníticas de Uranio en el batolito de Cabeza de Ar aya (provincia de Cáceres): El Saguazal, Brechas NNE y La Zafrilla. Stud. Geol. Salmant. 27.

Roger, F., Teyssier, C., Respaut, J.-P., Rey, P.F., Jolivet, M., Whitney, D.L., Paquette, J.-L., Brunel, M., 2015. Timing of formation and exhumation of the Montagne Noire double dome, French Massif Central. Tectonophysics 640–641, 53–69. http://dx.doi.org/10.1016/j.tecto.2014.12.002.

Schaltegger, U., 2000. U–Pb geochronology of the Southern Black Forest Batholith (Central Variscan Belt): timing of exhumation and granite emplacement. Int. J. Earth Sci. 88, 814–828. http://dx.doi.org/10.1007/s005310050308.

Sobel, E.R., Seward, D., 2010. Influence of etching conditions on apatite fission track etch pit diameter. Chem. Geol. 271, 59–69. http://dx.doi.org/10.1016/j. chemgeo.2009.12.012.

Stacey, J.S., Kramers, J.D., 1975. Approximation of terrestrial lead isotope evolution by a two-stage model.Earth Planet. Sci. Lett. 26, 207–221. http://dx.doi.org/10.1016/0012-821X(75)90088-6.

Tagami, T., 1987. Determination of zeta calibration constant for fission track dating. Int. J. Radiat. Appl. Instrum. Nucl. Tracks Radiat. Meas. 13, 127–130. http://dx.doi.org/10.1016/1359-0189(87)90023-9.

Tartèse, R., Boulvais, P., 2010. Differentiation of peraluminous leucogranites "en route" to the surface. Lithos 114, 353–368. http://dx.doi.org/10.1016/j.lithos.2009.09.011.

Tartèse, R., Poujol, M., Ruffet, G., Boulvais, P., Yamato, P., Košler, J., 2011a. New U-Pb zircon and $^{40}Ar/^{39}Ar$ muscovite age constraints on the emplacement of the Lizio syntectonic granite (Armorican Massif, France). Compt. Rendus Geosci. 343, 443–453. http://dx.doi.org/10.1016/j.crte.2011.07.005.

Tartèse, R., Ruffet, G., Poujol, M., Boulvais, P., Ireland, T.R., 2011b. Simultaneous resetting of the muscovite K-Ar and monazite U-Pb geochronometers: a story of fluids. Terra Nova 23, 390–398. http://dx.doi.org/10.1111/j.1365-3121.2011.01024.x.

Tartèse, R., Boulvais, P., Poujol, M., Chevalier, T., Paquette, J.-L., Ireland, T.R., Deloule, E., 2012. Mylonites of the South Armorican Shear Zone: insights for crustal-scale fluid flow and water–rock interaction processes. J. Geodyn. 56–57, 86–107. http://dx.doi.org/10.1016/j.jog.2011.05.003.

Tartèse, R., Boulvais, P., Poujol, M., Gloaguen, E., Cuney, M., 2013. Uranium mobilization from the Variscan Questembert syntectonic granite during fluid-rock interaction at depth. Econ. Geol. 108, 379–386. http://dx.doi.org/10.2113/econgeo.108.2.379.

Triboulet, C., Audren, C., 1988. Controls on P–T–t deformation path from amphibole zonation during progressive metamorphism of basic rocks (estuary of the River Vilaine, South Brittany, France). J. Metamorph. Geol. 6, 117–133. http://dx.doi.org/10.1111/j.1525-1314.1988.tb00412.x.

Turpin, L., Leroy, J.L., Sheppard, S.M.F., 1990. Isotopic systematics (O, H, C, Sr, Nd) of superimposed barren and U-bearing hydrothermal systems in a Hercynian granite, Massif Central, France. Chem. Geol. 88, 85–98. http://dx.doi.org/10.1016/0009-2541(90)90105-G.

Turrillot, P., Augier, R., Faure, M., 2009. The top-to-the-southeast Sarzeau shear zone and its place in the late-orogenic extensional tectonics of southern Armorica. Bull. Soc. Geol. Fr. 180, 247–261. http://dx.doi.org/10.2113/gssgfbull.180.3.247.

Valley, J.W., 2003. Oxygen isotopes in zircon. In: Hanchar, J.M., Hoskin, P.W.O. (Eds.), Zircon. Reviews in Mineralogy and Geochemistry vol. 53, pp. 343–385.

Valois, J., 1975. Les formations métamorphiques de Pénaran (presqu'île de Guérande, Loire Atlantique) et leur minéralisation uranifère (Thèse 3e cycle) Nancy (136 pp.).

Van Den Driessche, J., Brun, J.P., 1989. Un modèle cinématique de l'extension paléozoïque dans le Sud du Massif central. C. R. Acad. Sci. Paris II 309, 1607–1613.

Van Den Driessche, J., Brun, J.-P., 1992. Tectonic evolution of the Montagne Noire (french Massif Central): a model of extensional gneiss dome. Geodin. Acta 5, 85–97. http://dx.doi.org/10.1080/09853111.1992.11105221.

Velichkin, V.I., Vlasov, B.P., 2011. Domal structures and hydrothermal uranium deposits of the Erzgebirge, Saxony, Germany. Geol. Ore Deposit 53, 74–83. http://dx.doi.org/10.1134/S1075701511010053.

Vigneresse, J., 1983. Enracinement des granites armoricains estimé d'après la gravimétrie. Bulletin de la societé Géologique et minéralogique de Bretagne C 15 (1), pp. 1–15.

Vigneresse, J.L., 1995. Crustal regime of deformation and ascent of granitic magma. Tectonophysics 249, 187–202. http://dx.doi.org/10.1016/0040-1951(95)00005-8.

Vigneresse, J.L., Cuney, M., Jolivet, J., Bienfait, G., 1989. Selective heat-producing element enrichment in a crustal segment of the mid-European Variscan chain. Tectonophysics 159, 47–60. http://dx.doi.org/10.1016/0040-1951(89)90169-8.

Wendt, L., Lenz, H., Höhndorf, A., Bültemann, H., Bültemann, W.D., 1979. Das Alter der Pechblende der Lagerstätte Menzenschwand, Schwarzwald. Z. Dtsch. Geol. Ges. 130, 619–626 (with an abstract in English).

Zheng, Y.F., 1993. Calculation of oxygen isotope fractionation in anhydrous silicate minerals. Geochim. Cosmochim. Acta 57, 1079–1091.

Supplementary file 1: details about analytical protocols

1. *Analytic protocol for oxygen isotope analyses*

Oxygen isotope analyses were performed in the stable isotope laboratory at the University of Lausanne, Switzerland. The oxygen isotope composition of whole-rock samples and minerals from the Guérande granite, reported in the standard $\delta^{18}O$ notation, were measured using a CO_2-laser fluorination line coupled to a Finnigan MAT 253 mass spectrometer. Whole-rock samples (5 to 10 kg) were crushed following a standard protocol to obtain adequate powder using agate mortars. Silicate minerals (quartz and feldspar) were handpicked under a binocular microscope, to get purity higher than 98%, and then crushed in a tungsten carbide mortar. For each run, 1 - 2 mg of samples was loaded with at least 3 in-house quartz LS 1 standards (reference value: $\delta^{18}O$ = 18.1 ‰ vs. VSMOW: Vienna Standard Mean Ocean Water) in a platinum sample holder. The sample holder was dried in an oven at 110°C during at least one hour and then placed in the analysis chamber. The chamber was then evacuated to a vacuum better than 10-4 mbar before an overnight pre-fluorination. Samples were heated in the presence of F_2 using a CO_2 laser and the liberated oxygen was purified through an extraction line passing over a heated KCl salt. Oxygen was then absorbed onto a molecular sieve (13x) held at liquid nitrogen temperature and subsequently heated to expand the O_2 into the inlet of the mass spectrometer. For each run, the results, reported in per mill (‰) relative to the VSMOW, were normalized using the analyses carried out on the quartz standard LS1. The precision, based on replicate analyses of the standard run together with the samples was generally better than 0.2 permil.

2. *Analytic protocol for apatite fission tracks analyses*

Apatite fission track analysis was performed on three granite samples from the Guérande leucogranite. Apatite crystals were separated using classical magnetic and heavy liquid methods. The apatite grains were mounted on glass slides using epoxy resin and then polished. The spontaneous fission tracks were revealed by etching in 6.5 % HNO_3 (1.6M) for 45 s at 20°C (e.g. Seward et al., 2000; Jolivet et al., 2010). A Low-U external mica sheet used as external detector was then attached to the glass side before being irradiated with a neutron fluence rate of 1.0 x 10^{15} at SCK facility, Mol, Belgium. The induced tracks in the external detector were etched with 60% HF for 40 min at 20°C. The ages were calculated following the method recommended by the Fission Track Working Group of the IUGS Subcommission on Geochronology (Hurford, 1990) using the zeta calibration method (Hurford and Green, 1983). CN5 glass was used as a dosimeter.

The AFT age measurements were made in Géosciences Rennes using a Zeiss Axioplan 2 microscope with a 1250x magnification under dry lenses. For each samples, a total of 20 inclusion-free apatite grains oriented parallel to the c-axis were measured using the TrackWorks software developed by the Autoscan company (Australia). Age calculations were done using the TrackKey software (Dunkl, 2002). A weighted mean zeta value of 335.9 ± 6.8 yr cm² (CB) obtained on both Durango (McDowell et al., 2005) and Mount Dromedary (Green, 1985; Tagami, 1987) apatite standards was used. All ages

reported in this study are central ages (Galbraith and Laslett, 1993) reported at ± 2σ. Measurements of the horizontal track lengths and their respective angle with c axis, as well as the mean Dpar value (e.g. Jolivet et al., 2010; Sobel and Seward, 2010) were obtained for each sample. The Dpar value corresponds to the etched trace of the intersection of a fission track with the surface of the analyzed apatite (parallel to the c axis). The mean Dpar value used for each samples was obtained by measuring more than 300 Dpar.

3. Analytic protocol for LA-ICP-MS analyses on uranium-oxides

The rare earth elements (La, Ce, Pr, Nd, Sm, Eu, Gd, Tb, Dy, Ho, Er, Tm, Yb, Lu), Ti, V, Cu, Zn, Zr, W and Th concentrations in uranium oxides were quantified using a laser ablation-inductively coupled plasma mass spectrometry (LA-ICP-MS) system composed of a GeoLas excimer laser (ArF, 193 nm, Microlas) coupled to a conventional transmitted and reflected light microscope (Olympus BX51) for sample observation and laser beam focusing onto the sample and an Agilent 7500c quadrupole ICP-MS. The LA-ICP-MS system was optimized to have the highest sensitivity for all elements (from ^{7}Li to ^{238}U), ThO/Th ratio < 0.5% and Th/U ratio of ~1. Samples were ablated with laser spot sizes of 32, 60 or 120 µm depending on the suspected concentrations of the trace elements in the analyzed uranium oxides and the sample homogeneity (the freshest zones were selected and analyzed to obtain the primary trace and minor element concentrations). Trace and minor element quantifications by LA-ICP-MS were done in the same location as the U-Pb dating by SIMS. A fluence of ~ 7.5 J.cm^{2} and a repetition rate of 10 Hz were used, except for the sample "Pen Ar Ran: pseudo-spherulitic" for which a repetition rate of 3 Hz was used, this sample having a smaller thickness (30 µm in total; thin section) compared to the other samples (mounts). The carrier gas used was helium (0.5 l/min) which was mixed to argon (0.5 l/min) gas before entering the ICP-MS. The ICP-MS settings were the following: ICP RF Power at 1550 W, Cooling gas (Ar) at 15 l/min, auxiliary gas (Ar) at 0.96 l/min and dual detector mode was used. For each analysis, acquisition time was 30 s for background, 30 s for external standards (NIST 610 and NITS 612 silicate glasses (Pearce and al., 1997 for concentrations) and in-house UO2 standard Mistamisk for REE (Lach et al., 2013) and 30 s for uranium oxide minerals. The analytical procedure for one set of analyses (all the analytical conditions are similar) was the following: 2 analyses of NIST 610, 2 analyses of NIST612, 2 analyses of Mistamisk uranium oxides, between 4 to 20 analyses of uranium oxides, 2 analyses of NIST612 and 2 analyses of NIST610. The external standard was NIST610 and ^{238}U was mainly used as internal standard, as described in Lach et al. (2013). For the analyses of the samples "MN-granitic C.R." and "MN-metased. C.R." with a laser beam of 120 µm (to quantify low REE concentrations), ^{43}Ca was used instead of ^{238}U, as U concentration was too elevated (detector saturation using ^{238}U). NIST612 and Mistamisk uranium oxides were analyzed and considered as cross-calibration samples to control the quality of the analyses (precision, accuracy, repeatability), as described in Lach et al. (2013). No UO_2 standard has been developed for minor and trace elements except REE (only the REE concentrations have been characterized in the

Mistamisk uranium oxide by total digestion and ICP-MS measurement (Bonhoure et al., 2007) and the matrix effect using a silicate standard to quantify trace elements (concentrations below 10 ppm) in a uranium matrix is not known. Consequently, the concentrations proposed for Ti, V, Cu, Zn, Zr, W and Th in the different tested uranium oxides could present a bias for accuracy. U and Ca contents in uranium oxides were measured before LA-ICP-MS analyses using an electronic microprobe. These two elements present a relative constant concentration in the analyzed zones and a mean concentration was used for each sample. The U concentrations, in weight percent, used for internal standardization are the following: 70.6 for "PAR-prismatic", 72.2 for "PAR-spherulitic", 72.9 for "PAR-pseudo-spherulitic", 74.4 for "MN: granitic C.R." and, 74.8 for "MN-metased. C.R.". The Ca concentrations, in weight percent, used for internal standardization are the following: 4.92 for "MN- granitic C.R." and 5.57 for "MN-metased. C.R.". Acquisition times were the following: 0.01 s for all elements except W (0.1 s) and U (0.005 s). Total cycle time was 430 ms. Data treatment was done using the software "Iolite" (Paton et al., 2011), following Longerich et al. (1996) for data reduction.

Résumé de l'article #5 : la métallogénie de l'uranium dans les leucogranites peralumineux du complexe de Pontivy-Rostrenen (chaîne hercynienne armoricaine) : le résultat d'une altération hydrothermale oxydante à long terme lors d'une tectonique décrochante.

Au sein de la chaîne hercynienne armoricaine, la majorité des gisements d'uranium (U) hydrothermaux économiquement significatifs sont associés spatialement à des leucogranites peralumineux mis en place le long du cisaillement sud armoricain (CSA), une faille décrochante dextre d'échelle lithosphérique qui a enregistré une déformation ductile de ca. 315 à 300 Ma. Dans le complexe de Pontivy-Rostrenen, une intrusion composite, la minéralisation en U est associée à des structures fragiles qui se sont développées lors de la déformation le long du CSA. A l'opposé des monzogranites et des monzodiorites quartziques ($3 < [U] < 9$ ppm; $Th/U > 3$), les échantillons de leucogranites se caractérisent par des teneurs en U (~3 to 27 ppm) et des rapports Th/U très variables (~5 to 0.1) suggérant la cristallisation d'oxydes d'uranium magmatiques dans les facies les plus évolués puis leur lessivage lors d'épisodes hydrothermaux et/ou d'altération de surface. La datation U-Pb des oxydes d'uranium des gisements révèle qu'ils se sont, pour la plupart, formés entre ca. 300 et 270 Ma. Dans les monzogranites et les monzodiorites quartziques, les apatites se caractérisent par des textures magmatiques et des dates U-Pb à ca. 315 Ma reflétant la mise en place des intrusions. Au contraire, les grains d'apatite des leucogranites montrent des évidences texturales, géochimiques et géochronologiques d'interaction avec des fluides hydrothermaux oxydants riches en U de ca. 290 à 270 Ma. De 300 à 270 Ma, l'infiltration de fluides météoriques oxydants en profondeur a permis le lessivage des oxydes d'uranium magmatiques des leucogranites fertiles et la formation de gisements d'U. Ce phénomène a perduré grâce à une déformation fragile discrète dans la croûte supérieure et grâce à une anomalie thermique persistante associée à ces leucogranites.

Uranium metallogenesis in the peraluminous leucogranites from the Pontivy-Rostrenen magmatic complex (French Armorican Hercynian Belt): the result of long term oxidized hydrothermal alteration during strike-slip deformation.

Submitted to Mineralium Deposita

Ballouard C.[a]*, Poujol M.[a], Mercadier J.[b], Deloule E.[c], Boulvais P.[a], Cuney M.[b], Cathelineau M.[b],

[a] UMR CNRS 6118, Géosciences Rennes, OSUR, Université Rennes 1, 35042 Rennes Cedex, France
[b] Université de Lorraine, CNRS, CREGU, GeoRessources, Boulevard des Aiguillettes, BP 70239, 54506 Vandoeuvre-lès-Nancy, France
[c] CRPG, UMR 7358 CNRS-Université de Lorraine, BP20, 54501 Vandoeuvre Cedex, France

Keywords: Uranium deposits, syntectonic granites, apatite geochemistry and U-Pb dating, fluid-rock interactions, Variscan, South Armorican Shear Zone

Abstract

In the French Armorican Hercynian Belt, most of the economically significant hydrothermal U deposits are spatially associated with peraluminous leucogranites emplaced along the South Armorican Shear Zone (SASZ), a dextral lithospheric scale wrench fault that recorded ductile deformation from ca. 315 to 300 Ma. In the Pontivy-Rostrenen complex, a composite intrusion, the U mineralization is spatially associated with brittle structures related to deformation along the SASZ. In contrast to monzogranites and quartz monzodiorites ($3 < [U] < 9$ ppm; $Th/U > 3$), the leucogranite samples are characterized by highly variable U contents (~3 to 27 ppm) and Th/U ratios (~5 to 0.1) suggesting that the crystallization of magmatic uranium oxide in the more evolved facies was followed by uranium oxide leaching during hydrothermal alteration and/or surface weathering. U-Pb dating of uranium oxides from the deposits reveals that they mostly formed between ca. 300 and 270 Ma. In the monzogranites and quartz monzodiorites, apatite grains display magmatic textures and provide U-Pb dates of ca. 315 Ma reflecting the emplacement age of the intrusions. In contrast, apatite grains from the leucogranites display textural, geochemical and geochronological evidences for an interaction with U-rich oxidized hydrothermal fluids contemporaneously with U mineralizing events. From 300 to 270 Ma, infiltrations of surface-derived oxidized fluids were able to leach out magmatic uranium oxide from fertile leucogranites and to form U deposits. This phenomenon was sustained by brittle deformation and by the persistence of thermal anomalies associated with granitic bodies.

1. Introduction

Continental scale wrench faults represent common tectonic features in orogenic belts which act as channels for crustal and mantle derived magmas (Strong and Hanmer 1981; D'lemos et al. 1992; Hutton and Reavy 1992; De Saint Blanquat et al. 1998) as well as hydrothermal fluids (e.g. Sibson 1987, 1990; Faulkner et al. 2010; Cao and Neubauer 2016). Major strike-slip faults initiate deep within the crust and the lithospheric mantle due to rheological weakening contrast (Cao and Neubauer 2016). During the exhumation of these tectonic systems, a thermal evolution occurs: fragile deformation (cataclasites, pseudotachylytes) superimposes on ductile deformation (mylonites) and the ascent of magmas as well as hot lower crustal fluids and magmatic derived fluids is followed by the downward flow of cold surface derived waters. As a consequence, these tectonic features can control the location of various magmatic- and hydrothermal-related ore deposits such as orogenic gold (e.g. Mueller et al. 1988; Hagemann et al. 1992; Henley and Adams 1992; Cox 1999), porphyry copper (e.g. Pirajno 2010; Zengqian et al. 2003), iron in skarn (Wan et al. 2012), Ni-Cu sulfide, granite-related greisens or REE pegmatites (e.g. Pirajno 2010). These strike-slip deformation zones can also represent an important metallotect for hydrothermal uranium (U) deposits if they affect U fertile lithologies. Among U-rich igneous rocks, felsic volcanics and peraluminous leucogranites represent an ideal source for the formation of hydrothermal U deposits because most of their U can be hosted in easily leachable glass and uranium oxide, respectively (e.g. Cuney 2014). The relationships between U rich felsic volcanics, strike-slip faults and hydrothermal uranium deposits are for example well illustrated in South China along the southern termination of the Tan Lu fault (Li et al. 2001, 2002); the association between peraluminous leucogranites, wrench faults and U mineralization exists, for example, in Egypt along the El Sela shear zone (Gaafar et al. 2014; Gaafar 2015), in the European Hercynian belt (EHB): the Alentejo-Plasencia shear zone in Iberia (Pérez Del Villar and Moro 1991) and the north-western part of the French Massif Central (Cathelineau et al. 1990; Cuney et al. 1990; Gébelin et al. 2009).

The French Armorican Massif in the EHB represents a historical mining province for U where about 20000 t (~20 % of the French production; IRSN, 2004) have been extracted in the region before the end of the 90's. Few minor deposits are associated with Late Carboniferous metaluminous granites emplaced along the North Armorican Shear Zone (NASZ; Chauris 1984), a crustal-scale dextral strike slip fault with a limited displacement of ~20 km (Jégouzo 1980) (Fig. 1). The majority of the U deposits are spatially associated with Late Carboniferous peraluminous syntectonic leucogranites emplaced either along extensional deformation zones (Guérande leucogranite; Cathelineau 1981; Ballouard et al. 2017) or along the South Armorican Shear Zone (SASZ: Mortagne and Pontivy leucogranites; Cathelineau 1982; Cathelineau et al. 1990; Cuney et al. 1990), a lithospheric scale dextral wrench fault with a displacement of ~200 km (Berthé et al. 1979; Gapais and Le Corre 1980; Jégouzo 1980, Jégouzo and Rosselo 1988; Gumiaux et al. 2004a, 2004b; Tartèse et al. 2012) (Fig. 1). Recent studies on mylonites, leucogranites and quartz veins along the SASZ demonstrated that, during the Late Variscan

times, this fault acted as a major channel for lower crustal but also meteoric-derived oxidized hydrothermal fluids (Tartèse and Boulvais 2010; Tartèse et al. 2012; Lemarchand et al. 2012). These fluids were able to transport an important quantity of uranium in solution (Dubessy et al. 1987).

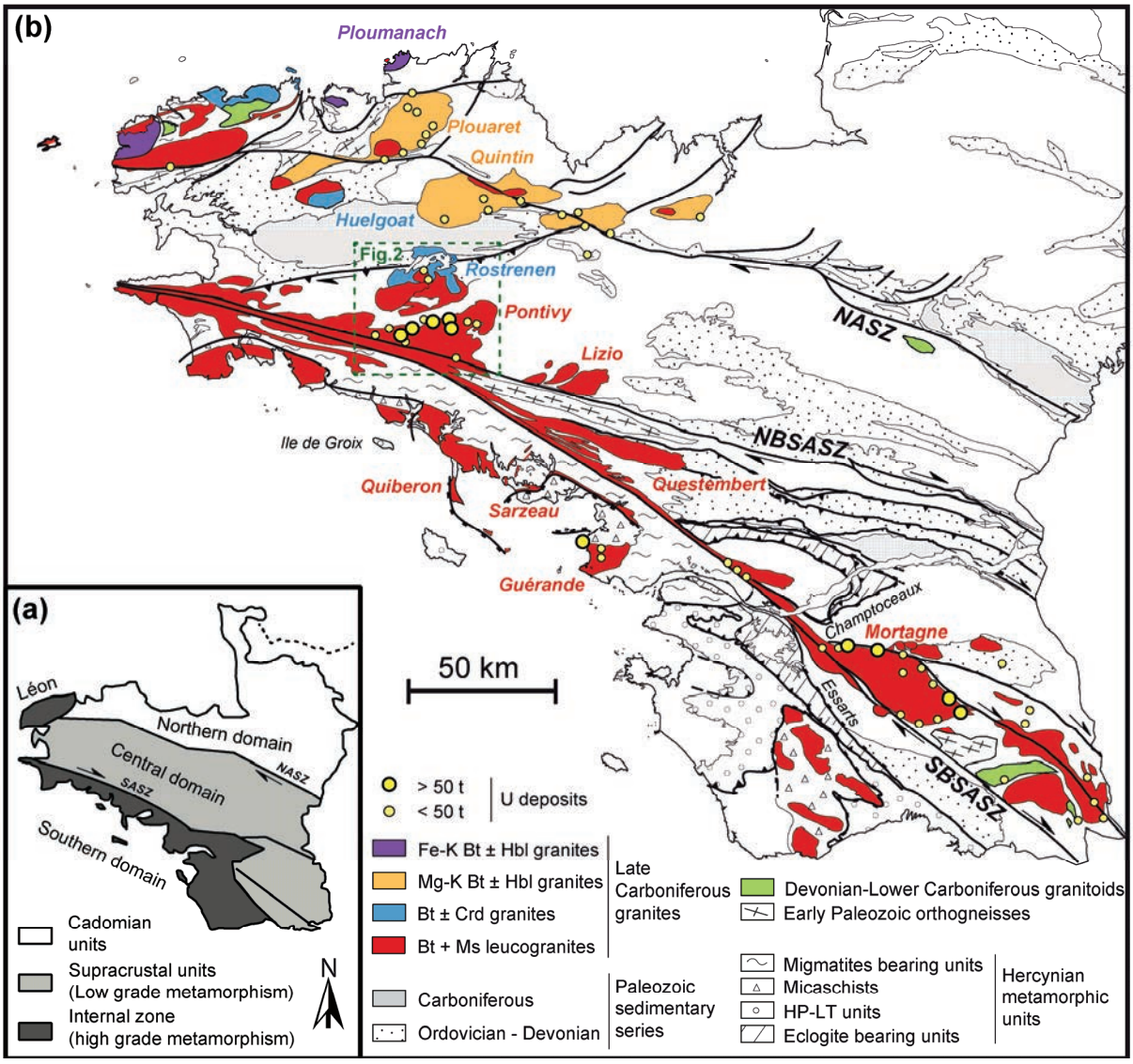

Figure 1: (a) Schematic structural map of the Armorican Massif. (b) General geological map of the Armorican Massif identifying the different type of Carboniferous granites according to Capdevila (2010) and localizing the uranium deposits. The geological map is modified from Chantraine et al. (2003) and Gapais et al. (2015). NASZ: North Armorican Shear Zone. SBSASZ: Southern Branch of the South Armorican Shear zone. NBSASZ: Northern Branch of the South Armorican Shear Zone. Fe-K granites: ferro-potassic granites. Mg-K granites: magnesio-potassic granites. Mineral abbreviations according to Kretz (1983).

The Pontivy-Rostrenen syntectonic composite intrusion hosts U intragranitic deposits associated with peraluminous leucogranites (Figs. 1 and 2). U was interpreted to originate from the leaching of uranium oxides present in the surrounding leucogranites (Marcoux 1982), although the metallogenic model remains poorly constrained. In this study, we use airborne radiometric data, geochemical analyses and U-Pb dating on apatite from the granitoids as well as U-Pb dating on uranium

oxides from the deposits to determine the timing and conditions of hydrothermal U mobilization and then its precipitation in the deposits. We then discuss this model in the geodynamic and metallogenic frameworks at the scale of the region and the northwestern part of the French Massif Central.

2. Geological framework

2.1. The Armorican Hercynian belt

The Armorican Massif belongs to the EHB, a Paleozoic orogenic belt which extends throughout the western (Iberian Massif) and central Europe (Bohemian Massif) and results from the collision of the supercontinents Laurussia and Gondwana (e.g. Ballèvre et al. 2009). The Armorican Massif is separated into three main continental domains by the NASZ and the SASZ (Fig. 1). The northern domain is mostly made of a Proterozoic basement (Brun et al. 2001), locally intruded by Hercynian granitoids (ex. Plouaret Massif, Fig. 1). The central domain is composed of Late Proterozoic (Brioverian) to Lower Carboniferous sediments mostly deformed under greenschist facies conditions during dextral wrenching along the NASZ and SASZ in Carboniferous times (Gumiaux et al. 2004a). The deformation in this area is marked by a vertical foliation which bears a sub-horizontal stretching lineation (e.g. Jégouzo 1980). The southern domain, which belongs to the internal part of the Hercynian belt, is characterized by a higher degree of deformation and by the presence of high grade metamorphic rocks (Gapais et al. 2015 and reference therein). Three tectono-metamorphic units can be distinguished in this domain and include, from top to bottom, HP-LT rocks, composed of blueschists and metavolcanics subducted and exhumed during early tectonic events from 370 to 350 Ma (Bosse et al. 2005), micaschists and migmatites bearing units (Fig. 1). Between 315 and 300 Ma (Tartèse et al. 2012), the SASZ acted as a transfer zone between the southern domain, where crustal extension lead to the exhumation of core complex cored by migmatites and syncinematic leucogranites, and the central domain submitted to pervasive dextral wrenching (Gapais et al. 2015).

During the Late Carboniferous, the Armorican Massif has been intruded by various granitoids ranging from peraluminous to metaluminous in composition (Capdevilla 2010; Fig. 1). To the south, muscovite (Ms) – biotite (Bt) peraluminous leucogranites are characteristic. They emplaced either along extensional deformation zone in the southern domain such as the Quiberon (Gapais et al. 1993, 2015), Sarzeau (Turrillot et al. 2009) and Guérande (309.7 ± 1.3 Ma: Zrn and Mnz U-Th-Pb, Ballouard et al. 2015) leucogranites or along the SASZ such as the Lizio (316.4 ± 5.6 Ma: Zrn U-Pb, Tartèse et al. 2011a), Questembert (316.1 ± 2.9 Ma: Zrn U-Pb, Tartèse et al. 2011b) and Pontivy (316.7 ± 2.5 Ma: Zrn U-Pb, Ballouard et al. submitted) leucogranites. To the north, the influence of mantle-derived magmatism increases as evidenced by the emplacement of Bt ± cordierite (Cd) peraluminous granites, such as the Rostrenen granite (315.5 ± 2.0 Ma, U-Pb Zrn, Ballouard et al. submitted), and two suites of Bt ± hornblende (Hbl) metaluminous granitoids including a magneso-potassic (Mg-K) and a ferro-potassic (Fe-K) association mostly emplaced between 320 and 300 Ma (Ballouard et al. submitted and

reference therein). On a regional scale, the crustal magmatism to the south of the SASZ is triggered by late-orogenic crustal extension. In contrast, to the north, the partial melting of the crust and the mantle, enriched during earlier subduction events, are triggered by an asthenosphere upwelling induced by pervasive wrenching (transtension) and the potential dismembering of an oceanic slab remnant at the lithosphere – asthenosphere transition (Ballouard et al. submitted).

U has been mostly mined in the district of Guérande, Pontivy and Mortagne (Fig. 1). In the Guérande district, the most important vein-type deposit (Pen Ar Ran), is perigranitic and localized above the apical zone of the Guérande leucogranite (Cathelineau 1981). The Guérande leucogranite itself was the main source for U (Ballouard et al. 2017). Trace elements and oxygen isotopes analyses suggest that leaching of the magmatic uranium oxides from the deformed facies from the apical zone of the intrusion was promoted by hydrothermal alteration with surface-derived oxidized fluids. The leached out U was then precipitated in the reducing environment represented by black shales and graphitic quartzites. Fluid inclusion analyses on a quartz comb from a quartz-uranium oxide vein from the Pen Ar Ran deposit indicate low salinity aqueous mineralizing fluids (1–6 wt.% NaCl eq.), consistent with the contribution of meteoric-derived waters, with trapping temperatures in the range 250-350 °C (Ballouard et al. 2017). Apatite fission track dating on the Guérande leucogranite suggests that the intrusion was still at temperature above 120°C, so at a depth greater than about 4 km (for a geothermal gradient of 30°C/km) during U deposits formation from ca. 300 to 275 Ma (uranium oxide U-Pb dating; Ballouard et al. 2017). The age of the U mineralizing events in the Guérande area is comparable with those in the Mortagne district and with other U deposits from the EHB (Cathelineau et al. 1990; Ballouard et al. 2017 and reference therein). The Questembert leucogranite (Fig. 1) is not associated with U deposits but the petro-geochemical and geochronological study of Tartèse et al. (2013) suggests that this intrusion liberated an important amount of uranium during a sub-solidus alteration event at depth with surface-derived oxidized fluids.

2.2. The Pontivy-Rostrenen magmatic complex.

2.2.1. General framework

Gravimetric data reveals that the Pontivy-Rostrenen complex represents a continuous intrusion with the main root (~6 km depth) localized to the north (Vigneresse and Brun 1983; Vigneresse 1999). The southern part of the complex is composed almost exclusively of peraluminous leucogranites whereas peraluminous leucogranites and monzogranites outcrop to the north with small stocks of mantle-derived metaluminous quartz monzodiorites (Euzen 1993; Ballouard et al. submitted) (Fig. 2). To the south, the leucogranites intrude Late-Proterozoic (Brioverian) sediments whereas to the north, leucogranites, monzogranites and quartz-monzodiorites intrude Late-Proterozoic and Paleozoic (Ordovician to Lower Carboniferous) sedimentary formations affected by contact metamorphism (Fig. 2). Based on the depth of the root of several intrusions across the EHB, including the Pontivy-Rostrenen

complex, Vigneresse (1999) estimated that these intrusions were emplaced at a depth around 6 – 8 km. The shape of the Pontivy leucogranite intrusion to the south marks the dextral shearing of the SASZ (Figs. 1 and 2) and, in the southern edge, syn-cooling shearing is revealed by the development of C/S structures (Gapais 1989) and mylonites in 100 m wide oriented N 100-110 dextral shear zones (Jégouzo 1980). The oxygen isotope study on mylonites from the Guilligomarch carry (Fig. 2) in the southern edge of the complex evidenced that some of these rocks experienced hydrothermal alteration with low $\delta^{18}O$ meteoric-derived fluids (Tartèse et al. 2012).

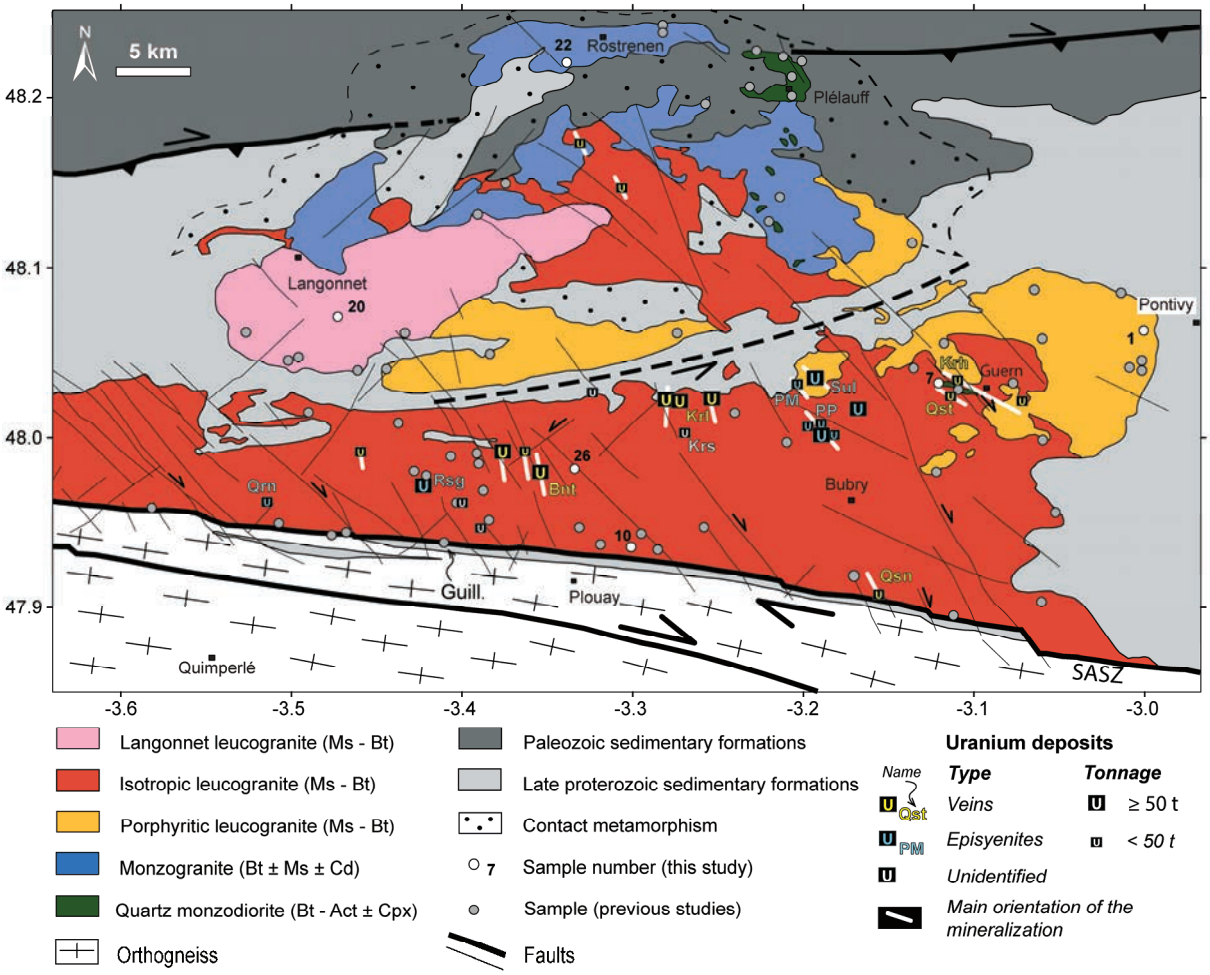

Figure 2: Geological map of the Pontivy-Rostrenen magmatic complex showing the different magmatic units and localizing the uranium deposits. Samples from this study and previous studies are localized on the map. The map is redrawn from Euzen (1993) and from the 1/50000 BRGM geological maps of Pontivy (Dadet et al. 1988), Rostrenen (Bos et al. 1997), Plouay (Bechennec et al. 2006) and Bubry (Bechennec and Thiéblemont 2009). SASZ: South Armorican Shear Zone. The types of uranium deposits and their main orientations are from Marcoux (1982) and Cuney (2006). Qst: Quistiave; Krh: Kerroch; PM: Prat Mérrien; PP: Poulprio; Sul: Sulliado; Qsn: Quistinic; Krl: Kerlech (Lignol); Bnt: Bonote; Rsg: Rosglas; Qrn: Quérrien (Kerjean); Krs: Kerségalec. Guill.: Guilligomarch..

2.2.2. Petrogeochemical characteristics

This section summarizes the petro-geochemical and geochronological study performed by Ballouard et al. (submitted) on the Pontivy-Rostrenen complex. Leucogranites contain quartz-feldspar-

muscovite with a variable amount of biotite. Biotite hosts most of the accessory minerals such as zircon, apatite, monazite and Fe-Ti oxides. Uranium oxides were not observed in our samples. This absence is likely the consequence of the instability of this mineral during post-crystallization alteration and/or weathering events because uranium oxides were commonly observed in the fresh drill cores realized in the leucogranites associated with U deposits such as in the Guérande leucogranite (Oudou 1984) (Fig. 1) or in the northwestern part of the French Massif Central (Friedrich et al. 1987). The leucogranites were divided into three main sub-facies (Fig. 2):

(1) The isotropic leucogranites are characterized by the abundance of porphyritic K-feldspar and a higher amount of biotite over muscovite.
(2) The isotropic leucogranites represent the most common type of leucogranites in the complex and are characterized by a low abundance or by the absence of porphyritic K-feldspar. In this complex, the proportion of biotite over muscovite is variable, biotite being even totally absent in some cases.
(3) The Langonnet leucogranite forms an elliptic stock which cartographically crosscuts the other facies. This leucogranite is rarely porphyritic and generally contains a low proportion of biotite.

In terms of alteration, chloritization of biotite and secondary muscovite are common while secondary muscovitization affects more particularly the Ms > Bt isotropic facies. Several veins of pegmatite and aplite crosscut the leucogranites. Moreover, pegmatite stocksheiders were described along the western edge of the Langonnet leucogranite and greisenization locally affects the most evolved terms of the isotropic and Langonnet leucogranites (Euzen 1993; Bos et al. 1997).

The monzogranites (Rostrenen granite s.s.) outcrop in the northern part of the complex (Fig. 2). This facies contains a quartz-feldspar-biotite assemblage with a small amount of muscovite and locally cordierite. The most common accessory minerals include zircon, monazite and Fe-Ti oxides. Mafic enclaves with a composition similar to the quartz-monzodiorites are commonly observed in this facies (Euzen 1993). The quartz-monzodiorite facies mostly appears as small stock of a few km² in the eastern part of the monzogranitic intrusion (Fig. 2). This facies generally contains quartz-feldspar-biotite-amphibole ± clinopyroxene as well as apatite, titanite, zircon and Fe-Ti oxide as accessory minerals. Ocellar quartz is frequently observed in this facies and interpreted as the result of a mixing with a felsic magma. Mingling features are visible at the contact between the quartz-monzodiorites and the monzogranites.

U-Pb dating of magmatic zircon grains revealed that the three magmatic facies forming the complex were emplaced synchronously at ca. 315 Ma whereas the Langonnet leucogranite was emplaced later at 304.7 ± 2.7 Ma. The three leucogranites (A/CNK > 1.10, εNd(t) from -4.79 to 2.08, inherited zircon grains with Archean to Paleozoic apparent ages) represent pure crustal melts formed by partial melting of Neoproterozoic metasedimentary rocks with the probable contribution of Paleozoic

peraluminous orthogneisses. The monzogranites (1.03 < A/CNK < 1.30, εNd(t) from -3.95 to -3.22, no inherited zircon grains, magmatic zircon grains with sub-chondritic εHf(t) values) were formed by the partial melting of an orthogneiss with a probable metaluminous composition. The metaluminous quartz monzodiorites (0.69 < A/CNK < 1.10, εNd(t) from-3.19 to -2.17, no inherited zircon grains, magmatic zircon grains with sub- to slightly superchondritic εHf(t) values) were formed by the partial melting of a metasomatized lithospheric mantle.

The evolution from high (~70 wt.%) to very high (~75 wt.%) SiO_2 leucogranite samples is likely explained by the fractional crystallization of a cumulate composed of Bt + Kfs + Pl as well as accessory minerals hosted in Bt such as Ap + Zrn + Mnz. The chemical evolution of monzogranites from high (~71 wt.%) to low (~65 wt.%) SiO_2 samples may reflect entrainment of peritectic minerals from the source (i.e. Cpx + Grt + Pl + Ilm) and/or a mixing with a mantle derived melt. The evolution of the quartz monzodiorite samples from ~ 54 wt.% to ~60 wt.% SiO_2 is likely the consequence of fractionation of a cumulate made of Pl + Bt + Cpx and mixing with an acid magma with a probable monzogranitic composition.

2.2.3. U mineralization

Most of the U deposits in the Pontivy-Rostrenen complex (~2000 t of U extracted; IRSN 2004) are spatially associated with the isotropic leucogranite facies (Fig. 2). They are generally localized close to contact with the sedimentary country rock or micaschistes enclaves (Marcoux 1982; Alabosi 1984; Cuney 2006). The most important U deposits occur as polyphazed, commonly hematized, quartz vein mostly oriented N170° and interpreted as tension gashes accommodating dextral wrenching along the SASZ (Marcoux 1982, Alabosi 1984) such as the Bonote (~400 t U extracted) or the Kerlech-Lignol deposit (~1000 t U extracted; Fig. 2). A second type of U deposits, with a main orientation of N120-130°, occur generally as brecciated quartz veins, such as in the Guern area (e.g. Quistiave and Kerroch deposits with ~40 t U extracted), in relation with second order faults which also likely developed due to deformation along the SASZ (Marcoux 1982, Alabosi 1984). The third type corresponds to episyenite-hosted deposits such as in the Prat Mérrien and Poulprio area (~ 100 t U extracted; Fig. 2) where the mineralized bodies follows N130-160° oriented faults (Alabosi 1984). The episyenitization of leucogranites during hydrothermal alteration resulted in the dissolution of magmatic quartz, the destabilization of plagioclase, the development of secondary muscovite and the geodic crystallization of adularia, quartz, montmorillonite and carbonate, U ore being disseminated in clay or in magmatic minerals (Alabosi 1984). A fourth type of deposit occurs as fracture fillings within Brioverian micaschist xenoliths (e.g., Kerségalec; Cuney 2006) (Fig. 2).

In addition to these U deposits, several metal deposits and occurrences (Pb, Zn, Sn and W) are spatially associated with the Pontivy-Rostrenen magmatic complex (Chauris 1977). Pb-Zn deposits are not spatially associated with a specific magmatic facies and galena can be abundant in some uranium

deposits (e.g. Quistiave), whereas Sn and W occurrences are exclusively associated with the Langonnet leucogranite (Marcoux 1982).

3. Analytical techniques

3.1. Whole rock major and trace elements analyses

Three samples of episyenites collected in the Prat Mérrien and Poulprio carries (Fig. 2) by Alabosi (1984) were crushed in the Geosciences Rennes Laboratory following a standard protocol to obtain adequate powder fractions using agate mortars. Chemical analyses were performed by the Service d'Analyse des Roches et des Minéraux (SARM; CRPG-CNRS, Nancy, France) using an ICP-AES for major-elements and an ICP-MS for trace-elements following the techniques described in Carignan et al. (2001). The results of the whole rock analyses are provided in Table 1.

3.2. Radiometric data

A detailed airbone radiometric survey was performed over the Armorican Massif by the BRGM (Bureau de Recherche Géologique et Minière). The detailed acquisition and treatment methods applied to the airborne radiometric data are provided in Bonijoly et al. (1999).

3.3. Apatite chemistry and U-Pb dating

Apatite crystals from the different magmatic facies forming the complex as well as an episyenite sample were separated using classical magnetic and heavy liquid methods in the Géosciences Rennes laboratory. Apatite grains were then handpicked under a binocular microscope before being embedded in epoxy resin and polished on a lap wheel. Apatite grains were imaged by cathodoluminesence (CL) using a Reliotron CL system equipped with a digital color camera available in Géosciences Rennes. Backscattered electron (BSE) images and chemical maps were performed using a Cameca SX-100 electron microprobe available at IFREMER, Plouzané, France.

3.3.1. Apatite chemistry

Apatite compositions were measured using a Cameca SX-100 electron microprobe at IFREMER, Plouzané, France. Analyses were performed using a 15 keV accelerating voltage and a beam diameter of 15 µm. A beam current of 10 nA and 20 nA were used for spot analyses and elemental mapping, respectively. Standards were: apatite (F Kα, TAP crystal, counting time of 30s; P Kα, LPET, 60s; Ca Kα, PET, 30s), albite (Si Kα, TAP, 30s; Na Kα, TAP, 30s), strontianite (Sr Lα, TAP, 30s), pyromorphyte (Cl Kα, LPET, 60s), Si-Al-Ca glass with 4w.% La (La Lα, LPET, 30s), Barium sulfate (S Kα, PET, 30s), Si-Al-Ca glass with 4w.% Ce (Ce Lα, PET, 60s), andradite (Fe Kα, LLIF, 60s), rhodonite (Mn Kα, LLIF, 60s), gallium arsenide (As Lα, TAP, 60s).

3.3.2. U-Pb dating

U-Pb geochronology of apatite was conducted by in-situ laser ablation inductively coupled plasma mass spectrometry (LA-ICP-MS) at Géosciences Rennes using a ESI NWR193UC excimer laser coupled to a quadripole Agilent 7700x ICP-MS equipped with a dual pumping system to enhance sensitivity. The methodology used to perform the analyses can be found in Pochon et al. (2016) and in Supplementary file 1. Ages, calculated using the ISOPLOT software (Ludwig, 2012), are provided with their 2σ uncertainties. All the isotopic ratios as well as the corresponding U and Pb contents in ppm are provided in Supplementary Table 2.

3.4. Uranium oxide U-Pb dating

Petrography, and imaging of selected polished thin sections and mounts of uranium oxide samples from different U deposits from the Pontivy-Rostrenen complex were carried out at the GeoRessources laboratory (Nancy, France) and the Centre de Recherches Pétrographiques et Géochimiques (CRPG, Nancy, France). U-Pb dating was carried out at the CRPG by secondary ion mass spectrometry (SIMS). The uranium oxide samples were first examined using reflected light microscopy. We then selected appropriate areas suitable for SIMS analyses (chemically homogenous area having high radiogenic lead content) based on BSE images obtained using a JEOL J7600F, a HITACHI S-4800 (GeoRessources) or a JEOL 6510 (CRPG) scanning electron microscope and major element analyses obtained using a CAMECA SX100 electron microprobe (GeoRessources). U-Pb isotope analyses were performed using a CAMECA IMS 1270 ion microprobe. The complete methodology is described in supplementary material. Due to the common Pb rich character of the uranium oxides ($50 < {}^{206}Pb/{}^{204}Pb < 11000$), a common lead correction based on the measured ^{204}Pb content and the Pb isotopic composition calculated using the model of Stacey and Kramers (1975) at the estimated age of the uranium oxide was applied to the analyses. All the isotopic ratios are provided in Supplementary Table 3 and ages, calculated using the ISOPLOT software (Ludwig 2012), are provided with their 2σ uncertainties.

4. Results

4.1. Whole rock geochemistry and U-Th distribution

The major elements compositions of whole rock samples from the Pontivy-Rostrenen complex are reported in the Q-P diagram (Fig 3a). Leucogranites, monzogranites and quartz monzodiorite plot mostly in the field defined for granites-adamellites, ademellites and quartz monzodiorite, respectively, whereas the episyenite sample from the Prat Mérrien deposit plots in the granite field and the two episyenite samples from the Poulprio deposit plot out of the field defined for magmatic rocks. The episyenites, which result from leucogranite metasomatism (Alabosi 1984), display evidence of an important dequartzification combined with potassic alteration for Poulprio and a slight dequartzification for Prat Mérrien (Fig. 3a). Lost on ignition (LOI) between ~4 and 8 wt.% in the episyenite samples reflect the presence of carbonates and clay minerals (montmorillonite; Alabosi 1984) whereas LOI are

below 2 wt.% for unaltered leucogranites. The episyenite sample from Part Mérrien is also enriched in P_2O_5 (1.19 wt.%; Table 1) compared to other episyenites (P_2O_5 < 0.7 wt.%; Table 1) and unaltered leucogranite samples (P_2O_5 < 0.5 wt.%; Ballouard et al. submitted). Moreover, all episyenites samples display elevated As content with values from 20 ppm (Poulprio: MS-81-32) to 95 ppm (Prat Mérrien; Table 1) whereas As contents are generally below 11 ppm in unaltered leucogranites (Ballouard et al. submitted).

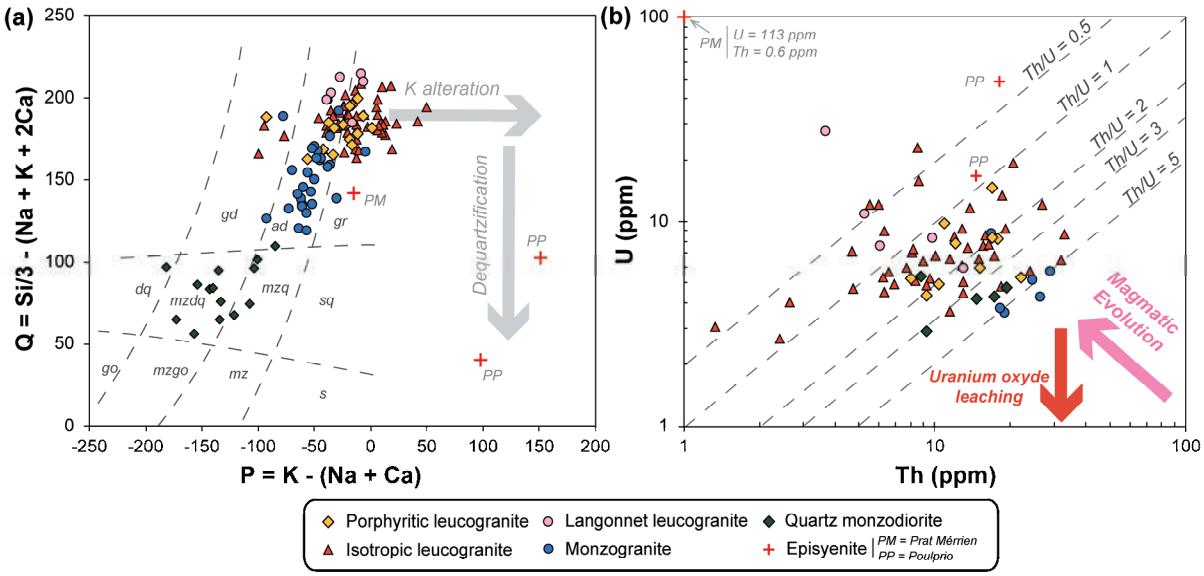

Figure 3: (a) Q-P diagram (after Debon and Le Fort 1988) and (b) Th/U diagram showing the whole rock compositions of samples from the Pontivy-Rostrenen magmatic complex. In (a), the fields in dashed delimitate the location of common igneous rock: gr = granite, ad = adamellite (monzogranite), gd = granodiorite, to = tonalite, sq = quartz syenite, mzq = quartz monzonite, mzdq = quartz monzodiorite, s = syenite, mz = monzonite, mzgo = monzogabbro and go = gabbro. Q-P parameters are expressed in molar proportion multiplied by 1000. The grey arrows represent the compositional evolution of leucogranites during episyenitization. In (b), the yellow arrow represents the theoretical evolution of a peraluminous leucogranitic melt during fractional crystallization whereas the green arrow represents the evolution of a sample during uranium oxide leaching. The sample compositions are from Ballouard et al. (submitted), Cotten (1975), Alabosi (1984), Euzen (1993), Bechennec et al. (2006, 2009) and Tartèse et al. (2012).

In the Th vs. U diagram (Fig. 3b), monzogranite and quartz monzodiorite samples are characterized by elevated Th/U values mostly above 3, low U contents from ~3 to 9 ppm and a poorly-defined correlation between Th and U. In contrast, the Th/U ratios and U contents are highly variable in the leucogranites and range from ~5 to 0.1 and ~3 to 27 ppm, respectively. Among the leucogranites, the lowest Th/U ratios (< 1) and higher U contents (> 15 ppm) are displayed by the isotropic leucogranites and the Langonnet leucogranites whereas Th/U ratios above 1 and U contents below or equal to 15 ppm are found in the porphyritic leucogranites. U correlates negatively with Th for the Langonnet leucogranite samples whereas no clear correlation appears for the porphyritic and isotropic leucogranites. In the episyenites, the Th/U ratios range from 0.9 to 0.01 with a U content from 17 to 48 ppm for Poulprio and of 113 ppm for Prat Mérrien.

Table 1: whole rock major and trace elements composition of episyenite samples

Sample		MS-81-66	MS-81-32	MS-81-40
location		Prat-Mérien (PM)	Poulprio (PP)	
SiO_2	Wt.%	62.97	55.95	58.24
Al_2O_3	Wt.%	17.55	19.84	21.14
Fe_2O_3	Wt.%	4.40	3.01	1.64
MnO	Wt.%	0.04	0.03	0.03
MgO	Wt.%	1.00	1.85	1.18
CaO	Wt.%	1.68	1.04	0.98
Na_2O	Wt.%	2.67	0.39	2.42
K_2O	Wt.%	4.77	8.59	9.08
TiO_2	Wt.%	0.13	0.43	0.39
P_2O_5	Wt.%	1.19	0.49	0.65
LOI	Wt.%	4.13	8.23	4.08
Total	Wt.%	100.52	99.85	99.82
Li	ppm	91	70	66
Cs	ppm	17.2	22.8	20.2
Rb	ppm	355	544	582
Sn	ppm	4.0	15.9	15.7
W	ppm	0.89	3.02	2.47
Ba	ppm	528	645	657
Sr	ppm	53.5	46.0	56.1
Be	ppm	8.1	34.4	8.2
U	ppm	113.20	48.42	16.53
Th	ppm	0.59	18.04	14.61
Nb	ppm	2.92	12.30	7.97
Ta	ppm	0.50	2.53	1.67
Zr	ppm	41.3	178.1	157.8
Hf	ppm	1.32	5.61	4.88
Bi	ppm	2.44	0.65	0.78
Cd	ppm	0.412	0.14	0.145
Co	ppm	7.05	1.48	3.25
Cr	ppm	14.72	9.441	8.305
Cu	ppm	25.55	< L.D.	7.167
Ga	ppm	24.3	30.7	32.4
Ge	ppm	1.18	1.37	1.20
In	ppm	< L.D.	0.523	0.139
Mo	ppm	< L.D.	< L.D.	< L.D.
Ni	ppm	15.54	< L.D.	< L.D.
Pb	ppm	52.1	30.5	25.4
Sc	ppm	3.36	3.71	2.94
Sb	ppm	2.403	2.229	5.07
V	ppm	22.0	22.5	16.0
Y	ppm	44.34	10.91	14.10
Zn	ppm	29.43	31.29	53.36
As	ppm	95.15	20.08	54.01
La	ppm	8.13	30.40	27.24
Ce	ppm	23.90	60.93	58.68
Pr	ppm	3.94	7.47	7.18
Nd	ppm	18.02	28.40	28.45
Sm	ppm	5.77	6.85	7.61
Eu	ppm	1.11	0.83	1.12
Gd	ppm	5.89	5.42	6.31
Tb	ppm	1.14	0.68	0.83
Dy	ppm	7.79	2.92	3.59
Ho	ppm	1.65	0.41	0.50
Er	ppm	4.45	0.84	1.00
Tm	ppm	0.66	0.11	0.13
Yb	ppm	4.35	0.68	0.77
Lu	ppm	0.61	0.10	0.11
A/NK		1.84	1.99	1.53
A/CNK		1.39	1.67	1.35

Bdl : below detection limit ; LOI : lost on ignition

On the Th/U airborne radiometric map (Fig. 4), monzogranitic and quartz monzodioritic zones are characterized by elevated Th/U values (orange, brown and white colors) whereas the leucogranitic zones are mostly characterized by low Th/U values (green, cream and blue colors). The lowest Th/U values (blue to cream) are mostly associated with the isotropic and the Langonnet leucogranites. On the map, the U deposits, mostly associated with the isotropic leucogranites, are almost exclusively located on cream-colored zones at the transition between high and low Th/U areas.

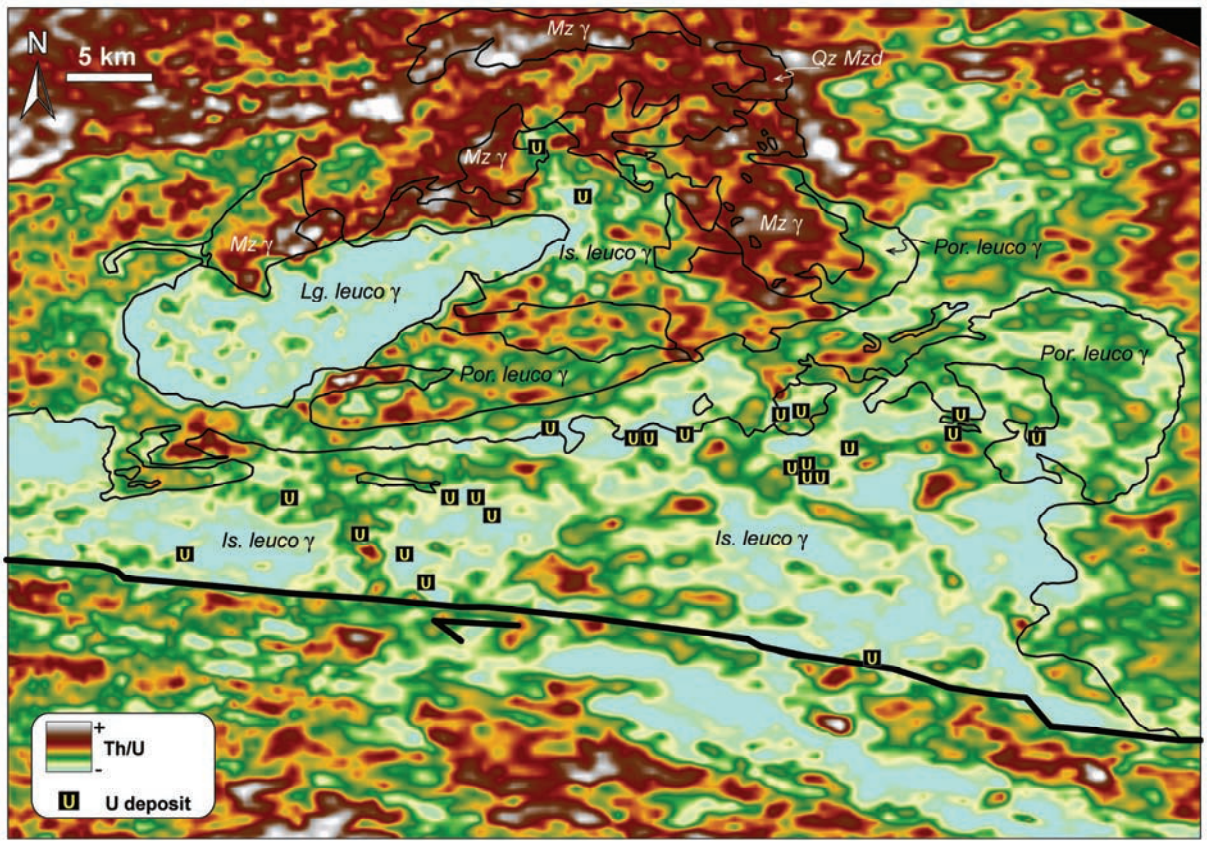

Figure 4: Airborne radiometric map of Th/U ratio in the Pontivy-Rostrenen magmatic complex area localizing the uranium deposits. The contour of the intrusions (see Fig. 2) are represented in black: Por. leuco γ = porphyritic leucogranite; Is. leuco γ = isotropic leucogranite; Lg leuco γ = Langonnet leucogranite. Mz γ = monzogranite; Qz Mzd = quartz monzodiorite.

4.2. Apatite petro-geochemistry

Apatite is a common accessory mineral in all the magmatic rocks from the Pontivy-Rostrenen complex. In this study, chemical analyses (Table 2) were performed on 10 to 15 separated apatite grains from one porphyritic leucogranite (PONT-1), two isotropic leucogranites (PONT-10 and 26), the Langonnet leucogranite (PONT-20), one episyenite (MS-81-66-PM), one monzogranite (PONT-22) and two quartz-monzodiorites (PONT-7 and 23). In all these samples, the F content in the apatite crystals is always above 0.75 apfu indicating that they are fluoroapatite (Table 2).

Table 2: Average chemical composition of apatite.

Facies	Por.leucogranite		Isotropic leucogranite											
Sample	PONT-1		PONT-10						PONT-26					
Location			Core		Rim		Unzoned		Core		Rim		Unzoned	
Color CL	Yellow		Yellow		Yellow		Yellow		Yellow		Yellow		Yellow	
Analyses	**n = 15**	**σ**	**n = 9**	**σ**	**n = 8**	**σ**	**n = 5**	**σ**	**n = 11**	**σ**	**n = 13**	**σ**	**n = 7**	**σ**
CaO	52.42	0.71	51.97	0.44	53.17	0.55	53.16	0.91	53.21	0.39	54.19	0.73	53.95	0.45
SrO	bdl		bdl		bdl		bdl		bdl		bdl		bdl	
FeO	0.65	0.21	0.65	0.20	0.34	0.20	0.51	0.26	0.56	0.16	0.34	0.19	0.26	0.19
MnO	1.08	0.30	1.89	0.30	1.13	0.28	1.10	0.49	0.84	0.16	0.55	0.29	0.48	0.26
Na_2O	0.10	0.05	0.06	0.03	0.04	0.03	0.03	0.03	0.09	0.04	0.06	0.04	0.04	0.03
P_2O_5	41.74	0.44	41.78	0.39	41.64	0.43	41.70	0.19	41.77	0.24	41.99	0.37	42.02	0.34
SiO_2	0.01	0.01	0.02	0.01	0.01	0.01	0.02	0.02	0.01	0.02	0.02	0.02	0.03	0.02
SO_2	0.01	0.02	0.02	0.02	0.01	0.01	0.02	0.02	0.01	0.01	0.01	0.02	0.02	0.02
As_2O_3	bdl		0.01	0.01	0.01	0.01	0.01	0.02	bdl		0.01	0.01	0.01	0.01
Ce_2O_3	0.07	0.05	0.09	0.05	0.07	0.04	0.05	0.04	0.06	0.04	0.03	0.03	0.06	0.05
La_2O_3	0.03	0.03	0.02	0.02	0.01	0.01	0.02	0.04	0.01	0.02	0.02	0.02	0.02	0.02
Cl	0.012	0.007	0.003	0.003	0.008	0.006	0.008	0.003	0.004	0.003	0.005	0.005	0.002	0.003
F	3.316	0.101	3.311	0.107	3.318	0.066	3.235	0.123	3.286	0.093	3.342	0.095	3.385	0.108
Total	99.46	0.84	99.83	0.51	99.76	0.57	99.89	0.42	99.85	0.26	100.56	0.45	100.29	0.37
O=F	1.40	0.04	1.39	0.04	1.40	0.03	1.36	0.05	1.38	0.04	1.41	0.04	1.43	0.05
O=Cl	0.00	0.00	0.00	0.00	0.00	0.00	0.00	0.00	0.00	0.00	0.00	0.00	0.00	0.00
Total*	98.06	0.81	98.43	0.49	98.36	0.58	98.52	0.41	98.47	0.25	99.15	0.44	98.86	0.36
	Structural formula on the basis of a 12.5 oxygen equivalent													
Ca	4.80	0.05	4.75	0.04	4.86	0.05	4.85	0.08	4.86	0.03	4.91	0.06	4.90	0.03
Sr	0.00	0.00	0.00	0.00	0.00	0.00	0.00	0.00	0.00	0.00	0.00	0.00	0.00	0.00
Fe	0.05	0.02	0.05	0.01	0.02	0.01	0.04	0.02	0.04	0.01	0.02	0.01	0.02	0.01
Mn	0.08	0.02	0.14	0.02	0.08	0.02	0.08	0.03	0.06	0.01	0.04	0.02	0.03	0.02
Na	0.02	0.01	0.01	0.00	0.01	0.00	0.00	0.00	0.02	0.01	0.01	0.01	0.01	0.00
P	3.02	0.02	3.02	0.01	3.01	0.01	3.01	0.01	3.01	0.01	3.01	0.02	3.01	0.01
Si	0.00	0.00	0.00	0.00	0.00	0.00	0.00	0.00	0.00	0.00	0.00	0.00	0.00	0.00
S	0.00	0.00	0.00	0.00	0.00	0.00	0.00	0.00	0.00	0.00	0.00	0.00	0.00	0.00
As	0.00	0.00	0.00	0.00	0.00	0.00	0.00	0.00	0.00	0.00	0.00	0.00	0.00	0.00
Ce	0.00	0.00	0.00	0.00	0.00	0.00	0.00	0.00	0.00	0.00	0.00	0.00	0.00	0.00
La	0.00	0.00	0.00	0.00	0.00	0.00	0.00	0.00	0.00	0.00	0.00	0.00	0.00	0.00
Cl	0.00	0.00	0.00	0.00	0.00	0.00	0.00	0.00	0.00	0.00	0.00	0.00	0.00	0.00
F	0.90	0.02	0.89	0.03	0.90	0.02	0.87	0.03	0.89	0.02	0.89	0.03	0.91	0.03
OH[a]	0.10	0.02	0.11	0.03	0.10	0.02	0.13	0.03	0.11	0.02	0.11	0.03	0.09	0.03

Facies	Lang. leucogranite		Episyenite						Monzogranite		Quartz monzodiorite			
Sample	PONT-20		MS-81-66 (PM)						PONT-22		PONT-7		PONT-23	
Color CL	Yellow		Light-blue		Dark-blue		Yellow		Yellow		Purple		Purple	
Analyses	n = 17	σ	n = 11	σ	n = 4	σ	n = 4	σ	n = 23	σ	n = 14	σ	n = 15	σ
CaO	52.41	0.67	54.47	0.30	52.42	0.67	53.03	1.36	53.21	0.63	53.62	0.51	53.87	0.41
SrO	bdl		bdl		0.08	0.01	bdl		bdl		bdl		0.01	0.01
FeO	0.77	0.24	0.01	0.02	0.05	0.03	0.42	0.28	0.23	0.05	0.05	0.02	0.04	0.02
MnO	0.75	0.12	0.03	0.03	bdl		1.04	0.66	0.31	0.04	0.05	0.02	0.04	0.02
Na_2O	0.12	0.02	0.01	0.01	0.02	0.02	0.08	0.06	0.12	0.02	0.02	0.01	0.02	0.02
P_2O_5	42.61	0.29	42.79	0.38	37.15	0.43	42.64	0.37	42.04	0.50	41.63	0.40	41.59	0.59
SiO_2	0.01	0.01	0.02	0.02	0.02	0.02	0.01	0.02	0.05	0.06	0.48	0.29	0.22	0.13
SO_2	0.01	0.02	0.01	0.02	0.01	0.02	0.00	0.00	0.01	0.01	0.01	0.02	0.02	0.02
As_2O_3	bdl		0.11	0.36	5.17	0.49	0.02	0.02	bdl		0.01	0.01	bdl	
Ce_2O_3	0.09	0.05	0.03	0.04	0.08	0.04	0.04	0.03	0.03	0.03	0.24	0.15	0.19	0.12
La_2O_3	0.03	0.02	0.01	0.01	0.04	0.04	0.03	0.03	0.01	0.01	0.06	0.05	0.07	0.06
Cl	0.011	0.004	0.005	0.005	0.007	0.010	0.078	0.054	0.030	0.009	0.055	0.014	0.090	0.030
F	3.323	0.107	3.377	0.136	2.784	0.114	3.305	0.126	3.395	0.097	3.332	0.094	3.430	0.090
Total	100.14	0.59	100.89	0.37	97.85	1.01	100.68	0.77	99.45	0.71	99.57	0.59	99.58	0.68
O=F	1.40	0.05	1.42	0.06	1.17	0.05	1.39	0.05	1.43	0.04	1.40	0.04	1.44	0.04
O=Cl	0.00	0.00	0.00	0.00	0.00	0.00	0.02	0.01	0.01	0.00	0.01	0.00	0.02	0.01
Total*	98.74	0.58	99.46	0.36	96.68	1.00	99.27	0.75	98.01	0.70	98.15	0.58	98.12	0.65
	Structural formula on the basis of a 12.5 oxygen equivalent													
Ca	4.75	0.05	4.89	0.02	5.02	0.02	4.78	0.08	4.86	0.05	4.89	0.06	4.93	0.03
Sr	0.00	0.00	0.00	0.00	0.00	0.00	0.00	0.00	0.00	0.00	0.00	0.00	0.00	0.00
Fe	0.05	0.02	0.00	0.00	0.00	0.00	0.03	0.02	0.02	0.00	0.00	0.00	0.00	0.00
Mn	0.05	0.01	0.00	0.00	0.00	0.00	0.07	0.05	0.02	0.00	0.00	0.00	0.00	0.00
Na	0.02	0.00	0.00	0.00	0.00	0.00	0.01	0.01	0.02	0.00	0.00	0.00	0.00	0.00
P	3.05	0.01	3.04	0.02	2.81	0.02	3.04	0.01	3.03	0.02	3.00	0.02	3.00	0.02
Si	0.00	0.00	0.00	0.00	0.00	0.00	0.00	0.00	0.00	0.01	0.04	0.02	0.02	0.01
S	0.00	0.00	0.00	0.00	0.00	0.00	0.00	0.00	0.00	0.00	0.00	0.00	0.00	0.00
As	0.00	0.00	0.01	0.02	0.28	0.03	0.00	0.00	0.00	0.00	0.00	0.00	0.00	0.00
Ce	0.00	0.00	0.00	0.00	0.00	0.00	0.00	0.00	0.00	0.00	0.01	0.00	0.01	0.00
La	0.00	0.00	0.00	0.00	0.00	0.00	0.00	0.00	0.00	0.00	0.00	0.00	0.00	0.00
Cl	0.00	0.00	0.00	0.00	0.00	0.00	0.01	0.01	0.00	0.00	0.01	0.00	0.01	0.00
F	0.89	0.03	0.90	0.03	0.79	0.03	0.88	0.03	0.91	0.03	0.90	0.03	0.93	0.02
OH[a]	0.11	0.03	0.10	0.03	0.21	0.03	0.11	0.03	0.08	0.03	0.09	0.03	0.06	0.02

Notes: oxide in wt.%, cationic contents in apfu. a: calculated OH cationic content. bdl: below detection limit

In the leucogranite and episyenite samples, apatite grains appear as squat prisms up to 500 µm in length. In the leucogranites, the crystals display generally yellow colors in cathodoluminescence (CL) with irregular patchy zoning (Fig. 5a) not visible in the BSE images. In these CL images, the dark yellow color characteristic of the grain cores generally evolves toward light yellow or even locally light blue colors for the rims. This change in color corresponds to a decrease in the Fe and Mn contents observed in the chemical maps (Fig. 5a) and in the Mn versus Fe diagram (Fig. 6). In samples PONT-10 and 26, where we performed systematic core and rim analyses, the cores are characterized by Mn and Fe content from 0.04 to 0.17 and 0.02 to 0.07 apfu, respectively, whereas in the rims, the Mn and Fe contents range from < 0.01 to 0.11 and < 0.01 to 0.06 apfu, respectively (Fig. 6). In the episyenite samples, apatite crystals generally display yellow or light blue colors with irregular zoning. These zones are locally characterized by a dark blue color in the CL images and a light color in the BSE images (Fig. 5b). Crystals or zones with a yellow color in the CL images are generally characterized by elevated Mn and Fe content from 0.08 to 0.12 and 0.03 to 0.04 apfu, respectively, whereas light blue crystals display Fe

and Mn content < 0.01 apfu (Fig. 6). Zones with a dark blue and a light color in the CL and BSE images, respectively, are characterized by the absence of Fe and Mn, an elevated average As content of 0.28 apfu (commonly < 0.01 apfu in other grains) and an elevated average OH content of 0.21 apfu (generally around 0.1 in other crystals; Table 2). This increase of the As and OH contents marks the evolution toward the johnbaumite pole [$Ca_5(AsO_4)_3(OH)$].

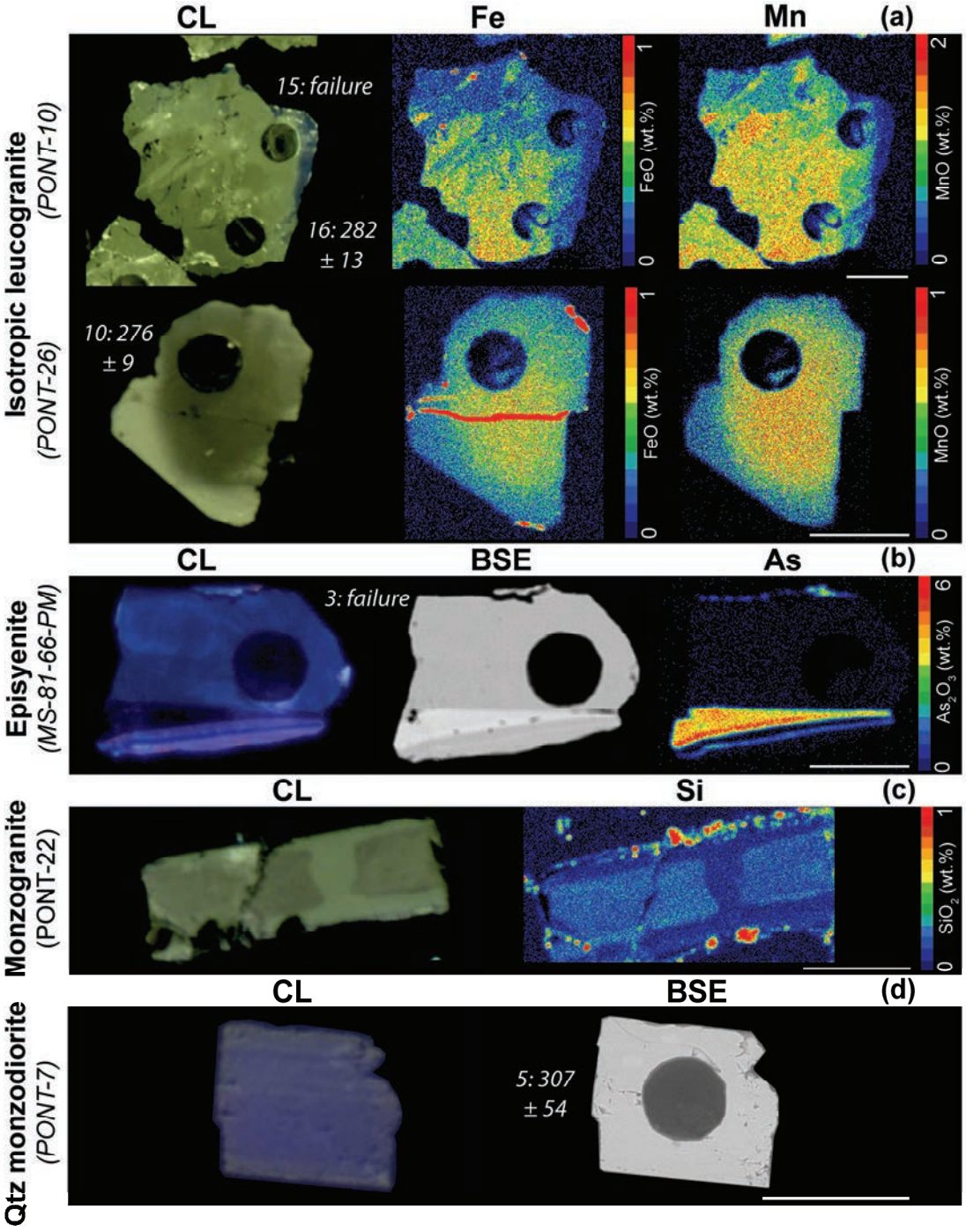

Figure 5: Cathodoluminescence (CL), backscattered electron images (BSE) and chemical maps of Fe, Mn, As or Si for representative apatite grains from magmatic rocks of the Pontivy-Rostrenen magmatic complex. Number in white represent the associated ^{207}Pb corrected age. The white bar represents 100 µm

In the monzogranite sample, apatite appears as squat or elongated prisms up to 500 µm in length displaying a yellow color in cathodoluminescence. Apatite crystals generally appear as homogeneous in the CL images, but may locally display regular zoning, not visible in the BSE images, with a dark yellow core and a light yellow rim (Fig. 5c). This change can be attributed to a slight decrease of the Si content from 0.02 to < 0.01 apfu. The Mn (0.02 – 0.03 apfu) and Fe (0.01 – 0.03 apfu) contents are generally lower than those found in the apatite grains from the leucogranites (Fig. 6). Regarding the quartz monzodiorite samples, apatite crystals appear as squat or elongated prisms up to 200 µm in length. These apatite crystals appear as homogenous in the BSE images and display purple colors in the CL images with commonly yellow rims (Fig. 5d) likely marking a slight decrease of the LREE content ([La + Ce] ~0.01 apfu to below detection limits), REE together with Mn representing some of the main activators for CL (e.g. Barbarand and Pagel 2001; Bouzari et al. 2016) (Fig. 5d). These crystals are characterized by low Fe and Mn contents below 0.01 apfu.

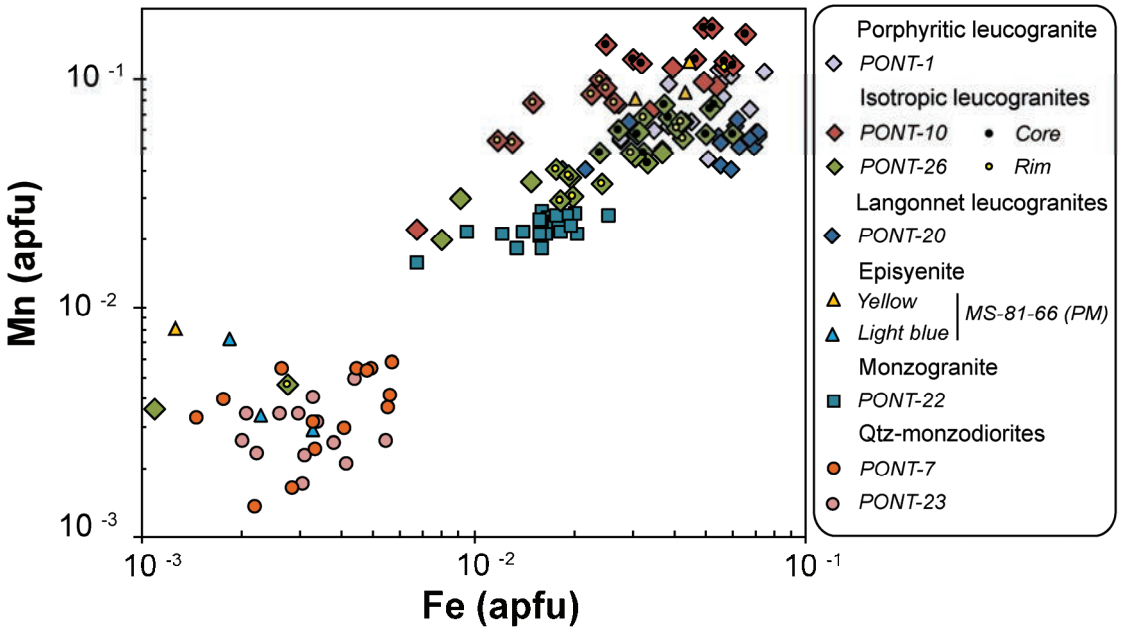

Figure 6: Fe versus Mn diagram displaying the analyses made on apatite grains. APFU = atoms per formula unit.

4.3. Apatite U-Pb dating

Apatite U-Pb analyses were performed for all the samples presented in the last section with the exception of the quartz monzodiorite PONT-23. The results are reported in Tera-Wasserburg diagrams (Fig. 7).

In the leucogranites, the analyses are discordant with $^{207}Pb/^{206}Pb$ ratios ranging from 0.148 to 0.537. Due to the small size of the rims observed in the CL images, analyses were almost exclusively performed on grains cores. For the porphyritic leucogranite sample PONT-1 (Fig. 7a), 23 analyses performed on 19 different grains define a poorly defined lower intercept date of 285.4 ± 8.5 Ma (MSWD = 6.8). If the discordia is forced to the composition of a common Pb calculated at 285 Ma (Stacey and

Kramers, 1975), a comparable poorly constrained date of 295.9 ± 6.0 (MSWD = 6.4) is obtained. Using the common Pb composition calculated at 285 Ma, the analyses yield two populations for the ^{207}Pb corrected dates; 307.2 ± 7.1 Ma (MSWD = 2.2, n = 9) and 286.2 ± 3.8 Ma (MSWD = 1.6, n = 14), respectively. For the isotropic leucogranite sample PONT-10 (18 analyses out of 16 grains; Fig. 7b), the unforced discordia yields a lower intercept date of 270.4 ± 6.7 Ma (MSWD =2.5) comparable with the lower intercept date of 277.1 ± 3.6 Ma (MSWD = 6.4) obtained if the discordia is anchored to the common Pb composition calculated at 270 Ma. Once again, two populations are obtained for the corrected ^{207}Pb dates, calculated using the common Pb composition at 270 Ma, and yield mean values of 294.9 ± 7.4 Ma (MSWD = 0.12) and 279.9 ± 2.9 Ma (MSWD = 0.42), respectively. For the isotropic leucogranite PONT-26 (21 analyses out of 15 grains; Fig. 7c), we obtain an unforced lower intercept date of 272.8 ± 2.9 Ma (MSWD = 1.2) slightly younger than the forced intercept date of 285.1 ± 4.2 Ma (MSWD = 5.8) obtained if the discordia is anchored at a common Pb composition calculated at 275 Ma. Two populations of ^{207}Pb corrected dates are obtained and yield mean values of 299.9 ± 4.3 Ma (MSWD = 0.26) and 279.6 ± 2.1 Ma (MSWD = 0.59), respectively. Then, for the Langonnet leucogranite sample (PONT-20; 24 analyses out of 18 grains; Fig. 7d), the poorly constrained unforced lower intercept date of 278.0 ± 11.0 Ma (MSWD = 8.7) is comparable with the forced lower intercept date of 289.8 ± 4.0 Ma (MSWD = 9.1) obtained if the discordia is anchored at the common Pb composition calculated at 280 Ma. The analyses yield two populations of ^{207}Pb corrected dates with a mean value of 297.1 ± 3.0 Ma (MSWD = 1.6) and 280.9 ± 2.1 Ma (MSWD = 0.63), respectively. There is no clear correlation between the apparent ^{207}Pb corrected dates obtained for the apatite grains from the leucogranites and their relative Mg and/or Fe contents.

For the episyenite sample (MS-81-66-PM; Fig. 7e), the discordant analyses display highly variable common Pb contents with ^{207}Pb/^{206}Pb values ranging from 0.122 to 0.861. No analyses were performed on the dark blue CL zones because of their small sizes. In this sample, 9 analyses out of 6 grains presenting yellow or light blue colors and characterized by ^{207}Pb/^{206}Pb values below 0.300, display a well-defined discordia and yield an unforced lower intercept date of 289.0 ± 10.0 Ma (MSWD =0.54). This date is identical within error with the lower intercept date of 287.3 ± 3.5 Ma (MSWD = 0.48), obtained by forcing the discordia at the common Pb composition calculated at 290 Ma, and with the mean ^{207}Pb corrected date of 286.5 ± 3.8 Ma (MSWD = 0.31). The other data characterized by a higher content in common Pb are more scattered and were therefore not used.

Figure 7: Tera-Wasserbug concordia diagrams with the corresponding ^{207}Pb corrected dates for analyses made on apatite grains from the Pontivy-Rostrenen complex. The red discordia in dashed is unforced whereas the grey discordia in solid line is anchored at the composition of common Pb (Stacey and Kramers, 1975) calculated at the unforced lower intercept date. 207Pb corrected dates are also calculated using the common Pb composition at the unforced lower intercept date (Stacey and Kramers, 1975). Dashed ellipses in (e) represent analyses not used for dates calculations. Ellipses and errors on ages are reported at 2σ. The main period of U deposit formation in the complex is reported for comparison (U).

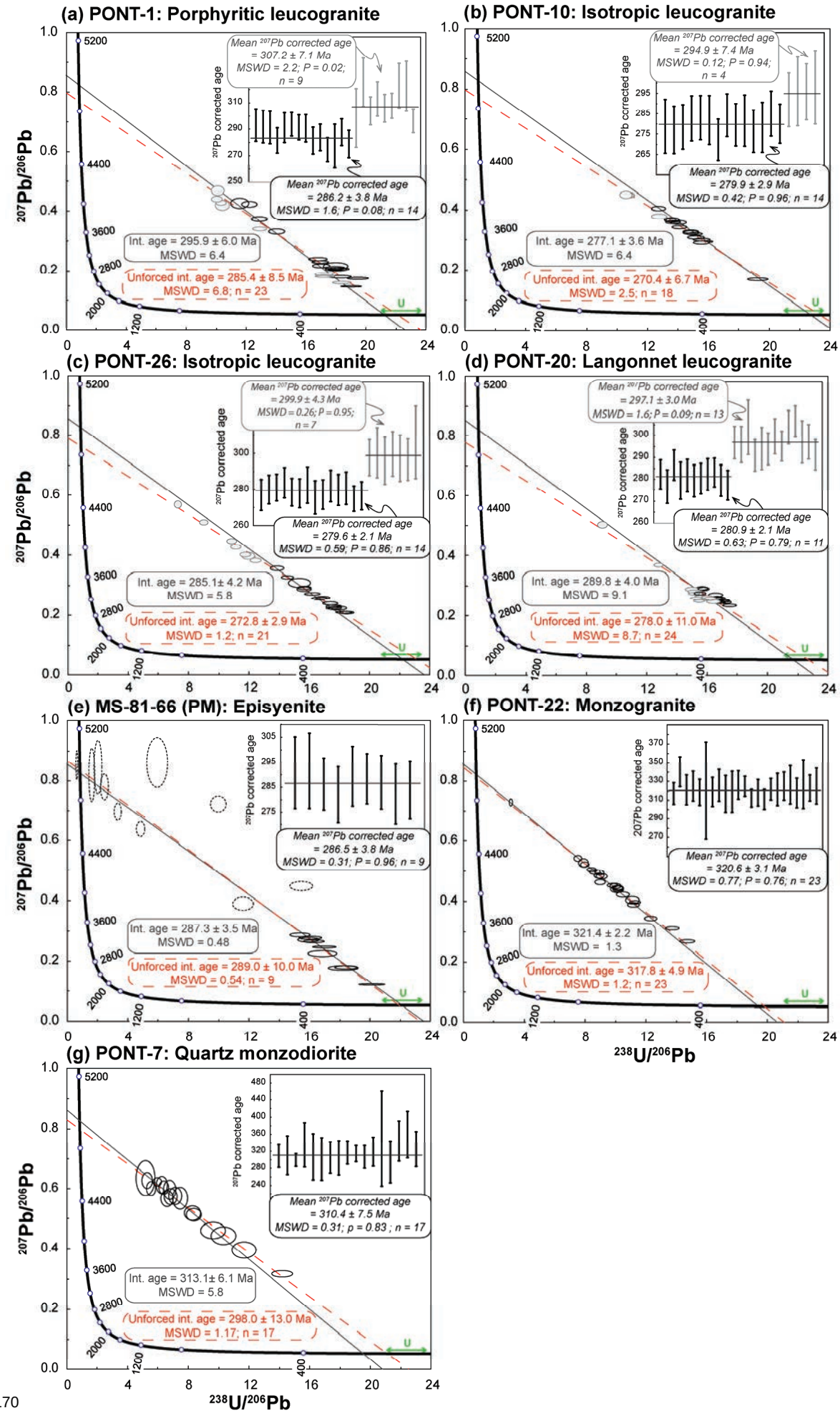
(a) PONT-1: Porphyritic leucogranite
Mean 207Pb corrected age = 307.2 ± 7.1 Ma MSWD = 2.2; P = 0.02; n = 9
Mean 207Pb corrected age = 286.2 ± 3.8 Ma MSWD = 1.6; P = 0.08; n = 14
Int. age = 295.9 ± 6.0 Ma MSWD = 6.4
Unforced int. age = 285.4 ± 8.5 Ma MSWD = 6.8; n = 23
(b) PONT-10: Isotropic leucogranite
Mean 207Pb corrected age = 294.9 ± 7.4 Ma MSWD = 0.12; P = 0.94; n = 4
Mean 207Pb corrected age = 279.9 ± 2.9 Ma MSWD = 0.42; P = 0.96; n = 14
Int. age = 277.1 ± 3.6 Ma MSWD = 6.4
Unforced int. age = 270.4 ± 6.7 Ma MSWD = 2.5; n = 18
(c) PONT-26: Isotropic leucogranite
Mean 207Pb corrected age = 299.9 ± 4.3 Ma MSWD = 0.26; P = 0.95; n = 7
Mean 207Pb corrected age = 279.6 ± 2.1 Ma MSWD = 0.59; P = 0.86; n = 14
Int. age = 285.1± 4.2 Ma MSWD = 5.8
Unforced int. age = 272.8 ± 2.9 Ma MSWD = 1.2; n = 21
(d) PONT-20: Langonnet leucogranite
Mean 207Pb corrected age = 297.1 ± 3.0 Ma MSWD = 1.6; P = 0.09; n = 13
Mean 207Pb corrected age = 280.9 ± 2.1 Ma MSWD = 0.63; P = 0.79; n = 11
Int. age = 289.8 ± 4.0 Ma MSWD = 9.1
Unforced int. age = 278.0 ± 11.0 Ma MSWD = 8.7; n = 24
(e) MS-81-66 (PM): Episyenite
Mean 207Pb corrected age = 286.5 ± 3.8 Ma MSWD = 0.31; P = 0.96; n = 9
Int. age = 287.3 ± 3.5 Ma MSWD = 0.48
Unforced int. age = 289.0 ± 10.0 Ma MSWD = 0.54; n = 9
(f) PONT-22: Monzogranite
Mean 207Pb corrected age = 320.6 ± 3.1 Ma MSWD = 0.77; P = 0.76; n = 23
Int. age = 321.4 ± 2.2 Ma MSWD = 1.3
Unforced int. age = 317.8 ± 4.9 Ma MSWD = 1.2; n = 23
(g) PONT-7: Quartz monzodiorite
Mean 207Pb corrected age = 310.4 ± 7.5 Ma MSWD = 0.31; p = 0.83 ; n = 17
Int. age = 313.1± 6.1 Ma MSWD = 5.8
Unforced int. age = 298.0 ± 13.0 Ma MSWD = 1.17; n = 17
207Pb/206Pb
238U/206Pb
207Pb corrected age

Regarding the monzogranite sample (PONT-22), the 23 out of 22 grains analyses are discordant and common Pb rich with $^{207}Pb/^{206}Pb$ values ranging from 0.268 to 0.729. The analyses yield a well-defined unforced lower intercept date of 317.8 ± 4.9 Ma (MSWD = 1.2) comparable with the lower intercept date of 321.4 ± 2.2 Ma (MSWD = 1.3) obtained if the discordia is anchored at the composition of common lead calculated at 315 Ma. The mean ^{207}Pb corrected date of 320.6 ± 3.1 Ma (MSWD = 0.76) is identical within error.

Finally, for the quartz-monzodiorite sample (PONT-7), the 17 out of 13 grains discordant analyses are common Pb rich and display $^{207}Pb/^{206}Pb$ values from 0.316 to 0.628. The data align on a discordia which yields a well-defined unforced intercept date of 298 ± 13 Ma (MSWD = 1.17) comparable with a lower intercept date, forced at the common Pb composition calculated at 300 Ma, of 313.1 ± 6.1 Ma (MSWD = 5.8). The mean ^{207}Pb corrected date of 310.4 ± 7.5 Ma (MSWD = 0.31) is comparable with the two lower intercept dates.

4.4. Uranium oxide petrography

In this study, uranium oxide U-Pb dating was performed on 6 mounts or thin sections belonging to the AREVA collection from the Kerlech (Lignol), Rosglas and Quérrien (Kerjean) deposits as well as three deposits in the region of Guern (Fig. 2: Quistiave, Kerroch and a sample referenced as "undifferentiated-Guern" in the AREVA collection).

In the Guern region, the mineralization is described as brecciated quartz veins, following N°120 – 130 oriented faults, which mostly occur in tectonized contacts between the porphyritic and isotropic leucogranites close to micashists enclaves and/or small stocks of quartz monzodiorites (Marcoux 1982; Cuney 2006) (Fig. 2). The Quistiave deposit consists of two veins orientated WNW-ESE and dipping SW, occurring about 80 m apart. The veins are more or less parallel to alternating bands of a porphyritic biotite-rich – muscovite granite and an equigranular muscovite-rich and biotite-poor leucogranite, and minor pegmatite veins. The uranium mineralization occurs as discontinuous lenses along these structures and has been mined to a depth of 95 m. The uranium oxide nodules (up to 50 cm in size) have grown on a ~1 cm thick quartz comb before the vein was filled by brecciated quartz, chalcopyrite, galena, sphalerite, marcasite, covellite and bismuthinite (Cuney 2006). The analyzed sample corresponds to a nodule of pseudo-spherultic to spherulitic uranium oxide (Ur1) brecciated by microfractures mainly filled with quartz (Qtz), chalcopyrite, galena (Gn), sphalerite and a product of alteration of Ur1 (Alt Ur1; Fig. 8a). In the sample from the Kerroch deposit, the mineralization occurs as clusters of millimeter sized spherultic uranium oxides disseminated in a leucogranitic granitic country rock and crosscut by micrometers large veinlets filled with quartz and sulfides (Fig. 8b). In the last sample from the Guern region (undifferentiated-Guern, Fig. 8c), hundred micrometers to millimeters large spherulitic to pseudo-spherultic quartz-uranium oxide veinlets crosscut the leucogranitic country rock.

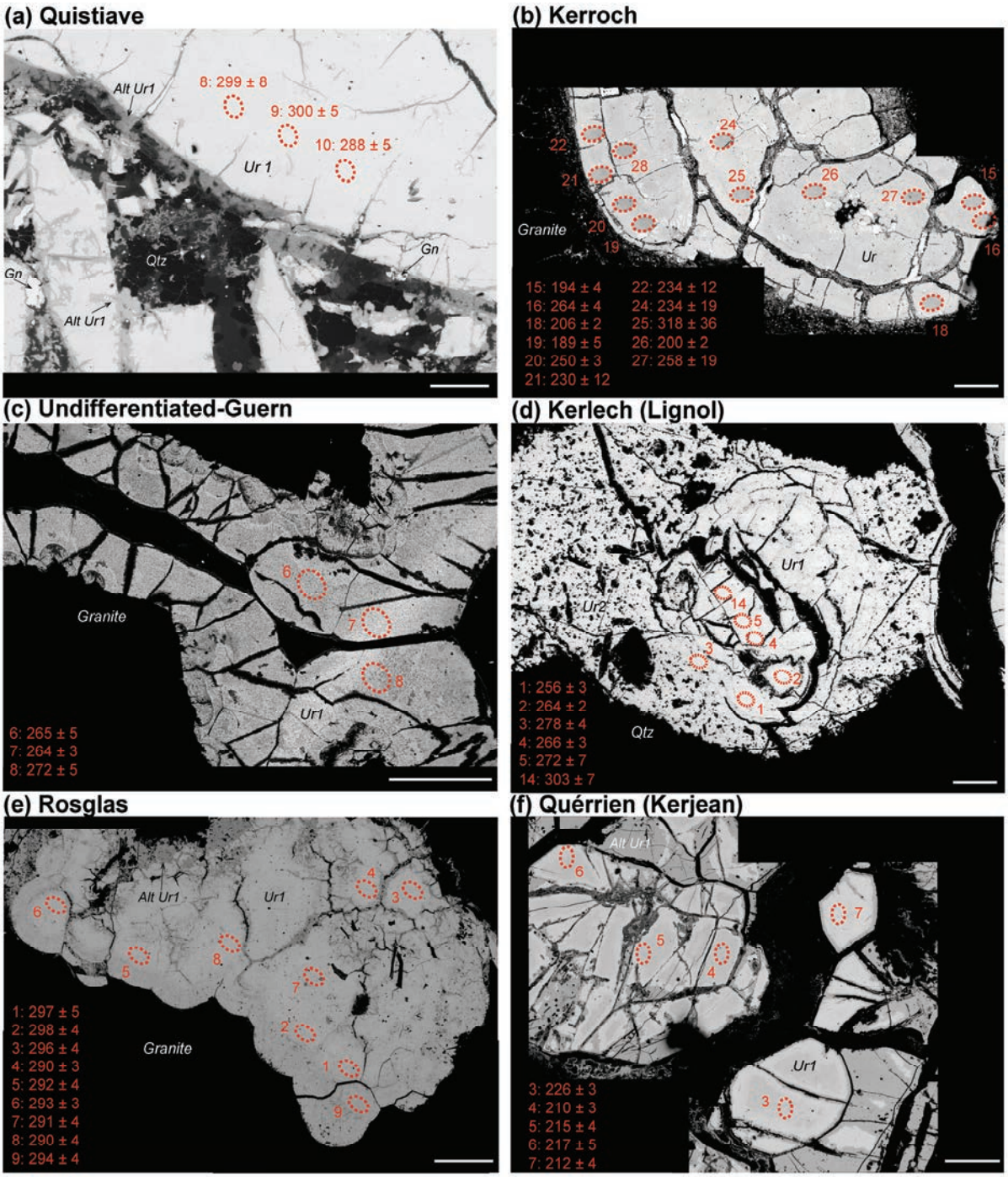

Figure 8: Backscattered electron images for uranium oxides (Ur) from uranium deposits of the Pontivy district. Red dashed ellipses represent the location of SIMS U-Pb analyses with the corresponding $^{207}Pb/^{206}Pb$ date. In samples, alt Ur1 corresponds to the alteration of the first generation of uranium oxide. In (d), a first generation of spherulitic uranium oxide (Ur1) is brechified by quartz and a second generation of uranium oxide (Ur2). The white bar represents 100 µm.

In the Kerlech (Lignol) deposit, 50 cm to 1 m sized mineralized quartz veins oriented N-S to N°170 crosscut the isotropic leucogranite from the contact with the sediments (Marcoux 1982; Cuney 2006) (Fig. 2). Vein infilling began with a quartz comb followed by fine grained quartz bearing uranium oxide and chalcopyrite. The last infilling event is represented by barren quartz (Cuney 2006). In the studied sample, a centimeter large cluster of uranium oxide spherules (Ur1) up to 500µm in length occurs

in fine grained (< 1 mm) quartz together with Fe oxides. The first generation of spherulitic uranium oxide (Ur1) is brecciated by a second generation of uranium oxide (Ur2) accompanied by quartz, galena and locally bismuthinite (Fig. 8d).

Rosglas and Quérrien (Kerjean) are both classified as episyenite type deposits and are found in the isotropic leucogranite facies (Fig. 2). At Rosglas the episyenite forms a nearly cylindric subvertical column at a tectonic intersection. In the Rosglas sample, the mineralization occurs as millimeter large clusters of uranium oxide spherules, with a diameter of 10 to 100 µm, disseminated inside an episyenitized leucogranitic country-rock (Fig.8e). In the Quérrien (Kerjean) sample, the mineralization occurs as brecciated millimeter large pseudo-spherulitic uranium oxides veinlets or clusters disseminated inside an episyenitized leucogranitic country rock. In the BSE images, uranium oxides, crosscut by numerous millimeter large fractures, are characterized by the presence of light grey zones interpreted as unaltered (Ur1) and dark grey zones interpreted as altered (Alt Ur 1; Fig. 8f).

4.5. Uranium oxide U-Pb dating

Uranium oxides areas selected for U-Pb analyses were chosen following a precise characterization by BSE images and EPMA analyses and as a consequence SIMS dating were realized only on chemically homogenous areas poorly affected by post-crystallization alteration (Fig. 8). Yet, most analyses plot in a discordant positon in Tera-Wasserburg (TW) and Wetherill concordia diagrams (Wc) (Fig. 9) suggesting Pb losses which could be the result of the alteration evidenced during the petrographic study (see above and Fig. 8).

For the Quistiave (Guern) deposit (Fig. 9a), the 8 analyses plot in a discordant position in the TW diagram and define a poorly constrained upper intercept date of 294 ± 67 Ma (MSWD = 6.6) and a lower intercept date of 10 ± 120 Ma. If the discordia is anchored at 0 Ma in the Wc diagram, assuming a recent Pb loss, an upper intercept date of 286 ± 10 Ma (MSWD = 3.5) is obtained. For the Kerroch (Guern) deposit (Fig. 9b), the 30 analyses, which reveal Pb loss, are discordant to sub-concordant and display an important scattering in the TW diagram. A poorly constrained upper intercept date of 268 ± 78 Ma (MSWD = 12) and a lower intercept date of 43 ± 110 Ma are obtained. If the concordia is anchored at 0 Ma in the Wc diagram, an upper intercept date of 248 ± 17 Ma (MSWD = 1.4) is obtained. For the last sample from the deposits of the Guern region (Guern – undifferentiated; Fig. 9c), the 15 discordant analyses, affected by Pb loss, define a relatively well constrained upper intercept date of 269 ± 10 Ma (MSWD = 2.0) and a lower intercept date of -12 ± 28 Ma in the TW diagram. Assuming a recent Pb loss, an upper intercept date of 273 ± 3 Ma (MSWD = 1.2) can be calculated. For the Kerlech (Lignol) deposit (Fig. 9d), the 13 analyses plot in a discordant position and display an important scattering in the TW diagram. The data define a poorly constrained upper intercept date of 280 ± 110 Ma (MSWD = 6.9) and a lower intercept date of 19 ± 170 Ma. If the discordia is anchored at 0 Ma in the Wc diagram, an upper intercept date of 267 ± 11 Ma (MSWD = 1.2) is obtained. Regarding the sample from the Rosglas

deposit (Fig. 9e), the 12 discordant analyses, affected by Pb loss, define a relatively well defined upper intercept date of 301 ± 21 Ma (MSWD = 1.2) and a lower intercept date of 27 ± 88 Ma. A comparable upper intercept date of 296 ± 4 Ma (MSWD = 0.5) is obtained by anchoring the discordia at 0 Ma. Finally, for the Quérrien (Kerjean) deposit, the 14 analyses plot in concordant to discordant (reverse or normal) positions in the TW diagram reflecting variable degrees of Pb loss. The data define a relatively well constrained upper intercept date of 220 ± 5 Ma (MSWD = 3.7) with a lower intercept date of -18 ± 81 Ma. By anchoring the discordia at 0 Ma, an identical upper intercept date of 219 ± 5Ma (MSWD = 0.8) is obtained.

5. Discussion

5.1. U behavior in the Pontivy-Rostrenen complex

In contrast to the quartz monzodiorite and monzogranite samples, characterized by low U contents (< 9 ppm) and elevated Th/U values mostly above 3, the leucogranites are characterized by both highly variable U contents (~3 to 27 ppm) and Th/U ratios (~5 to 0.1). The Th/U is an indicator of the nature of the U bearing minerals in granitoids and the elevated Th/U ratios (> 2) measured in some samples suggest that most of their U is hosted in refractory mineral phases such as zircon, titanite or allanite for quartz monzodiorites and zircon or monazite for leucogranites and monzogranites (e.g. Cuney 2014). On the other hand, low Th/U values (< 1) and U contents of tens ppm in peraluminous leucogranitic melts favor the crystallization of magmatic uranium oxides at the expense of monazite (Friedrich et al. 1987; Peiffert et al. 1994, 1996; Cuney 2014). In the magmas at the origin of the leucogranites, extraction of accessory minerals incorporating limited amounts of U, such as monazite and zircon, during fractional crystallization (see the negative correlation between SiO_2, Th and Zr documented by Ballouard et al. submitted, their Fig. 7) likely induced an increase of the U contents and a decrease of the Th/U values. Such behavior, well-illustrated by the correlation between Th and U in the Langonnet leucogranite (Fig. 3b), likely triggered the crystallization of uranium oxides in the most evolved leucogranitic melts. In contrast to the Langonnet leucogranite, there is no correlation between Th and U for the porphyritic and isotropic leucogranites (Fig. 3b). We propose that the very variable Th/U values displayed by these samples (isotropic facies more particularly) can be attributed to a combination between magmatic evolution (uranium oxides crystallization), hydrothermal alteration and/or surface weathering (uranium oxides leaching). In the Th/U radiometric map (Fig. 4), U deposits are almost exclusively located within isotropic leucogranites at the transition between low Th/U and high Th/U zones. This association suggests that hydrothermal U deposits formed close to the areas where U oxide leaching occurred (i.e. zones with local increase of Th/U values).

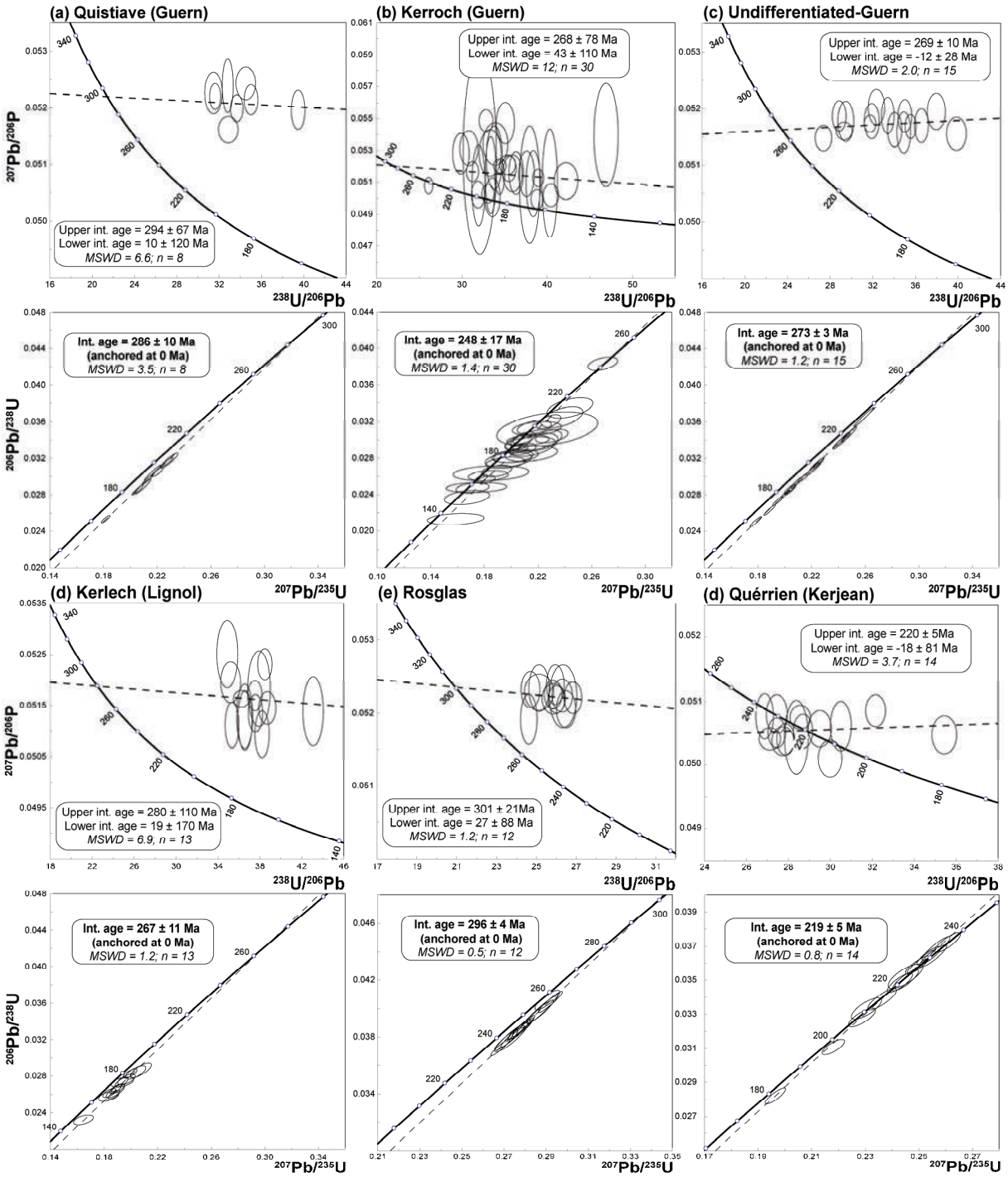

Figure 9: Tera Wasserburg and Wetherill concordia diagrams displaying the analyses made on uranium oxides from the uranium deposits from the Pontivy district. In the Wetherill diagrams, the discordia is anchored at 0 Ma. Ellipses and age errors are reported at 2 σ.

5.2. Age of the uranium mineralization

The results of uranium oxide U-Pb dating evidence different U mineralizing events in the Pontivy-Rostrenen complex. In the Guern region (Fig. 2), the sample Guern-undifferentiated provided a well constrained unforced upper intercept date of 269 ± 10 Ma which is identical within error with the upper intercept date of 273 ± 3 Ma obtained if the discordia is anchored at 0 Ma (Fig. 9c). As a

consequence, we suggest that this deposit formed 273 ± 3 Ma ago. For the Quistiave (Guern) deposit, uranium oxide analyses yield a poorly constrained unforced upper intercept date of 294 ± 67 Ma and a forced upper intercept date of 286 ± 10 Ma. The date of 286 ± 10 Ma, which seems slightly older than the age of 273 ± 3 Ma obtained on the previous sample is interpreted as the age of formation of the Quistiave U deposit. Regarding the Kerroch (Guern) deposit (Fig. 9b), the two poorly constrained upper intercept dates (268 ± 78 Ma and 248 ± 17 Ma) are comparable with the ages for the two other deposits in the area, but the scattering of the data prevents a precise estimation of the mineralization age. Analyses on uranium oxides from the Rosglas deposit yield a relatively well constrained unforced intercept date of 301 ± 21 Ma comparable to a forced upper intercept date of 296 ± 4 Ma that we interpret as the age of formation of this deposit (Fig. 9e). Regarding the Kerlech deposit, the scattering of the data in the Tera Wasserburg diagram leads to the calculation of a poorly constrained unforced upper intercept date of 287 ± 110 Ma (Fig. 9d). However, an upper intercept date of 267 ± 11 Ma comparable to the ages obtained on the Guern region is obtained by anchoring the discordia at 0 Ma and is interpreted to reflect the age of emplacement of the U mineralization. Finally, the uranium oxides from the Quérrien (Kerjean) deposit yield two identical upper intercept dates of 220 ± 5 Ma and 219 ± 5 Ma (Fig. 9d) interpreted as the age of their crystallization. To sum up, the hydrothermal U deposits from the Pontivy-Rostrenen complex mostly form during the Early Permian from ca. 300 to 270 Ma but U deposits formation or U remobilization also occurred during the Trias around 220 Ma such as illustrated in the Quérrien (Kerjean) deposit.

5.3. Apatite as a proxy to date emplacement and/or alteration ages?

The closure temperatures for Pb diffusion in apatite, determined from empirical or experimental studies, range from ~375 to 550°C (e.g. Chamberlain and Bowring 2000; Schoene and Bowring 2006; Cochrane et al. 2014) and are therefore lower than those calculated for zircon (> 900 °C; e.g. Cherniak and Watson 2001). The apatite U-Pb system could consequently represent a good tool to date the cooling of big size intrusions but also the emplacement ages of small size intrusive bodies (Pochon et al. 2016). In addition, apatite could represent a perfect mineral to study mineralizing systems because it can incorporate halogen and a large range of trace elements. It is also highly reactive to fluid circulations (e.g. Harlov 2015; Zirner et al. 2015; Bouzari et al. 2016). Therefore, the apatite U-Pb system could also represent a promising tool to date hydrothermal events.

5.3.1. Apatite dating in rocks non affected by fluids

In the quartz monzodiorite and the monzogranite, apatite grains are unzoned or display discrete regular zonation on CL images (Fig. 5c and d), which suggest that these crystals have kept their magmatic signature and were not affected by significant hydrothermal processes. U-Pb dating of apatite grains from the quartz monzodiorite yield a mean ^{207}Pb corrected date of 310.4 ± 7.5 Ma comparable with both unforced and forced lower intercept dates of 298.0 ± 13.0 Ma and 313.1 ± 6.1 Ma in the TW

diagram, respectively (Fig. 7g). These three dates are slightly younger than or identical within error to the zircon U-Pb date of 315.2 ± 2.9 Ma obtained on this facies (Ballouard et al. submitted) (Table 3). As a consequence, these apatite U-Pb dates can be interpreted as reflecting the emplacement or a cooling age for this quartz-monzodiorite intrusion. In the monzogranite, apatite grains provide a mean ^{207}Pb corrected date of 320.6 ± 3.1 Ma comparable with the unforced and forced intercept dates of 317.8 ± 4.9 Ma and 321.4 ± 2.2 Ma, respectively. The forced intercept date is slightly older than the zircon U-Pb age of 315.5 ± 2.0 obtained on this sample (Ballouard et al. submitted) (Table 3). This could be due to the fact that the common Pb value used to force the discordia and calculated using the model of Stacey and Kramers (1975) differs slightly from the real one. The two other dates are identical within error and can be interpreted as reflecting the emplacement age of the monzogranitic intrusion.

Table 3: comparison between the different U-Pb dates obtained on zircon (Ballouard et al., submitted) and apatite (this study) grains from samples of the Pontivy-Rostrenen complex.

Sample	***Emplacement age (U-Pb zircon)***	***Unforced discordia dates***	***Age used for common Pb***	***Forced discordia Dates***	***^{207}Pb corrected dates***
Porphyritic leucogranite (PONT-1)	316.7 ± 2.5 Ma *(MSWD = 1.2)*	285.4 ± 8.5 Ma *(MSWD=6.8)*	285 Ma	295.9 ± 6 Ma *(MSWD = 6.4)*	307.2 ± 7.1 Ma 286.2 ± 3.8 Ma
Isotropic leucogranite (PONT-10)	310.3 ± 4.7 Ma *(MSWD = 2.5)*	270.4 ± 6.7 Ma *(MSWD=2.5)*	270 Ma	277.1 ± 3.6 Ma *(MSWD = 6.4)*	294.9 ± 7.4 Ma 279.9 ± 2.9 Ma
Isotropic leucogranite (PONT-26)		272.8 ± 2.9 Ma *(MSWD = 1.2)*	275 Ma	285.1 ± 4.2 Ma (MSWD = 5.8)	299.9 ± 4.3 Ma 279.6 ± 2.1 Ma
Langonnet leucogranite (PONT-20)	304.7 ± 2.7 Ma *(MSWD = 0.57)*	278 ± 11 Ma *(MSWD = 8.7)*	280 Ma	289.8 ± 4 Ma (MSWD = 9.1)	297.1 ± 3 Ma 280.9 ± 2.1 Ma
Episyenite (MS-81-66-PM)		289 ± 10 Ma *(MSWD = 0.54)*	290	287.3 ± 3.5 Ma *(MSWD = 0.48)*	286.5 ± 3.8 Ma
Monzogranite (PONT-22)	315.5 ± 2.0 Ma *(MSWD = 1.5)*	317.8 ± 4.9 Ma *(MSWD = 1.2)*	315	321.4 ± 2.2 Ma *(MSWD = 1.3)*	320.6 ± 3.1 Ma
Monzodiorite Quartzique (PONT-7)	315.2 ± 2.9 Ma *(MSWD = 0.94)*	298 ± 13 Ma *(MSWD = 1.17)*	315	313.1 ± 6.1 Ma (MSWD = 5.8)	310.4 ± 7.5 Ma

5.3.2. Apatite dating in rocks affected by fluids

In contrast to the monzogranite and quartz monzodiorite apatite crystals, the apatite grains from the leucogranites and episyenite display petro-geochemical and geochronological evidence for pervasive hydrothermal alteration. Indeed, these apatite grains show patchy irregular zoning in the CL images and in the Fe and Mn chemical maps, likely reflecting fluid interactions processes (Fig.5a). The decrease in the Mn and Fe contents, generally observed from the core to the rim (Fig. 5a and 6) likely reflects the transition toward a more oxidized environment during this (or these) hydrothermal event(s). Indeed, Mn and Fe are more compatible in apatite in reduced conditions as Mn2+ and Fe2+ substitute easily to Ca2+ (e.g. Miles et al. 2014). In addition to the irregular patching zoning reflecting various Fe and Mn mobility, apatite grains from the episyenite also display complex zoning, probably hydrothermal in

origin, with some enrichment in As and OH characteristic of a substitution toward the johnbaumite pole (Fig. 5b). This OH enrichment suggests that these zones crystalized in a H_2O rich environment whereas the increase of the As content reflects the high oxygen fugacity of the involved hydrothermal fluids as As5+ will substitute more easily for P5+ than As3+.

In the episyenite sample MS-81-66 (Fig. 7e), apatite grains yield a mean ^{207}Pb corrected date of 286.5 ± 3.8 Ma (MSWD=0.31) identical within error with the forced (287.3 ± 3.5 Ma, MSWD=0.48) and unforced (289.0 ± 10 Ma; MSWD=0.54) lower intercept dates. These apatite grains display petro-geochemical evidence for an interaction with oxidizing hydrothermal fluids (see above). Therefore, we believe that the age of the episyenitization (i.e. the metasomatism of the leucogranite) is ca. 285 Ma old.

In each of the leucogranite samples, the data obtained by U-Pb dating of apatite reveal a complex behavior with regard to their U-Pb system. First of all, the unforced lower intercept dates obtained for the leucogranites are characterized by rather high MSWD values (between 2.5 and 8.7) with the exception of one of the isotropic leucogranite PONT-26 (MSWD=1.2). This probably means that the scattering of the data can be attributed to geological event(s) rather than to an analytical problem. This is further amplified by the fact that unforced lower intercept dates, forced lower intercept dates and ^{207}Pb corrected dates are systematically different and, when available, are always younger than the emplacement ages (Ballouard et al. submitted; see Table 3). As outlined earlier, all the apatite grains from these leucogranites show evidence for some interaction with fluids. At a first order, this means that the U-Pb system in these grains has been affected by these late fluid circulations.

It is also interesting to note that, in all cases, the mean 207Pb corrected dates are showing two different populations for each sample: A first one returning dates in the range 294.9 ± 7.4 Ma to 307.2 ± 7.1 Ma, and a second one with dates ranging from 279.6 ± 2.1 Ma to 286.2 ± 3.8 Ma (Fig. 7a-d). In figure 10, the calculated U contents in the apatite grains dated in this study are reported as a function of the corresponding ^{207}Pb corrected dates. Regarding the apatite grains from the monzogranite ([U] ~7 – 90 ppm), quartz-monzodiorite ([U] ~12 – 56 ppm), Langonnet leucogranite ([U] ~48 – 184 ppm) and episyenite ([U] ~95 – 263 ppm) samples, the U content are relatively constant and there is no correlation between the 207Pb corrected dates. In contrast, the U contents in the apatite from the isotropic and the porphyritic leucogranites increase as the ^{207}Pb corrected dates get younger. This correlation between the apatite grain apparent ages and their U contents likely shows that the fluids which interacted with these apatite grains were U-rich.

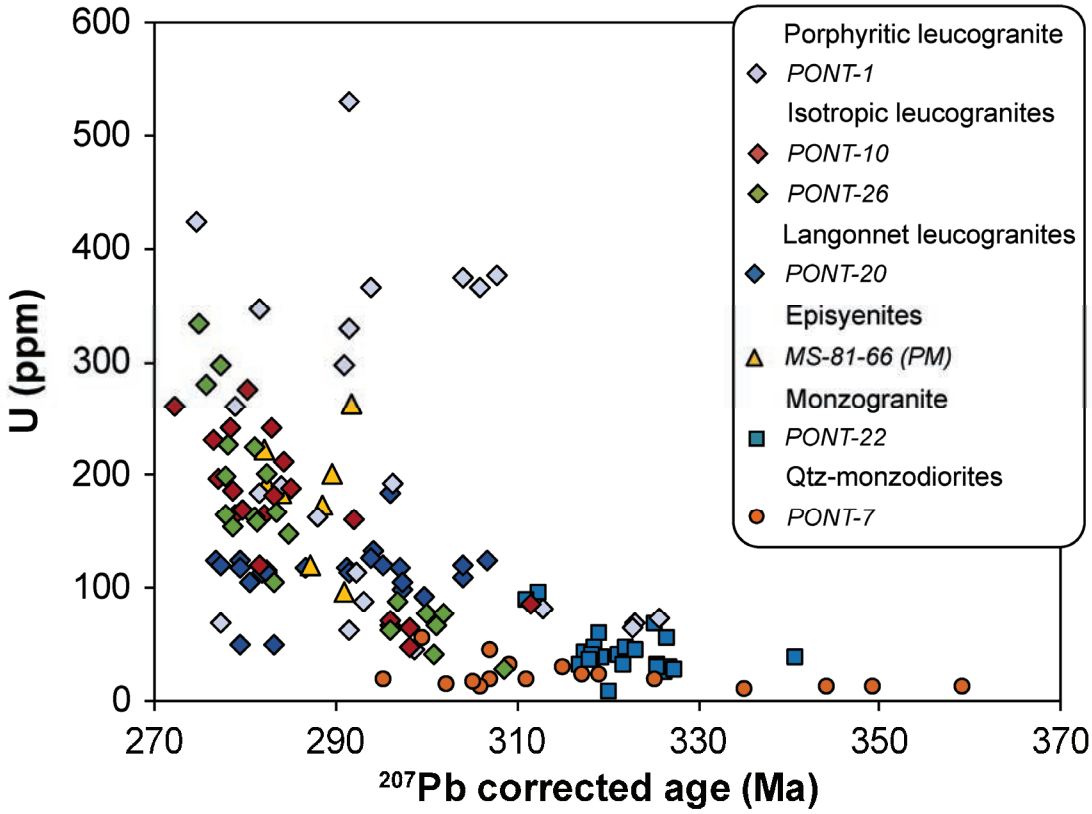

Figure 10: Diagram reporting the U content of apatite as a function of the corresponding ^{207}Pb corrected date.

In order to see if we can extract meaningful ages from this dataset, we decided, for each sample, to keep only the population returning the youngest ^{207}Pb-corrected dates (Fig. 11). The resulting unforced lower intercept dates are 285.9 ± 7.4 Ma (MSWD=2.1; PONT-1), 266 ± 11 Ma (MSWD=2.7; PONT-10), 272.8 ± 6.4 Ma (MSWD=0.39; PONT-26) and 278 ± 15 (MSWD=0.84; PONT-20). Individually, all these dates are comparable with their respective ^{207}Pb-corrected dates. We therefore conclude that these dates represent, for each sample, the best estimate of the time at which fluids interacted with the rocks. The other, older, dates probably represent partially reset apatite grains and are therefore considered as meaningless. Pb losses, as well as decrease of Mn and Fe contents, in apatite grains from the leucogranites should resulted mostly from diffusion processes because apatite recrystallization are not visible on BSE images.

As a conclusion, we evidence at least two major fluid circulation events between ca 290 Ma (episyenite and porphyritic leucogranite) and ca. 270 Ma (Isotropic leucogranites and Langonnet leucogranite). These events were responsible for the resetting (complete or uncomplete) of the U-Pb system in apatite grains within the leucogranites. This period is therefore contemporaneous with most of the ages obtained on most of the uranium deposits (Fig. 9). This together with the fact that the apatite grains affected by the fluids are richer in uranium than the ones that have been partly affected (or non-affected) suggest that these hydrothermal fluids were the same than those at the origin of the formation of U deposits (Fig. 10).

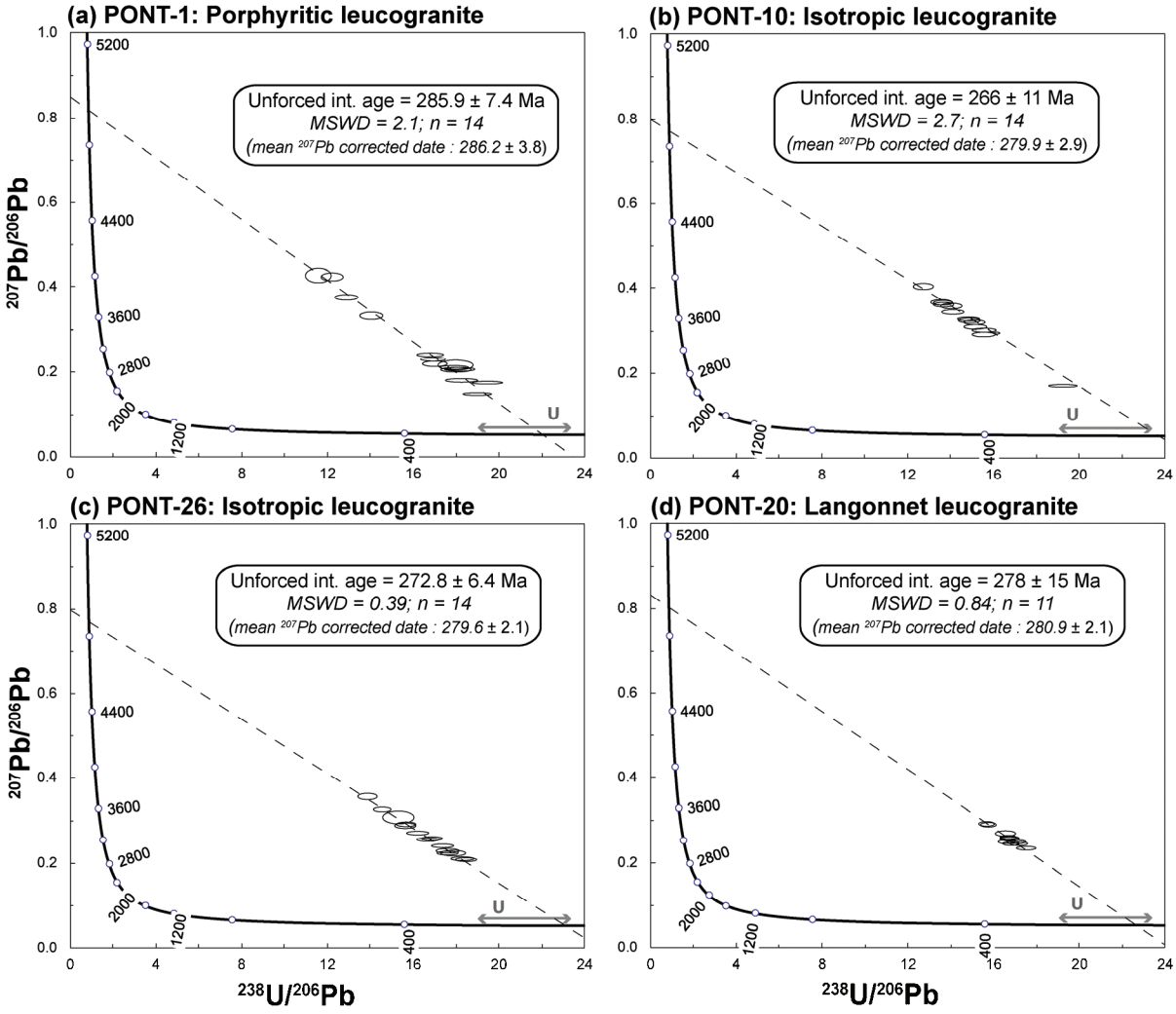

Figure 11: Tera-Wasserbug concordia diagrams reporting apatite analyses characterized by young ^{207}Pb corrected dates (second population) for the leucogranites. The main period of U deposits formation in the complex is reported for comparison (U). Ellipses and age errors are reported at 2σ.

5.4. Metallogenic model and regional implication

In the Pontivy-Rostrenen complex, the main U mineralization is hosted in N170° oriented quartz veins (Kerlech – Lignol, Bonote) or as brecciated quartz veins (Guern region) and episyenite bodies (Prat Mérrien, Poulprio) where the mineralized zone follows N120-130° and N130-160° oriented brittle lineaments, respectively. As illustrated in Figure 12 and proposed by Marcoux (1982), the N°170 oriented mineralized quartz veins can be interpreted as tension gashes accommodating late dextral movement along the SASZ while the formation of other deposits could be related to second order faulting also associated with deformation along the SASZ. Muscovite Ar-Ar and zircon or monazite U-Th-Pb dating on syntectonic leucogranites and mylonites from the SASZ (Tartèse et al. 2011b; 2012; Gapais et al. 2015) bracketed the ductile deformation along the SASZ between ca. 315 to 300 Ma.

According to uranium oxide and apatite U-Pb dating on U deposits and leucogranites from the Pontivy-Rostrenen complex, respectively, fragile deformation along the SASZ was still active from ca. 300 to 270 Ma.

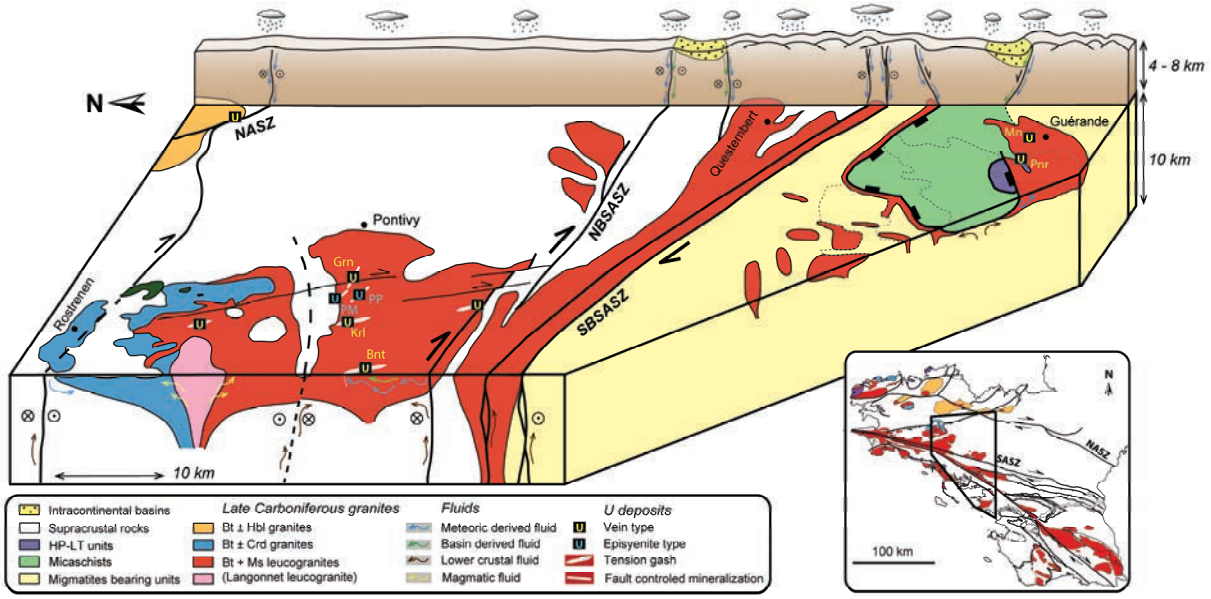

Figure 12: Schematic bloc diagram summarizing the geodynamic context of U mineralization formation in the Armorican Hercynian Belt from 300 to 270 Ma. In the Pontivy leucogranite the main mineralization occurs as N170° oriented quartz veins interpreted as tension gashes accommodating dextral wrenching along the SASZ whereas other deposits are represented by brecciated quartz veins or episyenite type deposits which are associated with second order faults (N120–160°) also related to the deformation along the SASZ. In the Guérande leucogranite area, the vein type mineralization is spatially associated with an extensional deformation zone which affected the Guérande leucogranite intrusion during its emplacement. Regional scale strike-slip faults and detachments represent major channels for surface-derived oxidized fluids which are able to dissolve magmatic uranium oxides in fertile leucogranites and then form U deposits. A schematic cross section representing the topography at the end of the Hercynian orogeny is represented in the background. Apatite fission track dating realized on the Guérande leucogranite suggest that these intrusions were at a temperature above 120 °C (so at a depth above 4 km for a geothermal gradient of 30°C/km) during U deposits formation (Ballouard et al. 2017). NASZ: North Armorican Shear Zone; NBSASZ: Northern Branch of the South Armorican Shear Zone; SBSASZ: Southern Branch of the South Armorican Shear Zone; Grn: Guern; PP: Poulprio; PM: Prat Mérrien; Krl: Kerlech (Lignol); Bnt: Bonote; Mn: Métairie-Neuve; Pnr: Pen Ar Ran.

On a regional scale, U deposition in the Pontivy-Rostrenen complex was contemporaneous with U mineralizing events from ca. 290 to 260 Ma and ca. 300 to 275 Ma in the Mortagne (Cathelineau et al. 1990) (Fig 13) and Guérande districts, respectively (Ballouard et al. 2017; Fig. 12 and 13). In the Guérande district, the main perigranitic vein type mineralization (Pen Ar Ran) occurs in a graben structure localized above the apical zone of the Guérande leucogranite. The formation of the graben and U mineralization relate to a brittle-ductile tectonic phase which followed the emplacement of the Guérande intrusion in an extensional deformation zone at ca. 310 Ma (Ballouard et al. 2015, 2017) (Fig. 12). From 310 to 300 Ma, the SASZ acted as a transfer zone between the South Armorican Massif, a thickened domain in extension, and the Central Armorican Massif, an unthickened domain submitted to pervasive dextral wrenching (e.g. Gumiaux et al. 2004a; Gapais et al. 2015). According to uranium

oxides U-Pb dating, this tectonic configuration was likely somewhat active until the middle Permian in mostly brittle conditions. U deposition in the Armorican Massif is contemporaneous with the main U mineralizing phase in the whole EHB (300 – 270 Ma, Ballouard et al. 2017 and references therein). In the northwestern part of the French Massif Central, hydrothermal U deposits formed in a similar context than the Armorican Massif as peraluminous leucogranites spatially associated with U mineralization were emplaced during the late Carboniferous (324 ± 4 Ma; Holliger et al. 1986) along major strike-slip shear zones link to the north-west with the SASZ and these intrusions are bounded at their roof by detachments (Gébelin et al. 2009) (Fig. 13). In this region, vein or episyenite types deposits follow Hercynian magmatic shear zones reactivated in fragile during Permian (eg. Cuney et al. 1990; Cuney and Kyser 2008).

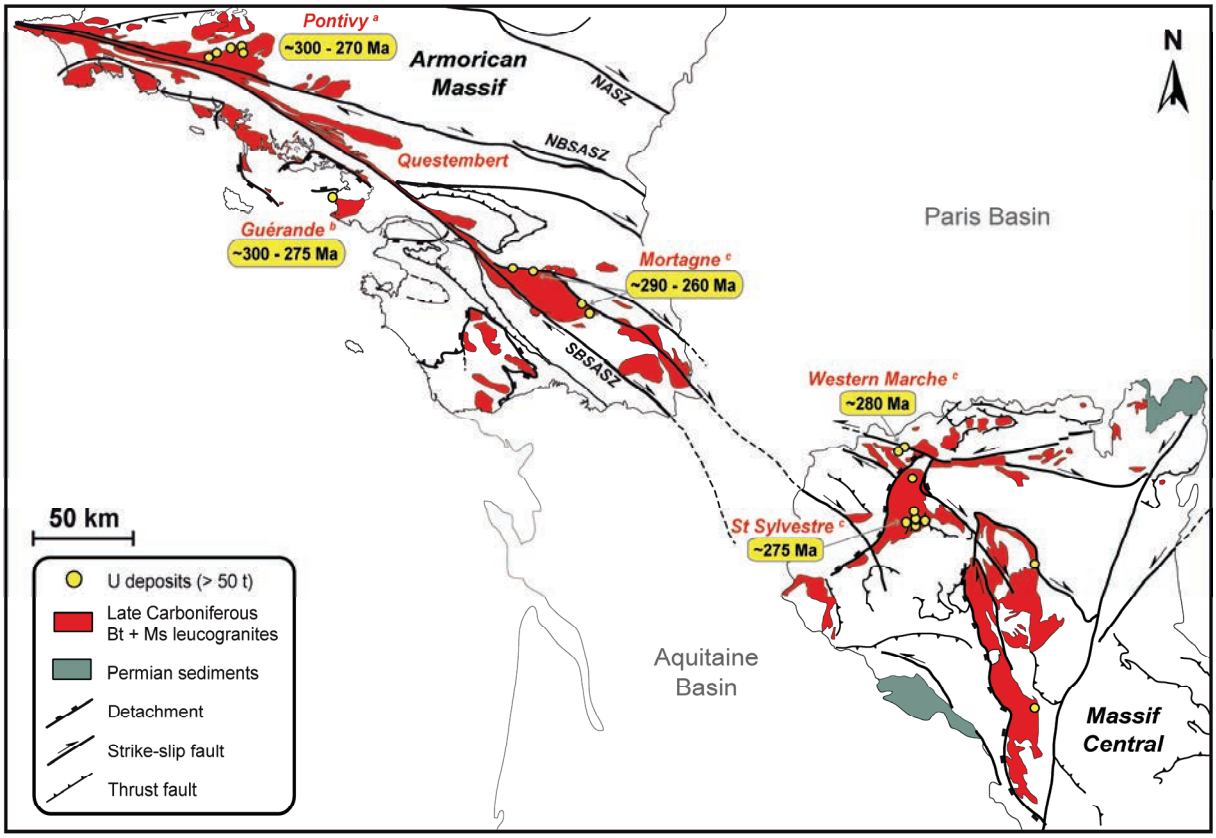

Figure 13: Simplified geological map (modified from Chantraine et al. 2003) of the southern part and the northern part of the Armorican Massif and the French Massif Central, respectively, showing the relationship between Late Carboniferous peraluminous leucogranites, strike-slip faults, detachments and U deposits. The age of U deposits formation is indicated (a: this study; b: Ballouard et al. 2017; c: Cathelineau et al. 1990).

As outlined earlier, the apatite grains from the leucogranite of the Pontivy-Rostrenen complex and their episyenites show evidence for an interaction with oxidized hydrothermal fluids. Concerning these oxidized fluids, a surface-derived origin is favored as numerous indications for the circulation of meteoric-derived fluids at depth, coming from oxygen isotopes and fluid inclusions studies, exist in rocks associated with the SASZ: quartz veins (Lemarchand et al. 2012), leucogranites (Tartèse and

Boulvais 2010) and mylonites (Tartèse et al. 2012). For example, a sedimentary derived mylonites from the Guillomarch quarry on the southern-edge of the Pontivy-Rostrenen complex (Guill. on Fig. 2) displays a whole rock $\delta^{18}O$ values as low as 1.7 ‰ which is the indubitable sign of an interaction with a low-$\delta^{18}O$ fluid derived from the surface (Tartèse et al. 2012). At the scale of the Pontivy-Rostrenen complex, U oxide deposits formation is contemporaneous with pervasive oxidizing hydrothermal alteration events as recorded by leucogranite apatite grains from ~ 290 to 270 Ma. Surface-derived fluids represent good candidates for the formation of U deposits because their oxidized character allows them to transport an important quantity of U in solution (Dubessy et al. 1987). During late Carboniferous and Early Permian, the SASZ and the detachments likely acted as major channels for surface-derived oxidized fluids which have the capacity to dissolve magmatic uranium oxides in fertile intrusions such as the Guérande (Ballouard et al. 2017), Questembert (Tartèse et al. 2013) and the Pontivy-Rostrenen leucogranites (Fig. 12).

In the Guérande district (Fig. 1), fluid inclusion analyses on a quartz comb from a quartz-uranium oxide vein of the Pen Ar Ran deposit, indicate a low salinity mineralizing fluid (1-6 wt.% eq. NaCl) with trapping temperatures in the range 250 – 350 °C (Ballouard et al. 2017). The trapping temperatures and the salinities of fluid inclusions in the Guérande district are overall comparable with those obtained in U deposits from the Mortagne district (Fig. 1) and the northwestern part of the French Massif Central (Saint Sylvestre; Fig. 13) with salinities and temperature generally in the range 0 – 7 wt.% eq. NaCl and 150-250 °C, respectively (e.g. Cathelineau 1982; Cathelineau et al. 1990; Lespinasse and Cathelineau 1990; Cuney and Kyser 2008). The low salinities measured in the fluid inclusions from these deposits are in agreement with the contribution of meteoric derived fluids although the elevated trapping temperatures and the salinity values variation suggest mixing processes with other fluids with a moderate salinity. For example, in the northwestern part of the French Massif Central (Saint Sylvestre; Fig. 13), the stable isotope studies of Turpin et al. (1990) on barren and U mineralized episyenites suggest that two fluids were involved in the mineralization genesis: an oxidized low $\delta^{18}O$ fluid of meteoric origin and a reduced high $\delta^{18}O$ fluid with a basin or metamorphic origin.

In the Guérande district, the precipitation of uranium occurred at the contact with reducing lithologies, such as black shales (Cathelineau et al. 1981; Ballouard et al. 2017). In the Pontivy-Rostrenen district, most deposits occurred close to the contact with sedimentary country rocks or micaschists enclaves, which likely play a role in the U precipitation processes. In parallel, regional scale strike slip faults can, in addition to surface derived fluids, act as channels for lower crustal reduced metamorphic fluids (as the ones documented in regional quartz veins along the SASZ; Lemarchand et al. 2012), which can be involved in U precipitation (Fig. 12). A reduced basin derived fluid can also be involved in the precipitation of U as suggested in the French Massif Central (Turpin et al. 1990) and the Bohemian massif (Kříbek et al. 2008; Dolníček et al. 2013). Permian basins were not preserved in the Armorican Massif, with the exception of its northeastern part where shales and red sandstones were

deposed in fluvial or lacustrine environments (Ballèvre et al. 2013). However, in the French Massif Central, bituminous shales deposed in intracontinental basins during early Permian, as in the Autun basin (e.g. McCann et al. 2006), could be the source of reducing waters able to precipitate the U (Turpin et al. 1990; Marignac and Cuney 1999). The formation of Permian basins in the French Massif Central resulted from the late-orogenic extension of the Hercynian belt which began at the end of the Carboniferous (e.g. Van Den Driessche and Brun 1989, 1992; Faure 1995). These basins with a dominant half-graben structural style can be strongly asymmetrical with an important transtensional character (e.g. McCann et al. 1990) attesting for the role of detachments and strike-slip faults in the control of the sedimentation as tentatively illustrated in Figure 12.

Around 300 Ma, convective fluid circulations in the Armorican Massif were enhanced by the heat provided during a regional late crustal magmatism event as evidenced by the emplacement of the Langonnet leucogranite in the Pontivy-Rostrenen district (304.7 ± 2.7 Ma; Ballouard et al. submitted) and leucogranitic dykes in the Guérande area (302.5 ± 2.0 Ma; Ballouard et al. 2015, 2017). Similarly, in the north-west French Massif Central (Saint-Sylvestre; Fig. 13), the emplacement of lamphrophyre dykes during lower Permian (285 ± 10 Ma; Leroy and Sonet 1976) likely contributed to the increase of the heat flux in the environment of the deposits. In the EHB, the Permian period is marked by an abnormal heat flux in the mantle, as evidenced by the emplacement of the Cornubian batholith in Cornwall (Chen et al. 1993) and the emplacement of post-orogenic granitoids in Iberia (Gutiérrez-Alonso et al. 2011 and references therein). This heat flux combined with the high heat producing character of the granites enriched in radioactive elements (Vigneresse et al. 1989) likely sustained an elevated geothermal gradient in the upper crust, which enhanced convective circulations of fluids (Scaillet et al. 1996). In the Guérande district, apatite fission tracks dating suggest that the leucogranite was at a temperature above 120°C (so at a depth above 4 km for a geothermal gradient of 30°C/km) during the formation of the deposits (Ballouard et al. 2017).

Finally, a last U mineralizing or remobilization event occurred at ca. 220 Ma in the Pontivy-Rostrenen district (Rosglas deposit; Figs. 2 and 7d). This mineralizing event is sub-contemporaneous with the emplacement of dolerite dikes in the western part of the Armorican Massif between 210 and 195 Ma which marks the first step of the Atlantic rifting (Caroff et al. 1995; Ballèvre et al. 2013). This tectonic event likely caused the circulation of hydrothermal fluids responsible for a late, discrete, U mobilization. Triassic and Lower Jurassic U mineralizing or mobilization events are also recorded in the Mortagne district (ca. 200 Ma) and the whole French Massif Central (ca. 210 – 170 Ma) and have been attributed to the tectonic movements at the origin of the opening of the Tethys (Cathelineau et al. 1990; Cathelineau et al. 2012). In parallel, several synsedimentary hydrothermal events affected the Paris Basin basement during the Trias and the Jurassic and are recorded in northern part of the French Central Massif and the western part of the Armorican Massif by the emplacement of F-Ba (Pb-Zn) mineralization (Guillocheau et al. 2000; Cathelineau et al. 2012).

In a more methodological point of view, this study demonstrates that the mineral apatite can be used to date the emplacement of magmatic rocks but also that it constitutes a powerful proxy to trace and date fluid/rock interaction events.

6. Conclusion

In the Late Carboniferous Pontivy-Rostrenen composite intrusion, intragranitic hydrothermal U mineralization are associated with the emplacement of peraluminous leucogranites. Mineralization is hosted in quartz veins associated with brittle structures related to strike-slip deformation along the SASZ. Our study of the U deposits and their magmatic country-rocks leads us to the following conclusions:

(1) In the peraluminous monzogranite and metaluminous quartz monzodiorite samples, low U contents (< 9 ppm) and elevated Th/U values (> 3) suggest that most of their U is hosted in refractory minerals such as zircon and monazite for the former and zircon, titanite or allanite for the latter. For the peraluminous leucogranites, the highly variable U contents (~3 – 27 ppm) and Th/U ratios (~0.1 to 5) suggest that in some samples, crystallization of magmatic uranium oxide followed by uranium oxide leaching during subsequent hydrothermal alteration and weathering occurred. On the Th/U airborne radiometric map, U deposits systematically occur at the transition between high and low Th/U zones suggesting that these hydrothermal deposits formed close to areas where uranium oxide leaching occurred.

(2) Apatite is a powerful tool both for dating and tracing fluids in the system. Apatite grains from the monzogranite and quartz monzodiorite samples are unzoned or display regular zonation in CL images suggesting that these crystals kept their magmatic signature. Apatite U-Pb dating of these samples yield dates around 315 Ma which can be interpreted as emplacement or cooling ages. Apatite grains from leucogranite or episyenites samples display irregular patchy zoning in CL (or BSE) images attributed to the mobility of Fe and Mn or As during an oxidized hydrothermal event involving surface-derived fluids. Apatite U-Pb dating of leucogranite samples yield ages from ca. 290 to 270 Ma, interpreted as representative of the previously evidenced oxidizing hydrothermal event. In leucogranite facies associated with U deposits, the younger apatite grains are enriched in U compared to older ones suggesting that these oxidized fluids were involved in the formation of U deposits.

(3) U-Pb dating of uranium oxide from the U deposits revealed a main Permian U mineralizing phase from 300 to 270 Ma synchronous with the oxidized hydrothermal event recorded by apatite grains from the leucogranites. A late U mineralization or remobilization event also occurred during the Trias at ca. 220 Ma.

On a regional scale, U deposition from 300 to 270 Ma in the Pontivy-Rostrenen complex is contemporaneous with the main U mineralizing phase in the Armorican Massif and the European Hercynian belt. During this period, late brittle dextral deformation along the SASZ was synchronous with a discrete extension in the South Armorican Domain suggesting a continuum of the ductile deformation which occurred in the region during Late Carboniferous from ca. 315 to 300 Ma. Detachment zones and regional scale strike slip faults acted as major channels for oxidized surface-derived fluids which were in turn able to dissolve magmatic uranium oxide from fertile peraluminous leucogranites and then form hydrothermal U deposits thanks to the interaction with reducing lithologies and/or crustal and basin derived fluids. In the French Massif Central, the peraluminous leucogranites spatially associated with U deposits where emplaced in a similar structural context suggesting a comparable metallogenic system.

Acknowledgment

This study was supported by 2012-2013 NEEDS-CNRS and 2015-CESSUR-INSU (CNRS) research grants attributed to Marc Poujol. We want to thank AREVA (in particular D. Virlogeux and J-M.Vergeau) for providing uranium oxide samples and for fruitful discussions. We are grateful to Y. Lepagnot (Geosciences, Rennnes) for crushing the samples. Many thanks to J. Langlade (IFREMER, Brest), O. Rouer, S. Matthieu and L. Salsi (SCMEM - Géoressources, Nancy) for their technical supports during EPMA and SEM analyses. Thank you to Nordine Bouden (CRPG, Nancy) for the help during SIMS analyses. We thank G. Martelet (BRGM) for providing the airborne radiometric data.

Supplementary Table 1: Operating conditions for the LA-ICP-MS equipment

	U-Pb apatite analyses
Laboratory & Sample Preparation	
Laboratory name	Géosciences Rennes, UMR CNRS 6118, Rennes, France
Sample type/mineral	Magmatic apatite
Sample preparation	Conventional mineral separation, 1 inch resin mount, 1µm polish to finish
Imaging	CL: RELION CL instrument, Olympus Microscope BX51WI, Leica Color Camera DFC 420C. Chemical maps: Cameca SX-100 electron microprobe (IFREMER, Plouzané, France).
Laser ablation system	
Make, Model & type	ESI NWR193UC, Excimer
Ablation cell	ESI NWR TwoVol2
Laser wavelength	193 nm
Pulse width	< 5 ns
Fluence	6 – 6.55 J/cm-2
Repetition rate	5 Hz
Spot size	55 - 60 µm (round spot)
Sampling mode / pattern	Single spot
Carrier gas	100% He, Ar make-up gas and N_2 (3 ml/mn) combined using in-house smoothing device
Background collection	20 seconds
Ablation duration	60 seconds
Wash-out delay	15 seconds
Cell carrier gas flow (He)	0.75 l/min
ICP-MS Instrument	
Make, Model & type	Agilent 7700x, Q-ICP-MS
Sample introduction	Via conventional tubing
RF power	1350W
Sampler, skimmer cones	Ni
Extraction lenses	X type
Make-up gas flow (Ar)	0.87 l/min
Detection system	Single collector secondary electron multiplier
Data acquisition protocol	Time-resolved analysis
Scanning mode	Peak hopping, one point per peak
Detector mode	Pulse counting, dead time correction applied, and analog mode when signal intensity > ~ 10^6 cps
Masses measured	^{43}Ca, ^{204}(Hg + Pb), ^{206}Pb, ^{207}Pb, ^{208}Pb, ^{232}Th, ^{238}U
Integration time per peak	10-30 ms
Sensitivity / Efficiency	28000 cps/ppm Pb (50µm, 10Hz)
Dwell time per isotope	5-70 ms depending on the masses
Data Processing	
Gas blank	20 seconds on-peak
Calibration strategy	Madagascar apatite used as primary reference material, Durango and McClure apatites used as secondary reference material (quality control)
Reference Material info	Madagascar (Thomson et al. 2012) Durango (McDowell et al. 2005) McClure (Schoene and Bowring 2006)
Data processing package used	Iolite (Paton et al. 2011), VizualAge_UcomPbine (Chew et al. 2014)
Quality control / Validation	Durango: Weighted average ^{207}Pb corrected age = 31.78 ± 0.39 Ma (N = 31; MSWD = 0.64; probability=0.93) McClure: Weighted average ^{207}Pb corrected age = 519.5 ± 3.6 Ma (N = 32; MSWD = 0.65; probability = 0.93)

Chapitre 2 : Traçage de la source des leucogranites fertiles en uranium du Massif armoricain

1. Introduction

Les leucogranites peralumineux (MPG ; Barbarin, 1999) peuvent représenter une source favorable pour la formation des gisements d'U hydrothermaux à condition qu'ils contiennent des oxydes d'uranium (e.g. Cuney, 2014, cf. chapitre 1). La capacité d'un magma peralumineux à cristalliser des oxydes d'uranium va dépendre d'une succession de processus « secondaires » qui incluent (Friedrich et al., 1987 ; Cuney et Kyser, 2008 ; Cuney, 2014) :

- un faible taux de fusion partielle.
- un degré de cristallisation fractionnée élevé du magma, induisant l'extraction des minéraux accessoires riches en Th qui incorporent une quantité limitée d'U comme la monazite, jusqu'à atteindre des faibles rapports Th/U (< ~1) et des teneurs en U suffisamment élevées (> ~10 ppm) permettant la saturation des oxydes d'uranium.
- une activité magmatique-hydrothermale significative qui semble favoriser l'enrichissement en U des leucogranites dans leur dernier stades d'évolution (Friedrich et al., 1987 ; cf. article #4).

Malgré le rôle essentiel de ces processus dans la genèse de leucogranites fertiles, un des facteurs les plus discriminants concerne la richesse en U de la source soumise à la fusion partielle et la proportion de cette U qui va être localisée en dehors de la structure des minéraux accessoires. En effet, la faible solubilité du zircon et de la monazite dans les liquides silicatés peralumineux les empêchent de participer de façon significative à la richesse du magma lors de la fusion partielle (Montel, 1993; Watson and Harrison, 1983). Au contraire, l'U adsorbé à la surface des minéraux ou localisé dans des microfractures va fractionner fortement en faveur du liquide silicaté. A titre d'exemple, les métavolcanites acides et les schistes noirs, avec des teneurs en U largement au-dessus du Clarke de la croûte continentale supérieure (> 2.7 ppm), peuvent représenter une source favorable pour former des leucogranites fertiles car une partie significative de leur U peut être associée, respectivement, à du verre ou à de la matière organique (e.g. Friedrich et al., 1987 ; Cuney, 2014).

Dans le Massif armoricain, la high heat production and flow belt (HHPFB) est une zone d'une cinquantaine de kilomètre de large et d'orientation NO-SE qui se caractérise par un flux de chaleur anormalement élevé et par la présence de granites avec une production de chaleur par deux fois supérieure à celle des formations géologiques environnantes (Jolivet et al., 1989 ; Vigneresse et al., 1989) (Fig. IV.1). Cette ceinture, sécante aux structures géologiques du Massif armoricain qui se prolongerait jusqu'en Cornwall et au NO du Massif central, englobe la majorité des occurrences et gisements uranifères de la région. Vigneresse et al. (1989) ont proposé que cette zone soit le reflet d'une croûte supérieure à moyenne préenrichie en éléments radioactifs dont la fusion partielle à la fin du

Carbonifère aurait induit la formation de leucogranites fertiles. Bien que l'existence de cette ceinture reste énigmatique elle permet de poser le problème de la source des leucogranites peralumineux associés à des gisements d'U au sein du Massif armoricain et de la chaîne hercynienne européenne.

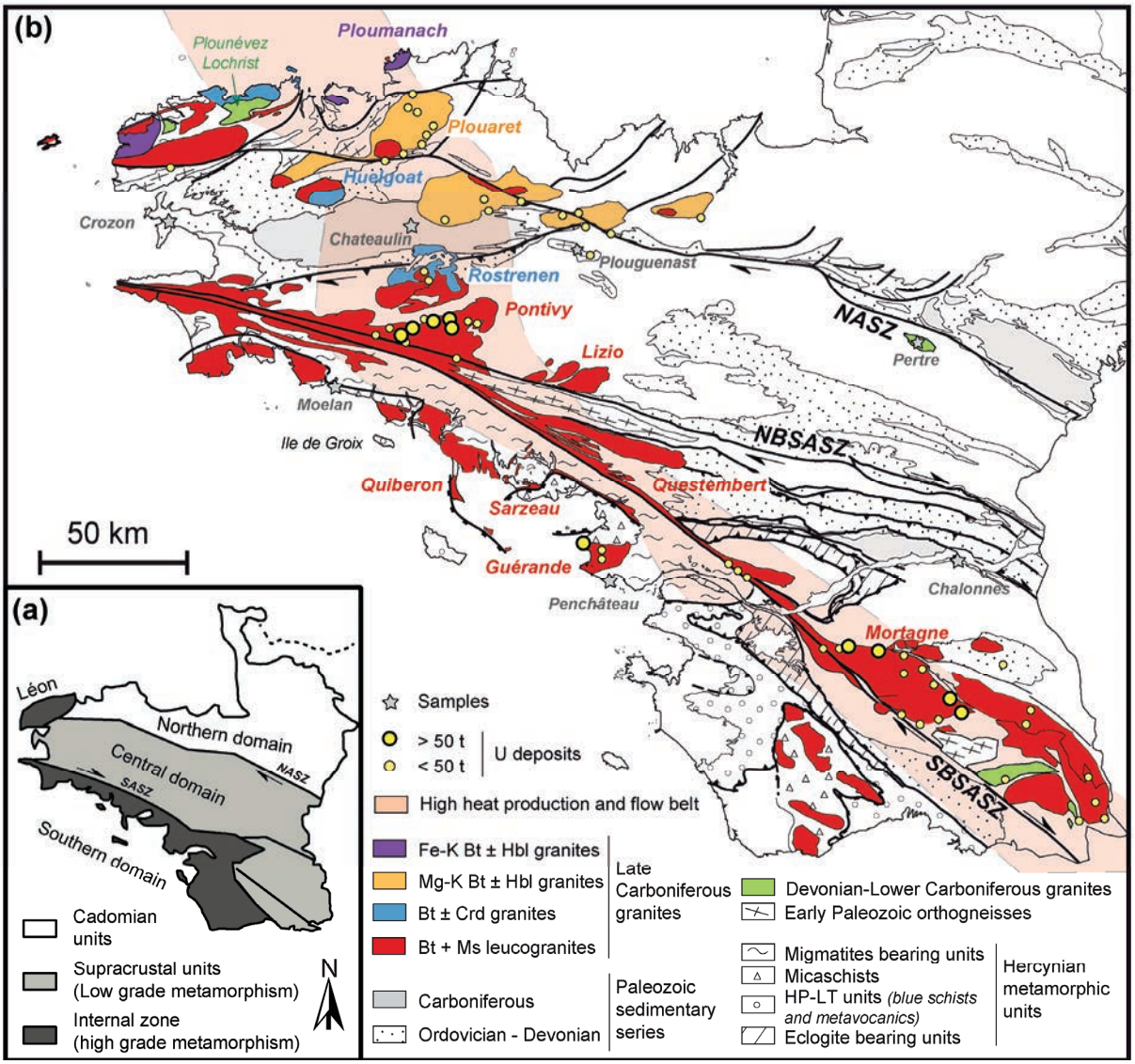

Figure IV.1 : (a) Domaines structuraux principaux du Massif armoricain. (b) Carte géologique générale du Massif armoricain [modifiée d'après Chantraine et al. (2003) et Gapais et al. (2015)] montrant les différents types de granites carbonifères d'après Capdevila (2010) et localisant les occurrences et gisements uranifères. NASZ: cisaillement nord armoricain; NBSASZ: branche nord du cisaillement sud armoricain. SBSASZ: branche sud du cisaillement sud armoricain. Fe-K granites: granites ferro-potassiques. Mg-K granites: granites magneso-potassiques. Calk-alk granites: granites calco-alcalins. La high heat production and flow belt de Vigneresse et al. (1989) et Jolivet et al. (1989) est indiquée.

Une identification préliminaire des sources méta-sédimentaires et méta-ignées impliquées dans la genèse des leucogranites de Guérande et de Pontivy a été réalisée dans la partie III principalement à partir de leur composition en éléments majeurs et en isotopes radiogéniques (Sr et Nd). Dans ce chapitre, une caractérisation plus précise, basée, en plus, sur la comparaison entre la signature isotopique (U-Pb et Hf) des cristaux de zircon hérités issus des leucogranites ainsi que des grains de zircons des orthogneiss et des formations sédimentaires de la région, est proposée. Afin de discuter ces résultats en

terme d'implication sur la genèse de leucogranites fertiles en U, des analyses roches totales en éléments majeurs et traces sur les sources potentielles de ces intrusions ont été réalisées et combinées avec des données issues de la littérature.

2. Méthodes analytiques

Une analyse en Sm-Nd complémentaire a été réalisée sur un grès Carbonifère inférieur du bassin de Châteaulin (Tableau IV.1 et 2). L'analyses a été réalisée à Géosciences Rennes et la méthode utilisée est la même que celle décrite dans l'article #3.

Les analyses roches totales en éléments majeurs et traces ont été réalisés au CRPG (Centre de Recherche Pétrographique et Géochimique) à Nancy selon la méthode décrite dans les articles #2, #3 et #5. Les échantillons sur lesquels ont été réalisés les analyses sont reportés dans la Tableau IV.1 et les résultats des analyses sont fournies en annexe de ce manuscrit.

Toutes les datations U-Pb sur zircon ont été réalisées au laboratoire Géosciences Rennes par LA-ICP-MS. La méthode utilisée est la même que celle décrite dans les articles #2 et #3 et les résultats des analyses avec un degré de concordance entre 90 et 110 % sont fournies en annexe de ce manuscrit avec une incertitude de 1σ. Lors des sessions analytiques, le zircon 91500 (Wiedenbeck et al., 1995 ; 1065 Ma) et le zircon Plešovice (Slama et al., 2008 ; 337.13 ± 0.13 Ma) utilisés comme standards externes ont fournies des âges concordia de, respectivement, 1060.9 ± 5.5 Ma (MSWD = 0.61 ; n = 20) et 337.6 ± 0.6 Ma (MSWD = 0.54 ; n = 239) permettant de valider la justesse des résultats obtenus.

Les analyses isotopiques en Hf sur zircon ont été réalisées à la Goethe-University à Frankfurt par LA-MC-ICP-MS en utilisant la méthode décrite dans l'article #3. Les valeurs d'εHf (t) fournies en annexes de ce manuscrit ont été calculées en utilisant l'âge de mise en place des intrusions pour les cristaux de zircons magmatiques (métagranitoïdes ; Tableau IV.1) alors que pour les grains hérités ou détritiques, avec un degré de concordance entre 90 et 110 %, c'est l'âge $^{206}Pb/^{238}U$ qui est utilisé pour les grains avec un âge $^{207}Pb/^{206}Pb$ < 1000 Ma et l'âge $^{207}Pb/^{206}Pb$ pour les grains avec un âge $^{207}Pb/^{206}Pb$ > 1000 Ma (Talavera et al., 2012).

Table IV.1 : Composition isotopique roche totale en Sm-Nd d'un échantillon de grès d'âge carbonifère inférieur de la carrière du bassin de Châteaulin. Les concentrations en Sm et Nd ont été obtenues par dilution isotopique.

Sample	Sm (ppm)	Nd (ppm)	$^{147}Sm/^{144}Nd$	$^{143}Nd/^{144}Nd$	±	εNd (310 Ma)	T_{DM}*
LOC-1	5.2	28	0.113189	0.512210	5	-5.0	1.4

** Two stages T_{DM} calculated using the equation of Liew and Hofmann (1988) for an age of 315 Ma.*

Sample	Locality / intrusion	Period - age	Formation - facies	Description	Longitude°	Latitude°	U-Pb	Hf	WR
LOC-1	Châteaulun basin	Lower Carboniferous	Locarn	Sandstone	-3.41852	48.31677	Yes	Yes	Yes
LOC-2	Châteaulun basin	Lower Carboniferous	Locarn	Carbonaceous shale	-3.41852	48.31677			Yes
CRO-14	Crozon	Upper Devonian	Porsguen	Black shale	-4.346333	48.343017			Yes
CRO-2	Crozon	Upper Devonian	Goasquelou	Sandstone	-4.537517	48.292633	Yes		Yes
CRO-1a	Crozon	Middle Devonian	Tibidi	Sandstone	-4.5395	48.291933	Yes		Yes
CRO-1b	Crozon	Middle Devonian	Tibidi	Siltstone	-4.5395	48.291933	Yes		Yes
CRO-12	Crozon	Lower Devonian	Bolast	Sandstone	-4.259033	48.30655	Yes		Yes
CRO-11	Crozon	Lower Devonian	Verveur	Sandstone	-4.539167	48.28615	Yes	Yes	Yes
CRO-10	Crozon	Silurian-Devonian	Plougastel	Sandstone	-4.582283	48.319383			Yes
CRO-6	Crozon	Silurian	Plougastel	Sandstone	-4.558633	48.218033	Yes	Yes	Yes
CRO-3a	Crozon	Silurian	Lostmarch	Sandstone	-4.5572	48.21485	Yes		Yes
CRO-3b	Crozon	Silurian	Lostmarch	Siltstone	-4.5572	48.21485	Yes		Yes
CRO-4a	Crozon	Silurian	Lostmarch	Sandstone	-4.5572	48.21485			Yes
CRO-4b	Crozon	Silurian	Lostmarch	Siltstone	-4.5572	48.21485			Yes
CRO-5	Crozon	Silurian	Lostmarch	Sandstone	-4.5572	48.21485			Yes
CRO-8	Crozon	Silurian	La Tavelle	Sandstone	-4.602917	48.260417			Yes
CRO-7	Crozon	Silurian	La Tavelle	Black shale	-4.602917	48.260417			Yes
CRO-17	Crozon	Ordovician-Silurian	Lamn Soaz	Sandstone	-4.602917	48.260417			Yes
CRO-16	Crozon	Ordovician	Kermeur	Sandstone	-4.607563	48.260786			Yes
CRO-15	Crozon	Ordovician	Postolonnec (kerloc'h)	Heavy minerals sandstone	?	?			Yes
CRO-9	Crozon	Brioverian		Sandstone	-4.62065	48.2781	Yes	Yes	Yes
PENCH-1	Penchâteau	Ordovician - Devonian?		Migmatitic paragneiss (Guérande leucogranite root)	-2.41883	47.2579	Yes		
PLG-1	Plouguenast	Ordovician (477.9 ± 2.9 Ma)		Metagranitoid (granite) Ms > Bt	-2.63975	48.274317	Yes	Yes	Yes
PLG-2	Plouguenast	Cambrian (502.3 ± 2.1 Ma)		Metagranitoid (tonalite) Bt > Ms	-2.545533	48.270633	Yes	Yes	Yes
PLG-3	Plouguenast	Ordovician	Saint Goueno	Metagranitoid (granite) Ms > Bt	-2.55685	48.255217	Yes		Yes
PLG-4	Plouguenast	Ordovician (482.6 ± 5.5 Ma)		Metagranitoid (tonalite) Ms >> Chl (Bt)	-2.615186	48.19458	Yes		Yes
QIMP-1	Moelan	Ordovician (466.8 ± 3.0 Ma)		Metagranitoid (tonalite) Ms > Bt	-3.740952	47.811525	Yes	Yes	Yes
GUE-3	Guérande	Upper Carboniferous (309.4 ± 1.9 Ma)	Coarse grained	Leucogranite Ms > Bt	−2.547297	47.368122	Yes	Yes	Yes
GUE-4	Guérande	Upper Carboniferous (309.7 ± 1.3 Ma)	Fine grained	Leucogranite Ms > Bt	−2.481191	47.342346	Yes	Yes	Yes
GUE-5	Guérande	Upper Carboniferous (302.5 ± 1.6 Ma)	Dyke	Leucogranite Ms >> Bt	−2.481191	47.342346	Yes	Yes	Yes
PONT-1	Pontivy	Upper Carboniferous (316.7 ± 2.5 Ma)	Porphyritic	Leucogranite Bt > Ms	-3.000557	48.062879	Yes	Yes	Yes
PONT-10	Pontivy	Upper Carboniferous	Isotropic	Leucogranite Ms>Bt	-3.300926	47.935201	Yes		Yes
PONT-14	Pontivy	Upper Carboniferous	Isotropic	Leucogranite Ms	-3.428067	47.980217	Yes		Yes
PONT-15	Pontivy	Upper Carboniferous	Isotropic	Leucogranite Ms>Bt	-3.5074	47.949383	Yes		Yes
PONT-26	Pontivy	Upper Carboniferous (310.3 ± 4.7 Ma)	Isotropic	Leucogranite Ms = Bt	-3.333955	47.981447	Yes	Yes	Yes
PONT-20	Langonnet	Upper Carboniferous (304.7 ± 2.7 Ma)		Leucogranite Bt > Ms	-3.472679	48.071121	Yes	Yes	Yes
QRT-08	Questembert	Upper Carboniferous (315.3 ± 1.6 Ma)		Leucogranite Bt - Ms	-2.59	47.72	Yes	Yes	Yes
LRT-10	Lizio	Upper Carboniferous (312.5 ± 2.4 Ma)		Leucogranite Bt - Ms	-2.57	47.88	Yes	Yes	Yes
HUEL-2	Huelgoat	Upper Carboniferous (314.8 ± 2.0 Ma)	Le Cloitre	Monzogranite Bt	-3.793344	48.363371	Yes		Yes
HUEL-3	Huelgoat	Upper Carboniferous (314.0 ± 2.8 Ma)	La Feuillée	Leucogranite Bt-Ms	-3.860646	48.394754	Yes		Yes

Tableau IV.2 : Localisation et description des échantillons sélectionnés pour les analyses en éléments majeurs et traces sur roches totales (WR) et/ou les analyses en U-Pb et Hf sur zircon. Les analyses en éléments majeurs et traces sur les sédiments, les métagranitoïdes et le granite de Huelgoat sont fournies en annexe de ce manuscrit mais celles sur les leucogranites sont fournies dans les articles #2 et #3. Les analyses en Hf et U-Pb sur zircon sont fournies en annexe du manuscrit.

.

3. *Résultats*

Dans cette étude, sont considérés comme leucogranites fertiles les leucogranites de Guérande (ca. 310 Ma) et Pontivy (ca. 315 Ma) car ils sont associés à des gisements d'uranium (cf. Partie IV, Chapitre 1, Fig. IV.1) mais aussi le leucogranite de Langonnet (ca. 305 Ma) ainsi que les leucogranites « jumeaux » de Lizio et Questembert (ca. 315 Ma, Fig. IV.1 et Tableau IV.2). En effet, l'étude de Tartèse et al. (2013) suggère que le leucogranite de Questembert a libéré plus d'une centaine de millier de tonnes d'U lors d'une phase d'altération hydrothermale en profondeur avec des fluides oxydants dérivés de la surface. Ainsi, le fait que ce leucogranite ne soit pas associé à des gisements d'U est vraisemblablement lié à un problème de piégeage de l'U ou de préservation de ces pièges. En parallèle, le leucogranite de Lizio est interprété comme un terme moins évolué du leucogranite de Questembert (Tartèse et Boulvais, 2010) et si la différentiation limitée de ce leucogranite a probablement proscrit la cristallisation d'oxydes d'uranium magmatiques, sa source doit rester comparable à celle du leucogranite de Questembert. Enfin, l'étude présentée dans l'article #5 suggère que le leucogranite de Langonnet a pu cristalliser des oxydes d'uranium mais que ce ceux-ci n'ont pas été lessivés. En revanche le granite de Huelgoat (cf. Partie III) (Fig. IV.1) n'est pas considéré comme un granite fertile.

3.1. *Données préliminaires (Rb-Sr et Sm-Nd) sur la source des leucogranites fertiles*

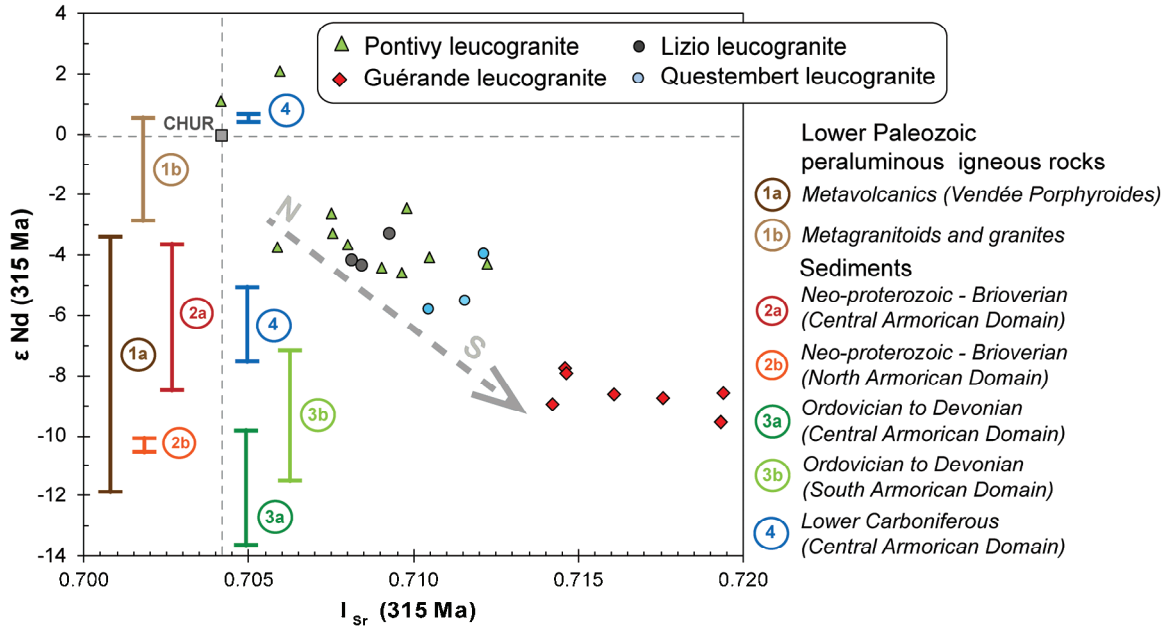

Figure IV.2 : Compositions en εNd(T) et en $^{87}Sr/^{86}Sr$ initial (I_{Sr}) calculées à 315 Ma pour les leucogranites peralumineux tardi-carbonifères du Massif armoricain (Tartèse et Boulvais, 2010 ; Euzen, 1993 ; chapitre III). Les compositions en εNd (315 Ma) des sédiments Briovérien (Dabard et al., 1996 ; Dabard, 1997) à Paléozoïques (Michard, 1985 ; Dabard et Peucat, 2001), des métavolcanites ordoviciennes (Ballèvre et al., 2012) et des métagranitoïdes ou granites paléozoïques inférieurs (article #3) sont reportées pour comparaison. Les échantillons du leucogranite de Langonnet et un échantillon du leucogranite de Pontivy avec des I_{Sr} anormalement faibles n'ont pas été intégrés car ces valeurs sont interprétées comme le résultat d'interactions fluides-roches (cf. article #3). La flèche indique l'évolution du nord vers le sud de la composition des leucogranites.

Les leucogranites sont tous fortement peralumineux (A/CNK > 1.1 ; Tartèse et Boulvais, 2010 ; cf. article #2 et #3) et se caractérisent, pour la quasi-totalité, par des valeurs en εNd(T) négatives (- 8 < εNd(T) < - 2) ainsi que des rapports en $^{87}Sr/^{86}Sr$ initiaux élevés (0.705 > I_{Sr} > 0.720) qui confirment leur nature purement crustale (Fig. IV.2). Deux échantillons du leucogranite de Pontivy présentent pourtant des valeurs en εNd(T) positives (1.1 et 2.1) associées à des valeurs en I_{Sr} relativement faibles (0.704 et 0.706). Comme mis en évidence par Bernard-Griffiths et al. (1985) et confirmé dans l'article #2, les valeurs d'I_{Sr} augmentent et les valeurs d'εNd(T) diminuent en allant du nord vers le sud depuis les leucogranites de Pontivy et Lizio mis en place sur la branche nord du CSA, le leucogranite de Questembert mis en place sur la branche sud du CSA et jusqu'au leucogranite de Guérande mis en place dans le domaine sud armoricain (Figs. IV.1 et IV.2).

Les échantillons du leucogranite de Guérande ont une composition en εNd(T) similaire à celle des métasédiments paléozoïques du domaine sud-armoricain (micaschistes ordoviciens à dévoniens ; Dabard et Peucat, 2001), des métavolcanites acides peralumineuses ordoviciennes (porphyroïdes de Vendée ; Ballèvre et al., 2012) et ils tombent à la limite du champ défini par les sédiments briovériens de Bretagne centrale. Pour les leucogranites de Pontivy, Lizio et Questembert, les échantillons présentent une composition isotopique comparable aux sédiments briovériens (Dabard et al., 1996 ; Dabard, 1997) du domaine centre armoricain ainsi qu'aux orthogneiss peralumineux paléozoïques inférieurs (métavolcanites ou métagranitoides : cf. article #3). De même certains échantillons avec les valeurs en εNd(T) les plus basses (Questembert) et les plus élevées (Pontivy) ont une composition comparable à celles des sédiments carbonifères inférieurs.

3.2. Datations U-Pb sur zircon

Les analyses U-Pb ont été réalisées sur (Tableau IV.1 ; Fig. IV.1) :

(1) les cristaux de zircon hérités des leucogranites fertiles de Pontivy, Langonnet, Guérande, Questembert et Lizio.
(2) les cristaux de zircon hérités d'un leucogranite et d'un monzogranite de Huelgoat.
(3) les cristaux de zircon magmatiques et hérités de métagranitoïdes peralumineux de la zone centre (Plouguenast) et sud armoricaine (Moelan).
(4) les grains de zircon détritiques de sédiments briovériens, siluriens et dévoniens de la presqu'île de Crozon et de sédiments carbonifères inférieurs du bassin de Châteaulin.
(5) les grains de zircon détritiques d'un paragneiss migmatitique localisé à l'extrémité SO du leucogranite de Guérande et interprétée comme sa zone d'alimentation (cf. article #2).

Ces analyses ont été complétées par des données de la littérature sur des cristaux hérités du leucogranites de Lizio (Tartèse et al., 2011a), des grains détritiques du dévonien de la région de Chalonnes (Ducassou et al., 2014 ; Fig. IV.1) et sur des cristaux magmatiques et hérités des

métavolcanites peralumineuses ordoviciennes de la zone sud armoricaine (porphyroïdes de Vendée ; Ballèvre et al., 2012 ; Fig. IV.1) et d'un leucogranite peralumineux Carbonifère inférieur (leucogranite du Pertre : ca. 340 Ma ; Vernhet et al., 2009 ; Fig. IV.1). Les dates U-Pb obtenues sur ces échantillons sont représentés dans la figure IV.3 sous la forme d'histogrammes et de diagrammes d'estimation par noyau (« Kernel density Estimate – KDE ») réalisés à partir du logiciel DensityPlotter (Vermeesch, 2012 ; « band width = 25 »).

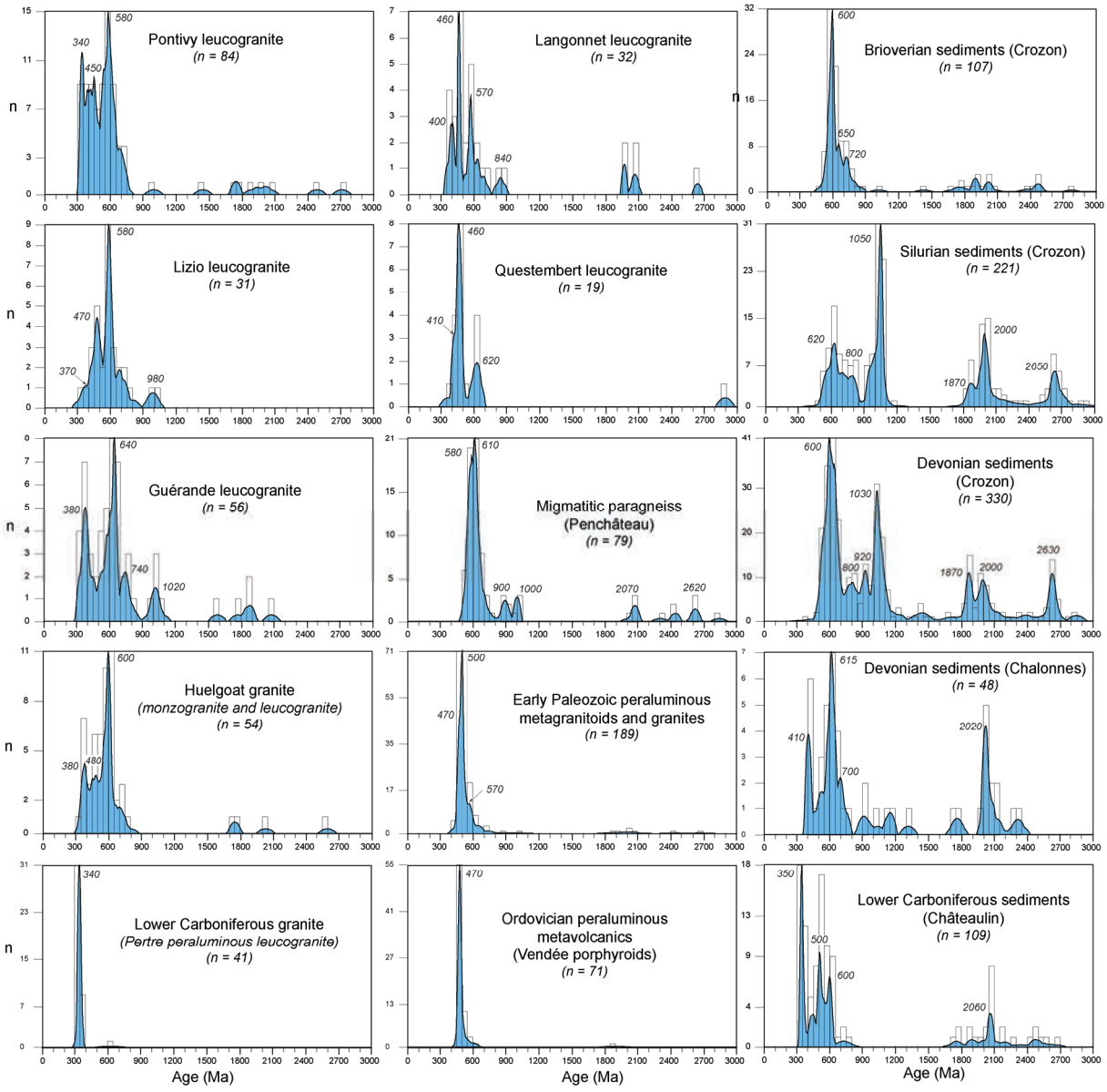

Figure IV.3 : Diagrammes d'estimation par noyau (« kernel density estimate - KDE ») et histogrammes représentant les dates U-Pb obtenues sur les cœurs hérités de zircon des leucogranites fertiles de Pontivy, Langonnet, Lizio, Questembert et Guérande ainsi que du granite de Huelgoat. Sont aussi reportés les dates U-Pb obtenues sur les grains de zircon des sédiments briovériens, siluriens, dévoniens de la presqu'île de Crozon, des sédiments dévoniens de la région de Chalonnes (Ducassou et al., 2014), des sédiments carbonifères inférieurs du bassin de Chateaulun, des métavolcanites ordoviciennes de la zone sud armoricaine (Ballèvre et al., 2012), d'un granite carbonifère inferieur (leucogranite du Pertre ; Vernhet et al., 2012), des métagranitoïdes ou granites paléozoïques inférieurs de la région de Moelan et de Plouguenast ainsi que d'un échantillon de paragneiss migmatitique prélevé à la racine du leucogranite de Guérande (Penchâteau). Pour les cœurs de zircon du leucogranites de Lizio des analyses complémentaires issues de Tartèse et al (2001a) ont été rajoutées. L'âge des pics obtenus par KDE est reporté sur chaque diagramme.

Les cristaux de zircon hérités issus des leucogranites de Pontivy (n = 84), Langonnet (n = 32), Lizio (n = 31) et Questembert (n = 19) ainsi que du granite de Huelgoat (n = 54), mis en place au nord de la branche sud du CSA, se caractérisent par des pics de populations d'âges similaires sur les diagrammes KDE avec généralement quelques dates dispersées archéennes à mésoprotérozoïques, un héritage néoprotérozoïque marqué par des pics entre ~620 et 580 Ma (cadomien - panafricain), un héritage paléozoïque inférieur (cambrio-ordovicien) avec des pics entre ~470 et 450 Ma et un héritage dévono-carbonifère inférieur marqué par des pics entre ~410 et 340 Ma. De rare grains de la base du Néoprotérozoïque (grenvillien) apparaissent dans les leucogranites de Lizio (~980 Ma) et Langonnet (~840 Ma). En ce qui concerne le leucogranite de Guérande (n =56), il est caractérisé par la présence de grains de zircon hérités archéens, un héritage grenvillien marqué par un pic vers 1020 Ma, un héritage cadomien avec deux pics à ~740 et 640 Ma et un héritage dévono-carbonifère inférieur marqué par un pic vers 380 Ma.

Les sédiments briovériens (n = 107) se caractérisent par une faible contribution archéenne à mésoprotérozoïque et une forte contribution cadomienne marquée par des pics entre ~720 et 600 Ma. En ce qui concerne les sédiments paléozoïques de Crozon d'âge silurien (n=221) et dévonien (n=330), ils révèlent quatre populations d'âges principales, avec une population archéenne marquée par des pics vers 2630 et 2650 Ma, une population paléoprotérozoïque marquée par des pics à ~1870 et 2000 Ma, une population grenvillienne avec des pics entre ~1050 et 920 Ma et une population cadomienne marquée par des pics à ~620 et 600 Ma. Ces deux spectres sont similaires à celui obtenu à partir d'un échantillon de grès d'âge ordovicien prélevé sur la presqu'île de Crozon (formation des grès armoricains, Mattteini et al., 2014). De même, le paragneiss migmatite prélevé à la racine du leucogranite de Guérande (n = 79) montre un spectre comparable à celui des sédiments ordoviciens à dévoniens de Crozon avec une population archéenne à paléoprotérozoïque montrant des pics vers 2620 et 2070Ma, une population grenvillienne marquée par des pics à ~1000 et 900 et une population cadomienne majeure avec des pics à ~610 et 580 Ma. Le Dévonien de Chalonnes au sud-est du Massif armoricain (n = 48 ; Ducassou et al., 2014) diffère du Dévonien de Crozon (Fig. IV.1) : il reste marqué par des populations mésoprotérozoïques et néoprotérozoïques (cadomiennes) importantes avec des pic à ~2020 Ma, 700 et 615 Ma mais il révèle aussi une contribution dévonienne significative avec un pic à ~410 Ma. En ce qui concerne l'échantillon de grès carbonifère inférieur (n = 109), il se caractérise par une population archéenne à paléoprotérozoïque marquée par un pic à ~2060 Ma, un pic cadomien à ~600Ma, une population paléozoïque inférieure avec un pic vers 500 Ma et un pic carbonifère inférieur vers 350 Ma.

Les orthogneiss (métagranitoïdes : n = 189 et metavolcanites : n =71, Ballèvre et al., 2012) révèlent deux pics majeurs cambrio-ordoviciens à ~470 et 500 Ma marqueurs de leur mise en place et indiquent un héritage cadomien avec un léger pic à ~570 Ma. Quant au leucogranite du Pertre (n =41), il est caractérisé par un pic vers 340 Ma indiquant l'âge de sa mise en place (Vernhet et al., 2012).

3.3. Analyses en Hf sur zircon

Les analyses en Hf sur zircon ont été réalisées sur des cristaux de zircon hérités des leucogranites de Pontivy, Langonnet, Lizio, Questembert et Guérande, sur des grains magmatiques de métagranitoïdes paléozoïques inférieurs et des grains détritiques des formations sédimentaires briovériennes à carbonifères inférieures (voir tableau IV.1 pour le détail des échantillons analysés). Dans le diagramme εHf (T) versus âge de la Figure IV.4, les valeurs d'εHf (T) des cristaux hérités des leucogranites varient de sub- à super-chondritiques (9.1 à -22.8) et il n'apparait pas de différences claires entre les différentes intrusions. En ce qui concerne les formations sédimentaires, les grains détritiques montrent une variation encore plus importante avec des valeurs en εHf (T) qui vont de fortement sub-chondritique (-37.4) à fortement super-chondritique (13.1). Pour les métagranitoïdes (othogneiss), les valeurs varient de chondritique (-0.9) à fortement super-chondritique (14.4).

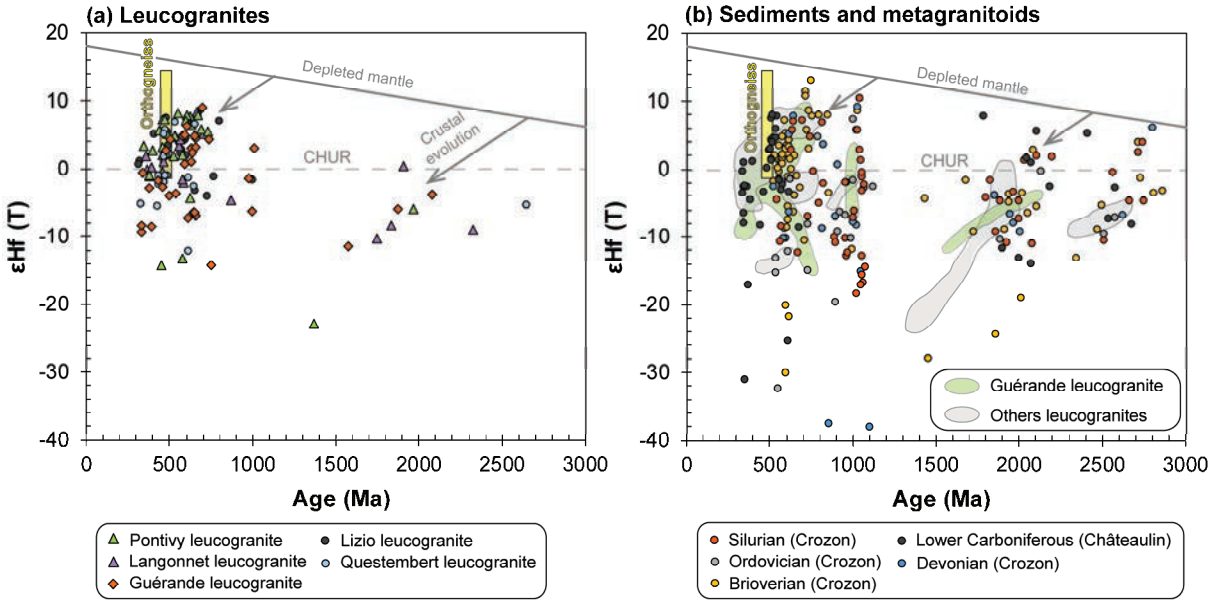

Figure IV.4 : Diagrammes εNd (T) en fonction des dates U-Pb pour (a) les cristaux de zircons hérités des leucogranites ainsi que pour (b) les grains de zircon détritiques des sédiments et des grains néoformés des métagranitoïdes palozoïques inférieurs (orthogneiss) du Massif armoricain. Les analyses sur les grains de zircon détritiques d'un grès briovérien et ordovicien de la presqu'île de Crozon réalisées par Matteini et al. (2014) ont été ajoutées.

3.4. Distribution de l'U dans les sources potentielles des leucogranites

Les analyses disponibles dans la littérature et réalisées sur les sources potentielles des leucogranites sont reportées dans un diagramme Th versus U (Fig. IV.5). Les sédiments paléozoïques et briovériens sont pour la majorité caractérisés par des teneurs en U entre 1 et 5 ppm mais les sédiments paléozoïques présentent généralement des rapports Th/U élevés > 4 alors que les sédiments briovériens sont pour la plupart caractérisés par des rapports Th/U compris entre 2 et 4. Les métavolcanites ordoviciennes présentent majoritairement des teneurs en U entre 1 et 6 ppm et des rapports Th/U > 2. Les métagranitoïdes paléozoïques inférieurs et le leucogranite carbonifère inférieur du Pertre sont

caractérisés par des teneurs en U entre 1 et 40 ppm et des rapports Th/U majoritairement compris entre 0.5 et 4.

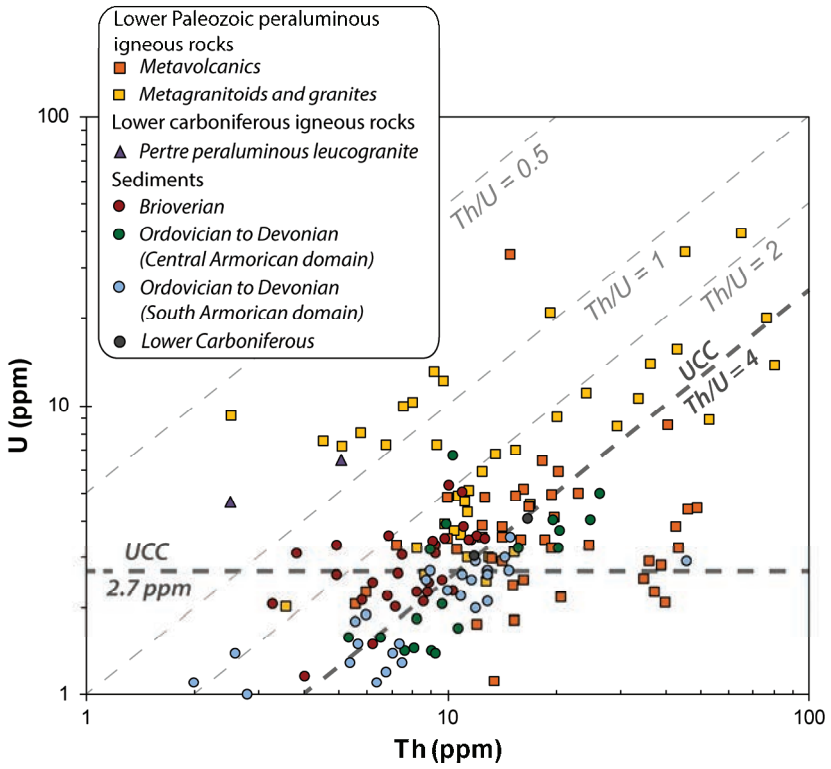

Figure IV.5 : Composition en U-Th des sources potentielles des granites peralumineux du Massif armoricain. Une partie des analyses sont issues de cette étude et les autres sont issues de Vigneresse et al. (1989), Dabard et Peucat (2001), Béchennec et Thiéblement (2013), Béchennec et al. (1996, 1999, 2001), Le Hébel (2002) et Trautmann et Carn (1997). La teneur en U (2.7 ppm) et le rapport Th/U (~4) de la croûte continentale supérieure (UCC ; Rudnick et Gao, 2005) est indiquée.

4. Discussion

4.1. Croisement des données et identification des sources impliquées dans la genèse des leucogranites uranifères et du granite de Huelgoat.

Tout d'abord, les données en εNd(T) et I_{Sr} de la Figure IV.2, permettent d'apporter les informations suivantes :

- La ou les source(s) du leucogranite de Guérande semblent différentes de celle(s) des leucogranites mis en place le long de la branche nord et sud du CSA.
- La signature isotopique en εNd(T) du leucogranite de Guérande est compatible avec la fusion de sédiments paléozoïques ordoviciens à dévoniens, la fusion de métavolcanites ordoviciennes et la contribution de sédiments briovériens.
- La signature en εNd(T) des leucogranites mis en place le long du CSA est compatible avec la fusion de sédiments briovériens ainsi que la fusion de métavolcanites ordoviciennes. En parallèle, les valeurs en εNd(T) positives obtenues suggèrent la contribution soit de métagranitoïdes paléozoïques inférieurs soit de sédiments carbonifères inferieurs. Une proportion majeure de sédiments ordoviciens à dévoniens dans la source des leucogranites de

Pontivy et Lizio semble proscrite. Néanmoins, la contribution de ces sédiments semble augmenter légèrement dans la source du leucogranite de Questembert expliquant ainsi l'évolution nord-sud de la signature isotopique des leucogranites dans la Figure IV.2 (cf. article #2).

Les leucogranites fertiles et le granite de Huelgoat montrent une forte variabilité des dates U-Pb sur zircon hérités (archéennes à paléozoïques ; Figs. IV.3 et IV.4) qui ne peut pas être expliquée exclusivement via la fusion de formations ignées (orthogneiss paléozoïques inférieurs ou granites carbonifères inférieurs), caractérisés par une gamme restreinte de dates U-Pb sur zircon, suggérant une forte contribution métasédimentaire dans la source de ces leucogranites uranifères. Une population de zircon cadomienne (~570 – 700 Ma) est observable sur tous les spectres KDE des leucogranites fertiles mais aussi sur la totalité des spectres des formations sédimentaires briovériennes à carbonifères inférieures (Fig. IV.3). Cette gamme d'héritage ne peut donc pas être utilisé pour discriminer la source des leucogranites. Ensuite, les leucogranites fertiles et le granite de Huelgoat sont caractérisés par une contribution dévono-carbonifère inférieur (~410 – 380 Ma) qu'on retrouve sur le spectre des sédiments carbonifères inférieurs du bassin de Châteaulin et évidemment sur celui du leucogranite carbonifère inférieur du Pertre (Fig. IV.3). Le pic à ~400 Ma observé sur le spectre des sédiments dévoniens de la région de Charonne est en revanche trop restreint pour expliquer la gamme d'héritage observée dans les leucogranites. Géochimiquement, les sédiments carbonifères inférieurs permettent d'expliquer la signature légèrement super-chondritique en εNd(T) de certains échantillons du leucogranite de Pontivy et une majeure partie de la gamme de variation des cristaux de zircon hérités des leucogranites dans le diagramme εHf(T) versus âge (Fig. IV.4). Néanmoins, la contribution de sédiments carbonifères inférieurs dans la source de tous ces granites tardi-carbonifères pose un problème structural majeur. En effet, le domaine centre armoricain a été peu épaissi pendant l'orogenèse hercynienne et il était en régime tectonique décrochant durant l'ensemble du Carbonifère (e.g. Gumiaux et al., 2004a). Ainsi, l'enfouissement de sédiments carbonifères dans la croûte inférieure jusqu'au granite de Huelgoat parait difficile (Fig. IV.1). En parallèle, la subduction de matériel continental sous la plaque armoricaine semble prendre fin entre vers 360 Ma avec l'exhumation des schistes bleus de l'Ile de Groix et des métavolcanites ordoviciennes (porhyroïdes de Vendée) de HP-BT (Bosse et al., 2005 ; Le Hébel, 2002) (Fig. IV.1). En ce qui concerne le leucogranite de Guérande, les analyses en Sm-Nd ne sont pas en accord avec une contribution significative de sédiments carbonifères inférieurs dans sa source (Fig. IV.2). En conséquence, on suggère que l'héritage dévono-carbonifère inférieur enregistré par les cristaux de zircon des leucogranites fertiles et du granite de Huelgoat reflète la fusion d'orthogneiss peralumineux. Les équivalents à l'affleurement de ces roches ignées sont représentés, par exemple, par le leucogranite peralumineux du Pertre et l'orthogneiss (monzogranite) peralumineux de Plounévez-Lochrist dans le Léon (Fig. IV.1).

Les granites tardi-carbonifères mis en place au nord de la branche sud du CSA sont caractérisés par un héritage cambrio-ordovicien (Paléozoïque inférieur) significatif, marqué par des pics entre ~480 et 450 Ma sur les diagrammes KDE (Fig. IV.3). Les grains de zircon détritiques d'âges cambrio-ordoviciens étant absent des sédiments siluriens ou dévoniens, cette héritage reflète vraisemblablement la contribution d'orthogneiss peralumineux paléozoïques inférieurs dans la source de ces leucogranites fertiles et du granite de Huelgoat. Cette hypothèse est en accord avec les signatures chondritiques à superchondritiques en εHf (T) comparable entre les cristaux de zircon hérités cambrio-ordoviciens des leucogranites au nord du CSA et celles des grains magmatiques issus des métagranitoïdes (Fig. IV.4). De plus, la signature légèrement super-chondritique en εNd (T) de certains échantillons du leucogranite de Pontivy est compatible avec la contribution de ces métagranitoïdes (Fig. IV.2 ; cf. article #3). Enfin, comme suggéré par la composition en εNd (T) des échantillons, l'héritage cadomien important enregistré par ces granites tardi-carbonifères (Fig.IV.3) reflète vraisemblablement la fusion de sédiments briovériens lors de leur genèse. Cette hypothèse est appuyée par la signature sub- à super-chondritique en εHf (T) comparable entre les grains hérités cadomiens des leucogranites et les grains détritiques des sédiments briovériens (Fig. IV.4).

Le leucogranite de Guérande se distingue des autres leucogranites mis en place le long du CSA par une proportion significative de zircon hérités avec des dates grenvilliennes et par l'absence d'heritage cambrio-ordovicien. Il est donc possible de conclure que la fusion d'orthogneiss paléozoïques inférieurs (métavolcanites ou métagranitoïdes) ne contribue pas de façon significative à la formation du leucogranite de Guérande mais qu'au contraire les sédiments ordoviciens à dévoniens représentent une proportion importante de sa source car les grains de zircon détritiques avec des dates méso-néoprotérozoiques (grenvilliennes) vers ~1000 Ma sont caractéristiques de ces formation sédimentaires (voir les sédiments dévoniens et siluriens de Crozon sur la Fig. IV.3). En parallèle, le paragneiss migmatitique échantillonné à la racine du leucogranite de Guérande, interprété comme un équivalent de sa source (cf. article #2), présente des dates U-Pb sur zircon comparables à celles des formations sédimentaires ordoviciennes à dévoniennes (Fig. IV.3), suggérant que le protholithe de cette migmatite est un sédiment ordovicien à dévonien.

Pour résumé, il est proposé que le leucogranite de Guérande provienne majoritairement de la fusion partielle de sédiments paléozoïques ordoviciens à dévoniens avec une contribution significative d'orthogneiss dévoniens à carbonifères inférieurs. Ensuite, il est suggéré que les leucogranites fertiles mis en place au nord de la branche sud du CSA et le granite de Huelgoat, soient issus en majeure partie de la fusion partielle de sédiments briovériens avec une contribution significative d'orthogneiss cambrio-ordoviciens et dévono-carbonifères inférieurs. Ainsi, il n'existe pas de différence de source majeure entre le granite de Huelgoat (leucogranite et monzogranite) et les leucogranites uranifères. Le fait qu'il n'est pas associé à des occurrences uranifères est vraisemblablement lié à des processus « secondaires » comme un taux de fusion partielle trop élevé, un faible degré de différentiation et une

interaction avec des magmas mantelliques (cf. Partie III). En parallèle, il semble que l'évolution nord-sud en εNd (T) et I_{Sr} enregistrée par les leucogranites reflète une augmentation de la contribution de sédiments ordoviciens à dévoniens au sein de leur source.

4.2. Implications sur la fertilité en uranium des leucogranites

En parallèle du taux de fusion partiel qui doit rester faible, la richesse en U du liquide silicaté peralumineux produit lors des réactions de fusion va être dépendant de la richesse en U de sa source, orthodérivée ou métasédimentaire, et de la proportion de cette U qui va être située en dehors des minéraux accessoires comme le zircon et la monazite qui sont peu solubles dans les liquides peralumineux. Le rapport Th/U est un indicateur des phases porteuse de l'U dans les roches et les rapports Th/U élevés supérieur à la valeur de la croute continentale supérieure (> 3.8 ; Rudnick et Gao, 2005) suggèrent qu'une majeure partie de cette U est incorporée dans les minéraux accessoires porteurs de Th comme la monazite. En revanche, la diminution des rapports Th/U suggère une augmentation de la proportion de l'U qui va être situé en dehors de la structure de ces minéraux accessoires réfractaires c'est-à-dire, en adsorption sur les minéraux majeurs, dans des microfractures ou même dans des oxydes d'uranium, pour les roches ignées avec des rapports Th/U <1 et des teneurs en U d'une dizaine de ppm (Friedrich et al., 1987 ; Cuney, 2014). Ainsi, les lithologies crustales considérées comme les plus à même à former des liquides silicatés riches en U lors de la fusion partielle sont celles avec une teneur en U au-dessus du Clarke de la croûte continentale supérieure (> 2.7 ppm) et avec un rapport Th/U < ~4.

Dans le Massif armoricain, les lithologies impliquées dans la genèse des leucogranites uranifères qui présentent, pour partie, ces caractéristiques (Th/U < 4 et [U] > 2.7 ppm) sont les sédiments briovériens et les roches ignées peralumineuses d'âges paléozoïques inférieurs et carbonifères inferieurs (Fig. IV.5). En revanche, les sédiments paléozoïques ordoviciens à dévoniens, avec généralement un rapport Th/U > 4 et/ou [U] < 2.7 ppm, ne représentent pas une source favorable pour la génération de leucogranites fertiles lors de la fusion partielle (Fig. IV.5). La différence de fertilité entre ces sources peut, potentiellement, permettre de comprendre la répartition des gisements d'uranium dans la région. En effet, malgré l'abondance des leucogranites peralumineux dans la zone sud armoricaine, seul le leucogranite de Guérande est associé à des gisements ou indices uranifères (Fig. IV.1). Cela pourrait s'expliquer par le fait que ces leucogranites proviennent en grande partie de la fusion de sédiments paléozoïques peu propice à générer des magmas riches en U lors de la fusion. Au contraire, les leucogranites mis en place au nord de la branche sud du CSA sont en grande parties issus de la fusion de sédiments briovériens et d'orthogneiss paléozoïques inférieurs qui sont vraisemblablement des lithologies à même de générer des magmas uranifères. Par exemple, le leucogranite peralumineux de Saint-Gouéno ([U] > 7 ppm ; Th/U < 1) dans le complexe orthogneissique paléozoïque inférieur de Plouguenast (Fig. IV.1) est associé à un indice uranifère intragranitique (Carric et al., 1980) et contient

potentiellement des oxydes d'uranium. Finalement, les seules sources qu'ont en commun le leucogranite de Guérande et les leucogranites fertiles mis en place au nord de la branche sud du CSA sont les orthogneiss dévono-carbonifères inférieurs. Il existe peu d'analyses sur ces formations mais le leucogranite du Pertre ([U] > 4 ppm ; Th/U < 1 ; Fig. IV.5) apparait comme une lithologie favorable à la génération de magma riche en U lors de la fusion partielle.

Ainsi, il semble que la différentiation de la croûte continentale par fusion successives de roches ignées felsiques peralumineuses est un point clé dans la genèse des leucogranites uranifères de la chaîne hercynienne armoricaine. Une source méta-ignée avait déjà été proposé pour les leucogranites peralumineux carbonifères du nord-ouest du Massif central comme Saint-Sylvestre qui sont connus pour être associés à des gisements d'U majeurs (Turpin et al., 1990) et ce processus d'enrichissement en U est potentiellement commun à tous les leucogranites uranifères de la chaîne hercynienne européenne.

En ce qui concerne la HHPFB, son existence et sa signification géologique restent incertaines. Cette ceinture semble toutefois reproduire la forme de l'anomalie de vitesse des ondes P qui a été mis en évidence par la tomographie du manteau, lithosphérique et asthénosphérique, sous le Massif armoricain et interprétée comme la trace d'une lithosphère océanique subductée (Judenherc et al., 2002 ; 2003 ; Gumiaux et al., 2004b) (Fig. IV.6). La subduction de matériel océanique et continental sous la plaque armoricaine jusqu'à la transition dévono-carbonifère entre ca. 370 et 350 Ma (Le Hébel, 2002 ; Bosse et al., 2005), suivi potentiellement d'un processus de « slab-break off » (e.g. Davies et von Blanckenburg., 1995), a pu provoquer la mise en place de nombreux granitoïdes peralumineux dont la fusion à la fin du Carbonifère a pu contribuer à la formation des leucogranites uranifères.

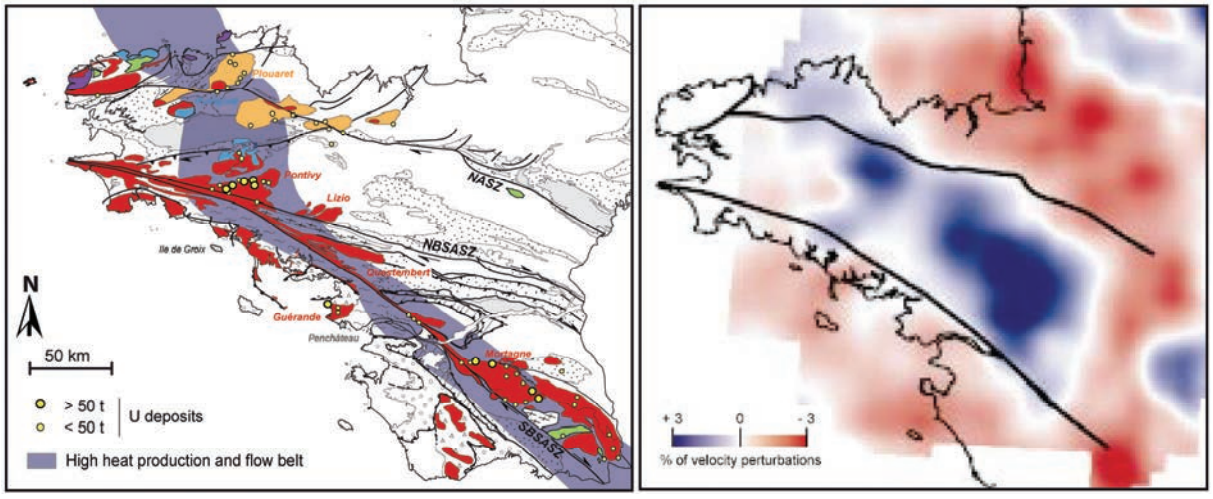

Figure IV.6 : Comparaison entre la high heat production and flow belt (Vigneresse et al., 1989 ; Jolivet et al., 1989) et une image tomographique du manteau asthénosphérique entre 165 et 200 km de profondeur (d'après Gumiaux et al., 2004). L'anomalie de vitesse des ondes P en bleue est interprétée comme la trace d'un panneau plongeant de lithosphère océanique (Judenherc et al., 2002 ; 2003 ; Gumiaux et al., 2004b).

5. Conclusion

Cette étude isotopique sur les roches totales et les grains de zircon des leucogranites fertiles en U du Massif armoricain ainsi que leurs sources potentielles permet de conclure sur les points suivants :

- Les leucogranites fertiles mis en place au nord de la branche sud du CSA (-6 < εNd (T) < 2 ; zircon hérités cadomiens, ordoviciens et dévono-carbonifères avec une signature en εHf (T) sub- à super-chondritique) proviennent majoritairement de la fusion de sédiments briovériens avec une contribution significative d'orthogneiss peralumineux paléozoïques inférieurs et dévono-carbonifères.
- Le leucogranite fertile de Guérande (-10 < εNd (T) < - 8 ; zircon hérités grenvilliens, cadomiens et dévono-carbonifères avec une signature en εHf (T) sub- à super-chondritique) provient en majorité de la fusion de sédiments ordoviciens à dévoniens avec une contribution significative d'othogneiss dévono-carbonifères. L'évolution nord-sud de la composition isotopique en εNd (T) et I_{Sr} des leucogranites est vraisemblablement liée à une augmentation de la contribution de sédiments ordoviciens à dévoniens dans leur source en allant vers le sud.
- Les formations géologiques du Massif armoricain les plus à même à générer des leucogranites uranifères, à condition d'un faible degré de fusion partielle, sont les sédiments briovériens ainsi que les orthogneiss peralumineux paléozoïques inférieurs et dévono-carbonifères car ils sont communément caractérisés par des rapports Th/U < 4 et des teneurs en U au-dessus du Clarke de la croûte continentale supérieure (> 2.7 ppm). Ces caractéristiques géochimiques suggèrent qu'une partie importante de leur U est localisée en dehors de la structure des minéraux accessoires peu solubles dans les magmas peralumineux. Au contraire, les sédiments ordoviciens à dévoniens avec généralement des rapports Th/U < 4 ne représentent pas une source favorable pour former des leucogranites uranifères lors de la fusion. La différence de fertilité entre ces sources permet potentiellement d'expliquer la répartition des gisements d'U à l'échelle du Massif armoricain. Les leucogranites peralumineux de la zone sud armoricaine sont rarement associés à des gisements car ils proviennent majoritairement de la fusion de sédiments ordoviciens à dévoniens. Au contraire, les leucogranites mis en place au nord du CSA sont communément associés à des gisements car ils proviennent en grande partie de la fusion de lithologies fertiles que sont les sédiments briovériens et les orthogneiss paléozoïques inférieurs. Les orthogneiss dévono-carbonifères apparaissent comme la source commune des leucogranites uranifères de la zone sud et centre armoricaine et doivent représenter une lithologie très favorable à la génération de magmas peralumineux riches en U lors de la fusion partielle.

A une échelle plus globale, la différentiation de la croûte continentale par fusions successives de différentes générations d'orthogneiss acides apparait comme un paramètre clé dans la formation d'une province métallogénique uranifère et la genèse de leucogranites fertiles.

Partie V : discussion préliminaire sur l'évolution mésozoïque du Massif armoricain

1. Introduction

La thermochronologie par la méthode des traces de fission sur apatite permet d'avoir accès à l'histoire thermique des échantillons dans une gamme de température comprise entre environs 120 et 60°C qui correspond à la zone de rétention partielle des traces de fission (PAZ). Cette méthode permet donc de contraindre le timing d'exhumation des roches dans les ~3 à 6 derniers km de la croûte continentale si on prend en compte un gradient géothermique normal de 20°C/km. Lors de cette thèse, des analyses par traces de fission sur apatite ont été réalisées sur plusieurs granites carbonifères du Massif armoricain en suivant un profil sud-nord partant du leucogranite de Guérande jusqu'au granite de Ploumanac'h (cette dernière donnée ayant été acquise par C. Dubois lors de son stage de master 2 en 2014) (Fig.V.1). Ces analyses s'ajoutent aux analyses non publiées réalisées par Siddall (1993) sur une grande partie de la côte du Massif armoricain mais sans données disponibles sur les longueurs des traces de fission (Fig. V.1). Les analyses ont été réalisées dans le but de mieux contraindre les conditions thermiques et de profondeur sous lesquels les leucogranites ont été lessivés de leur U et celles où les gisements d'U hydrothermaux associés se sont formés (cf. article #4). Nous allons voir que ces données permettent, en parallèle, d'apporter des informations sur l'évolution topographique post hercynienne du Massif armoricain et sur des événements hydrothermaux mésozoïques associés. Les données traces de fission obtenues sont aussi interprétées avec des données non publiées de datation U-Th-Pb sur monazite réalisées sur le granite de Guérande.

2. Contexte géologique générale du Massif armoricain du Permien au mésozoïque

Les bassins sédimentaires permiens sont rares dans le Massif armoricain et le rare exemple est localisé à l'extrémité nord-est au niveau de Carentan (Fig. V.1). Dans ce bassin, la sédimentation détritique terrigène se traduit par le dépôt de grès et d'argiles rouges (Ballèvre et al., 2013). Le bassin de Carentan est interprété comme l'extrémité méridionale de bassins plus importants, maintenant localisés sous la Manche (Western Approach, Fig. V.1), et alimentés par les produits d'érosion de la chaîne hercynienne armoricaine et de la partie sud-ouest de l'Angleterre. Le Massif armoricain est bordé par trois bassins sédimentaires mésozoïques à cénozoïques principaux qui sont la Manche (Western Approach) au nord, le bassin de Paris à l'est et la marge sud armoricaine au sud (Fig. V.1). Au Trias inférieur, le Massif armoricain représente un relief en érosion dont les sédiments alimentent des formations fluviatiles en Angleterre et à l'est de la France (Ballèvre et al., 2013). Au Trias supérieur une sédimentation détritique terrigène reprend sur la marge nord-est du Massif armoricain sous la forme de dépôt continentaux (Ballèvre et al., 2013) (Fig.V.1). La période du Jurassique (~200 - 145 Ma) est marquée par l'absence de sédimentation détritique importante dans les bassins autour du Massif armoricain et, dans le bassin de Paris, les sédiments jurassiques sont principalement constitués de carbonates et d'argiles (Guillocheau et al., 2000). A l'opposé du Jurassique, le début du Crétacé inférieur est marqué par une sédimentation silico-clastique importante dans tous les bassins autour du

Massif armoricain, dont la Manche (Fig. V.1), qui est interprétée comme le reflet de la surrection et l'érosion du Massif armoricain en réponse à l'initiation du rifting dans le Golfe de Gascogne au sud de la marge armoricaine (Guillocheau et al., 2000). A partir d'une cartographie détaillée des surfaces d'aplanissement du Massif armoricain, Bessin et al. (2015) suggèrent l'existence de deux phases majeures d'enfouissement et d'exhumation dans le Massif armoricain : (1) une phase d'enfouissement au Jurassique suivie d'une période de dénudation au crétacé inférieur puis (2) une phase d'enfouissement au crétacé supérieur suivie d'une période de dénudation entre la fin du Crétacé et le début de l'Eocène.

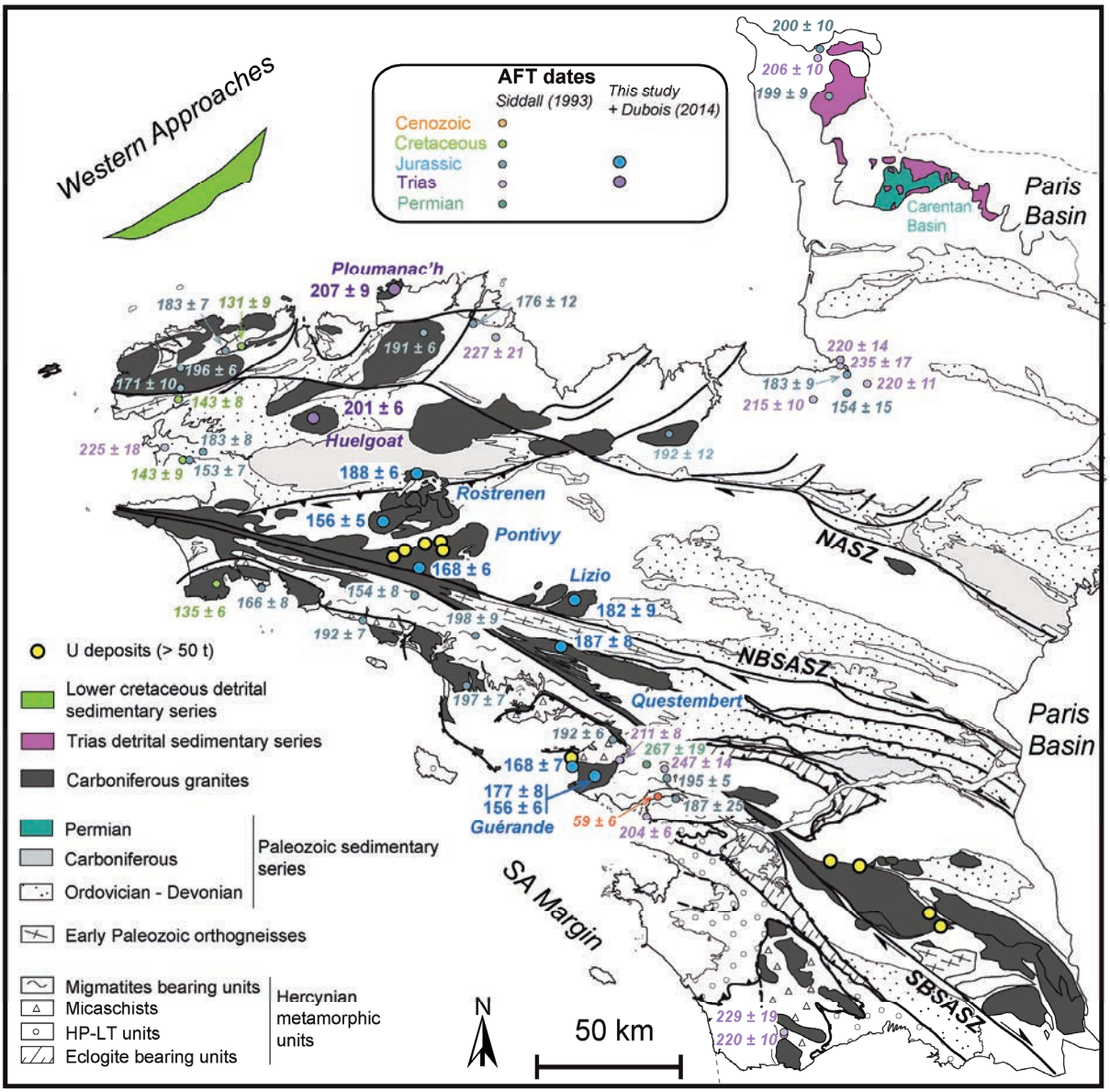

Figure V.1 : Carte géologique simplifiée du Massif armoricain [modifiée d'après Chantraine et al. (2003) et Gapais et al. (2015)] reportant les dates moyennes par traces de fission sur apatite (AFT) mesurées lors de cette étude ainsi que les dates obtenues par Dubois (2014 : granite de Ploumanac'h) et Siddall (1993) pour comparaison. SA Margin = marge sud armoricaine.

La période du Trias supérieur au Jurassique dans le bassin de Paris est marquée par plusieurs événements hydrothermaux synsédimentaires qui sont enregistrés de la bordure est du Massif armoricain aux Vosges, en passant par le Massif central (Guillocheau et al., 2000; Cathelineau et al., 2012). Un premier événement daté de la transition Trias-Jurassique inférieur (Rhétien-Héttangien : ~200 Ma) est associé à la mise en place de minéralisations en sphalérite, galène, fluorite, barytine et pyrite (Guillocheau et al., 2000; Montenat et al., 2006). Cet événement est synchrone de la mise en place de dykes de dolérite sur la bordure ouest du Massif armoricain entre ca. 210 et 195 Ma et interprétée comme le reflet des prémices de l'ouverture de l'Atlantique (Caroff, 1995). Ensuite, un événement hydrothermal d'âge Pliensbachien (~190 – 180 Ma) est enregistré du Massif armoricain au Massif central et associé à la mise en place de filons de barytines (Guillocheau et al., 2000). Clauer et al. (1995) suggèrent l'implication de fluides avec des températures de ~220 - 250°C lors de cette événement. Enfin, un évènement hydrothermal majeur, avec des températures de l'ordre de 100 – 200°C, associé à la mise en place de minéralisations en F-Ba (Pb-Zn) est enregistré dans le socle à la transition entre le bassin aquitain et le bassin de Paris pendant le Jurassique supérieur (ca. 146 – 156 Ma) (Cathelineau et al., 2012).

3. Méthode

3.1. Traces de fission sur apatite (AFT)

Les analyses en trace de fission sur apatite (AFT) ont été réalisées sur trois échantillons du granite de Guérande (cf. article #4) puis un échantillon des granites de Questembert, Lizio, Pontivy, Langonnet, Rostrenen et Huelgoat (Tableau IV.3). L'analyse d'un échantillon du granite de Ploumanac'h a été réalisée par Dubois (2014). Les grains d'apatite ont été séparés à Géosciences Rennes via un séparateur magnétique et des liqueurs denses. Les cristaux ont été montées sur une lame de verre grâce à de la résine époxy puis polies. Les traces de fission ont été révélées en plongeant les apatites dans de l'acide nitrique (HNO_3 – 1.6 M) à 20 °C pendant 45s (e.g. Seward et al., 2000; Jolivet et al., 2010). Une feuille de mica (dépourvue d'U) utilisée comme détecteur externe a ensuite été posée sur la lame de verre avant que les échantillons d'apatite soient envoyés à irradier dans un réacteur nucléaire à SCK, Mol, Belgique (flux de neutron = 1.0 $x10^{15}$; échantillons GUE-3, 4, 5 ; QRT-08 ; LRT-10 ; PL-1) ou à l'Oregon State University (flux de neutron = 1.0 x 10^{16} ; échantillons PONT-10, 20, 22, HUEL-3). Les traces induites dans les feuilles de mica, par la fission de l'U^{235} contenu dans l'apatite, ont été révélées en plongeant le mica dans de l'acide fluorhydrique à 20°C (HF-60%) pendant 40 min. Les âges ont été calculés en suivant la méthode recommandée par le groupe de travail sur les traces de fission de la subcommission IUGS de géochronologie (Hurford, 1990) en utilisant la méthode de calibration zeta. Le verre CN5, à chaque fois irradié avec les échantillons, a été utilisé comme dosimètre.

Le comptage et la mesure des traces de fission ont été réalisés à Géosciences Rennes en utilisant un microscope Zeiss Axioplan 2 avec une magnificence de 1250x. Pour chaque échantillon, un total de 20 ou 19 (QRT-08) grains d'apatite sans inclusions et avec leur surface parallèle à l'axe cristallographique <c>, ont été analysées par comptage des traces en utilisant le logiciel Trackworks développé par la compagnie Autoscan (Australie). Le calcul des âges a été effectué en utilisant le logiciel Trackkey (Dunkl, 2002). Les valeurs de zeta ont été obtenues à partir de l'apatite standards Durango (McDowell et al., 2005) et Mount Dromedary (Green, 1985 ; Tagami, 1987). Les valeurs moyenne pondérées utilisées sont de 335.9 ± 6.8 yr.cm² (CB: GUE-3, 4, 5; QRT-08; LRT-10), 338.4 ± 6.2 yr.cm² (CB: PONT-10, 20, 22; HUEL-3) et 311.7 ± 5.8 yr.cm² (CD: PL-1). Les dates reportées à 2σ sont l'âge centrale pour P (χ2) > 5 % et l'âge pooled pour P (χ2) < 5 %. La mesure de longueur des traces horizontales et de leur angle respectif avec l'axe <c> ainsi que des valeurs de D_{par} (e.g. Jolivet et al., 2010; Sobel and Seward, 2010) ont été obtenues pour chaque échantillons hormis PONT-20 et PL-1 (les longueurs ont été mesurées pour PL-1 mais pas les D_{par}). Le D_{par} correspond au diamètre de l'intersection des traces avec la surface parallèle à l'axe <c> des cristaux d'apatite analysés. La valeur moyenne des D_{par} utilisée pour chaque échantillon a été obtenue en mesurant plus de 300 D_{par}.

La modélisation de l'histoire thermique des échantillons a été réalisée à partir du logiciel QTQt (Gallagher et al., 2009; Gallagher, 2012) en utilisant le modèle d'effacement des traces de Ketcham et al. (2007) qui prend en compte la valeur de D_{par} pour contraindre la cinétique d'effacement des traces de fission dans l'apatite. Pour PL-1, une valeur classique de D_{par} de 1.5 a été utilisée. L'histoire temps-température des échantillons n'est bien contrainte par le modèle que dans la zone de rétention partielle des traces de fission (PAZ : 120 – 60°C).

3.2. Datation U-Th-Pb sur monazite (granite de Guérande)

Des datations U-Pb sur monazite par LA-ICP-MS ont été réalisés à Géosciences Rennes sur des échantillons du granite de Guérande en complément de celles publiées dans l'article #2. Les conditions analytiques sont exactement les même que dans l'article #2 et les résultats des analyses sont fournies an annexe de ce manuscrit avec un degré d'incertitude de 1σ. Les âges sont néanmoins calculés avec un degré d'incertitude de 2σ

4. Résultats

4.1. Thermochronologie par traces de fission sur apatite

Le résultat des analyses par traces de fission sur apatite sont reportées dans le Tableau V.1 et les Figures V.1 et V.2. Les dates AFT mesurées varient de 207 ± 9 Ma (Pl-1 ; Ploumanac'h) à 154 ± 5 Ma (PONT-20 : Langonnet) et sont cohérentes avec la grande hétérogénéité des dates obtenues par Siddall (1993) allant majoritairement du Trias au Crétacé inférieur (Fig. V.1). Le début de l'histoire thermique des échantillons dans le logiciel QTQt a été contraint à partir de la température de fermeture

du système ^{40}Ar-^{39}Ar sur muscovite (450 ± 100°C ; Harrison et al., 2009) pour les granites de Guérande (300 ± 10 Ma ; Le Hébel, 2002), Lizio (310 ± 10 Ma ; Tartèse et al., 2011a), Questembert (315 ± 10 Ma ; Tartèse et al., 2011b), Pontivy (310 ± 20 Ma ; Cosca et al., 2011) et Ploumanac'h (300 ± 10 Ma ; Ruffet, données non publiées), le système U-Pb sur apatite (450 ± 100 Ma ; e.g. Chamberlain and Bowring, 2000; Schoene and Bowring, 2006; Cochrane et al., 2014) pour le granite de Rostrenen (315 ± 10 ; cf. article #5) et le système U-Pb sur zircon (800 ± 100 Ma ; e.g. Cherniak and Watson, 2001) pour le granite de Huelgoat (315 ± 10 Ma, cf. Partie III). La longueur moyenne des traces de fission (MTL) varie de 12.5 µm (granite de Lizio) à 13.5 µm (granite de Questembert). La majorité des échantillons, excepté les granites de Lizio et Rostrenen, révèle une distribution unimodale des longueurs de traces de fission qui est cohérente avec un refroidissement régulier de ces échantillons de 120 à 60°C (Fig. IV.2). Le taux de refroidissement est faible et varie de ~4°C/ Ma pour les granites de Ploumanac'h et Huelgoat à ~2°C /Ma pour les granites de Questembert et Pontivy, le granite de Guérande révélant un taux intermédiaire de 3°C/Ma. A la différence des autres granites, les granites de Lizio et Rostrenen montrent une distribution hétérogène des traces de fission qui se traduit par un refroidissement régulier des échantillons de ca. 250 à 220 Ma (~2°C/Ma) puis un ralentissement de ce refroidissement de ca. 220 à 175 Ma (~0 à 0.5°C/Ma). L'âge minimum d'arrivée des échantillons à des températures inférieures à 60 °C va de ca. 210 Ma pour le granite de Ploumanac'h à ca. 140 Ma pour le granite de Lizio. A partir de ces dates tous les échantillons sont restés en sub-surface.

4.2. Géochronologie U-Th-Pb sur monazite.

Les analyses en U-Th-Pb réalisées sur les grains de monazite de deux échantillons du granite de Guérande sont reportées dans un diagramme Terra-Wasserburg (TW ; Fig. V.3). L'échantillon GUE-5 provient d'un dyke de leucogranite intrusif dans le leucogranite de Guérande s.s. alors que l'échantillon GUE-8 est un leucogranite à Ms-Bt appartenant au faciès principal de l'intrusion. Ces deux échantillons ne présentent pas d'évidence majeur d'altération hormis une chloritisation variable de la biotite (voir l'article #2 pour une localisation et une description précise des échantillons).

Pour l'échantillon GUE-5, 36 analyses à partir de 21 grains de monazite ont été réalisées. Les analyses ont une position concordante à discordante dans le diagramme TW et deux populations d'ellipse apparaissent. Un premier groupe de 18 analyses permet le calcul d'une date concordia à 302.9 ± 2.0 Ma (MSWD = 1.2) et 8 autres analyses permettent le calcul d'une date concordia à 227.8 ± 3.2 Ma (MSWD = 2.0). La position des autres ellipses en pointillés est majoritairement explicable par une contamination en Pb commun. La date concordia à ca. 303 Ma correspond à l'âge de mise en place de ce dyke publié dans l'article #2 (âge concordia calculé à 302.5 ± 1.6 Ma dans un diagramme $^{206}Pb/^{238}U$ versus $^{208}Pb/^{232}Th$) alors que la date à ca. 225 Ma est nettement plus jeune. Hormis pour un grain (n°7), les deux populations de dates apparentes ont été obtenues à partir de cristaux de monazite différents.

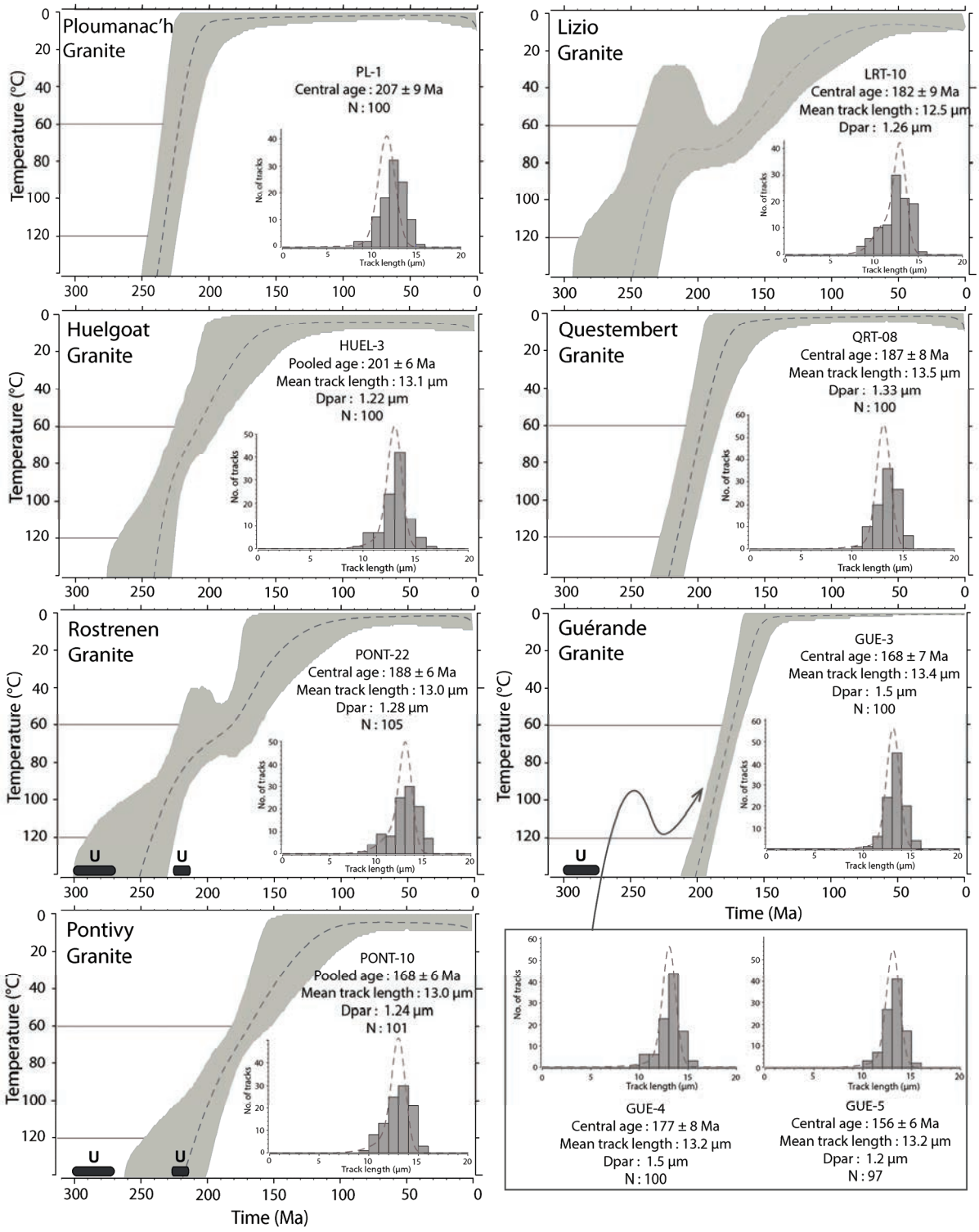

Figure V.2 : Modélisation de l'histoire thermique des échantillons de granite à partir des données traces de fission sur apatite (AFT) en utilisant le logiciel QTQt (Gallagher et al., 2009). Les histogrammes à l'intérieur des diagrammes temps-température représentent la distribution des longueurs de traces de fission mesurées dans chaque échantillon. La courbe en pointillée autour des histogrammes représente la distribution des traces calculées à partir du modèle. N = nombres de traces mesurées. Sur les diagrammes temps-température, les traits gris horizontaux représentent la zone de rétention partielle des traces de fission (PAZ) située entre 120 et 60°C. Le modèle n'est bien contraint que dans cette gamme de température. La zone grise représente l'histoire thermique de l'échantillon pour une probabilité de 95 %. La courbe grise en tirés représente la moyenne pondérée de l'histoire thermique attendue. Pour le leucogranite de Guérande la modélisation a été réalisée à partir de trois échantillons (cf. article #4). Pour le granite de Ploumanach (Dubois, 2014) un Dpar de 1.5 µm a été utilisé pour la modélisation. L'âge des minéralisations uranifères (U) dans les districts de Pontivy-Rostrenen et Guérande (cf. article #4 et #5) est reporté.

Pour l'échantillon GUE-8, 29 analyses à partir de 11 grains de monazite ont été réalisées et 17 analyses en position sub-concordante à concordante permettent le calcul d'une date concordia à 223.4 ± 1.5 Ma (MSWD = 1.4). La position des ellipses en pointillés est majoritairement explicable soit par une perte en Pb soit par une contamination en Pb commun. Cette date est largement plus jeune que l'âge de mise en place de l'intrusion de Guérande à ca. 310 Ma (cf. article #2) et comparable à la date la plus jeune obtenue sur les monazites de l'échantillon GUE-5.

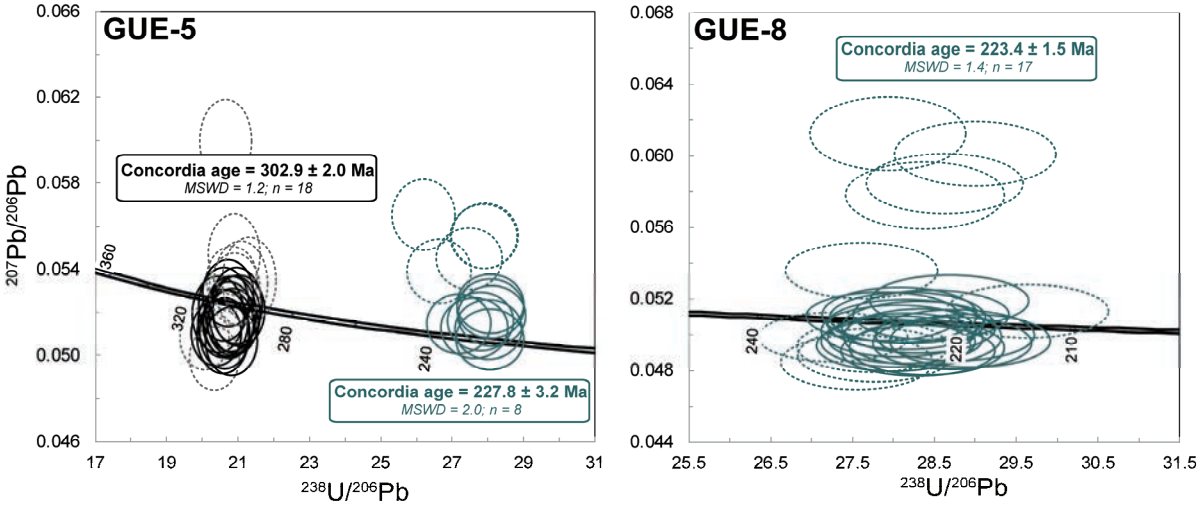

Figure V.3 : Diagrammes Terra-Wasserburg reportant les analyses U-Pb réalisées sur les cristaux de monazite des échantillons GUE-5 et GUE-8 du leucogranite de Guérande. Les ellipses et les âges sont reportées à 2σ. Les ellipses en pointillés représentent les analyses non utilisées pour le calcul des âges concordia.

5. Discussion

5.1. Exhumation des granites et implication sur l'évolution topographique du Massif armoricain.

Les dates AFT obtenus par Siddall (1993) et lors de cette étude sont très variables et vont majoritairement du Trias au Crétacé inférieur (Fig. V.1). Les dates AFT Crétacé inférieurs semblent se localiser exclusivement sur la bordure ouest du Massif armoricain mais aucun lien entre la date et la localisation des échantillons semble apparaitre pour le Trias et le Jurassique (Fig. V.1). Dans le diagramme de densité par noyau («Kernel density estimate » - KDE) de la Figure V.4, les dates AFT se répartissent en 3 pics majeurs à ~210-220 Ma (Trias), ~185-200 Ma (Jurassique inférieur) et ~150-160 Ma (Jurassique supérieur). Le pic triasique est comparable à la date AFT du granite de Ploumanac'h (207 ± 9 Ma ; Fig. V.2). L'histoire thermique de cette échantillon suggère un taux de refroidissement faible et régulier d'environ 4°C/Ma dans la PAZ qui correspond à un taux d'érosion de ~200 m/Ma en prenant en compte un gradient géothermique normal de 20°C/km (Fig. V.2). Le pic jurassique inférieur est caractéristique des granites de Huelgoat (201 ± 6 Ma) et Questembert (187 ± 8 Ma) dont le profil thermique indique un refroidissement lent et régulier à des taux d'environ 2 à 4°C/Ma, correspondant à des taux d'exhumation de 200 à 100m/Ma (gradient géothermique de 20°C/km ; Fig. V.2). Enfin, les dates AFT obtenues sur les granites de Guérande (168 ± 7 Ma, 177 ± 8

Ma, 156 ± 6 Ma) et Pontivy (168 ± 6 Ma) sont proches ou appartiennent à la dernière population jurassique supérieure. Comme pour les autres échantillons, l'histoire thermique de ces granites suggère un refroidissement lent et régulier à travers la PAZ avec un taux de 3 à 2°C/Ma correspondant à un taux d'exhumation de 100 à 150 m/Ma pour un gradient géothermique de 20°C/km.

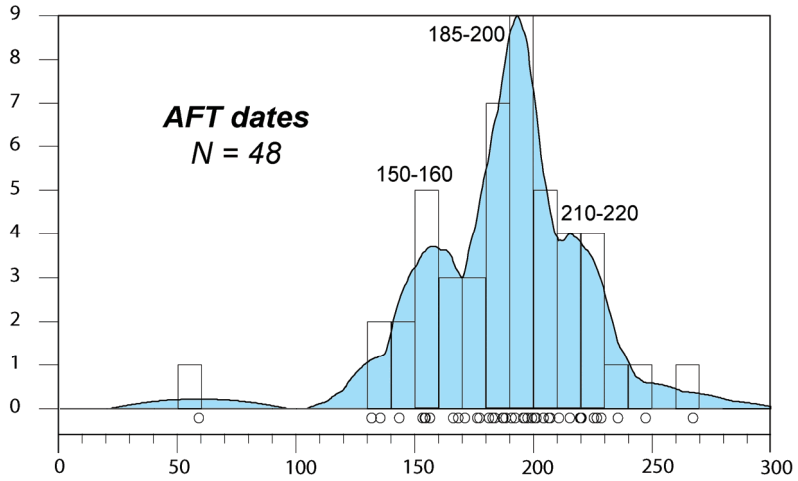

Figure V.4 : Diagramme d'estimation par noyau (« kernel density estimate – KDE) couplé à un histogramme réalisé à partir du logiciel DensityPlotter (Vermeesch, 2012 ; « band width = 10 »), reportant les dates AFT disponibles sur l'ensemble du Massif armoricain.

Les données AFT suggèrent donc que la majorité des échantillons ont été exhumés en sub-surface (~2-3 km de profondeur pour un gradient géothermique de 20°C/km) sur une période de temps qui va du Trias au Jurassique supérieur. Le pic d'exhumation triasique (~210 - 220 Ma) est synchrone du dépôt de formations détritiques fluviatiles au nord-est du Massif armoricain reflétant la fin de l'érosion des reliefs majeurs de la chaîne hercynienne armoricaine (Ballèvre et al., 2013) (Fig. V.1). Les deux pics d'exhumation jurassique ne sont cependant pas contemporains d'une sédimentation détritique dans les bassins qui entourent le Massif armoricain et la période jurassique du bassin de Paris est dominée par une sédimentation carbonatée et argileuse en milieu marin (Guillaucheau, 2000). Néanmoins, l'exhumation très lente du socle à cette période avec un taux de 100 à 200 m/Ma, comme indiqué par le profil thermique des granites (Fig. V.2), a dû être vraisemblablement accompagnée d'une très faible production détritique rendant possible le développement d'une plateforme carbonaté sur les marges du Massif armoricain. Les variations locales importantes des dates AFT qui sont observées sur la carte de la Fig.V.1, que ce soit pour nos échantillons ou ceux de Siddall (1993), pourraient être liées au taux de refroidissement très lent des échantillons qui perturberaient les cinétiques d'effacement des traces de fission. Bessin et al. (2015) ont suggéré un enfouissement du Massif armoricain durant le Jurassique. Cependant, l'exhumation en sub-surface de nombreux échantillons à cette période et l'absence d'évidence de ralentissement du refroidissement des granites durant le Jurassique (Fig. V.2) n'est pas en accord avec cette hypothèse. En parallèle, si le Massif armoricain avait été immergé à cette période le maximum d'enfouissement aurait été enregistré sur ses

bordures. Néanmoins, les nombreuses dates AFT triasiques enregistrées sur la côte, y compris par le granite de Ploumanac'h (Fig. V.1), suggèrent que le Massif armoricain n'a pas été enfoui de façon significative durant la période méso-cénozoïque. Plusieurs dates AFT crétacées supérieures sont enregistrées à l'ouest du Massif armoricain et reflètent vraisemblablement sa surrection en réponse à l'initiation du rifting dans le Golfe de Gascogne. Cet événement est marqué par une sédimentation détritique terrigène (Groupe de Wealden : ~145 – 125 Ma ; Bessin et al., 2015 et références y contenues) dans tous les bassins environnants comme la Manche (Fig.V.1).

5.2. Evidences d'un événement hydrothermal trias supérieur dans le Massif armoricain.

La datation U-Pb des oxydes d'uranium issus des gisements uranifères du district de Pontivy-Rostrenen (cf. article #5) (Fig. V.1) a mis en évidence un événement hydrothermal tardif à ca. 220 Ma qui est largement postérieure à la phase majeure de formation des gisements entre ca. 300 à 270 Ma. Les profils thermiques des granites de Rostrenen et Lizio révèlent un ralentissement de leur refroidissement entre ~220 et 175 Ma qui est synchrone de cette événement hydrothermal mobilisateur d'U (Fig. V.2). Indépendamment, la datation U-Pb de grains de monazite sur deux échantillons du leucogranite de Guérande révèlent des dates comparables à ca. 225 Ma (Fig. V.3). Nous suggérons que ces dates soient le reflet d'un événement hydrothermal d'âge Trias supérieur vraisemblablement généralisé à l'ensemble de la moitié sud du Massif armoricain. Des évidences de circulations de fluides hydrothermaux à la limite Trias-Jurassique inférieur (~200 Ma) existent de la bordure est du Massif armoricain aux Vosges (Guillaucheau, 2000 ; Montenat, 2006) et sont associées à des événements minéralisateurs en F, Ba, Pb et Zn. Ces circulations de fluides sont synchrones de la mise en place de dykes de dolérite entre 210 et 195 Ma à l'ouest du Massif armoricain et interprétée comme le reflet des prémices de l'ouverture de l'Atlantique (Caroff et al., 1995). Dans cette étude, nous mettons en évidence un événement hydrothermal qui semble légèrement plus précoce même si les profils thermiques des granites de Lizio et Rostrenen suggèrent que ces circulations de fluides ont pu perdurer jusqu'à 175 Ma (Fig. V.2).

6. Conclusion

Cette interprétation préliminaire des données AFT obtenues durant cette thèse permet de conclure les points suivants :

- L'exhumation post hercynienne du socle constituant le Massif armoricain s'est faite sur une période très longue allant du Permien jusqu'à la fin du Jurassique. Les taux d'exhumation du Trias au Jurassique sont très faibles et sont de l'ordre de 100 à 200 m/Ma. Les données AFT ne sont pas en accord avec un enfouissement du Massif armoricain au cours du Jurassique. En parallèle, aucun enfouissement majeur de ce domaine continental n'est enregistré pendant le Méso-Cénozoïque.

- Les données AFT suggèrent une surrection de la partie ouest du Massif armoricain au Crétacé inférieur en réponse à l'initiation du rifting dans le Golfe de Gascogne.
- Un événement hydrothermal généralisé à la moitié sud du Massif armoricain est mis en évidence à ca. 225Ma par trois méthodes de datation différentes (U-Pb sur monazite, U-Pb sur oxyde d'uranium et AFT).

Du point de vue métallogénique, les données AFT suggèrent que les leucogranites de Guérande et de Pontivy étaient effectivement en profondeur au moment de la période majeure de formation des gisements uranifères dans le Massif Armoricain de ca. 300 à 270 Ma (Fig. V.2).

Table V.1 : Données traces de fission sur apatite. ρd est la densité de traces de fission induites (par cm²) qui serait obtenue dans chaque échantillon si sa concentration en U était égale à celle du verre dosimètre CN5. ρs et ρi représentent, respectivement, la densité des traces de fissions spontanées et induites (par cm²) mesurée dans chaque échantillon. Les nombres entre parenthèses représentent le nombre total de traces comptées. U représente la concentration moyenne en U des apatites analysées. P (χ2) est la probabilité en %. L'âge considéré est l'âge central pour P (χ2) > 5 % et l'âge pooled pour P (χ2) < 5 %. MTL représente la longueur moyenne des traces de fission horizontales mesurées dans les cristaux d'apatite avec une surface parallèle à l'axe <c> (µm). Le D_{par} représente la moyenne des diamètres de l'intersection des traces de fission avec la surface parallèle à l'axe <c> des apatites analysée (en µm). Les âges ont été calculés en utilisant le logiciel Trackkey (Dunkl, 2002). Les données sur le granite de Ploumanach sont de Dubois (2014). * longueurs de traces non corrigées de l'angle avec l'axe <c>. Les cordonnées GPS des échantillons sont reportées dans le tableau IV.2.

Intrusion	Sample	Number of grains	ρd × 10^5 (cm²)	ρs × 10^5 (cm²)	ρi × 10^5 (cm²)	U (ppm)	P (χ^2) (%)	Age (Ma)	±2σ	MTL (µm)	SD (µm)	D_{par} (µm)	zeta (yr.cm²)	±
Guérande	GUE-3	20	3.409 (3421)	35.998 (4579)	12.17 (1548)	44	33.4	168	7	13.4	1.0	1.50		
	GUE-4	20	3.457 (3421)	56.923 (3404)	18.411 (1081)	61	97.4	177	8	13.2	1.1	1.46	335.9	6.8
	GUE-5	20	3.361 (3421)	55.589 (4058)	19.89 (1452)	69	35.2	156	6	13.2	1.0	1.19		
Questembert	QRT-08	19	3.288 (3421)	75.525 (5181)	22.099 (1516)	76	17.1	187	8	13.5	1.1	1.33	335.9	6.8
Lizio	LRT-10	20	3.264 (3421)	61.096 (4350)	18.23 (1298)	65	10.1	182	9	12.5	1.6	1.26	335.9	6.8
Pontivy	PONT-10	20	8.531 (9002)	42.067 (3277)	35.687 (2780)	51	7.2	168	6	13.0	1.3	1.24	338.4	6.2
Langonnet	PONT-20	19	9.069 (9002)	67.288 (4367)	65.532 (4253)	86	0	156	5				338.4	6.2
Rostrenen	PONT-22	20	9.473 (9002)	44.61 (4635)	37.44 (3890)	47	16	188	6	13.0	1.6	1.28	338.4	6.2
Huelgoat	HUEL-3	20	9.607 (9002)	59.01 (5482)	46.99 (4635)	56	0	201	6	13.1	1.2	1.22	338.4	6.2
Ploumanach	PL-1	20	3.864 (3646)	52.863 (7200)	15.117 (2059)	45	5.3	207	9	12.4*	1.4		311.7	5.8

Conclusion générale

Le travail réalisé a pour objectif principal d'améliorer la compréhension des processus contrôlant la formation des gisements d'uranium hydrothermaux associés aux leucogranites peralumineux dans la chaîne hercynienne européenne. Pour cela, une étude complète depuis la source des leucogranites, leur processus de différentiation et leur mise en place dans la croûte supérieure jusqu'au lessivage de l'U, la formation des gisements et leur exhumation a été réalisée au sein du Massif armoricain. En parallèle, cette étude apporte des précisions sur les conditions du magmatisme carbonifère dans la chaîne hercynienne, la tectonique permienne et l'évolution du Massif armoricain durant le Mésozoïque. Les événements et processus clés dans l'histoire des leucogranites et de leurs gisements associés sont résumés ci-dessous :

1. ***La fusion partielle d'un manteau métasomatisé et d'une croûte continentale différenciée et préenrichie en U entre ca. 320 Ma et 300 Ma.***

Le croisement de données isotopiques sur roches totales (Sr et Nd) et zircon (U-Pb et Hf) avec des analyses en éléments majeurs et traces obtenues sur les granitoïdes carbonifères du Massif armoricain et leurs sources potentielles nous a permis de tracer l'origine de ces intrusions. En parallèle les datations U-Th-Pb sur zircon et monazite nous ont aussi permis de dater leur mis en place.

Dans la zone interne de la chaîne hercynienne armoricaine au sud du cisaillement sud armoricain (CSA), de nombreux leucogranites peralumineux (MPG) avec une origine purement crustale se sont mis en place dans des zones de déformation extensive. Parmi eux le leucogranite de Guérande qui est daté par U-Th-Pb sur zircon et monazite à ca. 310 Ma est le seul à être associé à des gisements et occurrences uranifères. Le magma à l'origine de cette intrusion provient d'un faible taux de fusion partielle de métasédiments détritiques ordoviciens à dévoniens et d'une source métaignée, probablement peralumineuse, d'âge dévono-carbonifère. Les sédiments dévoniens caractérisés par des teneurs en U généralement en dessous du Clarke de la croûte continentale supérieure (< 2.7 ppm) et des rapports Th/U > 4 ne représentent pas une source propice à la formation de leucogranites fertiles. Néanmoins, les orthogneiss peralumineux avec des valeurs de Th/U < 4 et des teneurs en U > 2.7 ppm peuvent représenter une source favorable car une partie significative de leur U est potentiellement localisée en dehors de la structure des minéraux accessoires (i.e. monazite et zircon).

Au nord du CSA dans les zones externes de la chaîne, les occurrences de roches mantelliques augmentent du sud vers le nord et l'ascension des différents magmas a été facilitée par la déformation en régime décrochant de la zone centre armoricaine. Le long du CSA, le magmatisme exclusivement crustal est marqué par la mise en place vers 315 Ma de leucogranites peralumineux syntectoniques communément associés à des gisements ou occurrences uranifères comme le leucogranite de Pontivy. Ces leucogranites fertiles proviennent majoritairement d'un faible taux de fusion partielle de métasédiments détritiques briovériens ainsi que d'orthogneiss peralumineux d'âges paléozoïques inférieurs et dévono-carbonifères. Les trois lithologies, communément caractérisés par des rapports

Th/U < 4 et des teneurs en U > 2.7 ppm, représentent des sources favorables pour la formation de leucogranites uranifères. Cette différence de sources soumises à la fusion entre le domaine sud et centre armoricain permet vraisemblablement d'expliquer pourquoi la majorité des gisements d'U sont associés aux leucogranites situés au nord du CSA et pas ceux situés au sud. Plus au nord dans la zone externe, des monzogranites à cordiérite (CPG de Huelgoat et Rostrenen) se sont mis en place vers 315 Ma de façon synchrone avec des leucogranites peralumineux et des magmas mafiques métalumineux (monzodiorite et diorite quartziques). En parallèle, une intrusion leucogranitique tardive (MPG de Langonnet) se met en place à ca. 305 Ma. Les magmas à l'origine des CPG sont issus principalement d'un fort taux de fusion partielle d'orthogneiss métalumineux, pour le monzogranite de Rostrenen, et d'un mélange de métasédiments brioveriens et d'orthogneiss paléozoïques (cambrio-ordoviciens et dévono-carbonifères) pour le monzogranite de Huelgoat. Le fort taux de fusion partielle de sédiments et d'orthogneiss sous la zone centre armoricaine a été induit par le sous plaquage de magmas mafiques issus de la fusion partielle d'un manteau lithosphérique métasomatisé.

Au sud du CSA dans la zone interne et épaissie de la chaîne, la fusion crustale est contrôlée par un amincissement lithosphérique lui-même provoqué par l'extension tardi-orogénique de la chaîne. Au contraire, au nord du CSA dans la zone externe et peu épaissie de la chaîne, la fusion crustale et mantellique est induite par une remonté asthénosphérique provoquée par la déformation diffuse en décrochement, probablement transtensif, de la zone centre armoricaine et potentiellement le démembrement d'un vestige de panneau océanique à la transition lithosphère - asthénosphère. Le manteau sous continental au nord du CSA était potentiellement plus propice à la fusion partielle que le manteau situé au sud car ce premier a dû être enrichi par la subduction de matériels océaniques et continentaux jusqu'à la fin du dévonien (~360 Ma).

Du point de vue métallogénique, la fusion partielle d'orthogneiss peralumineux et donc la différentiation progressive de la croûte continentale apparait comme étant un paramètre clé dans la genèse de leucogranites uranifères.

2. Une différentiation par cristallisation fractionnée et par altération magmatique-hydrothermale synchrone de la mise en place

Les analyses en éléments majeurs et traces sur roches totales couplées à des analyses sur minéraux nous ont permis de contraindre les processus magmatiques et magmatiques-hydrothermaux impliqués dans l'évolution des leucogranites.

Contrairement au monzogranite de Rostrenen qui a évolué majoritairement via un mélange avec des magmas mantelliques et/ou l'entrainement de minéraux peritéctiques depuis la source, les leucogranites de Guérande et Pontivy ont évolués principalement par cristallisation fractionnée au cours de leur remonté vers la surface. L'extraction du magma de minéraux accessoires comme la monazite et le zircon a induit la diminution du rapport Th/U et l'enrichissement en U du liquide jusqu'à atteindre la

saturation en oxydes d'uranium magmatiques dans les facies les plus évolués. En parallèle, l'interaction sub-solidus avec des fluides orthomagmatiques a vraisemblablement contribuée à l'enrichissement en U de ces leucogranites. La diminution du rapport Nb/Ta à des valeurs inférieures à ~5 dans les leucogranites peralumineux est interprétée comme le résultat conjoint de la cristallisation fractionnée et d'une altération magmatique-hydrothermale diffuse. La valeur Nb/Ta ~5 peut être utilisée comme outil d'exploration pour différencier les leucogranites stériles des leucogranites évolués potentiellement minéralisés en oxydes d'uranium magmatiques et associés à des gisements.

3. Un lessivage syntectonique des oxydes d'uranium magmatiques durant la circulation de fluides hydrothermaux oxydants dérivés de la surface

Les analyses des inclusions fluides et la datation U-Pb des oxydes d'uranium des gisements couplées, entre autre, aux analyses isotopes stables, à la radiométrie spectrale et à la datation par U-Pb et traces de fission de l'apatite des leucogranites nous a permis de proposer un modèle métallogénique pour la formation des gisements d'U du Massif armoricain.

Dans le district de Guérande, le gisement d'U principale est périgranitique et localisé dans un graben au-dessus de la zone apicale du leucogranite où les analyses géochimiques et la radiométrie spectrale suggèrent un lessivage d'oxydes d'uranium. Entre ca. 310 et 300 Ma, l'apex de l'intrusion, où sont situés les facies les plus évolués, a été déformée de façon ductile dans une zone de déformation extensive. Vers 300 Ma, des circulations de fluides hydrothermaux oxydants d'origine météorique, mises en évidence par l'isotopie de l'oxygène dans les facies C/S de l'apex, ont induit la mise en solution d'oxydes d'uranium magmatiques. A cette époque, le flux de chaleur fourni par une activité magmatique tardive, se traduisant par la mise en place de dykes leucogranitiques, a aidé à maintenir les circulations de fluides convectives. Ensuite, ces fluides ont pu précipiter leur U dans les failles au contact avec des lithologies réductrices représentées par des schistes noirs ou des quartzites graphiteux. La datation des oxydes d'uranium issus des gisements suggère qu'un tel scénario a pu se reproduire plusieurs fois dans la région jusqu'à ca. 275 Ma et que la tectonique extensive fragile a dû persister jusqu'au milieu du Permien.

Dans le district de Pontivy, les minéralisations uranifères, localisées dans les leucogranites à proximité de l'encaissant sédimentaires ou d'enclaves micashisteuses, ont rempli des structures fragiles (fentes de tension par exemple) associées à la déformation décrochante le long du CSA. Les datations U-Pb sur les oxydes d'uranium des gisements révèlent que, comme dans le district de Guérande ou de Mortagne (Cathelineau et al., 1990), les minéralisations se mettent principalement en place entre ca. 300 et 270 Ma. Les données géochimiques et radiométriques suggèrent un lessivage d'oxydes d'uranium dans les facies leucogranitiques associés aux gisement et les données en isotopes de l'oxygène de Tartèse et al. (2012) sur les mylonites du CSA suggèrent des circulations de fluides hydrothermaux d'origine météoriques à partir de 300 Ma. En parallèle, les grains d'apatite des leucogranites montrent des

évidences texturales, géochimiques et géochronologiques de circulations de fluides oxydants riches en U au moment de la formation de la minéralisation uranifère. La mise en place du massif leucogranitique de Langonnet vers 305 Ma arrive peu de temps avant la formation des premières minéralisations uranifères et le flux de chaleur fourni par cette intrusion a pu favoriser les mouvements convectifs de fluides.

Au début du Permien, une activité tectonique fragile a persisté le long du CSA et des détachements de la zone sud armoricaine. Ces structures d'échelle crustale ont joué le rôle de conduits pour des fluides oxydants dérivés de la surface capable de lessiver les oxydes d'uranium des leucogranites. Les fluides ont ensuite pu précipiter leur U dans des structures fragiles à proximité ou au contact de lithologies sédimentaires avec un caractère réducteur variable. Les données en traces de fission sur apatite révèlent que les intrusions étaient encore à des températures au-dessus de 120°C et donc à une profondeur de plus de 3-4 km (pour un gradient géothermique élevé de 30°C/km) lors de la formation des gisements. La formation des gisements d'uranium dans le Massif armoricain de ca. 300 à 270 Ma est synchrone des événements minéralisateurs principaux de la chaîne hercynienne européenne. Au permien inférieur, un flux de chaleur anormal dans le manteau, révélé par exemple par la formation du batholithe de Cornwall de l'autre côté de la Manche (Chen et al., 1993) et la mise en place de granites post-orogéniques en Ibérie (e.g. Gutiérrez-Alonso et al., 2011), a pu aider un maintenir à un gradient géothermique élevé dans la croûte facilitant l'infiltration et la convection de fluides météoriques en profondeur.

Un dernier événement minéralisateur ou de remobilisation d'U a eu lieu au Trias vers 220 Ma dans le district de Pontivy. Cette événement hydrothermal, a eu vraisemblablement un impact régional car il est aussi enregistré via les données traces de fission sur apatite sur les granites de Rostrenen et de Lizio et via la datation U-Pb de monazite dans le granite de Guérande. Ces circulations de fluides sont précoces vis-à-vis de la mise en place de dykes de dolérites à l'ouest du Massif armoricain, entre ca. 210 et 195 Ma (Caroff et al., 1995), et de circulations hydrothermales généralisées à l'ensemble du bassin de Paris (~200 Ma ; e.g. Guillaucheau et al., 2000) interprétés comme le reflet des prémices de l'ouverture de l'Atlantique. Les analyses en traces de fission sur apatite indiquent que les granites carbonifères, y compris les leucogranites, s'exhument en sub-surface du Trias au Jurassique. Les données suggèrent que le Massif armoricain n'a pas été significativement enfoui durant le Mésozoïque ou le Cénozoïque.

4. Perspectives

Le travail réalisé sur les leucogranites uranifères du Massif armoricain et leurs gisements associés a permis d'apporter des informations sur le cycle de l'U dans la chaîne hercynienne européenne. Néanmoins cette étude amène de nouvelles questions et des pièces de ce puzzle restent à découvrir :

- *Indentification et caractérisation de la suite granitique dévono-carbonifère :* l'analyse U-Pb des cristaux de zircon hérités des leucogranites et des grains détritiques des sédiments carbonifères inférieurs ont mis en évidence un contribution dévono-carbonifère importante. Peu d'intrusions de cette âge ont été identifiées ou étudiées dans la Massif armoricain. Néanmoins, elles se mettent en place à une époque critique de la formation de la chaîne et leur étude pourrait apporter des informations clés sur la géodynamique de cette époque. Du point de vue métallogénique, leur fusion à la fin du carbonifère semble contribuer à la richesse en U des leucogranites fertiles.
- *Datation des granites métalumineux mis en place le long du cisaillement nord armoricain :* Aucunes données de datation moderne n'existe sur ces granites pourtant ils représentent une part importante du magmatisme tardi-carbonifère.
- *Contraintes expérimentales sur le comportement de l'U lors de la fusion partielle :* Dans cette étude, la fusion d'orthogneiss acides apparait comme un paramètre clé dans la genèse des leucogranites uranifères. La réalisation d'expériences de fusion partielle de sources sédimentaires et métaignées acides permettrait d'obtenir des contraintes sur le partitionnement de l'U entre le liquide et le résidu lors ce processus.
- *Contraintes expérimentales sur la solubilité de l'uraninite dans les liquides silicatés peralumineux :* les données expérimentales sur la solubilité de l'uraninite dans les liquides peralumineux obtenues par Peiffert et al. (2014, 2016) sont peu précises et de nouvelles expériences mériteraient d'être réalisées.
- *Contraintes expérimentales sur la solubilité du Nb et du Ta dans les saumures magmatiques :* Il existe très peu de contraintes expérimentales sur la solubilité du Nb et du Ta dans les fluides (Chevychelov et al., 2005 ; Zaraisky et al., 2014) et la majorité de ces expériences sont réalisées à partir de fluides aqueux peu salés et donc peu représentatifs des conditions magmatiques-hydrothermales. De nouvelles expériences avec des liquides, type saumure, de compositions intermédiaires entre un fluide aqueux et un liquide silicaté (liquide hydrosalin) mériteraient d'être réalisées.
- *Etude pétrographique minutieuse des oxydes d'uranium dans les leucogranites :* dans ce travail nous avons manqué de temps pour rechercher des oxydes d'uranium ou des évidences texturales de leur lessivage dans les leucogranites. Ce travail implique la réalisation de nombreuses lames minces et une étude pétrographique minutieuse.
- *Analyses en isotopes de l'oxygène ponctuelles sur les apatites des leucogranites :* les grains d'apatite des leucogranites de Pontivy montrent des évidences d'interaction avec des fluides oxydants d'origine météorique probable. Le minéral apatite apparait être un minéral très prometteur pour le traçage des circulations de fluides et il pourrait être intéressant de réaliser des analyses en $\delta^{18}O$ sur ces grains pour vérifier l'origine du fluide avec lequel elles ont interagi.

- *Evolution permienne du Massif armoricain.* La datation des oxydes d'uranium des gisements a permis d'apporter indirectement des contraintes sur la tectonique permienne dans le Massif armoricain. Néanmoins, nous ne disposons encore que de très peu d'informations sur cette période et cela car la plupart des bassins qui devaient être présents ont dû être érodés. La thermochronologie par analyses des traces de fission sur zircon (PAZ ~200 – 250 °C) permettrait potentiellement d'apporter de meilleurs contraintes sur la tectonique permienne du Massif armoricain.

Références bibliographiques

André, A.-S., Lespinasse, M., Cathelineaua, M., Boirona, M.-C., Cuneya, M., Leroy, J.L., 1999. Percolation de fluides tardi-hercyniens dans le granité de Saint-Sylvestre (Nord-Ouest du Massif central français) : données des inclusions fluides sur un profil Razès-Saint-Pardoux. Comptes Rendus Académie Sci. - Ser. IIA - Earth Planet. Sci. 329, 23–30. doi:10.1016/S1251-8050(99)80223-7

Annen, C., Sparks, R.S.J., 2002. Effects of repetitive emplacement of basaltic intrusions on thermal evolution and melt generation in the crust. Earth and Planetary Science Letters 203, 937–955. doi:10.1016/S0012-821X(02)00929-9

Alabosi, M., 1984. Les altérations hydrothermales associées aux gisements d'uranium de Ty Gallen, Poulprio et Prat Mérien (massif de Pontivy, Morbihan, France). Thesis INPL (Inst. Natl. Polytech. Lorraine), Nancy. 113 pp.

Ballèvre, M., Catalán, J.R.M., López-Carmona, A., Pitra, P., Abati, J., Fernández, R.D., Ducassou, C., Arenas, R., Bosse, V., Castiñeiras, P., Fernández-Suárez, J., Barreiro, J.G., Paquette, J.-L., Peucat, J.-J., Poujol, M., Ruffet, G., Martínez, S.S., 2014. Correlation of the nappe stack in the Ibero-Armorican arc across the Bay of Biscay: a joint French–Spanish project. Geological Society of London Special Publication 405, 77–113. doi:10.1144/SP405.13

Ballèvre, M., Bosse, V., Dabard, M.-P., Ducassou, C., Fourcade, S., Paquette, J.-L., Peucat, J.-J., Pitra, P., 2013. Histoire Géologique du massif Armoricain : Actualité de la recherche. Bulletin de la Société Géologique et Minéralogique de Bretagne (D), 10-11, 5–96.

Ballèvre, M., Bosse, V., Ducassou, C., Pitra, P., 2009. Palaeozoic history of the Armorican Massif: Models for the tectonic evolution of the suture zones. Comptes Rendus Geoscience 341, 174–201. doi:10.1016/j.crte.2008.11.009

Ballèvre, M., Fourcade, S., Capdevila, R., Peucat, J.-J., Cocherie, A., Fanning, C.M., 2012. Geochronology and geochemistry of Ordovician felsic volcanism in the Southern Armorican Massif (Variscan belt, France): Implications for the breakup of Gondwana. Gondwana Research 21, 1019–1036. doi:10.1016/j.gr.2011.07.030

Ballouard, C., Poujol, M., Boulvais, P., Zeh, A., submitted. Crustal recycling and juvenile addition during lithospheric wrenching: The Pontivy-Rostrenen magmatic complex, Armorican Massif (France), Hercynian Belt. Gondwana Research.

Ballouard, C., Poujol, M., Boulvais, P., Mercadier, J., Tartèse, R., Venneman, T., Deloule, E., Jolivet, M., Kéré, I., Cathelineau, M., Cuney, M., 2017. Magmatic and hydrothermal behavior of uranium in syntectonic leucogranites: The uranium mineralization associated with the Hercynian Guérande granite (Armorican Massif, France). Ore Geol. Rev. 80, 309–331. doi:10.1016/j.oregeorev.2016.06.034

Ballouard, C., Boulvais, P., Poujol, M., Gapais, D., Yamato, P., Tartèse, R., Cuney, M., 2015a. Tectonic record, magmatic history and hydrothermal alteration in the Hercynian Guérande leucogranite, Armorican Massif, France. Lithos 220–223, 1–22. doi:10.1016/j.lithos.2015.01.027

Ballouard, C., Poujol, M., Jolivet, M., Boulvais, P., Tartese, R., Dubois, C., Hallot, E., Dabard, M.-P., Ruffet, G., 2015b. Geochronological and Thermochronological Constraints on the Carboniferous Magmatism from the Armorican Massif: from the source to the exhumation. The Variscan belt: correlations and plate dynamics, Variscan Conference 2015, Rennes (France), 9-11 June 2015.

Barak, S., Klemperer, S.L., 2016. Rapid variation in upper-mantle rheology across the San Andreas fault system and Salton Trough, southernmost California, USA. Geology 44, 575–578. doi:10.1130/G37847.1

Barak, S., Klemperer, S.L., Lawrence, J.F., 2015. San Andreas Fault dip, Peninsular Ranges mafic lower crust and partial melt in the Salton Trough, Southern California, from ambient-noise tomography. Geochemistry, Geophysics, Geosystems 16, 3946–3972. doi:10.1002/2015GC005970

Barbarand, J., Pagel, M., 2001. Cathodoluminescence study of apatite crystals. Am. Mineral. 86, 473–484. doi:10.2138/am-2001-0411

Barbarin, B., 1999. A review of the relationships between granitoid types, their origins and their geodynamic environments. Lithos 46, 605–626. doi:10.1016/S0024-4937(98)00085-1

Barbarin, B., 1996. Genesis of the two main types of peraluminous granitoids. Geology 24, 295–298. doi:10.1130/0091-7613(1996)024<0295:GOTTMT>2.3.CO;2

Bau, M., 1996. Controls on the fractionation of isovalent trace elements in magmatic and aqueous systems: evidence from Y/Ho, Zr/Hf, and lanthanide tetrad effect. Contrib. Mineral. Petrol. 123, 323–333. doi:10.1007/s004100050159

Baxter, S., Feely, M., 2002. Magma mixing and mingling textures in granitoids: examples from the Galway Granite, Connemara, Ireland. Mineralogy and Petrology 76, 63–74. doi:10.1007/s007100200032

Bea, F., Fershtater, G.B., Montero, P., Smirnov, V.N., Molina, J.F., 2005. Deformation-driven differentiation of granitic magma: the Stepninsk pluton of the Uralides, Russia. Lithos 81, 209–233. doi:10.1016/j.lithos.2004.10.004

Bea, F., Pereira, M.D., Corretgé, L.G., Fershtater, G.B., 1994. Differentiation of strongly peraluminous, perphosphorus granites: The pedrobernardo pluton, central Spain. Geochim. Cosmochim. Acta 58, 2609–2627. doi:10.1016/0016-7037(94)90132-5

Béchennec, F., Thiéblemont, D., 2013. Baud, 384. Bureau de Recherches Géologiques et Minières.

Béchennec, F., Thiéblemont, D., Audru, J.C., 2006. Plouay, 348. Bureau de Recherches Géologiques et Minières.

Béchennec, F., Thiéblemont, D., 2009. Bubry, 349. Bureau de Recherches Géologiques et Minières.

Béchennec, F., Hallégouët, B., Thiéblemont, D., 2001. Rosporden, 347. Bureau de Recherches Géologiques et Minières.

Béchennec, F., Hallégouët, B., Thiéblemont, D., 1999. Quimper, 346. Bureau de Recherches Géologiques et Minières.

Béchennec, F., Guennoc, P., Guerrot, C., Lebret, P., Thiéblemont, D., 1996. Concarneau, 382. Bureau de Recherches Géologiques et Minières.

Bernard-Griffiths, J., Peucat, J.J., Sheppard, S., Vidal, P., 1985. Petrogenesis of Hercynian leucogranites from the southern Armorican Massif: contribution of REE and isotopic (Sr, Nd, Pb and O) geochemical data to the study of source rock characteristics and ages. Earth and Planetary Science Letters 74, 235–250. doi:10.1016/0012-821X(85)90024-X

Berthé, D., Choukroune, P., Jegouzo, P., 1979. Orthogneiss, mylonite and non coaxial deformation of granites: the example of the South Armorican Shear Zone. Journal of Structural Geology 1, 31–42. doi:10.1016/0191-8141(79)90019-1

Bessin, P., Guillocheau, F., Robin, C., Schroëtter, J.-M., Bauer, H., 2015. Planation surfaces of the Armorican Massif (western France):Denudation chronology of a Mesozoic land surface twice exhumed in response to relative crustal movements between Iberia and Eurasia. Geomorphology 233, 75–91. doi:10.1016/j.geomorph.2014.09.026

Blichert-Toft, J., Puchtel, I.S., 2010. Depleted mantle sources through time: Evidence from Lu–Hf and Sm–Nd isotope systematics of Archean komatiites. Earth Planet. Sci. Lett. 297, 598–606. doi:10.1016/j.epsl.2010.07.012

Bonhoure, J., Kister, P., Cuney, M., Deloule, E., 2007. Methodology for Rare Earth Element Determinations of Uranium Oxides by Ion Microprobe. Geostand. Geoanalytical Res. 31, 209–225. doi:10.1111/j.1751-908X.2007.00865.x

Bonijoly, D., Perrin, J., Truffert, C., Asfirane, F., 1999. Couverture géophysique aéroportée du Massif armoricain, magnétisme et radiométrie spectrale. Rapport B.R.G.M. R40471 (75 pp.).

Bonin, B., 2004. Do coeval mafic and felsic magmas in post-collisional to within-plate regimes necessarily imply two contrasting, mantle and crustal, sources? A review. Lithos 78, 1–24. doi:10.1016/j.lithos.2004.04.042

Bos, P., Castaing, C., Clément, J.P., Chantraine, J., Lemeille, F., 1997. Rostrenen, 312. Bureau de Recherches Géologiques et Minières.

Bosse, V., Ballevre, M., Vidal, O., 2002. Ductile Thrusting Recorded by the Garnet Isograd from Blueschist-Facies Metapelites of the Ile de Groix, Armorican Massif, France. Journal of Petrology 43, 485–510. doi:10.1093/petrology/43.3.485

Bosse, V., Féraud, G., Ballèvre, M., Peucat, J.-J., Corsini, M., 2005. Rb–Sr and $^{40}Ar/^{39}Ar$ ages in blueschists from the Ile de Groix (Armorican Massif, France): Implications for closure mechanisms in isotopic systems. Chemical Geology 220, 21–45. doi:10.1016/j.chemgeo.2005.02.019

Bossiere, G., 1988. Evolutions chimico-minéralogiques du grenat et de la muscovite au voisinage de l'isograde biotite-staurotide dans un métamorphisme prograde de type barrovien: un exemple en Vendée littorale (Massif Armoricain). Comptes Rendus Académie Sci. Sér. 2 Mécanique Phys. Chim. Sci. Univers Sci. Terre 306, 135–140.

Bouvier, A., Vervoort, J.D., Patchett, P.J., 2008. The Lu–Hf and Sm–Nd isotopic composition of CHUR: Constraints from unequilibrated chondrites and implications for the bulk composition of terrestrial planets. Earth and Planetary Science Letters 273, 48–57. doi:10.1016/j.epsl.2008.06.010

Bouzari, F., Hart, C.J.R., Bissig, T., Barker, S., 2016. Hydrothermal Alteration Revealed by Apatite Luminescence and Chemistry: A Potential Indicator Mineral for Exploring Covered Porphyry Copper Deposits. Econ. Geol. 111, 1397–1410. doi:10.2113/econgeo.111.6.1397

Breiter, K., 2012, Nearly contemporaneous evolution of the A- and S-type fractionated granites in the Krušné hory/Erzgebirge Mts., Central Europe: Lithos 151, 105–121, doi:10.1016/j.lithos.2011.09.022.

Brun, J.-P., Guennoc, P., Truffert, C., Vairon, J., 2001. Cadomian tectonics in northern Brittany: a contribution of 3-D crustal-scale modelling. Tectonophysics 331, 229–246. doi:10.1016/S0040-1951(00)00244-4

Canosa, F., Martin-Izard, A., Fuertes-Fuente, M., 2012, Evolved granitic systems as a source of rare-element deposits: The Ponte Segade case (Galicia, NW Spain): Lithos 153, 165–176, doi:10.1016/j.lithos.2012.06.029

Cao, S., Neubauer, F., 2016. Deep crustal expressions of exhumed strike-slip fault systems: Shear zone initiation on rheological boundaries. Earth-Sci. Rev. 162, 155–176. doi:10.1016/j.earscirev.2016.09.010

Capdevila, R., 2010. Les granites varisques du Massif Armoricain. Bulletin de la Société Géologique et Minéralogique de Bretagne, 7, 1-52.

Carignan, J., Hild, P., Mevelle, G., Morel, J., Yeghicheyan, D., 2001. Routine Analyses of Trace Elements in Geological Samples using Flow Injection and Low Pressure On-Line Liquid Chromatography Coupled to ICP-MS: A Study of Geochemical Reference Materials BR, DR-N, UB-N, AN-G and GH. Geostandards Newsletter 25, 187–198. doi:10.1111/j.1751-908X.2001.tb00595.x

Caroff, M., Labry, C., Le Gall, B., Authemayou, C., Grosjean, D.B., Guillong, M., 2015. Petrogenesis of late-Variscan high-K alkali-calcic granitoids and calc-alkalic lamprophyres: The Aber-Ildut/North-Ouessant complex, Armorican Massif, France. Lithos 238, 140–155. doi:10.1016/j.lithos.2015.09.025

Caroff, M., Bellon, H., Chauris, L., Carron, J.-P., Chevrier, S., Gardinier, A., Cotten, J., Moan, Y.L., Neidhart, Y., 1995. Magmatisme fissural triasico-liasique dans l'ouest du Massif armoricain (France): pétrologie, géochimie, âge, et modalités de la mise en place. Can. J. Earth Sci. 32, 1921–1936. doi:10.1139/e95-147

Carric, G., Chantraine, J., Dadet, P., Flageollet, J.C., Sagon, J.P., Talbot, H. 1980. Montcontour, 279. Bureau de Recherches Géologiques et Minières.

Carron, J.-P., Kerneizon, M.L.G. de, Nachit, H., 1994. Variscan Granites from Brittany, in: Chantraine, J., Rolet, J., Santallier, D.S., Piqué, A., Keppie, J.D. (Eds.), Pre-Mesozoic Geology in France and Related Areas, IGCP-Project 233. Springer Berlin Heidelberg, pp. 231–239.

Castaing, C., 1988. Huelgoat, 276. Bureau de Recherches Géologiques et Minières.

Castro, A., Patiño-Douce, A.E., Corretgé, L.G., Rosa, J.D. de la, El-Biad, M., El-Hmidi, H., 1999. Origin of peraluminous granites and granodiorites, Iberian massif, Spain: an experimental test of granite petrogenesis. Contrib. Mineral. Petrol. 135, 255–276. doi:10.1007/s004100050511

Cathelineau, M., 1982. Les gisements d'uranium liés spatialement aux leucogranites sudarmoricainset à leur encaissant métamorphique: relations et interactions entre les minéralisations et divers contextes géologiques et structuraux. Sciences de la Terre, Mémoires 42. Université de Nancy (375 pp.).

Cathelineau, M., 1981. Les Gisements Uraniferes de la Presqu'ile Guerandaise (Sud Bretagne); Approche Structurale et Metallogenique. Miner. Deposita 16, 227–240. doi:10.1007/BF00202737

Cathelineau, M., Boiron, M.-C., Fourcade, S., Ruffet, G., Clauer, N., Belcourt, O., Coulibaly, Y., Banks, D.A., Guillocheau, F., 2012. A major Late Jurassic fluid event at the basin/basement unconformity in western France: $^{40}Ar/^{39}Ar$ and K–Ar dating, fluid chemistry, and related geodynamic context. Chem. Geol. 322–323, 99–120. doi:10.1016/j.chemgeo.2012.06.008

Cathelineau, M., Boiron, M.C., Holliger, P., Poty, B., 1990. Metallogenesis of the French part of the Variscan orogen. Part II: Time-space relationships between U, Au and Sn-W ore deposition and geodynamic events — mineralogical and U-Pb data. Tectonophysics 177, 59–79. doi:10.1016/0040-1951(90)90274-C

Černý, P., 1991. Precambrian Granitoids Petrogenesis, Geochemistry and Metallogeny Fertile granites of Precambrian rare-element pegmatite fields: is geochemistry controlled by tectonic setting or source lithologies? Precambrian Res. 51, 429–468. doi:10.1016/0301-9268(91)90111-M

Černý, P., 1992. Minerals for Future MaterialsGeochemical and petrogenetic features of mineralization in rare-element granitic pegmatites in the light of current research. Appl. Geochem. 7, 393–416. doi:10.1016/0883-2927(92)90002-K

Chamberlain, K.R., Bowring, S.A., 2000. Apatite–feldspar U–Pb thermochronometer: a reliable, mid-range (~450°C), diffusion-controlled system. Chem. Geol. 172, 173–200. doi:10.1016/S0009-2541(00)00242-4

Chantraine, J., Carric, G., Dadet, P., Flageollet, J.C., Sagon, J.P., Talbo, H., Mulot, B., 1979. Moncontour, 279. Bureau de Recherches Géologiques et Minières.

Chantraine, J., Autran, A., Cavelier, C., 2003. Carte géologique de la France à 1/1 000 000 6ème édition révisée. Bureau de Recherches Géologiques et Minières.

Chappell, B.W., Hine, R., 2006, The Cornubian Batholith: an Example of Magmatic Fractionation on a Crustal Scale: Resource Geology, v. 56, 203–244, doi:10.1111/j.1751-3928.2006.tb00281.x.

Chappell, B.W., White, A.J.R., 1974. Two contrasting granite types. Pacific Geol. 8, 173–174.

Chappell, B.W., White, A.J.R., 1992. I- and S-type granites in the Lachlan Fold Belt. Geol. Soc. Am. Spec. Pap. 272, 1–26. doi:10.1130/SPE272-p1

Chappell, B.W., White, A.J.R., Wyborn, D., 1987. The Importance of Residual Source Material (Restite) in Granite Petrogenesis. Journal of Petrology. 28, 1111–1138. doi:10.1093/petrology/28.6.1111

Chauris, L., 1977. Les associations paragenetiques dans la metallogenie varisque du massif armoricain. Miner. Deposita 12, 353–371. doi:10.1007/BF00206172

Chauris, L., 1984. Accidents linéamentaires et minéralisations uranifères; L'exemple de la ceinture batholitique hercynienne medio-armoricaine (France). Bull. Soc. Geol. Fr. S7–XXVI, 1375–1380. doi:10.2113/gssgfbull.S7-XXVI.6.1375

Chen, Y., Clark, A.H., Farrar, E., Wasteneys, H.A.H.P., Hodgson, M.J., Bromley, A.V., 1993. Diachronous and independent histories of plutonism and mineralization in the Cornubian Batholith, southwest England. J. Geol. Soc. 150, 1183–1191. doi:10.1144/gsjgs.150.6.1183

Cherniak, D.J., Watson, E.B., 2001. Pb diffusion in zircon. Chem. Geol., What are we dating? Understanding the Crystallogernesis of U-Pb 172, 5–24. doi:10.1016/S0009-2541(00)00233-3

Chew, D.M., Petrus, J.A., Kamber, B.S., 2014. U–Pb LA–ICPMS dating using accessory mineral standards with variable common Pb. Chem. Geol. 363, 185–199. doi:10.1016/j.chemgeo.2013.11.006

Chin, E.J., Lee, C.-T.A., Barnes, J.D., 2014. Thickening, refertilization, and the deep lithosphere filter in continental arcs: Constraints from major and trace elements and oxygen isotopes. Earth and Planetary Science Letters 397, 184–200. doi:10.1016/j.epsl.2014.04.022

Claiborne, L.L., Miller, C.F., Walker, B.A., Wooden, J.L., Mazdab, F.K., Bea, F., 2006. Tracking magmatic processes through Zr/Hf ratios in rocks and Hf and Ti zoning in zircons: An example from the Spirit Mountain batholith, Nevada. Mineral. Mag. 70, 517–543. doi:10.1180/0026461067050348

Clauer, N., O'neil, J.R., Furlan, S., 1995. Clay Minerals as Records of Temperature Conditions and Duration of Thermal Anomalies in the Paris Basin, France. Clay Miner. 30, 1–13. doi:10.1180/claymin.1995.030.1.01

Clemens, J.D., Stevens, G., 2015. Comment on "Water-fluxed melting of the continental crust: A review" by R.F. Weinberg and P. Hasalová. Lithos 234–235, 100–101. doi:10.1016/j.lithos.2015.06.032

Clemens, J.D., Stevens, G., 2012. What controls chemical variation in granitic magmas? Lithos 134–135, 317–329. doi:10.1016/j.lithos.2012.01.001

Clemens, J.D., Stevens, G., Farina, F., 2011. The enigmatic sources of I-type granites: The peritectic connexion. Lithos 126, 174–181. doi:10.1016/j.lithos.2011.07.004

Clemens, J., Watkins, J., 2001. The fluid regime of high-temperature metamorphism during granitoid magma genesis. Contrib. Mineral. Petrol. 140, 600–606. doi:10.1007/s004100000205

Cochrane, R., Spikings, R.A., Chew, D., Wotzlaw, J.-F., Chiaradia, M., Tyrrell, S., Schaltegger, U., Van der Lelij, R., 2014. High temperature (>350 °C) thermochronology and mechanisms of Pb loss in apatite. Geochim. Cosmochim. Acta 127, 39–56. doi:10.1016/j.gca.2013.11.028

Conrad, W.K., Nicholls, I.A., Wall, V.J., 1988. Water-Saturated and -Undersaturated Melting of Metaluminous and Peraluminous Crustal Compositions at 10 kb: Evidence for the Origin of Silicic Magmas in the Taupo Volcanic Zone, New Zealand, and Other Occurrences. Journal of Petrology. 29, 765–803. doi:10.1093/petrology/29.4.765

Cosca, M., Stunitz, H., Bourgeix, A.-L., Lee, J.P., 2011. 40Ar∗ loss in experimentally deformed muscovite and biotite with implications for 40Ar/39Ar geochronology of naturally deformed rocks. Geochimica et Cosmochimica Acta 75, 7759–7778. doi:10.1016/j.gca.2011.10.012

Cotten, J., 1975. Etude des mégacristaux du granite de Rostrenen (Massif Armoricain) [Ph.D. thesis] : Université de Bretagne Occidentale, Brest.

Couzinié, S., Moyen, J.-F., Villaros, A., Paquette, J.-L., Scarrow, J.H., Marignac, C., 2014. Temporal relationships between Mg-K mafic magmatism and catastrophic melting of the Variscan crust in the southern part of Velay Complex (Massif Central, France). Journal of Geosciences 59, 69–86. doi:10.3190/jgeosci.155

Cuney, M., 2014. Felsic magmatism and uranium deposits. Bull. Soc. Geol. Fr. 185, 75–92. doi:10.2113/gssgfbull.185.2.75

Cuney, M., 2009. The extreme diversity of uranium deposits. Miner. Deposita 44, 3–9. doi:10.1007/s00126-008-0223-1

Cuney, M., 2006. Excursion « granites varisques et minéralisations uranifères ». L'exemple des masssifs de Ploumanac'h et de Pontivy. Partie II: Métallogenèse de l'uranium. Séminaire AREVA-BUM-DEX. (54 pp.).

Cuney, M., Kyser, T. K., 2008. Recent and not-so-recent developments in uranium deposits and implications for exploration. Mineral. Assoc. Canada, Short Course Series, 39, 257 p.

Cuney, M., Friedrich, M., Blumenfeld, P., Bourguignon, A., Boiron, M.C., Vigneresse, J.L., Poty, B., 1990. Metallogenesis in the French part of the Variscan orogen. Part I: U preconcentrations in pre-Variscan and Variscan formations — a comparison with Sn, W and Au. Tectonophysics 177, 39–57. doi:10.1016/0040-1951(90)90273-B

Dabard, M.P., Peucat, J.J., 2001. Les métasédiments de Bretagne sud. Rapport BRGM.

Dabard, M.P., Loi, A., Peucat, J.J., 1996. Zircon typology combined with Sm-Nd whole-rock isotope analysis to study Brioverian sediments from the Armorican Massif. Sedimentary Geology 101, 243–260. doi:10.1016/0037-0738(95)00068-2

Dabard, M. P., 1997. Les Formations à cherts carbonés (phtanites) de la chaîne cadomienne; genèse et signification géodynamique; exemple du segment Armoricain. Documents du BRGM. 267 (248 pp.).

Dadet, P., Bos, P., Chantraine, J., Laville, P., Sagon, J.P., 1988. Pontivy, 313. Bureau de Recherches Géologiques et Minières.

Davies, J.H., von Blanckenburg, F., 1995. Slab breakoff: A model of lithosphere detachment and its test in the magmatism and deformation of collisional orogens. Earth Planet. Sci. Lett. 129, 85–102. doi:10.1016/0012-821X(94)00237-S

Debon, F., Le Fort, P., 1988. A cationic classification of common plutonic rocks and their magmatic associations: principles, method, applications. Bulletin de Minéralogie 111 (5), 493–510.

Deveaud, S., Gumiaux, C., Gloaguen, E., Branquet, Y., 2013. Spatial statistical analysis applied to rare-element LCT-type pegmatite fields: an original approach to constrain faults-pegmatites-granites relationships. J. Geosci. 163–182. doi:10.3190/jgeosci.141

Deveaud, S., Millot, R., Villaros, A., 2015. The genesis of LCT-type granitic pegmatites, as illustrated by lithium isotopes in micas. Chem. Geol. 411, 97–111. doi:10.1016/j.chemgeo.2015.06.029

De Saint Blanquat, M., Tikoff, B., Teyssier, C., Vigneresse, J.L., 1998. Transpressional kinematics and magmatic arcs. Geological Society of London Special Publication 135, 327–340. doi:10.1144/GSL.SP.1998.135.01.21

DÍaz-Alvarado, J., Castro, A., Fernández, C., Moreno-Ventas, I., 2011. Assessing Bulk Assimilation in Cordierite-bearing Granitoids from the Central System Batholith, Spain; Experimental, Geochemical and Geochronological Constraints. Journal of Petrology 52, 223–256. doi:10.1093/petrology/egq078

Dill, H.G., Škoda, R., Weber, B., Berner, Z.A., Müller, A., Bakker, R.J., 2012. A Newly Discovered Swarm of Shear-Zone-Hosted Bi–As–Fe–Mg–P-Rich Aplites and Pegmatites in the Hagendorf–Pleystein Pegmatite Province, Southeastern Germany: A Step Closer to the Metamorphic Root of Pegmatites. Can. Mineral. 50, 943–974. doi:10.3749/canmin.50.4.943

Dill, H.G., 1983. Vein-andmetasedimentary-hosted carbonaceous matter and phosphorus from NE Bavaria (FR Germany) and their implication on syngenetic and epigenetic uranium concentration. Neues Jb. Mineral. Abh. 148, 1–21.

D'lemos, R.S., Brown, M., Strachan, R.A., 1992. Granite magma generation, ascent and emplacement within a transpressional orogen. Journal of the Geological Society 149, 487–490. doi:10.1144/gsjgs.149.4.0487

Dokuz, A., Uysal, İ., Dilek, Y., Karsli, O., Meisel, T., Kandemir, R., 2015. Geochemistry, Re–Os isotopes and highly siderophile element abundances in the Eastern Pontide peridotites (NE Turkey): Multiple episodes of melt extraction–depletion, melt–rock interaction and fertilization of the Rheic Ocean mantle. Gondwana Research 27, 612–628. doi:10.1016/j.gr.2013.12.010

Dolníček, Z., René, M., Hermannová, S., Prochaska, W., 2013. Origin of the Okrouhlá Radouň episyenite-hosted uranium deposit, Bohemian Massif, Czech Republic: fluid inclusion and stable isotope constraints. Miner. Deposita 49, 409–425. doi:10.1007/s00126-013-0500-5

Dostal, J., Chatterjee, A.K., 1995, Origin of topaz-bearing and related peraluminous granites of the Late Devonian Davis Lake pluton, Nova Scotia, Canada: crystal versus fluid fractionation: Chemical Geology, v. 123, 67–88, doi:10.1016/0009-2541(95)00047-P.

Dostal, J., Kontak, D.J., Gerel, O., Gregory Shellnutt, J., Fayek, M., 2015. Cretaceous ongonites (topaz-bearing albite-rich microleucogranites) from Ongon Khairkhan, Central Mongolia: Products of extreme magmatic fractionation and pervasive metasomatic fluid: rock interaction: Lithos, v. 236–237, 173–189. doi:10.1016/j.lithos.2015.08.003.

Dubessy, J., Ramboz, C., Nguyen Trung, C., Cathelineau, M., Charoy, B., Cuney, M., Leroy, J., Poty, B., Weisbrod, A., 1987. Physical and chemical control (pO_2, T, pH) of the opposite behaviour of U and Sn-W as exemplified by hydrothermal deposits in France and Great Britain, and solubility data. Bull. Minér. 262–281.

Dubois, C., 2014. Durée de construction, refroidissement et exhumation de l'intrusion composite de Ploumanac'h (Massif Armoricain) : contraintes géochronologiques et thermochronologiques. Rapport de Master 2 : Université de Rennes 1, 31p.

Ducassou, C., Poujol, M., Ruffet, G., Bruguier, O., Ballèvre, M., 2014. Relief variation and erosion of the Variscan belt: detrital geochronology of the Palaeozoic sediments from the Mauges Unit (Armorican Massif, France). Geol. Soc. Lond. Spec. Publ. 405, 137–167. doi:10.1144/SP405.6

Dunkl, I., 2002. Trackkey: a Windows program for calculation and graphical presentation of fission track data. Computers & Geosciences, 28, 3-12.

Euzen, T., 1993. Pétrogenèse des granites de collision post-épaississement. Le cas des granites crustaux et mantelliques du complexe de Pontivy-Rostrenen (Massif Armoricain, France). Memoires Géosciences Rennes 51 (360 pp.).

Euzen, T., Capdevila, R., 1991. Origine des enclaves microgrenues acides dans le granite peralumineux de Pontivy (Massif Armoricain, France). Comptes Rendus de l'Académie des Sciences, Paris, Série II 313, 413–420.

Evensen, N.M., Hamilton, P.J., O'Nions, R.K., 1978. Rare-earth abundances in chondritic meteorites. Geochimica et Cosmochimica Acta 42, 1199–1212. doi:10.1016/0016-7037(78)90114-X

Farina, F., Stevens, G., Gerdes, A., Frei, D., 2014. Small-scale Hf isotopic variability in the Peninsula pluton (South Africa): the processes that control inheritance of source 176. Contribution to Mineralogy and Petrology 168, 1–18. doi:10.1007/s00410-014-1065-8

Farina, F., Stevens, G., 2011. Source controlled $^{87}Sr/^{86}Sr$ isotope variability in granitic magmas: The inevitable consequence of mineral-scale isotopic disequilibrium in the protolith. Lithos 122, 189–200. doi:10.1016/j.lithos.2011.01.001

Farina, F., Stevens, G., Villaros, A., 2012, Multi-batch, incremental assembly of a dynamic magma chamber: the case of the Peninsula pluton granite (Cape Granite Suite, South Africa): Mineralogy and Petrology, v. 106, 193–216, doi:10.1007/s00710-012-0224-8.

Fernández-Suárez, J., Dunning, G.R., Jenner, G.A., Gutiérrez-Alonso, G., 2000. Variscan collisional magmatism and deformation in NW Iberia: constraints from U–Pb geochronology of granitoids. J. Geol. Soc. 157, 565–576. doi:10.1144/jgs.157.3.565

Fernández-Suárez, J., Gutierrez-Alonso, G., Johnston, S.T., Jeffries, T.E., Pastor-Galán, D., Jenner, G.A., Murphy, J.B., 2011. Iberian late-Variscan granitoids: Some considerations on crustal sources and the significance of "mantle extraction ages." Lithos 123, 121–132. doi:10.1016/j.lithos.2010.09.010

Förster, H.-J., Tischendorf, G., Trumbull, R.B., Gottesmann, B., 1999. Late-Collisional Granites in the Variscan Erzgebirge, Germany. Journal of Petrology 40, 1613–1645. doi:10.1093/petroj/40.11.1613

Friedrich, M., Cuney, M., Poty, B., 1987. Uranium geochemistry in peraluminous leucogranites. Uranium 3, 353–385.

Gaafar, I., 2015. Application of gamma ray spectrometric measurements and VLF-EM data for tracing vein type uranium mineralization, El-Sela area, South Eastern Desert, Egypt. NRIAG J. Astron. Geophys. 4, 266–282. doi:10.1016/j.nrjag.2015.10.001

Gaafar, I., Cuney, M., Gawad, A.A., 2014. Mineral Chemistry of Two-Mica Granite Rare Metals: Impact of Geophysics on the Distribution of Uranium Mineralization at El Sela Shear Zone, Egypt. Open J. Geol. 4, 137–160. doi:10.4236/ojg.2014.44011

Galbraith, R.F., Laslett, G.M., 1993. Statistical models for mixed fission track ages. Nucl. Tracks Radiat. Meas. 21, 459–470. doi:10.1016/1359-0189(93)90185-C

Gallagher, K., 2012. Transdimensional inverse thermal history modeling for quantitative thermochronology. J. Geophys. Res. Solid Earth 117, B02408. doi:10.1029/2011JB008825

Gallagher, K., Charvin, K., Nielsen, S., Sambridge, M., Stephenson, J., 2009. Markov chain Monte Carlo (MCMC) sampling methods to determine optimal models, model resolution and model choice for Earth Science problems. Mar. Pet. Geol., Thematic Set on Basin Modeling Perspectives 26, 525–535. doi:10.1016/j.marpetgeo.2009.01.003

Gapais, D., Brun, J.-P., Gumiaux, C., Cagnard, F., Ruffet, G., Le Carlier De Veslud, C., 2015. Extensional tectonics in the Hercynian Armorican belt (France). An overview. Bulletin de la Société Géologique de France 186, 117–129. doi:10.2113/gssgfbull.186.2-3.117

Gapais, D., Lagarde, J.L., Le Corre, C., Audren, C., Jegouzo, P., Casas Sainz, A., Van Den Driessche, J., 1993. La zone de cisaillement de Quiberon: témoin d'extension de la chaine varisque en Bretagne méridionale au Carbonifère. Comptes Rendus de l'Académie des Sciences, Paris, série II 316, 1123–1129.

Gapais, D., 1989. Shear structures within deformed granites: Mechanical and thermal indicators. Geology 17, 1144–1147. doi:10.1130/0091-7613(1989)017<1144:SSWDGM>2.3.CO;2

Gapais, D., Le Corre, C., 1980. Is the Hercynien belt of Brittany a major shear zone? Nature 288, 574–576. doi:10.1038/288574a0

Georget, Y., 1986, Nature et origine des granites peralumineux à cordiérite et des roches associées. Exemples des granitoides du Massif Armoricain (France): Pétrologie et géochimie [Ph.D. thesis] : Université Rennes 1, 298p.

Gardien, V., Lardeaux, J.-M., Ledru, P., Allemand, P., Guillot, S., 1997. Metamorphism during late orogenic extension; insights from the French Variscan belt. Bulletin de la Société Géologique de France 168, 271–286.

Gébelin, A., Roger, F., Brunel, M., 2009. Syntectonic crustal melting and high-grade metamorphism in a transpressional regime, Variscan Massif Central, France. Tectonophysics, 477, 229–243. doi:10.1016/j.tecto.2009.03.022

Gerdes, A., Zeh, A., 2006. Combined U–Pb and Hf isotope LA-(MC-)ICP-MS analyses of detrital zircons: Comparison with SHRIMP and new constraints for the provenance and age of an Armorican metasediment in Central Germany. Earth and Planetary Science Letters 249, 47–61. doi:10.1016/j.epsl.2006.06.039

Gerdes, A., Zeh, A., 2009. Zircon formation versus zircon alteration — New insights from combined U–Pb and Lu–Hf in-situ LA-ICP-MS analyses, and consequences for the interpretation of Archean zircon from the Central Zone of the Limpopo Belt. Chemical Geology, Accessory minerals as tracers of crustal processes 261, 230–243. doi:10.1016/j.chemgeo.2008.03.005

Gilder, S.A., Leloup, P.H., Courtillot, V., Chen, Y., Coe, R.S., Zhao, X., Xiao, W., Halim, N., Cogné, J.-P., Zhu, R., 1999. Tectonic evolution of the Tancheng-Lujiang (Tan-Lu) fault via Middle Triassic to Early Cenozoic paleomagnetic data. Journal of Geophysical Research, Solid Earth 104, 15365–15390. doi:10.1029/1999JB900123

Glazner, A.F., 2007. Thermal limitations on incorporation of wall rock into magma. Geology 35, 319–322. doi:10.1130/G23134A.1

Gloaguen, E., 2006, Apports d'une étude intégrée sur les relations entre granites et minéralisations filoniennes (Au et Sn-W) en contexte tardiorogénique (Chaîne Hercynienne, Galice centrale, Espagne) [Ph.D. thesis] : Université d'Orléans, 574p.

Goldschmidt, V.M., 1937. The principles of distribution of chemical elements in minerals and rocks. The seventh Hugo Müller Lecture, delivered before the Chemical Society on March 17th, 1937. J. Chem. Soc. Resumed 655–673. doi:10.1039/JR9370000655

Gordon Medaris Jr., L., Ackerman, L., Jelínek, E., Michels, Z.D., Erban, V., Kotková, J., 2015. Depletion, cryptic metasomatism, and modal metasomatism (refertilization) of Variscan lithospheric mantle: Evidence from major elements, trace elements, and Sr-Nd-Os isotopes in a Saxothuringian garnet peridotite. Lithos 226, 81–97. doi:10.1016/j.lithos.2014.10.007

Green, P.F., 1985. Comparison of zeta calibration baselines for fission-track dating of apatite, zircon and sphene. Chem. Geol. Isot. Geosci. Sect. 58, 1–22. doi:10.1016/0168-9622(85)90023-5

Guillocheau, F., Robin, C., Allemand, P., Bourquin, S., Brault, N., Dromart, G., Friedenberg, R., Garcia, J.-P., Gaulier, J.-M., Gaumet, F., Grosdoy, B., Hanot, F., Strat, P.L., Mettraux, M., Nalpas, T., Prijac, C., Rigoltet, C., Serrano, O., Grandjean, G., 2000. Meso-Cenozoic geodynamic evolution of the Paris Basin: 3D stratigraphic constraints. Geodin. Acta 13, 189–245. doi:10.1080/09853111.2000.11105372

Gumiaux, C., Gapais, D., Brun, J.P., Chantraine, J., Ruffet, G., 2004a. Tectonic history of the Hercynian Armorican Shear belt (Brittany, France). Geodinamica Acta 17, 289–307. doi:10.3166/ga.17.289-307

Gumiaux, C., Judenherc, S., Brun, J.-P., Gapais, D., Granet, M., Poupinet, G., 2004b. Restoration of lithosphere-scale wrenching from integrated structural and tomographic data (Hercynian belt of western France). Geology 32, 333–336. doi:10.1130/G20134.2

Gutiérrez-Alonso, G., Fernández-Suárez, J., Jeffries, T.E., Johnston, S.T., Pastor-Galán, D., Murphy, J.B., Franco, M.P., Gonzalo, J.C., 2011. Diachronous post-orogenic magmatism within a developing orocline in Iberia, European Variscides. Tectonics 30, TC5008. doi:10.1029/2010TC002845

Hagemann, S.G., Groves, D.I., Ridley, J.R., Vearncombe, J.R., 1992. The Archean lode gold deposits at Wiluna, Western Australia; high-level brittle-style mineralization in a strike-slip regime. Econ. Geol. 87, 1022–1053. doi:10.2113/gsecongeo.87.4.1022

Hanmer, S.K., Corre, C.L., Berthé, D., 1982. The role of Hercynian granites in the deformation and metamorphism of Brioverian and Palaeozoic rocks of Central Brittany. J. Geol. Soc. 139, 85–93. doi:10.1144/gsjgs.139.1.0085

Hans Wedepohl, K., 1995. The composition of the continental crust. Geochimica et Cosmochimica Acta 59, 1217–1232. doi:10.1016/0016-7037(95)00038-2

Harrison, T.M., Célérier, J., Aikman, A.B., Hermann, J., Heizler, M.T., 2009. Diffusion of ^{40}Ar in muscovite. Geochim. Cosmochim. Acta 73, 1039–1051. doi:10.1016/j.gca.2008.09.038

Harlov, D.E., 2015. Apatite: A Fingerprint for Metasomatic Processes. Elements 11, 171–176. doi:10.2113/gselements.11.3.171

Healy, B., Collins, W.J., Richards, S.W., 2004. A hybrid origin for Lachlan S-type granites: the Murrumbidgee Batholith example. Lithos 78, 197–216. doi:10.1016/j.lithos.2004.04.047

Hecht, L., Vigneresse, J.L., Morteani, G., 1997, Constraints on the origin of zonation of the granite complexes in the Fichtelgebirge (Germany and Czech Republic): evidence from a gravity and geochemical study: Geol. Rundsch, v. 86, S93–S109, doi:10.1007/PL00014669.

Henley, R.W., Adams, D.P.M., 1992. Strike-slip fault reactivation as a control on epithermal vein-style gold mineralization. Geology 20, 443–446. doi:10.1130/0091-7613(1992)020<0443:SSFRAA>2.3.CO;2

Hofmann, B., Eikenberg, J., 1991. The Krunkelbach uranium deposit, Schwarzwald, Germany; correlation of radiometric ages (U-Pb, U-Xe-Kr, K-Ar, ^{230}Th- ^{234}U). Econ. Geol. 86, 1031–1049. doi:10.2113/gsecongeo.86.5.1031

Hofmann, A.W., 1988. Chemical differentiation of the Earth: the relationship between mantle, continental crust, and oceanic crust. Earth Planet. Sci. Lett. 90, 297–314. doi:10.1016/0012-821X(88)90132-X

Houseman, G.A., McKenzie, D.P., Molnar, P., 1981. Convective instability of a thickened boundary layer and its relevance for the thermal evolution of continental convergent belts. Journal of Geophysical Research Solid Earth 86, 6115–6132. doi:10.1029/JB086iB07p06115

Huang, X.L., Wang, R.C., Chen, X.M., Hu, H., Liu, C.S., 2002. Vertical Variations in the Mineralogy of the Yichun Topaz–Lepidolite Granite, Jiangxi Province, Southern China. Can. Mineral. 40, 1047–1068. doi:10.2113/gscanmin.40.4.1047

Hurford, A.J., 1990. Standardization of fission track dating calibration: Recommendation by the Fission Track Working Group of the I.U.G.S. Subcommission on Geochronology. Chem. Geol. Isot. Geosci. Sect. 80, 171–178. doi:10.1016/0168-9622(90)90025-8

Hurford, A.J., Green, P.F., 1983. The zeta age calibration of fission-track dating.Chem. Geol. 41, 285–317. doi:10.1016/S0009-2541(83)80026-6

Huppert, H.E., Sparks, R.S.J., 1988. The Generation of Granitic Magmas by Intrusion of Basalt into Continental Crust. Journal of Petrology 29, 599–624. doi:10.1093/petrology/29.3.599

Hutton, D.H.W., 1988. Granite emplacement mechanisms and tectonic controls: inferences from deformation studies. Earth and Environemental Science Transaction of the Royal Society Edinburg 79, 245–255. doi:10.1017/S0263593300014255

Hutton, D.H.W., Reavy, R.J., 1992. Strike-slip tectonics and granite petrogenesis. Tectonics 11, 960–967. doi:10.1029/92TC00336

Huw Davies, J., von Blanckenburg, F., 1995. Slab breakoff: A model of lithosphere detachment and its test in the magmatism and deformation of collisional orogens. Earth and Planetary Science Letters 129, 85–102. doi:10.1016/0012-821X(94)00237-S

International Atomic Energy Agency (IAEA), 2009. UDEPO – World Distribution of Uranium Deposits.

IRSN, 2004. Inventaire national des sites miniers d'uranium. Institut de Radioprotection et de Sureté Nucléaire.

Jackson, S.E., Pearson, N.J., Griffin, W.L., Belousova, E.A., 2004. The application of laser ablation-inductively coupled plasma-mass spectrometry to in situ U–Pb zircon geochronology. Chem. Geol. 211, 47–69. doi:10.1016/j.chemgeo.2004.06.017

Jaguin, J., 2012, Datation et caractérisation de processus minéralisateurs à l'Archéen : Application à l'Antimony Line, Ceinture de Roches Vertes de Murchison, Afrique du Sud [Ph.D. thesis] : Université Rennes 1, 350p.

Jahns, R.H., Burnham, C.W., 1969. Experimental studies of pegmatite genesis; l, A model for the derivation and crystallization of granitic pegmatites. Econ. Geol. 64, 843–864. doi:10.2113/gsecongeo.64.8.843

Janoušek, V., Holub, F.V., 2007. The causal link between HP-HT metamorphism and ultrapotassic magmatism in collisional orogens: case study from the Moldanubian Zone of the Bohemian Massif. Proceeding of the Geologist Association 118, 75–86. doi:10.1016/S0016-7878(07)80049-6

Jébrak, M., Marcoux, É., 2008. Géologie des Ressources Minérales. Ministère des ressources naturelles et de la faune. 667 pp.

Jégouzo, P., Rossello, E. A., 1988. La Branche Nord du Cisaillement Sud-Armoricain (France): un essai d'évaluation du déplacement par l'analyse des mylonites. Comptes rendus de l'Académie des sciences. Série II 307(17), 1825-1831.

Jégouzo, P., 1980. The South Armorican Shear Zone. Journal of Structural Geology 2, 39–47. doi:10.1016/0191-8141(80)90032-2

Johnson, T.E., Hudson, N.F.C., Droop, G.T.R., 2001. Partial melting in the Inzie Head gneisses: the role of water and a petrogenetic grid in KFMASH applicable to anatectic pelitic migmatites. J. Metamorph. Geol. 19, 99–118. doi:10.1046/j.0263-4929.2000.00292.x

Jolivet, M., Dominguez, S., Charreau, J., Chen, Y., Li, Yongan, Wang, Qingchen, 2010. Mesozoic and Cenozoic tectonic history of the Central Chinese Tian Shan: reactivated tectonic structures and active deformation. Tectonics, 29, TC6019, doi:10.1029/2010TC002712.

Jolivet, J., Bienfait, G., Vigneresse, J.L., Cuney, M., 1989. Heat flow and heat production in Brittany (Western France). Tectonophysics 159, 61–72. doi:10.1016/0040-1951(89)90170-4

Jones, K.A., Brown, M., 1990. High-temperature "clockwise"P-T paths and melting in the development of regional migmatites: an example from southern Brittany, France. Journal of Metamorphic Geology 8, 551–578. doi:10.1111/j.1525-1314.1990.tb00486.x

Judenherc, S., Granet, M., Brun, J.-P., Poupinet, G., 2003. The Hercynian collision in the Armorican Massif: evidence of different lithospheric domains inferred from seismic tomography and anisotropy. Bull. Société Géologique Fr. 174, 45–57.

Judenherc, S., Granet, M., Brun, J.-P., Poupinet, G., Plomerová, J., Mocquet, A., Achauer, U., 2002. Images of lithospheric heterogeneities in the Armorican segment of the Hercynian Range in France. Tectonophysics, Structure of the continental lithosphere and upper mantle 358, 121–134. doi:10.1016/S0040-1951(02)00420-1

Ketcham, R.A., Carter, A., Donelick, R.A., Barbarand, J., Hurford, A.J., 2007. Improved modeling of fission-track annealing in apatite. Am. Mineral. 92, 799–810. doi:10.2138/am.2007.2281

Kontak, D.J., Creaser, R.A., Heaman, L.M., Archibald, D.A., 2005. U-Pb tantalite, Re-Os molybdenite, and ^{40}Ar/^{39}Ar muscovite dating of the Brazil Lake Pegmatite, Nova Scotia; a possible shear-zone related origin for an LCT-type pegmatite. Atl. Geol. 41, 17–29.

Kretz, R., 1983. Symbols for rock-forming minerals. American Mineralogist 68, 277–279.

Kříbek, B., Žák, K., Dobeš, P., Leichmann, J., Pudilová, M., René, M., Scharm, B., Scharmová, M., Hájek, A., Holeczy, D., Hein, U.F., Lehmann, B., 2008. The Rožná uranium deposit (Bohemian Massif, Czech Republic): shear zone-hosted, late Variscan and post-Variscan hydrothermal mineralization. Miner. Deposita 44, 99–128. doi:10.1007/s00126-008-0188-0

Lach, P., Mercadier, J., Dubessy, J., Boiron, M.-C., Cuney, M., 2013. In Situ Quantitative Measurement of Rare Earth Elements in Uranium Oxides by Laser Ablation-Inductively Coupled Plasma-Mass Spectrometry. Geostand. Geoanalytical Res. 37, 277–296. doi:10.1111/j.1751-908X.2012.00161.x

Laumonier, M., Scaillet, B., Arbaret, L., Andújar, J., Champallier, R., 2015. Experimental mixing of hydrous magmas. Chemical Geology 418, 158–170. doi:10.1016/j.chemgeo.2015.10.031

Laumonier, M., Scaillet, B., Pichavant, M., Champallier, R., Andujar, J., Arbaret, L., 2014. On the conditions of magma mixing and its bearing on andesite production in the crust. Nat. Commun. 5, 5607. doi:10.1038/ncomms6607

Laurent, O., Zeh, A., 2015. A linear Hf isotope-age array despite different granitoid sources and complex Archean geodynamics: Example from the Pietersburg block (South Africa). Earth and Planetary Science Letters 430, 326–338. doi:10.1016/j.epsl.2015.08.028.

Leake, B.E., 1978. Nomenclature of amphiboles. Canadian Mineralogist 16, 501–520.

Leloup, P.H., Ricard, Y., Battaglia, J., Lacassin, R., 1999. Shear heating in continental strike-slip shear zones:model and field examples. Geophysical Journal International 136, 19–40. doi:10.1046/j.1365-246X.1999.00683.x

Le Fort, P., Cuney, M., Deniel, C., France-Lanord, C., Sheppard, S.M.F., Upreti, B.N., Vidal, P., 1987. Deep Seated Processes in Collision Zones Crustal generation of the Himalayan leucogranites. Tectonophysics 134, 39–57. doi:10.1016/0040-1951(87)90248-4

Le Gall, B., Authemayou, C., Ehrhold, A., Paquette, J.L., Bussien, D., Chazot, G., Aouizerat, A., Pastol, Y., 2014. LiDAR offshore structural mapping and U/Pb zircon/monazite dating of Variscan strain in the Leon metamorphic domain, NW Brittany. Tectonophysics 630, 236–250. doi:10.1016/j.tecto.2014.05.026

Le Hébel, F., 2002. Déformation continentale et histoire des fluides au cours d'un cycle subduction, exhumation, extension. Exemple des porphyroïdes Sud-Armoricains 1 [Ph.D. thesis] : Université de Rennes 1, 218 p.

Le Hébel, F., Vidal, O., Kienast, J.-R., Gapais, D., 2002. Les « Porphyroïdes » de Bretagne méridionale : une unité de HP–BT dans la chaîne hercynienne. Comptes Rendus Geoscience 334, 205–211. doi:10.1016/S1631-0713(02)01746-7

Lemarchand, J., Boulvais, P., Gaboriau, M., Boiron, M.-C., Tartèse, R., Cokkinos, M., Bonnet, S., Jégouzo, P., 2012. Giant quartz vein formation and high-elevation meteoric fluid infiltration into the South Armorican Shear Zone: geological, fluid inclusion and stable isotope evidence. J. Geol. Soc. 169, 17–27. doi:10.1144/0016-76492010-186

Li, J., Zhou, M., Li, X., Fu, Z., Li, Z., 2002. Structural control on uranium mineralization in South China: Implications for fluid flow in continental strike-slip faults. Sci. China Ser. Earth Sci. 45, 851–864. doi:10.1007/BF02879519

Li, J.-W., Zhou, M.-F., Li, X.-F., Fu, Z.-R., Li, Z.-J., 2001. The Hunan-Jiangxi strike-slip fault system in southern China: southern termination of the Tan-Lu fault. J. Geodyn. 32, 333–354. doi:10.1016/S0264-3707(01)00033-3

Liew, T.C., Hofmann, A.W., 1988. Precambrian crustal components, plutonic associations, plate environment of the Hercynian Fold Belt of central Europe: indications from a Nd and Sr isotopic study. Contributions to Mineralogy and Petrology 98, 129–138.

Linnen, R.L., Keppler, H., 1997. Columbite solubility in granitic melts: consequences for the enrichment and fractionation of Nb and Ta in the Earth's crust. Contrib. Mineral. Petrol. 128, 213–227. doi:10.1007/s004100050304

Linnen, R.L., Keppler, H., 2002. Melt composition control of Zr/Hf fractionation in magmatic processes. Geochim. Cosmochim. Acta 66, 3293–3301. doi:10.1016/S0016-7037(02)00924-9

Linnen, R. L., Cuney, M., 2005. Granite-related rare-element deposits and experimental constraints on Ta-Nb-W-Sn-Zr-Hf mineralization, in Linnen RL and Samson IM, eds., rare-element geochemistry and mineral deposits. In Geological Association of Canada, GAC, Short Course

London, D., 2005. Granitic pegmatites: an assessment of current concepts and directions for the future. Lithos, Granitic SystemsIlmari Haapala VolumeSymposium "Granitic Systems –State of the Art and Future Avenues" 80, 281–303. doi:10.1016/j.lithos.2004.02.009

London, D., 1990. Internal differentiation of rare-element pegmatites; A synthesis of recent research. Geol. Soc. Am. Spec. Pap. 246, 35–50. doi:10.1130/SPE246-p35

London, D., 1987. Internal differentiation of rare-element pegmatites: Effects of boron, phosphorus, and fluorine. Geochim. Cosmochim. Acta 51, 403–420. doi:10.1016/0016-7037(87)90058-5

London, D., Morgan, G.B., 2012. The Pegmatite Puzzle. Elements 8, 263–268. doi:10.2113/gselements.8.4.263

Longerich, H.P., Jackson, S.E., Günther, D., 1996. Inter-laboratory note. Laser ablation inductively coupled plasma mass spectrometric transient signal data acquisition and analyte concentration calculation. J. Anal. At. Spectrom. 11, 899–904. doi:10.1039/JA9961100899

Ludwig, K.R., 2001. Isoplot/Ex Version 2.49. A Geochronological Toolkit for Microsoft Excel. Berkeley Geochronology Center, Special Publication vol. 1a, pp. 1–55.

MacDonald, M.A., Home, R.J., Corey, M.C., Ham, L.J., 1992, An overview of recent bedrock mapping and follow-up petrological studies of the South Mountain Batholith, southwestern Nova Scotia, Canada: Atlantic Geology, v. 28.

Marchildon, N., Brown, M., 2003. Spatial distribution of melt-bearing structures in anatectic rocks from Southern Brittany, France: implications for melt transfer at grain- to orogen-scale. Tectonophysics 364, 215–235. doi:10.1016/S0040-1951(03)00061-1

Marcoux, E., 1982. Etude géologique et métallogénique du district plombo-zincifère de Pontivy (Massif armoricain, France) : Relations avec les pragenèses stannifères et uranifères. Bulletin du BRGM (2), section II, n°1, 1-24.

Martin, H., 1994. The Archean Grey Gneisses and the Genesis of Continental Crust, in: Condie, K.C. (Ed.), Developments in Precambrian Geology, Archean Crustal Evolution. Elsevier, pp. 205–259.

Matteini, M., Pavanetto, P., Dabard, M.P., Hauser, N., Loi, A., Funedda, A., 2014 U–Pb ages and Hf isotopes on detrital zircons from Neoproterozoic sediments from the Armorican Massif (NW France): western Gondwana as possible source. 9th South American Symposium on Isotope Geology (SSAGI). 6–9 April 2014, Sao Paulo (Brazil) (2014), p. 216

Marignac, C., Cuney, M., 1999. Ore deposits of the French Massif Central: insight into the metallogenesis of the Variscan collision belt. Miner. Deposita 34, 472–504. doi:10.1007/s001260050216

McDowell, F.W., McIntosh, W.C., Farley, K.A., 2005. A precise ^{40}Ar–^{39}Ar reference age for the Durango apatite (U–Th)/He and fission-track dating standard. Chem. Geol. 214, 249–263. doi:10.1016/j.chemgeo.2004.10.002

Mercadier, J., Cuney, M., Cathelineau, M., Lacorde, M., 2010. U redox fronts and kaolinisation in basement-hosted unconformity-related U ores of the Athabasca Basin (Canada): late U remobilisation by meteoric fluids. Miner. Deposita 46, 105–135. doi:10.1007/s00126-010-0314-7

Michard, A., Gurriet, P., Soudant, M., Albarede, F., 1985. Nd isotopes in French Phanerozoic shales: external vs. internal aspects of crustal evolution. Geochimica et Cosmochimica Acta 49, 601–610. doi:10.1016/0016-7037(85)90051-1

Miles, A.J., Graham, C.M., Hawkesworth, C.J., Gillespie, M.R., Hinton, R.W., Bromiley, G.D., 2014. Apatite: A new redox proxy for silicic magmas? Geochim. Cosmochim. Acta 132, 101–119. doi:10.1016/j.gca.2014.01.040

Miller, C.F., Stoddard, E.F., Bradfish, L.J., Dollase, W.A., 1981. Composition of plutonic muscovite; genetic implications. Canadian Mineralogist 19, 25–34.

Montel, J.-M., 1993. Geochemistry of Accessory Minerals A model for monazite/melt equilibrium and application to the generation of granitic magmas. Chem. Geol. 110, 127–146. doi:10.1016/0009-2541(93)90250-M

Montel, J.-M., Vielzeuf, D., 1997. Partial melting of metagreywackes, Part II. Compositions of minerals and melts. Contrib. Mineral. Petrol. 128, 176–196. doi:10.1007/s004100050302

Montenat, C., Bessonnat, G., Roy, C., 2006. Manifestations précoces du rift de Biscaye au Lias inférieur sur la marge Sud-Armoricaine (Talmont-Saint-Hilaire, Vendée, Ouest France). Comptes Rendus Geosci. 338, 272–279. doi:10.1016/j.crte.2006.01.002

Morfin, S., Sawyer, E.W., Bandyayera, D., 2014. The geochemical signature of a felsic injection complex in the continental crust: Opinaca Subprovince, Quebec. Lithos 196–197, 339–355. doi:10.1016/j.lithos.2014.03.004

Molina, J.F., Montero, P., Bea, F., Scarrow, J.H., 2012. Anomalous xenocryst dispersion during tonalite–granodiorite crystal mush hybridization in the mid crust: Mineralogical and geochemical evidence from Variscan appinites (Avila Batholith, Central Iberia). Lithos 153, 224–242. doi:10.1016/j.lithos.2012.03.021

Molnar, P., Houseman, G.A., 2004. The effects of buoyant crust on the gravitational instability of thickened mantle lithosphere at zones of intracontinental convergence. Geophysical Journal International 158, 1134–1150. doi:10.1111/j.1365-246X.2004.02312.x

Morfin, S., Sawyer, E.W., Bandyayera, D., 2014. The geochemical signature of a felsic injection complex in the continental crust: Opinaca Subprovince, Quebec. Lithos 196–197, 339–355. doi:10.1016/j.lithos.2014.03.004

Moyen, J.-F., Laurent, O., Chelle-Michou, C., Couzinié, S., Vanderhaeghe, O., Zeh, A., Villaros, A., Gardien, V., in press. Collision vs. subduction-related magmatism: two contrasting ways of granite formation and implications for crustal growth. Lithos. doi:10.1016/j.lithos.2016.09.018

Mueller, A.G., Harris, L.B., Lungan, A., 1988. Structural control of greenstone-hosted Gold mineralization by transcurrent shearing: A new interpretation of the Kalgoorlie mining district, Western Australia. Ore Geol. Rev. 3, 359–387. doi:10.1016/0169-1368(88)90027-3

Müller, A., Seltmann, R., Halls, C., Siebel, W., Dulski, P., Jeffries, T., Spratt, J., Kronz, A., 2006, The magmatic evolution of the Land's End pluton, Cornwall, and associated pre-enrichment of metals: Ore Geology Reviews, v. 28, 329–367.

Nachit, H., Razafimahefa, N., Stussi, J.-M., Carron, J.-P., 1985. Composition chimique des biotites et typologie magmatique des granitoïdes. Comptes Rendus de l'Académie des Sciences, Paris Série II 301, 813–818.

Neiva, A.M.R., 2002, Portuguese granites associated with Sn-W and Au mineralizations: Bulletin of the Geological Society of Finland, v. 74, Parts 1–2, 79–101.

Nex, P.A.M., Kinnaird, J.A., Oliver, G.J.H., 2001. Petrology, geochemistry and uranium mineralisation of post-collisional magmatism around Goanikontes, southern Central Zone, Damaran Orogen, Namibia. J. Afr. Earth Sci., African Renaissance and Geosciences 33, 481–502. doi:10.1016/S0899-5362(01)00096-3

Norris, R.J., Cooper, A.F., 2000. Late Quaternary slip rates and slip partitioning on the Alpine Fault, New Zealand. Journal of Structural Geology 23, 507–520. doi:10.1016/S0191-8141(00)00122-X

Patiño-Douce, A.E., 1999. What do experiments tell us about the relative contributions of crust and mantle to the origin of granitic magmas? Geological Society of London Special Publication 168, 55–75. doi:10.1144/GSL.SP.1999.168.01.05

Patiño-Douce, A.E., 1997. Generation of metaluminous A-type granites by low-pressure melting of calc-alkaline granitoids. Geology 25, 743–746. doi:10.1130/0091-7613(1997)025<0743:GOMATG>2.3.CO;2

Patiño-Douce, A.E., Beard, J.S., 1995. Dehydration-melting of Biotite Gneiss and Quartz Amphibolite from 3 to 15 kbar. Journal of Petrology 36, 707–738. doi:10.1093/petrology/36.3.707

Patiño-Douce, A.E., Harris, N., 1998. Experimental Constraints on Himalayan Anatexis. Journal of Petrology 39, 689–710. doi:10.1093/petroj/39.4.689

Patiño-Douce, A.E., Johnston, A.D., 1991. Phase equilibria and melt productivity in the pelitic system: implications for the origin of peraluminous granitoids and aluminous granulites. Contribution to Mineralogy and Petrology 107, 202–218. doi:10.1007/BF00310707

Paton, C., Hellstrom, J., Paul, B., Woodhead, J., Hergt, J., 2011. Iolite: Freeware for the visualisation and processing of mass spectrometric data. J. Anal. At. Spectrom. 26, 2508–2518. doi:10.1039/C1JA10172B

Pearce, N.J.G., Perkins, W.T., Westgate, J.A., Gorton, M.P., Jackson, S.E., Neal, C.R., Chenery, S.P., 1997. A Compilation of New and Published Major and Trace Element Data for NIST SRM 610 and NIST SRM 612 Glass Reference Materials. Geostand. Newsl. 21, 115–144. doi:10.1111/j.1751-908X.1997.tb00538.x

Peiffert, C., Cuney, M., Nguyen-Trung, C., 1994. Uranium in granitic magmas: Part 1. Experimental determination of uranium solubility and fluid-melt partition coefficients in the uranium oxide-haplogranite-H_2O-Na_2CO_3 system at 720–770°C, 2 kbar. Geochim. Cosmochim. Acta 58, 2495–2507. doi:10.1016/0016-7037(94)90026-4

Peiffert, C., Nguyen-Trung, C., Cuney, M., 1996. Uranium in granitic magmas: Part 2. Experimental determination of uranium solubility and fluid-melt partition coefficients in the uranium oxide-haplogranite-H_2O-NaX (X = Cl, F) system at 770°C, 2 kbar. Geochim. Cosmochim. Acta 60, 1515–1529. doi:10.1016/0016-7037(96)00039-7

Pérez Del Villar, L., Moro, C., 1991. Las mineralizaciones intragraníticas de Uranio en el batolito de Cabeza de Ar aya (provincia de Cáceres): El Saguazal, Brechas NNE y La Zafrilla. Stud. Geol. Salmant. 27.

Petford, N., Gallagher, K., 2001. Partial melting of mafic (amphibolitic) lower crust by periodic influx of basaltic magma. Earth and Planetary Science Letters 193, 483–499. doi:10.1016/S0012-821X(01)00481-2

Peucat, J. J., Charlot, R., Mifdal, A., Chantraine, J., Autran, A. (1979). Définition géochronologique de la phase bretonne en Bretagne centrale. Etude Rb/Sr de granites du domaine centre armoricain. Bulletin du BRGM, 1(4), 349-356.

Peucat, J.-J., Auvray, B., Hirbec, Y., Calvez, J.-Y., 1984. Granites et cisaillements hercyniens dans le Nord du Massif Armoricain; geochronologie Rb-Sr. Bulletin de la Société Géologique de France S7–XXVI, 1365–1373. doi:10.2113/gssgfbull.S7-XXVI.6.1365

Pichavant, M., Kontak, D.J., Herrera, J.V., Clark, A.H., 1988a. The Miocene-Pliocene Macusani Volcanics, SE Peru. I. Mineralogy and magmatic evolution of a two-mica aluminisilicate-bearing ignimbrite suite. Contrib. Mineral. Petrol. 100, 300–324. doi:10.1007/BF00379741

Pichavant, M., Kontak, D.J., Briqueu, L., Herrera, J.V., Clark, A.H., 1988b. The Miocene-Pliocene Macusani Volcanics, SE Peru. II. Geochemistry and origin of a felsic peraluminous magma. Contrib. Mineral. Petrol. 100, 325–338. doi:10.1007/BF00379742

Pirajno, F., 2010. Intracontinental strike-slip faults, associated magmatism, mineral systems and mantle dynamics: examples from NW China and Altay-Sayan (Siberia). Journal of Geodynamic 50, 325–346. doi:10.1016/j.jog.2010.01.018

Pirajno, F., 2013. Effects of Metasomatism on Mineral Systems and Their Host Rocks: Alkali Metasomatism, Skarns, Greisens, Tourmalinites, Rodingites, Black-Wall Alteration and Listvenites, in: Metasomatism and the Chemical Transformation of Rock, Lecture Notes in Earth System Sciences. Springer Berlin Heidelberg, pp. 203–251.

Pitra, P., Boulvais, P., Antonoff, V., Diot, H., 2008.Wagnerite in a cordierite–gedrite gneiss: witness of long-term fluid-rock interaction in the continental crust (Ile d'Yeu, Armorican Massif, France). American Mineralogist 93, 315–326.

Pochon, A., Poujol, M., Eric, G., Branquet, Y., Cagnard, F., Gumiaux, C., Gapais, D., 2016. U-Pb LA-ICP-MS dating of apatite in mafic rocks: evidence for a major magmatic event at the Devonian-Carboniferous boundary in the Armorican Massif (France). American Mineralogist 101, 2430-2442. doi: 10.2138/am-2016-5844

Raimbault, L., Cuney, M., Azencott, C., Duthou, J.-L., Joron, J.L., 1995, Geochemical evidence for a multistage magmatic genesis of Ta-Sn-Li mineralization in the granite at Beauvoir, French Massif Central: Economic Geology, v. 90, 548–576. doi:10.2113/gsecongeo.90.3.548.

Ramirez, J.A., Grundvig, S., 2000. Causes of geochemical diversity in peraluminous granitic plutons: the Jálama pluton, Central-Iberian Zone (Spain and Portugal). Lithos 50, 171–190. doi:10.1016/S0024-4937(99)00047-X

Robb, L., 2005. Introduction to ore forming processes, Blackwell Publishing, 373 p.

Rocchi, S., Storti, F., Vincenzo, G.D., Rossetti, F., 2003. Intraplate strike-slip tectonics as an alternative to mantle plume activity for the Cenozoic rift magmatism in the Ross Sea region, Antarctica. Geol. Soc. Lond. Spec. Publ. 210, 145–158. doi:10.1144/GSL.SP.2003.210.01.09

Rolin, P., Cartannaz, C., Henry, P., Rossy, M., Cocherie, A., Salen, F., Delwaulle, B., Mauroux, B., 2006, Notice explicative, Carte géologique de la France, échelle : 1/50 000, feuille Saint-Sulpice-les-Champs (666), Orléans : BRGM, 178 p.

Rollinson, H.R., 1993. Using Geochemical Data: Evaluation, Presentation, Interpretation. Longman Scientific & Technical

Romer, R.L., Kroner, U., 2014. Sediment and weathering control on the distribution of Paleozoic magmatic tin–tungsten mineralization. Miner. Deposita 50, 327–338. doi:10.1007/s00126-014-0540-5

Rudnick, R., Gao, S., 2005. Composition of the continental crust, in Holland, H.D., and Turekian, K.K., eds., Treatise on Geochemistry: Amsterdam, Elsevier 3, 1–64.

Sawyer, E.W., 1998. Formation and Evolution of Granite Magmas During Crustal Reworking: the Significance of Diatexites. J. Petrol. 39, 1147–1167. doi:10.1093/petroj/39.6.1147

Scaillet, S., Cuney, M., le Carlier de Veslud, C., Cheilletz, A., Royer, J.J., 1996. Cooling pattern and mineralization history of the Saint Sylvestre and western Marche leucogranite pluton, French Massif Central: II. Thermal modelling and implications for the mechanisms of uranium mineralization. Geochim. Cosmochim. Acta 60, 4673–4688. doi:10.1016/S0016-7037(96)00292-X

Scarrow, J.H., Molina, J.F., Bea, F., Montero, P., 2009. Within-plate calc-alkaline rocks: Insights from alkaline mafic magma–peraluminous crustal melt hybrid appinites of the Central Iberian Variscan continental collision. Lithos 110, 50–64. doi:10.1016/j.lithos.2008.12.007

Schoene, B., Bowring, S.A., 2006. U–Pb systematics of the McClure Mountain syenite: thermochronological constraints on the age of the $^{40}Ar/^{39}Ar$ standard MMhb. Contrib. Mineral. Petrol. 151, 615. doi:10.1007/s00410-006-0077-4

Schwartz, M.O., Surjono, 1990. Greisenization and albitization at the Tikus tin-tungsten deposit, Belitung, Indonesia. Econ. Geol. 85, 691–713. doi:10.2113/gsecongeo.85.4.691

Seward, D., Spikings, R., Viola, G., Kounov, A., Ruiz, G.M.H., Naeser, N., 2000. Etch times and operator variation for spontaneous track lengths measurements in apatites: an intra-laboratory check. OnTrack 10, 16–21.

Shand, S., 1943. Eruptive Rocks. Their genesis, composition, classification, and their relations to ore-deposits 2. Wiley, New York, p. 444.

Scherer, E., Münker, C., Mezger, K., 2001. Calibration of the Lutetium-Hafnium Clock. Science 293, 683–687. doi:10.1126/science.1061372

Shaw, D.., 1968. A review of K-Rb fractionation trends by covariance analysis. Geochimica et Cosmochimica Acta 32, 573–601. doi:10.1016/0016-7037(68)90050-1

Sibson, R.H., 1990. Conditions for fault-valve behaviour. Geol. Soc. Lond. Spec. Publ. 54, 15–28. doi:10.1144/GSL.SP.1990.054.01.02

Sibson, R.H., 1987. Earthquake rupturing as a mineralizing agent in hydrothermal systems. Geology 15, 701–704. doi:10.1130/0091-7613(1987)15<701:ERAAMA>2.0.CO;2

Siddall, R., 1993. Thermotectonic evolution of the continental margins of the Bay of Biscay: application of apatite fission track analysis. PhD thesis (unpubl.), University of London.

Sláma, J., Košler, J., Condon, D.J., Crowley, J.L., Gerdes, A., Hanchar, J.M., Horstwood, M.S.A., Morris, G.A., Nasdala, L., Norberg, N., Schaltegger, U., Schoene, B., Tubrett, M.N., Whitehouse, M.J., 2008. Plešovice zircon — A new natural reference material for U–Pb and Hf isotopic microanalysis. Chem. Geol. 249, 1–35. doi:10.1016/j.chemgeo.2007.11.005

Sobel, E. R., and D. Seward (2010), Influence of etching conditions on apatite fission track etch pit diameter, Chem. Geol., 271, 59–69, doi:10.1016/j. chemgeo.2009.12.012.

Söderlund, U., Patchett, P.J., Vervoort, J.D., Isachsen, C.E., 2004. The 176Lu decay constant determined by Lu–Hf and U–Pb isotope systematics of Precambrian mafic intrusions.). Earth and Planetary Science Letters 219, 311–324. doi:10.1016/S0012-821X(04)00012-3

Solgadi, F., Moyen, J.-F., Vanderhaeghe, O., Sawyer, E.W., Reisberg, L., 2007. The Role of Crustal Anatexis and Mantle-Derived Magmas in the Genesis of Synorogenic Hercynian Granites of the Livradois Area, French Massif Central. Can. Mineral. 45, 581–606. doi:10.2113/gscanmin.45.3.581

Spicer, E.M., Stevens, G., Buick, I.S., 2004. The low-pressure partial-melting behaviour of natural boron-bearing metapelites from the Mt. Stafford area, central Australia. Contribution to Mineralogy and Petrology 148, 160–179. doi:10.1007/s00410-004-0577-z

Stacey, J.S., Kramers, J.D., 1975. Approximation of terrestrial lead isotope evolution by a two-stage model. Earth Planet. Sci. Lett. 26, 207–221. doi:10.1016/0012-821X(75)90088-6

Štemprok, M., Pivec, E., & Langrová, A., 2005, The petrogenesis of a wolframite-bearing greisen in the Vykmanov granite stock, Western Krušné hory pluton (Czech Republic): Bulletin of Geosciences, v. 80(3), 163-184.

Stepanov, A., Mavrogenes, J.A., Meffre, S., Davidson, P., 2014. The key role of mica during igneous concentration of tantalum. Contrib. Mineral. Petrol. 167, 1–8. doi:10.1007/s00410-014-1009-3

Stevens, G., Villaros, A., Moyen, J.-F., 2007. Selective peritectic garnet entrainment as the origin of geochemical diversity in S-type granites. Geology 35, 9–12. doi:10.1130/G22959A.1

Storti, F., Holdsworth, R.E., Salvini, F., 2003. Intraplate strike-slip deformation belts. Geol. Soc. Lond. Spec. Publ. 210, 1–14. doi:10.1144/GSL.SP.2003.210.01.01

Strong, D.F., 1988. A review and model for granite related mineral deposits. In Taylor R.P. and Strong D.F. (eds), Recent Advances in the Geology of Granite-related Mineral Deposits. Canadian Institute of Mining Metallurgy, Special Volume 39, 424–45.

Strong, D.F., Hanmer, S.K., 1981. The leucogranites of southern Brittany; origin by faulting, frictional heating, fluid flux and fractional melting. Canadian Mineralogist 19, 163–176.

Sylvester, A.G., 1988. Strike-slip faults. Geological Society America Bulletin 100, 1666–1703. doi:10.1130/0016-7606(1988)100<1666:SSF>2.3.CO;2

Tabaud, A.-S., Janousek, V., Skrzypek, E., Schulmann, K., Rossi, P., Whitechurch, H., Guerrot, C., Paquette, J.-L., 2015. Chronology, petrogenesis and heat sources for successive Carboniferous magmatic events in the Southern-Central Variscan Vosges Mts (NE France). J. Geol. Soc. 172, 87–102. doi:10.1144/jgs2013-123

Tagami, T., 1987. Determination of zeta calibration constant for fission track dating. Int. J. Radiat. Appl. Instrum. Part Nucl. Tracks Radiat. Meas. 13, 127–130. doi:10.1016/1359-0189(87)90023-9

Talavera, C., Montero, P., Martínez Poyatos, D., Williams, I.S., 2012. Ediacaran to Lower Ordovician age for rocks ascribed to the Schist-Graywacke Complex (Iberian Massif, Spain): evidence from detrital zircon SHRIMP U–Pb geochronology. Gondwana Res 22, 928–942

Tartèse, R., Boulvais, P., Poujol, M., Gloaguen, E., Cuney, M., 2013. Uranium Mobilization from the Variscan Questembert Syntectonic Granite During Fluid-Rock Interaction at Depth. Econ. Geol. 108, 379–386. doi:10.2113/econgeo.108.2.379

Tartèse, R., Boulvais, P., Poujol, M., Chevalier, T., Paquette, J.-L., Ireland, T.R., Deloule, E., 2012. Mylonites of the South Armorican Shear Zone: Insights for crustal-scale fluid flow and water–rock interaction processes. Journal of Geodynamics 56–57, 86–107. doi:10.1016/j.jog.2011.05.003

Tartèse, R., Poujol, M., Ruffet, G., Boulvais, P., Yamato, P., Košler, J., 2011a. New U-Pb zircon and $^{40}Ar/^{39}Ar$ muscovite age constraints on the emplacement of the Lizio syn-tectonic granite (Armorican Massif, France). Comptes Rendus Geoscience 343, 443–453. doi:10.1016/j.crte.2011.07.005

Tartèse, R., Ruffet, G., Poujol, M., Boulvais, P., Ireland, T.R., 2011b. Simultaneous resetting of the muscovite K-Ar and monazite U-Pb geochronometers: a story of fluids. Terra Nova 23, 390–398. doi:10.1111/j.1365-3121.2011.01024.x

Tartèse, R., Boulvais, P., 2010. Differentiation of peraluminous leucogranites “en route” to the surface. Lithos 114, 353–368. doi:10.1016/j.lithos.2009.09.011

Taylor, S.R., McLennan, S.M., 1985. The continental crust: its composition and evolution. Blackwell, Oxford, 312 pp.

Thomas, R., Davidson, P., 2012. Water in granite and pegmatite-forming melts. Ore Geol. Rev. 46, 32–46. doi:10.1016/j.oregeorev.2012.02.006

Thomas, R., Davidson, P., Beurlen, H., 2012. The competing models for the origin and internal evolution of granitic pegmatites in the light of melt and fluid inclusion research. Mineral. Petrol. 106, 55–73. doi:10.1007/s00710-012-0212-z

Thomson, S.N., Gehrels, G.E., Ruiz, J., Buchwaldt, R., 2012. Routine low-damage apatite U-Pb dating using laser ablation–multicollector–ICPMS. Geochem. Geophys. Geosystems 13, Q0AA21. doi:10.1029/2011GC003928

Trautmann, F., Carn, A., 1997. La Guerche-De-Bretagne, 354. Bureau de Recherches Géologiques et Minières.

Triboulet, C., Audren, C., 1988. Controls on P–T–t deformation path from amphibole zonation during progressive metamorphism of basic rocks (estuary of the River Vilaine, South Brittany, France). J. Metamorph. Geol. 6, 117–133. doi:10.1111/j.1525-1314.1988.tb00412.x

Turpin, L., Cuney, M., Friedrich, M., Bouchez, J.-L., Aubertin, M., 1990a. Meta-igneous origin of Hercynian peraluminous granites in N.W. French Massif Central: implications for crustal history reconstructions. Contrib. Mineral. Petrol. 104, 163–172. doi:10.1007/BF00306440

Turpin, L., Leroy, J.L., Sheppard, S.M.F., 1990b. Isotopic systematics (O, H, C, Sr, Nd) of superimposed barren and U-bearing hydrothermal systems in a Hercynian granite, Massif Central, France. Chem. Geol. 88, 85–98. doi:10.1016/0009-2541(90)90105-G

Turpin, L., Velde, D., Pinte, G., 1988. Geochemical comparison between minettes and kersantites from the Western European Hercynian orogen: trace element and Pb-Sr-Nd isotope constraints on their origin. Earth Planet. Sci. Lett. 87, 73–86. doi:10.1016/0012-821X(88)90065-9

Turrillot, P., Augier, R., Faure, M., 2009. The top-to-the-southeast Sarzeau shear zone and its place in the late-orogenic extensional tectonics of southern Armorica. Bulletin de la Société Géologique de France 180, 247–261. doi:10.2113/gssgfbull.180.3.247

Uysal, I., Ersoy, E.Y., Dilek, Y., Escayola, M., Sarıfakıoğlu, E., Saka, S., Hirata, T., 2015. Depletion and refertilization of the Tethyan oceanic upper mantle as revealed by the early Jurassic Refahiye ophiolite, NE Anatolia—Turkey. Gondwana Research 27, 594–611. doi:10.1016/j.gr.2013.09.008

Van de Zedde, D.M.A., Wortel, M.J.R., 2001. Shallow slab detachment as a transient source of heat at midlithospheric depths. Tectonics 20, 868–882. doi:10.1029/2001TC900018

Vanderhaeghe, O., Teyssier, C., 2001. Crustal-scale rheological transitions during late-orogenic collapse. Tectonophysics 335, 211–228. doi:10.1016/S0040-1951(01)00053-1

Vanderhaeghe, O., Duchêne, S., 2010. Crustal-scale mass transfer, geotherm and topography at convergent plate boundaries. Terra Nova 22, 315–323. doi:10.1111/j.1365-3121.2010.00952.x

Vauchez, A., Tommasi, A., 2003. Wrench faults down to the asthenosphere: geological and geophysical evidence and thermomechanical effects. Geological Society of London Special Publication 210, 15–34. doi:10.1144/GSL.SP.2003.210.01.02

Vernon, R.H., 1990. Crystallization and hybridism in microgranitoid enclave magmas: Microstructural evidence. Journal of Geophysical Research, Solid Earth 95, 17849–17859. doi:10.1029/JB095iB11p17849

Vermeesch, P., 2012. On the visualisation of detrital age distributions. Chemical Geology, v.312-313, 190-194, doi: 10.1016/j.chemgeo.2012.04.021 0.

Vernhet, Y., Plaine, J., Trautmann, F., Pivette, B. 2009. Cossé-Le-Vivien 355. Bureau de Recherches Géologiques et Minières.

Vielzeuf, D., Montel, J.M., 1994. Partial melting of metagreywackes. Part I. Fluid-absent experiments and phase relationships. Contrib. Mineral. Petrol. 117, 375–393. doi:10.1007/BF00307272

Vielzeuf, D., Holloway, J.R., 1988. Experimental determination of the fluid-absent melting relations in the pelitic system. Contribution to Mineralogy and Petrology 98, 257–276. doi:10.1007/BF00375178

Vigneresse, J.L., 1999. Intrusion level of granitic massifs along the Hercynian belt: balancing the eroded crust. Tectonophysics 307, 277–295. doi:10.1016/S0040-1951(99)00104-3

Vigneresse, J.L., Cuney, M., Jolivet, J., Bienfait, G., 1989. Selective heat-producing element enrichment in a crustal segment of the mid-European Variscan chain. Tectonophysics 159, 47–60. doi:10.1016/0040-1951(89)90169-8

Vigneresse, J.-L., Brun, J.-P., 1983. Les leucogranites armoricains marqueurs de la déformation régionale; apport de la gravimetrie. Bulletin de la société géologique de France 7, 357–366. doi:10.2113/gssgfbull.S7-XXV.3.357

Villaros, A., Buick, I.S., Stevens, G., 2011. Isotopic variations in S-type granites: an inheritance from a heterogeneous source? Contribution to Mineralogy and Petrology 163, 243–257. doi:10.1007/s00410-011-0673-9

Villaros, A., Stevens, G., Moyen, J.-F., Buick, I.S., 2009. The trace element compositions of S-type granites: evidence for disequilibrium melting and accessory phase entrainment in the source. Contribution to Mineralogy and Petrology 158, 543–561. doi:10.1007/s00410-009-0396-3

Wan, B., Xiao, W., Zhang, L., Han, C., 2012. Iron mineralization associated with a major strike–slip shear zone: Radiometric and oxygen isotope evidence from the Mengku deposit, NW China. Ore Geol. Rev. 44, 136–147. doi:10.1016/j.oregeorev.2011.09.011

Wang, Y., Fan, W., Sun, M., Liang, X., Zhang, Y., Peng, T., 2007, Geochronological, geochemical and geothermal constraints on petrogenesis of the Indosinian peraluminous granites in the South China Block: A case study in the Hunan Province: Lithos, v. 96, 475–502, doi:10.1016/j.lithos.2006.11.010.

Watson, E.B., Harrison, T.M., 1983. Zircon saturation revisited: temperature and composition effects in a variety of crustal magma types. Earth Planet. Sci. Lett. 64, 295–304. doi:10.1016/0012-821X(83)90211-X

Weil, A., Gutiérrez-alonso, G., Conan, J., 2010. New time constraints on lithospheric-scale oroclinal bending of the Ibero-Armorican Arc: a palaeomagnetic study of earliest Permian rocks from Iberia. Journal of the Geological Society 167, 127–143. doi:10.1144/0016-76492009-002

Weinberg, R.F., Hasalová, P., 2015a. Water-fluxed melting of the continental crust: A review. Lithos 212–215, 158–188. doi:10.1016/j.lithos.2014.08.021

Weinberg, R.F., Hasalová, P., 2015b. Reply to comment by J.D. Clemens and G. Stevens on "Water-fluxed melting of the continental crust: A review." Lithos 234–235, 102–103. doi:10.1016/j.lithos.2015.08.002

Wiedenbeck, M., Allé, P., Corfu, F., Griffin, W.l., Meier, M., Oberli, F., Quadt, A.V., Roddick, J.C., Spiegel, W., 1995. Three natural zircon standards for U–Th–Pb, Lu–Hf, trace element and REE analyses. Geostandards Newsletter 19, 1–23.

Woodhead, J.D., Hergt, J.M., 2005. A Preliminary Appraisal of Seven Natural Zircon Reference Materials for In Situ Hf Isotope Determination. Geostandards and Geoanalytical Research 29, 183–195. doi:10.1111/j.1751-908X.2005.tb00891.x

Xie, L., Wang, R.-C., Che, X.-D., Huang, F.-F., Erdmann, S., Zhang, W.-L., 2016. Tracking magmatic and hydrothermal Nb–Ta–W–Sn fractionation using mineral textures and composition: A case study from the late Cretaceous Jiepailing ore district in the Nanling Range in South China. Ore Geol. Rev. 78, 300–321. doi:10.1016/j.oregeorev.2016.04.003

Xu, B., Jiang, S.-Y., Wang, R., Ma, L., Zhao, K., Yan, X., 2015, Late Cretaceous granites from the giant Dulong Sn-polymetallic ore district in Yunnan Province, South China: Geochronology, geochemistry, mineral chemistry and Nd–Hf isotopic compositions: Lithos, v. 218–219, 54–72. doi:10.1016/j.lithos.2015.01.004.

Yamato, P., Duretz, T., May, D.A., Tartèse, R., 2015. Quantifying magma segregation in dykes. Tectonophysics 660, 132–147. doi:10.1016/j.tecto.2015.08.030

Yoshikawa, M., Kawamoto, T., Shibata, T., Yamamoto, J., 2010. Geochemical and Sr-Nd isotopic characteristics and pressure-temperature estimates of mantle xenoliths from the French Massif Central: evidence for melting and multiple metasomatism by silicate-rich carbonatite and asthenospheric melts. Geological Society of London Special Publication 337, 153–175. doi:10.1144/SP337.8

Zaraisky, G.P., Aksyuk, A.M., Devyatova, V.N., Udoratina, O.V., Chevychelov, V.Y., 2009, The Zr/Hf ratio as a fractionation indicator of rare-metal granites: Petrology, v. 17, 25–45, doi:10.1134/S0869591109010020.

Zeh, A., Gerdes, A., Klemd, R., Barton, J.M., 2007. Archaean to Proterozoic Crustal Evolution in the Central Zone of the Limpopo Belt (South Africa–Botswana): Constraints from Combined U–Pb and Lu–Hf Isotope Analyses of Zircon. Journal of Petrology 48, 1605–1639. doi:10.1093/petrology/egm032

Zeh, A., Gerdes, A., Barton Jr., J., Klemd, R., 2010. U–Th–Pb and Lu–Hf systematics of zircon from TTG's, leucosomes, meta-anorthosites and quartzites of the Limpopo Belt (South Africa): Constraints for the formation, recycling and metamorphism of Palaeoarchaean crust. Precambrian Research 179, 50–68. doi:10.1016/j.precamres.2010.02.012

Zengqian, H., Hongwen, M., Zaw, K., Yuquan, Z., Mingjie, W., Zeng, W., Guitang, P., Renli, T., 2003. The Himalayan Yulong Porphyry Copper Belt: Product of Large-Scale Strike-Slip Faulting in Eastern Tibet. Econ. Geol. 98, 125–145. doi:10.2113/gsecongeo.98.1.125

Zheng, Y.F., 1993a. Calculation of oxygen isotope fractionation in anhydrous silicate minerals. Geochim. Cosmochim. Acta 57, 1079–1091. doi:10.1016/0016-7037(93)90042-U

Zheng, Y.F., 1993b. Calculation of oxygen isotope fractionation in hydroxyl-bearing silicates. Earth Planet. Sci. Lett. 120, 247–263. doi:10.1016/0012-821X(93)90243-3

Zhong, Y., Wang, L., Zhao, J., Liu, L., Ma, C., Zheng, J., Zhang, Z., Luo, B., 2016. Partial melting of an ancient sub-continental lithospheric mantle in the early Paleozoic intracontinental regime and its contribution to petrogenesis of the coeval peraluminous granites in South China. Lithos 264, 224–238. doi:10.1016/j.lithos.2016.08.026

Zhu, Z.-Y., Wang, R.-C., Che, X.-D., Zhu, J.-C., Wei, X.-L., Huang, X. 'e, 2015. Magmatic–hydrothermal rare-element mineralization in the Songshugang granite (northeastern Jiangxi, China): Insights from an electron-microprobe study of Nb–Ta–Zr minerals. Ore Geol. Rev., Applications of Modern Analytical Techniques in the Study of Mineral Deposits 65, Part 4, 749–760. doi:10.1016/j.oregeorev.2014.07.021

Zirner, A.L.K., Marks, M.A.W., Wenzel, T., Jacob, D.E., Markl, G., 2015. Rare earth elements in apatite as a monitor of magmatic and metasomatic processes: The Ilímaussaq complex, South Greenland. Lithos 228–229, 12–22. doi:10.1016/j.lithos.2015.04.013

Annexes

Datations U-Pb sur zircon et monazite article # 2

LA-ICP-MS data for zircon from sample GUE-3, GUE-5 and GUE-8. Data in bold reprsent the analyses used for the calculation of the mean $^{206}Pb/^{238}U$ age for GUE 3 and the concordia ages for GUE-5 and GUE-8.

	Isotope ratios							Ages (Ma)						Content (ppm)		
Zircon	$^{207}Pb/^{235}U$	1 σ	$^{206}Pb/^{238}U$	1 σ	rho	$^{207}Pb/^{206}Pb$	1 σ	$^{207}Pb/^{235}U$	1 σ	$^{206}Pb/^{238}U$	1 σ	$^{207}Pb/^{206}Pb$	1 σ	Pb	U	Th / U
GUE-3																
1a	**0.3558**	**0.0048**	**0.0492**	**0.0006**	**0.9327**	**0.0525**	**0.0006**	**309**	**4**	**309**	**4**	**307**	**27**	**21**	**478**	**0.00**
1b	0.6790	0.0088	0.0816	0.0010	0.9708	0.0604	0.0007	526	5	506	6	617	24	33	427	0.06
1c	**0.3622**	**0.0054**	**0.0490**	**0.0006**	**0.8588**	**0.0536**	**0.0007**	**314**	**4**	**309**	**4**	**354**	**31**	**15**	**338**	**0.00**
3	0.4701	0.0062	0.0602	0.0008	0.9626	0.0567	0.0006	391	4	377	5	479	25	51	869	0.09
4	**0.3676**	**0.0070**	**0.0493**	**0.0007**	**0.7244**	**0.0541**	**0.0010**	**318**	**5**	**310**	**4**	**375**	**41**	**17**	**357**	**0.04**
5	0.4729	0.0069	0.0600	0.0008	0.8852	0.0572	0.0008	393	5	375	5	499	29	18	303	0.08
6a	0.5383	0.0080	0.0692	0.0009	0.8715	0.0564	0.0008	437	5	432	5	468	30	17	236	0.20
7a	**0.3593**	**0.0059**	**0.0486**	**0.0006**	**0.8012**	**0.0536**	**0.0008**	**312**	**4**	**306**	**4**	**353**	**34**	**12**	**268**	**0.00**
7b	3.3445	0.0423	0.2255	0.0028	0.9952	0.1076	0.0011	1492	10	1311	15	1759	19	151	609	0.22
7c	**0.3569**	**0.0058**	**0.0492**	**0.0007**	**0.8108**	**0.0527**	**0.0008**	**310**	**4**	**309**	**4**	**314**	**34**	**14**	**310**	**0.00**
8a	**0.3591**	**0.0062**	**0.0482**	**0.0006**	**0.7760**	**0.0541**	**0.0009**	**312**	**5**	**303**	**4**	**375**	**36**	**14**	**316**	**0.00**
8b	**0.3623**	**0.0058**	**0.0489**	**0.0006**	**0.8140**	**0.0538**	**0.0008**	**314**	**4**	**308**	**4**	**362**	**34**	**17**	**385**	**0.00**
9a	**0.3616**	**0.0053**	**0.0492**	**0.0006**	**0.8815**	**0.0533**	**0.0007**	**313**	**4**	**310**	**4**	**341**	**29**	**29**	**651**	**0.00**
9b	0.5089	0.0066	0.0625	0.0008	0.9778	0.0591	0.0006	418	4	391	5	570	24	101	1700	0.05
10a	**0.3744**	**0.0067**	**0.0506**	**0.0007**	**0.7592**	**0.0536**	**0.0009**	**323**	**5**	**318**	**4**	**356**	**39**	**10**	**206**	**0.01**
10b	0.3636	0.0056	0.0457	0.0006	0.8533	0.0578	0.0008	315	4	288	4	521	31	15	358	0.01
11a	0.3439	0.0130	0.0354	0.0007	0.5163	0.0706	0.0028	300	10	224	4	944	80	2	58	0.03
11b	0.4786	0.0068	0.0602	0.0008	0.9140	0.0576	0.0007	397	5	377	5	516	28	64	1065	0.13
11c	0.4715	0.0069	0.0596	0.0008	0.8868	0.0574	0.0008	392	5	373	5	506	28	40	680	0.11
12a	0.5025	0.0074	0.0635	0.0008	0.8782	0.0574	0.0008	413	5	397	5	507	29	14	221	0.12
12b	0.5302	0.0078	0.0674	0.0009	0.8838	0.0571	0.0008	432	5	420	5	495	29	33	451	0.30
12c	0.5832	0.0084	0.0732	0.0009	0.8963	0.0578	0.0007	467	5	455	6	523	28	18	231	0.23
13a	8.0153	0.1050	0.3327	0.0042	0.9730	0.1748	0.0019	2233	12	1851	21	2604	18	53	143	0.16
13b	6.2964	0.0828	0.2653	0.0034	0.9719	0.1721	0.0019	2018	12	1517	17	2579	19	50	173	0.13
14a	0.8685	0.0124	0.1031	0.0013	0.9025	0.0611	0.0008	635	7	632	8	644	27	23	204	0.35
14b	0.4025	0.0062	0.0523	0.0007	0.8505	0.0558	0.0008	344	5	329	4	444	31	15	311	0.00
14c	0.4135	0.0062	0.0529	0.0007	0.8671	0.0567	0.0008	351	4	332	4	479	30	13	279	0.01
15	0.3392	0.0122	0.0402	0.0008	0.5177	0.0613	0.0023	297	9	254	5	649	79	3	69	0.01
16a	4.0330	0.0543	0.2697	0.0035	0.9526	0.1085	0.0013	1641	11	1539	18	1774	21	79	274	0.23
16b	0.3361	0.0046	0.0453	0.0006	0.9285	0.0538	0.0006	294	4	286	4	361	27	66	1637	0.00
16c	0.3063	0.0043	0.0417	0.0005	0.9290	0.0533	0.0006	271	3	263	3	341	27	50	1333	0.00
17a	4.1599	0.0563	0.2537	0.0033	0.9494	0.1190	0.0014	1666	11	1458	17	1940	21	82	311	0.13
18a	3.7370	0.0508	0.2767	0.0036	0.9444	0.0980	0.0011	1579	11	1575	18	1586	21	164	472	0.62
18b	3.2338	0.0440	0.2394	0.0031	0.9452	0.0980	0.0011	1465	11	1384	16	1586	22	242	707	0.92
6b	0.4287	0.0061	0.0552	0.0007	0.9073	0.0564	0.0007	362	4	346	4	466	27	57	1071	0.08
19	0.7438	0.0110	0.0868	0.0011	0.8875	0.0622	0.0008	565	6	537	7	680	28	35	381	0.24
GUE-5																
11a	**0.3427**	**0.0056**	**0.0475**	**0.0006**	**0.8125**	**0.0523**	**0.0008**	**299**	**4**	**299**	**4**	**299**	**35**	**42**	**978**	**0.00**
11c	**0.3408**	**0.0055**	**0.0478**	**0.0006**	**0.8160**	**0.0518**	**0.0008**	**298**	**4**	**301**	**4**	**275**	**34**	**56**	**1313**	**0.00**

GUE-8																	
1a	**0.3593**	**0.0066**	**0.0493**	**0.0007**	**0.7794**	**0.0529**	**0.0009**	**312**	**5**	**310**	**4**	**325**	**38**	**18**	**376**	**0.10**
1b	**0.3592**	**0.0072**	**0.0478**	**0.0007**	**0.7294**	**0.0545**	**0.0010**	**312**	**5**	**301**	**4**	**391**	**42**	**14**	**291**	**0.13**
1c	**0.3568**	**0.0079**	**0.0478**	**0.0007**	**0.6823**	**0.0542**	**0.0012**	**310**	**6**	**301**	**4**	**378**	**48**	**13**	**273**	**0.12**
1d	**0.3646**	**0.0081**	**0.0499**	**0.0008**	**0.6789**	**0.0531**	**0.0011**	**316**	**6**	**314**	**5**	**331**	**48**	**12**	**236**	**0.11**
1e	**0.3576**	**0.0088**	**0.0487**	**0.0008**	**0.6280**	**0.0533**	**0.0013**	**310**	**7**	**307**	**5**	**341**	**55**	**13**	**271**	**0.13**
1f	**0.3740**	**0.0069**	**0.0504**	**0.0007**	**0.7563**	**0.0538**	**0.0010**	**323**	**5**	**317**	**4**	**364**	**40**	**28**	**552**	**0.11**
1g	0.3842	0.0082	0.0473	0.0007	0.6815	0.0589	0.0013	330	6	298	4	563	46	11	226	0.13
1h	0.3054	0.0079	0.0477	0.0007	0.5711	0.0465	0.0012	271	6	300	4	21	60	10	238	0.13

LA-ICP-MS data for monazite from sample GUE-3, GUE-4 and GUE-5. Data in bold represent the analyses used for the calculation of the concordia ages.

	Isotopes ratios								Ages (Ma)								Contents (ppm)		
Monazite	**$^{207}Pb/^{235}U$**	**1 σ**	**$^{206}Pb/^{238}U$**	**1 σ**	**$^{208}Pb/^{232}Th$**	**1 σ**	**$^{207}Pb/^{206}Pb$**	**1 σ**	**$^{207}Pb/^{235}U$**	**1 σ**	**$^{206}Pb/^{238}U$**	**1 σ**	**$^{208}Pb/^{232}Th$**	**1 σ**	**$^{207}Pb/^{206}Pb$**	**1 σ**	**Pb**	**U**	**Th**
GUE-3																			
4	**0.366**	**0.006**	**0.0489**	**0.0007**	**0.0153**	**0.0003**	**0.0542**	**0.0008**	**317**	**4**	**308**	**4**	**307**	**5**	**380**	**31**	**871**	**5015**	**48820**
5	0.446	0.007	0.0520	0.0008	0.0141	0.0003	0.0623	0.0009	375	5	327	5	282	5	684	30	820	4869	48551
6	**0.363**	**0.008**	**0.0493**	**0.0008**	**0.0151**	**0.0003**	**0.0534**	**0.0011**	**314**	**6**	**310**	**5**	**303**	**5**	**345**	**45**	**719**	**3435**	**42689**
7	**0.347**	**0.006**	**0.0496**	**0.0007**	**0.0152**	**0.0003**	**0.0508**	**0.0007**	**303**	**4**	**312**	**4**	**305**	**5**	**231**	**33**	**849**	**5612**	**45788**
8	**0.358**	**0.006**	**0.0494**	**0.0007**	**0.0160**	**0.0003**	**0.0526**	**0.0008**	**311**	**5**	**311**	**4**	**320**	**6**	**310**	**35**	**727**	**1941**	**44702**
9	**0.365**	**0.007**	**0.0502**	**0.0008**	**0.0152**	**0.0003**	**0.0527**	**0.0010**	**316**	**5**	**316**	**5**	**304**	**5**	**316**	**41**	**820**	**2861**	**51176**
10	**0.338**	**0.006**	**0.0507**	**0.0008**	**0.0147**	**0.0003**	**0.0484**	**0.0008**	**296**	**5**	**319**	**5**	**295**	**5**	**117**	**40**	**821**	**3406**	**51182**
11	**0.351**	**0.007**	**0.0493**	**0.0007**	**0.0153**	**0.0003**	**0.0515**	**0.0009**	**305**	**5**	**311**	**5**	**307**	**5**	**265**	**39**	**748**	**2923**	**45455**
12	**0.357**	**0.006**	**0.0495**	**0.0007**	**0.0153**	**0.0003**	**0.0523**	**0.0008**	**310**	**5**	**312**	**4**	**306**	**5**	**297**	**35**	**937**	**4240**	**55395**
13	**0.339**	**0.006**	**0.0491**	**0.0007**	**0.0152**	**0.0003**	**0.0501**	**0.0008**	**297**	**5**	**309**	**4**	**305**	**5**	**199**	**37**	**871**	**3649**	**52621**
17	**0.347**	**0.006**	**0.0493**	**0.0007**	**0.0148**	**0.0003**	**0.0510**	**0.0007**	**302**	**4**	**310**	**4**	**297**	**5**	**243**	**33**	**742**	**6758**	**35692**
18	**0.348**	**0.006**	**0.0493**	**0.0007**	**0.0159**	**0.0003**	**0.0512**	**0.0007**	**303**	**4**	**311**	**4**	**319**	**6**	**250**	**32**	**1056**	**10035**	**46158**
19	**0.349**	**0.006**	**0.0504**	**0.0007**	**0.0157**	**0.0003**	**0.0502**	**0.0008**	**304**	**5**	**317**	**5**	**315**	**6**	**204**	**36**	**785**	**7039**	**35469**
21	**0.348**	**0.006**	**0.0492**	**0.0007**	**0.0155**	**0.0003**	**0.0513**	**0.0007**	**303**	**4**	**310**	**4**	**311**	**6**	**254**	**33**	**879**	**11013**	**32288**
22	**0.348**	**0.006**	**0.0497**	**0.0007**	**0.0157**	**0.0003**	**0.0509**	**0.0008**	**304**	**4**	**312**	**4**	**315**	**6**	**236**	**34**	**1000**	**11298**	**39251**
25	**0.354**	**0.007**	**0.0490**	**0.0007**	**0.0148**	**0.0003**	**0.0524**	**0.0010**	**308**	**5**	**308**	**5**	**297**	**5**	**304**	**41**	**779**	**7794**	**35372**
26	**0.364**	**0.007**	**0.0489**	**0.0007**	**0.0150**	**0.0003**	**0.0539**	**0.0009**	**315**	**5**	**308**	**4**	**302**	**5**	**368**	**38**	**761**	**5821**	**38999**
GUE-4																			
1a	**0.342**	**0.005**	**0.0495**	**0.0007**	**0.0152**	**0.0003**	**0.0501**	**0.0006**	**299**	**4**	**311**	**4**	**305**	**5**	**201**	**25**	**1087**	**11977**	**45701**
1b	**0.342**	**0.005**	**0.0492**	**0.0007**	**0.0152**	**0.0003**	**0.0503**	**0.0005**	**298**	**4**	**310**	**4**	**306**	**5**	**211**	**25**	**1085**	**12721**	**43596**
1c	**0.366**	**0.005**	**0.0499**	**0.0007**	**0.0155**	**0.0003**	**0.0532**	**0.0006**	**317**	**4**	**314**	**4**	**311**	**6**	**337**	**24**	**1170**	**13296**	**46577**
1d	**0.366**	**0.005**	**0.0496**	**0.0007**	**0.0153**	**0.0003**	**0.0535**	**0.0006**	**317**	**4**	**312**	**4**	**306**	**5**	**351**	**24**	**1102**	**11854**	**46632**
1e	**0.342**	**0.005**	**0.0493**	**0.0007**	**0.0157**	**0.0003**	**0.0504**	**0.0006**	**299**	**4**	**310**	**4**	**315**	**6**	**212**	**25**	**1107**	**13078**	**42773**
1f	**0.351**	**0.005**	**0.0509**	**0.0007**	**0.0156**	**0.0003**	**0.0501**	**0.0005**	**306**	**4**	**320**	**4**	**313**	**6**	**202**	**25**	**1074**	**12063**	**42286**
1g	**0.343**	**0.005**	**0.0495**	**0.0007**	**0.0157**	**0.0003**	**0.0504**	**0.0006**	**300**	**4**	**311**	**4**	**314**	**6**	**211**	**25**	**1106**	**12825**	**43289**
1h	**0.345**	**0.005**	**0.0498**	**0.0007**	**0.0159**	**0.0003**	**0.0502**	**0.0006**	**301**	**4**	**313**	**4**	**318**	**6**	**205**	**26**	**1155**	**12799**	**45903**
1i	**0.390**	**0.005**	**0.0493**	**0.0007**	**0.0153**	**0.0003**	**0.0575**	**0.0006**	**335**	**4**	**310**	**4**	**307**	**6**	**511**	**23**	**1405**	**17016**	**54074**
1j	**0.350**	**0.005**	**0.0494**	**0.0007**	**0.0153**	**0.0003**	**0.0514**	**0.0006**	**305**	**4**	**311**	**4**	**306**	**5**	**257**	**25**	**1085**	**10935**	**47909**
1k	**0.346**	**0.005**	**0.0499**	**0.0007**	**0.0151**	**0.0003**	**0.0504**	**0.0006**	**302**	**4**	**314**	**4**	**303**	**5**	**212**	**28**	**1693**	**18896**	**70042**
2a	**0.335**	**0.005**	**0.0495**	**0.0007**	**0.0148**	**0.0003**	**0.0491**	**0.0006**	**293**	**4**	**311**	**4**	**297**	**5**	**152**	**27**	**703**	**6261**	**34320**
2b	**0.333**	**0.005**	**0.0495**	**0.0007**	**0.0155**	**0.0003**	**0.0489**	**0.0006**	**292**	**4**	**311**	**4**	**311**	**6**	**142**	**28**	**649**	**5868**	**29929**
2c	**0.342**	**0.005**	**0.0498**	**0.0007**	**0.0149**	**0.0003**	**0.0498**	**0.0006**	**298**	**4**	**313**	**4**	**299**	**5**	**187**	**30**	**741**	**6467**	**36050**
2d	**0.343**	**0.005**	**0.0492**	**0.0007**	**0.0154**	**0.0003**	**0.0505**	**0.0006**	**299**	**4**	**310**	**4**	**309**	**6**	**217**	**26**	**1028**	**10799**	**43814**

3b	**0.469**	**0.006**	**0.0495**	**0.0007**	**0.0153**	**0.0003**	**0.0687**	**0.0008**	**390**	**4**	**311**	**4**	**307**	**5**	**891**	**22**	**1581**	**15949**	**68248**
14a	**0.345**	**0.005**	**0.0493**	**0.0007**	**0.0154**	**0.0003**	**0.0507**	**0.0006**	**301**	**4**	**310**	**4**	**309**	**6**	**228**	**27**	**915**	**6131**	**48197**
14d	**0.440**	**0.006**	**0.0496**	**0.0007**	**0.0153**	**0.0003**	**0.0645**	**0.0007**	**371**	**4**	**312**	**4**	**306**	**5**	**757**	**23**	**1696**	**18724**	**68938**
11a	**0.340**	**0.005**	**0.0497**	**0.0007**	**0.0148**	**0.0003**	**0.0496**	**0.0007**	**297**	**4**	**313**	**4**	**296**	**5**	**176**	**31**	**929**	**4142**	**56577**
11b	0.358	0.005	0.0516	0.0007	0.0153	0.0003	0.0504	0.0006	311	4	324	4	306	5	214	28	924	4718	52333
11c	**0.331**	**0.005**	**0.0494**	**0.0007**	**0.0152**	**0.0003**	**0.0487**	**0.0006**	**291**	**4**	**311**	**4**	**305**	**5**	**131**	**31**	**838**	**3409**	**50459**
11d	**0.347**	**0.005**	**0.0496**	**0.0007**	**0.0153**	**0.0003**	**0.0508**	**0.0006**	**303**	**4**	**312**	**4**	**306**	**5**	**232**	**28**	**1089**	**7275**	**57611**
11e	0.332	0.005	0.0501	0.0007	0.0148	0.0003	0.0480	0.0007	291	4	315	4	297	5	97	35	953	3559	59800
11f	**0.341**	**0.005**	**0.0496**	**0.0007**	**0.0151**	**0.0003**	**0.0500**	**0.0007**	**298**	**4**	**312**	**4**	**302**	**5**	**194**	**30**	**1056**	**4557**	**63418**
4a	0.333	0.005	0.0475	0.0007	0.0148	0.0003	0.0510	0.0007	292	4	299	4	296	5	239	30	1052	4124	66083
4b	0.335	0.005	0.0480	0.0007	0.0144	0.0003	0.0506	0.0007	293	4	302	4	290	5	224	31	1103	4827	69297
4c	**0.361**	**0.005**	**0.0493**	**0.0007**	**0.0151**	**0.0003**	**0.0531**	**0.0006**	**313**	**4**	**310**	**4**	**303**	**5**	**334**	**27**	**1231**	**8117**	**66012**
4d	**0.330**	**0.005**	**0.0493**	**0.0007**	**0.0151**	**0.0003**	**0.0485**	**0.0006**	**289**	**4**	**310**	**4**	**302**	**5**	**124**	**31**	**1064**	**4427**	**64302**
5a	**0.337**	**0.005**	**0.0492**	**0.0007**	**0.0155**	**0.0003**	**0.0496**	**0.0006**	**295**	**4**	**310**	**4**	**311**	**6**	**178**	**28**	**991**	**9950**	**42650**
5b	0.381	0.006	0.0515	0.0007	0.0156	0.0003	0.0537	0.0007	328	4	324	4	314	6	359	29	727	4538	37674
10a	**0.343**	**0.005**	**0.0493**	**0.0007**	**0.0156**	**0.0003**	**0.0505**	**0.0006**	**299**	**4**	**310**	**4**	**312**	**6**	**216**	**27**	**978**	**10030**	**41244**
10b	**0.344**	**0.005**	**0.0493**	**0.0007**	**0.0154**	**0.0003**	**0.0506**	**0.0006**	**300**	**4**	**311**	**4**	**309**	**5**	**222**	**27**	**1533**	**16227**	**63945**
6a	**0.339**	**0.005**	**0.0496**	**0.0007**	**0.0158**	**0.0003**	**0.0496**	**0.0007**	**297**	**4**	**312**	**4**	**316**	**6**	**178**	**31**	**969**	**6286**	**49780**
6b	**0.398**	**0.006**	**0.0495**	**0.0007**	**0.0156**	**0.0003**	**0.0584**	**0.0008**	**341**	**5**	**312**	**4**	**312**	**6**	**544**	**31**	**986**	**5816**	**52659**
7a	**0.339**	**0.005**	**0.0494**	**0.0007**	**0.0156**	**0.0003**	**0.0498**	**0.0006**	**297**	**4**	**311**	**4**	**314**	**6**	**187**	**28**	**796**	**8717**	**31858**
7b	**0.339**	**0.005**	**0.0496**	**0.0007**	**0.0155**	**0.0003**	**0.0495**	**0.0006**	**296**	**4**	**312**	**4**	**310**	**6**	**173**	**28**	**992**	**10292**	**41509**
7e	**0.334**	**0.005**	**0.0495**	**0.0007**	**0.0153**	**0.0003**	**0.0489**	**0.0006**	**292**	**4**	**311**	**4**	**306**	**5**	**143**	**30**	**1539**	**13887**	**70891**
8a	0.321	0.005	0.0481	0.0007	0.0146	0.0003	0.0485	0.0007	283	4	303	4	292	5	122	33	994	3264	64457
8b	0.325	0.005	0.0484	0.0007	0.0153	0.0003	0.0488	0.0007	286	4	305	4	307	5	138	34	1035	3480	63646
9a	0.324	0.005	0.0474	0.0007	0.0149	0.0003	0.0495	0.0007	285	4	299	4	299	5	173	31	934	4810	54636
9b	**0.318**	**0.005**	**0.0494**	**0.0007**	**0.0147**	**0.0003**	**0.0467**	**0.0006**	**281**	**4**	**311**	**4**	**294**	**5**	**34**	**30**	**1303**	**13644**	**57048**
GUE-5																			
1a	**0.400**	**0.006**	**0.0484**	**0.0007**	**0.0146**	**0.0003**	**0.0600**	**0.0008**	**342**	**4**	**305**	**4**	**294**	**5**	**602**	**28**	**1196**	**5596**	**73702**
1b	0.350	0.006	0.0489	0.0007	0.0150	0.0003	0.0519	0.0007	305	4	308	4	301	5	281	31	1253	6206	74226
2a	**0.338**	**0.005**	**0.0491**	**0.0007**	**0.0151**	**0.0003**	**0.0499**	**0.0006**	**296**	**4**	**309**	**4**	**303**	**5**	**190**	**27**	**891**	**9297**	**39126**
3a	**0.345**	**0.005**	**0.0491**	**0.0007**	**0.0148**	**0.0003**	**0.0510**	**0.0006**	**301**	**4**	**309**	**4**	**298**	**5**	**242**	**27**	**1276**	**14672**	**53113**
4a	**0.349**	**0.006**	**0.0475**	**0.0007**	**0.0152**	**0.0003**	**0.0533**	**0.0008**	**304**	**4**	**299**	**4**	**306**	**5**	**343**	**34**	**1329**	**1446**	**91326**
5a	**0.354**	**0.005**	**0.0480**	**0.0007**	**0.0152**	**0.0003**	**0.0535**	**0.0006**	**308**	**4**	**302**	**4**	**305**	**5**	**352**	**26**	**1029**	**8906**	**50002**
7a	0.341	0.005	0.0479	0.0007	0.0153	0.0003	0.0516	0.0006	298	4	302	4	308	5	266	28	1272	11181	60762
7b	**0.349**	**0.005**	**0.0499**	**0.0007**	**0.0152**	**0.0003**	**0.0508**	**0.0006**	**304**	**4**	**314**	**4**	**306**	**5**	**231**	**27**	**1413**	**15359**	**58476**
7c	**0.343**	**0.005**	**0.0483**	**0.0007**	**0.0146**	**0.0003**	**0.0515**	**0.0006**	**299**	**4**	**304**	**4**	**292**	**5**	**262**	**28**	**1595**	**18268**	**67911**
7d	**0.345**	**0.005**	**0.0486**	**0.0007**	**0.0150**	**0.0003**	**0.0515**	**0.0006**	**301**	**4**	**306**	**4**	**301**	**5**	**263**	**28**	**1500**	**16215**	**64295**
8a	**0.336**	**0.005**	**0.0481**	**0.0007**	**0.0149**	**0.0003**	**0.0507**	**0.0006**	**294**	**4**	**303**	**4**	**298**	**5**	**225**	**29**	**1144**	**9311**	**58133**
8b	0.352	0.005	0.0483	0.0007	0.0149	0.0003	0.0529	0.0006	306	4	304	4	299	5	323	27	1922	18037	90674
10	**0.341**	**0.005**	**0.0486**	**0.0007**	**0.0144**	**0.0003**	**0.0509**	**0.0007**	**298**	**4**	**306**	**4**	**289**	**5**	**236**	**31**	**1743**	**18176**	**79391**
11	**0.341**	**0.005**	**0.0485**	**0.0007**	**0.0148**	**0.0003**	**0.0510**	**0.0007**	**298**	**4**	**305**	**4**	**298**	**5**	**242**	**30**	**928**	**9582**	**41336**
12a	0.341	0.005	0.0475	0.0007	0.0152	0.0003	0.0521	0.0007	298	4	299	4	304	5	289	29	843	10249	33032
13	0.350	0.005	0.0485	0.0007	0.0152	0.0003	0.0524	0.0007	305	4	306	4	305	5	301	30	1141	5350	66662
14	**0.346**	**0.006**	**0.0469**	**0.0007**	**0.0145**	**0.0003**	**0.0535**	**0.0008**	**302**	**4**	**296**	**4**	**291**	**5**	**349**	**34**	**892**	**5810**	**50589**
15a	0.343	0.005	0.0482	0.0007	0.0144	0.0003	0.0516	0.0007	300	4	304	4	289	5	269	32	812	7583	39427
15b	0.344	0.005	0.0481	0.0007	0.0153	0.0003	0.0519	0.0007	300	4	303	4	307	5	283	31	870	8058	39924
15c	0.344	0.005	0.0477	0.0007	0.0146	0.0003	0.0523	0.0007	300	4	301	4	292	5	299	31	988	9151	47820
18	0.342	0.005	0.0478	0.0007	0.0149	0.0003	0.0519	0.0007	299	4	301	4	298	5	280	32	2247	24838	95113
20a	**0.361**	**0.006**	**0.0479**	**0.0007**	**0.0154**	**0.0003**	**0.0547**	**0.0008**	**313**	**4**	**301**	**4**	**309**	**5**	**400**	**31**	**1175**	**1684**	**79341**
29a	**0.350**	**0.005**	**0.0478**	**0.0007**	**0.0157**	**0.0003**	**0.0531**	**0.0007**	**305**	**4**	**301**	**4**	**315**	**5**	**332**	**29**	**987**	**1623**	**64433**

Datations U-Pb sur zircon article # 3. *Data in bold represent the analyses used for the calculation of the concordia ages.*

PONT-1: porphyritic leucogranite

Zircon analyses	Isotope ratios							Ages						Concentrations (ppm)			Th/U
	Pb^{207}/Pb^{206}	1σ	Pb^{207}/U^{235}	1σ	Pb^{206}/U^{238}	1σ	rho	Pb^{207}/Pb^{206}	1σ	Pb^{206}/U^{238}	1σ	Pb^{207}/U^{235}	1σ	Pb	U	Th	
3	0.06396	0.00074	0.96319	0.01278	0.10923	0.00133	0.92	740.3	24.26	668.3	7.72	684.9	6.61	26.4	238.3	94.1	0.39
4	0.06142	0.00068	0.73139	0.00942	0.08638	0.00105	0.94	653.8	23.65	534.1	6.21	557.4	5.53	47.2	550.3	136.7	0.25
5	**0.0527**	**0.00056**	**0.3681**	**0.00461**	**0.05066**	**0.00061**	**0.96**	**315.8**	**24.06**	**318.6**	**3.75**	**318.2**	**3.42**	**41.4**	**907.8**	**15.6**	**0.02**
6	0.05877	0.00063	0.73134	0.00914	0.09026	0.00109	0.97	558.6	23.08	557.1	6.43	557.3	5.36	35.9	368.6	224.1	0.61
9	0.05438	0.0006	0.35973	0.00458	0.04798	0.00058	0.95	386.7	24.55	302.1	3.55	312	3.42	64.9	1300.8	620.4	0.48
15	0.05268	0.00056	0.39555	0.00484	0.05447	0.00064	0.96	314.9	23.92	341.9	3.94	338.4	3.52	86.3	1687.3	178.3	0.11
16	**0.05303**	**0.00056**	**0.3692**	**0.00449**	**0.0505**	**0.0006**	**0.98**	**330.1**	**23.68**	**317.6**	**3.66**	**319.1**	**3.33**	**131.1**	**2280.4**	**1833.6**	**0.80**
18	0.10709	0.00114	4.40295	0.05376	0.29822	0.00352	0.97	1750.6	19.27	1682.5	17.48	1712.9	10.1	67.1	165.8	251.4	1.52
19	0.06547	0.00071	0.87944	0.01092	0.09744	0.00115	0.95	789.5	22.72	599.4	6.75	640.7	5.9	53.7	541.0	124.5	0.23
20	0.05658	0.00063	0.50213	0.00635	0.06437	0.00076	0.93	474.6	24.78	402.1	4.59	413.1	4.29	38.5	592.1	159.1	0.27
22	0.05312	0.00058	0.36385	0.0045	0.04968	0.00058	0.94	334	24.6	312.6	3.57	315.1	3.35	168.0	3262.4	1197.9	0.37
23	0.06313	0.00078	0.85221	0.01157	0.09792	0.00115	0.87	712.6	26.14	602.2	6.77	625.9	6.34	16.4	158.8	64.0	0.40
24	**0.05297**	**0.00064**	**0.36657**	**0.00487**	**0.0502**	**0.00059**	**0.88**	**327.3**	**27.11**	**315.8**	**3.61**	**317.1**	**3.62**	**16.0**	**259.7**	**267.2**	**1.03**
26	**0.05293**	**0.00059**	**0.36874**	**0.00461**	**0.05054**	**0.00059**	**0.93**	**325.7**	**25.17**	**317.8**	**3.61**	**318.7**	**3.42**	**47.7**	**906.2**	**323.1**	**0.36**
27	**0.05232**	**0.00059**	**0.36349**	**0.00456**	**0.05039**	**0.00059**	**0.93**	**299.5**	**25.49**	**316.9**	**3.59**	**314.8**	**3.4**	**48.1**	**961.5**	**198.3**	**0.21**
28	0.05351	0.00059	0.34673	0.00427	0.047	0.00054	0.93	350.4	24.62	296.1	3.35	302.3	3.22	64.8	1409.0	199.0	0.14
30	0.05389	0.00063	0.34451	0.00429	0.04637	0.00051	0.88	366.4	26.27	292.2	3.16	300.6	3.24	66.7	1480.4	277.2	0.19
32	0.05988	0.00124	0.77198	0.01612	0.09352	0.00111	0.57	599.1	44.4	576.3	6.52	580.9	9.24	11.5	81.3	170.7	2.10
33	0.06496	0.00084	0.90437	0.01224	0.10098	0.00113	0.83	773.1	26.93	620.1	6.6	654.1	6.53	24.1	235.5	63.1	0.27
35	0.06885	0.00075	1.09887	0.01283	0.11577	0.00128	0.95	894.3	22.18	706.2	7.37	752.8	6.21	88.3	725.3	292.2	0.40
36	0.06426	0.00101	0.94498	0.01521	0.10667	0.00121	0.70	750.2	32.82	653.4	7.07	675.5	7.94	9.2	80.9	39.2	0.48
39	0.06063	0.00071	0.85815	0.01071	0.10267	0.00114	0.89	626.1	25.08	630	6.65	629.1	5.85	29.1	260.6	154.5	0.59
40	0.05552	0.0006	0.48409	0.00564	0.06324	0.0007	0.95	433	23.78	395.3	4.22	400.9	3.86	344.4	5963.6	9.7	0.00
41	**0.05221**	**0.00076**	**0.3719**	**0.00557**	**0.05166**	**0.00058**	**0.75**	**294.8**	**32.65**	**324.7**	**3.55**	**321.1**	**4.12**	**12.5**	**242.4**	**73.9**	**0.31**
42	0.05243	0.00065	0.34824	0.00454	0.04818	0.00053	0.84	304.1	27.8	303.3	3.29	303.4	3.42	29.8	634.7	133.4	0.21
43	0.06046	0.00089	0.79567	0.01216	0.09546	0.00108	0.74	619.9	31.61	587.8	6.34	594.4	6.87	10.4	96.8	69.0	0.71
49	0.05382	0.00065	0.3631	0.00467	0.04894	0.00054	0.86	363.3	27.23	308	3.33	314.5	3.48	46.5	985.8	169.4	0.17

PONT-7: quartz monzodiorite

Zircon analyses	Isotope ratios							Ages						Concentrations (ppm)			Th/U
	Pb^{207}/Pb^{206}	1σ	Pb^{207}/U^{235}	1σ	Pb^{206}/U^{238}	1σ	rho	Pb^{207}/Pb^{206}	1σ	Pb^{206}/U^{238}	1σ	Pb^{207}/U^{235}	1σ	Pb	U	Th	
1	**0.05327**	**0.0006**	**0.36906**	**0.00507**	**0.05025**	**0.00064**	**0.93**	**340.3**	**25.18**	**316.1**	**3.95**	**319**	**3.76**	**280.2**	**3025.9**	**3073.8**	**1.02**
2	0.05843	0.00065	0.42195	0.00577	0.05238	0.00067	0.94	545.9	24.3	329.1	4.11	357.4	4.12	149.3	1704.8	1342.5	0.79
4	0.05465	0.00064	0.35148	0.00494	0.04665	0.0006	0.92	398	25.82	293.9	3.68	305.8	3.71	174.1	2057.5	2229.0	1.08
5	0.05451	0.00061	0.39874	0.00543	0.05306	0.00068	0.94	392.3	24.77	333.3	4.16	340.7	3.94	95.2	1174.4	258.3	0.22
6	0.05536	0.00065	0.39739	0.00559	0.05207	0.00067	0.91	426.5	25.86	327.2	4.09	339.8	4.06	104.8	1185.2	810.8	0.68
7	0.05452	0.0006	0.38721	0.00521	0.05152	0.00066	0.95	392.5	24.43	323.8	4.03	332.3	3.81	128.9	1586.5	759.6	0.48
8	0.05387	0.0006	0.38866	0.00525	0.05234	0.00067	0.95	365.5	24.89	328.8	4.09	333.4	3.84	168.7	2163.2	331.9	0.15
10	**0.05298**	**0.00059**	**0.3657**	**0.00492**	**0.05007**	**0.00064**	**0.95**	**327.8**	**24.82**	**315**	**3.92**	**316.5**	**3.66**	**173.1**	**2070.7**	**1319.9**	**0.64**
12	**0.05358**	**0.00059**	**0.37275**	**0.00499**	**0.05047**	**0.00064**	**0.95**	**353.1**	**24.57**	**317.4**	**3.95**	**321.7**	**3.69**	**247.8**	**3006.8**	**1563.5**	**0.52**
13	**0.05242**	**0.00057**	**0.36474**	**0.00485**	**0.05048**	**0.00064**	**0.95**	**303.7**	**24.71**	**317.4**	**3.94**	**315.7**	**3.61**	**440.1**	**4302.3**	**5902.9**	**1.37**
14	0.05394	0.00061	0.37224	0.00503	0.05006	0.00064	0.95	368.4	25.2	314.9	3.91	321.3	3.72	137.9	1758.2	576.0	0.33
15	**0.05316**	**0.00059**	**0.37069**	**0.00499**	**0.05058**	**0.00064**	**0.94**	**335.5**	**25.05**	**318.1**	**3.95**	**320.2**	**3.7**	**200.6**	**2457.7**	**1066.6**	**0.43**
17	**0.05333**	**0.0006**	**0.3655**	**0.00495**	**0.04972**	**0.00063**	**0.94**	**342.7**	**25.26**	**312.8**	**3.88**	**316.3**	**3.68**	**138.8**	**1727.2**	**735.6**	**0.43**
18	0.05541	0.00063	0.37585	0.00512	0.0492	0.00063	0.94	428.7	25.12	309.6	3.84	324	3.78	115.7	1402.0	796.5	0.57

19	0.05321	0.00062	0.35206	0.00484	0.04799	0.00061	0.92	337.8	26.01	302.2	3.75	306.3	3.63	113.0	1574.0	245.1	0.16
20	**0.0529**	**0.00062**	**0.35494**	**0.0049**	**0.04867**	**0.00062**	**0.92**	**324.6**	**26.28**	**306.3**	**3.8**	**308.4**	**3.67**	**108.4**	**1360.8**	**669.0**	**0.49**
22	0.05253	0.00063	0.34034	0.00475	0.047	0.0006	0.91	308.5	26.88	296.1	3.68	297.4	3.6	186.5	2302.4	1500.1	0.65
23	0.05229	0.00062	0.33612	0.00466	0.04663	0.00059	0.91	298	26.7	293.8	3.65	294.2	3.54	316.3	3394.1	5241.4	1.54
24	0.05476	0.00064	0.36437	0.00499	0.04827	0.00061	0.92	402.4	25.54	303.9	3.77	315.5	3.72	173.1	2409.4	251.3	0.10

PONT-20: Langonnet leucogranite

Zircon analyses	Isotope ratios							Ages						Concentrations (ppm)			Th/U
	Pb^{207}/Pb^{206}	1σ	Pb^{207}/U^{235}	1σ	Pb^{206}/U^{238}	1σ	rho	Pb^{207}/Pb^{206}	1σ	Pb^{206}/U^{238}	1σ	Pb^{207}/U^{235}	1σ	Pb	U	Th	
1	0.06035	0.00067	0.75207	0.00927	0.0904	0.00104	0.93	616.2	23.75	557.9	6.15	569.4	5.37	52.84	566.45	257.07	0.45
2a	0.06408	0.00072	0.95574	0.01191	0.10819	0.00124	0.92	744.3	23.62	662.2	7.24	681.1	6.18	40.43	350.14	180.60	0.52
3	0.05716	0.00064	0.58048	0.00716	0.07367	0.00084	0.92	497	24.7	458.2	5.07	464.8	4.6	36.14	524.69	44.74	0.09
4a	0.05867	0.00063	0.75133	0.00897	0.0929	0.00106	0.96	554.7	23.16	572.7	6.26	569	5.2	90.26	941.39	402.30	0.43
4b	0.05437	0.00058	0.35384	0.00419	0.04721	0.00054	0.97	386.3	23.66	297.4	3.31	307.6	3.14	189.62	3982.08	1323.99	0.33
4c	**0.05264**	**0.00056**	**0.35209**	**0.00415**	**0.04851**	**0.00055**	**0.96**	**313.5**	**23.84**	**305.4**	**3.39**	**306.3**	**3.12**	**190.42**	**4344.74**	**51.43**	**0.01**
5a	0.17838	0.0019	10.66509	0.12645	0.43368	0.00495	0.96	2637.9	17.59	2322.3	22.24	2494.4	11.01	46.88	95.34	42.87	0.45
5c	0.12088	0.00127	4.83668	0.05658	0.29024	0.00329	0.97	1969.2	18.58	1642.7	16.44	1791.3	9.84	293.31	1042.81	18.58	0.02
27	0.05419	0.00091	0.42999	0.00736	0.05755	0.00066	0.67	379	37.21	360.7	4	363.2	5.23	6.16	110.64	23.01	0.21
7a	0.06376	0.00076	0.8989	0.01157	0.10226	0.00116	0.88	733.7	25.08	627.6	6.79	651.1	6.19	19.86	189.51	63.42	0.33
7b	0.06247	0.0007	0.64318	0.0079	0.07468	0.00084	0.92	690.3	23.87	464.3	5.06	504.3	4.88	41.24	573.10	59.02	0.10
8	0.05475	0.00059	0.33211	0.00395	0.044	0.00049	0.94	402	23.84	277.6	3.06	291.2	3.01	351.02	8490.14	310.80	0.04
9	0.12099	0.00131	5.18392	0.06144	0.31078	0.00349	0.95	1970.9	19.14	1744.5	17.19	1850	10.09	149.93	412.35	288.76	0.70
10	0.07235	0.00079	1.43325	0.0171	0.1437	0.00161	0.94	995.7	22.04	865.6	9.09	902.9	7.14	101.42	646.01	341.01	0.53
11	0.06312	0.00075	1.00252	0.01273	0.11521	0.0013	0.89	712.3	24.9	702.9	7.5	705.1	6.45	23.51	208.22	39.75	0.19
12	0.0575	0.00068	0.52938	0.00671	0.06678	0.00075	0.89	510.4	25.57	416.7	4.54	431.4	4.46	41.96	680.42	2.35	0.00
13	0.05869	0.00071	0.46242	0.00598	0.05715	0.00064	0.87	555.8	26.22	358.3	3.92	385.9	4.15	80.82	1062.10	1291.98	1.22
15a	0.05707	0.00098	0.4937	0.00861	0.06275	0.00072	0.66	493.8	37.42	392.3	4.39	407.4	5.85	14.16	217.37	77.63	0.36
15b	0.05684	0.0007	0.58636	0.00763	0.07482	0.00084	0.86	484.9	27.21	465.1	5.01	468.5	4.88	23.35	309.59	83.79	0.27
16a	0.06002	0.0008	0.78396	0.01093	0.09474	0.00106	0.80	604.4	28.59	583.5	6.26	587.7	6.22	14.84	138.20	93.36	0.68
17b	0.12678	0.00144	6.00172	0.07264	0.34339	0.0038	0.91	2053.8	19.9	1902.9	18.25	1976.1	10.53	109.76	191.06	476.79	2.50
18a	0.05711	0.00067	0.49845	0.00623	0.06332	0.0007	0.88	495	26.17	395.8	4.25	410.7	4.22	96.81	1591.58	130.21	0.08
18b	0.05669	0.00067	0.49454	0.00621	0.06328	0.0007	0.88	478.7	26.31	395.6	4.24	408	4.22	91.50	1512.75	90.08	0.06
20	0.06074	0.00074	0.53682	0.00688	0.06411	0.00071	0.86	630	26.1	400.6	4.29	436.3	4.55	54.37	735.03	472.95	0.64
24a	0.05577	0.0007	0.37064	0.00489	0.0482	0.00054	0.85	443	27.07	303.5	3.31	320.1	3.62	17.66	359.91	127.30	0.35
24b	**0.05271**	**0.00072**	**0.35349**	**0.00504**	**0.04865**	**0.00055**	**0.79**	**316.1**	**30.73**	**306.2**	**3.36**	**307.3**	**3.78**	**15.17**	**317.40**	**77.11**	**0.24**
26	0.0611	0.00075	0.8509	0.01105	0.10102	0.00113	0.86	642.7	26.11	620.4	6.6	625.1	6.06	14.69	157.55	3.05	0.02
28a	**0.05332**	**0.00084**	**0.35041**	**0.00569**	**0.04767**	**0.00054**	**0.70**	**342.2**	**35.3**	**300.2**	**3.34**	**305**	**4.28**	**21.82**	**491.55**	**34.04**	**0.07**
28b	**0.05298**	**0.00071**	**0.35395**	**0.00497**	**0.04846**	**0.00054**	**0.79**	**327.8**	**30.08**	**305.1**	**3.34**	**307.7**	**3.73**	**12.97**	**279.93**	**42.94**	**0.15**
28c	**0.05343**	**0.00069**	**0.35704**	**0.00486**	**0.04847**	**0.00054**	**0.82**	**346.9**	**28.91**	**305.1**	**3.34**	**310**	**3.63**	**15.98**	**348.09**	**43.44**	**0.12**
29	0.05635	0.00063	0.59413	0.00714	0.07648	0.00085	0.92	465.2	24.7	475.1	5.08	473.5	4.55	63.79	842.37	198.82	0.24
30a	**0.05204**	**0.00073**	**0.34709**	**0.0051**	**0.04838**	**0.00054**	**0.76**	**287.2**	**31.92**	**304.6**	**3.35**	**302.5**	**3.84**	**27.71**	**520.57**	**353.25**	**0.68**
30b	0.05574	0.00077	0.35903	0.00519	0.04672	0.00053	0.78	441.6	30.17	294.4	3.24	311.5	3.88	15.19	299.78	163.31	0.54
31	0.05774	0.00066	0.55547	0.00677	0.06978	0.00077	0.91	519.8	24.97	434.8	4.67	448.6	4.42	54.29	800.99	116.59	0.15
33a	0.0595	0.00067	0.71211	0.00859	0.08681	0.00096	0.92	585.4	24.15	536.7	5.71	546	5.09	51.63	543.79	299.75	0.55
34	0.06055	0.00067	0.75951	0.00906	0.09098	0.00101	0.93	623.4	23.68	561.3	5.96	573.7	5.23	69.12	715.83	326.34	0.46
35	0.05894	0.0007	0.65938	0.00838	0.08114	0.0009	0.87	565	25.82	502.9	5.39	514.2	5.13	50.21	614.61	183.67	0.30
36	0.05674	0.00064	0.57536	0.00695	0.07355	0.00082	0.92	480.9	24.88	457.5	4.9	461.5	4.48	63.18	717.02	649.62	0.91
38	0.05706	0.00063	0.57553	0.00689	0.07316	0.00081	0.92	493.2	24.65	455.2	4.87	461.6	4.44	122.07	1397.75	1297.64	0.93
40	0.06921	0.00078	1.28831	0.01552	0.13503	0.0015	0.92	904.9	22.92	816.5	8.51	840.5	6.89	125.18	979.60	71.59	0.07
41a	0.06225	0.00115	0.64224	0.01201	0.07484	0.00087	0.62	682.7	38.97	465.2	5.23	503.7	7.43	6.33	81.16	27.16	0.33

41b	0.06286	0.00088	0.8096	0.0118	0.09342	0.00105	0.77	703.6	29.55	575.7	6.22	602.2	6.62	11.84	116.91	59.09	0.51
42	0.12859	0.00146	5.82805	0.07084	0.32875	0.00366	0.92	2078.8	19.82	1832.3	17.75	1950.6	10.53	82.55	223.95	116.21	0.52

PONT-22: monzogranite

Zircon analyses	Isotope ratios							Ages						Concentrations (ppm)			Th/U
	Pb^{207}/Pb^{206}	1σ	Pb^{207}/U^{235}	1σ	Pb^{206}/U^{238}	1σ	rho	Pb^{207}/Pb^{206}	1σ	Pb^{206}/U^{238}	1σ	Pb^{207}/U^{235}	1σ	Pb	U	Th	
1	**0.05246**	**0.00068**	**0.36105**	**0.00494**	**0.04992**	**0.00056**	**0.82**	**305.5**	**29.17**	**314**	**3.47**	**313**	**3.69**	**16.8**	**357.7**	**44.5**	**0.12**
2	**0.05298**	**0.00083**	**0.36767**	**0.00596**	**0.05034**	**0.00058**	**0.71**	**327.8**	**35.2**	**316.6**	**3.55**	**317.9**	**4.43**	**17.2**	**336.3**	**120.9**	**0.36**
3	0.05518	0.00065	0.36732	0.00465	0.04828	0.00054	0.88	419.4	25.99	304	3.34	317.7	3.46	92.6	1770.1	1087.5	0.61
4	**0.05245**	**0.00078**	**0.36428**	**0.0056**	**0.05037**	**0.00057**	**0.74**	**305.1**	**33.3**	**316.8**	**3.52**	**315.4**	**4.17**	**9.5**	**180.7**	**87.4**	**0.48**
5	**0.0533**	**0.00079**	**0.36413**	**0.00558**	**0.04956**	**0.00056**	**0.74**	**341.3**	**32.93**	**311.8**	**3.47**	**315.3**	**4.15**	**11.1**	**221.4**	**81.5**	**0.37**
6	**0.05343**	**0.00062**	**0.36789**	**0.00457**	**0.04994**	**0.00056**	**0.90**	**347.2**	**25.81**	**314.1**	**3.44**	**318.1**	**3.39**	**56.6**	**1219.0**	**89.6**	**0.07**
7	0.0543	0.00059	0.39047	0.00465	0.05216	0.00058	0.93	383.4	24.52	327.8	3.57	334.7	3.39	149.7	3118.5	70.4	0.02
8	**0.05393**	**0.00071**	**0.37252**	**0.00518**	**0.0501**	**0.00057**	**0.82**	**368.1**	**29.66**	**315.1**	**3.47**	**321.5**	**3.83**	**22.8**	**430.6**	**216.3**	**0.50**
10	**0.05361**	**0.00076**	**0.37034**	**0.00546**	**0.05011**	**0.00057**	**0.77**	**354.6**	**31.72**	**315.2**	**3.48**	**319.9**	**4.05**	**13.6**	**271.8**	**85.9**	**0.32**
12	**0.05331**	**0.00064**	**0.37048**	**0.00473**	**0.0504**	**0.00056**	**0.87**	**342.1**	**26.79**	**317**	**3.46**	**320**	**3.5**	**51.8**	**818.3**	**972.3**	**1.19**
13	**0.05403**	**0.00071**	**0.37592**	**0.00521**	**0.05046**	**0.00057**	**0.82**	**372.2**	**29.61**	**317.4**	**3.48**	**324**	**3.85**	**17.7**	**361.0**	**76.3**	**0.21**
14	**0.05299**	**0.00084**	**0.36484**	**0.00591**	**0.04994**	**0.00057**	**0.70**	**328.3**	**35.28**	**314.2**	**3.5**	**315.8**	**4.4**	**8.9**	**178.6**	**53.3**	**0.30**
15	0.0532	0.00067	0.33786	0.00449	0.04607	0.00052	0.85	337.1	28.15	290.3	3.18	295.5	3.41	33.8	784.6	59.4	0.08
16	**0.05439**	**0.00077**	**0.37223**	**0.00547**	**0.04964**	**0.00056**	**0.77**	**387.1**	**31.32**	**312.3**	**3.44**	**321.3**	**4.05**	**18.3**	**389.2**	**34.1**	**0.09**
17	0.05237	0.00075	0.37995	0.00563	0.05262	0.00059	0.76	301.8	32.17	330.6	3.64	327	4.14	18.4	354.2	89.4	0.25
18	**0.05434**	**0.0007**	**0.37394**	**0.00505**	**0.04992**	**0.00056**	**0.83**	**385**	**28.61**	**314**	**3.43**	**322.6**	**3.73**	**26.1**	**526.1**	**149.2**	**0.28**
19	**0.05409**	**0.00099**	**0.37539**	**0.00696**	**0.05034**	**0.00058**	**0.62**	**374.6**	**40.67**	**316.6**	**3.57**	**323.6**	**5.14**	**6.2**	**121.1**	**42.4**	**0.35**
20	**0.05364**	**0.00068**	**0.36847**	**0.00491**	**0.04983**	**0.00056**	**0.84**	**355.8**	**28.36**	**313.5**	**3.42**	**318.5**	**3.65**	**44.5**	**921.3**	**157.3**	**0.17**
21	**0.05459**	**0.00066**	**0.37308**	**0.00479**	**0.04958**	**0.00055**	**0.86**	**395.3**	**26.8**	**311.9**	**3.39**	**321.9**	**3.54**	**114.6**	**2097.0**	**1320.9**	**0.63**
22	**0.05499**	**0.00075**	**0.38028**	**0.00538**	**0.05017**	**0.00056**	**0.79**	**411.6**	**29.81**	**315.5**	**3.45**	**327.2**	**3.96**	**16.6**	**339.1**	**58.7**	**0.17**
23	0.05691	0.00078	0.39314	0.00561	0.05011	0.00056	0.78	487.5	30.37	315.2	3.45	336.7	4.09	24.1	397.2	389.4	0.98
24	0.05261	0.00069	0.34115	0.0047	0.04704	0.00053	0.82	311.9	29.7	296.3	3.24	298	3.56	26.4	512.5	302.5	0.59
25	0.05363	0.00072	0.42213	0.00593	0.0571	0.00064	0.80	355.4	30.2	357.9	3.9	357.6	4.23	22.9	419.6	56.1	0.13
26	**0.05438**	**0.00077**	**0.37785**	**0.00553**	**0.0504**	**0.00057**	**0.77**	**386.9**	**31.38**	**317**	**3.47**	**325.5**	**4.08**	**26.0**	**549.5**	**32.8**	**0.06**
27	**0.05329**	**0.00072**	**0.36864**	**0.00516**	**0.05018**	**0.00056**	**0.80**	**341.2**	**30.04**	**315.6**	**3.44**	**318.6**	**3.83**	**35.9**	**676.6**	**312.1**	**0.46**
28	0.05231	0.00071	0.3954	0.00555	0.05483	0.00061	0.79	299.1	30.47	344.1	3.74	338.3	4.04	30.7	554.3	206.7	0.37

PONT-26: isotropic leucogranite

Zircon analyses	Isotope ratios							Ages						Concentrations (ppm)			Th/U
	Pb^{207}/Pb^{206}	1σ	Pb^{207}/U^{235}	1σ	Pb^{206}/U^{238}	1σ	rho	Pb^{207}/Pb^{206}	1σ	Pb^{206}/U^{238}	1σ	Pb^{207}/U^{235}	1σ	Pb	U	Th	
1a	0.05937	0.00065	0.63882	0.00752	0.07804	0.00086	0.94	580.8	23.66	484.4	5.12	501.6	4.66	110.7	1372.1	512.7	0.37
3	0.05435	0.00061	0.3352	0.00405	0.04474	0.00049	0.91	385.3	25.26	282.1	3.03	293.5	3.08	55.2	1319.4	85.3	0.06
4b	0.06449	0.00078	0.79509	0.01014	0.08943	0.00099	0.87	757.8	25.27	552.1	5.84	594.1	5.74	25.1	266.8	105.4	0.39
5	0.0593	0.00072	0.43482	0.00554	0.05319	0.00059	0.87	578.2	26.01	334.1	3.59	366.6	3.92	32.8	651.7	35.7	0.05
7	0.05698	0.00062	0.59268	0.0069	0.07545	0.00083	0.94	490.1	23.96	468.9	4.96	472.6	4.4	116.2	1673.8	29.8	0.02
8	0.05209	0.0006	0.33755	0.00413	0.04701	0.00052	0.90	289.2	26.04	296.1	3.18	295.3	3.14	44.3	936.6	282.2	0.30
8b	**0.05338**	**0.0006**	**0.36532**	**0.00435**	**0.04964**	**0.00054**	**0.91**	**345**	**24.99**	**312.3**	**3.34**	**316.2**	**3.24**	**32.3**	**611.0**	**149.8**	**0.25**
8c	0.05418	0.00064	0.3345	0.00415	0.04478	0.00049	0.88	378.5	26.35	282.4	3.03	293	3.16	28.3	579.2	177.7	0.31
8d	**0.05432**	**0.00061**	**0.36868**	**0.00438**	**0.04923**	**0.00054**	**0.92**	**384.1**	**24.94**	**309.8**	**3.31**	**318.7**	**3.25**	**35.1**	**669.5**	**162.1**	**0.24**
8e	0.05394	0.00067	0.32589	0.00426	0.04383	0.00049	0.86	368.20	27.72	276.50	3.00	286.40	3.26	97.2	1354.0	328.5	0.24
10	0.05984	0.00065	0.48615	0.00571	0.05893	0.00065	0.94	597.7	23.51	369.1	3.94	402.3	3.9	298.6	5470.7	28.4	0.01
11a	0.0618	0.00079	0.65189	0.0087	0.07651	0.00085	0.83	667.3	27.01	475.2	5.08	509.6	5.35	26.2	360.9	24.4	0.07
11b	0.05563	0.00065	0.41266	0.0051	0.0538	0.00059	0.89	437.4	25.15	337.8	3.63	350.8	3.66	65.5	1328.5	10.1	0.01
12	0.05587	0.00063	0.46696	0.00563	0.06063	0.00067	0.92	446.7	24.45	379.5	4.05	389.1	3.9	64.5	1161.4	4.8	0.00
13a	0.05586	0.00091	0.56152	0.00936	0.07291	0.00083	0.68	446.5	35.47	453.7	4.96	452.5	6.08	10.7	149.3	30.9	0.21
13b	0.05414	0.00062	0.39371	0.00481	0.05274	0.00058	0.90	376.9	25.74	331.3	3.56	337.1	3.51	51.1	1061.9	5.8	0.01
14	0.06052	0.00079	0.63075	0.00861	0.07559	0.00084	0.81	622.3	27.91	469.8	5.04	496.6	5.36	59.4	776.8	243.9	0.31
15	0.05739	0.00064	0.37656	0.00449	0.04759	0.00052	0.92	506.2	24.28	299.7	3.22	324.5	3.31	202.9	4592.2	56.8	0.01
16	0.0692	0.0008	1.14019	0.01401	0.11952	0.00132	0.90	904.6	23.57	727.8	7.6	772.6	6.65	55.4	436.2	186.1	0.43
17a	0.05477	0.00062	0.34442	0.00416	0.04562	0.0005	0.91	402.6	24.81	287.6	3.1	300.5	3.14	207.9	4843.7	572.8	0.12
17b	0.05745	0.00065	0.35926	0.00436	0.04536	0.0005	0.91	508.4	24.7	286	3.08	311.7	3.26	230.8	5492.3	74.9	0.01
19a	0.05991	0.00072	0.5668	0.00723	0.06863	0.00076	0.87	600.3	25.84	427.9	4.58	455.9	4.68	78.8	1089.4	471.3	0.43
19b	0.05758	0.0007	0.55354	0.00712	0.06973	0.00077	0.86	513.4	26.16	434.6	4.65	447.3	4.65	68.2	935.0	403.3	0.43
21	0.0598	0.0007	0.59395	0.00744	0.07205	0.0008	0.89	596.3	25.31	448.5	4.79	473.4	4.74	106.9	1429.7	508.8	0.36
22	0.05403	0.00065	0.3454	0.00438	0.04637	0.00051	0.87	372.3	26.86	292.2	3.16	301.3	3.31	125.6	2975.6	2.5	0.00
23a	0.06558	0.00073	0.8344	0.0099	0.09229	0.00101	0.92	792.9	23.1	569.1	5.98	616.1	5.48	36.1	364.5	77.3	0.21
27a	0.06617	0.0007	1.02887	0.01179	0.11279	0.00123	0.95	811.7	22.12	688.9	7.15	718.4	5.9	66.8	537.7	174.5	0.32
27b	0.05551	0.0006	0.36858	0.00427	0.04817	0.00053	0.95	432.4	23.79	303.3	3.24	318.6	3.17	82.8	1599.0	480.2	0.30
28	0.05826	0.00063	0.48612	0.00563	0.06053	0.00066	0.94	538.8	24.06	378.8	4.03	402.3	3.85	60.4	950.7	99.5	0.10
29	0.05935	0.00069	0.76835	0.00951	0.0939	0.00103	0.89	580.1	25.2	578.6	6.08	578.8	5.46	21.5	209.1	73.6	0.35
31	0.05264	0.00063	0.36355	0.0046	0.0501	0.00055	0.87	313.3	27.04	315.1	3.38	314.9	3.42	13.6	248.3	90.4	0.36
31	**0.05264**	**0.00063**	**0.36355**	**0.0046**	**0.0501**	**0.00055**	**0.87**	**313.3**	**27.04**	**315.1**	**3.38**	**314.9**	**3.42**	**13.6**	**248.3**	**90.4**	**0.36**
34	0.0611	0.0007	0.8552	0.01035	0.10152	0.00111	0.90	642.9	24.33	623.3	6.51	627.5	5.66	34.8	305.4	129.5	0.42
35	0.0569	0.00064	0.34349	0.00412	0.04379	0.00048	0.91	486.9	25.03	276.3	2.96	299.8	3.12	73.3	1661.8	23.6	0.01

38a	0.12178	0.00148	5.97572	0.07631	0.35592	0.00395	0.87	1982.5	21.56	1962.8	18.76	1972.3	11.11	10.2	20.7	22.6	1.09
38b	0.05396	0.00061	0.35266	0.00423	0.04741	0.00052	0.91	369.1	25.36	298.6	3.19	306.7	3.17	87.2	1834.8	56.8	0.03
39	**0.05383**	**0.00062**	**0.36239**	**0.00442**	**0.04884**	**0.00053**	**0.89**	**363.6**	**25.9**	**307.4**	**3.28**	**314**	**3.3**	**45.6**	**786.2**	**482.9**	**0.61**
39b	0.05529	0.00064	0.36307	0.00446	0.04763	0.00052	0.89	423.8	25.48	300	3.22	314.5	3.32	90.0	1738.8	1020.8	0.59
39d	0.05712	0.00069	0.37303	0.00476	0.04737	0.00052	0.86	495.50	26.60	298.40	3.23	321.90	3.52	101.1	1185.8	637.9	0.54
39e	0.05771	0.0007	0.36256	0.00467	0.04557	0.00051	0.87	518.50	26.73	287.30	3.12	314.10	3.48	75.1	933.7	420.6	0.45
41b	0.05974	0.00073	0.62155	0.00808	0.07547	0.00084	0.86	594.00	26.44	469.00	5.02	490.80	5.06	81.8	659.6	136.9	0.21
42	**0.05409**	**0.00062**	**0.35965**	**0.00437**	**0.04823**	**0.00053**	**0.90**	**374.8**	**25.32**	**303.6**	**3.24**	**312**	**3.27**	**81.6**	**1699.4**	**7.2**	**0.00**
42c	0.05744	0.00071	0.66747	0.00872	0.08428	0.00094	0.85	508.20	26.81	521.60	5.56	519.20	5.31	54.6	381.2	104.8	0.27
44a	0.05272	0.00062	0.35778	0.00448	0.04923	0.00054	0.88	316.5	26.57	309.8	3.35	310.6	3.35	13.7	2780.6	3.2	0.00
44a	**0.05272**	**0.00062**	**0.35778**	**0.00448**	**0.04923**	**0.00054**	**0.88**	**316.5**	**26.57**	**309.8**	**3.35**	**310.6**	**3.35**	**13.7**	**2780.6**	**3.2**	**0.00**
44b	0.06042	0.00078	0.80506	0.01085	0.09665	0.00108	0.83	618.7	27.51	594.7	6.33	599.7	6.1	6.7	319.1	204.9	0.64
45	0.05717	0.00071	0.39396	0.00518	0.04999	0.00056	0.85	497.50	27.48	314.40	3.41	337.30	3.78	99.0	1275.1	50.4	0.04
45	0.05717	0.00071	0.39396	0.00518	0.04999	0.00056	0.85	497.50	27.48	314.40	3.41	337.30	3.78	99.0	1275.1	50.4	0.04

Analyses Lu- Hf sur zircon - article #3

Results of magmatic zircon Lu-Hf isotope analyses

Facies	**Sample**	**zircon**	**$^{176}Yb/^{177}Hf$ [a]**	**±2s**	**$^{176}Lu/^{177}Hh$ [a]**	**±2s**	**$^{178}Hf/^{177}Hf$**	**$^{180}Hf/^{177}Hf$**	**Sig_{Hf} [b] (V)**	**$^{176}Hf/^{177}Hf$**	**±2s [c]**	**$^{176}Hf/^{177}Hf_{(t)}$ [d]**	**$eHf_{(t)}$ [d]**	**±2s [c]**	**T_{DM2} [e] (Ga)**	**age [*](Ma)**	**±2s**
Quartz-monzodiorite	PONT-7	1	0.0366	7	0.00115	2	1.46720	1.88646	9	0.282602	30	0.282596	0.3	1.1	1.23	315.2	2.9
		10	0.0314	29	0.00103	9	1.46720	1.88546	10	0.282569	31	0.282563	-0.9	1.1	1.29	315.2	2.9
		12	0.0444	30	0.00140	9	1.46715	1.88596	8	0.282611	28	0.282603	0.6	1.0	1.21	315.2	2.9
		13	0.0947	37	0.00279	10	1.46716	1.88618	7	0.282663	33	0.282647	2.1	1.2	1.13	315.2	2.9
		15	0.0444	23	0.00140	7	1.46719	1.88575	8	0.282630	32	0.282622	1.3	1.1	1.18	315.2	2.9
		17	0.0189	22	0.00061	6	1.46716	1.88684	11	0.282564	30	0.282561	-0.9	1.1	1.30	315.2	2.9
		20	0.0281	19	0.00092	5	1.46712	1.88595	9	0.282556	34	0.282551	-1.3	1.2	1.32	315.2	2.9
Monzogranite	PONT-22	1	0.0303	9	0.00098	3	1.46719	1.88626	11	0.282526	28	0.282520	-2.3	1.0	1.37	315.5	2.0
		2	0.0605	87	0.00176	27	1.46737	1.88099	7	0.282583	45	0.282572	-0.5	1.6	1.27	315.5	2.0
		4	0.0446	30	0.00141	9	1.46719	1.88706	8	0.282583	33	0.282574	-0.4	1.2	1.27	315.5	2.0
		5	0.0473	21	0.00148	7	1.46715	1.88661	8	0.282552	30	0.282543	-1.5	1.1	1.33	315.5	2.0
		6	0.0309	29	0.00091	9	1.46709	1.88823	9	0.282553	34	0.282547	-1.4	1.2	1.32	315.5	2.0
		8	0.0339	20	0.00105	6	1.46716	1.88627	8	0.282547	32	0.282540	-1.6	1.1	1.34	315.5	2.0
		10	0.0217	9	0.00067	3	1.46720	1.88716	9	0.282527	30	0.282523	-2.2	1.1	1.37	315.5	2.0
		12	0.0396	28	0.00120	9	1.46710	1.88686	7	0.282564	35	0.282556	-1.1	1.2	1.30	315.5	2.0
		14	0.0227	24	0.00070	8	1.46720	1.88785	8	0.282568	38	0.282564	-0.8	1.3	1.29	315.5	2.0
		18	0.0244	21	0.00081	7	1.46712	1.88744	8	0.282562	32	0.282557	-1.0	1.1	1.30	315.5	2.0
		21	0.0530	50	0.00161	15	1.46708	1.88589	8	0.282555	30	0.282546	-1.4	1.1	1.33	315.5	2.0
		22	0.0219	21	0.00065	7	1.46725	1.88748	9	0.282526	30	0.282522	-2.3	1.0	1.37	315.5	2.0
		26	0.0255	20	0.00081	7	1.46716	1.88678	11	0.282527	29	0.282523	-2.3	1.0	1.37	315.5	2.0
		27	0.0229	4	0.00080	1	1.46717	1.88650	8	0.282566	30	0.282561	-0.9	1.1	1.30	315.5	2.0
Porphyritic leucogranite	PONT-1	5	0.0222	24	0.00070	8	1.46724	1.88620	7	0.282537	29	0.282533	-1.9	1.0	1.35	316.7	2.5
		16	0.0253	15	0.00079	5	1.46724	1.88614	9	0.282573	36	0.282568	-0.6	1.3	1.28	316.7	2.5
		16b	0.0238	19	0.00072	7	1.46714	1.88734	12	0.282560	30	0.282556	-1.1	1.1	1.31	316.7	2.5
		22	0.0736	68	0.00248	24	1.46716	1.88687	7	0.282719	32	0.282704	4.2	1.1	1.02	316.7	2.5
		24	0.0220	7	0.00061	2	1.46721	1.88629	7	0.282700	34	0.282697	3.9	1.2	1.03	316.7	2.5

		24b	0.0238	16	0.00069	4	1.46710	1.88652	7	0.282737	33	0.282733	5.2	1.2	0.96	316.7	2.5
		27	0.0466	41	0.00138	12	1.46713	1.88633	10	0.282536	29	0.282528	-2.0	1.0	1.36	316.7	2.5
		41	0.0142	41	0.00038	11	1.46719	1.88739	8	0.282513	41	0.282510	-2.7	1.4	1.39	316.7	2.5
		49	0.0377	14	0.00109	2	1.46710	1.88526	8	0.282567	37	0.282561	-0.9	1.3	1.30	316.7	2.5
Langonnet leucogranite	PONT-20	28	0.0089	12	0.00029	5	1.46721	1.88647	9	0.282621	32	0.282619	0.9	1.1	1.19	304.7	2.7
Isotropic leucogranite	PONT-26	8	0.0202	4	0.00056	1	1.46723	1.88499	7	0.282559	52	0.282556	-1.2	1.8	1.31	310.3	4.7
		31	0.0383	14	0.00114	4	1.46717	1.88636	10	0.282605	33	0.282599	0.3	1.2	1.22	310.3	4.7
		39a	0.0479	61	0.00144	18	1.46715	1.88673	7	0.282665	29	0.282656	2.4	1.0	1.11	310.3	4.7
		39b	0.0385	50	0.00116	15	1.46720	1.88705	9	0.282633	31	0.282626	1.3	1.1	1.17	310.3	4.7
		44a	0.0348	8	0.00107	2	1.46718	1.88609	10	0.282515	35	0.282509	-2.9	1.2	1.40	310.3	4.7

Results of inherited zircon Lu-Hf isotope analyses

Facies	Sample	Zircon	$^{176}Yb/^{177}Hf$ [a]	±2s	$^{176}Lu/^{177}Hf$ [a]	±2s	$^{178}Hf/^{177}Hf$	$^{180}Hf/^{177}Hf$	Sig_{Hf} [b] (V)	$^{176}Hf/^{177}Hf$	±2s [c]	$^{176}Hf/^{177}Hf_{(t)}$ [d]	$eHf_{(t)}$ [d]	±2s [c]	T_{DM2} [e] (Ga)	age [f] (Ma)	±2s	Conc. (%)
Porphyritic leucogranite	PONT-1	33	0.0249	3	0.00080	1	1.46722	1.88699	8	0.282621	30	0.282612	7.7	1.1	1.06	620	7	105
	PONT-1	32	0.0294	11	0.00087	4	1.46723	1.88719	9	0.282056	36	0.282047	-13.3	1.3	2.18	576	7	101
	PONT-1	15	0.0612	13	0.00193	4	1.46711	1.88668	8	0.282679	36	0.282667	3.4	1.3	1.08	342	4	99
	PONT-1	39	0.0508	36	0.00160	12	1.46711	1.88624	7	0.282589	34	0.282570	6.4	1.2	1.14	630	7	100
	PONT-1	40	0.1607	61	0.00563	18	1.46716	1.88642	13	0.282653	31	0.282611	2.7	1.1	1.16	395	4	101
	PONT-1	3	0.0427	15	0.00124	4	1.46711	1.88698	6	0.282601	38	0.282586	7.9	1.4	1.09	668	8	102
	PONT-1	23	0.0241	7	0.00087	2	1.46720	1.88517	9	0.282641	31	0.282631	8.0	1.1	1.03	602	7	104
	PONT-1	28	0.0382	53	0.00129	16	1.46712	1.88673	7	0.282600	35	0.282587	4.8	1.2	1.15	529	6	101
Langonnet leucogranite	PONT-20	2a	0.0617	14	0.00211	5	1.46720	1.88643	7	0.282630	30	0.282603	8.4	1.1	1.06	662	7	103
	PONT-20	16	0.0324	7	0.00102	2	1.46721	1.88547	8	0.282540	44	0.282529	3.4	1.6	1.25	558	6	102
	PONT-20	3	0.0107	17	0.00032	3	1.46714	1.88670	10	0.282487	34	0.282484	-0.4	1.2	1.38	458	5	101
	PONT-20	5a	0.0189	7	0.00063	2	1.46717	1.88678	7	0.281071	34	0.281043	-9.0	1.2	3.32	2322	22	107
	PONT-20	27	0.0096	11	0.00030	4	1.46721	1.88662	9	0.282557	34	0.282555	-0.1	1.2	1.29	361	4	101
	PONT-20	26	0.0094	6	0.00026	2	1.46717	1.88597	13	0.282593	33	0.282590	7.0	1.2	1.10	620	7	101
	PONT-20	9a	0.0420	6	0.00135	2	1.46718	1.88720	11	0.281428	36	0.281383	-10.3	1.3	2.93	1745	17	106
	PONT-20	10	0.0191	7	0.00062	2	1.46720	1.88708	10	0.282119	31	0.282109	-4.6	1.1	1.93	866	9	104
	PONT-20	11	0.0290	14	0.00089	5	1.46705	1.88721	8	0.282501	32	0.282489	5.2	1.1	1.26	703	8	100
	PONT-20	13	0.0353	35	0.00089	9	1.46720	1.88478	6	0.282621	41	0.282615	1.9	1.4	1.17	358	4	108
	PONT-20	33a	0.0940	39	0.00282	11	1.46718	1.88675	7	0.282609	36	0.282580	4.7	1.3	1.16	537	6	102
	PONT-20	34	0.0710	19	0.00221	5	1.46721	1.88640	9	0.282576	37	0.282552	4.3	1.3	1.20	561	6	102
	PONT-20	15b	0.0137	17	0.00035	3	1.46717	1.88706	8	0.282527	34	0.282524	1.1	1.2	1.30	465	5	101
	PONT-20	15a	0.0143	10	0.00038	2	1.46720	1.88517	9	0.282550	32	0.282547	0.3	1.1	1.29	392	4	104
	PONT-20	17b	0.0296	28	0.00087	8	1.46711	1.88686	7	0.281615	36	0.281583	0.5	1.3	2.47	1903	18	104
	PONT-20	36	0.0373	24	0.00100	6	1.46717	1.88667	9	0.282562	31	0.282554	2.0	1.1	1.25	458	5	101
	PONT-20	16a	0.0271	17	0.00080	5	1.46709	1.88649	10	0.282371	38	0.282363	-1.9	1.3	1.56	584	6	101
	PONT-20	35	0.0554	56	0.00142	11	1.46726	1.88022	7	0.282544	52	0.282531	2.2	1.9	1.27	503	5	102
	PONT-20	38	0.0454	15	0.00158	6	1.46717	1.88554	5	0.282717	36	0.282703	7.3	1.3	0.96	455	5	101
	PONT-20	41	0.0214	12	0.00062	2	1.46707	1.88689	8	0.282384	35	0.282377	-1.6	1.2	1.54	576	6	105
	PONT-20	42	0.0163	10	0.00054	5	1.46708	1.88786	10	0.281402	76	0.281383	-8.3	2.7	2.89	1832	18	106
Isotropic leucogranite	PONT-26	1a	0.0570	43	0.00167	12	1.46713	1.88722	8	0.282639	32	0.282624	5.1	1.1	1.10	484	5	104
	PONT-26	27a	0.0155	17	0.00048	4	1.46712	1.88722	9	0.282519	33	0.282513	5.8	1.2	1.22	689	7	104
	PONT-26	4b	0.0190	10	0.00063	3	1.46721	1.88508	7	0.282678	32	0.282672	8.3	1.1	0.97	552	6	108
	PONT-26	28	0.0465	57	0.00151	15	1.46711	1.88626	5	0.282529	40	0.282518	-1.0	1.4	1.35	379	4	106
	PONT-26	29	0.0288	10	0.00090	3	1.46722	1.88705	8	0.282490	31	0.282480	2.1	1.1	1.34	579	6	100
	PONT-26	11a	0.0321	20	0.00110	8	1.46711	1.88514	6	0.282565	37	0.282556	2.5	1.3	1.24	475	5	107
	PONT-26	12	0.0432	22	0.00160	8	1.46723	1.88641	10	0.282535	31	0.282523	-0.8	1.1	1.34	380	4	103
	PONT-26	13a	0.0211	32	0.00072	12	1.46719	1.88704	9	0.282595	41	0.282589	3.2	1.5	1.18	454	5	100

PONT-26	16	0.0175	13	0.00059	3	1.46710	1.88635	9	0.282488	32	0.282480	5.5	1.1	1.27	728	8	106
PONT-26	34	0.0327	16	0.00109	6	1.46717	1.88835	9	0.282283	42	0.282270	-4.3	1.5	1.73	623	7	101
PONT-26	19	0.0338	25	0.00113	9	1.46721	1.88666	10	0.282682	30	0.282673	5.7	1.1	1.03	435	5	103
PONT-26	38a	0.0142	6	0.00039	2	1.46717	1.88593	8	0.281379	36	0.281364	-5.9	1.3	2.87	1963	19	100
PONT-26	21	0.0325	19	0.00112	6	1.46716	1.88720	9	0.282109	40	0.282100	-14.3	1.4	2.13	449	5	106
PONT-26	42c	0.0536	37	0.00188	14	1.46711	1.88671	9	0.282529	32	0.282511	1.9	1.1	1.30	522	6	100
PONT-26	43b	0.0180	9	0.00063	3	1.46716	1.88649	9	0.281293	42	0.281277	-22.8	1.5	3.31	1364	14	128
PONT-26	44b	0.0404	14	0.00132	4	1.46717	1.88628	7	0.282626	38	0.282612	7.1	1.4	1.07	595	6	101
PONT-26	41b	0.0389	24	0.00128	9	1.46725	1.88564	8	0.282707	46	0.282696	7.3	1.6	0.97	469	5	105

(a) $^{176}Yb/^{177}Hf = (^{176}Yb/^{173}Yb)_{true} \times (^{173}Yb/^{177}Hf)_{meas} \times (M_{173(Yb)}/M_{177(Hf)})^{\beta(Hf)}$, $\beta(Hf) = \ln(^{179}Hf/^{177}Hf \text{ true} / {}^{179}Hf/^{177}Hf_{measured}) / \ln(M_{179(Hf)}/M_{177(Hf)})$, M=mass of respective isotope. The $^{176}Lu/^{177}Hf$ were calculated in a similar way by using the $^{175}Lu/^{177}Hf$ and β (Yb). Quoted uncertainties (absolute) relate to the last quoted figure. The effect of the inter-element fractionation on the Lu/Hf was estimated to be about 6 % or less based on analyses of the GJ-1 and Plesoviče zircons. (b) Mean Hf signal in volt. (c) Uncertainties are quadratic additions of the within-run precision and the daily reproducibility of the zircon GJ-1. Uncertainties for GJ-1 is 2SD (2 standard deviation). (d) Initial $^{176}Hf/^{177}Hf$ and εHf calculated using the age (Ma), and the CHUR parameters: $^{176}Lu/^{177}Hf = 0.0336$, and $^{176}Hf/^{177}Hf = 0.282785$ (Bouvier et al., 2008). (e) two stage model age in billion years using the measured $^{176}Lu/^{177}Lu$, the estimated age (Ma), a value of 0.01113 for the average coninental crust (second stage), and a depleted mantle $^{176}Lu/^{177}Hf$ and $^{176}Hf/^{177}Hf$ of 0.03933 and 0.283294 (Blichert-Toft and Puchtel, 2010). (f) $^{206}Pb/^{238}U$ age for zircon <1.0 Ga, and $^{206}Pb/^{207}Pb$ age for zircon >1.0 Ga. *-intrusion age

Analyses U-Pb sur oxydes d'uranium - article #4

U-Pb isotopic data for uranium oxides from the Pen Ar Ran (PAR) and the Métairie Neuve (MN) deposits. Data in italic represents the analyses not used for the calculation of the concordia or the lower intercept ages.

		Analytical	Uncorrected ratio		Common Pb corrected ratio						Correl.	Common Pb corrected ages					
Sample	**position**	**point**	**$^{204}Pb/^{206}Pb$**	**±**	**$^{207}Pb/^{206}Pb$**	**±**	**$^{207}Pb/^{235}U$**	**±**	**$^{206}Pb/^{238}U$**	**±**	**Err.**	**$^{207}Pb/^{206}Pb$**	**±**	**$^{206}Pb/^{238}U$**	**±**	**$^{207}Pb/^{235}U$**	**±**
PAR-spherulitic	**core**	2	0.0099	0.0000	0.0532	0.0009	0.3612	0.0082	0.0493	0.0007	0.62	329.8	3.8	310.1	4.3	313.1	6.1
	core	3	0.0108	0.0000	0.0529	0.0009	0.3476	0.0083	0.0477	0.0008	0.66	317.7	3.2	300.2	4.7	302.9	6.2
	core	4	0.0119	0.0000	0.0510	0.0011	0.3380	0.0082	0.0480	0.0005	0.40	235.3	2.7	302.5	2.9	295.7	6.2
	core	5	0.0156	0.0001	0.0534	0.0016	0.3481	0.0120	0.0473	0.0008	0.48	338.8	3.3	297.9	4.8	303.3	9.0
	core	6	0.0160	0.0001	0.0522	0.0018	0.3324	0.0138	0.0462	0.0010	0.54	289.3	4.1	290.9	6.4	291.4	10.5
	core	7	0.0156	0.0001	0.0532	0.0016	0.3457	0.0126	0.0471	0.0010	0.57	332.6	2.2	296.7	6.0	301.5	9.4
	core	8	0.0149	0.0001	0.0515	0.0018	0.3290	0.0134	0.0464	0.0009	0.49	254.4	2.3	292.2	5.7	288.8	10.2
	core	9	0.0181	0.0001	0.0538	0.0023	0.3432	0.0161	0.0463	0.0008	0.37	355.6	1.9	291.7	4.9	299.6	12.1
	core	10	0.0179	0.0001	0.0530	0.0018	0.3389	0.0152	0.0464	0.0014	0.68	322.3	2.7	292.2	8.6	296.3	11.4
	core	11	0.0179	0.0001	0.0523	0.0017	0.3319	0.0141	0.0460	0.0013	0.67	293.9	2.8	289.9	8.1	291.0	10.7
	core	12	0.0157	0.0001	0.0498	0.0027	0.3125	0.0181	0.0455	0.0010	0.37	177.5	2.6	287.1	6.1	276.1	13.9
	core	13	0.0152	0.0001	0.0533	0.0020	0.3388	0.0148	0.0461	0.0011	0.53	335.1	3.3	290.5	6.5	296.3	11.1
	core	14	0.0157	0.0001	0.0541	0.0021	0.3476	0.0141	0.0466	0.0006	0.34	369.8	2.6	293.5	4.0	302.9	10.6
	core	15	0.0177	0.0001	0.0529	0.0018	0.3352	0.0160	0.0460	0.0015	0.69	316.1	2.2	289.9	9.3	293.5	12.1
	rim	*16*	*0.0046*	*0.0000*	*0.0533*	*0.0009*	*0.3150*	*0.0062*	*0.0429*	*0.0004*	*0.47*	*333.6*	*4.6*	*270.6*	*2.4*	*278.1*	*4.7*
	rim	*17*	*0.0049*	*0.0000*	*0.0525*	*0.0009*	*0.3243*	*0.0067*	*0.0448*	*0.0005*	*0.49*	*297.4*	*4.8*	*282.7*	*2.8*	*285.2*	*5.1*
	core	18	0.0189	0.0001	0.0494	0.0014	0.3088	0.0124	0.0454	0.0013	0.70	158.3	1.7	286.0	7.9	273.3	9.6
	core	19	0.0186	0.0001	0.0541	0.0029	0.3413	0.0207	0.0458	0.0013	0.47	367.9	2.7	288.5	8.0	298.2	15.5
PAR-pseudo-spherulitic		1	0.0053	0.0000	0.0514	0.0008	0.3028	0.0052	0.0428	0.0004	0.52	251.7	4.1	269.9	2.4	268.6	4.1
		2	0.0038	0.0000	0.0519	0.0008	0.3121	0.0053	0.0436	0.0003	0.46	276.9	3.6	275.1	2.1	275.8	4.1
		3	0.0037	0.0000	0.0516	0.0004	0.3075	0.0034	0.0432	0.0003	0.67	264.0	3.1	272.6	1.9	272.3	2.6

	4	0.0036	0.0000	0.0531	0.0009	0.3187	0.0057	0.0435	0.0003	0.40	329.7	3.2	274.5	1.9	280.9	4.4
	5	0.0037	0.0000	0.0515	0.0006	0.3091	0.0044	0.0435	0.0003	0.50	257.4	4.0	274.7	1.9	273.5	3.4
	6	0.0035	0.0000	0.0535	0.0008	0.3201	0.0053	0.0434	0.0004	0.51	345.5	4.3	273.8	2.3	281.9	4.0
	7	0.0035	0.0000	0.0525	0.0008	0.3146	0.0056	0.0435	0.0004	0.51	300.2	4.0	274.4	2.5	277.7	4.3
	8	0.0034	0.0000	0.0520	0.0005	0.3098	0.0044	0.0432	0.0005	0.78	280.2	3.4	272.7	3.0	274.0	3.4
	9	0.0034	0.0000	0.0518	0.0007	0.3074	0.0048	0.0430	0.0003	0.47	271.5	3.1	271.6	2.0	272.2	3.7
	10	0.0036	0.0000	0.0509	0.0006	0.3060	0.0045	0.0436	0.0003	0.53	233.1	3.7	274.9	2.1	271.1	3.5
	11	0.0035	0.0000	0.0524	0.0007	0.3130	0.0051	0.0433	0.0004	0.57	299.4	3.5	273.2	2.5	276.5	4.0
	12	0.0036	0.0000	0.0518	0.0006	0.3090	0.0044	0.0433	0.0004	0.62	272.3	2.2	273.0	2.3	273.4	3.4
	13	0.0051	0.0001	0.0526	0.0012	0.3137	0.0076	0.0432	0.0004	0.37	307.5	4.5	272.8	2.4	277.0	5.8
	14	0.0050	0.0001	0.0527	0.0011	0.3115	0.0073	0.0429	0.0004	0.37	310.5	4.9	270.6	2.3	275.3	5.6
	15	0.0052	0.0000	0.0520	0.0005	0.3078	0.0042	0.0429	0.0004	0.69	280.8	3.6	270.9	2.5	272.5	3.2
	16	0.0050	0.0000	0.0528	0.0007	0.3126	0.0051	0.0429	0.0004	0.53	315.3	3.1	271.0	2.3	276.2	3.9
	17	0.0049	0.0000	0.0523	0.0009	0.3093	0.0058	0.0429	0.0003	0.40	294.3	3.1	270.6	2.0	273.7	4.5
	18	0.0052	0.0000	0.0522	0.0007	0.3072	0.0050	0.0427	0.0004	0.52	286.3	2.9	269.7	2.3	272.0	3.9
	19	0.0055	0.0000	0.0514	0.0008	0.3058	0.0055	0.0432	0.0003	0.44	251.3	3.2	272.5	2.1	270.9	4.3
	20	0.0053	0.0001	0.0513	0.0010	0.3033	0.0063	0.0428	0.0004	0.42	250.5	3.7	270.4	2.3	269.0	4.9
	21	0.0052	0.0000	0.0513	0.0007	0.3055	0.0048	0.0432	0.0004	0.53	247.5	3.5	272.8	2.2	270.7	3.8
	22	0.0052	0.0000	0.0522	0.0008	0.3113	0.0055	0.0432	0.0004	0.48	289.7	3.5	272.9	2.3	275.2	4.3
	23	0.0051	0.0000	0.0504	0.0006	0.3008	0.0042	0.0433	0.0003	0.56	207.3	2.3	273.2	2.1	267.0	3.3
PAR-prismatic	1	0.0093	0.0000	0.0527	0.0010	0.3163	0.0066	0.0435	0.0004	0.47	309.4	2.8	274.7	2.6	279.0	5.1
	2	0.0100	0.0001	0.0511	0.0016	0.3108	0.0103	0.0441	0.0004	0.29	236.9	4.6	278.5	2.6	274.8	8.0
	3	0.0096	0.0001	0.0525	0.0013	0.3129	0.0083	0.0432	0.0004	0.32	300.2	3.4	272.9	2.2	276.5	6.4
	4	0.0120	0.0001	0.0520	0.0015	0.3311	0.0102	0.0462	0.0004	0.30	278.9	3.3	291.0	2.6	290.4	7.7
	5	0.0102	0.0001	0.0523	0.0013	0.3191	0.0085	0.0443	0.0004	0.36	290.9	2.8	279.3	2.6	281.2	6.5
	6	0.0103	0.0001	0.0518	0.0012	0.3143	0.0081	0.0440	0.0004	0.36	271.4	4.0	277.5	2.5	277.5	6.2
	7	0.0104	0.0001	0.0511	0.0019	0.3133	0.0119	0.0445	0.0005	0.28	238.6	3.2	280.4	2.9	276.8	9.2
	8	0.0102	0.0001	0.0523	0.0012	0.3162	0.0081	0.0439	0.0005	0.45	290.3	2.0	276.8	3.1	279.0	6.2
	9	0.0103	0.0000	0.0516	0.0011	0.3172	0.0077	0.0446	0.0005	0.45	260.9	3.8	281.2	3.0	279.8	5.9
	10	0.0104	0.0001	0.0522	0.0013	0.3164	0.0087	0.0439	0.0005	0.42	288.5	3.3	277.2	3.1	279.2	6.7
	11	0.0104	0.0001	0.0527	0.0014	0.3167	0.0089	0.0436	0.0004	0.32	309.9	2.8	274.9	2.4	279.3	6.9
	12	0.0105	0.0001	0.0515	0.0017	0.3082	0.0109	0.0434	0.0006	0.37	256.5	3.4	273.9	3.5	272.8	8.4
	13	0.0101	0.0000	0.0507	0.0011	0.3043	0.0069	0.0435	0.0004	0.40	220.9	2.0	274.5	2.4	269.7	5.3
	14	0.0101	0.0001	0.0535	0.0014	0.3236	0.0094	0.0438	0.0005	0.37	345.0	2.7	276.5	2.9	284.6	7.2
	15	0.0103	0.0001	0.0523	0.0014	0.3163	0.0091	0.0439	0.0004	0.31	289.6	3.5	277.0	2.4	279.1	7.0
	16	0.0097	0.0001	0.0538	0.0018	0.3252	0.0117	0.0439	0.0006	0.39	353.6	4.2	276.8	3.8	285.9	8.9
	17	0.0098	0.0001	0.0532	0.0015	0.3181	0.0096	0.0434	0.0004	0.32	327.9	2.7	273.9	2.6	280.5	7.4
	18	0.0095	0.0001	0.0522	0.0020	0.3196	0.0128	0.0444	0.0005	0.29	285.3	5.0	280.3	3.2	281.6	9.8
	19	0.0098	0.0001	0.0522	0.0011	0.3128	0.0073	0.0435	0.0004	0.42	287.0	2.8	274.2	2.6	276.3	5.7
	20	*0.0071*	*0.0001*	*0.0517*	*0.0016*	*0.1699*	*0.0058*	*0.0239*	*0.0004*	*0.43*	*259.1*	*4.0*	*152.0*	*2.2*	*159.3*	*5.0*
	21	0.0095	0.0001	0.0540	0.0012	0.3299	0.0081	0.0443	0.0004	0.34	365.6	3.8	279.3	2.3	289.5	6.2
	22	0.0098	0.0000	0.0528	0.0009	0.3171	0.0060	0.0435	0.0003	0.42	314.2	3.4	274.7	2.1	279.7	4.6
	23	0.0097	0.0001	0.0534	0.0013	0.3229	0.0085	0.0439	0.0004	0.34	338.4	4.3	276.7	2.5	284.2	6.5
	24	0.0097	0.0001	0.0524	0.0024	0.3205	0.0158	0.0443	0.0008	0.37	297.4	5.1	279.6	5.0	282.3	12.0
	25	0.0097	0.0001	0.0521	0.0023	0.3152	0.0154	0.0439	0.0009	0.41	282.5	12.1	276.8	5.4	278.2	11.8
	26	0.0096	0.0001	0.0545	0.0021	0.3282	0.0134	0.0437	0.0006	0.33	384.2	9.9	275.7	3.6	288.2	10.2
	27	0.0098	0.0001	0.0504	0.0016	0.2951	0.0114	0.0424	0.0009	0.54	208.2	7.9	267.8	5.5	262.5	8.9
	28	0.0097	0.0001	0.0538	0.0017	0.3234	0.0117	0.0436	0.0007	0.45	354.4	8.4	275.2	4.3	284.5	8.9
	29	0.0096	0.0001	0.0525	0.0014	0.3180	0.0093	0.0440	0.0006	0.43	297.7	4.7	277.3	3.4	280.3	7.2
MN-metased. C.R.	2	0.0005	0.0000	0.0525	0.0005	0.3242	0.0038	0.0448	0.0003	0.61	301.2	11.5	282.6	2.0	285.1	2.9
	3	0.0007	0.0000	0.0514	0.0006	0.3178	0.0043	0.0448	0.0003	0.54	253.4	10.8	282.8	2.0	280.2	3.3

	4	0.0005	0.0000	0.0523	0.0006	0.3241	0.0047	0.0449	0.0004	0.61	294.8	10.4	283.3	2.4	285.1	3.6
	5	0.0015	0.0000	0.0525	0.0006	0.3284	0.0050	0.0454	0.0004	0.58	302.2	14.1	286.1	2.5	288.4	3.8
	6	0.0008	0.0000	0.0523	0.0004	0.3256	0.0045	0.0452	0.0005	0.80	292.9	11.0	284.7	3.0	286.2	3.4
	7	0.0007	0.0000	0.0521	0.0005	0.3279	0.0037	0.0457	0.0003	0.61	283.7	10.1	287.8	1.9	288.0	2.8
	8	0.0010	0.0000	0.0525	0.0004	0.3326	0.0039	0.0459	0.0004	0.73	303.0	6.8	289.5	2.4	291.6	2.9
	9	0.0010	0.0000	0.0524	0.0006	0.3250	0.0047	0.0450	0.0004	0.59	294.9	9.7	283.9	2.4	285.8	3.6
	10	0.0011	0.0000	0.0531	0.0007	0.3358	0.0054	0.0459	0.0005	0.65	326.5	9.8	289.1	2.9	293.9	4.1
	11	0.0011	0.0000	0.0522	0.0008	0.3284	0.0060	0.0456	0.0005	0.57	287.4	11.7	287.7	2.9	288.4	4.6
	12	0.0007	0.0000	0.0521	0.0005	0.3255	0.0038	0.0453	0.0003	0.63	285.6	9.6	285.4	2.1	286.1	2.9
	13	0.0008	0.0000	0.0520	0.0005	0.3230	0.0043	0.0450	0.0005	0.76	280.4	12.4	283.9	2.8	284.2	3.3
MN-granitic C.R.	1	0.0020	0.0000	0.0512	0.0004	0.3275	0.0039	0.0464	0.0004	0.72	245.1	4.9	292.1	2.4	287.6	3.0
	2	0.0019	0.0000	0.0523	0.0006	0.3281	0.0048	0.0455	0.0004	0.65	294.3	6.5	286.6	2.6	288.1	3.6
	3	0.0020	0.0000	0.0518	0.0007	0.3252	0.0056	0.0455	0.0005	0.58	270.6	10.2	287.1	2.8	285.9	4.2
	4	0.0020	0.0000	0.0516	0.0005	0.3268	0.0045	0.0460	0.0004	0.64	260.3	4.5	289.7	2.5	287.1	3.4
	5	0.0020	0.0000	0.0523	0.0005	0.3316	0.0037	0.0460	0.0003	0.56	293.4	3.7	289.8	1.8	290.8	2.8
	6	0.0020	0.0000	0.0530	0.0005	0.3315	0.0041	0.0453	0.0004	0.64	324.6	5.6	285.8	2.2	290.7	3.1
	7	0.0020	0.0000	0.0531	0.0005	0.3332	0.0044	0.0455	0.0004	0.64	326.8	3.7	287.0	2.4	292.0	3.4
	8	0.0020	0.0000	0.0525	0.0005	0.3295	0.0042	0.0455	0.0003	0.58	300.7	6.7	287.1	2.1	289.2	3.2
	9	0.0021	0.0000	0.0514	0.0008	0.3154	0.0057	0.0445	0.0004	0.48	252.9	14.8	280.7	2.4	278.4	4.4
	10	0.0020	0.0000	0.0533	0.0005	0.3346	0.0040	0.0455	0.0004	0.67	335.2	5.5	287.0	2.2	293.1	3.0
	11	0.0021	0.0000	0.0526	0.0005	0.3274	0.0056	0.0451	0.0006	0.84	304.4	7.8	284.6	4.0	287.6	4.2
	12	0.0020	0.0000	0.0529	0.0009	0.3371	0.0067	0.0463	0.0005	0.54	314.9	13.6	291.5	3.1	295.0	5.1

Analyses U-Pb sur oxydes d'uranium - article #5

				Common Pb corrected ratios							Common Pb corrected ages					
Sample	**Analytical point**	**$^{204}Pb/^{206}Pb$**	**1σ**	**$^{207}Pb/^{206}Pb$**	**1σ**	**$^{207}Pb/^{235}U$**	**1σ**	**$^{206}Pb/^{238}U$**	**1σ**	**Correl. Err.**	**$^{207}Pb/^{206}Pb$**	**1σ**	**$^{206}Pb/^{238}U$**	**1σ**	**$^{207}Pb/^{235}U$**	**1σ**
Quistiave (Guern)	1	0.0002	0.0000	0.0520	0.00010	0.2128	0.0016	0.0297	0.0002	0.96	280.8	4.0	188.6	1.4	195.9	1.4
	3	0.0001	0.0000	0.0522	0.00009	0.2276	0.0016	0.0316	0.0002	0.94	290.6	3.8	200.7	1.3	208.2	1.4
	5	0.0001	0.0000	0.0516	0.00010	0.2166	0.0025	0.0304	0.0003	0.98	264.9	4.1	193.2	2.2	199.0	2.1
	7	0.0002	0.0000	0.0520	0.00014	0.1816	0.0014	0.0253	0.0002	0.89	279.5	5.7	161.3	1.1	169.4	1.2
	8	0.0001	0.0000	0.0524	0.00019	0.2202	0.0017	0.0305	0.0002	0.86	298.8	7.9	193.6	1.3	202.1	1.4
	9	0.0001	0.0000	0.0524	0.00012	0.2093	0.0025	0.0290	0.0003	0.95	300.2	4.8	184.0	2.0	193.0	2.1
	10	0.0001	0.0000	0.0521	0.00011	0.2052	0.0017	0.0285	0.0002	0.93	287.9	4.5	181.4	1.4	189.5	1.4
	11	0.0002	0.0000	0.0523	0.00015	0.2290	0.0027	0.0318	0.0003	0.92	293.3	6.0	201.6	2.1	209.3	2.2
Kerroch (Guern)	1	0.0060	0.0000	0.0508	0.0002	0.2685	0.0046	0.0383	0.0003	0.45	227.3	2.6	242.2	1.8	241.2	3.7
	2	0.0070	0.0000	0.0517	0.0003	0.2279	0.0037	0.0320	0.0003	0.60	265.4	2.9	202.7	1.9	208.2	3.0
	3	0.0095	0.0001	0.0531	0.0004	0.2379	0.0064	0.0325	0.0005	0.52	330.0	3.8	205.5	2.9	216.2	5.3
	4	0.0156	0.0001	0.0511	0.0005	0.1669	0.0069	0.0237	0.0003	0.33	238.0	2.6	150.4	2.0	156.1	6.0
	5	0.0075	0.0001	0.0503	0.0003	0.2174	0.0052	0.0314	0.0003	0.41	201.6	3.6	198.9	1.9	199.4	4.4
	6	0.0140	0.0001	0.0534	0.0005	0.2169	0.0074	0.0295	0.0005	0.51	340.6	3.3	186.5	3.2	198.7	6.2
	7	0.0117	0.0001	0.0521	0.0003	0.2031	0.0071	0.0283	0.0003	0.31	284.6	1.8	179.2	1.9	187.2	6.0
	8	0.0121	0.0001	0.0528	0.0005	0.2437	0.0070	0.0335	0.0005	0.47	316.1	3.6	211.6	2.8	220.8	5.7
	9	0.0129	0.0000	0.0549	0.0003	0.2303	0.0050	0.0304	0.0003	0.46	402.6	1.9	192.7	1.9	209.8	4.1
	10	0.0101	0.0000	0.0520	0.0002	0.2083	0.0043	0.0290	0.0003	0.43	282.4	1.5	184.0	1.6	191.6	3.6
	11	0.0092	0.0000	0.0515	0.0006	0.1890	0.0046	0.0266	0.0003	0.40	258.9	5.2	168.9	1.6	175.4	3.9
	12	0.0138	0.0001	0.0547	0.0005	0.2150	0.0080	0.0285	0.0003	0.33	396.5	3.2	180.5	2.2	197.1	6.7
	13	0.0151	0.0001	0.0528	0.0006	0.2187	0.0077	0.0300	0.0005	0.45	315.8	3.4	190.0	3.0	200.1	6.4

	14	0.0097	0.0001	0.0519	0.0003	0.2015	0.0061	0.0282	0.0003	0.32	273.8	2.9	178.7	1.7	185.9	5.1
	15	0.0117	0.0000	0.0501	0.0005	0.2057	0.0040	0.0298	0.0003	0.57	195.1	3.6	188.7	2.0	189.4	3.4
	16	0.0133	0.0001	0.0516	0.0005	0.1956	0.0059	0.0275	0.0003	0.31	264.3	3.5	174.3	1.6	180.8	5.0
	17	0.0143	0.0001	0.0516	0.0005	0.1979	0.0071	0.0278	0.0004	0.35	263.5	2.9	176.3	2.2	182.7	6.0
	18	0.0088	0.0000	0.0503	0.0002	0.2096	0.0035	0.0302	0.0003	0.53	206.0	2.1	191.6	1.7	192.9	3.0
	19	0.0032	0.0000	0.0500	0.0002	0.1774	0.0019	0.0258	0.0002	0.68	189.0	4.8	163.8	1.2	165.7	1.7
	20	0.0048	0.0000	0.0513	0.0002	0.1815	0.0027	0.0257	0.0002	0.46	250.2	3.3	163.3	1.1	169.2	2.3
	21	0.0102	0.0001	0.0509	0.0015	0.1848	0.0115	0.0264	0.0003	0.21	230.9	12.2	167.3	2.1	171.8	9.8
	22	0.0050	0.0001	0.0509	0.0008	0.1830	0.0061	0.0261	0.0002	0.26	233.8	12.0	165.7	1.4	170.5	5.2
	23	0.0167	0.0001	0.0540	0.0013	0.1586	0.0086	0.0213	0.0003	0.23	365.8	6.9	135.4	1.7	148.9	7.5
	24	0.0054	0.0001	0.0509	0.0014	0.1742	0.0093	0.0248	0.0002	0.18	234.3	18.8	157.7	1.5	162.9	8.0
	25	0.0049	0.0001	0.0528	0.0026	0.2270	0.0153	0.0312	0.0008	0.37	317.8	36.2	197.7	4.8	207.5	12.6
	26	0.0129	0.0001	0.0502	0.0003	0.1712	0.0051	0.0247	0.0002	0.30	199.8	2.0	157.1	1.4	159.9	4.4
	27	0.0032	0.0001	0.0515	0.0010	0.2126	0.0064	0.0300	0.0002	0.26	258.4	18.7	190.2	1.5	195.6	5.4
	28	0.0048	0.0001	0.0508	0.0010	0.2191	0.0075	0.0313	0.0003	0.29	228.9	15.3	198.4	1.9	201.0	6.2
	29	0.0121	0.0001	0.0525	0.0008	0.2141	0.0077	0.0296	0.0003	0.32	305.9	5.7	187.3	2.1	196.4	6.4
	30	0.0030	0.0000	0.0514	0.0005	0.2057	0.0029	0.0290	0.0002	0.51	253.8	8.9	184.5	1.3	189.8	2.4
Guern (undifferentiated)	1	0.0001	0.0000	0.0517	0.0001	0.2247	0.0017	0.0315	0.0002	0.97	269.9	2.7	200.0	1.4	205.8	1.4
	2	0.0002	0.0000	0.0516	0.0001	0.1783	0.0018	0.0251	0.0002	0.94	260.6	5.0	159.7	1.5	166.6	1.6
	3	0.0001	0.0000	0.0516	0.0001	0.2037	0.0017	0.0286	0.0002	0.89	262.7	6.2	182.1	1.4	188.3	1.5
	4	0.0001	0.0000	0.0519	0.0001	0.1886	0.0018	0.0263	0.0002	0.95	278.2	5.6	167.6	1.5	175.5	1.5
	5	0.0001	0.0000	0.0519	0.0001	0.2141	0.0017	0.0299	0.0002	0.93	276.0	5.6	190.1	1.3	196.9	1.4
	6	0.0001	0.0000	0.0516	0.0001	0.2089	0.0018	0.0294	0.0002	0.94	264.6	5.3	186.5	1.5	192.7	1.5
	7	0.0001	0.0000	0.0516	0.0001	0.2427	0.0026	0.0341	0.0004	0.98	263.9	2.6	216.2	2.2	220.6	2.1
	8	0.0001	0.0000	0.0518	0.0001	0.2238	0.0021	0.0313	0.0003	0.94	271.7	5.3	199.0	1.8	205.1	1.8
	9	0.0001	0.0000	0.0519	0.0001	0.2043	0.0017	0.0286	0.0002	0.92	275.3	5.0	181.6	1.4	188.7	1.4
	10	0.0001	0.0000	0.0517	0.0001	0.2004	0.0013	0.0281	0.0002	0.95	267.4	3.7	178.8	1.1	185.5	1.1
	11	0.0002	0.0000	0.0520	0.0001	0.2217	0.0023	0.0309	0.0003	0.95	282.4	5.2	196.2	1.9	203.3	1.9
	12	0.0002	0.0000	0.0515	0.0001	0.2591	0.0030	0.0365	0.0004	0.98	258.3	3.8	231.1	2.6	233.9	2.4
	13	0.0002	0.0000	0.0519	0.0001	0.2479	0.0024	0.0347	0.0003	0.96	275.7	4.6	219.6	2.0	224.8	2.0
	14	0.0001	0.0000	0.0518	0.0001	0.2422	0.0026	0.0339	0.0004	0.95	271.6	6.1	215.0	2.2	220.2	2.1
	15	0.0001	0.0000	0.0517	0.0001	0.1949	0.0016	0.0273	0.0002	0.93	268.1	5.2	173.9	1.3	180.8	1.3
Kerlech (Lignol)	1	0.0023	0.0000	0.0514	0.0001	0.1833	0.0032	0.0258	0.0002	0.50	255.6	3.0	164.4	1.4	170.8	2.7
	2	0.0019	0.0000	0.0516	0.0001	0.1966	0.0027	0.0276	0.0002	0.63	263.5	1.6	175.6	1.5	182.2	2.3
	3	0.0019	0.0000	0.0520	0.0002	0.2034	0.0031	0.0284	0.0003	0.70	278.5	4.0	180.5	1.9	188.0	2.7
	4	0.0021	0.0000	0.0517	0.0001	0.1900	0.0020	0.0267	0.0002	0.73	266.5	2.9	169.5	1.3	176.6	1.7
	5	0.0020	0.0000	0.0518	0.0003	0.1885	0.0028	0.0264	0.0003	0.77	272.0	7.3	167.8	1.9	175.3	2.4
	6	0.0016	0.0000	0.0512	0.0002	0.1930	0.0020	0.0273	0.0002	0.72	244.4	6.4	173.8	1.3	179.1	1.7
	7	0.0018	0.0000	0.0513	0.0003	0.1935	0.0034	0.0274	0.0002	0.47	247.8	6.6	174.0	1.4	179.5	2.9
	8	0.0018	0.0000	0.0523	0.0001	0.1875	0.0018	0.0260	0.0002	0.75	293.2	3.2	165.4	1.2	174.5	1.6
	9	0.0014	0.0000	0.0509	0.0002	0.1840	0.0020	0.0262	0.0002	0.67	232.2	5.3	166.6	1.2	171.4	1.7
	10	0.0017	0.0000	0.0511	0.0002	0.1994	0.0021	0.0283	0.0002	0.74	240.3	4.9	179.8	1.3	184.6	1.7
	11	0.0024	0.0000	0.0514	0.0003	0.1645	0.0030	0.0232	0.0002	0.51	252.0	6.1	147.9	1.4	154.6	2.6
	12	0.0027	0.0000	0.0531	0.0001	0.1725	0.0028	0.0236	0.0003	0.72	326.8	3.1	150.1	1.8	161.5	2.5
	13	0.0016	0.0000	0.0514	0.0001	0.1885	0.0018	0.0266	0.0002	0.77	250.5	4.0	169.3	1.2	175.3	1.6
	14	0.0019	0.0000	0.0525	0.0003	0.2074	0.0033	0.0287	0.0003	0.74	302.7	6.6	182.0	2.1	191.3	2.7
Rosglas	1	0.0002	0.0000	0.0523	0.0001	0.2872	0.0026	0.0398	0.0003	0.94	296.6	5.3	251.5	2.1	256.3	2.1
	2	0.0002	0.0000	0.0524	0.0001	0.2784	0.0021	0.0385	0.0003	0.94	298.5	4.5	243.8	1.7	249.4	1.7
	3	0.0002	0.0000	0.0523	0.0001	0.2920	0.0023	0.0405	0.0003	0.95	295.5	4.2	255.8	1.9	260.2	1.8
	4	0.0002	0.0000	0.0522	0.0001	0.2766	0.0020	0.0384	0.0003	0.91	289.9	3.1	243.1	1.6	248.0	1.6

	5	0.0002	0.0000	0.0522	0.0001	0.2740	0.0023	0.0380	0.0003	0.95	292.0	3.7	240.7	1.9	245.9	1.8
	6	0.0002	0.0000	0.0523	0.0001	0.2789	0.0021	0.0387	0.0003	0.93	292.6	3.2	244.8	1.7	249.8	1.7
	7	0.0002	0.0000	0.0522	0.0001	0.2683	0.0019	0.0373	0.0002	0.94	290.5	3.6	235.9	1.5	241.3	1.5
	8	0.0002	0.0000	0.0522	0.0001	0.2783	0.0026	0.0387	0.0004	0.96	289.8	3.5	244.6	2.2	249.3	2.1
	9	0.0003	0.0000	0.0523	0.0001	0.2868	0.0036	0.0398	0.0005	0.97	294.1	3.9	251.5	3.0	256.0	2.8
	10	0.0003	0.0000	0.0519	0.0001	0.2906	0.0024	0.0406	0.0003	0.84	277.7	5.5	256.6	1.7	259.1	1.9
	11	0.0003	0.0000	0.0521	0.0001	0.2710	0.0022	0.0378	0.0003	0.91	283.5	4.1	238.9	1.8	243.5	1.8
	12	0.0003	0.0000	0.0522	0.0002	0.2734	0.0033	0.0380	0.0004	0.92	291.1	6.8	240.2	2.6	245.4	2.6
Quérrien	1	0.0010	0.0000	0.0504	0.0002	0.2450	0.0027	0.0352	0.0003	0.76	211.3	7.6	223.2	1.8	222.5	2.2
	2	0.0013	0.0000	0.0501	0.0001	0.2304	0.0023	0.0333	0.0003	0.76	196.0	3.6	211.5	1.6	210.5	1.9
	3	0.0007	0.0000	0.0507	0.0001	0.2449	0.0020	0.0350	0.0002	0.85	225.5	2.7	221.8	1.5	222.4	1.6
	4	0.0006	0.0000	0.0504	0.0001	0.2563	0.0021	0.0369	0.0003	0.91	210.2	2.6	233.5	1.7	231.7	1.7
	5	0.0009	0.0000	0.0505	0.0001	0.2428	0.0019	0.0349	0.0002	0.82	215.4	3.7	220.8	1.4	220.7	1.6
	6	0.0005	0.0000	0.0506	0.0001	0.2363	0.0022	0.0339	0.0003	0.84	217.3	4.5	214.9	1.6	215.4	1.8
	7	0.0006	0.0000	0.0505	0.0001	0.1964	0.0016	0.0282	0.0002	0.86	212.4	4.4	179.4	1.2	182.1	1.3
	8	0.0004	0.0000	0.0504	0.0001	0.2493	0.0018	0.0359	0.0002	0.85	209.7	4.0	227.2	1.4	226.0	1.5
	9	0.0010	0.0000	0.0506	0.0002	0.2288	0.0020	0.0328	0.0002	0.77	218.7	5.2	208.0	1.4	209.2	1.7
	10	0.0002	0.0000	0.0508	0.0001	0.2552	0.0021	0.0364	0.0003	0.89	227.6	5.3	230.7	1.7	230.8	1.7
	11	0.0006	0.0000	0.0508	0.0001	0.2180	0.0017	0.0311	0.0002	0.76	229.8	3.8	197.4	1.2	200.2	1.4
	12	0.0002	0.0000	0.0505	0.0001	0.2537	0.0018	0.0364	0.0002	0.85	214.3	4.0	230.7	1.4	229.6	1.5
	13	0.0002	0.0000	0.0504	0.0001	0.2505	0.0020	0.0361	0.0003	0.97	208.5	3.9	228.4	1.7	227.0	1.6
	14	0.0006	0.0000	0.0508	0.0001	0.2606	0.0020	0.0372	0.0002	0.84	226.4	5.4	235.7	1.5	235.2	1.6

Analyses U-Pb sur apatite- article #5

Facies	Sample	Analyse	U (ppm)	Pb (ppm)	$^{238}U/^{206}Pb$	Error (2σ)	$^{207}Pb/^{206}Pb$	Error (2σ)	Final ^{207}Age	Error (2σ)
Porphyritic leucogranite	**PONT-1**	1	87.0	12.3	12.8816	0.4353	0.3745	0.0058	293.1	12.2
		2	113.1	12.6	14.0410	0.4354	0.3315	0.0068	292.1	12.2
		3	61.3	11.0	11.5607	0.4874	0.4261	0.0142	291.3	12.2
		4	345.2	16.8	17.9244	0.5377	0.2105	0.0032	281.6	9.5
		5	328.8	12.8	18.2482	0.6029	0.1794	0.0036	291.3	11.2
		6	45.3	10.4	10.1010	0.3549	0.4691	0.0136	298.5	22.1
		7	72.4	14.8	10.4058	0.3999	0.4208	0.0138	325.6	18.4
		8	373.1	17.0	17.1940	0.4943	0.1886	0.0036	303.9	10.6
		9	366.2	18.8	17.0039	0.4859	0.2178	0.0052	293.7	8.9
		10	80.2	9.3	12.9032	0.3930	0.3397	0.0056	312.8	12.9
		11	528.8	14.0	18.9898	0.5527	0.1481	0.00198	291.4	9.4
		12	295.9	16.5	16.9319	0.4687	0.2291	0.0034	290.8	10.2
		13	183.7	8.5	18.1686	0.5791	0.2052	0.0036	281.4	10.1
		14	190.0	8.9	17.9889	0.5707	0.2047	0.0038	283.8	10
		15	424.0	14.8	19.4477	0.5739	0.1743	0.0024	274.6	8.9
		16	68.0	11.5	12.2115	0.4082	0.4242	0.0082	277.3	16.4
		17	163.1	10.0	16.7813	0.5043	0.2397	0.0036	287.8	10.1
		18	260.5	12.9	17.9727	0.6622	0.2161	0.0098	278.9	10.3
		19	364.9	13.9	17.2741	0.5079	0.1818	0.003	305.8	10.5
		20	376.3	14.3	17.1438	0.4627	0.1816	0.0022	307.8	9.5
		21	68.5	12.7	10.3231	0.2928	0.4291	0.0066	322.9	16.9
		22	64.0	12.6	10.0442	0.3009	0.4405	0.008	322.6	18.8
		23	192.6	6.0	18.3722	0.5250	0.1611	0.0036	296.3	9.0
Isotropic leucogranite	**PONT-10**	1	163.4	24.1	12.7210	0.3913	0.4040	0.0057	278.8	13.2
		2	161	22.5	12.7763	0.4138	0.3781	0.0071	291.8	13.2
		3	195.5	22.8	14.0509	0.4139	0.3579	0.0052	277	11.6
		4	185	16.1	15.5739	0.4496	0.3009	0.0038	278.5	10.9
		5	241	21.7	15.1768	0.4395	0.308	0.0041	282.7	11
		6	180.6	21.7	13.6893	0.3908	0.3599	0.0044	283.1	10.8
		7	164.6	20.6	13.5833	0.4057	0.3665	0.0051	281.9	12
		8	47.52	14.7	8.3056	0.0860	0.5373	0.0056	298	23.1
		9	66.3	13.1	10.7945	0.3080	0.4475	0.0068	296	16.9
		10	69.76	13.9	10.7411	0.3027	0.4485	0.0064	295.8	13.8
		11	260	21.3	16.1760	0.0930	0.2942	0.0017	272.2	10.1
		12	212.4	17.1	15.5376	0.4380	0.2912	0.0043	284.2	10.5
		14	167.7	16.0	14.8721	0.4208	0.3239	0.0052	279.6	10.4
		16	119.3	14.9	13.6463	0.3700	0.3651	0.005	281.6	12.5
		17	85.7	18.6	9.9305	0.1100	0.4591	0.005	311.3	17.4
		19	231.2	21.8	15.1149	0.4138	0.3200	0.004	276.4	10.4
		20	240.6	23.6	14.8478	0.4177	0.3271	0.0044	278.3	12.3
		21	64.3	12.8	10.5943	0.3247	0.4497	0.0097	298	18
		23	187.9	20.7	14.1064	0.4114	0.3432	0.0046	285	11
		24	276.3	9.1	19.2530	0.5477	0.1704	0.0028	280.1	9.6
	PONT-26	1	76.5	11.1	11.9517	0.3585	0.3977	0.009	299.8	8.1
		2	153.3	12.4	15.3280	0.5994	0.3081	0.0122	278.5	7
		3	40.9	10.9	8.9912	0.2257	0.5089	0.0071	300.8	12.3
		4	201.0	14.5	16.2101	0.4090	0.2711	0.0041	282.4	7.9
		5	224.7	11.6	17.6243	0.4082	0.2231	0.0032	281	7.3
		6	146.3	14.8	14.5518	0.3381	0.3262	0.0044	284.7	8.6
		7	165.3	9.0	17.6118	0.4240	0.229	0.004	277.8	7.9
		8	197.6	11.4	17.3792	0.4090	0.2403	0.0043	277.8	8
		9	105.3	12.5	13.8677	0.3600	0.3564	0.0063	283.2	9.6
		10	279.0	14.1	17.8827	0.4798	0.2232	0.0046	275.5	9
		13	296.2	13.9	18.2882	0.4477	0.2092	0.0034	277.1	7.6
		14	166.3	12.8	15.6495	0.3994	0.2877	0.0058	283.4	7.4
		15	61.1	12.1	10.8507	0.2684	0.4457	0.0072	295.9	13
		16	162.3	10.6	16.6889	0.4264	0.2558	0.0038	280.9	8
		17	158.8	13.0	15.6789	0.3684	0.2914	0.004	281.1	8.4
		19	66.5	12.0	11.1359	0.2764	0.4281	0.0062	300.9	12
		20	76.4	11.9	11.7385	0.2977	0.402	0.0064	301.9	10.9
		21	88.0	12.6	12.4595	0.3033	0.3834	0.0062	296.6	11.7
		22	27.9	10.8	7.2780	0.1967	0.569	0.009	308.4	20.2
		23	334.2	15.2	18.4706	0.3940	0.2082	0.0032	274.8	7
		24	227.2	15.0	16.8805	0.3950	0.2575	0.0034	278	7.8
Langonnet leucogranite	**PONT-20**	2	114.8	9.2	15.6666	0.3064	0.2926	0.0044	282.3	6.7
		3	123.7	8.0	16.7392	0.3678	0.2557	0.0037	276.7	7.7
		4	117.7	8.5	15.5812	0.3154	0.2638	0.0042	286.5	6.9
		5	124.9	7.5	16.8039	0.3225	0.245	0.0035	279.4	8.5
		6	113.9	9.8	15.0083	0.3678	0.2884	0.005	281.7	7.5
		7	48.3	13.3	9.0662	0.2497	0.5029	0.0086	279.3	7.4
		8	104.6	7.6	16.5536	0.3894	0.2682	0.0053	280.3	7
		9	113.9	8.1	16.0205	0.3137	0.2621	0.0038	282.2	7.3
		10	48.5	6.6	12.7894	0.2549	0.3685	0.0053	283.2	6.6
		11	117.3	8.1	16.7448	0.3695	0.2565	0.0042	279.4	7.2
		12	118.5	7.5	17.1762	0.3250	0.2452	0.0034	277.3	6.8
		13	118.3	7.6	16.6223	0.3376	0.2496	0.0033	296.9	7.4
		14	184.0	15.1	15.7580	0.3040	0.2888	0.0047	296	8.3

		15	108.3	7.6	16.6722	0.3137	0.2589	0.0039	303.9	12.5
		16	118.3	7.5	17.0387	0.3668	0.2498	0.0036	291	7.2
		17	131.9	7.7	17.5070	0.3675	0.235	0.0033	294.1	9.6
		18	125.5	8.4	16.4096	0.3812	0.247	0.0051	293.9	7.3
		19	92.2	7.7	15.1999	0.4110	0.28	0.0045	299.7	8.1
		20	120.4	8.2	15.9286	0.2841	0.2549	0.0031	295.2	6.8
		21	119.9	8.5	15.2812	0.3085	0.2586	0.0035	303.9	7.7
		22	123.1	8.4	15.4655	0.2875	0.2495	0.0035	306.6	7.1
		23	98.5	7.4	15.1263	0.3105	0.2729	0.0038	297.2	9.7
		24	104.9	7.9	15.5159	0.3165	0.2751	0.0043	297.2	7.9
		25	112.4	7.6	16.2285	0.3215	0.2567	0.0038	291.3	7
Episyenite	**MS-81-66 (PP)**	1	95.4	3.439	18.2083	0.8036	0.1770	0.0068	290.8	14.3
		2	262.5	13.74	16.8350	0.7785	0.2252	0.0078	291.5	15
		3	0.1324	0.869	*0.6223*	*0.0438*	*0.8530*	*0.0400*	*-180*	*630*
		6	*35.09*	*4.671*	*15.4583*	*0.6240*	*0.4490*	*0.0124*	*204.9*	*16.4*
		7	154.7	2.768	20.1167	0.7166	0.1217	0.0020	286.3	10.4
		8	*9.38*	*5.85*	*4.8520*	*0.2257*	*0.6380*	*0.0200*	*348*	*60*
		10	*13.14*	*4.642*	*9.9701*	*0.4182*	*0.7230*	*0.0220*	*106*	*34.5*
		11	*3.457*	*3.59*	*3.3400*	*0.2037*	*0.6960*	*0.0240*	*379*	*68*
		12	*9.99*	*2.549*	*14.1243*	*0.7288*	*0.7650*	*0.0340*	*51.2*	*27.8*
		13	*9.38*	*1.395*	*11.6144*	*0.5542*	*0.3906*	*0.0172*	*314.7*	*27.1*
		15	221.7	13.5	16.9722	0.6297	0.2459	0.0032	282	11.3
		16	200.7	15.71	15.3752	0.5355	0.2858	0.0048	289.4	11.9
		17	*0.0935*	*0.226*	*1.6313*	*0.1555*	*0.8200*	*0.0740*	*110*	*390*
		18	173.2	6.236	18.4196	0.6189	0.1784	0.0048	288.4	10
		19	119.7	8.712	15.9185	0.5861	0.2708	0.0060	287	10.7
		20	0.908	0.67	*5.9277*	*0.5527*	*0.8610*	*0.0680*	*-7*	96
		21	*0.1852*	*0.361*	*2.0284*	*0.2060*	*0.8460*	*0.0740*	*70*	*300*
		22	*2.56*	*3.76*	*2.4510*	*0.2001*	*0.7800*	*0.0360*	*242*	*133*
		23	192.2	13.97	16.0436	0.6233	0.2761	0.0048	282.3	12.1
		24	184.6	12.8	16.2920	0.5462	0.2643	0.0034	283.9	11.6
Monzogranite	**PONT-22**	1	42.5	8.978	9.9940	0.2957	0.4506	0.0064	317.2	11.5
		2a	38.93	9.422	9.0025	0.2817	0.4637	0.0076	340.5	16
		3	39.69	8.815	9.8116	0.2724	0.4536	0.005	321.1	16
		4	31.88	8.695	8.6386	0.2705	0.497	0.0065	325.2	16
		5	47.29	8.429	11.1000	0.3711	0.4035	0.0095	318.4	13.9
		6	7.772	9.628	3.1319	0.0956	0.7289	0.0092	320	52
		7	60.6	10.156	11.2676	0.2999	0.3975	0.004	318.9	15.4
		8	25.86	9.006	7.5216	0.2237	0.5428	0.0072	326.1	17.1
		9	32.27	8.511	8.9262	0.2472	0.4952	0.0062	316.8	19.7
		10b	38.9	8.589	10.1657	0.3097	0.4422	0.009	319.1	22
		11	54.59	8.674	11.1894	0.3174	0.3895	0.006	326.5	15.2
		12	68.8	8.811	12.3213	0.3413	0.3441	0.0058	325.1	10.6
		13	96	7.645	14.7254	0.3923	0.2683	0.0042	312.2	9.4
		14	39.62	8.002	10.1792	0.2890	0.4428	0.0062	318	14
		15b	89.45	9.38	13.7363	0.3769	0.3104	0.0046	311	10.7
		16	46.48	9.25	10.1112	0.3554	0.4401	0.0082	321.8	11.4
		17	32.6	8.35	9.0975	0.2852	0.4834	0.0068	321.5	17.2
		18	29.99	8.487	8.4324	0.2450	0.5054	0.0056	325.2	15.1
		19	30.04	9.289	7.9821	0.2368	0.5228	0.007	326.6	20.6
		20	37	7.606	10.1348	0.2750	0.4448	0.0062	317.7	15.8
		21	27.82	8.882	7.8802	0.2613	0.5273	0.0118	327.1	26.2
		22	45.39	8.639	10.5009	0.3486	0.423	0.007	323	13.9
		24	29.01	7.915	8.9350	0.2696	0.4851	0.0074	325.3	19.4
Quartz monzodiorite	**PONT-7**	1	31.9	8.03	10.3199	0.6747	0.443	0.024	309	27
		2	18.17	10.29	7.1378	0.3444	0.575	0.024	311	45
		3	56.16	6.88	14.1864	0.5726	0.3163	0.0084	299.5	15
		4	9.99	7.57	5.2854	0.2690	0.628	0.022	335	52
		5	20.16	10.71	7.4683	0.4021	0.567	0.03	307	54
		6	15.32	8.96	6.2578	0.3136	0.613	0.024	302	50
		7	12.213	8.237	5.9524	0.2282	0.6229	0.0116	305.7	36.5
		8	16.29	9.62	6.3898	0.2730	0.6035	0.018	305	40
		9	22.51	7.43	8.3542	0.4122	0.5131	0.017	317.1	27.1
		10	30.8	8.63	9.6154	0.6683	0.46	0.022	314.8	19.1
		12	44.5	8.79	11.6686	0.6585	0.395	0.022	307	27
		14	24.27	10.7	8.2781	0.4241	0.518	0.02	319	34
		17	12.92	9.74	5.1921	0.4996	0.635	0.048	349	111
		18	18.42	10.82	6.7705	0.3446	0.596	0.026	295	49
		20	12.28	6.14	6.6138	0.3387	0.566	0.022	344	47
		21	12.89	8.88	5.5556	0.2579	0.601	0.0196	359	54
		22	19.38	11.5	6.8306	0.3586	0.573	0.022	325	41

Analyses U-Pb sur zircon – granite de Huelgoat

HUEL-2 zircon	Pb^{207}/Pb^{206}	1σ	Pb^{207}/U^{235}	1σ	Pb^{206}/U^{238}	1σ	rho	Pb^{207}/Pb^{206}	1σ	Pb^{206}/U^{238}	1σ	Pb^{207}/U^{235}	1σ	Pb (ppm)	U (ppm)	Th (ppm)
3	0.05395	0.00057	0.39509	0.00459	0.05312	0.0006	0.97	368.70	23.62	333.70	3.65	338.10	3.34	135.8	1592.2	22.4
5	0.05281	0.00057	0.35265	0.00421	0.04844	0.00055	0.95	320.60	24.48	304.90	3.35	306.70	3.16	125.5	1354.2	872.1
9	0.05786	0.00063	0.62151	0.00748	0.07792	0.00088	0.94	524.10	24.07	483.70	5.26	490.80	4.68	64.9	484.8	105.1
10	0.06184	0.00065	0.88706	0.0103	0.10404	0.00117	0.97	668.70	22.23	638.10	6.85	644.80	5.54	307.8	1624.4	698.3
11	0.05495	0.00059	0.47255	0.00558	0.06238	0.0007	0.95	410.30	23.45	390.10	4.27	392.90	3.85	136.7	1292.5	190.2
12	0.05927	0.00076	0.82972	0.01131	0.10155	0.00116	0.84	576.90	27.49	623.50	6.78	613.50	6.28	15.9	74.3	77.6
15	0.05568	0.00061	0.38797	0.00467	0.05055	0.00057	0.94	439.30	23.63	317.90	3.51	332.90	3.42	195.6	2402.3	69.2
16	0.06007	0.0007	0.81021	0.01027	0.09784	0.00111	0.90	606.10	25.00	601.70	6.53	602.60	5.76	46.3	248.8	149.9
20	0.05666	0.00063	0.36933	0.00453	0.04728	0.00054	0.93	477.70	24.72	297.80	3.31	319.20	3.36	237.3	2937.9	642.9
22	0.05453	0.00062	0.34899	0.00432	0.04642	0.00053	0.92	393.10	25.00	292.50	3.25	304.00	3.25	146.1	1952.1	72.1
24	0.05957	0.00069	0.77351	0.00979	0.09419	0.00108	0.91	587.90	24.91	580.30	6.34	581.80	5.61	11.7	102.9	26.5
26	0.05668	0.0006	0.40623	0.00477	0.05198	0.00059	0.97	478.50	23.32	326.70	3.61	346.20	3.45	55.5	929.6	109.5
27	0.05322	0.00057	0.39302	0.00466	0.05357	0.00061	0.96	338.00	23.92	336.40	3.72	336.60	3.40	39.7	667.2	55.5
29	0.06026	0.00063	0.82037	0.00959	0.09875	0.00112	0.97	612.90	22.46	607.10	6.56	608.30	5.35	88.7	725.0	229.1
31	0.05463	0.00061	0.37613	0.00464	0.04994	0.00057	0.93	397.00	24.82	314.20	3.48	324.20	3.42	42.4	754.4	66.8
32	**0.05315**	**0.00057**	**0.36787**	**0.00435**	**0.05021**	**0.00057**	**0.96**	**335.10**	**23.89**	**315.80**	**3.48**	**318.10**	**3.23**	**57.4**	**1001.3**	**116.2**
33	0.0585	0.00061	0.67121	0.00784	0.08323	0.00094	0.97	548.40	22.77	515.40	5.59	521.40	4.76	192.8	2082.0	106.4
35	0.05763	0.00065	0.69537	0.00855	0.08752	0.00099	0.92	515.50	24.14	540.80	5.87	536.00	5.12	20.4	196.5	41.8
37	0.05744	0.00062	0.39756	0.00472	0.0502	0.00057	0.96	508.20	23.47	315.80	3.48	339.90	3.43	91.8	1610.3	54.3
39	**0.05356**	**0.0006**	**0.36768**	**0.00447**	**0.04979**	**0.00056**	**0.93**	**352.70**	**24.88**	**313.20**	**3.45**	**317.90**	**3.32**	**44.8**	**627.0**	**448.8**
40	**0.05298**	**0.00067**	**0.36665**	**0.00493**	**0.0502**	**0.00057**	**0.84**	**327.80**	**28.22**	**315.70**	**3.50**	**317.20**	**3.66**	**19.7**	**332.9**	**59.4**
42	0.06373	0.00107	0.86505	0.0149	0.09845	0.00115	0.68	732.70	35.13	605.30	6.75	632.90	8.11	3.9	33.5	5.3
44	0.05762	0.00068	0.60035	0.00768	0.07558	0.00085	0.88	514.90	25.52	469.70	5.11	477.50	4.87	14.2	158.9	29.7
45	0.05346	0.00061	0.35661	0.0044	0.04839	0.00054	0.90	348.10	25.39	304.60	3.35	309.70	3.29	34.0	551.1	206.5
47	0.05622	0.00063	0.37194	0.00453	0.04799	0.00054	0.92	460.10	24.75	302.20	3.32	321.10	3.35	73.0	1359.5	55.2
48	**0.05338**	**0.00058**	**0.36551**	**0.00441**	**0.04967**	**0.00056**	**0.93**	**345.00**	**24.40**	**312.50**	**3.46**	**316.30**	**3.28**	**99.6**	**1187.5**	**227.5**
50	**0.05361**	**0.00058**	**0.3722**	**0.00443**	**0.05036**	**0.00057**	**0.95**	**354.70**	**24.00**	**316.70**	**3.50**	**321.30**	**3.28**	**273.1**	**3133.9**	**792.1**
52	0.05397	0.00059	0.42186	0.00508	0.0567	0.00064	0.94	369.70	24.53	355.50	3.91	357.40	3.63	60.2	628.5	124.6
55	0.05436	0.00067	0.35825	0.00472	0.04781	0.00054	0.86	385.70	27.31	301.10	3.34	310.90	3.53	38.8	474.3	99.1
56	0.06087	0.00065	0.83024	0.00981	0.09894	0.00112	0.96	634.70	22.84	608.20	6.55	613.70	5.44	149.4	773.9	536.6
57	0.05773	0.00068	0.54174	0.00691	0.06807	0.00077	0.89	519.20	25.86	424.50	4.66	439.60	4.55	124.1	1039.8	257.1
58	0.05268	0.00056	0.351	0.00415	0.04833	0.00054	0.95	314.90	24.12	304.30	3.35	305.50	3.12	188.8	2340.6	304.4
59	0.05297	0.00057	0.34875	0.00414	0.04776	0.00054	0.95	327.50	24.23	300.70	3.31	303.80	3.12	149.6	1944.4	28.4
61	0.05895	0.00068	0.61877	0.00772	0.07614	0.00086	0.91	565.30	24.81	473.00	5.16	489.10	4.85	108.6	806.1	255.8
64	**0.05305**	**0.00058**	**0.3663**	**0.00437**	**0.05009**	**0.00056**	**0.94**	**330.80**	**24.45**	**315.10**	**3.46**	**316.90**	**3.25**	**268.2**	**3252.5**	**225.1**
65	0.05421	0.00066	0.36692	0.00478	0.0491	0.00055	0.86	379.70	27.20	309.00	3.41	317.40	3.55	96.4	1068.6	449.0
67	0.05965	0.00067	0.77059	0.0094	0.09371	0.00105	0.92	591.00	24.10	577.40	6.21	580.10	5.39	94.3	560.4	194.5
68	0.0578	0.00064	0.58044	0.00698	0.07284	0.00082	0.94	522.10	24.17	453.30	4.92	464.70	4.48	224.2	1544.7	1134.8
69	0.06138	0.00073	0.85179	0.01085	0.10066	0.00114	0.89	652.60	25.18	618.30	6.65	625.60	5.95	59.7	248.9	401.6
70	0.05386	0.00068	0.38778	0.00523	0.05223	0.00059	0.84	365.00	28.45	328.20	3.62	332.70	3.83	35.3	369.2	155.2
14a	0.05665	0.00061	0.53214	0.00635	0.06814	0.00077	0.95	477.10	23.93	425.00	4.65	433.20	4.21	129.5	1129.1	161.1
14b	0.05917	0.00076	0.80292	0.01097	0.09843	0.00113	0.84	573.50	27.55	605.20	6.60	598.50	6.18	26.6	154.9	46.4
17b	0.05968	0.0007	0.79743	0.01012	0.09693	0.0011	0.89	591.80	25.07	596.40	6.48	595.40	5.72	38.1	229.5	54.7
18b	0.27942	0.00299	23.09753	0.27438	0.59963	0.0068	0.95	3359.70	16.63	3028.30	27.39	3231.10	11.56	1179.7	994.8	119.2
1a	0.05644	0.00075	0.36958	0.00522	0.0475	0.00054	0.80	469.00	29.51	299.10	3.33	319.30	3.87	25.4	293.7	144.1
1b	**0.05322**	**0.00055**	**0.36377**	**0.00418**	**0.04958**	**0.00056**	**0.98**	**338.20**	**23.23**	**311.90**	**3.42**	**315.00**	**3.11**	**299.8**	**3758.0**	**217.2**
23a	0.0654	0.00105	0.82506	0.01371	0.09151	0.00108	0.71	787.20	33.25	564.50	6.36	610.90	7.63	3.8	33.8	8.3

23b	**0.05299**	**0.00055**	**0.36806**	**0.0043**	**0.05038**	**0.00057**	**0.97**	**328.40**	**23.44**	**316.90**	**3.51**	**318.20**	**3.19**	**78.6**	**1451.1**	**13.7**
2a	0.05388	0.00063	0.43036	0.00543	0.05794	0.00065	0.89	365.80	26.12	363.10	3.99	363.40	3.85	29.2	271.6	141.5
2b	0.05312	0.00055	0.34054	0.00389	0.0465	0.00052	0.98	334.10	23.09	293.00	3.21	297.60	2.95	427.5	5726.0	80.3
34a	0.06229	0.0007	0.68072	0.0084	0.07927	0.0009	0.92	684.00	23.91	491.80	5.37	527.20	5.08	79.6	842.0	153.3
34b	0.06165	0.00066	0.88014	0.01046	0.10355	0.00117	0.95	662.10	22.87	635.20	6.83	641.10	5.65	50.1	387.0	127.0
36a	**0.05337**	**0.00062**	**0.36734**	**0.00463**	**0.04992**	**0.00057**	**0.91**	**344.70**	**25.93**	**314.00**	**3.47**	**317.70**	**3.44**	**121.4**	**2228.6**	**39.9**
36b	0.06735	0.00083	1.0093	0.01329	0.1087	0.00124	0.87	848.70	25.27	665.20	7.20	708.50	6.72	11.9	84.0	33.9
41a	**0.05303**	**0.00058**	**0.36931**	**0.00442**	**0.05051**	**0.00057**	**0.94**	**330.20**	**24.48**	**317.60**	**3.49**	**319.10**	**3.28**	**74.2**	**1329.2**	**60.9**
41b	0.05411	0.00064	0.37708	0.00483	0.05054	0.00057	0.88	375.70	26.67	317.90	3.50	324.90	3.56	15.7	250.5	80.1
46a	0.05875	0.00069	0.731	0.00921	0.09025	0.00102	0.90	557.90	25.25	557.00	6.01	557.10	5.40	31.2	306.6	22.8
46b	0.05994	0.00067	0.72241	0.0089	0.08743	0.00099	0.92	601.30	24.06	540.30	5.89	552.10	5.24	80.4	518.3	179.4
49a	**0.05345**	**0.0008**	**0.36262**	**0.0057**	**0.04921**	**0.00057**	**0.74**	**347.80**	**33.56**	**309.70**	**3.50**	**314.20**	**4.25**	**19.1**	**205.5**	**127.1**
49b	0.05288	0.00056	0.43098	0.00508	0.05912	0.00067	0.96	323.50	23.87	370.30	4.07	363.90	3.61	136.2	1423.9	79.4
4a	0.06071	0.00067	0.81932	0.00993	0.09789	0.0011	0.93	629.10	23.71	602.00	6.48	607.70	5.54	57.7	306.6	199.1
4b	0.05799	0.00062	0.41813	0.00493	0.0523	0.00059	0.96	529.10	23.65	328.60	3.61	354.70	3.53	148.6	1740.9	61.5
51a	0.06484	0.00076	0.82708	0.01053	0.09252	0.00105	0.89	769.20	24.46	570.40	6.21	612.00	5.85	111.5	611.3	424.3
51b	**0.05368**	**0.00056**	**0.36629**	**0.00426**	**0.0495**	**0.00056**	**0.97**	**357.40**	**23.30**	**311.40**	**3.43**	**316.90**	**3.16**	**274.4**	**3415.9**	**113.7**
54a	0.10773	0.00111	4.3218	0.0499	0.29101	0.00328	0.98	1761.30	18.73	1646.60	16.39	1697.50	9.52	977.0	1994.7	8.7
62b	0.0552	0.00061	0.39003	0.00472	0.05125	0.00058	0.94	420.30	24.34	322.20	3.54	334.40	3.45	96.6	1138.3	100.6
63a	0.06298	0.00071	0.95966	0.01175	0.11052	0.00125	0.92	707.70	23.72	675.80	7.23	683.10	6.09	92.1	381.5	447.4
63b	0.05277	0.0006	0.43937	0.00543	0.0604	0.00068	0.91	318.90	25.63	378.00	4.14	369.80	3.83	82.4	830.4	50.0
8a	0.05482	0.00059	0.36118	0.00426	0.04779	0.00054	0.96	405.00	23.49	300.90	3.31	313.10	3.18	267.4	3468.8	81.6
8b	0.06177	0.00066	0.82685	0.00973	0.0971	0.00109	0.95	666.20	22.63	597.40	6.43	611.90	5.41	103.6	559.7	326.0

HUEL-3

Zircon	Pb^{207}/Pb^{206}	1σ	Pb^{207}/U^{235}	1σ	Pb^{206}/U^{238}	1σ	rho	Pb^{207}/Pb^{206}	1σ	Pb^{206}/U^{238}	1σ	Pb^{207}/U^{235}	1σ	Pb ppm	Uppm	Thppm
26	0.05349	0.00098	0.29122	0.00541	0.03949	0.00046	0.63	349.50	40.84	249.70	2.84	259.50	4.25	45.2	689.7	76.2
12b	0.05375	0.00107	0.29838	0.006	0.04027	0.00048	0.59	360.30	44.25	254.50	2.97	265.10	4.69	29.9	446.2	92.4
21b	0.0538	0.00065	0.33665	0.00434	0.04539	0.00051	0.87	362.50	26.93	286.20	3.16	294.60	3.30	118.3	1611.2	151.2
17	0.05456	0.0006	0.34448	0.00415	0.04579	0.00052	0.94	394.30	24.39	288.60	3.18	300.60	3.13	479.6	6639.3	39.6
20f	0.05322	0.00055	0.33904	0.00394	0.04621	0.00052	0.97	338.30	23.33	291.20	3.22	296.40	2.99	433.4	5721.9	585.6
31b	0.05284	0.00068	0.33735	0.00459	0.0463	0.00052	0.83	322.10	28.93	291.80	3.21	295.20	3.48	71.9	933.5	127.7
20d	0.05681	0.00066	0.36329	0.00454	0.04638	0.00052	0.90	483.60	25.71	292.30	3.20	314.70	3.38	51.8	632.2	185.6
23	0.0565	0.00058	0.36453	0.00413	0.0468	0.00052	0.98	471.30	22.87	294.80	3.19	315.60	3.08	1614.4	21168.7	308.3
20c	0.05297	0.00062	0.34492	0.00431	0.04724	0.00053	0.90	327.30	26.09	297.50	3.25	300.90	3.25	54.5	659.2	199.4
1	0.05475	0.00057	0.36453	0.0042	0.04829	0.00055	0.99	402.20	22.91	304.00	3.35	315.60	3.13	347.5	4573.5	71.9
35	0.05422	0.0006	0.36441	0.00438	0.04875	0.00054	0.92	380.00	24.89	306.80	3.34	315.50	3.26	550.9	7031.6	84.0
27c	0.05687	0.0006	0.38621	0.00448	0.04926	0.00055	0.96	485.80	23.53	310.00	3.36	331.60	3.28	209.9	2573.8	196.2
31a	**0.05397**	**0.00073**	**0.36856**	**0.00523**	**0.04953**	**0.00056**	**0.80**	**369.80**	**30.25**	**311.60**	**3.43**	**318.60**	**3.88**	**16.6**	**192.3**	**55.1**
20a	**0.05413**	**0.00067**	**0.37125**	**0.00493**	**0.04975**	**0.00056**	**0.85**	**376.10**	**27.91**	**313.00**	**3.46**	**320.60**	**3.65**	**19.9**	**229.5**	**78.7**
20b	**0.05301**	**0.00059**	**0.36393**	**0.00439**	**0.0498**	**0.00056**	**0.93**	**329.00**	**24.80**	**313.30**	**3.44**	**315.10**	**3.26**	**411.6**	**5092.0**	**573.2**
48b	**0.05176**	**0.00054**	**0.35588**	**0.00413**	**0.04988**	**0.00056**	**0.97**	**274.70**	**23.73**	**313.80**	**3.45**	**309.10**	**3.09**	**856.6**	**10753.9**	**131.6**
38b	**0.05294**	**0.00057**	**0.36477**	**0.00428**	**0.04998**	**0.00056**	**0.95**	**326.10**	**24.20**	**314.40**	**3.42**	**315.80**	**3.19**	**529.4**	**6596.2**	**112.7**
38c	**0.05359**	**0.00058**	**0.37115**	**0.00436**	**0.05023**	**0.00056**	**0.95**	**353.90**	**24.11**	**315.90**	**3.43**	**320.50**	**3.23**	**606.9**	**7501.1**	**166.7**
27a	0.05789	0.00061	0.40415	0.00463	0.05064	0.00056	0.97	525.20	23.04	318.50	3.45	344.70	3.35	204.4	2424.3	188.1
15	0.05851	0.00063	0.41304	0.00491	0.0512	0.00058	0.95	549.10	23.50	321.90	3.53	351.10	3.53	324.9	3923.3	214.0
45b	0.05473	0.00058	0.38683	0.0046	0.05127	0.00058	0.95	401.20	23.92	322.30	3.57	332.10	3.37	341.4	4143.2	111.3
20e	0.05195	0.00078	0.3785	0.00595	0.05285	0.00061	0.73	283.40	33.94	332.00	3.75	325.90	4.38	16.6	181.5	55.2
37	0.05705	0.00082	0.43274	0.00647	0.05502	0.00062	0.75	492.90	31.69	345.30	3.82	365.10	4.59	36.3	367.4	131.2

24	0.05341	0.00057	0.44708	0.00522	0.06072	0.00067	0.95	346.20	23.96	380.00	4.10	375.20	3.66	185.9	1862.2	142.8
22	0.05652	0.00066	0.4961	0.0062	0.06367	0.00071	0.89	471.90	25.79	397.90	4.31	409.10	4.21	48.2	449.1	56.2
14b	0.05407	0.00071	0.50212	0.00701	0.06736	0.00077	0.82	373.70	29.52	420.20	4.63	413.10	4.74	31.5	279.6	51.6
48a	0.05908	0.00065	0.59417	0.00723	0.07296	0.00083	0.93	569.90	23.95	453.90	4.97	473.50	4.61	81.9	550.9	411.1
32b	0.05945	0.00064	0.67686	0.00797	0.08258	0.00092	0.95	583.70	23.31	511.50	5.47	524.90	4.83	78.4	569.5	67.5
13	0.06365	0.00078	0.73011	0.00959	0.08321	0.00094	0.86	729.90	25.75	515.20	5.62	556.60	5.63	45.1	311.1	80.4
41	0.05896	0.00084	0.72051	0.01067	0.08864	0.001	0.76	565.50	30.57	547.50	5.95	551.00	6.30	9.0	56.5	20.2
38a	0.05703	0.00066	0.72877	0.00909	0.09269	0.00104	0.90	492.20	25.69	571.40	6.11	555.80	5.34	33.6	200.2	81.5
14a	0.06108	0.00074	0.78952	0.01032	0.09376	0.00106	0.86	642.10	25.98	577.70	6.27	590.90	5.86	25.1	147.2	73.8
9a	0.06576	0.00081	0.86647	0.01148	0.09557	0.00109	0.86	798.70	25.73	588.40	6.41	633.60	6.25	67.7	411.4	80.9
6a	0.06064	0.00065	0.83765	0.00988	0.1002	0.00113	0.96	626.40	22.87	615.60	6.63	617.80	5.46	67.3	368.5	187.1
29	0.06878	0.0011	1.09141	0.01786	0.1151	0.00133	0.71	892.00	32.59	702.30	7.69	749.20	8.67	21.5	84.5	103.8
42	0.06886	0.00104	1.12018	0.01772	0.118	0.00139	0.74	894.50	30.92	719.10	7.99	763.10	8.49	24.3	98.8	93.3
7	0.0633	0.00069	1.05106	0.01257	0.12043	0.00136	0.94	718.40	22.94	733.10	7.83	729.40	6.22	43.8	214.5	54.1
47	0.07141	0.00085	1.29354	0.01664	0.13139	0.0015	0.89	969.20	23.99	795.80	8.55	842.90	7.37	64.9	265.2	127.7
30a	0.10675	0.00115	3.9793	0.04671	0.2704	0.00301	0.95	1744.60	19.63	1542.80	15.29	1630.00	9.53	78.5	140.6	113.6
40a	0.12537	0.00136	6.41082	0.07581	0.3709	0.00413	0.94	2034.10	19.09	2033.60	19.44	2033.80	10.39	164.2	240.4	73.2
10	0.17404	0.00181	10.04778	0.11595	0.41875	0.00471	0.97	2596.90	17.25	2254.80	21.41	2439.20	10.66	908.7	1223.2	36.2

Analyses U-Pb sur zircon – Orthogneiss paléozoïques inférieurs

		Isotope ratios							Ages						Concentrations (ppm)			Th/U
Sample	Zircon analyses	Pb^{207}/Pb^{206}	1σ	Pb^{207}/U^{235}	1σ	Pb^{206}/U^{238}	1σ	rho	Pb^{207}/Pb^{206}	1σ	Pb^{206}/U^{238}	1σ	Pb^{207}/U^{235}	1σ	Pb	U	Th	
PLG-1	5	0.05669	0.00064	0.58448	0.00708	0.07478	0.00082	0.91	478.8	25.17	464.9	4.93	467.3	4.54	134.3	1058.3	256.1	0.24
PLG-1	9	0.05724	0.00065	0.59193	0.00715	0.07501	0.00082	0.91	500.4	25.05	466.2	4.93	472.1	4.56	140.8	1112.0	236.5	0.21
PLG-1	26	0.05644	0.0007	0.58524	0.00749	0.07521	0.00082	0.85	469.1	27.23	467.5	4.9	467.8	4.8	126.8	989.0	198.6	0.20
PLG-1	19	0.05659	0.00069	0.58676	0.00747	0.07521	0.00082	0.86	474.8	26.94	467.5	4.93	468.8	4.78	109.1	837.1	233.1	0.28
PLG-1	35	0.05668	0.00066	0.59044	0.00726	0.07557	0.00082	0.88	478.2	25.86	469.6	4.94	471.1	4.64	89.0	696.1	187.7	0.27
PLG-1	38	0.05623	0.00067	0.58984	0.00739	0.07609	0.00083	0.87	460.5	26.47	472.8	4.96	470.8	4.72	102.5	788.2	229.6	0.29
PLG-1	34	0.05709	0.00065	0.60150	0.00726	0.07642	0.00083	0.90	494.6	25.3	474.7	4.99	478.2	4.6	145.4	1112.7	342.1	0.31
PLG-1	7	0.05790	0.00065	0.61114	0.00731	0.07657	0.00084	0.92	525.5	24.67	475.6	5.03	484.3	4.61	135.0	1034.0	262.0	0.25
PLG-1	13	0.05699	0.00067	0.60374	0.00747	0.07685	0.00084	0.88	490.4	25.98	477.3	5.04	479.6	4.73	123.2	973.2	114.6	0.12
PLG-1	30	0.05757	0.00071	0.61223	0.00782	0.07715	0.00084	0.85	513	26.58	479.1	5.01	485	4.93	203.2	1567.8	225.1	0.14
PLG-1	37b	0.05738	0.00067	0.61238	0.00749	0.07741	0.00084	0.89	505.6	25.42	480.7	5.04	485.1	4.72	171.9	1349.1	199.8	0.15
PLG-1	42	0.05748	0.00069	0.61375	0.00762	0.07745	0.00084	0.87	509.5	25.92	480.9	5	485.9	4.8	110.0	840.4	184.3	0.22
PLG-1	33	0.05676	0.00078	0.60660	0.00861	0.07753	0.00086	0.78	481.3	30.38	481.3	5.13	481.4	5.44	23.1	177.1	45.3	0.26
PLG-1	49	0.05737	0.00073	0.61544	0.00801	0.07781	0.00084	0.83	505.4	27.65	483	5	487	5.03	91.7	682.7	181.9	0.27
PLG-1	37a	0.05690	0.00074	0.61177	0.00830	0.07798	0.00086	0.81	487.1	28.97	484.1	5.12	484.7	5.23	48.3	356.3	121.9	0.34
PLG-1	46	0.05719	0.00073	0.61862	0.00811	0.07846	0.00085	0.83	498.2	28.1	486.9	5.06	489	5.09	56.8	417.7	121.3	0.29
PLG-1	18	0.05721	0.00068	0.61977	0.00772	0.07859	0.00086	0.88	498.9	26.15	487.7	5.13	489.7	4.84	103.4	763.0	201.9	0.26
PLG-1	27	0.05714	0.0007	0.62002	0.00787	0.07871	0.00085	0.85	496.5	27.01	488.4	5.11	489.9	4.93	165.2	1236.0	222.8	0.18
PLG-1	25	0.05748	0.00073	0.63305	0.00831	0.07989	0.00087	0.83	509.7	27.44	495.4	5.2	498	5.17	66.6	502.9	52.1	0.10
PLG-1	23	0.05720	0.00068	0.63241	0.00789	0.08019	0.00087	0.87	498.9	26.33	497.3	5.2	497.6	4.91	149.5	1150.5	38.0	0.03
PLG-1	44	0.05783	0.00073	0.64604	0.00842	0.08103	0.00088	0.83	523.2	27.74	502.2	5.22	506	5.2	71.5	528.5	85.2	0.16
PLG-1	1	0.05739	0.00071	0.64584	0.00838	0.08164	0.00090	0.85	505.9	26.77	505.9	5.39	505.9	5.17	41.3	298.6	69.4	0.23
PLG-1	22	0.05734	0.00069	0.64940	0.00811	0.08215	0.00089	0.87	504.3	26.13	508.9	5.32	508.1	4.99	134.0	950.0	210.3	0.22
PLG-1	39	0.05779	0.00078	0.65578	0.00909	0.08230	0.00090	0.79	521.8	29.41	509.9	5.37	512	5.57	24.9	177.5	50.4	0.28
PLG-1	21	0.05674	0.00068	0.64638	0.00814	0.08263	0.00090	0.86	480.8	26.69	511.8	5.36	506.3	5.02	113.8	804.0	191.8	0.24
PLG-1	43	0.05807	0.00076	0.66411	0.00893	0.08295	0.00090	0.81	532	28.84	513.7	5.36	517.1	5.45	38.0	266.5	73.2	0.27

PLG-1	17	0.05790	0.00074	0.60151	0.00796	0.07535	0.00083	0.83	525.7	27.89	468.3	4.96	478.2	5.04	108.2	862.3	119.1	0.14
PLG-1	48	0.05796	0.00072	0.60312	0.00770	0.07549	0.00081	0.84	527.7	27.33	469.1	4.86	479.2	4.88	145.1	1123.2	272.5	0.24
PLG-1	4	0.05829	0.00065	0.61979	0.00743	0.07713	0.00085	0.92	539.9	24.98	479	5.08	489.7	4.66	123.2	939.5	237.1	0.25
PLG-1	6	0.05841	0.00071	0.62419	0.00801	0.07751	0.00086	0.86	545.2	26.36	481.3	5.12	492.5	5	57.6	425.1	140.7	0.33
PLG-1	28	0.05843	0.00074	0.62066	0.00814	0.07705	0.00084	0.83	546	27.49	478.5	5.02	490.3	5.1	80.7	600.0	170.4	0.28
PLG-1	14	0.05829	0.00072	0.59105	0.00766	0.07356	0.00081	0.85	539.9	27.52	457.5	4.85	471.5	4.89	127.3	1003.4	266.4	0.27
PLG-1	29	0.05879	0.00087	0.61039	0.00922	0.07531	0.00083	0.73	559.4	32.03	468.1	4.98	483.8	5.81	63.5	480.7	134.6	0.28
PLG-1	8	0.05831	0.00067	0.56103	0.00684	0.06979	0.00077	0.90	540.9	25.56	434.9	4.62	452.2	4.45	179.7	1504.5	380.5	0.25
PLG-1	15	0.05929	0.0007	0.59244	0.00736	0.07248	0.00079	0.88	577.8	25.46	451.1	4.77	472.4	4.7	152.8	1240.2	237.3	0.19
PLG-1	41	0.05902	0.00071	0.56103	0.00698	0.06895	0.00075	0.87	567.8	25.95	429.8	4.49	452.2	4.54	187.6	1613.4	315.3	0.20
PLG-1	45	0.06165	0.001	0.59256	0.00970	0.06972	0.00077	0.67	661.9	34.44	434.5	4.66	472.5	6.18	27.1	220.2	60.4	0.27
PLG-1	32	0.05761	0.00062	0.68705	0.00790	0.08651	0.00094	0.94	514.5	23.16	534.9	5.59	531	4.76	650.0	4744.4	263.4	0.06
PLG-1	2	0.05965	0.00067	0.76106	0.00916	0.09254	0.00102	0.92	591	24.21	570.6	6.01	574.6	5.28	98.3	668.4	11.6	0.02
PLG-1	24	0.06130	0.00086	0.79997	0.01152	0.09465	0.00104	0.76	649.9	29.89	583	6.14	596.8	6.5	55.9	218.4	482.1	2.21
PLG-1	10	0.06201	0.00076	0.81846	0.01050	0.09573	0.00106	0.86	674.6	25.86	589.4	6.21	607.2	5.86	57.6	313.2	213.1	0.68
PLG-1	3	0.06732	0.00073	1.18043	0.01378	0.12720	0.00140	0.94	847.6	22.42	771.9	7.99	791.5	6.42	288.2	1159.4	777.3	0.67
PLG-1	36	0.06753	0.00074	1.31560	0.01537	0.14130	0.00154	0.93	854.3	22.7	852	8.67	852.6	6.74	256.0	1037.1	366.6	0.35
PLG-1	31	0.12491	0.00137	6.81847	0.07977	0.39595	0.00434	0.94	2027.6	19.29	2150.4	20.03	2088.1	10.36	170.3	207.3	190.6	0.92
PLG-2	101	0.05766	0.00066	0.62716	0.00793	0.07890	0.00091	0.91	516.6	24.48	489.5	5.45	494.3	4.95	134.7	1044.8	409.2	0.39
PLG-2	86	0.05773	0.00066	0.63763	0.00810	0.08011	0.00093	0.91	519.4	25.23	496.8	5.54	500.8	5.02	33.4	282.7	17.4	0.06
PLG-2	2b	0.05722	0.00063	0.63265	0.00760	0.08021	0.00090	0.93	499.3	24.19	497.3	5.4	497.7	4.73	59.0	427.2	105.3	0.25
PLG-2	42	0.05789	0.00068	0.64086	0.00810	0.08030	0.00091	0.90	525.3	25.7	497.9	5.41	502.8	5.01	31.6	222.8	79.7	0.36
PLG-2	71	0.05724	0.00071	0.63433	0.00828	0.08038	0.00090	0.86	500.4	27.1	498.4	5.35	498.8	5.15	18.5	134.3	25.8	0.19
PLG-2	70	0.05725	0.00075	0.63485	0.00876	0.08044	0.00090	0.81	500.6	28.81	498.7	5.38	499.1	5.44	12.1	88.2	15.5	0.18
PLG-2	98	0.05657	0.00082	0.62801	0.00969	0.08052	0.00095	0.76	474.3	32.19	499.2	5.65	494.9	6.04	15.1	121.4	25.2	0.21
PLG-2	50	0.05735	0.00066	0.63709	0.00785	0.08058	0.00090	0.91	504.5	25.01	499.6	5.37	500.5	4.87	33.3	246.6	33.2	0.13
PLG-2	88	0.05741	0.00063	0.63837	0.00787	0.08066	0.00093	0.94	506.8	24.09	500.1	5.56	501.3	4.88	103.5	794.4	290.8	0.37
PLG-2	8	0.05755	0.00062	0.64067	0.00759	0.08075	0.00090	0.94	512.4	23.4	500.6	5.4	502.7	4.7	118.8	813.5	306.3	0.38
PLG-2	94	0.05709	0.00065	0.63575	0.00800	0.08077	0.00093	0.92	494.6	25.11	500.7	5.57	499.7	4.96	57.7	437.4	172.8	0.40
PLG-2	4a	0.05714	0.00064	0.63743	0.00784	0.08092	0.00091	0.91	496.3	24.99	501.6	5.45	500.7	4.86	36.7	256.7	86.2	0.34
PLG-2	2a	0.05766	0.00068	0.64322	0.00826	0.08092	0.00092	0.89	516.4	25.43	501.6	5.47	504.3	5.1	19.2	139.8	28.7	0.21
PLG-2	105	0.05766	0.00069	0.64385	0.00847	0.08099	0.00094	0.88	516.7	26.42	502	5.6	504.7	5.23	41.1	324.4	81.6	0.25
PLG-2	30	0.05768	0.00076	0.64472	0.00895	0.08108	0.00092	0.82	517.4	28.87	502.5	5.48	505.2	5.53	31.2	225.4	48.4	0.21
PLG-2	12	0.05765	0.00075	0.64494	0.00886	0.08115	0.00092	0.83	516.1	28.59	503	5.47	505.4	5.47	11.5	82.8	17.3	0.21
PLG-2	1	0.05782	0.00063	0.64692	0.00780	0.08116	0.00092	0.94	522.7	24.07	503	5.47	506.6	4.81	54.5	375.3	140.5	0.37
PLG-2	26	0.05752	0.00067	0.64634	0.00810	0.08151	0.00091	0.89	511	25.2	505.1	5.44	506.2	4.99	54.3	407.8	19.9	0.05
PLG-2	15	0.05748	0.00068	0.64635	0.00818	0.08156	0.00091	0.88	509.6	25.61	505.4	5.45	506.2	5.05	25.0	180.7	29.5	0.16
PLG-2	59	0.05708	0.00066	0.64205	0.00799	0.08159	0.00091	0.90	494.1	25.72	505.6	5.42	503.6	4.94	26.1	182.2	54.4	0.30
PLG-2	56	0.05750	0.00064	0.64713	0.00782	0.08163	0.00091	0.92	510.4	24.24	505.9	5.42	506.7	4.82	35.8	251.5	67.0	0.27
PLG-2	78	0.05685	0.00073	0.63995	0.00886	0.08166	0.00095	0.84	484.9	28.29	506	5.68	502.3	5.49	14.8	117.8	22.9	0.19
PLG-2	17	0.05673	0.00065	0.63918	0.00791	0.08172	0.00091	0.90	480.3	25.5	506.4	5.44	501.8	4.9	38.7	268.9	75.1	0.28
PLG-2	28	0.05811	0.00077	0.65516	0.00916	0.08177	0.00093	0.81	533.5	29.26	506.7	5.52	511.7	5.62	9.6	68.8	12.7	0.18
PLG-2	14	0.05783	0.00065	0.65348	0.00799	0.08196	0.00092	0.92	523.2	24.87	507.8	5.46	510.6	4.91	45.0	314.3	85.9	0.27
PLG-2	55	0.05749	0.00066	0.64996	0.00799	0.08200	0.00091	0.90	510	24.74	508.1	5.45	508.5	4.92	27.0	189.5	47.5	0.25
PLG-2	10	0.05775	0.00065	0.65961	0.00804	0.08284	0.00093	0.92	520.2	24.69	513.1	5.53	514.4	4.92	45.9	315.1	92.7	0.29
PLG-2	53	0.05706	0.00064	0.65222	0.00790	0.08291	0.00092	0.92	493.4	24.81	513.5	5.5	509.8	4.85	33.1	233.1	50.7	0.22
PLG-2	93	0.05815	0.0007	0.66645	0.00875	0.08313	0.00096	0.88	535	26.53	514.8	5.74	518.6	5.33	27.5	206.3	67.3	0.33
PLG-2	6	0.05753	0.00066	0.66411	0.00831	0.08374	0.00094	0.90	511.4	24.99	518.4	5.62	517.1	5.07	26.0	182.9	34.4	0.19
PLG-2	23	0.05777	0.00067	0.67009	0.00837	0.08413	0.00094	0.89	521	25.5	520.7	5.6	520.8	5.09	23.2	159.9	37.7	0.24
PLG-2	29	0.05726	0.00063	0.66632	0.00803	0.08441	0.00094	0.92	501.1	24.43	522.4	5.62	518.5	4.89	39.8	281.3	41.1	0.15
PLG-2	33	0.05718	0.00069	0.66979	0.00863	0.08497	0.00096	0.88	497.8	26.52	525.7	5.69	520.6	5.25	19.4	134.4	27.4	0.20
PLG-2	92	0.05805	0.00066	0.68955	0.00873	0.08615	0.00100	0.92	531.4	25.28	532.8	5.92	532.5	5.25	45.5	329.2	106.7	0.32
PLG-2	91	0.05664	0.00071	0.66261	0.00900	0.08486	0.00099	0.86	476.6	27.62	525.1	5.87	516.2	5.5	36.1	280.1	43.2	0.15

PLG-2	87	0.05711	0.00064	0.67864	0.00843	0.08619	0.00100	0.93	495.3	24.72	533	5.92	526	5.1	57.2	418.9	127.6	0.30
PLG-2	96	0.05703	0.00074	0.66849	0.00939	0.08502	0.00099	0.83	492.1	28.81	526	5.89	519.8	5.71	16.5	122.7	36.8	0.30
PLG-2	22	0.05656	0.00067	0.63517	0.00804	0.08145	0.00091	0.88	473.8	26.1	504.8	5.43	499.3	4.99	19.9	144.3	24.7	0.17
PLG-2	83	0.05643	0.00068	0.62526	0.00826	0.08037	0.00093	0.88	468.6	26.65	498.3	5.57	493.1	5.16	23.4	189.5	39.6	0.21
PLG-2	27	0.05872	0.00067	0.69151	0.00848	0.08542	0.00096	0.92	556.6	24.52	528.4	5.68	533.7	5.09	32.1	217.4	51.8	0.24
PLG-2	40	0.05774	0.00063	0.63050	0.00753	0.07921	0.00089	0.94	519.5	23.99	491.4	5.32	496.4	4.69	123.1	850.3	387.4	0.46
PLG-2	51	0.05793	0.00062	0.64067	0.00748	0.08022	0.00089	0.95	526.7	23.59	497.5	5.33	502.7	4.63	76.0	555.1	108.7	0.20
PLG-2	13	0.05804	0.00069	0.64727	0.00824	0.08089	0.00091	0.88	530.9	26.22	501.4	5.42	506.8	5.08	25.1	172.1	65.7	0.38
PLG-2	103	0.05833	0.0007	0.65785	0.00860	0.08180	0.00095	0.89	541.5	26.53	506.9	5.65	513.3	5.27	51.8	406.6	96.9	0.24
PLG-2	60	0.05801	0.0007	0.63693	0.00822	0.07964	0.00089	0.87	529.7	26.75	494	5.31	500.4	5.1	18.3	134.0	27.0	0.20
PLG-2	76	0.05851	0.0007	0.66750	0.00848	0.08275	0.00092	0.88	548.9	25.92	512.5	5.48	519.2	5.17	25.7	174.1	56.7	0.33
PLG-2	31	0.05848	0.00065	0.66464	0.00800	0.08244	0.00092	0.93	547.8	23.96	510.7	5.5	517.5	4.88	47.8	348.6	41.6	0.12
PLG-2	100	0.05843	0.00071	0.66012	0.00873	0.08195	0.00095	0.88	545.9	26.2	507.7	5.67	514.7	5.34	34.6	267.0	74.9	0.28
PLG-2	19a	0.05899	0.00067	0.69447	0.00848	0.08539	0.00095	0.91	566.8	24.45	528.2	5.65	535.5	5.08	51.9	359.2	56.9	0.16
PLG-2	54	0.05791	0.00062	0.62476	0.00731	0.07825	0.00087	0.95	526.1	23.65	485.7	5.2	492.8	4.57	87.8	622.2	238.3	0.38
PLG-2	37	0.05773	0.00062	0.61278	0.00725	0.07699	0.00086	0.94	519.2	23.72	478.2	5.17	485.3	4.56	181.6	1436.2	117.9	0.08
PLG-2	5	0.05811	0.00065	0.63637	0.00775	0.07943	0.00089	0.92	533.5	24.72	492.7	5.34	500.1	4.81	50.4	353.2	136.1	0.39
PLG-2	16	0.05846	0.00069	0.65626	0.00831	0.08142	0.00091	0.88	547.2	25.65	504.6	5.44	512.3	5.1	30.9	220.3	43.0	0.19
PLG-2	32	0.05856	0.00076	0.66203	0.00907	0.08200	0.00093	0.83	550.9	27.98	508	5.53	515.9	5.54	12.6	90.7	16.7	0.18
PLG-2	38	0.05839	0.00065	0.64930	0.00784	0.08066	0.00091	0.93	544.3	23.99	500.1	5.41	508	4.83	63.2	476.3	40.2	0.08
PLG-2	66	0.05850	0.00068	0.65475	0.00810	0.08119	0.00090	0.90	548.5	25.01	503.2	5.38	511.4	4.97	28.2	198.3	52.8	0.27
PLG-2	57	0.05828	0.00071	0.63842	0.00832	0.07946	0.00089	0.86	539.7	27.24	492.9	5.31	501.3	5.16	24.5	174.5	54.3	0.31
PLG-2	45	0.05807	0.00066	0.62025	0.00764	0.07748	0.00087	0.91	531.9	25.01	481	5.23	490	4.79	125.5	938.6	245.2	0.26
PLG-2	106	0.05775	0.0007	0.59690	0.00795	0.07497	0.00087	0.87	520	26.76	466.1	5.22	475.3	5.05	63.0	500.6	241.8	0.48
PLG-2	74	0.05914	0.00069	0.71310	0.00888	0.08746	0.00097	0.89	572.4	25.18	540.5	5.76	546.6	5.26	31.4	210.0	36.5	0.17
PLG-2	43	0.05707	0.0007	0.70020	0.00918	0.08899	0.00101	0.87	493.7	27.04	549.6	5.97	538.9	5.48	51.7	352.0	40.1	0.11
PLG-2	18	0.06024	0.00099	0.75382	0.01275	0.09077	0.00104	0.68	612.2	35.25	560.1	6.17	570.4	7.38	7.9	35.8	61.3	1.71
PLG-2	73	0.06033	0.00067	0.77592	0.00928	0.09329	0.00103	0.92	615.4	23.81	575	6.09	583.2	5.3	107.7	604.2	337.4	0.56
PLG-2	90	0.06004	0.00067	0.78318	0.00974	0.09461	0.00109	0.93	605.1	23.97	582.8	6.44	587.3	5.55	65.0	467.0	22.2	0.05
PLG-2	99	0.06022	0.00081	0.81326	0.01178	0.09795	0.00115	0.81	611.6	28.95	602.4	6.72	604.3	6.6	16.9	86.3	98.7	1.14
PLG-2	82	0.06125	0.00064	0.89173	0.01058	0.10561	0.00122	0.97	648	22.34	647.2	7.1	647.3	5.68	304.4	1969.2	59.3	0.03
PLG-2	46	0.06274	0.00077	1.02533	0.0135	0.11853	0.00135	0.87	699.6	25.91	722.1	7.76	716.6	6.77	20.1	90.4	51.3	0.57
PLG-2	35	0.07240	0.00079	1.69691	0.02033	0.17002	0.00191	0.94	997.1	22.14	1012.2	10.51	1007.4	7.65	57.2	167.3	142.4	0.85
PLG-2	36	0.11506	0.00135	5.32109	0.06718	0.33546	0.00381	0.90	1880.7	20.99	1864.8	18.39	1872.3	10.79	26.1	29.1	63.8	2.19
PLG-2	80	0.29600	0.00307	27.68851	0.32566	0.67852	0.00784	0.98	3449.4	15.98	3338.7	30.09	3408.1	11.53	365.4	242.9	275.4	1.13
PLG-2	20	0.06021	0.0007	0.58041	0.00728	0.06993	0.00078	0.89	611	25.05	435.7	4.71	464.7	4.67	54.4	475.5	11.5	0.02
PLG-2	3	0.05731	0.00063	0.55532	0.00666	0.07029	0.00079	0.94	502.8	24.01	437.9	4.77	448.5	4.35	105.6	935.4	4.5	0.00
PLG-2	58	0.05957	0.00065	0.60094	0.00708	0.07318	0.00081	0.94	587.9	23.38	455.3	4.88	477.8	4.49	157.7	1306.9	58.1	0.04
PLG-2	25	0.06067	0.00067	0.62386	0.00744	0.07459	0.00083	0.93	627.5	23.47	463.7	4.99	492.3	4.65	65.6	539.9	11.0	0.02
PLG-2	95	0.05819	0.00074	0.60317	0.00833	0.07518	0.00088	0.85	536.5	28.23	467.3	5.25	479.2	5.28	54.9	458.6	131.2	0.29
PLG-2	21	0.06133	0.00065	0.65658	0.0076	0.07765	0.00086	0.96	650.8	22.54	482.1	5.16	512.5	4.66	141.7	1094.7	75.0	0.07
PLG-2	9	0.05833	0.00065	0.62959	0.00763	0.07829	0.00088	0.93	541.5	24.88	485.9	5.25	495.8	4.75	117.4	832.8	304.8	0.37
PLG-2	68	0.05853	0.00067	0.63596	0.00781	0.07882	0.00088	0.91	549.6	24.81	489.1	5.23	499.8	4.85	51.5	359.0	148.8	0.41
PLG-2	4b	0.06045	0.00082	0.67396	0.00967	0.08088	0.00092	0.79	619.6	29.08	501.3	5.51	523.1	5.87	8.7	62.6	12.6	0.20
PLG-2	48	0.05978	0.00068	0.66858	0.00817	0.08112	0.00091	0.92	595.1	24.88	502.8	5.4	519.8	4.97	54.9	383.3	117.3	0.31
PLG-2	7	0.06421	0.0007	0.71897	0.00857	0.08122	0.00091	0.94	748.6	22.81	503.4	5.44	550.1	5.06	68.3	499.2	43.9	0.09
PLG-2	47	0.05913	0.00067	0.66245	0.00807	0.08126	0.00091	0.92	571.9	24.3	503.7	5.41	516.1	4.93	37.8	266.7	72.7	0.27
PLG-2	19b	0.06325	0.00066	0.71155	0.00814	0.0816	0.00091	0.97	716.6	21.99	505.7	5.4	545.7	4.83	157.0	1167.4	20.4	0.02
PLG-2	65	0.05940	0.00081	0.67252	0.00957	0.08212	0.00092	0.79	581.9	29.26	508.8	5.51	522.2	5.81	9.1	63.0	16.9	0.27
PLG-2	97	0.06246	0.00072	0.72777	0.00932	0.08452	0.00098	0.91	689.9	24.56	523	5.82	555.2	5.48	48.5	344.7	142.8	0.41
PLG-2	34	0.06389	0.00074	0.75774	0.00945	0.08603	0.00097	0.90	738	24.26	532	5.74	572.7	5.46	25.9	165.8	60.4	0.36
PLG-2	75	0.06073	0.00069	0.72589	0.00882	0.08671	0.00096	0.91	629.6	24.23	536	5.7	554.1	5.19	65.4	411.5	165.4	0.40
PLG-2	72	0.06053	0.00068	0.73501	0.00888	0.08808	0.00098	0.92	622.6	24.08	544.2	5.78	559.5	5.2	60.6	369.0	174.8	0.47

PLG-2	102	0.06428	0.00078	0.82513	0.01099	0.0931	0.00108	0.87	751	25.56	573.9	6.38	610.9	6.12	33.8	194.3	161.1	0.83
PLG-2	79	0.06365	0.00081	0.8241	0.0114	0.09391	0.0011	0.85	730.2	26.83	578.6	6.46	610.3	6.35	17.1	94.4	95.5	1.01
PLG-2	85	0.06189	0.00069	0.81081	0.01006	0.09503	0.0011	0.93	670.3	23.63	585.2	6.47	602.9	5.64	58.1	375.8	135.6	0.36
PLG-2	24	0.12460	0.00129	5.58605	0.06359	0.3252	0.00362	0.98	2023.1	18.22	1815.1	17.6	1913.9	9.8	172.8	305.4	13.2	0.04
PLG-3	1	0.05876	0.00067	0.60039	0.00817	0.07411	0.00094	0.93	558.3	24.58	460.9	5.65	477.5	5.18	113.1	990.1	489.1	0.49
PLG-3	2	0.05970	0.00076	0.86243	0.01265	0.10479	0.00134	0.87	593	26.75	642.4	7.81	631.5	6.89	35.6	204.6	107.5	0.53
PLG-3	3	0.06039	0.00068	0.78839	0.01071	0.0947	0.0012	0.93	617.4	24.28	583.3	7.08	590.3	6.08	135.9	848.2	597.1	0.70
PLG-3	6a	0.05996	0.00074	0.73074	0.01056	0.0884	0.00113	0.88	602.2	26.64	546.1	6.68	557	6.19	49.3	352.7	103.7	0.29
PLG-3	7a	0.05689	0.00065	0.60314	0.0082	0.07691	0.00098	0.94	486.5	25.14	477.6	5.84	479.2	5.19	273.6	2474.8	39.7	0.02
PLG-3	8b	0.06085	0.00068	0.87523	0.01177	0.10432	0.00132	0.94	634.1	23.87	639.7	7.72	638.4	6.38	104.6	656.1	145.8	0.22
PLG-3	9	0.05915	0.00065	0.6864	0.00915	0.08417	0.00107	0.95	572.8	23.77	520.9	6.34	530.6	5.51	257.8	1902.3	917.8	0.48
PLG-3	10	0.05832	0.00065	0.72188	0.00971	0.08978	0.00114	0.94	541.3	24.94	554.2	6.74	551.8	5.73	129.7	930.5	258.0	0.28
PLG-3	11	0.05835	0.00068	0.64155	0.00885	0.07975	0.00101	0.92	542.9	25.19	494.6	6.05	503.3	5.48	265.7	2263.9	252.0	0.11
PLG-3	12	0.05707	0.00084	0.67167	0.01104	0.08537	0.0011	0.78	493.5	32.57	528.1	6.54	521.7	6.71	43.8	333.7	81.3	0.24
PLG-3	14a	0.06047	0.00072	0.74594	0.01047	0.08948	0.00114	0.91	620.5	25.5	552.4	6.74	565.9	6.09	130.5	861.4	493.8	0.57
PLG-3	15	0.06252	0.00075	0.84488	0.01192	0.09803	0.00125	0.90	691.9	25.39	602.8	7.32	621.8	6.56	110.0	682.7	288.0	0.42
PLG-3	16	0.05984	0.00069	0.78076	0.01075	0.09464	0.0012	0.92	597.7	24.87	582.9	7.08	585.9	6.13	449.6	2865.3	1417.0	0.49
PLG-3	17	0.05881	0.00081	0.64901	0.01013	0.08005	0.00103	0.82	560	29.84	496.4	6.13	507.9	6.24	46.5	275.7	431.1	1.56
PLG-4	1	0.06347	0.00083	0.81091	0.01163	0.09267	0.0011	0.83	724.1	27.65	571.3	6.5	603	6.52	33.0	232.5	50.1	0.22
PLG-4	3	0.05790	0.00076	0.7119	0.01016	0.08918	0.00105	0.82	525.8	28.73	550.7	6.24	545.9	6.03	15.5	114.5	25.1	0.22
PLG-4	4	0.05577	0.00066	0.64455	0.00848	0.08383	0.00098	0.89	442.9	25.6	519	5.85	505.1	5.23	38.6	299.6	78.8	0.26
PLG-4	6	0.06187	0.00068	0.90994	0.0113	0.10669	0.00124	0.94	669.4	23.31	653.5	7.25	657	6	81.3	421.6	355.1	0.84
PLG-4	7	0.05758	0.00066	0.6409	0.00821	0.08074	0.00094	0.91	513.5	24.7	500.5	5.62	502.9	5.08	51.7	427.6	65.5	0.15
PLG-4	8b	0.05957	0.00098	0.70099	0.01229	0.08535	0.00107	0.72	588.1	35.42	528	6.36	539.4	7.34	36.2	257.3	74.7	0.29
PLG-4	9	0.05750	0.0007	0.72708	0.00969	0.09173	0.00107	0.88	510.2	26.18	565.8	6.32	554.8	5.7	22.4	159.8	33.8	0.21
PLG-4	10	0.05640	0.00073	0.65419	0.00923	0.08414	0.00099	0.83	467.4	28.75	520.8	5.86	511.1	5.67	23.2	167.2	83.4	0.50
PLG-4	13	0.06103	0.00071	0.81341	0.01044	0.09667	0.00111	0.89	640.5	24.89	594.9	6.55	604.4	5.85	41.6	257.2	120.2	0.47
PLG-4	14	0.05690	0.00068	0.73208	0.0096	0.09333	0.00108	0.88	486.9	26.59	575.2	6.35	557.8	5.63	49.2	334.5	94.6	0.28
PLG-4	16	0.05878	0.0007	0.75445	0.00975	0.09311	0.00107	0.89	558.8	25.61	573.9	6.3	570.8	5.64	40.6	296.6	8.0	0.03
PLG-4	17	0.15898	0.0018	10.14381	0.12604	0.46283	0.00532	0.93	2444.8	19	2452	23.44	2448	11.48	39.8	42.2	45.4	1.08
PLG-4	18	0.11741	0.00133	5.20227	0.06454	0.32139	0.00368	0.92	1917.2	20.12	1796.5	17.95	1853	10.57	137.9	257.0	55.8	0.22
PLG-4	19	0.18141	0.00202	12.95991	0.15839	0.51818	0.00589	0.93	2665.8	18.35	2691.4	25.02	2676.7	11.52	109.6	115.3	54.6	0.47
PLG-4	20	0.06220	0.00088	1.00137	0.01485	0.11677	0.00135	0.78	681.1	29.84	711.9	7.78	704.5	7.53	41.2	218.9	61.6	0.28
PLG-4	21	0.12878	0.00146	7.05823	0.08703	0.39754	0.00451	0.92	2081.4	19.77	2157.7	20.81	2118.8	10.97	84.1	118.9	65.5	0.55
PLG-4	22	0.06068	0.00074	0.88601	0.01163	0.10591	0.0012	0.86	627.9	26.14	648.9	7.02	644.2	6.26	44.4	227.7	186.5	0.82
PLG-4	23	0.05965	0.00079	0.83974	0.01173	0.10212	0.00117	0.82	590.8	28.35	626.8	6.82	619	6.47	48.4	259.3	199.1	0.77
PLG-4	24	0.05689	0.00066	0.66767	0.00837	0.08512	0.00096	0.90	486.7	25.69	526.6	5.71	519.3	5.1	95.5	751.3	32.2	0.04
PLG-4	25	0.06018	0.00077	0.93506	0.01266	0.11269	0.00128	0.84	610.1	27.31	688.4	7.42	670.3	6.64	25.9	129.4	84.4	0.65
PLG-4	26	0.06253	0.0008	1.0085	0.01362	0.11697	0.00133	0.84	692.4	26.91	713.1	7.66	708.1	6.89	23.4	118.1	54.8	0.46
PLG-4	27	0.05679	0.00088	0.60215	0.0096	0.0769	0.00089	0.73	482.7	34.11	477.6	5.3	478.6	6.08	29.5	246.3	40.7	0.17
PLG-4	28	0.05640	0.00072	0.66402	0.00901	0.08539	0.00097	0.84	467.6	28.37	528.2	5.74	517.1	5.5	36.0	266.9	56.7	0.21
PLG-4	31	0.05894	0.00072	0.63184	0.00906	0.07776	0.00099	0.89	564.8	26.54	482.8	5.91	497.2	5.64	61.1	515.9	79.1	0.15
PLG-4	34	0.05735	0.00069	0.62339	0.00871	0.07885	0.00098	0.89	504.6	26.41	489.3	5.88	492	5.45	47.2	378.9	90.6	0.24
PLG-4	35	0.05940	0.00069	0.67175	0.00912	0.08203	0.00102	0.92	581.8	25.07	508.3	6.08	521.8	5.54	134.3	1073.1	111.4	0.10
PLG-4	36	0.06741	0.00083	0.986	0.01372	0.1061	0.00131	0.89	850.5	25.24	650.1	7.63	696.7	7.01	87.3	502.1	130.2	0.26
PLG-4	11c	0.06701	0.00097	0.856	0.01364	0.09267	0.00117	0.79	838	29.89	571.3	6.9	627.9	7.46	28.5	157.0	139.0	0.89
PLG-4	15a	0.05667	0.00076	0.60116	0.00858	0.07695	0.00089	0.81	477.9	29.51	477.9	5.34	478	5.44	53.7	459.1	70.8	0.15
QIMP-1	1	0.05659	0.00065	0.58635	0.00709	0.07516	0.00082	0.90	474.9	25.39	467.1	4.9	468.5	4.54	96.7	739.5	221.2	0.30
QIMP-1	2	0.05682	0.0007	0.58111	0.00751	0.07418	0.00081	0.84	484	27.41	461.3	4.86	465.2	4.82	42.5	326.0	112.2	0.34
QIMP-1	5	0.05775	0.00074	0.61024	0.0081	0.07665	0.00084	0.83	519.9	27.99	476.1	5.03	483.7	5.11	56.2	409.8	154.4	0.38
QIMP-1	6	0.05611	0.00072	0.57554	0.00766	0.0744	0.00082	0.83	456.5	27.81	462.6	4.89	461.6	4.94	36.2	277.2	95.5	0.34
QIMP-1	7	0.05653	0.00066	0.57969	0.00711	0.07438	0.00081	0.89	472.7	25.78	462.5	4.86	464.3	4.57	83.8	643.5	205.4	0.32
QIMP-1	9	0.05766	0.00071	0.59735	0.00766	0.07514	0.00082	0.85	516.7	26.96	467.1	4.93	475.6	4.87	48.1	363.4	128.4	0.35

QIMP-1	14	0.05672	0.00069	0.57261	0.0073	0.07322	0.0008	0.86	480.1	26.9	455.5	4.82	459.7	4.72	128.5	994.1	369.5	0.37
QIMP-1	18	0.05708	0.00071	0.5856	0.00765	0.07441	0.00082	0.84	494.1	27.66	462.7	4.91	468.1	4.9	76.9	589.1	201.3	0.34
QIMP-1	19	0.05609	0.00071	0.5836	0.00768	0.07546	0.00083	0.84	455.7	27.33	469	4.97	466.8	4.92	52.8	396.2	146.2	0.37
QIMP-1	23	0.05613	0.00073	0.58671	0.00797	0.07582	0.00084	0.82	457	28.32	471.1	5.02	468.8	5.1	57.3	390.1	283.6	0.73
QIMP-1	25	0.05675	0.00083	0.59747	0.00896	0.07636	0.00085	0.74	481.3	32.18	474.4	5.1	475.6	5.7	32.0	244.2	69.0	0.28

Analyses U-Pb sur zircon – sédiment briovérien

		Isotope ratios							Ages						Concentrations (ppm)		
Sample	Zircon analyses	Pb^{207}/Pb^{206}	1σ	Pb^{207}/U^{235}	1σ	Pb^{206}/U^{238}	1σ	rho	Pb^{207}/Pb^{206}	1σ	Pb^{206}/U^{238}	1σ	Pb^{207}/U^{235}	1σ	Pb	U	Th
CRO-9	1	0.06333	0.00088	1.01803	0.01548	0.11660	0.00142	0.80	719.4	29.37	711	8.18	712.9	7.79	7.7	40.9	12.6
CRO-9	2	0.05909	0.00067	0.72791	0.00939	0.08935	0.00107	0.93	570.6	24.04	551.7	6.33	555.3	5.52	29.2	208.9	45.6
CRO-9	3	0.05903	0.00067	0.72486	0.00941	0.08907	0.00107	0.93	568.3	24.94	550	6.32	553.5	5.54	27.5	192.1	59.6
CRO-9	4	0.05899	0.00069	0.76966	0.01022	0.09464	0.00114	0.91	566.7	25.3	582.9	6.68	579.6	5.86	20.6	133.8	46.9
CRO-9	5	0.06010	0.00069	0.78006	0.01022	0.09415	0.00113	0.92	607.1	24.71	580	6.65	585.5	5.83	24.5	157.0	66.1
CRO-9	6	0.06015	0.0007	0.82340	0.01085	0.09929	0.00119	0.91	609	24.89	610.3	6.98	609.9	6.04	29.5	153.3	160.7
CRO-9	7	0.06042	0.00073	0.81948	0.01111	0.09839	0.00118	0.88	618.5	25.84	605	6.93	607.8	6.2	19.8	128.3	27.7
CRO-9	8	0.05889	0.00069	0.74292	0.00981	0.09151	0.00110	0.91	563.1	25.18	564.4	6.47	564.1	5.72	26.8	176.2	79.2
CRO-9	9	0.06423	0.0007	1.08684	0.01372	0.12274	0.00147	0.95	749.2	22.98	746.3	8.41	747	6.68	48.6	252.8	48.7
CRO-9	10	0.05962	0.00066	0.78503	0.01002	0.09551	0.00114	0.94	589.8	23.94	588.1	6.71	588.3	5.7	40.0	255.7	93.6
CRO-9	11	0.06082	0.00074	0.79268	0.01081	0.09454	0.00113	0.88	632.9	26.03	582.3	6.68	592.7	6.12	54.3	302.2	283.2
CRO-9	13	0.05985	0.00065	0.75921	0.00948	0.09201	0.00109	0.95	598.3	23.26	567.4	6.46	573.6	5.47	98.5	629.9	308.6
CRO-9	15	0.05840	0.00065	0.68439	0.00874	0.08501	0.00101	0.93	544.8	24.24	525.9	6.02	529.4	5.27	43.6	337.1	37.2
CRO-9	16	0.06556	0.00081	1.08200	0.01494	0.11972	0.00144	0.87	792.3	25.8	729	8.27	744.6	7.28	16.4	79.5	44.0
CRO-9	17	0.05994	0.00069	0.75788	0.00990	0.09172	0.00109	0.91	601.3	24.74	565.7	6.46	572.8	5.72	31.4	208.3	77.1
CRO-9	18	0.06092	0.00069	0.84308	0.01090	0.10039	0.00120	0.92	636.2	24.27	616.7	7.01	620.8	6	60.3	337.2	224.7
CRO-9	19	0.06060	0.0008	0.81456	0.01184	0.09749	0.00117	0.83	625.2	28.33	599.7	6.89	605	6.63	13.1	87.6	10.7
CRO-9	21	0.05867	0.00084	0.70856	0.01097	0.08760	0.00106	0.78	554.9	31.02	541.3	6.27	543.9	6.52	22.3	159.6	39.5
CRO-9	23	0.05983	0.00076	0.74890	0.01053	0.09080	0.00109	0.85	597.4	27.34	560.3	6.42	567.6	6.11	42.0	260.3	171.7
CRO-9	25	0.05862	0.00073	0.82228	0.01139	0.10175	0.00122	0.87	553.1	27.04	624.6	7.11	609.3	6.35	21.5	131.2	37.8
CRO-9	26	0.11256	0.00123	4.46423	0.05607	0.28768	0.00341	0.94	1841.2	19.73	1629.9	17.08	1724.3	10.42	220.1	475.9	60.7
CRO-9	28	0.06217	0.0008	0.92859	0.01316	0.10835	0.00130	0.85	679.8	27.27	663.2	7.54	666.9	6.93	17.8	84.9	75.5
CRO-9	29	0.06065	0.00071	0.81905	0.01084	0.09797	0.00116	0.89	626.7	25.19	602.5	6.84	607.5	6.05	38.9	226.3	135.7
CRO-9	30	0.05894	0.00064	0.78971	0.00968	0.09719	0.00113	0.95	564.9	23.51	597.9	6.63	591	5.49	47.0	295.9	73.5
CRO-9	31	0.06741	0.0007	1.21147	0.01443	0.13037	0.00151	0.97	850.4	21.58	789.9	8.62	805.9	6.63	112.3	510.3	154.8
CRO-9	32	0.10376	0.00111	3.59178	0.04342	0.25110	0.00292	0.96	1692.4	19.55	1444.2	15.05	1547.7	9.6	43.2	92.6	56.4
CRO-9	33	0.06462	0.00086	0.95238	0.01367	0.10691	0.00126	0.82	761.9	27.78	654.8	7.34	679.3	7.11	20.1	100.8	71.8
CRO-9	34	0.15046	0.00171	9.30728	0.11809	0.44870	0.00529	0.93	2351.2	19.35	2389.5	23.53	2368.7	11.63	22.7	20.9	39.2
CRO-9	35	0.06074	0.00069	0.86647	0.01098	0.10347	0.00121	0.92	630.1	24.25	634.7	7.04	633.6	5.97	30.2	160.5	104.8
CRO-9	36	0.11564	0.00125	5.31195	0.06494	0.33320	0.00389	0.95	1889.8	19.35	1853.9	18.79	1870.8	10.45	49.9	71.4	81.8
CRO-9	37	0.06036	0.00069	0.88130	0.01127	0.10592	0.00124	0.92	616.3	24.56	649	7.2	641.7	6.08	24.9	145.3	31.1
CRO-9	38	0.05938	0.00067	0.75349	0.00952	0.09204	0.00107	0.92	581.2	24.31	567.6	6.33	570.2	5.51	33.4	210.1	97.8
CRO-9	39	0.06404	0.00073	1.07818	0.01378	0.12213	0.00143	0.92	742.8	24.03	742.8	8.19	742.7	6.73	26.0	119.7	65.4
CRO-9	40	0.06515	0.0012	1.04823	0.02001	0.11670	0.00142	0.64	779.2	38.37	711.6	8.2	728	9.92	4.0	19.4	9.6
CRO-9	41	0.07229	0.0008	1.70663	0.02125	0.17125	0.00200	0.94	994.1	22.3	1019	11	1011	7.97	44.2	143.8	83.3
CRO-9	42	0.06098	0.00069	0.92503	0.01174	0.11003	0.00129	0.92	638.7	24.18	672.9	7.46	665	6.19	36.5	172.0	153.2
CRO-9	44	0.06874	0.00097	1.32716	0.01999	0.14004	0.00167	0.79	891.1	28.77	844.9	9.42	857.6	8.72	10.7	42.1	26.4
CRO-9	45	0.06051	0.00073	0.81783	0.01093	0.09804	0.00115	0.88	621.7	25.88	602.9	6.75	606.8	6.1	22.9	142.1	40.0
CRO-9	46	0.06085	0.00071	0.83308	0.01087	0.09931	0.00116	0.90	633.8	25.04	610.4	6.82	615.3	6.02	29.5	165.4	102.1

CRO-9	47	0.05938	0.0007	0.79630	0.01038	0.09727	0.00114	0.90	581.1	25.23	598.4	6.69	594.7	5.87	30.1	178.6	84.6
CRO-9	48	0.16220	0.00176	9.26921	0.11426	0.41452	0.00485	0.95	2478.7	18.23	2235.6	22.12	2365	11.3	48.0	60.5	37.3
CRO-9	49	0.10827	0.0012	4.41124	0.05507	0.29554	0.00346	0.94	1770.4	20.08	1669.2	17.22	1714.5	10.33	51.5	91.6	65.7
CRO-9	50	0.06033	0.00068	0.79755	0.01008	0.09590	0.00112	0.92	615.3	24.01	590.3	6.6	595.4	5.69	79.5	455.1	293.9
CRO-9	51	0.06026	0.00068	0.78892	0.00997	0.09497	0.00111	0.92	612.8	24.03	584.9	6.54	590.6	5.66	63.9	403.1	138.1
CRO-9	52	0.12494	0.00136	5.92641	0.07328	0.34406	0.00403	0.95	2028	19.14	1906.2	19.31	1965.1	10.74	137.4	193.0	206.3
CRO-9	54	0.06041	0.00069	0.82099	0.01048	0.09858	0.00116	0.92	618.3	24.3	606.1	6.78	608.6	5.84	84.1	515.5	160.2
CRO-9	55	0.05990	0.00069	0.79542	0.01032	0.09632	0.00113	0.90	600	24.9	592.8	6.65	594.2	5.84	52.2	333.6	83.9
CRO-9	57	0.06449	0.00076	1.11854	0.01464	0.12581	0.00148	0.90	757.7	24.51	763.9	8.47	762.3	7.02	32.5	157.9	43.4
CRO-9	58	0.05996	0.00069	0.65186	0.00839	0.07886	0.00093	0.92	602	24.6	489.3	5.53	509.6	5.16	91.8	767.5	27.5
CRO-9	59	0.12467	0.00138	6.27493	0.07885	0.36510	0.00428	0.93	2024.1	19.51	2006.3	20.22	2015	11.01	100.1	163.2	31.6
CRO-9	60	0.11666	0.00122	5.60948	0.06802	0.34881	0.00413	0.98	1905.7	18.67	1928.9	19.73	1917.6	10.45	71.5	112.0	65.6
CRO-9	61	0.06218	0.00065	0.93841	0.01135	0.10947	0.00129	0.97	680.4	22.11	669.7	7.51	672.1	5.95	150.1	756.4	509.4
CRO-9	62	0.09023	0.00096	3.08497	0.03796	0.24801	0.00293	0.96	1430.3	20.25	1428.2	15.16	1429	9.44	50.6	108.6	82.5
CRO-9	63	0.06586	0.00071	1.02614	0.01266	0.11302	0.00133	0.95	802	22.33	690.2	7.73	717	6.35	66.4	375.4	49.2
CRO-9	64	0.16382	0.00169	10.51405	0.12601	0.46557	0.00549	0.98	2495.5	17.26	2464.1	24.14	2481.2	11.11	242.6	283.8	128.2
CRO-9	65	0.05997	0.00069	0.76750	0.00999	0.09283	0.00110	0.91	602.6	24.82	572.3	6.48	578.3	5.74	23.5	154.8	44.7
CRO-9	66	0.15674	0.00162	9.43163	0.11310	0.43649	0.00514	0.98	2420.8	17.43	2334.9	23.06	2380.9	11.01	165.9	223.7	30.6
CRO-9	67	0.06207	0.00077	0.88644	0.01212	0.10360	0.00123	0.87	676.4	26.16	635.5	7.19	644.5	6.52	20.6	105.3	87.5
CRO-9	68	0.06841	0.00078	1.22369	0.01567	0.12975	0.00153	0.92	881	23.28	786.5	8.75	811.5	7.16	45.9	187.2	151.5
CRO-9	69	0.06530	0.00076	1.14659	0.01491	0.12737	0.00150	0.91	784	24.13	772.8	8.61	775.6	7.05	25.9	109.1	85.2
CRO-9	70	0.06073	0.00068	0.82362	0.01044	0.09837	0.00116	0.93	629.7	23.97	604.9	6.79	610.1	5.81	58.5	343.5	168.0
CRO-9	72	0.06083	0.00074	0.81901	0.01105	0.09766	0.00115	0.87	633.3	26.02	600.7	6.77	607.5	6.17	23.4	114.2	144.8
CRO-9	73	0.06802	0.00075	1.32246	0.01649	0.14103	0.00165	0.94	869.1	22.61	850.5	9.34	855.6	7.21	61.8	260.5	95.4
CRO-9	74	0.05891	0.00069	0.72025	0.00941	0.08869	0.00104	0.90	563.7	25.28	547.8	6.17	550.8	5.55	23.4	163.8	35.4
CRO-9	75	0.19446	0.00207	14.06706	0.17101	0.52471	0.00615	0.96	2780.3	17.33	2719.1	25.98	2754.2	11.52	143.6	139.8	86.9
CRO-9	76	0.06206	0.00075	0.79694	0.01064	0.09315	0.00110	0.88	676	25.56	574.1	6.46	595.1	6.01	73.4	392.5	396.4
CRO-9	77	0.06026	0.00065	0.75649	0.00931	0.09106	0.00106	0.95	612.8	23.21	561.8	6.28	572	5.38	179.9	1102.3	647.1
CRO-9	78	0.12002	0.00144	4.77298	0.06332	0.28845	0.00342	0.89	1956.6	21.29	1633.8	17.09	1780.2	11.14	27.6	35.0	78.9
CRO-9	79	0.06046	0.00066	0.80936	0.01000	0.09710	0.00113	0.94	620.1	23.34	597.4	6.66	602.1	5.61	113.6	661.8	333.5
CRO-9	80	0.11684	0.0013	4.92159	0.06152	0.30553	0.00357	0.93	1908.5	19.83	1718.7	17.62	1806	10.55	62.2	79.1	167.8
CRO-9	81	0.06333	0.00081	1.02664	0.01424	0.11760	0.00138	0.85	719.2	26.76	716.7	7.96	717.2	7.14	17.3	71.0	81.8
CRO-9	83	0.05929	0.00068	0.71818	0.00918	0.08787	0.00102	0.91	577.7	24.73	542.9	6.06	549.6	5.43	88.7	567.7	297.1
CRO-9	84	0.06722	0.00078	0.90352	0.01166	0.09749	0.00114	0.91	844.7	24	599.7	6.67	653.6	6.22	63.4	384.9	121.5
CRO-9	85	0.06067	0.00072	0.81602	0.01073	0.09757	0.00114	0.89	627.4	25.44	600.2	6.68	605.8	6	42.0	198.1	270.9
CRO-9	86	0.06036	0.00072	0.82699	0.01087	0.09939	0.00116	0.89	616.4	25.51	610.8	6.79	611.9	6.04	35.8	218.6	55.6
CRO-9	87	0.06375	0.00077	1.04360	0.01384	0.11875	0.00138	0.88	733.4	25.34	723.3	7.97	725.7	6.88	35.3	160.6	107.3
CRO-9	88	0.06392	0.0008	1.05426	0.01444	0.11963	0.00140	0.85	739.1	26.37	728.5	8.05	731	7.14	36.1	167.1	99.8
CRO-9	89	0.12396	0.0014	6.32925	0.07952	0.37037	0.00430	0.92	2014	19.86	2031.1	20.23	2022.5	11.02	85.2	100.4	154.6
CRO-9	90	0.05896	0.00079	0.77319	0.01126	0.09513	0.00113	0.82	565.5	28.85	585.8	6.63	581.6	6.45	11.4	71.7	25.1
CRO-9	91	0.06060	0.00066	0.83391	0.01031	0.09982	0.00117	0.95	624.9	23.33	613.4	6.84	615.8	5.71	62.3	384.2	106.0
CRO-9	92	0.06078	0.0007	0.80199	0.01033	0.09572	0.00112	0.91	631.4	24.61	589.2	6.6	597.9	5.82	76.2	388.0	482.3
CRO-9	93	0.16155	0.00168	10.50933	0.12554	0.47186	0.00550	0.98	2472	17.46	2491.7	24.1	2480.7	11.08	185.4	164.3	289.2
CRO-9	94	0.05943	0.00074	0.66190	0.00906	0.08079	0.00095	0.86	582.8	26.83	500.8	5.67	515.8	5.53	44.2	316.8	145.5
CRO-9	95	0.06739	0.00092	1.04469	0.01540	0.11245	0.00134	0.81	849.8	28.21	687	7.74	726.3	7.65	25.8	124.6	85.7
CRO-9	96	0.06143	0.00068	0.89256	0.01117	0.10539	0.00123	0.93	654.4	23.64	645.9	7.18	647.7	5.99	56.6	292.5	210.5
CRO-9	97	0.06008	0.00077	0.80565	0.01131	0.09727	0.00115	0.84	606.5	27.61	598.4	6.73	600	6.36	16.2	98.2	39.2
CRO-9	98	0.06197	0.00079	0.94306	0.01314	0.11038	0.00130	0.85	673.2	27.07	675	7.54	674.5	6.87	16.9	85.6	53.2
CRO-9	99	0.06108	0.00071	0.87976	0.01136	0.10447	0.00122	0.90	642.2	24.71	640.5	7.13	640.9	6.14	48.3	285.4	65.6
CRO-9	100	0.06127	0.00068	0.88224	0.01097	0.10444	0.00122	0.94	648.9	23.53	640.4	7.1	642.2	5.92	62.3	268.5	409.6
CRO-9	101	0.05983	0.00068	0.79107	0.01008	0.09591	0.00112	0.92	597.3	24.51	590.4	6.58	591.8	5.72	65.8	418.0	116.5
CRO-9	102	0.06065	0.00069	0.90685	0.01154	0.10847	0.00126	0.91	626.7	24.35	663.8	7.35	655.4	6.14	33.7	193.0	39.4
CRO-9	103	0.06405	0.00081	1.06088	0.01470	0.12014	0.00141	0.85	743.4	26.65	731.3	8.12	734.3	7.24	14.6	64.4	48.7

CRO-9	104	0.06061	0.00068	0.85129	0.01072	0.10188	0.00119	0.93	625.5	24.04	625.4	6.94	625.4	5.88	52.0	310.1	86.4
CRO-9	105	0.06549	0.00079	0.87066	0.01162	0.09643	0.00113	0.88	790.3	25.26	593.4	6.63	635.9	6.31	29.3	161.8	115.5
CRO-9	106	0.05868	0.00067	0.69066	0.00877	0.08538	0.00099	0.91	555.1	24.61	528.2	5.9	533.2	5.27	42.4	272.7	187.8
CRO-9	107	0.06279	0.00072	0.86575	0.01107	0.10002	0.00116	0.91	701	24.25	614.5	6.82	633.3	6.02	58.0	304.5	230.2
CRO-9	108	0.12815	0.00138	6.26251	0.07615	0.35446	0.00412	0.96	2072.8	18.81	1955.9	19.59	2013.2	10.65	144.0	227.6	91.8
CRO-9	109	0.05949	0.0008	0.71994	0.01040	0.08778	0.00103	0.81	585.1	28.82	542.4	6.11	550.6	6.14	16.2	108.2	42.6
CRO-9	110	0.11645	0.00133	5.28964	0.06711	0.32950	0.00384	0.92	1902.4	20.36	1836	18.63	1867.2	10.83	42.1	62.8	60.3
CRO-9	111	0.05954	0.00068	0.81492	0.01037	0.09928	0.00115	0.91	586.8	24.63	610.2	6.76	605.2	5.8	42.0	254.6	78.3
CRO-9	112	0.23404	0.00253	19.68174	0.24016	0.61000	0.00707	0.95	3079.9	17.19	3070	28.31	3075.9	11.79	146.2	135.3	1.8
CRO-9	113	0.06071	0.00077	0.78562	0.01081	0.09387	0.00110	0.85	628.9	27	578.4	6.46	588.7	6.14	26.7	168.6	61.4
CRO-9	114	0.06180	0.00071	0.93947	0.01193	0.11028	0.00128	0.91	667.1	24.26	674.3	7.43	672.6	6.24	51.8	262.9	134.3
CRO-9	115	0.05905	0.0007	0.78097	0.01023	0.09594	0.00112	0.89	568.8	25.54	590.6	6.56	586	5.83	65.0	428.8	66.1
CRO-9	116	0.06019	0.00084	0.76735	0.01145	0.09248	0.00109	0.79	610.3	29.93	570.2	6.42	578.2	6.58	15.7	96.5	49.3
CRO-9	117	0.06029	0.00093	0.77186	0.01254	0.09287	0.00110	0.73	614	33.04	572.5	6.49	580.8	7.19	10.6	63.2	36.4
CRO-9	118	0.10717	0.00119	4.67620	0.05793	0.31649	0.00366	0.93	1751.9	20.07	1772.6	17.93	1763	10.36	131.0	221.5	141.7
CRO-9	119	0.05916	0.0007	0.75679	0.00982	0.09278	0.00108	0.90	573.2	25.38	572	6.35	572.2	5.67	35.8	235.9	58.3

Analyses U-Pb sur zircon – sédiments siluriens

Sample	Zircon analyses	Pb^{207}/Pb^{206}	1σ	Pb^{207}/U^{235}	1σ	Pb^{206}/U^{238}	1σ	rho	Pb^{207}/Pb^{206}	1σ	Pb^{206}/U^{238}	1σ	Pb^{207}/U^{235}	1σ	Pb	U	Th
CRO-6	1	0.21215	0.00221	15.48080	0.18276	0.52931	0.00611	0.98	2922	16.75	2738.5	25.76	2845.3	11.26	205.6	205.5	75.9
CRO-6	2	0.06206	0.00071	0.86474	0.01095	0.10107	0.00117	0.91	676.2	24.23	620.7	6.84	632.7	5.96	29.3	154.0	117.3
CRO-6	3	0.07417	0.00079	1.80341	0.02168	0.17636	0.00203	0.96	1046.2	21.38	1047.1	11.14	1046.7	7.85	59.9	200.6	65.5
CRO-6	4	0.17370	0.00185	11.66676	0.13996	0.48720	0.00564	0.96	2593.6	17.67	2558.5	24.44	2578	11.22	37.0	38.5	26.6
CRO-6	5	0.07587	0.00084	1.83917	0.02274	0.17583	0.00203	0.93	1091.7	22.06	1044.2	11.13	1059.6	8.13	40.6	130.2	73.4
CRO-6	6	0.07451	0.0008	1.80061	0.02176	0.17530	0.00202	0.95	1054.9	21.82	1041.3	11.08	1045.7	7.89	51.8	162.5	97.1
CRO-6	7	0.07496	0.0008	1.82443	0.02198	0.17655	0.00203	0.95	1067.4	21.41	1048.1	11.14	1054.3	7.9	51.7	162.2	93.2
CRO-6	8	0.06222	0.00067	0.88688	0.01073	0.10339	0.00119	0.95	681.8	22.87	634.2	6.95	644.7	5.77	105.2	647.2	57.5
CRO-6	9	0.18649	0.00193	13.41166	0.15695	0.52165	0.00599	0.98	2711.4	16.93	2706.2	25.38	2709.1	11.06	294.1	272.9	237.2
CRO-6	10	0.06566	0.00078	1.12628	0.01464	0.12443	0.00144	0.89	795.4	24.68	756	8.25	766	6.99	26.1	118.1	61.0
CRO-6	11	0.07840	0.00089	1.81944	0.02292	0.16833	0.00194	0.91	1157.1	22.47	1002.9	10.72	1052.5	8.25	42.5	145.4	51.2
CRO-6	12	0.07436	0.00126	1.78610	0.03132	0.17422	0.00209	0.68	1051.3	33.78	1035.3	11.48	1040.4	11.42	4.2	12.9	9.5
CRO-6	13	0.06122	0.00066	0.72879	0.00878	0.08636	0.00099	0.95	646.8	22.96	533.9	5.88	555.8	5.16	113.1	552.1	998.3
CRO-6	14	0.17432	0.00182	11.38546	0.13389	0.47376	0.00543	0.97	2599.5	17.28	2500	23.74	2555.2	10.98	266.0	313.8	69.1
CRO-6	15	0.19115	0.002	13.91674	0.16405	0.52810	0.00605	0.97	2752.1	17.1	2733.4	25.53	2744.1	11.17	204.8	194.3	131.0
CRO-6	16	0.06408	0.00087	0.86502	0.01256	0.09792	0.00114	0.80	744.1	28.56	602.2	6.7	632.9	6.84	16.9	92.3	60.6
CRO-6	17	0.06962	0.00075	1.27429	0.01539	0.13276	0.00152	0.95	917.2	22.11	803.6	8.66	834.3	6.87	75.4	314.4	207.7
CRO-6	18	0.05894	0.00066	0.73310	0.00905	0.09022	0.00104	0.93	564.8	24.06	556.9	6.12	558.4	5.3	42.5	305.0	10.0
CRO-6	19	0.11069	0.00121	4.27389	0.05182	0.28008	0.00322	0.95	1810.7	19.66	1591.8	16.19	1688.3	9.98	58.5	104.1	92.6
CRO-6	20	0.06778	0.0008	1.26073	0.01620	0.13493	0.00155	0.89	861.7	24.19	815.9	8.81	828.2	7.28	21.2	91.8	32.7
CRO-6	21	0.07247	0.00081	1.59607	0.01975	0.15975	0.00183	0.93	999.1	22.6	955.4	10.18	968.7	7.73	50.9	153.0	173.3
CRO-6	22	0.06359	0.00075	1.03805	0.01334	0.11841	0.00136	0.89	728	24.74	721.4	7.84	722.9	6.65	38.2	139.5	230.0
CRO-6	23	0.06346	0.00072	0.98584	0.01225	0.11269	0.00129	0.92	723.6	23.73	688.3	7.48	696.6	6.26	61.1	328.9	70.7
CRO-6	24	0.13663	0.00148	7.61014	0.09161	0.40400	0.00462	0.95	2185	18.72	2187.4	21.21	2186.1	10.8	96.4	126.1	70.9
CRO-6	25	0.16652	0.00181	10.79797	0.13016	0.47035	0.00538	0.95	2523	18.11	2485.1	23.59	2505.9	11.2	97.4	109.2	52.9
CRO-6	26	0.06158	0.00068	0.84323	0.01033	0.09932	0.00114	0.94	659.5	23.59	610.4	6.66	620.9	5.69	84.3	549.0	8.5
CRO-6	27	0.06208	0.00073	0.87823	0.01131	0.10261	0.00118	0.89	677	25.05	629.7	6.88	640	6.11	36.1	217.2	32.8
CRO-6	28	0.05945	0.00069	0.73154	0.00933	0.08926	0.00102	0.90	583.6	25.14	551.1	6.05	557.5	5.47	29.9	215.5	10.8
CRO-6	29	0.06183	0.00068	0.86649	0.01056	0.10165	0.00116	0.94	668.2	23.43	624.1	6.79	633.7	5.75	116.7	744.8	4.5

CRO-6	30	0.07504	0.00097	1.78912	0.02482	0.17294	0.00201	0.84	1069.6	25.76	1028.3	11.03	1041.5	9.04	10.7	34.3	18.1
CRO-6	31	0.06142	0.00067	0.82143	0.01002	0.09701	0.00111	0.94	654	23.39	596.8	6.52	608.8	5.58	49.2	283.7	152.2
CRO-6	32	0.07440	0.00082	1.80813	0.02201	0.17628	0.00202	0.94	1052.4	21.95	1046.6	11.05	1048.4	7.96	38.2	115.8	78.2
CRO-6	33	0.11563	0.00122	5.19649	0.06120	0.32597	0.00372	0.97	1889.8	18.8	1818.8	18.08	1852	10.03	122.3	170.5	228.6
CRO-6	34	0.12218	0.00131	6.09692	0.07268	0.36196	0.00414	0.96	1988.3	18.91	1991.5	19.58	1989.8	10.4	46.4	66.8	44.9
CRO-6	35	0.06748	0.0008	1.20876	0.01556	0.12993	0.00149	0.89	852.7	24.33	787.5	8.5	804.6	7.15	24.7	94.7	93.2
CRO-6	36	0.07611	0.00094	1.79043	0.02396	0.17063	0.00197	0.86	1098	24.61	1015.6	10.83	1042	8.72	15.5	43.9	49.0
CRO-6	37	0.06445	0.00069	1.07838	0.01292	0.12137	0.00138	0.95	756.3	22.56	738.5	7.94	742.8	6.31	63.5	326.2	39.6
CRO-6	38	0.07569	0.00092	1.81570	0.02396	0.17400	0.00200	0.87	1086.9	24.25	1034.1	10.99	1051.1	8.64	22.8	65.8	62.9
CRO-6	39	0.07256	0.0008	1.59642	0.01941	0.15960	0.00182	0.94	1001.6	22.15	954.5	10.11	968.8	7.59	60.2	194.2	156.5
CRO-6	40	0.06953	0.0008	1.39963	0.01760	0.14601	0.00167	0.91	914.5	23.48	878.6	9.37	888.8	7.45	31.9	126.6	36.4
CRO-6	41	0.07416	0.00082	1.72261	0.02090	0.16848	0.00192	0.94	1045.9	22.01	1003.7	10.57	1017	7.8	61.2	174.5	192.2
CRO-6	42	0.07423	0.0008	1.69501	0.02028	0.16563	0.00188	0.95	1047.7	21.62	988	10.4	1006.7	7.64	85.3	291.6	119.8
CRO-6	43	0.07248	0.00078	1.34315	0.01605	0.13442	0.00152	0.95	999.4	21.75	813	8.66	864.6	6.95	128.5	478.9	297.5
CRO-6	44	0.07434	0.00085	1.82899	0.02292	0.17845	0.00203	0.91	1050.8	22.94	1058.5	11.12	1055.9	8.23	30.4	87.8	67.0
CRO-6	46	0.07377	0.0008	1.65063	0.01979	0.16231	0.00184	0.95	1035.1	21.48	969.6	10.2	989.8	7.58	71.3	258.3	69.4
CRO-6	47	0.06695	0.00076	1.10402	0.01374	0.11960	0.00136	0.91	836.4	23.54	728.3	7.82	755.3	6.63	33.3	163.2	46.7
CRO-6	48	0.07451	0.00085	1.80790	0.02244	0.17599	0.00200	0.92	1055.1	22.98	1045	10.96	1048.3	8.12	34.5	104.9	64.6
CRO-6	49	0.07212	0.00079	1.57414	0.01896	0.15831	0.00179	0.94	989.5	22.07	947.4	9.97	960.1	7.48	70.9	247.3	127.3
CRO-6	50	0.06855	0.00077	1.26234	0.01548	0.13357	0.00151	0.92	885.2	23	808.2	8.59	829	6.95	99.5	421.2	195.7
CRO-6	51	0.06224	0.00079	0.92473	0.01253	0.10776	0.00123	0.84	682.5	26.86	659.7	7.15	664.9	6.61	15.9	90.2	14.4
CRO-6	52	0.11593	0.00131	5.31188	0.06533	0.33233	0.00377	0.92	1894.4	20.14	1849.7	18.24	1870.8	10.51	37.4	52.1	61.2
CRO-6	53	0.07188	0.0008	1.59689	0.01946	0.16115	0.00182	0.93	982.5	22.51	963.1	10.1	969	7.61	76.5	242.9	196.3
CRO-6	54	0.07526	0.00087	1.73390	0.02183	0.16711	0.00189	0.90	1075.5	23.13	996.1	10.45	1021.2	8.11	32.8	97.6	87.8
CRO-6	55	0.05947	0.00073	0.75255	0.00988	0.09179	0.00104	0.86	584.2	26.32	566.1	6.15	569.7	5.73	20.3	128.1	44.5
CRO-6	56	0.07271	0.00095	1.67328	0.02321	0.16692	0.00191	0.82	1006	26.3	995.1	10.54	998.4	8.82	17.3	47.6	62.4
CRO-6	57	0.13022	0.00149	6.79411	0.08440	0.37844	0.00429	0.91	2100.9	19.96	2069	20.07	2085	11	31.2	41.2	30.8
CRO-6	58	0.12366	0.0014	6.16318	0.07573	0.36151	0.00409	0.92	2009.7	19.91	1989.3	19.35	1999.2	10.74	52.1	68.9	68.3
CRO-6	59	0.11902	0.00134	5.69422	0.06997	0.34702	0.00392	0.92	1941.6	20.07	1920.3	18.76	1930.5	10.61	52.6	68.2	93.2
CRO-6	60	0.07325	0.00078	1.73746	0.02067	0.17205	0.00196	0.96	1020.9	21.43	1023.4	10.8	1022.5	7.67	57.8	197.1	59.0
CRO-6	61	0.11514	0.00119	5.37422	0.06250	0.33857	0.00386	0.98	1882.1	18.52	1879.8	18.57	1880.8	9.96	209.9	271.3	408.0
CRO-6	62	0.06083	0.00071	0.87156	0.01111	0.10392	0.00119	0.90	633.3	24.87	637.4	6.95	636.4	6.03	20.7	121.9	22.5
CRO-6	64	0.07123	0.00077	1.55456	0.01870	0.15830	0.00181	0.95	964.1	21.93	947.3	10.06	952.3	7.43	51.4	175.0	108.7
CRO-6	65	0.06762	0.00076	1.09743	0.01354	0.11772	0.00135	0.93	856.9	23.04	717.4	7.76	752.1	6.56	31.1	146.7	70.4
CRO-6	67	0.05991	0.00066	0.73299	0.00890	0.08875	0.00101	0.94	600.2	23.53	548.1	6	558.3	5.22	72.9	428.9	317.7
CRO-6	68	0.11258	0.00117	4.96754	0.05783	0.32007	0.00364	0.98	1841.4	18.63	1790.1	17.79	1813.8	9.84	308.7	553.0	144.3
CRO-6	69	0.13217	0.00137	7.00693	0.08176	0.38455	0.00438	0.98	2127	18.07	2097.5	20.38	2112.3	10.37	205.3	284.7	144.9
CRO-6	70	0.13573	0.00143	7.31048	0.08605	0.39068	0.00445	0.97	2173.4	18.19	2126	20.63	2150.1	10.51	176.2	248.4	99.8
CRO-6	71	0.07466	0.00079	1.82272	0.02167	0.17709	0.00202	0.96	1058.9	21.61	1051.1	11.05	1053.7	7.79	121.6	364.6	241.8
CRO-6	73	0.18372	0.00192	13.20952	0.15501	0.52154	0.00594	0.97	2686.7	17.19	2705.7	25.15	2694.7	11.08	320.2	285.6	288.0
CRO-6	75	0.12500	0.00134	6.34626	0.07570	0.36826	0.00420	0.96	2028.8	18.82	2021.2	19.79	2024.9	10.46	72.0	109.8	34.6
CRO-6	76	0.05907	0.00064	0.70551	0.00848	0.08663	0.00099	0.95	569.9	23.58	535.6	5.85	542.1	5.05	105.9	699.4	283.2
CRO-6	77	0.05954	0.00064	0.71068	0.00852	0.08658	0.00099	0.95	586.8	23.2	535.3	5.85	545.1	5.06	115.8	861.4	11.9
CRO-6	78	0.07451	0.00094	1.82146	0.02482	0.17731	0.00205	0.85	1055.2	25.58	1052.2	11.21	1053.2	8.93	24.2	61.6	85.2
CRO-6	79	0.07430	0.00084	1.78757	0.02232	0.17452	0.00200	0.92	1049.6	22.71	1036.9	10.95	1040.9	8.13	41.7	133.9	61.4
CRO-6	80	0.07398	0.00081	1.78352	0.02170	0.17486	0.00199	0.94	1041	21.99	1038.8	10.94	1039.5	7.92	79.4	263.6	86.7
CRO-6	81	0.07216	0.00083	1.59471	0.02021	0.16031	0.00183	0.90	990.4	23.34	958.5	10.19	968.1	7.91	62.6	205.0	148.6
CRO-6	82	0.17664	0.00191	12.21300	0.14703	0.50152	0.00572	0.95	2621.5	17.89	2620.3	24.54	2620.9	11.3	140.2	134.9	112.4
CRO-6	83	0.11942	0.0013	5.80593	0.07007	0.35265	0.00402	0.94	1947.6	19.28	1947.2	19.15	1947.3	10.45	157.1	238.4	126.0
CRO-6	84	0.17963	0.00195	12.62475	0.15229	0.50980	0.00581	0.94	2649.4	17.89	2655.8	24.8	2652.1	11.35	179.1	167.6	147.6
CRO-6	85	0.07284	0.0009	1.48783	0.01996	0.14817	0.00170	0.86	1009.4	24.99	890.7	9.57	925.4	8.15	38.6	146.5	64.3
CRO-6	86	0.12046	0.00132	5.89911	0.07181	0.35521	0.00405	0.94	1963.1	19.43	1959.4	19.26	1961.1	10.57	116.6	177.9	83.0
CRO-6	87	0.07242	0.00081	1.70372	0.02114	0.17064	0.00195	0.92	997.8	22.69	1015.6	10.72	1009.9	7.94	87.8	285.3	141.7

CRO-6	88	0.06246	0.00074	0.93445	0.01205	0.10851	0.00124	0.89	690	25.01	664.1	7.22	670	6.33	43.5	167.6	300.2
CRO-6	89	0.07536	0.00085	1.86690	0.02325	0.17969	0.00205	0.92	1078.1	22.53	1065.3	11.21	1069.4	8.23	97.1	241.9	377.5
CRO-6	90	0.07406	0.00083	1.77111	0.02184	0.17345	0.00197	0.92	1043.2	22.55	1031.1	10.83	1034.9	8	33.3	96.4	86.3
CRO-6	91	0.15366	0.00158	8.72779	0.10017	0.41199	0.00466	0.99	2387.1	17.35	2224	21.25	2310	10.46	714.6	972.5	194.3
CRO-6	92	0.17784	0.00182	11.29973	0.12977	0.46090	0.00521	0.98	2632.8	16.94	2443.5	22.99	2548.2	10.71	791.8	838.8	635.9
CRO-6	93	0.07254	0.00075	1.48321	0.01716	0.14831	0.00168	0.98	1001.1	20.88	891.5	9.42	923.5	7.02	240.8	1023.0	36.9
CRO-6	94	0.07140	0.00081	1.56226	0.01947	0.15871	0.00181	0.92	968.9	23.07	949.6	10.06	955.4	7.71	28.8	89.7	89.0
CRO-6	95	0.12410	0.00129	6.10480	0.07072	0.35681	0.00404	0.98	2016	18.29	1967.1	19.2	1990.9	10.11	188.0	275.4	167.6
CRO-6	96	0.12662	0.00131	6.58134	0.07638	0.37701	0.00427	0.98	2051.6	18.22	2062.3	20	2056.9	10.23	143.8	218.8	46.7
CRO-6	97	0.07418	0.00081	1.76770	0.02133	0.17286	0.00196	0.94	1046.3	21.86	1027.8	10.8	1033.7	7.82	68.1	195.1	193.4
CRO-6	99	0.06040	0.00087	0.84996	0.01288	0.10207	0.00118	0.76	618	30.78	626.5	6.91	624.6	7.07	8.5	39.6	45.7
CRO-6	100	0.07186	0.0008	1.58897	0.01939	0.16040	0.00183	0.93	981.9	22.37	959	10.14	965.9	7.61	40.0	133.3	85.1
CRO-6	101	0.07293	0.00079	1.64991	0.01988	0.16409	0.00187	0.95	1012.1	21.87	979.5	10.35	989.5	7.62	66.3	233.5	77.0
CRO-6	102	0.06184	0.00066	0.83522	0.00989	0.09797	0.00111	0.96	668.6	22.54	602.5	6.54	616.5	5.47	205.6	1344.2	45.5
CRO-6	103	0.06472	0.00081	1.11465	0.01500	0.12493	0.00144	0.86	765.2	26.06	758.9	8.23	760.4	7.2	21.2	94.0	50.4
CRO-6	104	0.06101	0.00078	0.84415	0.01165	0.10036	0.00116	0.84	639.5	27.42	616.5	6.77	621.4	6.42	18.4	69.9	158.9
CRO-6	106	0.12353	0.00133	6.24674	0.07506	0.36681	0.00419	0.95	2007.8	19.06	2014.4	19.75	2011	10.52	58.1	84.4	46.7
CRO-6	108	0.07376	0.00083	1.75877	0.02182	0.17297	0.00198	0.92	1034.8	22.26	1028.5	10.87	1030.4	8.03	55.9	179.4	90.5
CRO-6	109	0.12748	0.00138	6.38306	0.07684	0.36320	0.00415	0.95	2063.5	18.92	1997.3	19.63	2029.9	10.57	120.2	197.6	13.5
CRO-6	110	0.12509	0.00135	6.40534	0.07700	0.37141	0.00424	0.95	2030.1	18.94	2036.1	19.95	2033	10.56	152.4	226.7	89.3
CRO-6	111	0.12183	0.00135	5.78213	0.07104	0.34425	0.00395	0.93	1983.2	19.63	1907.1	18.93	1943.7	10.64	55.5	72.0	97.2
CRO-6	112	0.05923	0.00067	0.74089	0.00923	0.09073	0.00104	0.92	575.6	24.3	559.9	6.14	562.9	5.38	55.8	368.2	99.5
CRO-6	113	0.12310	0.00135	5.29018	0.06444	0.31171	0.00357	0.94	2001.7	19.27	1749.1	17.54	1867.3	10.4	207.0	363.7	153.8
CRO-6	114	0.06361	0.00089	0.96587	0.01437	0.11014	0.00128	0.78	728.6	29.44	673.6	7.45	686.3	7.42	17.2	83.3	56.2
CRO-6	115	0.06917	0.00082	1.20707	0.01565	0.12658	0.00146	0.89	903.8	24.24	768.3	8.34	803.8	7.2	30.3	120.3	98.9
CRO-6	116	0.11299	0.00124	4.71686	0.05781	0.30281	0.00347	0.93	1848	19.8	1705.2	17.18	1770.2	10.27	141.3	216.1	261.4
CRO-6	117	0.12313	0.00136	5.52237	0.06798	0.32531	0.00373	0.93	2002.1	19.49	1815.6	18.16	1904.1	10.58	118.0	177.2	174.6
CRO-6	118	0.06090	0.00119	0.81304	0.01625	0.09683	0.00117	0.60	635.8	41.55	595.8	6.87	604.2	9.1	3.0	19.4	1.3
CRO-3	112	0.07421	0.00089	1.84483	0.02389	0.18032	0.00205	0.88	1047.2	24.09	1068.7	11.17	1061.6	8.53	20.4	64.8	26.3
CRO-3	69	0.07167	0.00087	1.66246	0.02168	0.16826	0.00192	0.88	976.4	24.48	1002.5	10.57	994.3	8.27	20.0	53.5	75.1
CRO-3	91	0.07344	0.00078	1.76744	0.02089	0.17457	0.00198	0.96	1026	21.41	1037.3	10.84	1033.6	7.66	79.7	236.2	186.7
CRO-3	105	0.06590	0.00094	1.21504	0.01825	0.13374	0.00154	0.77	803.2	29.73	809.2	8.76	807.5	8.36	8.8	30.8	38.0
CRO-3	113	0.06183	0.00072	0.94649	0.01194	0.11103	0.00125	0.89	668.4	24.76	678.7	7.28	676.3	6.23	39.4	190.0	121.5
CRO-3	84	0.06563	0.00078	1.19936	0.01541	0.13256	0.00151	0.89	794.5	24.67	802.5	8.58	800.3	7.12	30.9	145.7	9.8
CRO-3	15	0.12397	0.00131	6.30167	0.07474	0.36872	0.00422	0.96	2014.1	18.68	2023.4	19.89	2018.7	10.39	116.2	169.4	95.0
CRO-3	88	0.07180	0.00076	1.63854	0.01924	0.16552	0.00187	0.96	980.4	21.36	987.4	10.36	985.2	7.4	91.1	323.4	99.2
CRO-3	86	0.05692	0.00061	0.62418	0.00744	0.07954	0.00090	0.95	487.8	23.83	493.4	5.38	492.5	4.65	70.1	490.0	259.8
CRO-3	44	0.05955	0.00066	0.78708	0.00953	0.09587	0.00108	0.93	587.4	23.79	590.1	6.36	589.5	5.41	59.8	339.9	198.5
CRO-3	27	0.06248	0.0007	0.97813	0.01209	0.11355	0.00130	0.93	690.6	23.83	693.3	7.5	692.6	6.21	78.1	340.4	348.9
CRO-3	39	0.12161	0.00129	6.04271	0.07089	0.36041	0.00407	0.96	1980	18.81	1984.1	19.28	1982	10.22	117.9	145.4	201.6
CRO-3	73	0.12361	0.00148	6.23964	0.08061	0.36615	0.00420	0.89	2009	21.12	2011.3	19.83	2010	11.31	14.4	17.6	23.2
CRO-3	70b	0.06355	0.00081	1.04668	0.01426	0.11947	0.00136	0.84	726.6	26.81	727.5	7.85	727.2	7.07	13.3	61.9	26.1
CRO-3	54	0.11980	0.00136	5.85019	0.07199	0.35420	0.00401	0.92	1953.3	20.09	1954.6	19.07	1953.9	10.67	35.3	54.2	23.2
CRO-3	29	0.12372	0.00129	6.24428	0.07235	0.36610	0.00414	0.98	2010.5	18.35	2011	19.54	2010.7	10.14	113.8	178.0	43.4
CRO-3	94	0.18713	0.00195	13.52932	0.15680	0.52441	0.00593	0.98	2717.1	17.04	2717.9	25.07	2717.3	10.96	159.2	149.3	103.8
CRO-3	60a	0.11393	0.0012	5.26357	0.06151	0.33511	0.00378	0.97	1863.1	18.96	1863.1	18.24	1863	9.97	65.1	101.1	62.1
CRO-3	11	0.12094	0.00134	5.95682	0.07304	0.35728	0.00412	0.94	1970.1	19.55	1969.3	19.58	1969.6	10.66	39.7	55.0	51.6
CRO-3	97	0.12425	0.0013	6.29346	0.07330	0.36739	0.00415	0.97	2018.1	18.5	2017.1	19.55	2017.5	10.2	193.4	280.4	142.6
CRO-3	92	0.05906	0.00072	0.75057	0.00992	0.09218	0.00105	0.86	569.3	25.88	568.4	6.2	568.6	5.75	17.9	101.5	77.4
CRO-3	3	0.05916	0.00071	0.75519	0.00995	0.09259	0.00107	0.88	573.1	25.98	570.8	6.33	571.2	5.76	19.0	113.5	70.8
CRO-3	10	0.07215	0.00096	1.64610	0.02340	0.16550	0.00193	0.82	990.1	26.77	987.3	10.68	988.1	8.98	11.6	35.3	34.2

CRO-3	9	0.17786	0.00183	12.34120	0.14412	0.50332	0.00577	0.98	2633	17.04	2628	24.76	2630.7	10.97	306.7	323.6	147.7
CRO-3	76	0.07215	0.00081	1.64367	0.02023	0.16525	0.00187	0.92	990.1	22.7	985.9	10.35	987.1	7.77	47.8	164.0	65.1
CRO-3	106	0.06106	0.00068	0.87499	0.01070	0.10394	0.00117	0.92	641.4	23.9	637.4	6.85	638.3	5.8	67.7	321.2	319.4
CRO-3	42	0.17717	0.00186	12.22738	0.14248	0.50060	0.00564	0.97	2626.6	17.38	2616.4	24.24	2622	10.94	152.6	157.9	72.9
CRO-3	87	0.06445	0.00094	1.09719	0.01682	0.12349	0.00143	0.76	756.4	30.56	750.6	8.22	752	8.15	7.2	29.8	24.7
CRO-3	2a	0.06179	0.00081	0.91872	0.01294	0.10786	0.00126	0.83	666.7	27.74	660.3	7.31	661.7	6.85	12.5	58.0	59.0
CRO-3	8	0.07290	0.00082	1.70095	0.02120	0.16923	0.00195	0.92	1011.3	22.62	1007.9	10.76	1008.9	7.97	30.8	107.1	38.6
CRO-3	40	0.06094	0.00068	0.86248	0.01055	0.10266	0.00116	0.92	637.2	23.89	630	6.78	631.5	5.75	41.8	226.5	115.7
CRO-3	51	0.12205	0.00134	6.03913	0.07238	0.35892	0.00405	0.94	1986.3	19.35	1977.1	19.19	1981.5	10.44	90.3	129.7	83.3
CRO-3	85	0.06362	0.00077	1.03831	0.01363	0.11839	0.00135	0.87	728.9	25.53	721.3	7.8	723.1	6.79	19.9	76.0	104.8
CRO-3	12	0.07418	0.00083	1.79489	0.02229	0.17552	0.00202	0.93	1046.3	22.48	1042.4	11.07	1043.6	8.1	33.1	105.2	57.9
CRO-3	77	0.17742	0.00192	12.20102	0.14582	0.49881	0.00564	0.95	2628.9	17.89	2608.7	24.27	2620	11.22	113.0	111.9	75.3
CRO-3	38	0.20380	0.00217	15.50625	0.18238	0.55188	0.00625	0.96	2856.9	17.22	2833	25.97	2846.9	11.22	54.4	46.7	38.8
CRO-3	46	0.11500	0.00125	5.31986	0.06346	0.33554	0.00379	0.95	1879.9	19.43	1865.2	18.29	1872.1	10.2	66.3	99.3	77.7
CRO-3	1b	0.06112	0.00067	0.86484	0.01055	0.10263	0.00118	0.94	643.6	23.23	629.8	6.92	632.8	5.74	44.7	258.3	93.3
CRO-3	63	0.06345	0.00068	1.01491	0.01202	0.11603	0.00131	0.95	723.2	22.61	707.7	7.55	711.4	6.06	70.0	355.4	92.9
CRO-3	68	0.18666	0.00202	13.25979	0.15779	0.51527	0.00584	0.95	2713	17.7	2679.1	24.86	2698.3	11.24	37.1	37.6	14.6
CRO-3	70a	0.06253	0.00082	0.95292	0.01330	0.11054	0.00126	0.82	692.2	27.74	675.9	7.34	679.6	6.91	10.3	58.7	3.3
CRO-3	48	0.07158	0.00082	1.57820	0.01967	0.15993	0.00181	0.91	973.9	23.24	956.4	10.05	961.7	7.75	32.8	118.1	40.5
CRO-3	110	0.05866	0.00069	0.70479	0.00894	0.08715	0.00099	0.90	554.6	25.39	538.6	5.84	541.7	5.33	33.7	225.9	75.0
CRO-3	90	0.06690	0.00075	1.24550	0.01531	0.13504	0.00153	0.92	834.7	23.18	816.6	8.71	821.4	6.92	31.0	132.1	50.8
CRO-3	66	0.12017	0.00141	5.79531	0.07346	0.34982	0.00400	0.90	1958.7	20.72	1933.7	19.1	1945.7	10.98	17.8	24.1	24.5
CRO-3	56	0.06344	0.00072	1.00480	0.01236	0.11489	0.00129	0.91	723	23.82	701.1	7.48	706.2	6.26	84.1	441.7	92.3
CRO-3	102	0.06749	0.00089	1.27699	0.01792	0.13725	0.00157	0.82	852.9	27.25	829.1	8.92	835.5	7.99	12.4	50.9	23.1
CRO-3	13	0.07316	0.00082	1.70379	0.02116	0.16892	0.00194	0.92	1018.4	22.57	1006.2	10.71	1010	7.95	39.7	109.3	142.6
CRO-3	61	0.06621	0.00071	1.18292	0.01402	0.12959	0.00146	0.95	813.1	22.31	785.5	8.33	792.7	6.52	67.6	279.2	167.1
CRO-3	95	0.18630	0.00194	13.07560	0.15144	0.50909	0.00575	0.98	2709.8	17.05	2652.7	24.54	2685.1	10.92	302.5	336.8	35.3
CRO-3	79	0.13912	0.00151	7.68242	0.09222	0.40054	0.00453	0.94	2216.3	18.75	2171.5	20.86	2194.5	10.79	120.5	175.1	15.1
CRO-3	26	0.18023	0.00197	12.30758	0.14900	0.49534	0.00566	0.94	2655	18.05	2593.7	24.4	2628.2	11.37	77.4	80.3	45.2
CRO-3	7	0.12026	0.00125	5.75629	0.06756	0.34720	0.00399	0.98	1960.1	18.35	1921.2	19.08	1939.9	10.15	173.0	262.8	175.8
CRO-3	43	0.07331	0.00081	1.70888	0.02070	0.16908	0.00191	0.93	1022.5	22.21	1007.1	10.53	1011.9	7.76	48.0	148.2	106.7
CRO-3	17	0.06276	0.00082	0.94560	0.01319	0.10930	0.00127	0.83	700	27.44	668.7	7.36	675.8	6.88	12.6	59.1	52.1
CRO-3	108	0.06135	0.00067	0.85469	0.01030	0.10105	0.00114	0.94	651.5	23.43	620.6	6.67	627.2	5.64	109.4	637.7	184.5
CRO-3	18	0.07218	0.00082	1.59248	0.01991	0.16003	0.00184	0.92	991	22.92	957	10.21	967.3	7.8	35.3	115.6	92.1
CRO-3	4	0.17712	0.00185	11.91894	0.14073	0.48812	0.00562	0.98	2626.1	17.27	2562.6	24.37	2598.1	11.06	97.0	82.5	140.9
CRO-3	101	0.11375	0.00122	5.12452	0.06077	0.32676	0.00369	0.95	1860.2	19.29	1822.7	17.94	1840.2	10.08	85.9	128.0	125.6
CRO-3	14b	0.07463	0.0008	1.80148	0.02160	0.17509	0.00201	0.96	1058.3	21.78	1040.1	11	1046	7.83	82.0	255.6	158.7
CRO-3	35	0.11630	0.00123	5.35278	0.06289	0.33384	0.00378	0.96	1900.1	18.95	1857	18.25	1877.3	10.05	75.8	106.9	119.1
CRO-3	64	0.11406	0.00134	5.13622	0.06504	0.32662	0.00373	0.90	1865.1	20.98	1822	18.12	1842.1	10.76	17.3	23.4	32.2
CRO-3	80	0.07489	0.00085	1.81774	0.02252	0.17606	0.00200	0.92	1065.5	22.62	1045.4	10.94	1051.9	8.12	51.6	152.9	108.4
CRO-3	28	0.07216	0.00077	1.57954	0.01859	0.15877	0.00180	0.96	990.6	21.43	949.9	10	962.2	7.32	79.4	283.1	121.1
CRO-3	52	0.12184	0.00132	5.87603	0.06994	0.34982	0.00394	0.95	1983.3	19.21	1933.7	18.8	1957.7	10.33	174.6	289.5	49.1
CRO-3	111	0.06174	0.00077	0.86640	0.01153	0.10179	0.00116	0.86	665.1	26.41	624.9	6.76	633.6	6.27	22.7	119.8	74.8
CRO-3	98	0.12501	0.00132	6.15175	0.07202	0.35695	0.00403	0.96	2028.9	18.57	1967.7	19.15	1997.6	10.22	125.8	200.4	51.8
CRO-3	21b	0.16488	0.00178	10.34791	0.12411	0.45524	0.00520	0.95	2506.3	18.05	2418.5	23.05	2466.4	11.11	87.5	100.7	54.3
CRO-3	83	0.07423	0.00098	1.75980	0.02474	0.17196	0.00198	0.82	1047.8	26.45	1022.9	10.87	1030.8	9.1	22.1	34.4	167.5
CRO-3	37	0.07258	0.00077	1.64015	0.01917	0.16391	0.00185	0.97	1002.3	21.26	978.4	10.24	985.8	7.37	150.1	555.1	88.6
CRO-3	50	0.12728	0.00137	6.35865	0.07519	0.36237	0.00408	0.95	2060.8	18.84	1993.4	19.29	2026.6	10.38	339.2	486.1	285.9
CRO-3	49	0.05904	0.00064	0.68553	0.00818	0.08422	0.00095	0.95	568.7	24.09	521.3	5.63	530.1	4.93	164.1	1107.4	447.8
CRO-3	65	0.14675	0.00157	8.34379	0.09860	0.41242	0.00466	0.96	2308.4	18.28	2226	21.29	2269.1	10.71	47.7	58.6	37.3
CRO-3	59	0.12078	0.00125	5.71698	0.06591	0.34334	0.00386	0.98	1967.7	18.37	1902.7	18.54	1933.9	9.96	186.2	244.7	302.6
CRO-3	32	0.13126	0.00136	6.74287	0.07804	0.37261	0.00421	0.98	2114.9	18.1	2041.7	19.78	2078.3	10.23	125.5	182.6	79.9

CRO-3	109	0.07344	0.00086	1.69845	0.02158	0.16775	0.00190	0.89	1026.2	23.6	999.7	10.49	1007.9	8.12	36.2	122.4	50.8
CRO-3	36	0.12601	0.00131	6.21404	0.07201	0.35769	0.00404	0.97	2043.1	18.3	1971.2	19.17	2006.4	10.14	140.9	227.9	41.6
CRO-3	6	0.07390	0.00077	1.72861	0.02044	0.16968	0.00195	0.97	1038.7	21	1010.3	10.74	1019.2	7.6	125.6	414.1	223.1
CRO-3	47	0.11439	0.00123	5.08994	0.06023	0.32275	0.00363	0.95	1870.3	19.27	1803.1	17.71	1834.4	10.04	140.5	226.7	136.0
CRO-3	71	0.07234	0.00077	1.55239	0.01833	0.15566	0.00176	0.96	995.5	21.54	932.6	9.79	951.4	7.29	230.2	814.0	416.8
CRO-3	53	0.07232	0.00082	1.54641	0.01902	0.15509	0.00175	0.92	995.1	22.81	929.4	9.76	949.1	7.58	60.9	212.9	120.3
CRO-3	78	0.06306	0.00091	0.91955	0.01396	0.10577	0.00122	0.76	710.4	30.49	648.1	7.12	662.1	7.38	13.7	62.2	67.2
CRO-3	58	0.12152	0.00126	5.73407	0.06595	0.34225	0.00385	0.98	1978.7	18.37	1897.5	18.48	1936.5	9.94	223.9	300.5	355.2
CRO-3	22	0.12335	0.00133	5.88673	0.07051	0.34618	0.00395	0.95	2005.2	19.02	1916.3	18.92	1959.3	10.4	137.5	233.9	38.8
CRO-3	89	0.07183	0.0008	1.49968	0.01832	0.15144	0.00172	0.93	981.2	22.48	909	9.63	930.3	7.44	34.5	123.5	71.6
CRO-3	23	0.17672	0.00193	11.38764	0.13767	0.46741	0.00535	0.95	2622.3	18.06	2472.2	23.5	2555.4	11.28	65.9	76.0	26.1
CRO-3	21a	0.06141	0.00077	0.78623	0.01058	0.09287	0.00107	0.86	653.7	26.55	572.5	6.31	589	6.01	31.3	219.7	0.5
CRO-3	100	0.07531	0.0008	1.80270	0.02118	0.17362	0.00196	0.96	1076.9	21.15	1032	10.76	1046.4	7.67	165.9	554.4	187.0
CRO-3	20	0.07430	0.00094	1.72947	0.02363	0.16883	0.00195	0.85	1049.7	25.42	1005.7	10.78	1019.6	8.79	15.4	53.1	19.4
CRO-3	82	0.07455	0.0009	1.74238	0.02275	0.16952	0.00193	0.87	1056.2	24.45	1009.5	10.65	1024.3	8.42	21.2	70.4	29.9
CRO-3	33	0.06273	0.00067	0.85676	0.01012	0.09907	0.00112	0.96	699.2	22.56	608.9	6.57	628.4	5.53	75.7	467.5	83.1
CRO-3	72	0.07480	0.00085	1.75257	0.02164	0.16995	0.00193	0.92	1063.2	22.58	1011.8	10.61	1028.1	7.98	33.0	106.7	53.4
CRO-3	41	0.07423	0.00082	1.70828	0.02070	0.16693	0.00189	0.93	1047.7	22.13	995.2	10.42	1011.6	7.76	83.9	262.3	183.8
CRO-3	75	0.14366	0.00154	7.66125	0.09075	0.38682	0.00437	0.95	2271.8	18.34	2108.1	20.3	2192.1	10.64	228.2	338.0	43.2
CRO-3	114	0.18015	0.00202	11.42423	0.13956	0.45998	0.00521	0.93	2654.3	18.48	2439.5	22.98	2558.4	11.41	41.1	43.7	30.5
CRO-3	57	0.07333	0.00089	1.64019	0.02131	0.16224	0.00184	0.87	1023	24.25	969.2	10.23	985.8	8.2	24.4	72.6	73.6
CRO-3	81	0.18359	0.002	11.76877	0.14116	0.46498	0.00526	0.94	2685.6	17.86	2461.5	23.14	2586.2	11.22	208.4	246.6	43.2
CRO-3	74	0.07499	0.00089	1.75381	0.02254	0.16964	0.00193	0.89	1068.2	23.7	1010.1	10.64	1028.6	8.31	23.1	65.1	70.4
CRO-3	30	0.12291	0.00127	5.61363	0.06469	0.33128	0.00374	0.98	1999	18.2	1844.6	18.12	1918.2	9.93	191.3	333.9	66.0
CRO-3	5	0.18080	0.00189	11.33806	0.13372	0.45487	0.00524	0.98	2660.2	17.2	2416.9	23.21	2551.3	11	60.1	67.8	41.6
CRO-3	14a	0.07450	0.00081	1.69902	0.02063	0.16543	0.00190	0.95	1054.6	22.12	986.9	10.5	1008.2	7.76	71.2	219.2	195.5
CRO-3	34a	0.12056	0.00126	5.30834	0.06177	0.31937	0.00361	0.97	1964.6	18.53	1786.7	17.64	1870.2	9.94	107.7	150.9	200.2
CRO-3	67	0.07515	0.00127	1.73267	0.03018	0.16724	0.00198	0.68	1072.5	33.68	996.9	10.92	1020.7	11.21	7.0	13.7	42.2
CRO-3	55	0.12414	0.00135	5.58444	0.06674	0.32631	0.00367	0.94	2016.5	19.24	1820.5	17.84	1913.7	10.29	232.8	376.4	196.0
CRO-3	103	0.07443	0.00082	1.67544	0.02023	0.16327	0.00185	0.94	1053.2	22.01	974.9	10.22	999.3	7.68	102.3	374.1	88.9
CRO-3	107	0.07441	0.00085	1.67077	0.02083	0.16287	0.00184	0.91	1052.5	22.95	972.7	10.22	997.5	7.92	34.9	112.1	77.7
CRO-3	19	0.16971	0.00182	9.80053	0.11718	0.41889	0.00479	0.96	2554.8	17.87	2255.4	21.78	2416.2	11.02	94.5	105.0	109.9
CRO-3	45	0.07089	0.0008	1.22787	0.01508	0.12563	0.00142	0.92	954.3	22.86	762.9	8.13	813.4	6.87	58.5	188.0	324.4
CRO-3	96	0.07463	0.00083	1.65304	0.02018	0.16067	0.00182	0.93	1058.1	22.57	960.5	10.11	990.7	7.72	59.6	190.0	147.0
CRO-3	31	0.07421	0.00086	1.60737	0.02027	0.15711	0.00179	0.90	1047.1	23.21	940.7	9.96	973.1	7.89	23.6	74.3	69.5
CRO-3	99	0.17563	0.00184	9.55762	0.11110	0.39473	0.00445	0.97	2612	17.31	2144.7	20.57	2393.1	10.68	444.0	537.7	541.8

Analyses U-Pb sur zircon – sédiments dévoniens

		Isotope ratios							Ages						Concentrations (ppm)		
Sample	Zircon analyses	Pb^{207}/Pb^{206}	1σ	Pb^{207}/U^{235}	1σ	Pb^{206}/U^{238}	1σ	rho	Pb^{207}/Pb^{206}	1σ	Pb^{206}/U^{238}	1σ	Pb^{207}/U^{235}	1σ	Pb	U	Th
CRO-11	1	0.06227	0.00066	0.93539	0.01141	0.10897	0.00128	0.96	683.2	22.49	666.8	7.46	670.5	5.98	68.9	427.7	52.9
CRO-11	4	0.06012	0.00068	0.73154	0.00928	0.08826	0.00104	0.93	608	24.09	545.2	6.16	557.5	5.44	71.1	509.1	172.9
CRO-11	6	0.12258	0.0013	6.13711	0.07432	0.36316	0.00426	0.97	1994.1	18.68	1997.1	20.15	1995.5	10.57	50.4	77.8	52.0
CRO-11	7	0.07135	0.00076	1.55996	0.01900	0.15859	0.00186	0.96	967.4	21.63	948.9	10.33	954.5	7.54	63.0	241.6	108.6
CRO-11	8	0.07609	0.0008	1.92940	0.02319	0.18392	0.00215	0.97	1097.4	20.85	1088.4	11.71	1091.3	8.04	144.8	392.9	487.5
CRO-11	9	0.20472	0.00211	12.30441	0.14619	0.43595	0.00509	0.98	2864.2	16.7	2332.5	22.85	2627.9	11.16	276.8	343.3	174.8
CRO-11	11	0.05970	0.00066	0.79242	0.00993	0.09627	0.00113	0.94	593.2	23.54	592.5	6.62	592.5	5.63	35.3	232.6	76.6
CRO-11	13	0.11331	0.00122	4.47576	0.05458	0.28651	0.00335	0.96	1853.2	19.31	1624.1	16.77	1726.5	10.12	84.2	173.8	66.7

CRO-11	14	0.11889	0.00124	5.52009	0.06598	0.33679	0.00392	0.97	1939.6	18.59	1871.2	18.9	1903.7	10.27	302.1	586.7	18.9
CRO-11	15	0.07438	0.00084	1.58940	0.02008	0.15501	0.00181	0.92	1051.7	22.62	929	10.09	966.1	7.87	86.4	325.5	175.9
CRO-11	16	0.05894	0.00072	0.76687	0.01024	0.09438	0.00110	0.87	564.8	26.23	581.4	6.5	578	5.88	34.2	195.8	175.3
CRO-11	17	0.06325	0.00095	1.05127	0.01673	0.12057	0.00143	0.75	716.5	31.65	733.8	8.25	729.5	8.28	9.2	42.4	30.8
CRO-11	18	0.06224	0.00133	0.89121	0.01935	0.10387	0.00128	0.57	682.3	44.86	637	7.47	647	10.39	2.8	15.9	8.3
CRO-11	19	0.07638	0.00087	1.86619	0.02374	0.17723	0.00206	0.91	1105	22.72	1051.8	11.3	1069.2	8.41	83.5	262.8	189.0
CRO-11	21	0.06100	0.0009	0.81333	0.01274	0.09672	0.00115	0.76	639.2	31.56	595.1	6.73	604.3	7.13	29.7	177.1	125.4
CRO-11	22	0.19635	0.00215	14.53762	0.17830	0.53706	0.00623	0.95	2796.1	17.79	2771.1	26.14	2785.5	11.65	109.5	111.1	53.6
CRO-11	23	0.05985	0.00073	0.81986	0.01098	0.09937	0.00116	0.87	598.1	26.32	610.7	6.78	608	6.13	33.5	213.9	62.7
CRO-11	25	0.07479	0.00084	1.83478	0.02300	0.17795	0.00207	0.93	1062.9	22.48	1055.8	11.32	1058	8.24	31.7	101.0	62.6
CRO-11	26	0.05731	0.00079	0.77204	0.01142	0.09771	0.00115	0.80	503.1	30.14	601	6.75	580.9	6.54	26.5	119.2	216.0
CRO-11	28	0.07368	0.00106	1.69440	0.02583	0.16682	0.00198	0.78	1032.6	28.76	994.6	10.95	1006.4	9.73	10.4	37.9	14.2
CRO-11	29	0.11296	0.00117	5.13889	0.06064	0.33001	0.00382	0.98	1847.5	18.65	1838.4	18.52	1842.6	10.03	140.0	239.5	135.1
CRO-11	31	0.09344	0.001	3.44356	0.04162	0.26731	0.00310	0.96	1496.9	20.13	1527.2	15.79	1514.4	9.51	119.3	275.6	73.5
CRO-11	32	0.11601	0.00124	4.91537	0.05918	0.30735	0.00357	0.96	1895.6	19.05	1727.7	17.6	1804.9	10.16	80.8	146.8	91.1
CRO-11	33	0.07300	0.00084	1.66215	0.02120	0.16516	0.00193	0.92	1013.9	23.12	985.4	10.65	994.2	8.08	31.6	94.1	117.6
CRO-11	34	0.07462	0.0008	1.84974	0.02239	0.17981	0.00209	0.96	1058	21.75	1065.9	11.4	1063.3	7.98	92.9	296.1	182.3
CRO-11	35	0.06479	0.00078	1.11482	0.01482	0.12482	0.00146	0.88	767.5	25.31	758.2	8.37	760.5	7.12	26.7	128.3	63.7
CRO-11	36	0.07329	0.00079	1.72190	0.02098	0.17043	0.00198	0.95	1022	21.73	1014.5	10.91	1016.7	7.83	55.5	183.2	120.9
CRO-11	37	0.07027	0.00078	1.49346	0.01861	0.15416	0.00179	0.93	936.4	22.67	924.2	10.02	927.7	7.58	38.8	156.7	49.3
CRO-11	38	0.06190	0.0007	0.84840	0.01065	0.09942	0.00116	0.93	670.7	23.87	611	6.79	623.8	5.85	31.7	201.5	55.9
CRO-11	39	0.05737	0.00094	0.73122	0.01256	0.09246	0.00110	0.69	505.3	35.52	570.1	6.52	557.3	7.37	5.2	39.1	0.4
CRO-11	42	0.06088	0.00067	0.88984	0.01097	0.10603	0.00123	0.94	635	23.42	649.6	7.19	646.3	5.89	64.0	374.0	137.8
CRO-11	43	0.05826	0.00096	0.67359	0.01156	0.08387	0.00101	0.70	539	36.16	519.2	5.99	522.9	7.01	12.1	77.0	72.4
CRO-11	44	0.06072	0.00068	0.82598	0.01033	0.09868	0.00115	0.93	629.3	23.87	606.7	6.75	611.4	5.75	64.2	402.8	143.5
CRO-11	45	0.07499	0.0009	1.65492	0.02188	0.16009	0.00188	0.89	1068.1	23.95	957.3	10.44	991.4	8.37	33.2	111.2	101.1
CRO-11	46	0.07097	0.00078	1.51171	0.01863	0.15450	0.00180	0.95	956.7	22.21	926.2	10.05	935.1	7.53	97.6	412.1	61.5
CRO-11	48	0.07406	0.00084	1.75533	0.02216	0.17192	0.00201	0.93	1043.2	22.62	1022.7	11.05	1029.1	8.17	64.7	194.3	214.1
CRO-11	49	0.07398	0.00104	1.74109	0.02618	0.17071	0.00203	0.79	1041.1	28.17	1016	11.2	1023.9	9.7	12.3	39.8	28.6
CRO-11	50	0.06271	0.00103	0.98805	0.01695	0.11429	0.00138	0.70	698.4	34.58	697.6	7.97	697.7	8.65	9.5	49.7	25.4
CRO-11	51	0.07232	0.00087	1.65975	0.02200	0.16649	0.00195	0.88	994.8	24.26	992.8	10.8	993.3	8.4	45.2	132.2	172.4
CRO-11	52	0.10608	0.00118	4.16018	0.05191	0.28448	0.00332	0.94	1733.2	20.25	1613.9	16.68	1666.2	10.21	146.9	305.3	129.8
CRO-11	53	0.11751	0.00142	5.68683	0.07506	0.35107	0.00413	0.89	1918.6	21.47	1939.7	19.71	1929.4	11.4	31.5	38.5	72.7
CRO-11	54	0.06116	0.00069	0.79886	0.01006	0.09475	0.00110	0.92	645	24.13	583.6	6.47	596.2	5.68	55.8	328.0	234.6
CRO-11	55	0.12803	0.00135	6.61939	0.07886	0.37506	0.00434	0.97	2071.1	18.41	2053.2	20.34	2061.9	10.51	109.4	174.0	51.5
CRO-11	56	0.10373	0.00112	3.57468	0.04336	0.25000	0.00290	0.96	1691.8	19.75	1438.5	14.93	1543.9	9.62	98.5	229.0	106.1
CRO-11	57	0.12530	0.00131	6.40678	0.07589	0.37091	0.00428	0.97	2033.1	18.35	2033.7	20.15	2033.2	10.4	91.2	131.4	100.2
CRO-11	59	0.07181	0.00081	1.57534	0.01979	0.15914	0.00185	0.93	980.5	22.82	952	10.26	960.5	7.8	36.9	118.9	124.6
CRO-11	60	0.07356	0.00084	1.65609	0.02096	0.16332	0.00190	0.92	1029.3	22.88	975.2	10.51	991.9	8.01	54.8	198.0	90.9
CRO-11	61	0.07566	0.00088	1.82567	0.02345	0.17505	0.00204	0.91	1086	23.12	1039.9	11.16	1054.7	8.42	27.7	86.1	64.8
CRO-11	62	0.06185	0.00069	0.73542	0.00916	0.08626	0.00100	0.93	668.8	23.7	533.4	5.93	559.7	5.36	105.4	712.0	357.3
CRO-11	63	0.07743	0.00105	2.02042	0.02924	0.18929	0.00223	0.81	1132.2	26.65	1117.5	12.09	1122.4	9.83	11.2	35.6	13.6
CRO-11	64	0.17623	0.00185	11.94425	0.14203	0.49165	0.00568	0.97	2617.8	17.36	2577.8	24.54	2600	11.14	278.4	291.9	219.6
CRO-11	65	0.07468	0.00089	1.72948	0.02268	0.16800	0.00196	0.89	1059.9	23.85	1001.1	10.79	1019.6	8.44	28.1	93.6	65.2
CRO-11	66	0.07572	0.00091	1.86889	0.02463	0.17905	0.00209	0.89	1087.6	23.9	1061.8	11.41	1070.1	8.72	39.0	121.8	82.6
CRO-11	67	0.07132	0.001	1.47866	0.02215	0.15041	0.00178	0.79	966.5	28.47	903.2	9.95	921.7	9.07	26.5	101.0	57.2
CRO-11	68	0.08702	0.00101	2.78494	0.03574	0.23216	0.00270	0.91	1360.9	22.23	1345.8	14.13	1351.5	9.59	66.1	174.9	51.5
CRO-11	70	0.07426	0.00083	1.82828	0.02282	0.17860	0.00207	0.93	1048.5	22.42	1059.3	11.31	1055.7	8.19	52.1	170.7	88.8
CRO-11	71	0.07378	0.00088	1.67513	0.02196	0.16471	0.00192	0.89	1035.3	23.61	982.9	10.6	999.1	8.34	35.5	110.8	112.7
CRO-11	72	0.06306	0.00082	0.90185	0.01260	0.10374	0.00121	0.83	710.3	27.25	636.3	7.08	652.7	6.73	43.3	248.1	113.3
CRO-11	74	0.06994	0.00078	1.42788	0.01771	0.14810	0.00171	0.93	926.6	22.66	890.3	9.61	900.7	7.41	97.8	398.6	160.6
CRO-11	75	0.07366	0.00085	1.78061	0.02280	0.17535	0.00203	0.90	1032.3	22.97	1041.5	11.15	1038.4	8.32	30.8	105.7	42.7
CRO-11	76	0.06694	0.00081	1.24873	0.01647	0.13533	0.00157	0.88	835.9	24.88	818.2	8.93	822.8	7.44	23.5	109.8	25.4

CRO-11	77	0.06145	0.0008	0.87929	0.01234	0.10379	0.00121	0.83	655.2	27.65	636.6	7.08	640.6	6.67	41.4	229.7	138.6
CRO-11	78	0.06454	0.00094	0.95265	0.01473	0.10708	0.00126	0.76	759.3	30.54	655.8	7.36	679.5	7.66	28.4	163.2	53.6
CRO-11	79	0.06080	0.00074	0.83163	0.01111	0.09923	0.00115	0.87	632	26.13	609.9	6.76	614.5	6.16	47.8	251.3	258.5
CRO-11	80	0.06058	0.00073	0.85784	0.01128	0.10273	0.00119	0.88	624.3	25.65	630.4	6.97	628.9	6.17	37.8	198.0	162.4
CRO-11	81	0.06037	0.00099	0.76880	0.01316	0.09237	0.00110	0.70	616.9	35.08	569.5	6.5	579.1	7.55	22.8	114.7	174.6
CRO-11	82	0.11999	0.00141	6.01528	0.07760	0.36364	0.00425	0.91	1956	20.77	1999.4	20.1	1978.1	11.23	21.9	30.5	31.7
CRO-11	83	0.06866	0.0008	1.32757	0.01708	0.14025	0.00163	0.90	888.5	23.88	846.1	9.19	857.8	7.45	52.9	222.6	111.4
CRO-11	84	0.12362	0.00128	5.17699	0.06093	0.30376	0.00350	0.98	2009.2	18.27	1709.9	17.29	1848.8	10.02	531.4	1114.2	59.0
CRO-11	85	0.06275	0.0009	0.92941	0.01417	0.10743	0.00126	0.77	699.9	30.3	657.8	7.36	667.3	7.46	16.4	79.2	80.8
CRO-11	86	0.05985	0.00082	0.76786	0.01127	0.09306	0.00109	0.80	598.2	29.43	573.6	6.43	578.5	6.47	18.0	111.3	65.6
CRO-11	87	0.12276	0.00133	6.30701	0.07689	0.37268	0.00431	0.95	1996.7	19.16	2042	20.26	2019.4	10.68	58.6	87.0	55.8
CRO-11	88	0.07417	0.00087	1.79619	0.02331	0.17566	0.00204	0.89	1046.1	23.58	1043.2	11.19	1044.1	8.46	35.7	101.2	116.8
CRO-11	89	0.06158	0.00082	0.83691	0.01201	0.09859	0.00115	0.81	659.5	28.38	606.1	6.77	617.4	6.64	17.5	120.1	3.8
CRO-11	90	0.06728	0.00073	1.23870	0.01516	0.13355	0.00154	0.94	846.4	22.54	808.1	8.77	818.3	6.88	104.2	413.7	361.2
CRO-11	91	0.06648	0.00088	1.02409	0.01465	0.11174	0.00131	0.82	821.6	27.54	682.8	7.58	716	7.35	18.3	89.4	74.5
CRO-11	92	0.11414	0.00127	5.02291	0.06223	0.31922	0.00370	0.94	1866.3	19.91	1785.9	18.09	1823.2	10.49	98.6	160.4	144.2
CRO-11	94	0.06001	0.00078	0.81931	0.01145	0.09904	0.00115	0.83	603.9	27.7	608.8	6.77	607.7	6.39	14.2	90.7	25.7
CRO-11	95	0.06398	0.00081	0.90083	0.01232	0.10213	0.00119	0.85	741.1	26.42	626.9	6.96	652.2	6.58	52.6	234.0	373.6
CRO-11	96	0.08521	0.00094	2.66030	0.03277	0.22646	0.00262	0.94	1320.3	21.25	1315.9	13.76	1317.5	9.09	71.9	183.7	90.2
CRO-11	97	0.05847	0.00066	0.68677	0.00859	0.08521	0.00098	0.92	547.2	24.35	527.1	5.85	530.9	5.17	88.1	679.6	94.7
CRO-11	98	0.12561	0.00136	5.48403	0.06682	0.31671	0.00366	0.95	2037.4	19.08	1773.6	17.93	1898.1	10.46	177.0	308.1	186.7
CRO-11	99	0.07120	0.00082	1.56883	0.01998	0.15984	0.00185	0.91	963.1	23.31	955.9	10.29	958	7.9	27.7	102.0	51.0
CRO-11	100	0.17510	0.00188	11.73211	0.14204	0.48604	0.00562	0.96	2607	17.82	2553.5	24.38	2583.3	11.33	123.4	139.9	80.9
CRO-11	101	0.13733	0.00147	6.53392	0.07897	0.34514	0.00398	0.95	2193.8	18.54	1911.4	19.09	2050.5	10.64	303.9	551.4	24.5
CRO-11	102	0.06134	0.00068	0.89323	0.01107	0.10563	0.00122	0.93	651.3	23.64	647.3	7.11	648.1	5.94	84.5	546.7	6.0
CRO-11	103	0.05980	0.00097	0.74365	0.01257	0.09021	0.00107	0.70	596.2	34.68	556.8	6.35	564.5	7.32	10.3	76.7	4.2
CRO-11	104	0.12325	0.00139	6.33624	0.07927	0.37294	0.00433	0.93	2003.8	19.83	2043.2	20.32	2023.5	10.97	81.5	112.3	104.0
CRO-11	106	0.06376	0.00086	0.94038	0.01362	0.10699	0.00125	0.81	733.7	28.36	655.2	7.3	673.1	7.13	43.6	238.1	130.6
CRO-11	107	0.06773	0.0009	1.21318	0.01729	0.12993	0.00152	0.82	860.3	27.26	787.5	8.68	806.6	7.93	29.1	136.6	50.2
CRO-11	108	0.07308	0.00082	1.73404	0.02177	0.17213	0.00199	0.92	1016.2	22.7	1023.8	10.95	1021.3	8.09	82.5	284.3	153.3
CRO-11	109	0.12440	0.00139	6.33329	0.07885	0.36931	0.00428	0.93	2020.3	19.7	2026.1	20.14	2023.1	10.92	94.3	131.3	124.6
CRO-11	110	0.11962	0.00138	5.64003	0.07199	0.34202	0.00398	0.91	1950.6	20.49	1896.4	19.1	1922.2	11.01	54.2	85.7	61.3
CRO-11	112	0.06533	0.00105	0.79357	0.01306	0.08812	0.00102	0.70	784.9	33.33	544.4	6.03	593.2	7.4	52.1	371.8	7.1
CRO-11	113	0.05985	0.00161	0.77621	0.02070	0.09408	0.00119	0.47	598	57.06	579.6	7	583.3	11.84	9.2	48.6	43.9
CRO-11	114	0.06237	0.00105	0.73823	0.01272	0.08586	0.00100	0.68	686.7	35.57	531	5.92	561.4	7.43	40.6	237.8	191.8
CRO-11	115	0.06870	0.00079	1.43903	0.01785	0.15194	0.00170	0.90	889.8	23.64	911.8	9.52	905.3	7.43	66.0	248.5	88.4
CRO-11	116	0.06494	0.00117	0.92126	0.01692	0.10290	0.00121	0.64	772.4	37.62	631.4	7.07	663	8.94	32.3	164.7	111.7
CRO-11	118	0.07386	0.00106	1.69777	0.02540	0.16674	0.00191	0.77	1037.7	28.81	994.1	10.56	1007.7	9.56	50.8	141.9	167.5
CRO-11	121	0.06172	0.00152	0.90467	0.02221	0.10633	0.00132	0.51	664.3	51.85	651.4	7.68	654.2	11.84	10.9	52.1	40.9
CRO-11	122	0.07081	0.00082	1.56024	0.01947	0.15984	0.00179	0.90	951.9	23.6	955.9	9.95	954.6	7.72	121.0	440.5	115.6
CRO-11	123	0.18030	0.00196	12.55875	0.14862	0.50525	0.00565	0.94	2655.7	17.95	2636.3	24.18	2647.1	11.13	159.8	127.7	205.1
CRO-11	124	0.11315	0.00132	5.13276	0.06424	0.32906	0.00370	0.90	1850.6	20.97	1833.8	17.97	1841.5	10.64	111.5	161.9	156.5
CRO-11	125	0.06103	0.001	0.81469	0.01373	0.09683	0.00112	0.69	640.2	34.98	595.8	6.58	605.1	7.68	35.7	169.1	215.6
CRO-11	127	0.07735	0.0011	1.91060	0.02833	0.17917	0.00205	0.77	1130.3	28.15	1062.4	11.22	1084.8	9.88	48.5	156.6	40.2
CRO-11	128	0.09078	0.00124	2.67516	0.03826	0.21377	0.00245	0.80	1441.8	25.88	1248.8	12.99	1321.6	10.57	74.3	169.3	162.1
CRO-11	130	0.07334	0.00085	1.75794	0.02194	0.17387	0.00195	0.90	1023.3	23.36	1033.4	10.69	1030.1	8.08	138.5	488.5	43.2
CRO-11	131	0.17933	0.00202	12.41798	0.15091	0.50231	0.00562	0.92	2646.7	18.56	2623.7	24.12	2636.5	11.42	232.6	226.0	155.8
CRO-11	132	0.06141	0.00108	0.85222	0.01525	0.10066	0.00117	0.65	653.7	37.26	618.3	6.87	625.9	8.36	22.5	132.9	26.6
CRO-11	133	0.06442	0.00096	0.96550	0.01493	0.10872	0.00124	0.74	755.3	31.23	665.3	7.23	686.1	7.71	25.9	132.7	58.9
CRO-11	134	0.07281	0.0009	1.67029	0.02185	0.16639	0.00187	0.86	1008.8	24.77	992.2	10.34	997.3	8.31	68.0	224.8	104.8
CRO-11	135	0.07332	0.00105	1.52724	0.02266	0.1511	0.00173	0.77	1022.7	28.62	907.1	9.66	941.4	9.11	48.1	166.7	108.8
CRO-11	136	0.20279	0.00261	15.70966	0.21272	0.56193	0.00651	0.86	2848.8	20.8	2874.6	26.87	2859.3	12.93	36.4	28.9	30.7
CRO-11	138	0.11428	0.00136	4.87084	0.06177	0.30917	0.00347	0.89	1868.5	21.26	1736.6	17.1	1797.2	10.68	240.0	340.9	473.1

CRO-11	139	0.15536	0.00188	8.22554	0.10601	0.38404	0.00434	0.88	2405.8	20.44	2095.1	20.21	2256.2	11.67	97.3	110.9	140.6
CRO-11	140	0.07518	0.00098	1.85614	0.02549	0.1791	0.00202	0.82	1073.2	25.97	1062.1	11.07	1065.6	9.06	91.0	286.9	107.9
CRO-11	24a	0.06774	0.0008	1.18867	0.01538	0.12729	0.00148	0.90	860.5	24.18	772.4	8.45	795.3	7.13	42.5	209.9	54.2
CRO-11	24b	0.06599	0.00071	1.19133	0.01443	0.13096	0.00152	0.96	805.9	22.35	793.3	8.65	796.6	6.69	68.6	333.0	82.6
CRO-11	40a	0.06396	0.00097	0.99679	0.01595	0.11304	0.00135	0.75	740.4	31.76	690.4	7.81	702.2	8.11	10.7	57.2	23.5
CRO-11	40b	0.06275	0.00075	0.98825	0.01306	0.11423	0.00134	0.89	699.9	25.37	697.3	7.73	697.8	6.67	30.7	155.1	95.3
CRO-12	24	0.06377	0.00093	1.12919	0.01721	0.12845	0.00149	0.761094	734	30.61	779	8.49	767.4	8.21	58.3	251.0	156.4
CRO-12	28	0.07631	0.00088	2.00828	0.02505	0.19091	0.00217	0.9112711	1103.3	22.78	1126.3	11.73	1118.3	8.46	103.9	352.0	19.8
CRO-12	125	0.0687	0.00079	1.43903	0.01785	0.15194	0.0017	0.9020039	889.8	23.64	911.8	9.52	905.3	7.43	66.0	248.5	88.4
CRO-12	140	0.07334	0.00085	1.75794	0.02194	0.17387	0.00195	0.8986227	1023.3	23.36	1033.4	10.69	1030.1	8.08	138.5	488.5	43.2
CRO-12	79	0.05914	0.00077	0.7766	0.0107	0.09524	0.00107	0.8154137	572.4	28.15	586.5	6.32	583.5	6.11	41.9	276.0	36.7
CRO-12	146	0.20279	0.00261	15.70966	0.21272	0.56193	0.00651	0.8555733	2848.8	20.8	2874.6	26.87	2859.3	12.93	36.4	28.9	30.7
CRO-12	10	0.06082	0.00067	0.87794	0.01047	0.10471	0.00117	0.9369488	632.8	23.38	642	6.85	639.9	5.66	102.7	611.9	109.3
CRO-12	100	0.05737	0.00116	0.65116	0.01323	0.08233	0.00097	0.5798845	505.4	44.2	510	5.79	509.2	8.14	17.6	135.6	0.1
CRO-12	132	0.07081	0.00082	1.56024	0.01947	0.15984	0.00179	0.8974144	951.9	23.6	955.9	9.95	954.6	7.72	121.0	440.5	115.6
CRO-12	7	0.07447	0.00081	1.82216	0.02156	0.17748	0.00199	0.9476357	1054	22.02	1053.2	10.89	1053.5	7.76	89.5	302.3	88.2
CRO-12	81	0.17439	0.00195	11.88848	0.14358	0.49449	0.00552	0.9243021	2600.2	18.49	2590.1	23.79	2595.7	11.31	280.7	285.1	176.4
CRO-12	133	0.1803	0.00196	12.55875	0.14862	0.50525	0.00565	0.9449553	2655.7	17.95	2636.3	24.18	2647.1	11.13	159.8	127.7	205.1
CRO-12	141	0.17933	0.00202	12.41798	0.15091	0.50231	0.00562	0.9206561	2646.7	18.56	2623.7	24.12	2636.5	11.42	232.6	226.0	155.8
CRO-12	72	0.06119	0.00075	0.87134	0.01139	0.10328	0.00116	0.8592226	646.1	26.13	633.6	6.78	636.3	6.18	57.5	329.1	111.5
CRO-12	131	0.06172	0.00152	0.90467	0.02221	0.10633	0.00132	0.5056613	664.3	51.85	651.4	7.68	654.2	11.84	10.9	52.1	40.9
CRO-12	134	0.11315	0.00132	5.13276	0.06424	0.32906	0.0037	0.8984048	1850.6	20.97	1833.8	17.97	1841.5	10.64	111.5	161.9	156.5
CRO-12	58	0.06411	0.00087	1.05931	0.0152	0.11985	0.00137	0.7966398	745.4	28.53	729.7	7.89	733.5	7.5	139.6	668.6	327.1
CRO-12	93	0.06047	0.00072	0.81977	0.0104	0.09834	0.00109	0.8736852	620.5	25.58	604.6	6.4	607.9	5.8	94.8	535.3	228.2
CRO-12	60	0.07061	0.00199	1.507	0.04212	0.15482	0.00202	0.4668197	946.1	56.53	927.9	11.27	933.2	17.06	4.1	16.4	4.0
CRO-12	112	0.11798	0.0014	5.59057	0.07193	0.34369	0.00391	0.884211	1925.9	21.17	1904.4	18.78	1914.6	11.08	181.9	254.2	243.9
CRO-12	111	0.11016	0.0014	4.83625	0.06567	0.31845	0.00366	0.8464115	1802	22.99	1782.1	17.89	1791.2	11.43	54.6	89.6	57.9
CRO-12	123	0.05985	0.00161	0.77621	0.0207	0.09408	0.00119	0.4743059	598	57.06	579.6	7	583.3	11.84	9.2	48.6	43.9
CRO-12	108	0.06234	0.00086	0.93671	0.01359	0.109	0.00124	0.784117	685.6	29.21	666.9	7.23	671.2	7.13	58.2	321.3	57.0
CRO-12	150	0.07518	0.00098	1.85614	0.02549	0.1791	0.00202	0.8212903	1073.2	25.97	1062.1	11.07	1065.6	9.06	91.0	286.9	107.9
CRO-12	33	0.06073	0.00071	0.8285	0.01041	0.09895	0.00111	0.8927893	629.8	24.94	608.3	6.53	612.8	5.78	97.2	530.0	365.0
CRO-12	97	0.06984	0.00092	1.43333	0.01973	0.14886	0.00167	0.8149999	923.7	26.74	894.6	9.39	902.9	8.23	29.2	112.0	33.6
CRO-12	114	0.07593	0.00106	1.90589	0.02812	0.18206	0.0021	0.7817849	1093.3	27.79	1078.2	11.47	1083.1	9.83	24.5	71.3	48.3
CRO-12	71	0.05924	0.00067	0.72071	0.00887	0.08825	0.00099	0.9115015	575.8	24.58	545.2	5.85	551.1	5.23	169.4	1220.0	85.3
CRO-12	20	0.07385	0.00083	1.74603	0.02139	0.17152	0.00194	0.9232682	1037.2	22.59	1020.5	10.66	1025.7	7.91	101.8	363.1	89.8
CRO-12	29	0.06068	0.00076	0.80944	0.0109	0.09676	0.00111	0.8518935	628	26.93	595.4	6.5	602.1	6.12	78.9	511.5	101.9
CRO-12	23	0.06448	0.00085	1.05485	0.01476	0.11868	0.00136	0.8189657	757.3	27.65	723	7.83	731.3	7.3	50.3	255.5	81.3
CRO-12	144	0.07281	0.0009	1.67029	0.02185	0.16639	0.00187	0.859122	1008.8	24.77	992.2	10.34	997.3	8.31	68.0	224.8	104.8
CRO-12	142	0.06141	0.00108	0.85222	0.01525	0.10066	0.00117	0.6495473	653.7	37.26	618.3	6.87	625.9	8.36	22.5	132.9	26.6
CRO-12	62	0.18143	0.00191	12.37111	0.14322	0.49461	0.00553	0.9657556	2666	17.35	2590.6	23.85	2633	10.88	322.0	352.0	105.6
CRO-12	105	0.06275	0.00073	0.93367	0.01172	0.10793	0.00121	0.8931183	699.6	24.62	660.7	7.05	669.6	6.16	87.5	487.1	86.9
CRO-12	82	0.06602	0.00099	1.1407	0.01771	0.12533	0.00143	0.7349095	807.1	31.09	761.1	8.21	772.8	8.4	27.3	100.5	128.5
CRO-12	135	0.06103	0.001	0.81469	0.01373	0.09683	0.00112	0.6863252	640.2	34.98	595.8	6.58	605.1	7.68	35.7	169.1	215.6
CRO-12	106	0.06036	0.00112	0.77136	0.01456	0.0927	0.00109	0.6229347	616.4	39.58	571.5	6.44	580.5	8.34	15.6	92.0	49.9
CRO-12	96	0.06104	0.00098	0.79873	0.01309	0.09492	0.00109	0.7006952	640.5	34.03	584.6	6.39	596.1	7.39	43.8	290.3	1.7
CRO-12	1	0.06049	0.00072	0.75751	0.00961	0.09083	0.00102	0.8851887	621.3	25.34	560.5	6.03	572.6	5.55	47.2	324.6	51.9
CRO-12	14	0.06185	0.00084	0.83947	0.01196	0.09845	0.00112	0.7985025	669	28.73	605.3	6.6	618.9	6.6	50.5	264.1	233.9
CRO-12	70	0.12898	0.00143	6.44308	0.07755	0.36236	0.00407	0.933181	2084.1	19.39	1993.3	19.24	2038.2	10.58	156.3	243.5	77.9
CRO-12	101	0.07202	0.00083	1.50693	0.01877	0.15177	0.0017	0.8992735	986.6	23.4	910.9	9.5	933.2	7.6	135.0	501.4	212.8
CRO-12	119	0.11968	0.00148	5.51781	0.07374	0.33441	0.00385	0.8614798	1951.4	21.94	1859.7	18.58	1903.4	11.49	100.8	171.4	48.1
CRO-12	12	0.05931	0.00074	0.66813	0.00888	0.08171	0.00093	0.8563588	578.5	26.89	506.3	5.52	519.6	5.41	77.9	540.3	287.4
CRO-12	107	0.24238	0.00265	19.21218	0.22961	0.57495	0.00644	0.9372202	3135.7	17.28	2928.1	26.38	3052.5	11.53	865.0	728.5	402.6
CRO-12	67	0.12687	0.00137	6.16994	0.07262	0.35277	0.00395	0.9513277	2055	18.9	1947.8	18.81	2000.2	10.28	239.1	402.8	58.0

CRO-12	9	0.17026	0.00182	10.62862	0.1245	0.45282	0.00509	0.9596209	2560.2	17.81	2407.8	22.58	2491.2	10.87	144.4	159.4	120.7
CRO-12	104	0.11484	0.00133	5.03206	0.06286	0.31784	0.00358	0.9016664	1877.4	20.78	1779.2	17.51	1824.7	10.58	122.8	194.1	135.5
CRO-12	128	0.07386	0.00106	1.69777	0.0254	0.16674	0.00191	0.7656648	1037.7	28.81	994.1	10.56	1007.7	9.56	50.8	141.9	167.5
CRO-12	50	0.06606	0.00078	1.07365	0.01361	0.11789	0.00133	0.889978	808.4	24.41	718.4	7.67	740.5	6.66	186.2	866.6	522.5
CRO-12	59	0.06087	0.00147	0.74381	0.0179	0.08864	0.0011	0.5156701	634.7	50.98	547.5	6.52	564.6	10.42	19.7	119.8	84.9
CRO-12	143	0.06442	0.00096	0.9655	0.01493	0.10872	0.00124	0.7375725	755.3	31.23	665.3	7.23	686.1	7.71	25.9	132.7	58.9
CRO-12	80	0.1206	0.00139	5.50068	0.06819	0.33084	0.00371	0.9045896	1965.1	20.4	1842.4	17.98	1900.7	10.65	184.8	286.2	209.8
CRO-12	98	0.06411	0.00088	0.92907	0.01335	0.10513	0.00119	0.7877483	745.2	28.86	644.4	6.92	667.1	7.03	77.9	356.8	330.1
CRO-12	46	0.07282	0.00081	1.60765	0.01947	0.16014	0.0018	0.9281074	1009	22.4	957.5	10	973.2	7.58	167.0	572.8	368.4
CRO-12	34	0.06389	0.00073	0.90832	0.01117	0.10312	0.00116	0.9147466	738.1	23.87	632.7	6.77	656.2	5.94	100.2	590.3	155.0
CRO-12	148	0.11428	0.00136	4.87084	0.06177	0.30917	0.00347	0.8850308	1868.5	21.26	1736.6	17.1	1797.2	10.68	240.0	340.9	473.1
CRO-12	30	0.0726	0.00099	1.58167	0.0227	0.15805	0.00182	0.8023556	1002.7	27.37	945.9	10.15	963	8.93	112.3	302.9	545.4
CRO-12	137	0.07735	0.0011	1.9106	0.02833	0.17917	0.00205	0.7716347	1130.3	28.15	1062.4	11.22	1084.8	9.88	48.5	156.6	40.2
CRO-12	91	0.07172	0.00103	1.38855	0.02059	0.14045	0.00159	0.7634499	977.9	28.99	847.2	8.97	884.1	8.75	62.0	228.6	150.7
CRO-12	52	0.12055	0.0014	5.37228	0.06731	0.32328	0.00366	0.9036106	1964.3	20.51	1805.7	17.81	1880.4	10.73	209.3	382.4	83.2
CRO-12	63	0.06397	0.00072	0.87127	0.01058	0.0988	0.00111	0.9251947	740.6	23.51	607.3	6.49	636.3	5.74	210.4	1374.3	25.2
CRO-12	84	0.12386	0.00141	5.6103	0.06882	0.32856	0.00367	0.9105898	2012.5	20.08	1831.4	17.79	1917.7	10.57	307.1	432.1	522.9
CRO-12	126	0.06494	0.00117	0.92126	0.01692	0.1029	0.00121	0.6402533	772.4	37.62	631.4	7.07	663	8.94	32.3	164.7	111.7
CRO-12	68	0.07323	0.00136	1.599	0.03018	0.15838	0.00189	0.6322527	1020.4	36.97	947.8	10.52	969.8	11.79	34.5	116.2	76.2
CRO-12	11	0.08077	0.00087	2.12033	0.02497	0.19043	0.00214	0.9542525	1215.8	21.02	1123.7	11.58	1155.4	8.13	251.1	760.0	313.3
CRO-12	36	0.06667	0.0011	1.01994	0.01725	0.11097	0.00129	0.6873369	827.5	34.04	678.4	7.51	713.9	8.67	37.2	176.9	138.2
CRO-12	118	0.06546	0.00127	0.93925	0.01859	0.10407	0.00126	0.6117117	789.1	40.31	638.2	7.33	672.5	9.73	21.7	119.3	46.3
CRO-12	75	0.17693	0.00199	10.55317	0.12843	0.43265	0.00486	0.9230304	2624.3	18.62	2317.7	21.89	2484.6	11.29	449.3	607.9	7.0
CRO-12	124	0.06237	0.00105	0.73823	0.01272	0.08586	0.001	0.6759486	686.7	35.57	531	5.92	561.4	7.43	40.6	237.8	191.8
CRO-12	17	0.09383	0.00102	3.04239	0.03626	0.2352	0.00265	0.9453566	1504.8	20.46	1361.7	13.82	1418.3	9.11	332.1	853.9	143.7
CRO-12	21	0.07328	0.00083	1.58126	0.01953	0.15652	0.00177	0.9155972	1021.8	22.85	937.4	9.87	962.9	7.68	194.3	785.6	110.1
CRO-12	103	0.07537	0.00092	1.7161	0.02227	0.16517	0.00186	0.867769	1078.3	24.21	985.4	10.29	1014.6	8.32	105.6	361.9	128.5
CRO-12	45	0.0715	0.00133	1.28053	0.02411	0.12991	0.00155	0.633697	971.7	37.4	787.4	8.85	837.1	10.73	24.2	77.1	134.7
CRO-12	113	0.07143	0.00092	1.26915	0.01749	0.12888	0.00147	0.8276657	969.7	26.14	781.5	8.41	832	7.83	114.0	503.4	195.0
CRO-12	35	0.06736	0.00073	1.0044	0.01187	0.10817	0.00121	0.9465303	848.8	22.32	662.1	7.05	706	6.01	331.9	1849.3	485.6
CRO-12	149	0.15536	0.00188	8.22554	0.10601	0.38404	0.00434	0.8768612	2405.8	20.44	2095.1	20.21	2256.2	11.67	97.3	110.9	140.6
CRO-12	47	0.07442	0.00098	1.63655	0.02273	0.15952	0.00182	0.8214594	1052.8	26.26	954.1	10.12	984.4	8.75	63.9	227.9	106.4
CRO-12	53	0.17624	0.002	10.13298	0.125	0.41707	0.00471	0.9154595	2617.8	18.79	2247.2	21.42	2447	11.4	252.3	336.9	103.3
CRO-12	110	0.06369	0.00089	0.76722	0.01123	0.08738	0.001	0.7818584	731.2	29.26	540	5.92	578.2	6.45	144.9	973.7	261.4
CRO-12	4	0.17597	0.00184	10.05167	0.11535	0.41436	0.00463	0.9736969	2615.2	17.29	2234.8	21.1	2439.5	10.6	609.2	839.7	129.4
CRO-12	8	0.07464	0.00081	1.64325	0.01945	0.15969	0.00179	0.9470204	1058.6	22.02	955	9.95	987	7.47	207.9	672.1	561.0
CRO-12	3	0.11621	0.00147	4.67458	0.06237	0.29179	0.00334	0.8579123	1898.7	22.53	1650.5	16.68	1762.7	11.16	51.0	64.6	157.2
CRO-12	18	0.06627	0.00074	0.87502	0.01067	0.09577	0.00108	0.9248	815.1	23.27	589.6	6.35	638.3	5.78	144.1	971.0	43.1
CRO-12	145	0.07332	0.00105	1.52724	0.02266	0.1511	0.00173	0.7716654	1022.7	28.62	907.1	9.66	941.4	9.11	48.1	166.7	108.8
CRO-12	102	0.103	0.00114	3.56364	0.04278	0.25097	0.0028	0.9293713	1678.8	20.29	1443.5	14.44	1541.5	9.52	221.4	528.3	40.8
CRO-12	122	0.06533	0.00105	0.79357	0.01306	0.08812	0.00102	0.7033439	784.9	33.33	544.4	6.03	593.2	7.4	52.1	371.8	7.1
CRO-12	138	0.09078	0.00124	2.67516	0.03826	0.21377	0.00245	0.8013535	1441.8	25.88	1248.8	12.99	1321.6	10.57	74.3	169.3	162.1
CRO-12	61	0.13534	0.00144	6.05545	0.07055	0.32454	0.00363	0.9600366	2168.4	18.4	1811.9	17.67	1983.9	10.15	130.2	185.7	183.1
CRO-12	99	0.07271	0.00113	1.47511	0.02352	0.14716	0.00169	0.7202512	1006	31.17	885	9.51	920.2	9.65	38.3	126.3	110.5
CRO-12	25	0.12462	0.00142	5.15961	0.06392	0.30034	0.00341	0.9164765	2023.4	20.06	1693	16.91	1846	10.54	220.2	369.6	306.5
CRO-12	115	0.07555	0.00108	1.64681	0.02477	0.15809	0.00183	0.7695984	1083.3	28.44	946.2	10.2	988.3	9.5	44.9	130.3	173.9
CRO-1	45	0.05673	0.00104	0.80697	0.01480	0.10318	0.00115	0.61	480.4	40.41	633	6.75	600.8	8.32	9.5	50.5	15.4
CRO-1	27	0.06020	0.00093	0.85985	0.01351	0.10360	0.00116	0.71	610.7	32.98	635.5	6.76	630	7.38	24.0	139.0	3.4
CRO-1	7	0.06158	0.00074	0.93865	0.01185	0.11057	0.00121	0.87	659.4	25.59	676.1	7.02	672.2	6.2	52.5	262.5	63.5
CRO-1	18	0.06666	0.00099	1.26216	0.01919	0.13733	0.00153	0.73	827.3	30.73	829.6	8.7	828.9	8.62	40.8	158.6	57.5
CRO-1	37	0.05941	0.0009	0.77613	0.01188	0.09477	0.00104	0.72	582	32.51	583.7	6.11	583.3	6.79	15.5	96.4	2.5
CRO-1	44	0.13005	0.00143	6.89168	0.07923	0.38439	0.00412	0.93	2098.6	19.24	2096.8	19.16	2097.6	10.19	105.3	144.0	33.0
CRO-1	22	0.06054	0.00154	0.82602	0.02088	0.09897	0.00121	0.48	622.8	54.01	608.4	7.07	611.4	11.61	6.6	37.6	9.7

CRO-1	40	0.06038	0.00112	0.80815	0.01499	0.09709	0.00109	0.61	617.1	39.57	597.3	6.43	601.4	8.42	15.1	76.2	54.1
CRO-1	28	0.11525	0.00132	5.29385	0.06387	0.33319	0.00363	0.90	1883.7	20.48	1853.8	17.53	1867.9	10.3	297.8	474.8	140.6
CRO-1	4	0.06155	0.00071	0.86843	0.01063	0.10234	0.00112	0.89	658.6	24.71	628.1	6.53	634.7	5.78	94.9	553.2	24.0
CRO-1	48	0.06039	0.00073	0.79438	0.00991	0.09541	0.00102	0.86	617.6	25.88	587.5	6.03	593.7	5.61	162.1	983.3	82.6
CRO-1	11	0.06918	0.00076	1.37057	0.01599	0.14370	0.00156	0.93	904.2	22.47	865.6	8.8	876.4	6.85	166.8	610.1	280.3
CRO-1	51	0.16534	0.00184	10.44645	0.12093	0.45828	0.00490	0.92	2511.1	18.55	2432	21.68	2475.2	10.73	197.7	223.1	43.8
CRO-1	16	0.06274	0.00077	0.92755	0.01195	0.10723	0.00117	0.85	699.5	26.07	656.6	6.83	666.3	6.3	33.0	166.9	61.9
CRO-1	29	0.07041	0.00111	1.42226	0.02263	0.14652	0.00163	0.70	940.4	32.05	881.4	9.15	898.3	9.48	28.7	93.7	71.0
CRO-1	15b	0.06671	0.00078	1.16209	0.01423	0.12636	0.00138	0.89	828.8	24.08	767	7.88	782.9	6.68	61.9	260.3	123.8
CRO-1	30	0.06343	0.00071	0.94256	0.01102	0.10778	0.00115	0.91	722.8	23.67	659.8	6.7	674.2	5.76	116.4	548.3	289.2
CRO-1	31	0.06093	0.00078	0.77656	0.01025	0.09245	0.00100	0.82	636.7	27.47	570	5.88	583.5	5.86	60.8	365.8	80.6
CRO-1	20	0.06499	0.00168	1.00990	0.02581	0.11271	0.00138	0.48	774.1	53.33	688.5	8.02	708.8	13.04	5.1	27.0	0.5
CRO-1	32	0.05891	0.00103	0.62612	0.01094	0.07709	0.00086	0.64	563.9	37.52	478.7	5.15	493.7	6.83	33.5	251.4	22.3
CRO-1	12	0.06214	0.00078	0.82051	0.01075	0.09577	0.00105	0.84	679.1	26.64	589.6	6.18	608.3	5.99	58.8	359.1	33.2
CRO-1	53	0.06570	0.00094	1.03892	0.01513	0.11471	0.00125	0.75	796.7	29.79	700	7.26	723.4	7.54	58.5	276.0	92.2
CRO-1	42	0.06171	0.00072	0.78594	0.00945	0.09239	0.00099	0.89	664	24.65	569.6	5.84	588.9	5.37	146.9	790.3	505.3
CRO-1	57	0.17799	0.00204	11.23026	0.13337	0.45767	0.00492	0.91	2634.2	18.87	2429.3	21.74	2542.4	11.07	142.7	142.2	95.5
CRO-1	38	0.06016	0.00079	0.68246	0.00912	0.08228	0.00089	0.81	609.5	27.96	509.7	5.29	528.3	5.5	75.0	507.1	108.6
CRO-1	46	0.11188	0.00125	4.66175	0.05425	0.30225	0.00324	0.92	1830.1	20.13	1702.4	16.03	1760.4	9.73	97.4	155.4	102.8
CRO-1	15a	0.06655	0.00075	1.06597	0.01271	0.11619	0.00126	0.91	823.6	23.36	708.6	7.3	736.8	6.25	171.9	760.9	392.7
CRO-1	25	0.06246	0.00105	0.79477	0.01353	0.09229	0.00104	0.66	690	35.49	569.1	6.16	593.9	7.65	19.8	123.9	18.9
CRO-1	2	0.06046	0.0008	0.66883	0.00919	0.08024	0.00088	0.80	620.1	28.35	497.6	5.28	520	5.59	62.8	466.9	26.1
CRO-1	58	0.06245	0.00076	0.74276	0.00936	0.08628	0.00093	0.86	689.4	25.87	533.5	5.51	564	5.45	208.9	1402.7	68.9
CRO-1	50	0.11482	0.00134	4.70575	0.05692	0.29728	0.00320	0.89	1877	20.92	1677.8	15.91	1768.3	10.13	79.5	131.5	74.1
CRO-1	52	0.11196	0.00129	4.46822	0.05330	0.28948	0.00311	0.90	1831.5	20.69	1638.9	15.54	1725.1	9.9	142.1	220.7	193.5
CRO-1	55	0.06293	0.00074	0.74765	0.00909	0.08618	0.00092	0.88	705.8	24.79	532.9	5.48	566.9	5.28	271.2	1636.9	736.5
CRO-1	17	0.07341	0.00092	1.56678	0.02047	0.15481	0.00170	0.84	1025.3	25.18	927.9	9.5	957.2	8.1	74.6	255.8	101.6
CRO-1	14	0.06770	0.00118	0.95268	0.01671	0.10207	0.00117	0.65	859.3	35.68	626.6	6.82	679.5	8.69	39.4	136.2	318.5
CRO-1	26	0.17108	0.00195	9.12895	0.10950	0.38704	0.00421	0.91	2568.3	18.89	2109.1	19.58	2351	10.98	251.6	327.2	113.7
CRO-1	49	0.26918	0.00297	18.26868	0.21046	0.49229	0.00528	0.93	3301.2	17.23	2580.6	22.8	3004	11.09	322.0	304.9	89.4
CRO-2	56	0.05455	0.00077	0.45411	0.00660	0.06039	0.00067	0.76	393.7	31.38	378	4.1	380.2	4.61	54.0	478.4	260.6
CRO-2	36	0.05757	0.00086	0.64987	0.01003	0.08188	0.00093	0.74	513.2	32.66	507.3	5.57	508.4	6.17	28.6	179.4	136.3
CRO-2	38	0.05800	0.00111	0.65750	0.01276	0.08223	0.00096	0.60	529.3	41.72	509.4	5.73	513.1	7.82	9.3	71.4	1.3
CRO-2	17	0.06471	0.00083	0.73701	0.00996	0.08262	0.00093	0.83	764.8	26.75	511.7	5.54	560.7	5.82	131.1	724.4	1105.7
CRO-2	24	0.06053	0.00088	0.70946	0.01068	0.08501	0.00096	0.75	622.7	31.08	526	5.72	544.4	6.34	43.8	296.3	101.6
CRO-2	25	0.05803	0.00081	0.70375	0.01021	0.08797	0.00099	0.78	530.4	30.71	543.5	5.87	541	6.09	48.2	289.5	192.2
CRO-2	94	0.06484	0.00095	0.79633	0.01198	0.08909	0.00100	0.75	769.3	30.48	550.2	5.93	594.8	6.77	30.7	188.3	89.3
CRO-2	109	0.06065	0.00083	0.75316	0.01074	0.09009	0.00101	0.79	626.7	29.21	556.1	5.98	570.1	6.22	40.8	228.1	192.7
CRO-2	91	0.05993	0.00082	0.74870	0.01065	0.09063	0.00101	0.78	601.2	29.42	559.3	5.96	567.5	6.19	29.6	196.3	28.7
CRO-2	5	0.06024	0.00074	0.76576	0.01007	0.09220	0.00104	0.86	612.3	26.38	568.5	6.14	577.3	5.79	55.7	365.4	67.7
CRO-2	23	0.06072	0.0008	0.78161	0.01078	0.09337	0.00105	0.82	629.4	28.09	575.4	6.18	586.4	6.14	50.0	296.2	137.5
CRO-2	37	0.05942	0.00071	0.77311	0.00991	0.09438	0.00106	0.88	582.5	25.78	581.4	6.24	581.5	5.67	107.7	558.8	567.6
CRO-2	2	0.06375	0.00073	0.83853	0.01041	0.09541	0.00107	0.90	733.3	24.1	587.5	6.32	618.3	5.75	85.6	507.1	200.0
CRO-2	51	0.06513	0.00088	0.86246	0.01208	0.09606	0.00107	0.80	778.5	28	591.3	6.32	631.5	6.58	79.9	492.9	58.1
CRO-2	76	0.06382	0.00087	0.85295	0.01218	0.09695	0.00109	0.79	735.5	28.76	596.5	6.41	626.3	6.68	31.1	200.2	1.5
CRO-2	105	0.06441	0.00111	0.86597	0.01519	0.09753	0.00112	0.65	755.2	36.01	599.9	6.6	633.4	8.27	15.3	97.3	1.1
CRO-2	19	0.05951	0.00087	0.80273	0.01214	0.09784	0.00111	0.75	585.9	31.32	601.7	6.52	598.4	6.84	23.9	129.7	86.0
CRO-2	90	0.06219	0.00079	0.84672	0.01127	0.09877	0.00109	0.83	680.8	26.95	607.2	6.41	622.8	6.2	91.8	370.5	659.8
CRO-2	35	0.06120	0.00083	0.85233	0.01210	0.10102	0.00114	0.79	646.2	28.73	620.4	6.7	625.9	6.63	34.9	149.3	223.5
CRO-2	95	0.06132	0.00072	0.85581	0.01066	0.10124	0.00112	0.89	650.6	25.01	621.7	6.53	627.8	5.83	104.5	618.5	94.2
CRO-2	32	0.06140	0.00074	0.85926	0.01111	0.10150	0.00114	0.87	653.4	25.69	623.2	6.69	629.7	6.07	84.2	493.7	105.8
CRO-2	39	0.06080	0.00077	0.86003	0.01153	0.10260	0.00115	0.84	632.3	26.99	629.6	6.75	630.1	6.29	47.7	249.3	145.0
CRO-2	60	0.06175	0.00076	0.87465	0.01142	0.10275	0.00115	0.86	665.4	26.14	630.5	6.72	638.1	6.19	48.4	274.2	74.2

CRO-2	64	0.06236	0.00075	0.90178	0.01157	0.10490	0.00117	0.87	686.4	25.54	643.1	6.83	652.7	6.18	55.0	307.1	83.2
CRO-2	52	0.06421	0.00083	0.93167	0.01256	0.10525	0.00117	0.82	748.5	26.97	645.1	6.83	668.5	6.6	198.3	778.6	1302.4
CRO-2	78	0.06484	0.00079	0.96957	0.01254	0.10846	0.00121	0.86	769.2	25.52	663.8	7.03	688.2	6.46	74.6	389.9	142.1
CRO-2	46	0.06216	0.00081	0.94479	0.01295	0.11025	0.00124	0.82	679.6	27.62	674.2	7.18	675.4	6.76	45.3	209.2	160.2
CRO-2	72	0.06653	0.00077	1.02507	0.01268	0.11177	0.00124	0.90	822.9	23.96	683	7.2	716.5	6.36	212.1	1123.5	192.0
CRO-2	110	0.06980	0.001	1.18322	0.01752	0.12297	0.00139	0.76	922.3	29.07	747.7	8	792.8	8.15	59.4	244.5	196.0
CRO-2	54	0.06624	0.00085	1.16644	0.01559	0.12773	0.00142	0.83	814.1	26.45	774.9	8.11	785	7.31	81.6	329.9	219.5
CRO-2	69	0.06964	0.0008	1.29014	0.01592	0.13438	0.00149	0.90	917.8	23.53	812.8	8.49	841.4	7.06	142.2	507.1	515.0
CRO-2	8	0.07189	0.00095	1.34563	0.01878	0.13578	0.00155	0.82	982.7	26.73	820.8	8.77	865.7	8.13	59.1	244.7	102.7
CRO-2	93	0.06967	0.00096	1.32797	0.01888	0.13829	0.00155	0.79	918.5	27.95	835	8.75	858	8.24	30.3	112.6	79.7
CRO-2	20	0.06812	0.00096	1.30602	0.01913	0.13907	0.00158	0.78	872.2	28.89	839.4	8.94	848.4	8.42	38.9	153.9	67.6
CRO-2	112	0.07079	0.00093	1.37024	0.01884	0.14041	0.00158	0.82	951.4	26.57	847	8.92	876.3	8.07	99.3	330.2	308.9
CRO-2	44	0.06668	0.001	1.29200	0.02005	0.14054	0.00160	0.73	827.9	31.05	847.7	9.06	842.2	8.88	87.6	335.2	143.0
CRO-2	77	0.07235	0.00101	1.50673	0.02177	0.15106	0.00171	0.78	995.9	28	906.9	9.56	933.1	8.82	25.0	82.7	65.2
CRO-2	107	0.06963	0.00083	1.45681	0.01845	0.15177	0.00169	0.88	917.5	24.33	910.9	9.43	912.7	7.62	151.8	607.1	63.7
CRO-2	81	0.06970	0.00091	1.46457	0.01994	0.15242	0.00171	0.82	919.6	26.49	914.5	9.54	915.9	8.22	33.9	122.7	55.4
CRO-2	73	0.07165	0.00107	1.51390	0.02325	0.15327	0.00175	0.74	976	30.06	919.2	9.77	936	9.39	28.4	90.1	86.9
CRO-2	31	0.07176	0.00081	1.56977	0.01929	0.15869	0.00178	0.91	979	22.93	949.5	9.91	958.3	7.62	121.5	447.0	121.4
CRO-2	68	0.07106	0.00103	1.56773	0.02349	0.16005	0.00182	0.76	959	29.01	957	10.12	957.5	9.29	65.6	191.3	220.7
CRO-2	62	0.07237	0.00099	1.63701	0.02336	0.16407	0.00186	0.79	996.5	27.53	979.4	10.29	984.6	9	42.4	140.1	73.3
CRO-2	85	0.07249	0.00089	1.66722	0.02163	0.16682	0.00186	0.86	999.9	24.77	994.6	10.26	996.1	8.23	90.3	263.4	246.4
CRO-2	111	0.07268	0.00105	1.69105	0.02524	0.16877	0.00192	0.76	1005.1	28.96	1005.4	10.58	1005.2	9.52	42.6	130.7	89.2
CRO-2	33	0.07276	0.00099	1.67922	0.02391	0.16741	0.00191	0.80	1007.2	27.24	997.8	10.53	1000.7	9.06	26.9	85.9	50.7
CRO-2	21	0.07288	0.0009	1.48896	0.01944	0.14819	0.00166	0.86	1010.7	24.82	890.8	9.32	925.9	7.93	157.0	576.7	299.9
CRO-2	65	0.07308	0.00087	1.82255	0.02314	0.18091	0.00202	0.88	1016.2	23.96	1071.9	11.03	1053.6	8.33	63.5	187.5	110.5
CRO-2	3	0.07394	0.00094	1.70835	0.02303	0.16760	0.00190	0.84	1039.8	25.38	998.9	10.51	1011.7	8.63	32.2	103.4	58.4
CRO-2	26	0.07485	0.00108	1.72467	0.02580	0.16714	0.00190	0.76	1064.4	28.85	996.3	10.5	1017.8	9.61	54.9	164.4	133.8
CRO-2	79	0.07485	0.00085	1.73251	0.02114	0.16790	0.00186	0.91	1064.5	22.77	1000.5	10.27	1020.7	7.86	212.3	686.5	343.3
CRO-2	29	0.07610	0.00094	1.77357	0.02313	0.16905	0.00189	0.86	1097.7	24.57	1006.9	10.4	1035.8	8.47	102.7	327.4	175.2
CRO-2	18	0.07624	0.00116	1.81997	0.02859	0.17315	0.00200	0.74	1101.5	30.2	1029.4	10.96	1052.7	10.29	30.1	86.1	76.2
CRO-2	71	0.07687	0.00089	1.93378	0.02399	0.18249	0.00203	0.90	1117.7	23	1080.6	11.07	1092.8	8.3	96.1	266.5	211.7
CRO-2	92	0.07959	0.00092	1.90372	0.02333	0.17352	0.00191	0.90	1186.9	22.63	1031.5	10.5	1082.4	8.16	151.2	515.5	236.4
CRO-2	97	0.08054	0.00099	2.01566	0.02601	0.18156	0.00201	0.86	1210.2	23.93	1075.5	10.99	1120.8	8.76	35.1	106.3	54.4
CRO-2	104	0.08076	0.00097	2.30426	0.02941	0.20697	0.00230	0.87	1215.7	23.52	1212.7	12.29	1213.6	9.04	46.9	127.1	46.0
CRO-2	45	0.08919	0.0011	2.67330	0.03486	0.21741	0.00244	0.86	1408.2	23.35	1268.2	12.9	1321.1	9.64	92.5	247.6	43.7
CRO-2	98	0.08963	0.00105	2.59131	0.03211	0.20974	0.00232	0.89	1417.6	22.12	1227.4	12.36	1298.2	9.08	160.7	355.7	394.1
CRO-2	34	0.11379	0.00129	5.53921	0.06782	0.35308	0.00397	0.92	1860.9	20.29	1949.3	18.91	1906.7	10.53	122.9	181.6	109.5
CRO-2	66	0.11384	0.00125	4.75484	0.05626	0.30298	0.00337	0.94	1861.6	19.63	1706.1	16.65	1777	9.93	321.5	482.7	584.0
CRO-2	28	0.11429	0.00135	5.36493	0.06749	0.34050	0.00379	0.88	1868.7	21.23	1889.1	18.23	1879.3	10.77	205.2	249.8	411.4
CRO-2	80	0.11556	0.00138	5.65655	0.07168	0.35507	0.00396	0.88	1888.6	21.36	1958.8	18.85	1924.8	10.93	73.7	105.5	68.7
CRO-2	59	0.12158	0.00152	5.87447	0.07698	0.35050	0.00388	0.84	1979.5	22.16	1937	18.54	1957.5	11.37	216.1	311.2	195.2
CRO-2	70	0.12168	0.00132	6.16666	0.07231	0.36761	0.00407	0.94	1981	19.2	2018.2	19.18	1999.7	10.24	421.9	644.8	157.2
CRO-2	41	0.12207	0.00136	5.81139	0.07003	0.34532	0.00384	0.92	1986.7	19.74	1912.2	18.41	1948.1	10.44	489.3	690.1	619.3
CRO-2	1	0.12248	0.00136	5.78535	0.07013	0.34263	0.00387	0.93	1992.6	19.66	1899.3	18.57	1944.2	10.49	91.6	127.3	129.2
CRO-2	27	0.12470	0.00145	6.57889	0.08165	0.38270	0.00425	0.89	2024.5	20.5	2088.9	19.83	2056.5	10.94	481.8	723.4	106.4
CRO-2	15	0.13058	0.00146	6.80464	0.08238	0.37800	0.00423	0.92	2105.7	19.55	2066.9	19.79	2086.3	10.72	133.1	177.5	122.5
CRO-2	50	0.13274	0.00156	6.94040	0.08675	0.37926	0.00420	0.89	2134.5	20.43	2072.8	19.64	2103.8	11.09	453.4	661.4	147.1
CRO-2	10	0.13875	0.00149	7.50847	0.08833	0.39254	0.00439	0.95	2211.6	18.56	2134.6	20.32	2174	10.54	510.3	672.6	388.5
CRO-2	58	0.14913	0.00183	8.42395	0.10861	0.40975	0.00453	0.86	2336	20.87	2213.8	20.72	2277.8	11.7	569.6	752.4	164.2
CRO-2	67	0.14948	0.0016	8.09142	0.09423	0.39266	0.00435	0.95	2340	18.26	2135.1	20.14	2241.3	10.52	488.3	637.3	331.2
CRO-2	82	0.15963	0.00185	10.47684	0.12941	0.47609	0.00529	0.90	2451.7	19.48	2510.2	23.11	2477.9	11.45	244.3	260.1	141.4
CRO-2	4	0.17277	0.00187	11.80618	0.13964	0.49567	0.00557	0.95	2584.7	17.93	2595.2	24.02	2589.2	11.07	177.5	179.8	112.9
CRO-2	63	0.17571	0.0019	11.10685	0.13035	0.45852	0.00510	0.95	2612.8	17.91	2433	22.54	2532.1	10.93	238.2	220.0	302.7

CRO-2	12	0.17624	0.00193	12.33343	0.14662	0.50762	0.00568	0.94	2617.8	18.1	2646.4	24.27	2630.1	11.17	326.8	340.4	117.4
CRO-2	89	0.17723	0.00212	10.74869	0.13608	0.43992	0.00490	0.88	2627.1	19.75	2350.3	21.92	2501.6	11.76	219.4	232.1	204.0
CRO-2	61	0.17799	0.00201	11.82828	0.14372	0.48205	0.00542	0.93	2634.2	18.67	2536.2	23.56	2590.9	11.38	148.0	137.3	151.3
CRO-2	13	0.17865	0.00199	11.15316	0.13422	0.45286	0.00508	0.93	2640.3	18.35	2407.9	22.53	2536	11.21	322.6	345.4	253.0
CRO-2	53	0.18257	0.00219	12.68896	0.16091	0.50415	0.00559	0.87	2676.4	19.71	2631.6	23.96	2656.8	11.94	514.8	512.2	248.5
CRO-2	48	0.18314	0.00211	13.81679	0.16996	0.54724	0.00609	0.90	2681.5	18.89	2813.7	25.36	2737.2	11.65	426.8	408.0	113.5

Analyses U-Pb sur zircon – sédiments carbonifères inférieurs

		Isotope ratios							Ages						Concentrations (ppm)		
Sample	Zircon analyses	Pb^{207}/Pb^{206}	1σ	Pb^{207}/U^{235}	1σ	Pb^{206}/U^{238}	1σ	rho	Pb^{207}/Pb^{206}	1σ	Pb^{206}/U^{238}	1σ	Pb^{207}/U^{235}	1σ	Pb	U	Th
LOC-1	1	0.12742	0.00132	6.57953	0.07745	0.37455	0.00432	0.98	2062.6	18.19	2050.8	20.26	2056.6	10.38	95.1	144.0	36.2
LOC-1	5	0.06146	0.00072	0.84291	0.01086	0.09948	0.00115	0.90	655.4	24.93	611.4	6.75	620.8	5.98	25.8	131.9	115.2
LOC-1	8	0.05633	0.00065	0.54109	0.00688	0.06967	0.00080	0.90	464.8	25.52	434.2	4.84	439.1	4.53	40.3	307.5	167.5
LOC-1	10	0.05925	0.00085	0.75167	0.01141	0.09202	0.00107	0.77	576.4	30.9	567.5	6.35	569.2	6.61	12.4	60.4	81.3
LOC-1	11	0.10765	0.00119	4.64213	0.05699	0.31281	0.00360	0.94	1760	20.08	1754.5	17.7	1756.9	10.26	37.2	63.2	33.9
LOC-1	12	0.05836	0.00081	0.70962	0.01047	0.08820	0.00103	0.79	543.2	30.12	544.9	6.09	544.5	6.22	24.6	157.0	66.9
LOC-1	14	0.06101	0.00083	0.82883	0.01202	0.09854	0.00115	0.80	639.7	29.08	605.8	6.72	613	6.67	20.6	133.3	0.4
LOC-1	16	0.05953	0.00131	0.71418	0.01598	0.08703	0.00106	0.54	586.4	47.22	537.9	6.27	547.2	9.47	2.6	17.2	7.7
LOC-1	17	0.05882	0.0011	0.74021	0.01425	0.09129	0.00109	0.62	560.3	40.43	563.2	6.42	562.5	8.31	4.8	24.1	32.0
LOC-1	18	0.12242	0.00141	6.11518	0.07680	0.36235	0.00418	0.92	1991.8	20.27	1993.3	19.78	1992.4	10.96	22.5	31.5	22.1
LOC-1	20	0.05765	0.00074	0.61692	0.00852	0.07763	0.00089	0.83	516.1	28.39	481.9	5.34	487.9	5.35	25.7	187.3	79.4
LOC-1	21	0.05664	0.00071	0.64247	0.00870	0.08228	0.00094	0.84	476.9	27.9	509.7	5.63	503.8	5.38	21.7	147.9	64.7
LOC-1	22	0.11754	0.00134	5.58266	0.06954	0.34453	0.00395	0.92	1919.2	20.31	1908.4	18.94	1913.4	10.73	27.1	38.7	32.0
LOC-1	23	0.11566	0.00126	5.40440	0.06514	0.33894	0.00386	0.94	1890.2	19.55	1881.6	18.6	1885.6	10.33	93.1	125.4	147.3
LOC-1	25	0.0542	0.00062	0.46339	0.00580	0.06202	0.00071	0.91	379.3	25.74	387.9	4.29	386.6	4.02	45.8	469.9	2.2
LOC-1	26	0.05701	0.00065	0.63762	0.00790	0.08113	0.00092	0.92	491.2	25.14	502.9	5.51	500.8	4.9	74.9	504.9	255.1
LOC-1	27	0.0581	0.0009	0.70990	0.01145	0.08863	0.00103	0.72	533.1	34.06	547.4	6.1	544.7	6.8	8.1	45.2	43.1
LOC-1	28	0.155	0.00175	8.94616	0.11020	0.41866	0.00478	0.93	2401.9	19.07	2254.4	21.74	2332.5	11.25	78.1	75.3	127.3
LOC-1	29	0.10885	0.00117	4.78826	0.05722	0.31910	0.00365	0.96	1780.1	19.45	1785.3	17.86	1782.8	10.04	56.9	96.3	45.0
LOC-1	31	0.05765	0.00093	0.65833	0.01102	0.08283	0.00097	0.70	516.3	35.21	513	5.79	513.6	6.75	7.1	49.5	17.3
LOC-1	35	0.06102	0.00082	0.81129	0.01167	0.09644	0.00112	0.81	640	28.75	593.5	6.59	603.2	6.54	41.7	238.4	116.0
LOC-1	37	0.05783	0.00066	0.68500	0.00862	0.08591	0.00099	0.92	523.3	25.1	531.3	5.86	529.8	5.19	43.5	301.6	72.8
LOC-1	38	0.0599	0.00071	0.80688	0.01047	0.09771	0.00113	0.89	600	25.5	601	6.61	600.7	5.88	32.7	180.9	103.3
LOC-1	42	0.05271	0.00058	0.39930	0.00492	0.05495	0.00063	0.93	316.3	25.02	344.8	3.85	341.1	3.57	83.3	871.9	313.9
LOC-1	43	0.05928	0.00082	0.75809	0.01121	0.09277	0.00108	0.79	577.3	29.96	571.9	6.38	572.9	6.48	12.3	75.3	30.7
LOC-1	44	0.05675	0.0007	0.53871	0.00725	0.06886	0.00080	0.86	481.1	27.46	429.3	4.8	437.6	4.78	78.6	724.1	27.7
LOC-1	45	0.05662	0.00065	0.63475	0.00803	0.08132	0.00094	0.91	476.1	25.41	504	5.58	499.1	4.99	49.6	373.1	63.2
LOC-1	46	0.05835	0.0007	0.68144	0.00889	0.08471	0.00098	0.89	543	25.9	524.2	5.81	527.6	5.37	53.4	363.0	131.7
LOC-1	47	0.05279	0.00067	0.38844	0.00536	0.05337	0.00062	0.84	319.9	28.75	335.2	3.78	333.2	3.92	33.7	323.9	269.7
LOC-1	49	0.0531	0.00077	0.41359	0.00637	0.05650	0.00066	0.76	333.2	32.61	354.3	4.03	351.5	4.57	22.2	230.0	72.6
LOC-1	50	0.05691	0.00074	0.63426	0.00888	0.08084	0.00094	0.83	487.5	28.8	501.1	5.6	498.7	5.52	25.9	185.1	68.8
LOC-1	51	0.05271	0.00061	0.39055	0.00496	0.05375	0.00062	0.91	316.1	25.94	337.5	3.79	334.8	3.62	73.0	773.0	316.8
LOC-1	52	0.05629	0.00068	0.54561	0.00720	0.07032	0.00081	0.87	462.9	26.73	438.1	4.9	442.1	4.73	37.2	307.9	100.9
LOC-1	53	0.05709	0.00073	0.63745	0.00883	0.08100	0.00094	0.84	494.3	28.43	502.1	5.61	500.7	5.48	33.5	250.3	49.9
LOC-1	55	0.05324	0.00064	0.38785	0.00508	0.05284	0.00061	0.88	339.1	26.83	331.9	3.74	332.8	3.72	55.7	578.3	316.4
LOC-1	56	0.05352	0.00074	0.39701	0.00583	0.05381	0.00063	0.80	350.8	30.76	337.9	3.84	339.5	4.24	15.0	159.9	66.1
LOC-1	57	0.05372	0.00059	0.39844	0.00492	0.05380	0.00062	0.93	359.2	24.68	337.8	3.81	340.5	3.57	72.1	854.9	60.4
LOC-1	58	0.06289	0.00078	1.05587	0.01425	0.12179	0.00142	0.86	704.4	26.06	740.8	8.16	731.8	7.04	22.4	100.2	62.4

LOC-1	60	0.05293	0.00067	0.41443	0.00568	0.05679	0.00066	0.85	325.9	28.25	356.1	4.04	352.1	4.08	32.0	350.2	54.8
LOC-1	61	0.05654	0.00083	0.57851	0.00897	0.07422	0.00088	0.76	472.9	32.28	461.5	5.26	463.5	5.77	35.0	299.5	26.3
LOC-1	63	0.05707	0.00076	0.57817	0.00830	0.07348	0.00086	0.82	493.8	29.46	457.1	5.18	463.3	5.34	44.5	377.2	53.8
LOC-1	64	0.05461	0.00058	0.46905	0.00568	0.06230	0.00072	0.95	396.2	23.65	389.6	4.38	390.5	3.92	190.9	1997.9	7.3
LOC-1	65	0.05442	0.00062	0.43214	0.00546	0.05760	0.00067	0.92	388.4	25.17	361	4.08	364.7	3.87	72.8	723.6	297.4
LOC-1	67	0.05663	0.00068	0.64786	0.00860	0.08298	0.00097	0.88	476.4	26.63	513.9	5.77	507.2	5.3	34.4	244.2	86.2
LOC-1	68	0.05477	0.00061	0.41020	0.00516	0.05432	0.00063	0.92	402.9	24.67	341	3.87	349	3.71	81.1	868.9	321.6
LOC-1	71	0.05729	0.00066	0.62464	0.00803	0.07909	0.00092	0.90	502	25.35	490.7	5.52	492.8	5.02	53.7	419.2	80.1
LOC-1	72	0.05773	0.00067	0.72101	0.00933	0.09059	0.00106	0.90	519.3	25.58	559	6.26	551.3	5.51	47.9	324.2	61.6
LOC-1	73	0.05347	0.00062	0.42260	0.00546	0.05733	0.00067	0.90	348.7	25.94	359.3	4.08	357.9	3.9	77.8	813.8	232.3
LOC-1	74	0.05339	0.00061	0.42850	0.00549	0.05822	0.00068	0.91	345.3	25.68	364.8	4.14	362.1	3.91	71.5	681.2	388.7
LOC-1	75	0.05678	0.00075	0.67004	0.00956	0.08559	0.00101	0.83	482.5	29.09	529.4	5.99	520.7	5.81	44.6	334.2	25.1
LOC-1	77	0.05631	0.00066	0.62600	0.00813	0.08064	0.00095	0.91	463.7	25.75	499.9	5.64	493.6	5.08	111.5	901.1	24.1
LOC-1	79	0.05431	0.00062	0.40459	0.00518	0.05403	0.00063	0.91	384	25.53	339.2	3.87	345	3.75	106.6	1152.1	444.2
LOC-1	83	0.05491	0.00066	0.42044	0.00558	0.05554	0.00065	0.88	408.5	26.23	348.4	3.99	356.4	3.99	91.4	972.8	318.3
LOC-1	84	0.12971	0.00152	6.96732	0.09085	0.38962	0.00460	0.91	2094	20.39	2121.1	21.36	2107.3	11.58	55.2	70.0	64.5
LOC-1	86	0.05714	0.00062	0.64580	0.00791	0.08198	0.00095	0.95	496.5	24.22	507.9	5.63	505.9	4.88	96.7	760.8	15.2
LOC-1	87	0.05392	0.00073	0.38951	0.00568	0.05240	0.00061	0.80	367.6	30.5	329.2	3.75	334	4.15	45.7	504.0	203.3
LOC-1	89	0.05379	0.00061	0.39872	0.00501	0.05378	0.00062	0.92	362	25.36	337.7	3.8	340.7	3.64	61.5	651.5	285.5
LOC-1	90	0.05361	0.0007	0.40985	0.00578	0.05546	0.00065	0.83	354.5	29.2	348	3.95	348.8	4.16	91.2	931.0	443.1
LOC-1	91	0.06017	0.0007	0.81549	0.01044	0.09832	0.00114	0.91	609.6	24.8	604.5	6.69	605.5	5.84	43.4	224.9	103.3
LOC-1	92	0.17099	0.0018	10.76132	0.12851	0.45653	0.00527	0.97	2567.3	17.53	2424.2	23.34	2502.7	11.09	359.4	409.0	206.0
LOC-1	94	0.12765	0.00136	6.85663	0.08229	0.38964	0.00450	0.96	2065.8	18.6	2121.2	20.89	2093.1	10.64	161.0	237.8	53.1
LOC-1	95	0.13612	0.00148	7.17828	0.08778	0.38252	0.00444	0.95	2178.4	18.84	2088.1	20.69	2133.8	10.9	161.7	174.6	315.4
LOC-1	96	0.0569	0.0007	0.60629	0.00817	0.07729	0.00090	0.86	487.2	27.29	479.9	5.39	481.2	5.16	36.3	271.3	111.3
LOC-1	97	0.13737	0.00148	7.46991	0.09072	0.39444	0.00457	0.95	2194.3	18.61	2143.4	21.14	2169.4	10.88	140.0	188.6	99.3
LOC-1	98	0.0613	0.00074	0.92710	0.01232	0.10970	0.00128	0.88	649.9	25.79	671	7.43	666.1	6.49	34.1	164.0	121.7
LOC-1	99	0.12772	0.00138	6.75896	0.08237	0.38385	0.00445	0.95	2066.9	18.95	2094.2	20.74	2080.4	10.78	181.0	214.0	274.7
LOC-1	101	0.18204	0.00197	13.15371	0.16020	0.52413	0.00609	0.95	2671.5	17.78	2716.7	25.74	2690.7	11.49	206.1	192.3	148.7
LOC-1	104	0.06039	0.00067	0.82211	0.01017	0.09874	0.00115	0.94	617.7	23.62	607	6.72	609.2	5.67	140.7	747.3	552.8
LOC-1	105	0.0638	0.00074	1.14802	0.01475	0.13053	0.00152	0.91	734.9	24.33	790.9	8.67	776.3	6.97	69.4	285.5	186.6
LOC-1	106	0.12819	0.0014	6.45431	0.07937	0.36522	0.00424	0.94	2073.3	19.12	2006.9	20.04	2039.7	10.81	513.6	759.5	331.2
LOC-1	107	0.16695	0.00183	11.10165	0.13677	0.48233	0.00561	0.94	2527.3	18.27	2537.4	24.39	2531.7	11.48	528.7	564.4	309.3
LOC-1	108	0.12565	0.00139	6.38190	0.07916	0.36842	0.00429	0.94	2038	19.41	2021.9	20.2	2029.8	10.89	208.0	307.9	132.3
LOC-1	110	0.16175	0.0018	10.88999	0.13579	0.48834	0.00569	0.93	2474.1	18.65	2563.5	24.65	2513.8	11.6	158.1	167.5	97.7
LOC-1	111	0.12683	0.00144	6.40758	0.08122	0.36647	0.00428	0.92	2054.4	19.93	2012.7	20.2	2033.3	11.13	154.6	225.4	120.6
LOC-1	112	0.0531	0.00064	0.40848	0.00539	0.05580	0.00065	0.88	332.8	26.84	350.1	3.98	347.8	3.89	59.6	629.1	208.8
LOC-1	113	0.06023	0.00138	0.75130	0.01743	0.09048	0.00114	0.54	611.8	48.79	558.4	6.73	569	10.11	4.1	22.7	22.8
LOC-1	114	0.23397	0.00267	20.64267	0.26275	0.63997	0.00751	0.92	3079.4	18.12	3188.9	29.52	3122	12.33	70.5	52.1	41.5
LOC-1	115	0.11568	0.0013	5.45757	0.06874	0.34221	0.00399	0.93	1890.5	20.12	1897.3	19.17	1893.9	10.81	380.8	607.5	290.9
LOC-1	116	0.12786	0.00137	6.62078	0.08024	0.37560	0.00436	0.96	2068.7	18.75	2055.7	20.42	2062.1	10.69	187.4	273.3	118.9
LOC-1	119	0.05432	0.00066	0.47021	0.00631	0.06279	0.00074	0.88	384	27.19	392.6	4.46	391.3	4.36	39.4	323.5	280.0
LOC-1	121	0.12387	0.00138	6.63332	0.08329	0.38842	0.00455	0.93	2012.7	19.62	2115.5	21.15	2063.8	11.08	122.2	175.8	68.0
LOC-1	13a	0.06016	0.00066	0.83700	0.01016	0.10093	0.00116	0.95	609.2	23.43	619.8	6.77	617.5	5.61	57.4	341.9	69.1
LOC-1	13b	0.05948	0.00069	0.82983	0.01058	0.10119	0.00116	0.90	584.8	25.07	621.4	6.81	613.5	5.87	32.9	194.7	40.5
LOC-1	76a	0.05835	0.00124	0.67747	0.01466	0.08421	0.00104	0.57	543.1	45.65	521.2	6.17	525.2	8.87	4.8	29.9	24.4
LOC-1	76b	0.05668	0.00078	0.62959	0.00932	0.08057	0.00096	0.80	478.4	30.39	499.5	5.7	495.8	5.81	40.4	284.0	153.7
LOC-1	36	0.05973	0.00077	0.67885	0.00938	0.08244	0.00095	0.83	594	27.6	510.6	5.68	526.1	5.68	54.4	378.9	131.4
LOC-1	125	0.12975	0.00148	6.39523	0.08247	0.35751	0.00422	0.92	2094.6	19.97	1970.4	20.05	2031.6	11.32	298.6	430.3	316.0
LOC-1	88	0.05802	0.0008	0.56589	0.00830	0.07075	0.00083	0.80	530.2	30.16	440.7	4.99	455.4	5.38	32.1	275.3	61.0
LOC-1	24	0.0609	0.00127	0.72820	0.01533	0.08674	0.00106	0.58	635.6	44.21	536.2	6.26	555.5	9.01	8.6	56.8	21.2
LOC-1	9	0.05592	0.00059	0.42888	0.00507	0.05563	0.00064	0.97	448.7	22.78	349	3.9	362.4	3.61	215.1	2290.0	601.5
LOC-1	102	0.0627	0.00073	0.82554	0.01062	0.09551	0.00111	0.90	698	24.55	588	6.54	611.1	5.91	64.9	350.7	277.2

LOC-1	100	0.06346	0.00071	0.87162	0.01093	0.09963	0.00116	0.93	723.6	23.65	612.3	6.78	636.4	5.93	77.4	408.1	298.5
LOC-1	80	0.05582	0.00066	0.41528	0.00545	0.05396	0.00063	0.89	444.9	25.58	338.8	3.88	352.7	3.91	58.8	634.0	246.4
LOC-1	32	0.05601	0.00064	0.42312	0.00529	0.05479	0.00063	0.92	452.6	24.63	343.9	3.84	358.3	3.78	89.2	895.6	452.1
LOC-1	122	0.067	0.00075	1.08425	0.01373	0.11738	0.00138	0.93	837.7	23.22	715.5	7.94	745.7	6.69	202.7	1005.6	350.9
LOC-1	120	0.05622	0.00067	0.43100	0.00568	0.05561	0.00065	0.89	460.2	26.25	348.9	3.98	363.9	4.03	50.5	524.1	212.0
LOC-1	15	0.06291	0.00101	0.81810	0.01363	0.09432	0.00111	0.71	705.3	33.78	581.1	6.56	607	7.61	16.2	79.3	95.3
LOC-1	41	0.05871	0.00079	0.56074	0.00808	0.06928	0.00081	0.81	556.5	29.17	431.8	4.86	452	5.25	41.0	353.8	82.3
LOC-1	3a	0.05635	0.00064	0.41609	0.00522	0.05356	0.00062	0.92	465.5	25	336.3	3.79	353.3	3.74	79.7	865.2	289.9
LOC-1	117	0.06481	0.00078	0.88666	0.01172	0.09923	0.00116	0.88	768.2	25.02	609.9	6.8	644.6	6.31	94.7	489.4	392.6
LOC-1	81	0.05681	0.00069	0.41539	0.00556	0.05304	0.00062	0.87	483.5	26.74	333.1	3.82	352.8	3.99	91.7	1028.3	306.4
LOC-1	7	0.06453	0.00099	0.85686	0.01376	0.09632	0.00114	0.74	758.9	31.99	592.8	6.7	628.4	7.52	16.0	76.9	92.9
LOC-1	118	0.06039	0.00082	0.60594	0.00883	0.07278	0.00086	0.81	617.4	28.94	452.9	5.16	481	5.59	42.0	355.1	59.8
LOC-1	2	0.1618	0.00166	8.78622	0.10250	0.39387	0.00454	0.99	2474.6	17.21	2140.8	20.97	2316.1	10.63	376.1	536.8	89.4
LOC-1	4	0.10472	0.0012	3.82573	0.04828	0.26500	0.00308	0.92	1709.3	20.88	1515.4	15.69	1598.2	10.16	51.1	98.3	67.5
LOC-1	62	0.05882	0.00069	0.47926	0.00619	0.05910	0.00069	0.90	560.3	25.2	370.2	4.18	397.6	4.25	68.0	656.2	261.3
LOC-1	124	0.06573	0.00079	0.85936	0.01150	0.09483	0.00112	0.88	797.9	25.03	584	6.6	629.8	6.28	88.3	483.1	371.8
LOC-1	103	0.14477	0.00157	6.96562	0.08513	0.34901	0.00405	0.95	2285	18.56	1929.9	19.36	2107.1	10.85	238.5	354.3	192.6
LOC-1	69	0.05909	0.00074	0.46035	0.00630	0.05651	0.00066	0.85	570.3	27.01	354.4	4.04	384.5	4.38	56.0	579.1	177.8
LOC-1	54	0.05975	0.00073	0.46204	0.00618	0.05609	0.00065	0.87	594.4	26.61	351.8	3.97	385.7	4.29	40.1	413.5	121.3

Analyses U-Pb sur zircon – migmatite prélevé à la racine du granite de Guérande

		Isotope ratios							Ages						Concentrations (ppm)		
Sample	Zircon analyses	Pb^{207}/Pb^{206}	1σ	Pb^{207}/U^{235}	1σ	Pb^{206}/U^{238}	1σ	rho	Pb^{207}/Pb^{206}	1σ	Pb^{206}/U^{238}	1σ	Pb^{207}/U^{235}	1σ	Pb	U	Th
PENCH-1	2	2023.7	0.00144	5.95008	0.07896	0.34628	0.00424	0.92	2023.7	20.32	1916.8	20.29	1968.6	11.54	91.8	149.0	70.1
PENCH-1	3	683.1	0.00075	0.95225	0.01310	0.11094	0.00135	0.88	683.1	25.68	678.2	7.84	679.3	6.81	58.9	303.7	162.8
PENCH-1	4	629.3	0.00076	0.86606	0.01218	0.10346	0.00126	0.87	629.3	26.67	634.7	7.37	633.4	6.62	22.7	127.0	67.0
PENCH-1	5	1000.7	0.00079	1.68744	0.02153	0.16878	0.00204	0.95	1000.7	22.03	1005.4	11.26	1003.8	8.13	164.0	601.0	141.2
PENCH-1	6	2449.7	0.00169	10.03964	0.12543	0.45677	0.00552	0.97	2449.7	17.85	2425.3	24.43	2438.4	11.54	216.0	214.5	299.8
PENCH-1	11	650.9	0.0009	0.86621	0.01374	0.10244	0.00125	0.77	650.9	31.24	628.7	7.33	633.5	7.48	12.8	68.7	48.8
PENCH-1	12	876.8	0.00092	0.95888	0.01417	0.10188	0.00124	0.82	876.8	27.73	625.4	7.23	682.7	7.34	28.5	152.9	93.8
PENCH-1	14	2069.8	0.0014	6.11938	0.07714	0.34696	0.00414	0.95	2069.8	19.2	1920.1	19.82	1993	11	281.6	434.2	259.3
PENCH-1	15	675.5	0.00071	0.84142	0.01089	0.09838	0.00117	0.92	675.5	24.15	604.9	6.89	619.9	6.01	85.8	512.7	207.7
PENCH-1	17	629.0	0.00086	0.85398	0.01303	0.10203	0.00123	0.79	629	30.18	626.3	7.2	626.8	7.14	16.2	84.1	66.2
PENCH-1	18	649.9	0.00084	0.90409	0.01345	0.10697	0.00129	0.81	649.9	29.19	655.1	7.49	653.9	7.17	18.5	99.3	47.3
PENCH-1	19	825.2	0.00082	1.32445	0.01815	0.14426	0.00172	0.87	825.2	25.62	868.7	9.7	856.5	7.93	37.9	147.0	82.9
PENCH-1	20	728.4	0.00094	0.86600	0.01371	0.09876	0.00120	0.77	728.4	31.1	607.2	7.01	633.4	7.46	24.5	132.7	89.4
PENCH-1	22	689.8	0.00082	1.00931	0.01442	0.11722	0.00140	0.84	689.8	27.65	714.5	8.09	708.5	7.28	25.7	125.2	59.1
PENCH-1	23	2626.2	0.00184	10.02626	0.12345	0.41058	0.00496	0.98	2626.2	17.17	2217.6	22.69	2437.2	11.37	372.8	511.0	145.8
PENCH-1	27	748.6	0.00076	1.11269	0.01506	0.12570	0.00153	0.90	748.6	24.88	763.3	8.77	759.5	7.24	31.3	154.2	40.8
PENCH-1	29	2637.0	0.00194	11.57349	0.14750	0.47087	0.00574	0.96	2637	17.99	2487.4	25.15	2570.5	11.91	128.0	153.7	46.3
PENCH-1	30	712.5	0.00073	0.93285	0.01241	0.10719	0.00130	0.91	712.5	24.38	656.4	7.6	669.1	6.52	56.4	306.7	147.4
PENCH-1	32	643.8	0.00078	0.81909	0.01167	0.09720	0.00119	0.86	643.8	27.03	598	6.99	607.5	6.51	27.7	161.4	97.6
PENCH-1	34	2608.0	0.00192	12.54200	0.16073	0.51926	0.00632	0.95	2608	18.11	2696.1	26.83	2645.9	12.05	170.8	180.3	88.8
PENCH-1	35	712.3	0.00076	0.88185	0.01209	0.10134	0.00124	0.89	712.3	25.36	622.3	7.25	642	6.52	63.9	331.1	304.8
PENCH-1	36	675.9	0.0008	0.88065	0.01271	0.10294	0.00126	0.85	675.9	27.31	631.6	7.38	641.3	6.86	45.2	250.3	149.6
PENCH-1	37	679.4	0.00091	0.95674	0.01523	0.11166	0.00138	0.78	679.4	30.92	682.4	8.03	681.6	7.9	40.5	216.0	89.3
PENCH-1	38	2437.6	0.00178	10.10165	0.13207	0.46288	0.00565	0.93	2437.6	18.93	2452.2	24.92	2444.1	12.08	93.0	94.2	119.6

PENCH-1	40	649.0	0.0008	0.85318	0.01249	0.10099	0.00124	0.84	649	27.87	620.2	7.27	626.4	6.84	31.5	192.4	58.3
PENCH-1	41	656.3	0.00079	0.72649	0.01044	0.08571	0.00105	0.85	656.3	27.19	530.1	6.25	554.5	6.14	68.3	484.0	170.3
PENCH-1	43	670.9	0.00078	0.80807	0.01154	0.09468	0.00116	0.86	670.9	26.88	583.1	6.85	601.4	6.48	45.3	285.3	124.9
PENCH-1	44	735.1	0.00075	0.84469	0.01141	0.09603	0.00117	0.90	735.1	24.65	591.1	6.9	621.7	6.28	112.8	712.3	235.8
PENCH-1	45	698.2	0.00073	1.04714	0.01427	0.12114	0.00150	0.91	698.2	24.75	737.1	8.64	727.5	7.08	63.1	264.4	286.5
PENCH-1	46	602.9	0.00087	0.80736	0.01292	0.09764	0.00123	0.79	602.9	31.12	600.5	7.21	601	7.26	12.5	70.1	52.8
PENCH-1	47	535.6	0.00073	0.78579	0.01123	0.09799	0.00122	0.87	535.6	27.67	602.6	7.17	588.8	6.39	35.2	213.6	94.3
PENCH-1	48	625.3	0.0009	0.75056	0.01224	0.08983	0.00113	0.77	625.3	31.74	554.5	6.71	568.5	7.1	24.6	170.4	47.7
PENCH-1	49	661.5	0.00072	0.78763	0.01077	0.09270	0.00115	0.91	661.5	24.96	571.5	6.8	589.8	6.12	93.0	425.7	842.1
PENCH-1	51	740.2	0.00086	0.94048	0.01428	0.10667	0.00134	0.83	740.2	28.3	653.4	7.83	673.1	7.47	18.2	102.6	40.3
PENCH-1	54	622.4	0.0007	0.88033	0.01195	0.10550	0.00132	0.92	622.4	24.63	646.6	7.69	641.2	6.45	63.6	342.5	216.4
PENCH-1	57	633.4	0.00069	0.84838	0.01147	0.10116	0.00127	0.93	633.4	24.26	621.2	7.44	623.8	6.3	81.6	469.5	260.9
PENCH-1	59	741.7	0.00076	0.83461	0.01165	0.09459	0.00119	0.90	741.7	24.92	582.6	7.02	616.2	6.45	109.1	620.3	538.0
PENCH-1	60	793.6	0.00076	0.90489	0.01246	0.10006	0.00126	0.91	793.6	24.2	614.8	7.39	654.3	6.64	72.2	448.1	143.5
PENCH-1	62	627.8	0.00084	0.80887	0.01264	0.09670	0.00124	0.82	627.8	29.48	595	7.27	601.8	7.09	15.6	99.8	35.0
PENCH-1	66	716.7	0.00074	0.73591	0.01008	0.08439	0.00106	0.92	716.7	24.52	522.3	6.29	560	5.9	113.0	714.9	603.5
PENCH-1	70	614.7	0.00077	0.89323	0.01300	0.10743	0.00135	0.86	614.7	27.3	657.8	7.84	648.1	6.97	31.5	172.6	90.5
PENCH-1	72	663.2	0.00076	0.79330	0.01124	0.09328	0.00116	0.88	663.2	26.31	574.9	6.84	593	6.37	59.2	331.4	319.1
PENCH-1	73	720.0	0.00076	0.85309	0.01177	0.09768	0.00121	0.90	720	25.15	600.8	7.12	626.3	6.45	49.7	288.2	170.0
PENCH-1	75	833.5	0.00078	0.91519	0.01244	0.09929	0.00123	0.91	833.5	24.26	610.2	7.2	659.8	6.6	84.2	484.8	261.9
PENCH-1	77	602.3	0.00079	0.72815	0.01071	0.08808	0.00109	0.84	602.3	28.19	544.2	6.46	555.5	6.29	36.2	262.9	41.7
PENCH-1	80	594.0	0.00088	0.94609	0.01515	0.11488	0.00143	0.78	594	31.55	701	8.26	676.1	7.9	20.5	97.3	66.5
PENCH-1	81	984.2	0.00087	1.65953	0.02281	0.16733	0.00205	0.89	984.2	24.36	997.4	11.34	993.2	8.71	72.2	239.3	152.0
PENCH-1	82	598.9	0.0007	0.73912	0.00996	0.08955	0.00109	0.90	598.9	25.25	552.9	6.48	561.9	5.82	63.9	419.9	178.6
PENCH-1	85	622.7	0.00086	0.71682	0.01106	0.08589	0.00106	0.80	622.7	30.23	531.2	6.27	548.8	6.54	57.7	399.3	129.3
PENCH-1	87	636.9	0.00076	0.88244	0.01230	0.10504	0.00128	0.87	636.9	26.56	643.9	7.45	642.3	6.63	65.0	334.4	242.9
PENCH-1	88	579.9	0.00088	0.82094	0.01311	0.10033	0.00123	0.77	579.9	31.86	616.4	7.23	608.6	7.31	19.2	123.5	11.5
PENCH-1	89	710.1	0.00075	0.83120	0.01130	0.09561	0.00116	0.89	710.1	25.19	588.6	6.85	614.3	6.27	66.6	397.4	190.3
PENCH-1	90	2843.8	0.00216	15.02333	0.18882	0.53901	0.00655	0.97	2843.8	17.31	2779.3	27.46	2816.7	11.97	142.2	135.8	76.6
PENCH-1	92	696.1	0.00076	0.77885	0.01069	0.09018	0.00110	0.89	696.1	25.53	556.6	6.51	584.8	6.1	75.1	467.0	234.1
PENCH-1	93	599.6	0.00075	0.79018	0.01120	0.09570	0.00117	0.86	599.6	27.03	589.2	6.9	591.3	6.35	32.5	152.1	250.5
PENCH-1	96	590.7	0.00072	0.73240	0.01015	0.08908	0.00109	0.88	590.7	26.09	550.1	6.47	558	5.95	31.6	213.4	74.2
PENCH-1	98	834.7	0.00127	1.03859	0.02054	0.11261	0.00145	0.65	834.7	38.92	687.9	8.4	723.2	10.23	4.4	25.5	0.6
PENCH-1	100	958.2	0.00091	1.47138	0.02129	0.15027	0.00186	0.86	958.2	25.92	902.5	10.45	918.7	8.75	48.3	167.1	146.0
PENCH-1	102	740.1	0.00082	0.82413	0.01194	0.09348	0.00116	0.86	740.1	26.84	576.1	6.84	610.3	6.65	26.5	168.7	60.7
PENCH-1	103	815.7	0.00085	0.81374	0.01181	0.08904	0.00111	0.86	815.7	26.55	549.9	6.55	604.6	6.61	104.5	607.5	548.6
PENCH-1	104	616.0	0.00085	0.77215	0.01209	0.09282	0.00116	0.80	616	30.25	572.2	6.84	581	6.93	14.9	93.9	45.4
PENCH-1	105	656.2	0.00076	0.86553	0.01230	0.10212	0.00127	0.88	656.2	26.42	626.8	7.41	633.1	6.7	48.8	260.0	190.4
PENCH-1	106	685.2	0.00075	0.89709	0.01247	0.10441	0.00130	0.90	685.2	25.37	640.2	7.57	650.2	6.68	75.5	446.2	135.0
PENCH-1	107	785.8	0.00082	0.96799	0.01396	0.10744	0.00134	0.86	785.8	26.24	657.8	7.8	687.4	7.2	50.6	273.6	132.4
PENCH-1	108	2306.5	0.00169	7.67563	0.10420	0.37982	0.00472	0.92	2306.5	19.71	2075.4	22.06	2193.8	12.2	143.8	220.2	62.3
PENCH-1	109	2090.7	0.00152	6.72945	0.09247	0.37705	0.00470	0.91	2090.7	20.51	2062.5	21.99	2076.5	12.15	77.8	110.8	77.6
PENCH-1	110	2083.1	0.00155	6.25913	0.08725	0.35221	0.00440	0.90	2083.1	20.94	1945.2	20.98	2012.8	12.2	87.4	133.0	90.7
PENCH-1	111	668.9	0.00083	0.85245	0.01296	0.09998	0.00125	0.82	668.9	28.6	614.3	7.35	626	7.1	31.3	181.0	100.6
PENCH-1	28a	953.1	0.0008	1.50687	0.01966	0.15427	0.00187	0.93	953.1	22.91	924.9	10.47	933.2	7.96	47.5	176.8	95.8
PENCH-1	42a	703.3	0.00074	0.78723	0.01062	0.09085	0.00111	0.91	703.3	24.73	560.6	6.56	589.6	6.03	180.3	1101.4	735.4
PENCH-1	42b	772.6	0.00092	0.80334	0.01253	0.08972	0.00111	0.79	772.6	29.65	553.9	6.58	598.7	7.06	42.1	257.7	179.8
PENCH-1	55a	604.6	0.00075	0.76547	0.01106	0.09250	0.00116	0.87	604.6	26.95	570.3	6.86	577.2	6.36	26.3	169.1	79.5
PENCH-1	61a	765.0	0.00102	0.74246	0.01284	0.08322	0.00108	0.75	765	32.97	515.3	6.4	563.8	7.48	22.9	137.2	175.8
PENCH-1	69a	894.9	0.00092	1.41984	0.02140	0.14954	0.00189	0.84	894.9	27.32	898.4	10.6	897.3	8.98	15.2	61.1	26.9
PENCH-1	69b	904.7	0.00094	1.39722	0.02128	0.14646	0.00185	0.83	904.7	27.7	881.1	10.41	887.8	9.01	17.1	65.1	44.7
PENCH-1	7a	1009.4	0.00087	1.53975	0.02080	0.15334	0.00186	0.90	1009.4	23.97	919.7	10.38	946.4	8.32	45.7	161.1	118.4
PENCH-1	7b	982.6	0.00083	1.67537	0.02213	0.16907	0.00204	0.91	982.6	23.36	1007	11.26	999.2	8.4	48.4	155.4	112.7

PENCH-1	95a	616.6	0.00069	0.77726	0.01034	0.09340	0.00114	0.92	616.6	24.61	575.6	6.73	583.9	5.91	58.2	385.2	91.9
PENCH-1	95b	749.7	0.00087	0.83161	0.01255	0.09390	0.00116	0.82	749.7	28.5	578.6	6.85	614.5	6.96	18.6	113.2	58.9

Analyses U-Pb sur zircon – grains hérités des leucogranites de Pontivy et Langonnet

		Isotope ratios							Ages						Concentrations (ppm)		
Sample	**Zircon analyses**	**Pb^{207}/Pb^{206}**	**1σ**	**Pb^{207}/U^{235}**	**1σ**	**Pb^{206}/U^{238}**	**1σ**	**rho**	**Pb^{207}/Pb^{206}**	**1σ**	**Pb^{206}/U^{238}**	**1σ**	**Pb^{207}/U^{235}**	**1σ**	**Pb**	**U**	**Th**
PONT-1	3	0.06396	0.00074	0.96319	0.01278	0.10923	0.00133	0.92	740.3	24.26	668.3	7.72	684.9	6.61	26.4	238.3	94.1
PONT-1	4	0.06142	0.00068	0.73139	0.00942	0.08638	0.00105	0.94	653.8	23.65	534.1	6.21	557.4	5.53	47.2	550.3	136.7
PONT-1	6	0.05877	0.00063	0.73134	0.00914	0.09026	0.00109	0.97	558.6	23.08	557.1	6.43	557.3	5.36	35.9	368.6	224.1
PONT-1	15	0.05268	0.00056	0.39555	0.00484	0.05447	0.00064	0.96	314.9	23.92	341.9	3.94	338.4	3.52	86.3	1687.3	178.3
PONT-1	18	0.10709	0.00114	4.40295	0.05376	0.29822	0.00352	0.97	1750.6	19.27	1682.5	17.48	1712.9	10.1	67.1	165.8	251.4
PONT-1	19	0.06547	0.00071	0.87944	0.01092	0.09744	0.00115	0.95	789.5	22.72	599.4	6.75	640.7	5.9	53.7	541.0	124.5
PONT-1	20	0.05658	0.00063	0.50213	0.00635	0.06437	0.00076	0.93	474.6	24.78	402.1	4.59	413.1	4.29	38.5	592.1	159.1
PONT-1	23	0.06313	0.00078	0.85221	0.01157	0.09792	0.00115	0.87	712.6	26.14	602.2	6.77	625.9	6.34	16.4	158.8	64.0
PONT-1	32	0.05988	0.00124	0.77198	0.01612	0.09352	0.00111	0.57	599.1	44.4	576.3	6.52	580.9	9.24	11.5	81.3	170.7
PONT-1	33	0.06496	0.00084	0.90437	0.01224	0.10098	0.00113	0.83	773.1	26.93	620.1	6.6	654.1	6.53	24.1	235.5	63.1
PONT-1	35	0.06885	0.00075	1.09887	0.01283	0.11577	0.00128	0.95	894.3	22.18	706.2	7.37	752.8	6.21	88.3	725.3	292.2
PONT-1	36	0.06426	0.00101	0.94498	0.01521	0.10667	0.00121	0.70	750.2	32.82	653.4	7.07	675.5	7.94	9.2	80.9	39.2
PONT-1	39	0.06063	0.00071	0.85815	0.01071	0.10267	0.00114	0.89	626.1	25.08	630	6.65	629.1	5.85	29.1	260.6	154.5
PONT-1	40	0.05552	0.0006	0.48409	0.00564	0.06324	0.0007	0.95	433	23.78	395.3	4.22	400.9	3.86	344.4	5963.6	9.7
PONT-1	43	0.06046	0.00089	0.79567	0.01216	0.09546	0.00108	0.74	619.9	31.61	587.8	6.34	594.4	6.87	10.4	96.8	69.0
PONT-10	1	0.06535	0.0008	0.86555	0.01117	0.09608	0.00106	0.85	785.5	25.52	591.4	6.24	633.1	6.08	34.4	201.2	111.5
PONT-10	2b	0.06032	0.00069	0.79219	0.00964	0.09526	0.00105	0.91	615.2	24.49	586.5	6.16	592.4	5.46	48.1	310.0	71.6
PONT-10	3a	0.05633	0.0007	0.48695	0.00638	0.0627	0.00069	0.84	464.8	27.55	392	4.2	402.8	4.36	110.9	1114.4	172.9
PONT-10	3b	0.05687	0.0008	0.54829	0.008	0.06993	0.00078	0.76	486	31.21	435.7	4.7	443.9	5.25	33.2	287.5	82.4
PONT-10	5	0.06186	0.00072	0.60004	0.00742	0.07037	0.00077	0.88	669.1	24.76	438.4	4.66	477.3	4.71	48.1	416.5	82.5
PONT-10	6	0.05833	0.00102	0.5277	0.00939	0.06562	0.00075	0.64	541.5	38.6	409.7	4.54	430.3	6.24	31.5	291.3	76.5
PONT-10	7	0.06071	0.00067	0.53283	0.00631	0.06367	0.0007	0.93	628.8	23.66	397.9	4.23	433.7	4.18	179.7	1782.1	173.5
PONT-10	8b	0.06028	0.00068	0.5726	0.00693	0.0689	0.00076	0.91	613.7	24.33	429.5	4.56	459.7	4.47	78.6	663.4	253.0
PONT-10	9	0.05863	0.00076	0.45359	0.00612	0.05611	0.00062	0.82	553.5	27.91	351.9	3.79	379.8	4.27	137.9	1555.0	195.5
PONT-10	11b	0.06039	0.00069	0.80552	0.00978	0.09674	0.00106	0.90	617.7	24.41	595.3	6.24	599.9	5.5	88.6	559.6	141.3
PONT-10	12	0.06288	0.00075	0.7282	0.00921	0.084	0.00093	0.88	704.3	25.26	519.9	5.5	555.5	5.41	64.1	454.0	140.3
PONT-10	13	0.05716	0.00074	0.55636	0.00752	0.0706	0.00078	0.82	497.2	28.5	439.8	4.71	449.2	4.91	35.4	308.6	73.7
PONT-10	14	0.06105	0.00082	0.71674	0.01006	0.08516	0.00095	0.79	640.9	28.76	526.9	5.63	548.7	5.95	42.7	288.9	131.3
PONT-10	18	0.0625	0.00088	0.69848	0.01012	0.08106	0.00091	0.77	691.4	29.58	502.4	5.4	537.9	6.05	31.8	226.8	87.4
PONT-10	19	0.05669	0.0007	0.52875	0.00688	0.06765	0.00075	0.85	479	27.36	422	4.51	431	4.57	95.5	776.3	504.4
PONT-14	2	0.06133	0.00068	0.87257	0.01045	0.10321	0.00115	0.93	650.7	23.72	633.2	6.7	637	5.67	96.5	947.9	197.4
PONT-14	3	0.06565	0.00121	0.78861	0.01465	0.08713	0.00102	0.63	795.2	38.08	538.6	6.06	590.4	8.32	12.9	137.4	72.2
PONT-14	4	0.16265	0.00174	8.67379	0.10034	0.38682	0.0043	0.96	2483.4	17.88	2108.1	19.97	2304.3	10.53	79.5	185.0	65.0
PONT-14	6	0.06443	0.00075	1.08738	0.01353	0.12241	0.00137	0.90	755.9	24.4	744.4	7.84	747.2	6.58	37.7	273.8	195.8
PONT-14	12	0.05999	0.00081	0.809	0.01145	0.09783	0.0011	0.79	603.1	29.01	601.7	6.49	601.9	6.43	13.3	136.9	37.9
PONT-14	15	0.1065	0.0012	4.45094	0.05393	0.30316	0.00339	0.92	1740.3	20.53	1706.9	16.76	1721.9	10.05	53.5	155.8	102.2
PONT-14	18	0.05871	0.00088	0.75571	0.01167	0.09337	0.00106	0.74	556.2	32.23	575.5	6.27	571.5	6.75	11.0	104.2	79.4
PONT-14	21	0.06077	0.00076	0.7797	0.01036	0.09306	0.00105	0.85	631.1	26.79	573.6	6.17	585.3	5.91	31.0	360.3	9.2
PONT-14	23	0.06413	0.00082	1.04219	0.01408	0.11787	0.00133	0.84	746.1	26.8	718.3	7.67	725	7	30.0	252.4	83.5
PONT-14	25	0.06172	0.00075	0.86148	0.01121	0.10124	0.00114	0.87	664.4	25.98	621.7	6.66	630.9	6.12	94.6	916.6	339.3
PONT-14	26	0.0597	0.00071	0.47609	0.00606	0.05785	0.00065	0.88	593.1	25.16	362.5	3.95	395.4	4.17	133.7	2447.4	158.9
PONT-14	28	0.05866	0.00068	0.42076	0.00527	0.05203	0.00058	0.89	554.5	25.24	327	3.57	356.6	3.77	417.3	8615.0	88.0

PONT-14	38	0.18654	0.002	13.47376	0.15522	0.52391	0.00574	0.95	2711.9	17.57	2715.7	24.29	2713.4	10.89	44.3	353.4	262.1
PONT-14	40	0.11589	0.00128	5.10785	0.06042	0.31969	0.00352	0.93	1893.8	19.79	1788.2	17.18	1837.4	10.05	5.0	234.8	86.9
PONT-14	41a	0.0608	0.00069	0.863	0.01045	0.10295	0.00113	0.91	632.3	24.31	631.7	6.62	631.8	5.69	9.6	490.8	104.4
PONT-14	41b	0.05918	0.00066	0.74341	0.00881	0.09112	0.001	0.93	573.7	23.91	562.1	5.91	564.4	5.13	9.6	1594.9	223.4
PONT-14	42	0.05853	0.00075	0.42316	0.0057	0.05244	0.00058	0.82	549.7	27.87	329.5	3.57	358.3	4.07	3.8	724.7	22.3
PONT-15	3	0.05829	0.00072	0.70064	0.00912	0.08718	0.00097	0.85	540.1	27.44	538.8	5.73	539.2	5.45	19.8	220.3	91.1
PONT-15	5	0.05591	0.00065	0.48572	0.00599	0.06302	0.00069	0.89	448.4	25.16	394	4.21	402	4.1	35.3	562.4	147.9
PONT-15	8b	0.09089	0.00102	3.12998	0.03736	0.24978	0.00273	0.92	1444.2	21.31	1437.4	14.08	1440.1	9.18	56.6	213.5	87.0
PONT-15	8c	0.05555	0.00062	0.40999	0.00485	0.05353	0.00058	0.92	434.2	24.55	336.2	3.57	348.9	3.49	153.7	3104.7	92.5
PONT-15	14a	0.06304	0.00074	0.78878	0.00975	0.09076	0.001	0.89	709.6	24.62	560	5.9	590.5	5.53	71.0	772.6	227.5
PONT-15	15a	0.07212	0.0008	1.66084	0.01965	0.16704	0.00183	0.93	989.3	22.39	995.8	10.1	993.7	7.5	86.9	489.9	217.5
PONT-15	16	0.06545	0.00074	0.99885	0.01201	0.11069	0.00121	0.91	788.9	23.55	676.8	7.04	703.2	6.1	100.4	848.8	398.6
PONT-15	18	0.05448	0.00062	0.4147	0.00504	0.05521	0.0006	0.89	390.9	25.44	346.4	3.69	352.3	3.61	63.5	1248.1	19.0
PONT-15	20	0.06088	0.0008	0.72987	0.01	0.08696	0.00096	0.81	634.9	28.15	537.6	5.7	556.5	5.87	38.6	413.9	210.3
PONT-15	21a	0.05738	0.00081	0.66126	0.00966	0.08359	0.00093	0.76	505.6	30.75	517.5	5.52	515.4	5.9	18.5	221.4	59.7
PONT-15	21b	0.05941	0.00091	0.63478	0.00996	0.07751	0.00087	0.72	582	33	481.2	5.19	499.1	6.19	19.2	244.9	74.8
PONT-15	37	0.05495	0.00061	0.41935	0.00493	0.05535	0.0006	0.92	410.2	24.37	347.3	3.68	355.6	3.53	115.2	2245.8	93.0
PONT-15	45	0.06745	0.00085	0.98418	0.01292	0.10584	0.00117	0.84	851.6	25.85	648.5	6.82	695.7	6.61	35.5	293.1	147.6
PONT-15	46	0.13663	0.00167	7.05679	0.09043	0.37463	0.00417	0.87	2184.9	21.09	2051.2	19.57	2118.6	11.4	24.2	59.4	23.2
PONT-26	1a	0.05937	0.00065	0.63882	0.00752	0.07804	0.00086	0.94	580.8	23.66	484.4	5.12	501.6	4.66	110.7	1372.1	512.7
PONT-26	4b	0.06449	0.00078	0.79509	0.01014	0.08943	0.00099	0.87	757.8	25.27	552.1	5.84	594.1	5.74	25.1	266.8	105.4
PONT-26	5	0.0593	0.00072	0.43482	0.00554	0.05319	0.00059	0.87	578.2	26.01	334.1	3.59	366.6	3.92	32.8	651.7	35.7
PONT-26	7	0.05698	0.00062	0.59268	0.0069	0.07545	0.00083	0.94	490.1	23.96	468.9	4.96	472.6	4.4	116.2	1673.8	29.8
PONT-26	10	0.05984	0.00065	0.48615	0.00571	0.05893	0.00065	0.94	597.7	23.51	369.1	3.94	402.3	3.9	298.6	5470.7	28.4
PONT-26	11a	0.0618	0.00079	0.65189	0.0087	0.07651	0.00085	0.83	667.3	27.01	475.2	5.08	509.6	5.35	26.2	360.9	24.4
PONT-26	11b	0.05563	0.00065	0.41266	0.0051	0.0538	0.00059	0.89	437.4	25.15	337.8	3.63	350.8	3.66	65.5	1328.5	10.1
PONT-26	12	0.05587	0.00063	0.46696	0.00563	0.06063	0.00067	0.92	446.7	24.45	379.5	4.05	389.1	3.9	64.5	1161.4	4.8
PONT-26	13a	0.05586	0.00091	0.56152	0.00936	0.07291	0.00083	0.68	446.5	35.47	453.7	4.96	452.5	6.08	10.7	149.3	30.9
PONT-26	13b	0.05414	0.00062	0.39371	0.00481	0.05274	0.00058	0.90	376.9	25.74	331.3	3.56	337.1	3.51	51.1	1061.9	5.8
PONT-26	14	0.06052	0.00079	0.63075	0.00861	0.07559	0.00084	0.81	622.3	27.91	469.8	5.04	496.6	5.36	59.4	776.8	243.9
PONT-26	16	0.0692	0.0008	1.14019	0.01401	0.11952	0.00132	0.90	904.6	23.57	727.8	7.6	772.6	6.65	55.4	436.2	186.1
PONT-26	19b	0.05758	0.0007	0.55354	0.00712	0.06973	0.00077	0.86	513.4	26.16	434.6	4.65	447.3	4.65	68.2	935.0	403.3
PONT-26	21	0.0598	0.0007	0.59395	0.00744	0.07205	0.0008	0.89	596.3	25.31	448.5	4.79	473.4	4.74	106.9	1429.7	508.8
PONT-26	23a	0.06558	0.00073	0.8344	0.0099	0.09229	0.00101	0.92	792.9	23.1	569.1	5.98	616.1	5.48	36.1	364.5	77.3
PONT-26	27a	0.06617	0.0007	1.02887	0.01179	0.11279	0.00123	0.95	811.7	22.12	688.9	7.15	718.4	5.9	66.8	537.7	174.5
PONT-26	28	0.05826	0.00063	0.48612	0.00563	0.06053	0.00066	0.94	538.8	24.06	378.8	4.03	402.3	3.85	60.4	950.7	99.5
PONT-26	29	0.05935	0.00069	0.76835	0.00951	0.0939	0.00103	0.89	580.1	25.2	578.6	6.08	578.8	5.46	21.5	209.1	73.6
PONT-26	34	0.0611	0.0007	0.8552	0.01035	0.10152	0.00111	0.90	642.9	24.33	623.3	6.51	627.5	5.66	34.8	305.4	129.5
PONT-26	38a	0.12178	0.00148	5.97572	0.07631	0.35592	0.00395	0.87	1982.5	21.56	1962.8	18.76	1972.3	11.11	10.2	20.7	22.6
PONT-26	41b	0.05974	0.00073	0.62155	0.00808	0.07547	0.00084	0.86	594.00	26.44	469.00	5.02	490.80	5.06	81.8	659.6	136.9
PONT-26	42c	0.05744	0.00071	0.66747	0.00872	0.08428	0.00094	0.85	508.20	26.81	521.60	5.56	519.20	5.31	54.6	381.2	104.8
PONT-26	44b	0.06042	0.00078	0.80506	0.01085	0.09665	0.00108	0.83	618.7	27.51	594.7	6.33	599.7	6.1	6.7	319.1	204.9
PONT-20	1	0.06035	0.00067	0.75207	0.00927	0.0904	0.00104	0.93	616.2	23.75	557.9	6.15	569.4	5.37	52.8	566.5	257.1
PONT-20	2a	0.06408	0.00072	0.95574	0.01191	0.10819	0.00124	0.92	744.3	23.62	662.2	7.24	681.1	6.18	40.4	350.1	180.6
PONT-20	3	0.05716	0.00064	0.58048	0.00716	0.07367	0.00084	0.92	497	24.7	458.2	5.07	464.8	4.6	36.1	524.7	44.7
PONT-20	4a	0.05867	0.00063	0.75133	0.00897	0.0929	0.00106	0.96	554.7	23.16	572.7	6.26	569	5.2	90.3	941.4	402.3
PONT-20	5a	0.17838	0.0019	10.66509	0.12645	0.43368	0.00495	0.96	2637.9	17.59	2322.3	22.24	2494.4	11.01	46.9	95.3	42.9
PONT-20	5c	0.12088	0.00127	4.83668	0.05658	0.29024	0.00329	0.97	1969.2	18.58	1642.7	16.44	1791.3	9.84	293.3	1042.8	18.6
PONT-20	27	0.05419	0.00091	0.42999	0.00736	0.05755	0.00066	0.67	379	37.21	360.7	4	363.2	5.23	6.2	110.6	23.0
PONT-20	7a	0.06376	0.00076	0.8989	0.01157	0.10226	0.00116	0.88	733.7	25.08	627.6	6.79	651.1	6.19	19.9	189.5	63.4
PONT-20	7b	0.06247	0.0007	0.64318	0.0079	0.07468	0.00084	0.92	690.3	23.87	464.3	5.06	504.3	4.88	41.2	573.1	59.0
PONT-20	9	0.12099	0.00131	5.18392	0.06144	0.31078	0.00349	0.95	1970.9	19.14	1744.5	17.19	1850	10.09	149.9	412.3	288.8
PONT-20	10	0.07235	0.00079	1.43325	0.0171	0.1437	0.00161	0.94	995.7	22.04	865.6	9.09	902.9	7.14	101.4	646.0	341.0

PONT-20	11	0.06312	0.00075	1.00252	0.01273	0.11521	0.0013	0.89	712.3	24.9	702.9	7.5	705.1	6.45	23.5	208.2	39.7
PONT-20	12	0.0575	0.00068	0.52938	0.00671	0.06678	0.00075	0.89	510.4	25.57	416.7	4.54	431.4	4.46	42.0	680.4	2.4
PONT-20	13	0.05869	0.00071	0.46242	0.00598	0.05715	0.00064	0.87	555.8	26.22	358.3	3.92	385.9	4.15	80.8	1062.1	1292.0
PONT-20	15a	0.05707	0.00098	0.4937	0.00861	0.06275	0.00072	0.66	493.8	37.42	392.3	4.39	407.4	5.85	14.2	217.4	77.6
PONT-20	15b	0.05684	0.0007	0.58636	0.00763	0.07482	0.00084	0.86	484.9	27.21	465.1	5.01	468.5	4.88	23.4	309.6	83.8
PONT-20	16a	0.06002	0.0008	0.78396	0.01093	0.09474	0.00106	0.80	604.4	28.59	583.5	6.26	587.7	6.22	14.8	138.2	93.4
PONT-20	17b	0.12678	0.00144	6.00172	0.07264	0.34339	0.0038	0.91	2053.8	19.9	1902.9	18.25	1976.1	10.53	109.8	191.1	476.8
PONT-20	18b	0.05669	0.00067	0.49454	0.00621	0.06328	0.0007	0.88	478.7	26.31	395.6	4.24	408	4.22	91.5	1512.7	90.1
PONT-20	20	0.06074	0.00074	0.53682	0.00688	0.06411	0.00071	0.86	630	26.1	400.6	4.29	436.3	4.55	54.4	735.0	472.9
PONT-20	26	0.0611	0.00075	0.8509	0.01105	0.10102	0.00113	0.86	642.7	26.11	620.4	6.6	625.1	6.06	14.7	157.5	3.1
PONT-20	29	0.05635	0.00063	0.59413	0.00714	0.07648	0.00085	0.92	465.2	24.7	475.1	5.08	473.5	4.55	63.8	842.4	198.8
PONT-20	31	0.05774	0.00066	0.55547	0.00677	0.06978	0.00077	0.91	519.8	24.97	434.8	4.67	448.6	4.42	54.3	801.0	116.6
PONT-20	33a	0.0595	0.00067	0.71211	0.00859	0.08681	0.00096	0.92	585.4	24.15	536.7	5.71	546	5.09	51.6	543.8	299.7
PONT-20	34	0.06055	0.00067	0.75951	0.00906	0.09098	0.00101	0.93	623.4	23.68	561.3	5.96	573.7	5.23	69.1	715.8	326.3
PONT-20	35	0.05894	0.0007	0.65938	0.00838	0.08114	0.0009	0.87	565	25.82	502.9	5.39	514.2	5.13	50.2	614.6	183.7
PONT-20	36	0.05674	0.00064	0.57536	0.00695	0.07355	0.00082	0.92	480.9	24.88	457.5	4.9	461.5	4.48	63.2	717.0	649.6
PONT-20	38	0.05706	0.00063	0.57553	0.00689	0.07316	0.00081	0.92	493.2	24.65	455.2	4.87	461.6	4.44	122.1	1397.8	1297.6
PONT-20	40	0.06921	0.00078	1.28831	0.01552	0.13503	0.0015	0.92	904.9	22.92	816.5	8.51	840.5	6.89	125.2	979.6	71.6
PONT-20	41a	0.06225	0.00115	0.64224	0.01201	0.07484	0.00087	0.62	682.7	38.97	465.2	5.23	503.7	7.43	6.3	81.2	27.2
PONT-20	41b	0.06286	0.00088	0.8096	0.0118	0.09342	0.00105	0.77	703.6	29.55	575.7	6.22	602.2	6.62	11.8	116.9	59.1
PONT-20	42	0.12859	0.00146	5.82805	0.07084	0.32875	0.00366	0.92	2078.8	19.82	1832.3	17.75	1950.6	10.53	82.5	224.0	116.2

Analyses U-Pb sur zircon – grains hérités du leucogranite de Guérande

		Isotope ratios							Ages						Concentrations (ppm)		
Sample	Zircon analyses	Pb^{207}/Pb^{206}	1σ	Pb^{207}/U^{235}	1σ	Pb^{206}/U^{238}	1σ	rho	Pb^{207}/Pb^{206}	1σ	Pb^{206}/U^{238}	1σ	Pb^{207}/U^{235}	1σ	Pb	U	Th
GUE-3	1b	0.06037	0.00067	0.67896	0.00883	0.08158	0.00103	0.9708162	616.9	23.88	505.5	6.12	526.1	5.34	33.5	426.9	26.4
GUE-3	3	0.05669	0.00064	0.47014	0.00617	0.06016	0.00076	0.9626043	478.8	24.93	376.6	4.61	391.3	4.26	50.6	869.5	74.7
GUE-3	5	0.05721	0.00075	0.47287	0.00686	0.05996	0.00077	0.8852109	499.1	28.73	375.4	4.69	393.2	4.73	17.9	302.8	24.9
GUE-3	6a	0.0564	0.00077	0.53832	0.00803	0.06923	0.0009	0.8715116	467.5	30.07	431.5	5.41	437.3	5.3	16.8	235.7	46.4
GUE-3	9b	0.05908	0.00064	0.50894	0.00658	0.06249	0.00079	0.9778163	570	23.7	390.8	4.79	417.7	4.43	100.5	1700.2	78.0
GUE-3	11c	0.05739	0.00075	0.47146	0.00687	0.05959	0.00077	0.8867587	506.1	28.39	373.2	4.7	392.2	4.74	40.1	680.4	72.9
GUE-3	12a	0.05741	0.00076	0.50248	0.00739	0.06349	0.00082	0.8781786	507	28.64	396.8	4.99	413.4	5	13.8	221.1	26.8
GUE-3	12b	0.05711	0.00075	0.53023	0.00775	0.06735	0.00087	0.8837802	495.4	28.92	420.1	5.28	432	5.15	33.0	450.6	136.2
GUE-3	12c	0.05783	0.00073	0.5832	0.00836	0.07316	0.00094	0.8963248	523.1	27.85	455.2	5.67	466.5	5.36	17.5	231.5	52.2
GUE-3	14a	0.06113	0.00077	0.86846	0.01242	0.10305	0.00133	0.9024681	643.9	26.88	632.3	7.79	634.7	6.75	23.4	204.2	71.2
GUE-3	14b	0.05579	0.00079	0.4025	0.00624	0.05233	0.00069	0.8505104	443.8	30.77	328.8	4.22	343.5	4.52	14.7	311.0	0.7
GUE-3	14c	0.0567	0.00077	0.41349	0.00622	0.0529	0.00069	0.8670977	479.1	29.99	332.3	4.23	351.4	4.47	13.4	279.4	1.5
GUE-3	6b	0.05636	0.0007	0.42871	0.00608	0.05518	0.00071	0.9072703	465.6	27.31	346.3	4.36	362.3	4.32	56.6	1071.5	88.9
GUE-3	19	0.06217	0.00082	0.7438	0.01101	0.08678	0.00114	0.8874708	680	27.91	536.5	6.74	564.6	6.41	34.8	381.0	91.6
GUE-3	16a	0.10847	0.00125	4.03298	0.05431	0.26973	0.00346	0.9525617	1773.7	20.86	1539.4	17.57	1640.9	10.96	79.5	274.5	62.2
GUE-3	18a	0.09797	0.00113	3.73699	0.05077	0.27669	0.00355	0.9443863	1585.9	21.48	1574.7	17.94	1579.3	10.88	163.8	472.3	291.4
GUE-4	20a	0.05592	0.00186	0.48283	0.01547	0.06264	0.00108	0.538116	448.9	72.42	391.7	6.57	400	10.59	9.4	162.9	3.8
GUE-4	5a	0.06022	0.00191	0.81267	0.02538	0.09789	0.00159	0.5200935	611.4	67.25	602	9.36	604	14.22	4.0	42.6	3.6
GUE-4	19b	0.06085	0.00109	0.93082	0.01715	0.11097	0.00155	0.7581021	634.1	38.07	678.4	9	668.1	9.02	37.1	346.8	33.4
GUE-4	3a	0.06309	0.00157	0.98969	0.02437	0.11377	0.00176	0.6282443	711.4	51.86	694.6	10.19	698.6	12.44	6.7	55.8	16.8
GUE-4	24	0.06427	0.00116	1.06864	0.01969	0.12065	0.00168	0.7557317	750.6	37.64	734.3	9.66	738.1	9.66	58.5	506.2	40.1
GUE-4	1a	0.06479	0.00118	0.81423	0.01541	0.09115	0.00131	0.7593799	767.5	38.02	562.4	7.72	604.8	8.62	16.7	177.9	38.8
GUE-4	21a	0.06518	0.00117	0.96594	0.0178	0.10752	0.0015	0.7570632	780.1	37.3	658.3	8.75	686.4	9.19	23.6	213.8	41.4

GUE-4	20b	0.06533	0.00118	0.77911	0.01448	0.08652	0.00121	0.7524871	785	37.64	534.9	7.2	585	8.26	23.6	240.2	80.4
GUE-4	19a	0.06898	0.00144	1.02241	0.02134	0.10752	0.00158	0.7040419	898.3	42.45	658.3	9.19	715.1	10.71	13.8	117.2	32.0
GUE-4	13a	0.07541	0.00135	1.95987	0.03604	0.18852	0.0027	0.778841	1079.5	35.48	1113.4	14.63	1101.8	12.36	28.5	137.6	44.2
GUE-4	2	0.11456	0.00152	4.59685	0.06809	0.29105	0.00395	0.9162342	1872.9	23.67	1646.8	19.73	1748.7	12.35	47.4	155.4	32.2
GUE-4	6a	0.12855	0.00174	5.72533	0.08585	0.32304	0.00441	0.9104215	2078.3	23.68	1804.5	21.49	1935.2	12.96	36.1	103.4	24.8
GUE-5	1	0.05877	0.00105	1.01835	0.01896	0.1257	0.00173	0.7392129	558.6	38.43	763.3	9.92	713.1	9.54	31.7	233.0	76.4
GUE-5	11b	0.05845	0.00088	0.75808	0.01215	0.0941	0.00125	0.828818	546.6	32.44	579.7	7.36	572.9	7.02	55.1	578.0	108.8
GUE-5	2	0.05922	0.00081	0.80702	0.01226	0.09886	0.00131	0.8722571	575	29.59	607.7	7.66	600.8	6.89	84.6	798.7	255.8
GUE-5	17a	0.0605	0.00118	0.86305	0.01697	0.1035	0.00146	0.7174087	621.4	41.6	634.9	8.53	631.8	9.25	18.9	189.6	17.4
GUE-5	10	0.06502	0.00107	1.10616	0.01904	0.12342	0.00168	0.7908147	775.1	34.33	750.2	9.65	756.3	9.18	29.4	228.1	54.2
GUE-5	16	0.06458	0.00099	1.0742	0.01735	0.12068	0.0016	0.8208624	760.7	31.94	734.5	9.23	740.8	8.49	63.9	548.5	49.9
GUE-5	15	0.05387	0.00098	0.39952	0.0074	0.05381	0.00074	0.7424642	365.4	40.41	337.9	4.52	341.3	5.37	29.0	563.6	35.3
GUE-5	9	0.11566	0.00154	5.21269	0.07645	0.32698	0.00428	0.8924975	1890.2	23.73	1823.7	20.79	1854.7	12.49	161.8	477.0	74.1
GUE-5	8	0.06889	0.00119	1.23479	0.02204	0.13003	0.0018	0.7755512	895.5	35.3	788	10.28	816.5	10.01	28.3	164.8	117.7
GUE-5	21c	0.06495	0.00107	0.96279	0.01637	0.10755	0.00144	0.7874717	772.7	34.4	658.5	8.4	684.7	8.47	76.6	733.2	57.6
GUE-5	6c	0.06534	0.00097	0.95088	0.01514	0.10557	0.00141	0.8388386	785.4	30.77	647	8.23	678.6	7.88	50.7	469.5	89.9
GUE-8	21			1.25201	0.02645	0.13478	0.002	0.7024035	849.8	43.37	815.1	11.34	824.3	11.93	15.4	110.0	18.4
GUE-8	23			0.7122	0.0136	0.08603	0.00121	0.7365437	605.6	39.89	532	7.2	546.1	8.07	24.8	272.4	68.6
GUE-8	13			0.49623	0.00944	0.0612	0.00087	0.7472722	560.7	39.71	382.9	5.29	409.2	6.4	38.0	641.7	54.4
GUE-8	18b			0.86963	0.01571	0.09548	0.00133	0.7710767	808.7	36.01	587.9	7.85	635.4	8.53	34.5	380.8	13.3
GUE-8	10a			0.61479	0.01154	0.07221	0.00103	0.7599077	666.2	38.33	449.4	6.19	486.6	7.25	27.2	358.1	72.9
GUE-8	26	0.06176	0.00111	0.81994	0.01519	0.09631	0.00135	0.7566355	665.7	38.17	592.7	7.92	608	8.47	28.1	254.0	97.9
GUE-8	27	0.06455	0.00121	0.93395	0.01781	0.10495	0.00148	0.7395014	759.7	38.98	643.4	8.66	669.7	9.35	17.6	169.1	18.8
GUE-8	28	0.0593	0.0012	0.87731	0.01798	0.10732	0.00154	0.7001699	578.1	43.49	657.2	8.95	639.5	9.73	12.9	118.8	21.1
GUE-8	29	0.06425	0.00154	0.94096	0.02205	0.10624	0.00164	0.6587466	749.8	49.73	650.9	9.56	673.4	11.53	37.3	353.7	42.3
GUE-8	33	0.05691	0.00115	0.60535	0.01233	0.07716	0.0011	0.6999128	487.2	44.06	479.2	6.61	480.6	7.8	16.4	210.9	39.3
GUE-8	34	0.07237	0.00117	1.73732	0.02958	0.17414	0.00238	0.8027126	996.4	32.63	1034.9	13.08	1022.5	10.97	33.5	150.9	98.3
GUE-8	37	0.06398	0.00112	0.84612	0.0153	0.09593	0.00133	0.7667216	741.1	36.55	590.5	7.82	622.5	8.41	20.2	206.7	32.5
GUE-8	40	0.06442	0.00133	0.91423	0.01897	0.10295	0.0015	0.7021874	755.3	43.11	631.7	8.79	659.3	10.06	22.6	210.2	49.7
GUE-8	47	0.06576	0.00171	0.92667	0.02351	0.10222	0.00163	0.6285274	798.8	53.68	627.4	9.51	665.9	12.39	8.4	79.9	9.9
GUE-8	38a	0.07318	0.00126	1.50087	0.02668	0.14877	0.00207	0.7827305	1019.1	34.44	894	11.62	930.7	10.83	82.7	517.9	146.9
GUE-8	38b	0.07268	0.00113	1.67131	0.02748	0.16681	0.00226	0.8239989	1005	31.11	994.5	12.46	997.7	10.45	43.7	248.1	59.8
GUE-8	24a	0.06931	0.00096	1.55856	0.02365	0.16312	0.00216	0.8726476	907.9	28.38	974.1	11.96	953.9	9.39	83.7	457.2	162.9

Analyses U-Pb sur zircon – grains hérités du leucogranite de Lizio

		Isotope ratios							Ages						Concentrations (ppm)		
Sample	**Zircon analyses**	**Pb^{207}/Pb^{206}**	**1σ**	**Pb^{207}/U^{235}**	**1σ**	**Pb^{206}/U^{238}**	**1σ**	**rho**	**Pb^{207}/Pb^{206}**	**1σ**	**Pb^{206}/U^{238}**	**1σ**	**Pb^{207}/U^{235}**	**1σ**	**Pb**	**U**	**Th**
LRT-10	32	0.05248	0.00067	0.38069	0.0051	0.05262	0.00058	0.82277	306.3	28.92	330.6	3.56	327.5	3.75	58.6	654.9	231.5
LRT-10	2	0.05632	0.00065	0.49945	0.00604	0.06433	0.0007	0.8997867	464.1	25.37	401.9	4.24	411.3	4.09	198.3	1554.1	1400.2
LRT-10	31a	0.056	0.00066	0.5525	0.00688	0.07157	0.00079	0.8864208	452	25.56	445.6	4.73	446.6	4.5	64.1	531.9	170.9
LRT-10	13	0.05794	0.0007	0.615	0.00776	0.077	0.00084	0.8645736	527	26.41	478.2	5.05	486.7	4.88	56.2	433.1	136.0
LRT-10	26	0.05844	0.00071	0.62741	0.00807	0.07787	0.00086	0.8586302	546.4	26.44	483.4	5.14	494.5	5.03	80.8	597.2	254.8
LRT-10	25	0.05812	0.00075	0.63616	0.00857	0.07939	0.00088	0.8228154	533.8	28.46	492.5	5.25	499.9	5.32	75.4	562.1	183.6
LRT-10	31b	0.05719	0.00072	0.64997	0.00859	0.08244	0.00091	0.8352251	498.3	27.79	510.7	5.43	508.5	5.29	55.6	393.8	139.9
LRT-10	22	0.0588	0.00075	0.72849	0.00974	0.08986	0.00099	0.8240118	559.8	27.61	554.7	5.88	555.7	5.72	74.0	490.1	156.8
LRT-10	30	0.059	0.00075	0.74534	0.00989	0.09163	0.00101	0.8306954	567.3	27.09	565.2	5.99	565.5	5.75	61.1	413.4	81.2
LRT-10	20	0.05921	0.00069	0.75779	0.00935	0.09284	0.00102	0.8904352	574.8	25.15	572.3	6.01	572.7	5.4	105.6	681.7	199.2
LRT-10	5	0.06033	0.00078	0.78527	0.0105	0.09442	0.00104	0.8237569	615.5	27.56	581.6	6.11	588.5	5.97	35.7	221.6	70.7

LRT-10	21	0.05919	0.00074	0.77216	0.01009	0.09462	0.00104	0.8411366	574.3	26.85	582.8	6.15	581	5.78	50.3	290.2	181.2
LRT-10	1	0.05985	0.00076	0.78968	0.01039	0.09571	0.00105	0.8338109	598.1	27.18	589.2	6.17	591	5.9	30.8	176.2	102.1
LRT-10	15	0.06257	0.0008	0.83329	0.01105	0.09661	0.00107	0.8352098	693.5	26.87	594.5	6.26	615.4	6.12	68.1	406.0	125.6
LRT-10	14	0.0592	0.00087	0.79493	0.01197	0.0974	0.00109	0.7431941	574.6	31.55	599.2	6.38	594	6.77	27.7	171.1	47.8
LRT-10	11	0.06001	0.00072	0.85871	0.01086	0.10379	0.00114	0.8684924	604.1	25.84	636.6	6.64	629.4	5.93	50.1	309.3	16.4
LRT-10	16	0.06283	0.00069	0.92012	0.01083	0.10623	0.00116	0.9277412	702.5	23.34	650.8	6.76	662.4	5.73	456.8	2428.1	1211.3
LRT-10	38	0.06704	0.0009	1.01473	0.01415	0.10979	0.00122	0.7968767	839	27.74	671.6	7.09	711.3	7.13	55.7	273.6	161.1
LRT-10	4	0.06467	0.00079	1.05331	0.01344	0.11815	0.00129	0.855683	763.7	25.52	719.9	7.46	730.5	6.65	41.4	182.6	140.3
LRT-10	8	0.07156	0.00096	1.3007	0.01797	0.13186	0.00146	0.801436	973.3	27.01	798.5	8.31	846	7.93	32.5	109.7	147.8
LRT-10	35	0.07255	0.00087	1.66897	0.02117	0.16686	0.00184	0.8693472	1001.5	24.26	994.8	10.17	996.8	8.05	160.0	522.2	307.6

Analyses U-Pb sur zircon – grains hérités leucogranite de Questembert

		Isotope ratios							Ages						Concentrations (ppm)		
Sample	**Zircon analyses**	**Pb^{207}/Pb^{206}**	**1σ**	**Pb^{207}/U^{235}**	**1σ**	**Pb^{206}/U^{238}**	**1σ**	**rho**	**Pb^{207}/Pb^{206}**	**1σ**	**Pb^{206}/U^{238}**	**1σ**	**Pb^{207}/U^{235}**	**1σ**	**Pb**	**U**	**Th**
QRT-08	3	0.24338	0.00263	17.09994	0.1976	0.50965	0.0056	0.9508755	3142.2	17.03	2655.2	23.92	2940.5	11.08	197.7	181.9	134.0
QRT-08	8	0.05972	0.00086	0.86707	0.01284	0.10533	0.00117	0.7501065	593.5	30.61	645.6	6.85	634	6.98	22.9	107.7	108.3
QRT-08	17	0.06031	0.00071	0.57497	0.00717	0.06916	0.00076	0.8812206	614.7	25.37	431.1	4.56	461.2	4.62	257.4	1925.1	1532.3
QRT-08	18	0.06596	0.00083	0.89875	0.01178	0.09885	0.00109	0.8412856	805	26.07	607.6	6.38	651.1	6.3	88.8	465.2	414.3
QRT-08	23	0.06108	0.00072	0.7219	0.00898	0.08574	0.00094	0.8813432	641.9	25.24	530.3	5.56	551.8	5.3	126.8	823.1	373.6
QRT-08	24	0.05864	0.00072	0.62755	0.00807	0.07764	0.00085	0.8513501	553.7	26.59	482	5.08	494.6	5.03	74.6	597.2	52.8
QRT-08	29	0.06109	0.00067	0.83477	0.00983	0.09913	0.00108	0.9251922	642.4	23.58	609.3	6.35	616.3	5.44	138.8	774.7	410.2
QRT-08	37	0.05662	0.00063	0.52847	0.00629	0.06772	0.00074	0.9180883	476	24.78	422.4	4.46	430.8	4.18	142.6	1366.5	14.3
QRT-08	40	0.06045	0.00087	0.88165	0.01311	0.10581	0.00118	0.7499785	619.6	30.91	648.4	6.87	641.9	7.08	20.6	103.7	75.7
QRT-08	42	0.05642	0.00063	0.53321	0.00632	0.06857	0.00075	0.9228016	468.1	24.69	427.5	4.51	433.9	4.19	194.5	1838.2	26.3
QRT-08	43	0.20803	0.0023	14.50278	0.17026	0.50577	0.00553	0.9313452	2890.3	17.8	2638.5	23.67	2783.2	11.15	286.3	289.9	129.3
QRT-08	47	0.05857	0.00076	0.60112	0.00815	0.07445	0.00082	0.8123678	551.3	28.22	462.9	4.93	477.9	5.17	42.5	325.1	133.8
QRT-08	52	0.05647	0.00071	0.58547	0.00769	0.07521	0.00083	0.8401964	470.3	27.87	467.5	4.96	468	4.93	85.2	556.3	586.5
QRT-08	56	0.05804	0.00071	0.46957	0.00598	0.05869	0.00064	0.8562785	530.9	26.85	367.7	3.92	390.9	4.13	115.1	1190.7	412.3
QRT-08	25a	0.06124	0.00128	0.66023	0.01383	0.07821	0.00092	0.5615632	647.7	44.4	485.4	5.48	514.8	8.46	17.2	127.8	41.0
QRT-08	25b	0.058	0.00079	0.59379	0.00836	0.07427	0.00082	0.7842003	529.4	29.99	461.8	4.92	473.3	5.33	66.1	548.7	75.2
QRT-08	38a	0.05774	0.0007	0.53899	0.00685	0.06772	0.00074	0.8598148	519.8	26.54	422.4	4.49	437.8	4.52	95.0	787.5	374.0
QRT-08	38b	0.05657	0.00071	0.59395	0.00777	0.07617	0.00084	0.8429934	474	27.75	473.2	5.01	473.4	4.95	71.9	577.3	102.8
QRT-08	5a	0.05611	0.00081	0.57411	0.00849	0.07423	0.00083	0.7561119	456.2	31.24	461.6	4.96	460.7	5.48	41.2	343.4	47.9
QRT-08	5b	0.05713	0.00063	0.59253	0.00702	0.07524	0.00082	0.9198951	495.9	24.63	467.6	4.93	472.5	4.47	107.8	887.8	119.2

Analyses U-Pb sur zircon – grains hérités granite de Huelgoat

		Isotope ratios							Ages						Concentrations (ppm)		
Sample	**Zircon analyses**	**Pb^{207}/Pb^{206}**	**1σ**	**Pb^{207}/U^{235}**	**1σ**	**Pb^{206}/U^{238}**	**1σ**	**rho**	**Pb^{207}/Pb^{206}**	**1σ**	**Pb^{206}/U^{238}**	**1σ**	**Pb^{207}/U^{235}**	**1σ**	**Pb**	**U**	**Th**
HUEL-2	52	0.05397	0.00059	0.42186	0.00508	0.0567	0.00064	0.9373495	369.7	24.53	355.5	3.91	357.4	3.63	60.2	628.5	124.6
HUEL-2	2a	0.05388	0.00063	0.43036	0.00543	0.05794	0.00065	0.88913342	365.8	26.12	363.1	3.99	363.4	3.85	29.2	271.6	141.5
HUEL-2	49b	0.05288	0.00056	0.43098	0.00508	0.05912	0.00067	0.96146567	323.5	23.87	370.3	4.07	363.9	3.61	136.2	1423.9	79.4
HUEL-2	63b	0.05277	0.0006	0.43937	0.00543	0.0604	0.00068	0.91096679	318.9	25.63	378	4.14	369.8	3.83	82.4	830.4	50.0

HUEL-2	11	0.05495	0.00059	0.47255	0.00558	0.06238	0.0007	0.95031205	410.3	23.45	390.1	4.27	392.9	3.85	136.7	1292.5	190.2
HUEL-2	57	0.05773	0.00068	0.54174	0.00691	0.06807	0.00077	0.88684522	519.2	25.86	424.5	4.66	439.6	4.55	124.1	1039.8	257.1
HUEL-2	14a	0.05665	0.00061	0.53214	0.00635	0.06814	0.00077	0.94697993	477.1	23.93	425	4.65	433.2	4.21	129.5	1129.1	161.1
HUEL-2	68	0.0578	0.00064	0.58044	0.00698	0.07284	0.00082	0.93615083	522.1	24.17	453.3	4.92	464.7	4.48	224.2	1544.7	1134.8
HUEL-2	44	0.05762	0.00068	0.60035	0.00768	0.07558	0.00085	0.87913452	514.9	25.52	469.7	5.11	477.5	4.87	14.2	158.9	29.7
HUEL-2	61	0.05895	0.00068	0.61877	0.00772	0.07614	0.00086	0.90531044	565.3	24.81	473	5.16	489.1	4.85	108.6	806.1	255.8
HUEL-2	9	0.05786	0.00063	0.62151	0.00748	0.07792	0.00088	0.93838326	524.1	24.07	483.7	5.26	490.8	4.68	64.9	484.8	105.1
HUEL-2	34a	0.06229	0.0007	0.68072	0.0084	0.07927	0.0009	0.92007425	684	23.91	491.8	5.37	527.2	5.08	79.6	842.0	153.3
HUEL-2	33	0.0585	0.00061	0.67121	0.00784	0.08323	0.00094	0.96691949	548.4	22.77	515.4	5.59	521.4	4.76	192.8	2082.0	106.4
HUEL-2	46b	0.05994	0.00067	0.72241	0.0089	0.08743	0.00099	0.91911205	601.3	24.06	540.3	5.89	552.1	5.24	80.4	518.3	179.4
HUEL-2	35	0.05763	0.00065	0.69537	0.00855	0.08752	0.00099	0.91997859	515.5	24.14	540.8	5.87	536	5.12	20.4	196.5	41.8
HUEL-2	46a	0.05875	0.00069	0.731	0.00921	0.09025	0.00102	0.89703773	557.9	25.25	557	6.01	557.1	5.4	31.2	306.6	22.8
HUEL-2	23a	0.0654	0.00105	0.82506	0.01371	0.09151	0.00108	0.71023697	787.2	33.25	564.5	6.36	610.9	7.63	3.8	33.8	8.3
HUEL-2	51a	0.06484	0.00076	0.82708	0.01053	0.09252	0.00105	0.8914004	769.2	24.46	570.4	6.21	612	5.85	111.5	611.3	424.3
HUEL-2	67	0.05965	0.00067	0.77059	0.0094	0.09371	0.00105	0.9185417	591	24.1	577.4	6.21	580.1	5.39	94.3	560.4	194.5
HUEL-2	24	0.05957	0.00069	0.77351	0.00979	0.09419	0.00108	0.90594577	587.9	24.91	580.3	6.34	581.8	5.61	11.7	102.9	26.5
HUEL-2	17b	0.05968	0.0007	0.79743	0.01012	0.09693	0.0011	0.89422443	591.8	25.07	596.4	6.48	595.4	5.72	38.1	229.5	54.7
HUEL-2	8b	0.06177	0.00066	0.82685	0.00973	0.0971	0.00109	0.95394022	666.2	22.63	597.4	6.43	611.9	5.41	103.6	559.7	326.0
HUEL-2	16	0.06007	0.0007	0.81021	0.01027	0.09784	0.00111	0.89502196	606.1	25	601.7	6.53	602.6	5.76	46.3	248.8	149.9
HUEL-2	4a	0.06071	0.00067	0.81932	0.00993	0.09789	0.0011	0.92716849	629.1	23.71	602	6.48	607.7	5.54	57.7	306.6	199.1
HUEL-2	14b	0.05917	0.00076	0.80292	0.01097	0.09843	0.00113	0.84026564	573.5	27.55	605.2	6.6	598.5	6.18	26.6	154.9	46.4
HUEL-2	42	0.06373	0.00107	0.86505	0.0149	0.09845	0.00115	0.67816764	732.7	35.13	605.3	6.75	632.9	8.11	3.9	33.5	5.3
HUEL-2	29	0.06026	0.00063	0.82037	0.00959	0.09875	0.00112	0.97022415	612.9	22.46	607.1	6.56	608.3	5.35	88.7	725.0	229.1
HUEL-2	56	0.06087	0.00065	0.83024	0.00981	0.09894	0.00112	0.95803365	634.7	22.84	608.2	6.55	613.7	5.44	149.4	773.9	536.6
HUEL-2	69	0.06138	0.00073	0.85179	0.01085	0.10066	0.00114	0.88910023	652.6	25.18	618.3	6.65	625.6	5.95	59.7	248.9	401.6
HUEL-2	12	0.05927	0.00076	0.82972	0.01131	0.10155	0.00116	0.83800578	576.9	27.49	623.5	6.78	613.5	6.28	15.9	74.3	77.6
HUEL-2	34b	0.06165	0.00066	0.88014	0.01046	0.10355	0.00117	0.95072701	662.1	22.87	635.2	6.83	641.1	5.65	50.1	387.0	127.0
HUEL-2	10	0.06184	0.00065	0.88706	0.0103	0.10404	0.00117	0.96850371	668.7	22.23	638.1	6.85	644.8	5.54	307.8	1624.4	698.3
HUEL-2	36b	0.06735	0.00083	1.0093	0.01329	0.1087	0.00124	0.86633814	848.7	25.27	665.2	7.2	708.5	6.72	11.9	84.0	33.9
HUEL-2	63a	0.06298	0.00071	0.95966	0.01175	0.11052	0.00125	0.92373769	707.7	23.72	675.8	7.23	683.1	6.09	92.1	381.5	447.4
HUEL-2	54a	0.10773	0.00111	4.3218	0.0499	0.29101	0.00328	0.97618033	1761.3	18.73	1646.6	16.39	1697.5	9.52	977.0	1994.7	8.7
HUEL-2	18b	0.27942	0.00299	23.09753	0.27438	0.59963	0.0068	0.95463785	3359.7	16.63	3028.3	27.39	3231.1	11.56	1179.7	994.8	119.2
HUEL-3	37	0.05705	0.00082	0.43274	0.00647	0.05502	0.00062	0.75369193	492.9	31.69	345.3	3.82	365.1	4.59	36.3	367.4	131.2
HUEL-3	24	0.05341	0.00057	0.44708	0.00522	0.06072	0.00067	0.94505651	346.2	23.96	380	4.1	375.2	3.66	185.9	1862.2	142.8
HUEL-3	22	0.05652	0.00066	0.4961	0.0062	0.06367	0.00071	0.89227975	471.9	25.79	397.9	4.31	409.1	4.21	48.2	449.1	56.2
HUEL-3	14b	0.05407	0.00071	0.50212	0.00701	0.06736	0.00077	0.81880059	373.7	29.52	420.2	4.63	413.1	4.74	31.5	279.6	51.6
HUEL-3	48a	0.05908	0.00065	0.59417	0.00723	0.07296	0.00083	0.93490114	569.9	23.95	453.9	4.97	473.5	4.61	81.9	550.9	411.1
HUEL-3	32b	0.05945	0.00064	0.67686	0.00797	0.08258	0.00092	0.9461358	583.7	23.31	511.5	5.47	524.9	4.83	78.4	569.5	67.5
HUEL-3	13	0.06365	0.00078	0.73011	0.00959	0.08321	0.00094	0.86004668	729.9	25.75	515.2	5.62	556.6	5.63	45.1	311.1	80.4
HUEL-3	41	0.05896	0.00084	0.72051	0.01067	0.08864	0.001	0.76180856	565.5	30.57	547.5	5.95	551	6.3	9.0	56.5	20.2
HUEL-3	38a	0.05703	0.00066	0.72877	0.00909	0.09269	0.00104	0.89955363	492.2	25.69	571.4	6.11	555.8	5.34	33.6	200.2	81.5
HUEL-3	14a	0.06108	0.00074	0.78952	0.01032	0.09376	0.00106	0.86491157	642.1	25.98	577.7	6.27	590.9	5.86	25.1	147.2	73.8
HUEL-3	9a	0.06576	0.00081	0.86647	0.01148	0.09557	0.00109	0.86082834	798.7	25.73	588.4	6.41	633.6	6.25	67.7	411.4	80.9
HUEL-3	6a	0.06064	0.00065	0.83765	0.00988	0.1002	0.00113	0.95612873	626.4	22.87	615.6	6.63	617.8	5.46	67.3	368.5	187.1
HUEL-3	29	0.06878	0.0011	1.09141	0.01786	0.1151	0.00133	0.70612696	892	32.59	702.3	7.69	749.2	8.67	21.5	84.5	103.8
HUEL-3	42	0.06886	0.00104	1.12018	0.01772	0.118	0.00139	0.74465805	894.5	30.92	719.1	7.99	763.1	8.49	24.3	98.8	93.3
HUEL-3	7	0.0633	0.00069	1.05106	0.01257	0.12043	0.00136	0.94427057	718.4	22.94	733.1	7.83	729.4	6.22	43.8	214.5	54.1
HUEL-3	47	0.07141	0.00085	1.29354	0.01664	0.13139	0.0015	0.88747369	969.2	23.99	795.8	8.55	842.9	7.37	64.9	265.2	127.7
HUEL-3	30a	0.10675	0.00115	3.9793	0.04671	0.2704	0.00301	0.94832374	1744.6	19.63	1542.8	15.29	1630	9.53	78.5	140.6	113.6
HUEL-3	40a	0.12537	0.00136	6.41082	0.07581	0.3709	0.00413	0.94163004	2034.1	19.09	2033.6	19.44	2033.8	10.39	164.2	240.4	73.2
HUEL-3	10	0.17404	0.00181	10.04778	0.11595	0.41875	0.00471	0.97468762	2596.9	17.25	2254.8	21.41	2439.2	10.66	908.7	1223.2	36.2

Analyses en Hf sur zircon : orthogneiss paléozoïques

	$^{176}Yb/^{177}Hf$ [a]	±2s	$^{176}Lu/^{177}Hf$ [a]	±2s	$^{178}Hf/^{177}Hf$	$^{180}Hf/^{177}Hf$	Sig_{Hf} [b] (V)	$^{176}Hf/^{177}Hf$	±2s [c]	$^{176}Hf/^{177}Hf_{(t)}$ [d]	$\varepsilon Hf_{(t)}$ [d]	±2s [c]	T_{DM2} [e] (Ga)	age [f] (Ma)	±2s
QIMP-1-1	0.0249	12	0.00075	3	1.46720	1.88661	9	0.282573	35	0.282566	2.7	1.2	1.22	466.8	3.0
QIMP-1-2	0.0233	9	0.00067	2	1.46709	1.88663	10	0.282565	33	0.282559	2.4	1.2	1.23	466.8	3.0
QIMP-1-5	0.1028	102	0.00236	23	1.46717	1.88451	8	0.282644	44	0.282623	4.7	1.6	1.11	466.8	3.0
QIMP-1-6	0.0319	44	0.00082	9	1.46720	1.88656	9	0.282622	31	0.282615	4.4	1.1	1.12	466.8	3.0
QIMP-1-7	0.0438	47	0.00125	12	1.46722	1.88667	9	0.282593	31	0.282582	3.2	1.1	1.19	466.8	3.0
QIMP-1-9	0.0277	8	0.00081	2	1.46719	1.88677	8	0.282567	35	0.282560	2.4	1.3	1.23	466.8	3.0
QIMP-1-14	0.1416	122	0.00343	30	1.46733	1.88349	6	0.282679	31	0.282649	5.6	1.1	1.06	466.8	3.0
QIMP-1-19	0.0424	39	0.00126	11	1.46721	1.88595	7	0.282639	46	0.282628	4.8	1.6	1.10	466.8	3.0
QIMP-1-18	0.1029	84	0.00257	18	1.46712	1.88671	11	0.282660	34	0.282638	5.2	1.2	1.08	466.8	3.0
QIMP-1-25	0.0538	32	0.00155	9	1.46714	1.88665	8	0.282581	33	0.282568	2.7	1.2	1.22	466.8	3.0
PLG-2-94	0.0500	20	0.00164	6	1.46717	1.88579	7	0.282601	33	0.282586	4.2	1.2	1.17	502.3	2.1
PLG-2-17	0.0492	49	0.00168	15	1.46715	1.88684	7	0.282658	35	0.282642	6.2	1.2	1.06	502.3	2.1
PLG-2-88	0.0597	48	0.00195	15	1.46713	1.88734	9	0.282613	36	0.282595	4.5	1.3	1.15	502.3	2.1
PLG-2-16	0.0453	15	0.00155	4	1.46713	1.88713	7	0.282620	59	0.282605	4.8	2.1	1.13	502.3	2.1
PLG-2-14	0.0598	18	0.00194	6	1.46715	1.88721	7	0.282643	34	0.282625	5.5	1.2	1.09	502.3	2.1
PLG-2-15	0.0332	13	0.00114	4	1.46712	1.88635	9	0.282596	29	0.282585	4.1	1.0	1.17	502.3	2.1
PLG-2-8	0.2014	41	0.00641	12	1.46716	1.88694	7	0.282841	33	0.282781	11.1	1.2	0.78	502.3	2.1
PLG-2-1	0.0657	61	0.00218	19	1.46715	1.88671	8	0.282662	33	0.282641	6.1	1.2	1.06	502.3	2.1
PLG-2-30b	0.0265	5	0.00094	2	1.46724	1.88670	7	0.282617	31	0.282608	4.9	1.1	1.12	502.3	2.1
PLG-2-78	0.0338	8	0.00115	2	1.46715	1.88669	7	0.282601	29	0.282590	4.3	1.0	1.16	502.3	2.1
PLG-2-86b	0.0446	33	0.00155	10	1.46713	1.88709	7	0.282654	34	0.282640	6.1	1.2	1.06	502.3	2.1
PLG-1-1	0.0817	18	0.00261	5	1.46717	1.88602	7	0.282665	36	0.282641	5.6	1.3	1.07	477.9	2.9
PLG-1-18	0.0545	19	0.00189	6	1.46719	1.88658	9	0.282854	32	0.282837	12.5	1.1	0.68	477.9	2.9
PLG-1-19	0.0961	44	0.00308	8	1.46714	1.88762	8	0.282822	42	0.282794	11.0	1.5	0.77	477.9	2.9
PLG-1-21	0.0808	39	0.00256	9	1.46714	1.88696	9	0.282829	34	0.282807	11.4	1.2	0.74	477.9	2.9
PLG-1-23	0.0657	45	0.00210	14	1.46717	1.88678	10	0.282614	31	0.282595	3.9	1.1	1.16	477.9	2.9
PLG-1-22	0.0714	9	0.00220	3	1.46715	1.88660	9	0.282786	32	0.282766	10.0	1.1	0.82	477.9	2.9
PLG-1-25	0.0212	36	0.00062	12	1.46720	1.88625	10	0.282578	31	0.282572	3.1	1.1	1.20	477.9	2.9
PLG-1-26	0.0519	17	0.00177	6	1.46705	1.88735	10	0.282841	35	0.282825	12.1	1.2	0.71	477.9	2.9
PLG-1-27	0.0630	13	0.00214	4	1.46718	1.88610	9	0.282829	33	0.282810	11.5	1.2	0.74	477.9	2.9
PLG-1-29	0.0446	38	0.00127	10	1.46721	1.88677	9	0.282556	29	0.282544	2.1	1.0	1.26	477.9	2.9
PLG-1-35	0.0722	22	0.00254	8	1.46716	1.88658	9	0.282914	33	0.282891	14.4	1.2	0.58	477.9	2.9
PLG-1-38	0.0757	33	0.00245	7	1.46710	1.89051	8	0.282896	37	0.282874	13.8	1.3	0.61	477.9	2.9
PLG-1-39	0.0355	127	0.00096	35	1.46719	1.88689	9	0.282623	32	0.282615	4.6	1.1	1.12	477.9	2.9
PLG-1-42	0.0749	25	0.00245	9	1.46711	1.88663	10	0.282845	31	0.282823	12.0	1.1	0.71	477.9	2.9
PLG-1-43	0.0558	11	0.00186	3	1.46715	1.88662	8	0.282601	32	0.282584	3.6	1.1	1.18	477.9	2.9
PLG-1-46	0.0080	14	0.00026	5	1.46717	1.88634	9	0.282462	32	0.282460	-0.9	1.2	1.42	477.9	2.9

Analyses en Hf sur zircon : sédiment briovérien

	$^{176}Yb/^{177}Hf$ [a]	±2s	$^{176}Lu/^{177}Hf$ [a]	±2s	$^{178}Hf/^{177}Hf$	$^{180}Hf/^{177}Hf$	Sig_{Hf} [b] (V)	$^{176}Hf/^{177}Hf$	±2s [c]	$^{176}Hf/^{177}Hf_{(t)}$ [d]	$\varepsilon Hf_{(t)}$ [d]	±2s [c]	T_{DM2} [e] (Ga)	age [f] (Ma)	±2s	conc.[g]
CRO-9-1-co	0.0197	3	0.00083	1	1.46716	1.88667	7	0.282672	34	0.282661	11.5	1.2	0.92	711	8	100
CRO-9-2	0.0573	11	0.00187	4	1.46717	1.88681	9	0.282498	30	0.282478	1.5	1.1	1.35	552	6	101
CRO-9-3	0.0472	17	0.00154	5	1.46718	1.88669	10	0.282446	29	0.282430	-0.3	1.0	1.45	550	6	101
CRO-9-4	0.0414	19	0.00139	6	1.46721	1.88670	8	0.282189	36	0.282174	-8.6	1.3	1.93	583	7	99
CRO-9-6-co	0.0221	8	0.00070	3	1.46723	1.88642	8	0.281795	33	0.281787	-21.7	1.2	2.66	610	7	100
CRO-9-5	0.0141	5	0.00049	2	1.46722	1.88645	10	0.282632	33	0.282626	7.3	1.2	1.05	580	7	101
CRO-9-7	0.0215	8	0.00075	3	1.46722	1.88601	10	0.282385	28	0.282376	-1.0	1.0	1.53	605	7	100
CRO-9-9	0.0544	19	0.00177	7	1.46716	1.88648	9	0.282563	30	0.282538	8.0	1.1	1.15	746	8	100
CRO-9-10	0.0350	10	0.00108	3	1.46720	1.88626	10	0.282576	31	0.282564	5.3	1.1	1.17	588	7	100
CRO-9-15	0.0766	18	0.00245	5	1.46700	1.88759	9	0.282534	35	0.282510	2.0	1.2	1.30	526	6	101
CRO-9-16	0.0219	6	0.00073	1	1.46715	1.88646	8	0.282580	31	0.282570	8.7	1.1	1.09	729	8	102
CRO-9-21-rim	0.0131	2	0.00043	1	1.46721	1.88663	8	0.282456	31	0.282452	0.3	1.1	1.41	541	6	100
CRO-9-23	0.0211	10	0.00064	3	1.46721	1.88636	8	0.282473	35	0.282466	1.2	1.2	1.37	560	6	101
CRO-9-31	0.0334	18	0.00100	6	1.46722	1.88645	11	0.282529	33	0.282514	8.1	1.2	1.18	790	9	102
CRO-9-32	0.0196	8	0.00064	2	1.46725	1.88650	8	0.281096	33	0.281079	-28.0	1.2	3.65	1444	15	109
CRO-9-33	0.0186	3	0.00064	1	1.46722	1.88627	8	0.282355	35	0.282347	-0.9	1.2	1.56	655	7	104
CRO-9-35	0.0175	3	0.00055	1	1.46717	1.88676	8	0.282216	37	0.282209	-6.2	1.3	1.84	635	7	100
CRO-9-36	0.0178	11	0.00057	3	1.46716	1.88671	8	0.280938	30	0.280918	-24.3	1.1	3.78	1854	19	101
CRO-9-38	0.0308	10	0.00107	4	1.46715	1.88627	7	0.282574	33	0.282563	4.8	1.2	1.18	568	6	100
CRO-9-39	0.0801	11	0.00234	4	1.46720	1.88661	7	0.282719	34	0.282687	13.1	1.2	0.86	743	8	100
CRO-9-40	0.0185	6	0.00059	2	1.46723	1.88663	8	0.282648	33	0.282640	10.8	1.2	0.96	712	8	102
CRO-9-41	0.0261	20	0.00081	6	1.46725	1.88588	7	0.282400	34	0.282384	8.7	1.2	1.32	1019	11	99
CRO-9-44	0.0107	24	0.00039	8	1.46727	1.88716	9	0.282483	37	0.282476	8.0	1.3	1.22	845	9	102
CRO-9-45	0.0313	4	0.00105	1	1.46717	1.88659	8	0.282519	31	0.282507	3.6	1.1	1.27	603	7	101
CRO-9-47	0.0370	17	0.00110	5	1.46716	1.88675	8	0.282519	33	0.282507	3.5	1.2	1.28	598	7	99
CRO-9-49	0.0219	4	0.00074	1	1.46716	1.88633	8	0.281703	34	0.281680	-1.5	1.2	2.39	1669	17	103
CRO-9-50-rim	0.0225	9	0.00069	2	1.46718	1.88636	9	0.281852	32	0.281845	-20.1	1.1	2.56	590	7	101
CRO-9-52	0.0334	12	0.00104	3	1.46731	1.88517	7	0.281355	39	0.281317	-8.9	1.4	2.99	1906	19	103
CRO-9-54-rim	0.0292	7	0.00096	2	1.46722	1.88653	9	0.282482	33	0.282471	2.4	1.2	1.34	606	7	100
CRO-9-55	0.0332	17	0.00105	5	1.46723	1.88630	9	0.282507	33	0.282495	3.0	1.2	1.30	593	7	100
CRO-9-60	0.0044	1	0.00012	0	1.46724	1.88642	9	0.281455	28	0.281451	-3.6	1.0	2.72	1929	20	99
CRO-9-62-co	0.0210	3	0.00066	1	1.46715	1.88655	8	0.281773	29	0.281755	-4.3	1.0	2.36	1428	15	100
CRO-9-64	0.0123	3	0.00040	1	1.46716	1.88658	8	0.280975	30	0.280956	-8.8	1.1	3.42	2464	24	101
CRO-9-65	0.0256	10	0.00081	3	1.46723	1.88614	8	0.282480	33	0.282472	1.7	1.2	1.36	572	6	101
CRO-9-66	0.0118	3	0.00038	1	1.46713	1.88640	8	0.280936	33	0.280920	-13.1	1.2	3.55	2335	23	102
CRO-9-70	0.0148	3	0.00053	1	1.46716	1.88650	7	0.282258	34	0.282252	-5.4	1.2	1.77	605	7	101
CRO-9-73	0.0361	12	0.00113	4	1.46723	1.88537	9	0.282166	35	0.282148	-3.5	1.2	1.86	851	9	101
CRO-9-74	0.0293	6	0.00096	2	1.46711	1.88653	8	0.282547	34	0.282537	3.4	1.2	1.24	548	6	101
CRO-9-75	0.0230	10	0.00076	3	1.46723	1.88638	10	0.281040	32	0.281001	-1.2	1.2	3.20	2719	26	101
CRO-9-80	0.0143	4	0.00049	1	1.46721	1.88690	9	0.281449	31	0.281433	-9.1	1.1	2.85	1719	18	106
CRO-9-81	0.0262	12	0.00092	4	1.46718	1.88667	6	0.282510	35	0.282498	5.9	1.3	1.24	717	8	100
CRO-9-86	0.0453	11	0.00149	4	1.46719	1.88664	8	0.282537	33	0.282520	4.2	1.2	1.25	611	7	100
CRO-9-93	0.0249	4	0.00077	2	1.46716	1.88685	8	0.281072	35	0.281035	-5.3	1.2	3.25	2492	24	100
CRO-9-96	0.0298	7	0.00095	2	1.46718	1.88569	8	0.282448	36	0.282437	2.1	1.3	1.39	646	7	100
CRO-9-97	0.0227	9	0.00077	3	1.46724	1.88658	8	0.282176	31	0.282167	-8.5	1.1	1.94	598	7	100
CRO-9-98-rim	0.0117	1	0.00040	1	1.46717	1.88653	7	0.282291	35	0.282286	-2.6	1.2	1.67	675	8	100
CRO-9-99	0.0342	24	0.00095	3	1.46714	1.88637	9	0.282286	40	0.282274	-3.8	1.4	1.71	641	7	100

CRO-9-111	0.0266	32	0.00082	10	1.46724	1.88686	9	0.282503	34	0.282494	3.3	1.2	1.30	610	7	99
CRO-9-112-co	0.0546	10	0.00196	3	1.46722	1.88661	10	0.280906	32	0.280790	-0.5	1.1	3.43	3070	28	100

Analyses en Hf sur zircon : sédiment silurien

	$^{176}Yb/^{177}Hf$	±2s	$^{176}Lu/^{177}Hf$ [a]	±2s	$^{178}Hf/^{177}Hf$	$^{180}Hf/^{177}Hf$	Sig_{Hf} [b] (V)	$^{176}Hf/^{177}Hf$	±2s [c]	$^{176}Hf/^{177}Hf_{(t)}$	$\varepsilon Hf_{(t)}$ [d]	±2s [c]	T_{DM2} [e] (Ga)	age [f] (Ma)	±2s	conc.[g]
CRO-6-18	0.0180	11	0.00062	4	1.46712	1.88667	9	0.282141	31	0.282135	-10.6	1.1	2.02	557	6	100
CRO-6-20-rim	0.0109	4	0.00036	1	1.46723	1.88628	8	0.282219	36	0.282214	-2.0	1.3	1.75	816	9	102
CRO-6-3-rim	0.0203	11	0.00067	3	1.46718	1.88625	10	0.282104	31	0.282091	-1.1	1.1	1.88	1047	11	100
CRO-6-21	0.0317	10	0.00102	3	1.46719	1.88827	10	0.281837	35	0.281818	-12.8	1.2	2.45	955	10	101
CRO-6-22	0.0339	11	0.00111	3	1.46715	1.88640	6	0.282151	34	0.282136	-6.9	1.2	1.94	721	8	100
CRO-6-23	0.0169	11	0.00069	5	1.46716	1.88832	11	0.282564	42	0.282555	7.3	1.5	1.14	688	7	101
CRO-6-24	0.0209	6	0.00064	3	1.46715	1.88668	9	0.281464	34	0.281437	1.9	1.2	2.62	2187	21	100
CRO-6-15	0.0474	12	0.00158	4	1.46714	1.88694	8	0.281221	34	0.281138	4.0	1.2	2.92	2733	26	100
CRO-6-14	0.0084	5	0.00026	2	1.46740	1.88478	7	0.280897	37	0.280885	-10.5	1.3	3.54	2500	24	102
CRO-6-27	0.0626	24	0.00194	7	1.46716	1.88693	8	0.282575	32	0.282552	5.8	1.1	1.17	630	7	102
CRO-6-12-co	0.0216	5	0.00071	1	1.46719	1.88663	7	0.282226	32	0.282212	2.9	1.1	1.65	1035	11	101
CRO-6-29	0.0083	11	0.00030	4	1.46718	1.88665	10	0.282475	34	0.282471	2.8	1.2	1.33	624	7	102
CRO-6-10	0.0160	5	0.00055	1	1.46714	1.88646	8	0.282310	32	0.282302	-0.2	1.1	1.60	756	8	101
CRO-6-4-rim	0.0114	4	0.00039	2	1.46720	1.88627	8	0.281150	33	0.281131	-0.4	1.2	3.03	2559	24	101
CRO-6-1	0.0174	5	0.00068	2	1.46717	1.88627	8	0.280927	36	0.280891	-4.7	1.3	3.41	2739	26	103
CRO-6-6	0.0373	25	0.00123	8	1.46718	1.88564	8	0.282189	34	0.282165	1.4	1.2	1.74	1041	11	101
CRO-6-7	0.0273	11	0.00094	4	1.46714	1.88679	9	0.282050	32	0.282031	-3.2	1.1	2.00	1048	11	101
CRO-6-37	0.0285	16	0.00097	4	1.46723	1.88578	7	0.282468	34	0.282454	4.8	1.2	1.32	739	8	101
CRO-6-35	0.0205	3	0.00067	1	1.46719	1.88660	8	0.282157	30	0.282147	-5.0	1.0	1.89	788	9	102
CRO-6-59-co	0.0173	8	0.00055	3	1.46716	1.88633	10	0.281275	30	0.281255	-10.8	1.1	3.10	1920	19	101
CRO-6-34-rim	0.0211	8	0.00070	3	1.46728	1.88499	7	0.281408	36	0.281381	-4.6	1.3	2.82	1992	20	100
CRO-6-32-co	0.0170	2	0.00056	1	1.46712	1.88624	9	0.282123	31	0.282112	-0.3	1.1	1.84	1047	11	100
CRO-6-33	0.0338	19	0.00113	6	1.46715	1.88646	9	0.281619	31	0.281580	-1.6	1.1	2.52	1819	18	102
CRO-6-57-co	0.0156	3	0.00047	1	1.46714	1.88616	7	0.281172	34	0.281154	-10.9	1.2	3.23	2069	20	101
CRO-6-58-co	0.0206	5	0.00066	1	1.46722	1.88668	8	0.281337	34	0.281312	-7.1	1.2	2.96	1989	19	101
CRO-6-60	0.0211	11	0.00070	4	1.46718	1.88652	10	0.282315	32	0.282301	5.8	1.1	1.48	1023	11	100
CRO-6-56	0.0183	2	0.00057	1	1.46718	1.88668	9	0.281965	32	0.281954	-7.1	1.1	2.17	995	11	101
CRO-6-55	0.0327	11	0.00106	3	1.46720	1.88586	8	0.282204	39	0.282193	-8.3	1.4	1.90	566	6	101
CRO-6-44	0.0173	10	0.00055	3	1.46714	1.88675	9	0.282065	31	0.282054	-2.1	1.1	1.95	1059	11	100
CRO-6-40-rim	0.0177	4	0.00051	1	1.46723	1.88663	9	0.281957	32	0.281948	-10.0	1.1	2.24	879	9	101
CRO-6-41-co	0.0340	4	0.00116	1	1.46719	1.88661	9	0.281999	31	0.281977	-6.1	1.1	2.12	1004	11	103
CRO-6-48-co	0.0167	17	0.00060	6	1.46717	1.88666	8	0.281697	31	0.281685	-15.5	1.1	2.67	1045	11	101
CRO-6-49	0.0497	32	0.00175	11	1.46729	1.88654	6	0.281930	36	0.281899	-10.2	1.3	2.30	947	10	101
CRO-6-52	0.0161	2	0.00051	0	1.46722	1.88661	7	0.281362	33	0.281344	-9.2	1.2	2.96	1850	18	101
CRO-6-50	0.0202	9	0.00069	4	1.46718	1.88621	9	0.282480	32	0.282470	6.9	1.1	1.25	808	9	103
CRO-6-75	0.0269	16	0.00096	6	1.46722	1.88654	7	0.281571	41	0.281534	1.5	1.4	2.51	2021	20	100
CRO-6-73	0.1027	133	0.00282	28	1.46723	1.88556	7	0.281260	35	0.281114	2.5	1.2	2.99	2706	25	100
CRO-6-61	0.0334	20	0.00115	6	1.46719	1.88637	8	0.281495	32	0.281454	-4.6	1.1	2.73	1880	19	100
CRO-6-62	0.0375	7	0.00116	2	1.46724	1.88684	8	0.282599	33	0.282585	7.2	1.2	1.11	637	7	100
CRO-6-64	0.0280	4	0.00096	1	1.46718	1.88554	7	0.282149	32	0.282132	-1.9	1.1	1.85	947	10	101
CRO-6-71	0.0203	4	0.00063	1	1.46722	1.88654	10	0.281773	30	0.281761	-12.7	1.0	2.52	1051	11	100
CRO-6-79	0.1166	390	0.00291	83	1.46718	1.88644	8	0.282481	31	0.282424	10.5	1.1	1.24	1037	11	101
CRO-6-78-co	0.0254	10	0.00078	3	1.46712	1.88662	8	0.281665	31	0.281649	-16.6	1.1	2.73	1052	11	100

CRO-6-81	0.0098	14	0.00037	4	1.46714	1.88723	9	0.281840	31	0.281833	-12.2	1.1	2.42	959	10	101
CRO-6-80	0.0323	7	0.00101	2	1.46724	1.88624	10	0.281666	32	0.281646	-17.1	1.1	2.75	1039	11	100
CRO-6-67	0.0496	34	0.00154	9	1.46731	1.88534	8	0.282415	43	0.282399	-1.4	1.5	1.51	548	6	102
CRO-6-69	0.0175	13	0.00057	4	1.46723	1.88576	7	0.281523	39	0.281501	2.0	1.4	2.54	2098	20	101
CRO-6-68	0.0310	14	0.00110	5	1.46725	1.88530	8	0.281566	34	0.281528	-4.1	1.2	2.63	1790	18	102
CRO-6-84	0.0172	11	0.00055	3	1.46719	1.88700	9	0.280976	32	0.280948	-4.6	1.1	3.34	2656	25	100
CRO-6-76	0.0719	54	0.00215	13	1.46720	1.88612	11	0.282343	32	0.282321	-4.5	1.1	1.67	536	6	101
CRO-6-87-rim	0.0337	18	0.00116	7	1.46707	1.88649	10	0.281649	32	0.281627	-18.3	1.1	2.79	1016	11	99
CRO-6-86-co	0.0611	33	0.00200	10	1.46717	1.88624	9	0.281515	35	0.281440	-3.3	1.2	2.72	1959	19	100
CRO-6-85	0.0206	9	0.00055	2	1.46721	1.88675	9	0.281928	30	0.281918	-10.7	1.1	2.29	891	10	109
CRO-6-88	0.0156	11	0.00046	3	1.46724	1.88620	9	0.282026	29	0.282020	-12.2	1.0	2.19	664	7	101
CRO-6-89	0.0230	27	0.00075	7	1.46724	1.88659	8	0.281719	47	0.281703	-14.4	1.7	2.62	1065	11	101

Analyses en Hf sur zircon : sédiment dévonien

	$^{176}Yb/^{177}Hf$	±2s	$^{176}Lu/^{177}Hf$ [a]	±2s	$^{178}Hf/^{177}Hf$	$^{180}Hf/^{177}Hf$	Sig_{Hf} [b] (V)	$^{176}Hf/^{177}Hf$	±2s [c]	$^{176}Hf/^{177}Hf_{(t)}$	$\varepsilon Hf_{(t)}$ [d]	±2s [c]	T_{DM2} [e] (Ga)	age [f] (Ma)	±2s	conc.[g]
CRO-11-11	0.0466	28	0.00174	8	1.46720	1.88589	8	0.282143	34	0.282124	-10.2	1.2	2.02	593	7	100
CRO-11-8	0.0287	11	0.00106	3	1.46727	1.88503	8	0.281041	32	0.281019	-38.0	1.1	3.91	1097	21	101
CRO-11-14	0.0184	16	0.00067	3	1.46721	1.88570	10	0.281388	32	0.281363	-6.5	1.1	2.88	1940	19	102
CRO-11-23	0.0410	15	0.00123	4	1.46716	1.88762	8	0.282237	33	0.282223	-6.2	1.2	1.82	611	7	100
CRO-11-22-co	0.0336	10	0.00116	4	1.46713	1.88555	8	0.281217	46	0.281154	6.0	1.6	2.86	2796	18	100
CRO-11-25-rim	0.0255	14	0.00082	4	1.46715	1.88538	8	0.282051	34	0.282035	-2.7	1.2	1.99	1063	22	100
CRO-11-29-co	0.0148	6	0.00054	2	1.46714	1.88653	8	0.281516	41	0.281497	-3.9	1.5	2.66	1848	19	100
CRO-11-33	0.0325	19	0.00104	7	1.46727	1.88755	6	0.281931	39	0.281911	-8.2	1.4	2.25	1014	23	102
CRO-11-36	0.0669	42	0.00253	16	1.46715	1.88743	7	0.282446	31	0.282397	9.2	1.1	1.30	1022	22	101
CRO-11-38	0.0327	21	0.00094	5	1.46721	1.88525	5	0.282554	38	0.282543	5.1	1.3	1.20	611	7	102
CRO-11-43	0.0079	1	0.00023	0	1.46724	1.88642	7	0.282390	34	0.282388	-2.5	1.2	1.54	519	6	101
CRO-11-49	0.0308	15	0.00105	4	1.46719	1.88637	7	0.281720	34	0.281700	-15.1	1.2	2.64	1041	28	102
CRO-11-51	0.0252	13	0.00082	4	1.46717	1.88554	9	0.281955	32	0.281939	-7.7	1.1	2.20	993	11	100
CRO-11-70	0.0384	24	0.00120	7	1.46714	1.88680	10	0.282120	29	0.282096	-0.9	1.0	1.87	1049	22	99
CRO-11-74	0.0284	10	0.00089	3	1.46719	1.88629	8	0.282041	32	0.282026	-6.9	1.1	2.08	890	10	101
CRO-11-76-co	0.0132	2	0.00047	1	1.46720	1.88549	8	0.282379	33	0.282372	3.7	1.2	1.44	818	9	101
CRO-11-77	0.0189	10	0.00068	3	1.46730	1.88545	7	0.282614	36	0.282606	7.9	1.3	1.07	637	7	101
CRO-11-67	0.0070	11	0.00015	2	1.46719	1.88563	11	0.282238	28	0.282236	0.8	1.0	1.67	903	10	102
CRO-11-64	0.0243	21	0.00079	6	1.46717	1.88583	9	0.280952	31	0.280913	-6.7	1.1	3.42	2618	17	101
CRO-11-81-rim	0.0340	68	0.00087	13	1.46719	1.88648	8	0.282384	33	0.282375	-1.8	1.2	1.55	570	7	102
CRO-11-82	0.0210	7	0.00068	2	1.46706	1.88593	6	0.281340	36	0.281315	-7.8	1.3	2.97	1956	21	99
CRO-11-83	0.0295	6	0.00099	2	1.46725	1.88605	10	0.281210	34	0.281194	-37.4	1.2	3.68	846	9	889
CRO-11-86	0.0182	9	0.00058	3	1.46721	1.88695	7	0.282144	46	0.282138	-10.1	1.6	2.00	574	6	598
CRO-11-87	0.0120	5	0.00038	1	1.46716	1.88609	9	0.281265	31	0.281251	-9.2	1.1	3.07	1997	19	99
CRO-11-90	0.0349	14	0.00119	5	1.46715	1.88591	7	0.282045	39	0.282027	-8.8	1.4	2.11	808	9	101
CRO-11-99	0.0402	22	0.00140	7	1.46716	1.88632	9	0.282153	32	0.282128	-1.9	1.1	1.85	956	10	100
CRO-11-108-co	0.0593	88	0.00182	18	1.46720	1.88585	7	0.282339	43	0.282304	5.8	1.5	1.48	1016	23	100

Analyses en Hf sur zircon : sédiment carbonifère inférieur

	$^{176}Yb/^{177}Hf$	±2s	$^{176}Lu/^{177}Hf$ [a]	±2s	$^{178}Hf/^{177}Hf$	$^{180}Hf/^{177}Hf$	Sig_{Hf} [b] (V)	$^{176}Hf/^{177}Hf$	±2s[c]	$^{176}Hf/^{177}Hf_{(t)}$	$\varepsilon Hf_{(t)}$ [d]	±2s[c]	T_{DM2} [e] (Ga)	age [f] (Ma)	±2s	conc.[g]
LOC-1-5-co	0.0187	6	0.00062	2	1.46718	1.88639	8	0.282312	31	0.282305	-3.3	1.1	1.66	611	7	102
LOC-1-8	0.0351	41	0.00125	15	1.46709	1.88621	8	0.282292	32	0.282282	-8.1	1.1	1.79	434	5	101
LOC-1-10	0.0175	5	0.00055	2	1.46721	1.88570	7	0.282372	47	0.282366	-2.2	1.7	1.56	568	6	100
LOC-1-10	0.0175	5	0.00055	2	1.46721	1.88570	7	0.282372	47	0.282353	24.5	1.7	1.02	1760	20	100
LOC-1-16-rim	0.0060	3	0.00022	1	1.46718	1.88645	7	0.282670	33	0.282667	7.8	1.2	0.99	538	6	102
LOC-1-17	0.0388	4	0.00139	2	1.46723	1.88550	6	0.282362	31	0.282347	-2.9	1.1	1.60	563	6	100
LOC-1-18	0.0140	8	0.00042	2	1.46719	1.88616	7	0.281158	39	0.281142	-13.1	1.4	3.28	1992	20	100
LOC-1-23-co	0.0140	10	0.00044	3	1.46716	1.88658	8	0.281265	32	0.281249	-11.7	1.1	3.12	1890	20	100
LOC-1-25-co	0.0018	2	0.00005	1	1.46721	1.88646	11	0.282419	26	0.282419	-4.5	0.9	1.54	379	26	100
LOC-1-26	0.0401	27	0.00121	9	1.46719	1.88584	7	0.282695	32	0.282684	7.6	1.1	0.97	503	6	100
LOC-1-27-co	0.0518	21	0.00170	8	1.46722	1.88521	8	0.282412	34	0.282395	-1.6	1.2	1.52	547	6	100
LOC-1-28	0.0382	14	0.00123	4	1.46723	1.88586	7	0.281449	35	0.281392	5.3	1.2	2.60	2402	19	103
LOC-1-29	0.0230	14	0.00073	5	1.46718	1.88648	8	0.281895	44	0.281870	7.8	1.6	1.97	1780	19	100
LOC-1-31	0.0216	7	0.00084	3	1.46718	1.88661	7	0.282696	33	0.282687	8.0	1.2	0.96	513	6	100
LOC-1-37-co	0.0356	33	0.00117	9	1.46717	1.88587	9	0.282631	33	0.282619	6.0	1.2	1.09	531	6	100
LOC-1-38-rim	0.0213	2	0.00076	1	1.46722	1.88633	7	0.281699	38	0.281690	-25.4	1.3	2.85	601	7	100
LOC-1-38	0.0213	2	0.00076	1	1.46722	1.88633	7	0.281699	38	0.281694	-30.9	1.3	2.94	345	4	99
LOC-1-45	0.0254	17	0.00084	4	1.46715	1.88670	9	0.282519	33	0.282511	1.5	1.2	1.31	504	6	99
LOC-1-49	0.0166	8	0.00055	2	1.46722	1.88655	8	0.282497	34	0.282493	-2.4	1.2	1.41	354	4	99
LOC-1-50	0.0534	34	0.00161	9	1.46727	1.88510	6	0.282605	36	0.282590	4.3	1.3	1.16	501	6	100
LOC-1-51	0.0245	3	0.00080	1	1.46717	1.88628	9	0.282507	29	0.282502	-2.5	1.0	1.40	338	4	99
LOC-1-53-co	0.0288	9	0.00100	3	1.46724	1.88568	8	0.282520	34	0.282510	1.5	1.2	1.31	502	6	100
LOC-1-63-rim	0.0255	11	0.00077	4	1.46730	1.88418	7	0.282409	36	0.282403	-3.3	1.3	1.54	457	5	101
LOC-1-55	0.0325	15	0.00097	4	1.46718	1.88656	8	0.282485	32	0.282479	-3.5	1.1	1.45	332	4	100
LOC-1-56	0.0270	12	0.00087	4	1.46717	1.88670	8	0.282609	28	0.282603	1.1	1.0	1.20	338	4	100
LOC-1-57	0.0214	58	0.00054	15	1.46716	1.88670	10	0.282353	31	0.282350	-7.9	1.1	1.69	338	4	101
LOC-1-64-rim	0.0032	13	0.00008	3	1.46720	1.88638	11	0.282577	29	0.282576	1.3	1.0	1.23	390	4	100
LOC-1-65	0.0239	7	0.00084	3	1.46718	1.88565	11	0.282081	33	0.282076	-17.1	1.2	2.21	361	4	101
LOC-1-67	0.0572	25	0.00180	7	1.46717	1.88639	10	0.282609	32	0.282591	4.6	1.1	1.15	514	6	99
LOC-1-68	0.0246	2	0.00086	1	1.46721	1.88636	10	0.282509	31	0.282503	-2.4	1.1	1.40	341	4	102
LOC-1-71-rim	0.0184	23	0.00054	7	1.46722	1.88667	12	0.282561	30	0.282556	2.9	1.1	1.23	491	6	100
LOC-1-79	0.0249	7	0.00083	2	1.46716	1.88621	9	0.282397	33	0.282392	-6.4	1.2	1.61	339	4	102
LOC-1-75	0.0329	45	0.00096	13	1.46714	1.88684	11	0.282594	32	0.282585	4.7	1.1	1.16	529	6	98
LOC-1-77-rim	0.0354	29	0.00114	11	1.46721	1.88559	9	0.282567	36	0.282556	3.1	1.3	1.22	500	6	99
LOC-1-84	0.0106	3	0.00034	1	1.46721	1.88698	10	0.281618	42	0.281605	5.7	1.5	2.33	2094	20	99
LOC-1-85	0.0272	16	0.00079	4	1.46720	1.88585	9	0.282586	31	0.282579	4.0	1.1	1.18	508	6	100
LOC-1-87	0.0294	7	0.00107	2	1.46716	1.88585	7	0.282577	36	0.282571	-0.2	1.3	1.27	329	4	101
LOC-1-92-co	0.0198	17	0.00071	4	1.46718	1.88478	6	0.281093	40	0.281058	-2.7	1.4	3.17	2567	18	103
LOC-1-94	0.0041	3	0.00015	1	1.46717	1.88652	10	0.281498	29	0.281493	1.0	1.0	2.57	2066	19	99
LOC-1-95	0.0018	1	0.00005	0	1.46723	1.88666	10	0.281322	31	0.281320	-2.5	1.1	2.85	2178	19	102
LOC-1-96	0.0444	33	0.00139	11	1.46715	1.88660	9	0.282501	47	0.282489	0.2	1.7	1.36	480	5	100
LOC-1-98	0.0308	18	0.00103	5	1.46722	1.88590	6	0.282135	41	0.282122	-8.5	1.5	1.99	671	7	99
LOC-1-99	0.0119	3	0.00035	1	1.46723	1.88599	9	0.281087	32	0.281074	-13.8	1.2	3.38	2067	19	99
LOC-1-101	0.0199	7	0.00062	2	1.46727	1.88544	9	0.280871	39	0.280840	-8.1	1.4	3.54	2672	18	99
LOC-1-107	0.0206	6	0.00070	2	1.46720	1.88656	9	0.280994	31	0.280960	-7.2	1.1	3.38	2527	18	100
LOC-1-108	0.0308	4	0.00102	1	1.46723	1.88681	10	0.281569	31	0.281529	1.7	1.1	2.51	2038	19	100

Analyses en Hf sur zircon : grains hérités du leucogranite de Guérande

	$^{176}Yb/^{177}Hf$ [a]	±2s	$^{176}Lu/^{177}Hf$ [a]	±2s	$^{178}Hf/^{177}Hf$	$^{180}Hf/^{177}Hf$	Sig_{Hf} [b] (V)	$^{176}Hf/^{177}Hf$	±2s [c]	$^{176}Hf/^{177}Hf_{(t)}$ [d]	$\varepsilon Hf_{(t)}$ [d]	±2s [c]	T_{DM2} [e] (Ga)	age [f] (Ma)	±2s	conc.[g]
GUE-3-14a-co	0.0139	18	0.00051	6	1.46722	1.88671	7	0.282477	34	0.282471	3.0	1.2	1.33	632	8	100
GUE-3-14b-rim	0.0029	1	0.00011	1	1.46726	1.88495	8	0.282314	35	0.282314	-9.4	1.3	1.77	329	4	104
GUE-3-14c-rim	0.0025	3	0.00009	1	1.46725	1.88209	4	0.282340	44	0.282340	-8.4	1.6	1.72	332	4	106
GUE-3-12c	0.0547	62	0.00174	19	1.46714	1.88702	7	0.282439	37	0.282424	-2.6	1.3	1.50	455	6	102
GUE-3-9b-co	0.0087	23	0.00028	7	1.46711	1.88745	9	0.282301	33	0.282299	-8.5	1.2	1.77	391	5	107
GUE-3-1b-co	0.0321	18	0.00113	6	1.46708	1.88746	7	0.282602	37	0.282591	4.4	1.3	1.15	506	6	104
GUE-3-18	0.0209	3	0.00068	1	1.46713	1.88666	10	0.281480	30	0.281459	-11.5	1.1	2.87	1575	18	100
GUE-3-3co	0.0830	94	0.00266	30	1.46717	1.88636	8	0.282486	45	0.282467	-2.9	1.6	1.45	377	5	104
GUE-3-6a-co	0.0320	20	0.00107	5	1.46721	1.88661	8	0.282472	33	0.282464	-1.7	1.2	1.43	432	5	101
GUE-3-19-co	0.0042	7	0.00013	3	1.46727	1.88596	9	0.282347	32	0.282346	-3.6	1.1	1.62	537	7	105
GUE-4-2	0.0101	1	0.00034	0	1.46714	1.88672	10	0.281436	37	0.281424	-5.9	1.3	2.80	1873	24	107
GUE-4-3a-co	0.0240	8	0.00078	3	1.46716	1.88665	12	0.282612	31	0.282602	9.1	1.1	1.05	695	10	101
GUE-4-5a-co	0.0238	16	0.00075	5	1.46721	1.88625	7	0.282594	37	0.282585	6.4	1.3	1.12	602	9	100
GUE-4-6a-co	0.0117	2	0.00039	1	1.46716	1.88706	10	0.281363	26	0.281348	-3.8	0.9	2.84	2078	24	107
GUE-4-9-co	0.0145	10	0.00048	3	1.46716	1.88700	9	0.282364	26	0.282359	-4.0	0.9	1.61	497	8	119
GUE-4-21a-co	0.0171	25	0.00054	9	1.46716	1.88706	11	0.282469	32	0.282463	3.3	1.1	1.34	658	9	104
GUE-4-19a	0.0267	10	0.00084	3	1.46723	1.88591	10	0.282187	31	0.282177	-6.8	1.1	1.89	658	9	109
GUE-4-24-co	0.0260	19	0.00080	4	1.46724	1.88577	9	0.282456	34	0.282445	4.4	1.2	1.34	734	10	101
GUE-5-2-co	0.0149	11	0.00056	4	1.46721	1.88644	14	0.282205	38	0.282198	-7.2	1.3	1.87	608	8	99
GUE-5-21c-co	0.0190	7	0.00055	2	1.46719	1.88724	11	0.282502	32	0.282495	4.5	1.1	1.27	659	8	104
GUE-5-6c-co	0.0416	36	0.00136	12	1.46719	1.88643	11	0.282531	30	0.282515	4.9	1.1	1.24	647	8	105
GUE-5-10	0.0238	12	0.00076	3	1.46733	1.88653	10	0.281922	45	0.281911	-14.2	1.6	2.36	750	10	101
GUE-5-11b-co	0.0281	38	0.00092	13	1.46715	1.88709	9	0.282565	37	0.282555	4.8	1.3	1.19	580	7	99
GUE-5-11b-co	0.0281	38	0.00092	13	1.46715	1.88709	9	0.282565	37	0.282559	-0.5	1.3	1.29	338	5	101
GUE-5-17a-co	0.0233	20	0.00081	5	1.46720	1.88680	9	0.282460	34	0.282450	2.3	1.2	1.37	635	9	100
GUE-8-1a	0.0349	16	0.00130	5	1.46716	1.88697	10	0.282152	34	0.282128	-1.4	1.2	1.84	974	12	98
GUE-5-3-co	0.0489	20	0.00156	6	1.46720	1.88365	6	0.282451	35	0.282434	0.8	1.3	1.42	593	8	103
GUE-8-4	0.0160	5	0.00053	2	1.46722	1.88661	9	0.282204	35	0.282198	-6.4	1.2	1.86	643	9	104
GUE-8-6	0.0261	8	0.00079	3	1.46718	1.88687	11	0.282204	37	0.282195	-6.4	1.3	1.86	651	10	103
GUE-8-23-co	0.0575	13	0.00175	4	1.46721	1.88667	11	0.282443	28	0.282422	1.2	1.0	1.43	627	10	106
GUE-8-14b	0.0176	16	0.00049	4	1.46747	1.88371	8	0.282243	32	0.282234	3.0	1.1	1.62	1005	31	101
GUE-8-13	0.0224	26	0.00077	9	1.46721	1.88620	9	0.282561	31	0.282553	5.0	1.1	1.19	591	8	105
GUE-8-11	0.0331	20	0.00099	5	1.46717	1.88571	11	0.281996	37	0.281977	-6.3	1.3	2.13	996	33	99
GUE-8-10-co	0.0355	11	0.00102	4	1.46711	1.88715	12	0.282567	42	0.282558	2.6	1.5	1.23	479	7	100

Analyses en Hf sur zircon : grains hérités des leucogranites de Lizio et Questembert

	$^{176}Yb/^{177}Hf$ [a]	±2s	$^{176}Lu/^{177}Hf$ [a]	±2s	$^{178}Hf/^{177}Hf$	$^{180}Hf/^{177}Hf$	Sig_{Hf} [b] (V)	$^{176}Hf/^{177}Hf$	±2s [c]	$^{176}Hf/^{177}Hf_{(t)}$ [d]	$\varepsilon Hf_{(t)}$ [d]	±2s [c]	T_{DM2} [e] (Ga)	age [f] (Ma)	±2s	conc.[g]
Questembert																
QRT-08-4	0.0178	3	0.00055	1	1.46719	1.88645	9	0.282440	32	0.282437	-5.1	1.1	1.53	323	3	103
QRT-08-5-co	0.0306	19	0.00097	6	1.46718	1.88632	11	0.282450	31	0.282442	-1.9	1.1	1.46	462	5	100
QRT-08-8-co	0.0213	4	0.00068	1	1.46721	1.88690	10	0.282315	29	0.282307	-2.5	1.0	1.64	646	7	98
QRT-08-17	0.0488	78	0.00153	25	1.46718	1.88703	10	0.282500	34	0.282487	-0.9	1.2	1.39	431	5	107
QRT-08-18-co	0.0397	31	0.00126	10	1.46718	1.88670	9	0.282075	30	0.282061	-12.1	1.1	2.14	608	6	107
QRT-08-23-co	0.0556	9	0.00172	3	1.46715	1.88634	8	0.282665	31	0.282648	7.0	1.1	1.03	530	6	104
QRT-08-24-co	0.0262	8	0.00078	4	1.46724	1.88590	9	0.282465	31	0.282458	-0.8	1.1	1.42	482	5	103
QRT-08-25b-co	0.0420	13	0.00133	4	1.46720	1.88667	9	0.282560	32	0.282549	1.9	1.1	1.26	462	5	102
QRT-08-29-co	0.0160	5	0.00069	3	1.46722	1.88641	11	0.282376	31	0.282368	-1.2	1.1	1.54	609	6	101
QRT-08-37	0.0383	50	0.00133	17	1.46724	1.88668	11	0.282379	32	0.282368	-5.3	1.1	1.62	422	4	102
QRT-08-38-co	0.0531	36	0.00165	11	1.46713	1.88681	8	0.282665	32	0.282651	5.8	1.1	1.05	473	5	100
QRT-08-40-co	0.0730	62	0.00230	20	1.46716	1.88573	8	0.282592	30	0.282564	6.7	1.1	1.14	648	7	99
QRT-08-42	0.0482	14	0.00146	3	1.46715	1.88672	10	0.282465	31	0.282454	-2.2	1.1	1.46	428	5	101
QRT-08-43-co	0.0493	5	0.00167	2	1.46722	1.88634	10	0.281026	32	0.280942	-5.2	1.1	3.36	2639	24	104
QRT-08-47	0.0355	12	0.00118	4	1.46716	1.88681	9	0.282652	31	0.282641	5.2	1.1	1.07	463	5	103
QRT-08-52-co	0.0516	41	0.00153	12	1.46723	1.88734	9	0.282480	31	0.282466	-0.9	1.1	1.41	468	5	100
Lizio																
LRT-10-1-co	0.0309	6	0.00095	2	1.46722	1.88675	9	0.282548	35	0.282538	4.4	1.2	1.22	589	6	100
LRT-10-2-co	0.0540	39	0.00166	12	1.46717	1.88591	8	0.282692	39	0.282679	5.2	1.4	1.03	402	4	102
LRT-10-4-co	0.0426	18	0.00136	5	1.46723	1.88818	9	0.282236	52	0.282217	-4.0	1.8	1.79	720	7	101
LRT-10-8-co	0.0456	15	0.00144	4	1.46726	1.88384	6	0.282504	37	0.282482	7.2	1.3	1.23	799	8	106
LRT-10-11-co	0.0329	46	0.00101	12	1.46729	1.88692	10	0.282585	52	0.282573	6.7	1.8	1.13	637	7	99
LRT-10-12-co	0.0169	17	0.00050	5	1.46731	1.88656	10	0.282283	32	0.282276	-1.0	1.1	1.65	760	8	122
LRT-10-13-co	0.0390	34	0.00124	11	1.46716	1.88726	9	0.282709	30	0.282698	7.6	1.1	0.96	478	5	102
LRT-10-14-co	0.0444	18	0.00146	5	1.46723	1.88624	7	0.282556	34	0.282540	4.7	1.2	1.21	599	6	99
LRT-10-15-co	0.0489	34	0.00139	10	1.46713	1.88652	10	0.282483	33	0.282468	2.0	1.2	1.35	595	6	104
LRT-10-16-co	0.0521	15	0.00154	5	1.46722	1.88597	10	0.282304	45	0.282285	-3.2	1.6	1.68	651	7	102
LRT-10-20-co	0.0346	20	0.00119	6	1.46720	1.88648	11	0.282516	30	0.282503	2.8	1.1	1.30	572	6	100
LRT-10-22-co	0.0452	16	0.00128	4	1.46720	1.88675	9	0.282559	32	0.282546	3.9	1.1	1.22	555	6	100
LRT-10-23	0.0446	31	0.00134	9	1.46714	1.88674	8	0.282626	35	0.282618	1.2	1.2	1.18	319	3	100
LRT-10-25-co	0.0334	20	0.00116	6	1.46719	1.88663	7	0.282585	38	0.282575	3.5	1.4	1.19	493	5	102
LRT-10-26-co	0.0455	14	0.00145	5	1.46718	1.88646	8	0.282650	32	0.282637	5.6	1.1	1.07	483	5	102
LRT-10-30-co	0.0334	5	0.00103	1	1.46709	1.88708	8	0.282509	34	0.282498	2.5	1.2	1.31	565	6	100
LRT-10-31a	0.0353	14	0.00116	5	1.46716	1.88627	7	0.282667	32	0.282658	5.4	1.1	1.05	446	5	100
LRT-10-33	0.0185	8	0.00060	3	1.46723	1.88661	7	0.282615	33	0.282612	0.8	1.2	1.20	310	3	101
LRT-10-35-co	0.0612	27	0.00178	8	1.46714	1.88691	9	0.282145	36	0.282112	-1.5	1.3	1.87	995	10	100
LRT-10-38-co	0.0660	22	0.00202	7	1.46720	1.88725	8	0.282618	41	0.282593	8.2	1.5	1.08	672	7	106

Analyses U-Th-Pb sur monazite complémentaires sur le leucogranite de Guérande

	Isotopes ratios								Ages (Ma)							
GUE-8	**Pb^{207}/Pb^{206}**	**1σ**	**Pb^{207}/U^{235}**	**1σ**	**Pb^{206}/U^{238}**	**1σ**	**Pb^{208}/Th^{232}**	**1σ**	**Pb^{207}/Pb^{206}**	**1σ**	**Pb^{206}/U^{238}**	**1σ**	**Pb^{207}/U^{235}**	**1σ**	**Pb^{208}/Th^{232}**	**1σ**
6a	*0.06121*	*0.00084*	*0.30208*	*0.00467*	*0.0358*	*0.0005*	*0.01609*	*0.00028*	*646.8*	*29.16*	*226.8*	*3.14*	*268*	*3.64*	*322.6*	*5.57*
5a	0.05842	0.00069	0.28119	0.00397	0.03493	0.00048	0.01526	0.00026	545.4	25.72	221.3	3	251.6	3.15	306.1	5.26
5b	0.0513	0.00061	0.23854	0.00336	0.03374	0.00046	0.01541	0.00027	254.2	26.99	213.9	2.9	217.2	2.76	309.1	5.32
4b	0.05101	0.00056	0.25226	0.00341	0.03588	0.00049	0.01616	0.00028	241.3	25.26	227.3	3.05	228.4	2.77	324	5.55
2a	0.05108	0.00057	0.24731	0.00336	0.03513	0.00048	0.01563	0.00027	244.2	25.47	222.6	2.99	224.4	2.73	313.5	5.37
2b	0.05054	0.00057	0.24742	0.00339	0.03552	0.00049	0.01577	0.00027	220	25.95	225	3.03	224.5	2.76	316.3	5.42
2c	*0.04984*	*0.00056*	*0.25198*	*0.00343*	*0.03668*	*0.0005*	*0.01549*	*0.00027*	*187.4*	*25.86*	*232.2*	*3.12*	*228.2*	*2.78*	*310.7*	*5.32*
2d	*0.05188*	*0.0006*	*0.24928*	*0.00344*	*0.03486*	*0.00048*	*0.01556*	*0.00027*	*280.2*	*26.08*	*220.9*	*2.98*	*226*	*2.8*	*312.1*	*5.34*
2e	0.04977	0.00057	0.24377	0.00333	0.03553	0.00049	0.01561	0.00027	184.5	26.27	225.1	3.03	221.5	2.72	313.2	5.36
1a	0.05018	0.00059	0.24647	0.00343	0.03563	0.00049	0.01557	0.00027	203.5	26.94	225.7	3.04	223.7	2.79	312.3	5.34
1b	0.05038	0.00059	0.24527	0.0034	0.03532	0.00048	0.01567	0.00027	212.5	26.76	223.8	3.02	222.7	2.77	314.3	5.37
1c	*0.04932*	*0.00058*	*0.24508*	*0.00341*	*0.03605*	*0.00049*	*0.01553*	*0.00027*	*163.1*	*27.16*	*228.3*	*3.08*	*222.6*	*2.78*	*311.6*	*5.32*
1d	0.04939	0.00058	0.24309	0.00338	0.03571	0.00049	0.0157	0.00027	166.2	27.2	226.2	3.05	221	2.76	314.8	5.37
1e	0.04949	0.00059	0.23754	0.00333	0.03482	0.00048	0.01594	0.00027	171.2	27.5	220.6	2.98	216.4	2.73	319.6	5.45
8a	*0.05357*	*0.00064*	*0.26746*	*0.00374*	*0.03622*	*0.0005*	*0.01544*	*0.00027*	*352.9*	*26.57*	*229.4*	*3.1*	*240.7*	*3*	*309.6*	*5.29*
7a	0.04996	0.00058	0.23953	0.0033	0.03478	0.00048	0.01549	0.00027	193.2	26.77	220.4	2.97	218	2.7	310.7	5.3
7b	0.04908	0.00057	0.23898	0.00328	0.03533	0.00048	0.01569	0.00027	151.6	26.83	223.8	3.01	217.6	2.69	314.7	5.37
7c	0.04958	0.00058	0.24363	0.00337	0.03564	0.00049	0.01566	0.00027	175.5	27.12	225.8	3.04	221.4	2.75	314.1	5.35
7d	0.05092	0.00059	0.24914	0.00343	0.03549	0.00049	0.01572	0.00027	237.1	26.64	224.8	3.03	225.9	2.78	315.2	5.36
3a	*0.05779*	*0.00076*	*0.28065*	*0.00415*	*0.03523*	*0.00049*	*0.01531*	*0.00026*	*521.5*	*28.7*	*223.2*	*3.05*	*251.2*	*3.29*	*307.1*	*5.23*
3b	0.04963	0.0006	0.2365	0.00333	0.03456	0.00048	0.01549	0.00027	177.9	28.02	219.1	2.96	215.6	2.74	310.7	5.28
9	0.05108	0.00063	0.25081	0.00355	0.03562	0.00049	0.01581	0.00027	244.4	27.95	225.6	3.05	227.2	2.88	317	5.39
10	0.04924	0.00061	0.23897	0.00339	0.0352	0.00048	0.01512	0.00026	159.5	28.54	223	3.02	217.6	2.78	303.4	5.16
11	*0.04883*	*0.0006*	*0.24234*	*0.00342*	*0.036*	*0.0005*	*0.01576*	*0.00027*	*139.7*	*28.43*	*228*	*3.08*	*220.3*	*2.8*	*316.1*	*5.37*
11b	*0.0601*	*0.00074*	*0.28568*	*0.00406*	*0.03448*	*0.00048*	*0.01539*	*0.00026*	*607.3*	*26.49*	*218.5*	*2.96*	*255.2*	*3.2*	*308.6*	*5.24*
1f	0.04986	0.00064	0.24241	0.00355	0.03527	0.00049	0.01528	0.00026	188.3	29.76	223.4	3.04	220.4	2.9	306.6	5.21
1g	*0.04844*	*0.00061*	*0.2424*	*0.00347*	*0.03629*	*0.0005*	*0.01549*	*0.00026*	*120.9*	*29.18*	*229.8*	*3.11*	*220.4*	*2.83*	*310.7*	*5.27*

GUE-5	Pb^{207}/Pb^{206}	1σ	Pb^{207}/U^{235}	1σ	Pb^{206}/U^{238}	1σ	Pb^{208}/Th^{232}	1σ	Pb^{207}/Pb^{206}	1σ	Pb^{206}/U^{238}	1σ	Pb^{207}/U^{235}	1σ	Pb^{208}/Th^{232}	1σ
1a	*0.05995*	*0.00079*	*0.40025*	*0.00611*	*0.04842*	*0.0007*	*0.01463*	*0.00026*	*601.8*	*28.13*	*304.8*	*4.28*	*341.8*	*4.43*	*293.6*	*5.17*
1b	0.0519	0.00072	0.35008	0.00556	0.04893	0.00071	0.01501	0.00027	280.9	31.48	307.9	4.33	304.8	4.18	301.1	5.31
2a	*0.04988*	*0.00059*	*0.33797*	*0.00486*	*0.04914*	*0.00069*	*0.01508*	*0.00027*	*189.5*	*27.35*	*309.3*	*4.26*	*295.6*	*3.69*	*302.5*	*5.33*
3a	*0.05102*	*0.00061*	*0.34515*	*0.005*	*0.04906*	*0.00069*	*0.01484*	*0.00026*	*241.9*	*27.45*	*308.8*	*4.26*	*301.1*	*3.78*	*297.7*	*5.25*
4a	*0.05334*	*0.00081*	*0.34897*	*0.00585*	*0.04745*	*0.00069*	*0.01524*	*0.00027*	*343.4*	*33.69*	*298.8*	*4.25*	*303.9*	*4.41*	*305.8*	*5.36*
5a	*0.05354*	*0.00062*	*0.35442*	*0.00502*	*0.04801*	*0.00067*	*0.01522*	*0.00027*	*351.8*	*25.87*	*302.3*	*4.15*	*308*	*3.76*	*305.3*	*5.36*
7a	0.05156	0.00064	0.34077	0.005	0.04794	0.00067	0.01534	0.00027	265.9	28.04	301.8	4.15	297.8	3.78	307.6	5.39
7b	*0.05077*	*0.00059*	*0.34914*	*0.00493*	*0.04987*	*0.0007*	*0.01523*	*0.00027*	*230.6*	*26.52*	*313.8*	*4.28*	*304.1*	*3.71*	*305.5*	*5.34*
7c	*0.05148*	*0.00063*	*0.34262*	*0.00498*	*0.04827*	*0.00068*	*0.01457*	*0.00026*	*262.3*	*27.66*	*303.9*	*4.16*	*299.2*	*3.76*	*292.4*	*5.12*
7d	*0.05149*	*0.00064*	*0.34497*	*0.00507*	*0.04859*	*0.00068*	*0.015*	*0.00026*	*262.9*	*28.25*	*305.9*	*4.2*	*300.9*	*3.83*	*301*	*5.27*
8a	*0.05065*	*0.00064*	*0.3356*	*0.00499*	*0.04806*	*0.00068*	*0.01488*	*0.00026*	*225*	*28.95*	*302.6*	*4.16*	*293.8*	*3.79*	*298.4*	*5.22*
8b	0.05287	0.00064	0.35202	0.00508	0.04829	0.00068	0.01488	0.00026	323.3	27.09	304	4.15	306.2	3.82	298.5	5.21
10	*0.05088*	*0.0007*	*0.34092*	*0.00535*	*0.0486*	*0.00069*	*0.01441*	*0.00025*	*235.5*	*31.49*	*305.9*	*4.24*	*297.9*	*4.05*	*289.1*	*5.07*
11	*0.05103*	*0.00067*	*0.3411*	*0.00517*	*0.04848*	*0.00068*	*0.01484*	*0.00026*	*242.3*	*29.83*	*305.2*	*4.2*	*298*	*3.91*	*297.8*	*5.21*
12a	0.05208	0.00067	0.34131	0.0051	0.04754	0.00067	0.01516	0.00027	288.7	28.99	299.4	4.11	298.2	3.86	304.2	5.31
13	0.05235	0.0007	0.35022	0.00539	0.04853	0.00068	0.01519	0.00027	300.7	30.33	305.5	4.2	304.9	4.05	304.8	5.3
14	*0.05348*	*0.00081*	*0.346*	*0.00577*	*0.04693*	*0.00067*	*0.01448*	*0.00025*	*349.3*	*33.89*	*295.6*	*4.14*	*301.7*	*4.35*	*290.6*	*5.07*
15a	0.05164	0.00073	0.34327	0.00546	0.04822	0.00068	0.01438	0.00025	269.4	32.15	303.6	4.19	299.6	4.12	288.7	5.03
15b	0.05194	0.00072	0.34427	0.00537	0.04808	0.00068	0.01529	0.00027	282.8	31.22	302.7	4.16	300.4	4.06	306.6	5.33
15c	0.05231	0.00073	0.34409	0.00539	0.04772	0.00067	0.01455	0.00025	299.2	31.29	300.5	4.13	300.3	4.07	292	5.07
18	0.05188	0.00073	0.34197	0.00539	0.04782	0.00067	0.01486	0.00026	280.3	31.86	301.1	4.14	298.7	4.08	298.1	5.17
20a	*0.05469*	*0.00077*	*0.36068*	*0.00579*	*0.04785*	*0.00068*	*0.01542*	*0.00027*	*400.1*	*30.61*	*301.3*	*4.17*	*312.7*	*4.32*	*309.3*	*5.37*
29a	0.05307	0.00068	0.34996	0.00519	0.04784	0.00067	0.0157	0.00027	331.9	28.59	301.3	4.09	304.7	3.91	314.8	5.42
20b	*0.0565*	*0.00067*	*0.29737*	*0.00426*	*0.03818*	*0.00053*	*0.0164*	*0.00029*	*471.5*	*26.1*	*241.5*	*3.28*	*264.3*	*3.33*	*328.8*	*5.71*
7e	0.05448	0.00058	0.27324	0.00371	0.03638	0.0005	0.01626	0.00028	391	23.83	230.4	3.1	245.3	2.96	326	5.65
7f	0.05238	0.00056	0.25718	0.00347	0.03562	0.00049	0.01583	0.00028	302.2	24.06	225.6	3.03	232.4	2.81	317.4	5.5
7g	0.05218	0.00056	0.25624	0.00346	0.03563	0.00049	0.01577	0.00028	293.4	24.11	225.7	3.03	231.6	2.8	316.3	5.48
21a	0.05555	0.00061	0.27433	0.00375	0.03583	0.00049	0.01559	0.00027	434.1	24.06	226.9	3.06	246.1	2.99	312.7	5.42
21b	0.05158	0.00056	0.25575	0.00347	0.03597	0.00049	0.01565	0.00027	266.8	24.6	227.8	3.06	231.2	2.81	313.9	5.43
23	*0.05389*	*0.00061*	*0.27903*	*0.00388*	*0.03756*	*0.00052*	*0.01581*	*0.00028*	*366.5*	*25.36*	*237.7*	*3.21*	*249.9*	*3.08*	*317*	*5.48*
24b	0.05147	0.00057	0.26088	0.00358	0.03678	0.0005	0.01538	0.00027	261.8	25.26	232.8	3.13	235.4	2.88	308.4	5.32
25	0.05554	0.00061	0.27448	0.00374	0.03586	0.00049	0.01587	0.00028	433.6	24.19	227.1	3.06	246.3	2.98	318.3	5.5
26	0.05121	0.00057	0.25188	0.00346	0.03569	0.00049	0.01574	0.00027	250.2	25.47	226.1	3.05	228.1	2.81	315.7	5.45
27a	0.05184	0.00058	0.25412	0.00349	0.03557	0.00049	0.01569	0.00027	278.3	25.33	225.3	3.04	229.9	2.82	314.8	5.43
27b	0.05126	0.00057	0.25569	0.00351	0.03619	0.0005	0.01562	0.00027	252.6	25.49	229.2	3.09	231.2	2.84	313.2	5.4
29b	0.05074	0.00058	0.24921	0.00345	0.03564	0.00049	0.01562	0.00027	229.1	26.04	225.7	3.04	225.9	2.8	313.2	5.39

Analyses en éléments majeurs et traces des sédiments et orthogneiss paléozoïques

Nature		**grès**	**schiste-noir**	**schiste-noir**	**grès**	**grès**	**silt**	**grès**	**grès**	**grès**	**grès**	**grès**	**silt**	**grès**
Age		**Carb inf**	**Carb inf**	**Dev**	**Dev**	**Dev**	**Dev**	**Dev**	**Dev**	**Sil-dev**	**Sil**	**Sil**	**Sil**	**Sil**
Echant		**LOC-1**	**LOC-2**	**CRO-14**	**CRO-2**	**CRO-1a**	**CRO-1b**	**CRO-12**	**CRO-11**	**CRO-10**	**CRO-6**	**CRO-3a**	**CRO-3b**	**CRO-4a**
SiO_2	%	72.77	57.64	54.86	65.2	61.83	82.14	86.26	79.01	94.54	94.09	50.63	87.27	59.43
Al_2O_3	%	12.794	19.863	27.113	16.795	15.72	6.151	3.961	6.481	1.132	1.441	29.897	4.068	23.21
Fe_2O_3	%	4.143	8.435	1.255	7.961	10.36	6.421	6.314	9.034	1.95	2.45	4.589	5.114	6.534
MnO	%	0.0334	0.0697	0.0008	0.0595	0.014	0.0486	0.1547	0.0892	0.0048	0.0187	0.0413	0.0556	0.0528
MgO	%	1.3	2.624	0.438	0.855	0.933	0.528	0.671	1.037	0.176	0.368	0.485	0.365	0.656
CaO	%	0.34	0.322	0.376	0.137	0.629	0.033	0.037	0.083	0.137	0.076	0.06	0.418	0.164
Na_2O	%	2.25	0.995	0.377	0.338	0.365	0.146	0.077	0.091	< L.D.	< L.D.	1.506	0.089	0.364
K_2O	%	2.129	4.213	.204	1.199	0.986	0.297	0.156	0.297	< L.D.	< L.D.	4.21	0.171	1.865
TiO_2	%	0.691	0.985	0.883	1.086	1.098	0.525	0.463	0.443	0.338	0.462	1.425	0.491	1.287
P_2O_5	%	0.14	0.19	0.08	0.2	0.69	< L.D.	0.05	0.08	0.11	0.07	0.12	0.35	0.17
PF	%	2.48	5.4	9.5	5.34	6.55	3.01	2.08	3.27	0.66	0.82	6.15	1.54	4.97
Total	%	99.07	100.73	100.09	99.17	99.18	99.2996	100.22	99.91	99.05	99.80	99.1	99.93	98.7
U	ppm	3.013	4.08	3.213	4.05	3.237	1.419	1.421	1.394	1.577	1.699	4.038	2.075	3.689
Th	ppm	11.88	16.75	15.74	19.61	20.29	9.091	7.671	9.287	6.541	10.74	24.98	9.672	20.58
Li	ppm	32.00	65	82	96	109	51	25	48	12	6	54	15.7	58
Nb	ppm	10.81	15.8	15.68	19.66	19.14	9.151	7.822	7.612	4.681	6.42	23.23	7.032	21
Ta	ppm	1.038	1.427	1.296	1.807	1.709	0.787	0.716	0.648	0.445	0.584	2.082	0.624	1.869
Zr	ppm	303	169.1	90.02	501.5	513.8	346	437.4	418.3	510.5	586	311.1	512.2	348.6
Hf	ppm	7.745	4.632	2.567	16.26	13.38	8.227	10.45	9.848	12	15.73	8.374	11.8	9.344
Sn	ppm	2.979	4.974	4.214	4.229	3.22	1.442	0.854	1.266	0.581	0.657	6.349	0.989	4.607
Cs	ppm	3.789	9.414	22.23	2.418	1.803	0.734	0.274	0.829	< L.D.	< L.D.	5.968	0.315	3.531
W	ppm	1.745	2.696	2.393	2.085	2.048	0.965	0.941	0.874	0.468	0.619	2.369	0.719	2.115
Rb	ppm	96.68	184.9	229	58.54	40.51	11.42	5.804	12.32	< L.D.	< L.D.	177.1	6.653	87.26
As	ppm	11.62	10.73	27.88	4.197	17.68	8.036	5.695	14.19	< L.D.	< L.D.	8.149	4.634	13.28
Ba	ppm	345	648.5	381.1	209	214.1	80.49	41.84	47.58	2.229	3.624	947.2	49.55	337.1
Be	ppm	2.036	3.928	5.696	2.427	2.678	1.008	0.403	0.913	< L.D.	< L.D.	5.007	< L.D.	2.653
Bi	ppm	0.109	0.666	0.201	0.208	0.198	< L.D.	< L.D.	0.126	< L.D.	< L.D.	0.301	< L.D.	0.323
Cd	ppm	0.292	0.209	< L.D.	0.39	0.348	0.228	0.334	0.29	0.35	0.489	0.248	0.37	0.246
Ce	ppm	62.7	96.77	96.7	92.5	142.9	37.99	45.81	47.01	37.98	51.56	150.6	52.51	122
Co	ppm	9.76	19.73	0.448	17.98	15.55	12.95	7.785	17.56	3.285	4.639	10.81	6.462	14.99
Cr	ppm	81.64	118.5	122.8	97.75	97.82	45.11	32.32	45.46	80.33	58.03	154.2	64.8	119.1
Cu	ppm	12.6	50.71	12.92	23.94	12.85	6.774	< L.D.	8.213	10.78	< L.D.	23.23	10.58	30.9
Dy	ppm	4.226	6.319	5.71	8.605	13.57	4.582	3.93	4.522	2.646	3.086	6.268	5.159	7.628
Er	ppm	2.348	3.401	2.255	5.127	6.422	2.608	2.157	2.404	1.61	1.829	3.651	3.019	4.12
Eu	ppm	1.15	1.761	2.863	1.903	3.836	0.849	0.726	1.053	0.468	0.413	2.408	0.942	2.168
Ga	ppm	16.46	27.64	36.09	25.05	25.42	9.544	5.121	9.34	2.32	2.694	39.44	7.38	31.3
Gd	ppm	4.547	6.958	8.575	8.174	15.66	3.986	3.86	4.476	2.781	3.056	7.601	4.926	8.206
Ge	ppm	1.764	2.3	2.451	2.388	2.277	2.274	2.316	2.676	1.196	1.17	1.955	1.535	2.361
Ho	ppm	0.876	1.274	0.934	1.871	2.63	0.992	0.826	0.911	0.587	0.672	1.308	1.116	1.567
In	ppm	< L.D.	0.098	0.179	0.096	0.114	< L.D.	< L.D.	< L.D.	< L.D.	< L.D.	0.11	< L.D.	0.099
La	ppm	31.46	48.47	49.32	47.97	59.29	16.11	21.24	22.33	18.08	24.24	78.25	23.53	61.06
Lu	ppm	0.367	0.523	0.341	0.802	0.819	0.383	0.327	0.364	0.282	0.329	0.595	0.472	0.622
Mo	ppm	< L.D.	0.923	6.328	0.511	0.592	< L.D.	< L.D.	< L.D.	< L.D.	< L.D.	0.674	< L.D.	< L.D.
Nd	ppm	27.62	43.57	43.31	43.57	73.89	17.86	20.38	21.6	16	21.66	61.55	23.91	52.12
Ni	ppm	29.63	55.18	7.898	51.74	54.61	30.45	19.43	40.82	7.393	7.15	41.71	16.74	40.79
Pb	ppm	14.3625	31.0115	346.510 4	19.145	17.7721	21.5049	18.779 7	24.194 6	8.0455	1.4175	9.3807	2.7689	9.7424
Pr	ppm	7.378	11.43	11.5	11.49	17.83	4.454	5.387	5.597	4.259	5.862	17.1	6.116	13.99
Sc	ppm	10.79	22.98	20.81	18.2	18.76	7.9	3.29	8.33	1.79	2.62	26.78	6.83	21.38
Sb	ppm	1.107	1.332	15.6	0.272	0.245	< L.D.	< L.D.	0.235	0.294	< L.D.	0.225	< L.D.	0.359
Sm	ppm	5.48	8.789	10.32	9.024	17.03	4.126	4.1	4.49	3.182	3.719	10.72	5.109	9.993
Sr	ppm	69.97	56.13	138.8	103.2	128.7	35.66	28.68	34.87	10.29	7.572	286.7	32.56	129.9
Tb	ppm	0.692	1.049	1.178	1.354	2.382	0.7	0.629	0.726	0.426	0.502	1.068	0.809	1.249
Tm	ppm	0.346	0.499	0.335	0.757	0.859	0.385	0.314	0.349	0.234	0.271	0.543	0.444	0.599
V	ppm	72.96	161.6	130.5	89.5	119.6	40.75	17.61	75.97	11.11	26.44	156.4	59.23	125.3
Y	ppm	23.16	33.37	16.32	49.44	62.57	25.98	22.19	24.23	16.44	18.17	34.12	31.35	40.25
Yb	ppm	2.41	3.382	2.262	5.23	5.571	2.661	2.127	2.333	1.683	1.943	3.79	3.07	4.095
Zn	ppm	69.75	137	14.37	137.5	126	74.91	48.74	114.3	21.47	14.61	57.88	36.39	50.93

Nature		silt	grès	grès	schiste -noir	grès	grès	grès à mx lourds	grès	Orthog	Orthog	Orthog	Orthog	Granit
Age		Sil	Sil	Sil	Sil	Ord-sil	Ord	Ord	Brio	ord	ord	ord	Ord	ord
Echant		CRO-4b	CRO-5	CRO-8	CRO-7	CRO-17	CRO-16	CRO-15	CRO-9	PLG-2	PLG-1	PLG-4	QIMP-1	PLG-3
SiO_2	%	93.2	83.51	84.35	61.88	86.35	86.91	87.41	76.37	71.72	72.81	74.77	78.73	74.33
Al_2O_3	%	1.845	4.725	7.344	18.728	7.568	7.417	2.251	8.236	15.15	14.075	14.108	12.602	14.043
Fe_2O_3	%	3.569	8.511	1.905	2.167	0.604	0.246	1.168	8.089	3.025	1.661	1.215	0.977	1.354
MnO	%	0.0253	0.0724	0.0026	0.0021	0.0004	0.0028	0.0061	0.0734	0.0433	0.0331	0.0103	0.0032	0.0254
MgO	%	0.232	0.554	0.298	0.513	0.176	0.087	0.173	2.32	0.741	0.375	0.326	0.098	0.238
CaO	%	0.046	0.167	< L.D.	< L.D.	< L.D.	< L.D.	0.45	0.071	2.374	1.428	1.998	0.137	0.505
Na_2O	%	< L.D.	0.011	0.273	0.333	0.144	0.056	< L.D.	0.055	4.11	3.566	5.564	6.076	3.421
K_2O	%	< L.D.	0.016	0.938	4.441	1.47	1.672	0.361	0.982	1.838	3.334	0.214	1.268	4.316
TiO_2	%	0.483	0.405	0.848	0.593	0.506	1.5	6.077	0.438	0.325	0.209	0.102	0.071	0.134
P_2O_5	%	< L.D.	0.14	0.04	0.04	< L.D.	< L.D.	0.49	0.09	0.08	0.15	0.12	< L.D.	0.36
PF	%	0.91	2.01	3.31	11.43	2.23	1.97	0.91	2.91	1.15	1.2	0.88	0.79	1.14
Total	%	100.31	100.12	99.31	100.13	99.05	99.86	99.30	99.63	100.56	98.84	99.3	100.75	99.86
U	ppm	1.829	1.452	3.901	6.748	3.205	4.983	21.53	1.59	2.469	3.238	2.025	15.64	8.065
Th	ppm	8.268	8.117	9.97	10.42	9.005	26.45	140	5.361	12.9	8.252	3.576	43.41	5.771
Li	ppm	9.1	21	144	6.1	3.9	3.6	7.6	54	28	25	6.9	8.3	94
Nb	ppm	6.987	6.074	13.11	10.5	8.39	24.37	80.27	5.455	6.092	3.744	2.145	77.21	9.628
Ta	ppm	0.629	0.548	1.206	0.868	0.782	2.641	8.118	0.485	0.441	0.436	0.399	8.204	2.098
Zr	ppm	520.4	325.4	642.9	79.52	524.1	2134	8000	157.8	171.2	120.9	63	146.8	54.48
Hf	ppm	14.62	7.563	17.87	2.061	15.1	59.49	218.2	4.049	5.207	3.303	2.011	6.894	1.97
Sn	ppm	0.731	0.791	1.903	3.601	1.23	1.372	8.475	1.378	0.856	1.902	1.013	3.738	11.53
Cs	ppm	< L.D.	< L.D.	2.642	7.198	0.824	0.977	0.169	0.99	1.915	2.426	0.296	0.408	16.09
W	ppm	0.719	0.568	1.201	1.371	0.905	1.834	17.73	1.84	0.256	< L.D.	< L.D.	1.633	0.665
Rb	ppm	0.524	0.783	46.86	206.7	52.62	48.68	15.54	39.41	55.14	131.2	6.359	58.27	249.4
As	ppm	3.712	5.01	7.664	17.17	5.836	< L.D.	3.595	3.573	< L.D.	< L.D.	< L.D.	< L.D.	< L.D.
Ba	ppm	6.877	10.92	340.3	2106	382.1	186.7	144.6	125.7	532.2	302.6	456.8	32.05	165.4
Be	ppm	< L.D.	< L.D.	0.443	1.863	0.923	0.625	0.92	0.663	1.345	1.69	6.188	4.112	0.544
Bi	ppm	< L.D.	0.12	< L.D.	0.306	< L.D.	< L.D.	0.203	0.117	< L.D.	0.105	0.119	< L.D.	1.035
Cd	ppm	0.513	0.486	0.767	0.792	0.445	1.659	5.767	< L.D.	0.129	0.185	< L.D.	0.129	< L.D.
Ce	ppm	37.02	48.28	59.62	72.88	58.06	138.5	432.8	35.8	81.78	32.9	13.45	38.22	21.39
Co	ppm	5.163	15.98	2.62	4.779	0.587	0.529	1.904	17.35	4.378	2.138	1.934	0.449	1.179
Cr	ppm	69.49	65.27	48.09	112.6	26.7	47.86	131	64.67	16.54	8.869	13.7	19	18.22
Cu	ppm	13.09	36.47	19.06	110.7	< L.D.	< L.D.	18.73	24.49	< L.D.	< L.D.	6.58	< L.D.	< L.D.
Dy	ppm	2.925	3.325	5.242	5.444	3.23	5.695	19.24	2.759	5.337	3.008	1.902	4.576	2.6
Er	ppm	1.788	1.814	3.304	2.822	1.981	3.467	11.32	1.537	3.115	1.531	1.15	2.87	1.02
Eu	ppm	0.333	0.662	0.871	1.601	0.629	1.406	3.903	0.816	1.121	0.638	0.428	0.085	0.293
Ga	ppm	3.438	9.782	10.01	26.14	7.867	8.597	5.859	10.06	18.51	18.41	13.56	28.13	19.52
Gd	ppm	2.576	3.45	4.225	5.892	3.281	6.759	23.85	3.027	6.163	3.536	1.629	3.264	2.61
Ge	ppm	1.709	1.847	1.605	1.659	1.422	1.372	2.478	2.062	1.382	1.366	1.271	1.561	2.198
Ho	ppm	0.649	0.681	1.193	1.11	0.703	1.207	4	0.577	1.119	0.589	0.408	0.966	0.447
In	ppm	< L.D.	0.289	< L.D.	< L.D.	< L.D.	< L.D.	< L.D.	< L.D.	< L.D.	< L.D.	< L.D.	< L.D.	0.085
La	ppm	18.34	22.11	30.56	40.24	28.86	62.75	204.1	17.48	39.91	19.53	7.298	15.98	10.05
Lu	ppm	0.327	0.304	0.554	0.374	0.352	0.722	2.456	0.24	0.508	0.24	0.219	0.566	0.125
Mo	ppm	< L.D.	0.61	4.106	85.19	0.558	< L.D.	0.836	< L.D.	< L.D.	< L.D.	< L.D.	2.1	< L.D.
Nd	ppm	15.47	20.25	25.02	36.66	23.79	52.96	169.5	15.94	36.65	17.44	7.085	16.63	10.19
Ni	ppm	10.11	25.15	12.96	53.76	5.188	< L.D.	9.335	48.85	6.172	< L.D.	< L.D.	< L.D.	< L.D.
Pb	ppm	65.4208	38.851	14.4263	32.6427	6.2823	13.7279	53.0547	4.6142	16.1959	14.9541	9.4974	5.2086	19.3918
Pr	ppm	4.202	5.285	6.842	9.56	6.578	14.56	45.69	4.188	9.621	4.559	1.856	4.743	2.687
Sc	ppm	3.04	7.12	7.11	16.65	4.01	5.12	11.51	7.94	8.32	3.47	2.56	< L.D.	4.79
Sb	ppm	< L.D.	< L.D.	3.576	28.32	0.715	1.91	5.171	2.945	< L.D.	< L.D.	< L.D.	0.217	< L.D.
Sm	ppm	2.936	3.934	4.669	7.203	4.266	9.353	31.66	3.352	7.337	4.243	1.752	4.215	2.773
Sr	ppm	10.21	19.45	76.7	75.18	12.82	27.48	124.2	12.4	189.1	78.83	584.7	13.4	25.94
Tb	ppm	0.436	0.544	0.762	0.886	0.51	0.972	3.352	0.463	0.879	0.529	0.288	0.659	0.454
Tm	ppm	0.272	0.265	0.483	0.405	0.309	0.552	1.843	0.219	0.472	0.222	0.187	0.504	0.14
V	ppm	13.89	62.33	180.3	1783	56.64	40.46	88.81	53.83	21.24	12.37	8.253	< L.D.	5.638
Y	ppm	17.93	17.81	33.62	30.56	18.97	32.16	104.8	15.05	29.59	16.91	11.65	20.69	12.84
Yb	ppm	1.972	1.915	3.429	2.556	2.172	4.12	13.77	1.543	3.245	1.499	1.351	3.822	0.885
Zn	ppm	34.86	580.1	21.13	34.6	< L.D.	< L.D.	55.17	117.3	53.56	63.73	< L.D.	18.12	64.31

Forum Comment

doi: 10.1130/G38086C.1

Nb-Ta fractionation in peraluminous granites: A marker of the magmatic-hydrothermal transition

Aleksandr S. Stepanov[1], Sebastien Meffre[1], John Mavrogenes[2], and Jeff Steadman[1]
[1]ARC Centre of Excellence in Ore Deposits (CODES), School of Physical Sciences, University of Tasmania, Private Bag 79, Tas 7001, Australia
[2]Research School of Earth Sciences, Australian National University, Canberra, ACT 0200, Australia

On the basis of geochemical and mineralogical features, Ballouard et al. (2016) argue that magmatic fractionation alone cannot explain the formation of leucogranites with low Nb/Ta ratios. Instead, they propose that low ratios are better explained by post-magmatic interaction with F-bearing fluids. Although fluids may certainly play an important role in the formation of rare metal leucogranites, the model proposed by Ballouard et al. lacks key details. We contend that the principal features they attribute to magmatic-hydrothermal processes are better explained by the magmatic fractionation model.

Ballouard et al. propose greater mobilization of Nb than Ta during post-magmatic alteration. Although fluid removal of Nb may decrease Nb/Ta ratios, it does not explain the high Ta concentrations in leucogranites, which vary from crustal values (≈1 ppm) to >100 ppm in the most evolved leucogranites (Stepanov et al., 2014; Ballouard et al., 2016, their figure 1B). In fluid-driven models, Ta enrichment in leucogranites may either be attributed to removal of silicate component (the removal scenario) or to addition of Ta by the fluid (the addition scenario). The removal scenario requires the extraction of 90 wt% of the silicates from the rock mass for a tenfold enrichment in Ta, which is not feasible. The Ta addition scenario is equivalent to the formation of Ta mineralization by hydrothermal processes. However, Ta-rich granites have igneous contacts with their host rocks, and do not display textures typical for hydrothermal ores (e.g., London, 2008).

Stepanov et al. (2014) demonstrated that the fractionation of micas and ilmenite have an opposite effect on Nb/Ta ratios. Ballouard et al. take this argument too far by proposing that effect of mica fractionation can be counterbalanced by the fractionation of 0.5 wt% of ilmenite. However, peraluminous granites evolving to low Nb/Ta values commonly have Ti contents much lower than 0.26 wt% TiO_2, which is equivalent to 0.5 wt% of ilmenite (Stepanov et al., 2014; Ballouard et al., 2016). Moreover, biotite and muscovite are significant hosts of Ti, and their presence further reduces the amount of produced ilmenite. Therefore, peraluminous granites evolving to low Nb/Ta contain insufficient ilmenite to counteract the decrease in Nb/Ta due to fractionation of mica.

Leucogranites with low Nb/Ta also contain low concentrations of Fe, Mg, Zr, light rare earth elements (LREEs) and Ti (Stepanov et al., 2014). If this were due to post-magmatic alteration, as proposed by Ballouard et al., fluid removal of all these "immobile" elements and simultaneous enrichment in "mobile" elements (e.g., Sn, Li, Cs, and F) would be required. By contrast, the magmatic differentiation model explains decreasing concentrations of Fe, Mg, Zr, LREEs, and Ti through the fractionation of minor and accessory minerals present in granites (London, 2008; Stepanov et al., 2014), while enrichments of Sn Li, Cs, and F are attributed to incompatible behavior during crystallization.

The metallogenic arguments put forward by Ballouard et al. are also problematic. Whereas Li, Cs, Rb, and Be can be transported by fluids, the highest concentrations of these elements are found in magmatic intrusions of pegmatites and leucogranites, and are commonly associated with elevated Ta (London, 2008). On the other hand, granite-related hydrothermal Sn and W deposits are not known to be significant sources of Li, Cs, Rb, Be, and Ta. Ballouard et al. argue that negative correlations of Sn contents with Nb/Ta ratios in granites are "markers of magmatic–hydrothermal alteration." However, Lehmann (1990) demonstrated that magmatic fractionation of tin granites increases Sn content, while fluid loss and alteration decreases Sn concentrations in granites, contrary to the proposal by Ballouard et al.

Ballouard et al. further argue that the correlation of decreasing Nb/Ta with increasing alteration of micas supports Nb-Ta fractionation by hydrothermal fluids. However, magmatic fractionation increases the concentrations of water and F in the melt. Upon exsolution, these components impose increasing post-magmatic alteration of fractionated leucogranites. Therefore, both decreased Nb/Ta and post-magmatic alteration can be the result of magmatic evolution.

Tantalite overgrowths on columbite in ongonite grains (Dostal et al., 2015) are cited by Ballouard et al. as an example of Ta hydrothermal transport. This contradicts their own statement that Nb is more mobile than Ta in hydrothermal fluids. Zonation with an increasing Ta from core to the rim of tantalite-columbite grains is common in leucogranites and pegmatites, and this zonation is best explained by the lower solubility of columbite relative to tantalite in melts (Linnen, 1998).

Extreme granite fractionation is required to explain the genesis of rare metal pegmatites (London, 2008) and Sn granites (Lehmann, 1982). Occam's razor demands that the simplest explanation should be preferred. That magmatic processes explain most features of rare metal leucogranites and pegmatites suggests that hydrothermal processes may not be required to fractionate Nb from Ta, although there are still many unknowns regarding the origin of rare metal granites.

REFERENCES CITED

Ballouard, C., Poujol, M., Boulvais, P., Branquet, Y., Tartèse, R., and Vigneresse, J.-L., 2016, Nb-Ta fractionation in peraluminous granites: A marker of the magmatic-hydrothermal transition: Geology, v. 44, p. 231–234, doi:10.1130/G37475.1.

Dostal, J., Kontak, D.J., Gerel, O., Gregory Shellnutt, J., and Fayek, M., 2015, Cretaceous ongonites (topaz-bearing albite-rich microleucogranites) from Ongon Khairkhan, Central Mongolia: Products of extreme magmatic fractionation and pervasive metasomatic fluid: rock interaction: Lithos, v. 236–237, p. 173–189, doi:10.1016/j.lithos.2015.08.003.

Lehmann, B., 1990, Metallogeny of Tin: Lecture Notes in Earth Sciences: Berlin, Springer Verlag, 211 p.

Lehmann, B., 1982, Metallogeny of tin: Magmatic differentiation versus geochemical heritage: Economic Geology and the Bulletin of the Society of Economic Geologists, v. 77, p. 50–59, doi:10.2113/gsecongeo.77.1.50.

Linnen, R.L., 1998, The solubility of Nb-Ta-Zr-Hf-W in granitic melts with Li and Li + F: Constraints for mineralization in rare metal granites and pegmatites: Economic Geology, v. 93, p. 1013–1025, doi:10.2113/gsecongeo.93.7.1013.

London, D., 2008, Pegmatites: The Canadian Mineralogist, Special Publication 10, 347 p.

Stepanov, A., Mavrogenes, J.A., Meffre, S., and Davidson, P., 2014, The key role of mica during igneous concentration of tantalum: Contributions to Mineralogy and Petrology, v. 167, p. 1–8, doi:10.1007/s00410-014-1009-3.